

Universitat Politècnica de València  
Departamento de Máquinas y Motores  
Térmicos

---



STUDY OF THE POTENTIAL OF ELECTRIFIED  
POWERTRAINS WITH DUAL-FUEL COMBUSTION  
TO ACHIEVE THE 2025 EMISSIONS TARGETS IN  
HEAVY-DUTY APPLICATIONS

Doctoral Thesis

Presented by:

Santiago Daniel Martinez Boggio

Supervised by:

Dr. Javier Monsalve Serrano

València, September 2022





## Doctoral Thesis

# STUDY OF THE POTENTIAL OF ELECTRIFIED POWERTRAINS WITH DUAL-FUEL COMBUSTION TO ACHIEVE THE 2025 EMISSIONS TARGETS IN HEAVY-DUTY APPLICATIONS

Presented by: Santiago Daniel Martinez Boggio  
Supervised by: Dr. Javier Monsalve Serrano

### Examining Board:

President: Dr. Raúl Payri Marín  
Secretary: Dr. José Rodríguez Fernández  
Examiner: Dr. Felix Leach

### Reviewing Board:

Dr. Felix Leach  
Dr. Chiara Guido  
Dr. Juan José Hernández Adrover

València, September 2022



## **Abstract**

The transport of people, as well as cargo, has evolved and grown tremendously over the recent years. Technological development had to be adapted to the different government measures for controlling polluting emissions. Since the Paris agreement in 2015 limits have also been imposed on the CO<sub>2</sub> emissions from road vehicles to keep global temperature growth below 1.5°C. For the heavy transport sector, fleet limits of 15% for 2025 and 30% for 2030 CO<sub>2</sub> reduction have been introduced with respect to the limits of 2019. Therefore, the current restriction of very low levels of polluting emissions, as well as greenhouse gases, makes the transport sector face a great technological challenge. In 2021, 99% of freight transport was powered by an internal combustion engine with Diesel as fuel and without any type of electrical assistance in the propulsion system. Moreover, polluting emission limits such as the Euro 6 are achieved with complex post-treatment systems that also add to the consumption of Urea.

Previous research and prototype systems have shown that it is possible to achieve polluting emission targets with advanced combustion control methods, thus reducing the complexity of post-treatment in the exhaust gas. With greater success, the concept of Reactivity Controlled Combustion Ignition can reach values below the Euro 6 with similar efficiency to Diesel combustion. Unfortunately, it does not solve the CO<sub>2</sub> emission problems. On the other hand, in passenger vehicles, the application of electric motors in the propulsion system has been shown to successfully improve the overall efficiency of the vehicle. The extreme case is the purely electric vehicles, where efficiencies above 70% are achieved against 35% of the non-electrified vehicles. However, limitations of vehicle range, charging time, payload reduction and an unclear overall reduction in greenhouse emissions bring this propulsion system under discussion. For vehicles with some degree of electrification, polluting gas emissions continue to be a problem as for the non-electrified case.

Therefore, this doctoral Thesis addresses the problem of polluting emissions and CO<sub>2</sub> combined with advanced modes of combustion with electrified propulsion systems. The application of these technologies focuses on the heavy road transport sector. In particular, an 18-ton maximum load truck that originally was equipped with an 8-liter six-cylinder engine with conventional Diesel combustion. The present work uses experimental tools such as measurements on the engine bench as well as on the road to feed and validate numerical models of the engine, after-treatment system, and the vehicle. The latter is the central point of the work since it allows addressing systems such as mild hybrid, full hybrid, and plug-in hybrid. Experimental engine calibration dedicated to hybrid propulsion systems is presented with synthetic fuels in order to reach the limits of the Euro 7.

## Resumen

El transporte de personas, así como de carga ha evolucionado y crecido tremendamente en los últimos años. El desarrollo tecnológico debió ser adaptado a las diferentes medidas gubernamentales en términos de control de emisiones contaminantes. Desde el acuerdo de París en 2015 para mantener el crecimiento de la temperatura global por debajo de 1.5°C, se han impuesto también límites para las emisiones de CO<sub>2</sub> por parte de vehículos de carretera. Para el sector del transporte pesado, se han impuesto límites de flota de 15% para 2025 y 30% para 2030 de reducción del CO<sub>2</sub> con respecto a 2019. Por lo tanto, esta doble restricción de muy bajos niveles de emisiones contaminantes, así como de gases de efecto invernadero hacen que el sector del transporte este ante un gran desafío tecnológico. En 2022, el transporte de carga tiene un 99% de vehículos propulsados a motor de combustión interna con Diesel como combustible y sin ningún tipo de ayuda eléctrica en el sistema de propulsión. Los límites de emisiones contaminantes como Euro 6 son alcanzados con complejos sistemas de postratamiento que además agregan el consumo de Urea.

Trabajos previos en la bibliografía, así como sistemas prototipo han demostrado que es posible alcanzar los objetivos de emisiones contaminantes con métodos avanzados de control de la combustión y así disminuyendo la complejidad del post tratamiento en la salida de gases. Con mayor éxito, el concepto de Reactivity Controlled Combustion Ignition puede alcanzar valores por debajo de Euro 6 con eficiencia similar a la combustión de Diesel. Sin embargo, no soluciona los problemas de emisiones de CO<sub>2</sub>. Por otro lado, en vehículos de pasajeros fue demostrado con suceso la aplicación de motores eléctricos en el sistema de propulsión para mejorar la eficiencia global del vehículo. El caso extremo son los vehículos puramente electricos donde se alcanza eficiencias por arriba del 70% contra 35% de los vehículos no electrificados. Sin embargo, limitaciones de autonomía, tiempo de carga y la no clara reducción global de la contaminación debido a las emisiones de la energía de la red eléctrica y la contaminación de las baterías de ion-litio hacen que este sistema de propulsión este bajo discusión. Para los vehículos con

algún grado de electrificación, las emisiones de gases contaminantes siguen siendo un problema como para el caso no electrificado.

Por lo tanto, esta tesis doctoral aborda el problema de emisiones contaminantes, así como de CO<sub>2</sub> combinado modos avanzados de combustión con sistemas de propulsión electrificado. La aplicación de estas tecnologías se centra en el sector del transporte de carretera pesado. En particular, un camión de 18 toneladas de carga máxima que originalmente en 2022 equipa un motor seis cilindros de 8 litros con combustión convencional Diesel. El presente trabajo utiliza herramientas experimentales como son medidas en banco motor, así como en carretera para alimentar y validar modelos numéricos de motor, sistema de postratamiento, así como de vehículo. Este último es el punto central del trabajo ya que permite abordar sistemas como el mild hybrid, full hybrid y plug-in hybrid. Calibración de motor experimental dedicada a sistemas de propulsión híbrido es presentada con combustibles sintéticos y/o para llegar a los límites de Euro 7.

## Resum

El transport de persones, així com de càrrega ha evolucionat i crescut tremendament en els últims anys. El desenvolupament tecnològic degué ser adaptat a les diferents mesures governamentals en termes de control d'emissions contaminants. Des de l'acord de Paris en 2015 per a mantindre el creixement de la temperatura global per davall de 1.5°C, s'han imposat també límits per a les emissions de CO<sub>2</sub> per part de vehicles de carretera. Per al sector del transport pesat, s'han imposat límits de flota de 15% per a 2025 i 30% per a 2030 de reducció del CO<sub>2</sub> respecte a 2019. Per tant, aquesta doble restricció de molt baixos nivells d'emissions contaminants, així com de gasos d'efecte d'hivernacle fan que el sector del transport aquest davant un gran desafiament tecnològic. En 2022, el transport de càrrega té un 99% de vehicles propulsats a motor de combustió interna amb Dièsel com a combustible i sense cap mena d'ajuda elèctrica en el sistema de propulsió. Els límits d'emissions contaminants com a Euro 6 són aconseguits amb complexos sistemes de posttractament que a més agreguen el consum d'Urea.

Treballs previs en la bibliografia, així com sistemes prototip han demostrat que és possible aconseguir els objectius d'emissions contaminants amb mètodes avançats de control de la combustió i així disminuint la complexitat del post tractament en l'eixida de gasos. Amb major èxit, el concepte de Reactivity Controlled Combustion Ignition pot aconseguir valors per davall d'Euro 6 amb eficiència similar a la combustió de Dièsel. No obstant això, no soluciona els problemes d'emissions de CO<sub>2</sub>. D'altra banda, en vehicles de passatgers va ser demostrat amb succés l'aplicació de motors elèctrics en el sistema de propulsió per a millorar l'eficiència global del vehicle. El cas extrem són els vehicles purament electicos on s'aconsegueix eficiències per dalt del 70% contra 35% dels vehicles no electrificats. No obstant això, limitacions d'autonomia, temps de càrrega i la no clara reducció global de la contaminació a causa de les emissions de l'energia de la xarxa elèctrica i la contaminació de les bateries d'ió-liti fan que aquest sistema de propulsió aquest baix discussió. Per als vehicles amb algun grau d'electrificació, les

emissions de gasos contaminants continuen sent un problema com per al cas no electrificat.

Per tant, aquesta tesi doctoral aborda el problema d'emissions contaminants, així com de CO<sub>2</sub> combinat maneres avançades de combustió amb sistemes de propulsió electrificat. L'aplicació d'aquestes tecnologies se centra en el sector del transport de carretera pesat. En particular, un camió de 18 tones de càrrega màxima que originalment en 2022 equipa un motor sis cilindres de 8 litres amb combustió convencional Dièsel. El present treball utilitza eines experimentals com són mesures en banc motor, així com en carretera per a alimentar i validar models numèrics de motor, sistema de posttractament, així com de vehicle. Est ultime és el punt central del treball ja que permet abordar sistemes com el mild hybrid, full \*hybrid i plug-in hybrid. Calibratge de motor experimental dedicada a sistemes de propulsió hibride és presentada amb combustibles sintètics i/o per a arribar als límits d'Euro 7.



*Everything can be taken from a man but one thing:  
**the last of the human freedoms**  
to choose one's attitude in any given set of circumstances,  
to choose one's own way.*

*Viktor Frankl*



## Acknowledgments

This work was done with the aid and support of several people whom I would like to express my gratitude to.

First, I would like to thank the director board of CMT-Motores Térmicos for the opportunity of joining this outstanding research group and for providing me with the tools to perform my investigation over these years. I would like to be grateful particularly to Jesús Benajes for welcoming me into the combustion group and supporting me during this investigation.

Second, to my advisor Javier Monsalve Serrano and Electrified Powertrain leader Antonio García. I certainly learned numerous things during these years together. I would like to express my gratitude for the formal education, timeless discussions, and teachings in the engine area. Thank you for the professional and personal growth that you have provided me.

My acknowledgment also to my teammates Rafael Lago, David Villalta, Álvaro Fogué Robles, María Gabriela Guzmán, Diego Golke, and Rafael Soria. Thank you for the valuable scientific discussions and good times together working as well as enjoying the time.

I would also like to thank my friends in CMT department: Felipe Lewiski, Cassio Spohr, Jacson Beltrao, André Nakaema, Douglas Pinto, Augusto Perin, and Vitor Vielmo. All contributed for the development of the work and made life easy during this time with the talks and time spent together during this journey. Your help has been fundamental to this work.

I would also like to thank the technician department of CMT Gabriel Alcantarilla, Juan Antonio López, and Omar Huerta for all the time spent together in front of the engine and battery test cells solving numerous issues. Thank you for your talks and for easing the path.

My gratitude to Aramco Overseas and Volvo Group Trucks Technology for funding the work in this Thesis. Thanks to Patrick Gaillard and Oliver

Poussin for following closely the different projects that we have developed together during all these years. It was a pleasure to be part of this investigation together with you.

I would like to express my gratitude to the University of Bath for welcoming me into their laboratories and giving me all the support during the internship. Especially, I sincerely appreciate the advice of Dr. Richard Burke as well as the reception and talking from Dr. Tom Fletcher and Davide Di Blasio during my stay in Bath.

I also want to thank Dr. Pedro Curto for his unconditional support. From my beginnings in Mechanical Engineering and in its orientation in the research area. Always motivating and guiding me on this wonderful path that is the academy. Also, I want to thank Dr. Simona Merola and Dr. Adrian Irimescu for opening the doors of Europe to me. They train me in the academic field but also in the personal aspect. His words and advice were essential to get to this moment.

My last words in this section were saved for my family. During this academic journey, many were the times given up, but their support and unconditional love have kept me on the path. My eternal gratitude to my parents, Daniel and Lilian. I would like to thank my brothers, Guillermo and Guzman, for making life easier by connecting the worlds in our family and being so dedicated and worried with me during life. I would also like to thank my girlfriend Eglè for her enormous support during the Ph.D. Thank you for always bringing me back to the path.

This Doctoral Thesis has been partially supported by the Universitat Politècnica de València through the predoctoral contract of the author (Subprograma 2), which is included within the framework of Programa de Apoyo para la Investigación y Desarrollo (PAID).

# Table of Contents

<b>Chapter 1: Introduction .....</b>	<b>1</b>
1.1 Introduction.....	2
1.2 Energy and emissions impact of the transport sector .....	2
1.3 Future CO <sub>2</sub> European targets .....	14
1.4 Euro VI and VII pollutant emissions limits for the Heavy-Duty transport.....	19
1.4.1 ATS solution for Euro VII .....	20
1.4.2 Advanced combustion concepts for Euro VII .....	22
1.5 Summary .....	24
1.6 Document content and structure .....	25
 <b>Chapter 2: Electrified powertrains and advanced combustion modes for Heavy-Duty vehicles.....</b>	 <b>29</b>
2.1 Introduction.....	31
2.2 Overview of the Heavy-Duty sector .....	31
2.3 Current powertrain challenges .....	35
2.4 Advanced combustion modes for emission reduction.....	49
2.4.1 RCCI: Reactivity Controlled Compression Ignition .....	52
2.4.2 Alternative fuels for compression ignition engines.....	63
2.5 Powertrain electrification for CO <sub>2</sub> and battery reduction .....	69
2.5.1 Hybrid powertrain classification.....	72
2.5.2 Battery storage system .....	77
2.5.3 Electric machine and power electronics.....	82
2.5.4 Control strategies.....	88

2.5.5	Life Cycle Analysis in Transportation.....	92
2.5.6	Hybrids in the Heavy-Duty sector .....	99
2.6	Literature review conclusions.....	104
2.7	The objective of the study and proposed methodology.....	106

**Chapter 3: Tools and methodology .....109**

3.1	Introduction.....	110
3.2	Experimental facilities .....	110
3.3	Fuels properties and calibration maps.....	119
3.4	Numerical tools.....	127
3.4.1	Vehicle model .....	128
3.4.2	Internal combustion engine model.....	140
3.4.3	Aftertreatment system model.....	149
3.4.4	Electric motor model .....	153
3.4.5	Lithium-Ion battery model.....	159
3.4.6	Regenerative braking .....	174
3.4.7	Driving cycles .....	178
3.4.8	Energy management and optimization strategy .....	182
3.4.9	Life cycle analysis .....	184
3.5	Conclusions.....	189

**Chapter 4: Impact of mild hybridization on dual-fuel concept.....191**

4.1	Introduction.....	192
4.2	Engine model calibration with e-Components .....	193
4.2.1.	Single path configuration for EGR.....	194

4.2.2. e-EGR pump.....	199
4.2.3. e-Turbo.....	204
4.2.4. e-EGR pump and e-Turbo .....	209
4.3 e-DOC model calibration .....	216
4.4 e-Component CO <sub>2</sub> tailpipe emissions.....	226
4.5 Driving cycle assessment with DOC and e-DOC.....	236
4.6 Conclusions.....	242

**Chapter 5: Full hybridization dual-fuel concept for achieving 2025 emission targets .....245**

5.1 Introduction.....	246
5.2 Parallel (P2) hybrid optimization .....	247
5.2.1. Methodology .....	249
5.2.2. Results.....	257
5.3 Series hybrid optimization .....	262
5.3.1. Methodology .....	264
5.3.2. Results.....	272
5.4 Power split hybrid optimization.....	277
5.4.1. Methodology .....	279
5.4.2. Results.....	292
5.5 Comparison between architectures.....	297
5.6 DOC behavior in the full hybrid truck.....	305
5.7 Conclusions.....	311

**Chapter 6: Dual-fuel combustion concept for 2030 targets.....313**

6.1	Introduction.....	314
6.2	Synthetic fuels for WTW CO <sub>2</sub> reduction.....	314
6.2.1.	Synthetic high reactivity fuel.....	315
6.2.2.	Synthetic low reactivity fuel .....	329
6.3	Potential of dual-fuel combustion for EUVII.....	338
6.3.1.	Methodology .....	338
6.3.2.	Results.....	342
6.4	Plug-in Hybrid towards 2030 LCA CO <sub>2</sub> targets .....	347
6.4.1.	Methodology .....	348
6.4.2.	Results.....	355
6.5	Conclusions.....	369
<b>Chapter 7: Conclusions, outcomes, and suggestions for future work .....</b>		<b>371</b>
7.1	Introduction.....	372
7.2	Summary and conclusions.....	372
7.3	Contributions and publications .....	377
7.4	Suggestions for future work.....	380
7.4.1	Assessment of the particle composition in dual-mode dual fuel with conventional and synthetic fuels. ....	381
7.4.2	Impact of aggressive transient engine operation in Dual-Mode Dual-Fuel combustion.....	381
7.4.3	Implementation in a real truck demonstrator.....	382
7.5	Bibliography .....	383



# Index of Figures

<i>Figure 1-1. Global greenhouse gas emissions sector by sector in 2016 [5].</i>	3
<i>Figure 1-2. Mean tropospheric NO<sub>2</sub> concentration (μmol/m<sup>2</sup>) in 2019 (1<sup>st</sup> March–18<sup>th</sup> May) (a), and the percent deviation of NO<sub>2</sub> concentration in 2020 (b)[9].</i>	5
<i>Figure 1-3. Present average relative percentage deviation (RPD) of tropospheric NO<sub>2</sub> concentration during the effective lockdown period in 2020 (8<sup>th</sup> March–8<sup>th</sup> May) in Madrid, Milan, and Paris. Adapted from [9].</i>	5
<i>Figure 1-4. Heavy-Duty emission limits [14] (a) and evolution of the Euro emissions standard for NO<sub>x</sub> and PM [15] (b).</i>	7
<i>Figure 1-5. Worldwide emission legislation overview HD on-road CI engines in 2020.</i>	8
<i>Figure 1-6. Timeline of the HD emissions standards implementation in major vehicle markets [16].</i>	8
<i>Figure 1-7. Worldwide CO<sub>2</sub> emission regulations will be tightened for commercial vehicles: in US and CN are already effective, EU recently introduced standards for 2025 and 2030 [17].</i>	9
<i>Figure 1-8. Lithium-Ion battery prices from 2010 to 2020. Cost is in €/kWh of battery storage energy. Adapted from [20].</i>	11
<i>Figure 1-9. Total electricity generated by 2050 in the energy transitions commission indicative pathways. Adapted from [18].</i>	12
<i>Figure 1-10. Required growth of installed wind and solar capacity in GW [18].</i>	13

<i>Figure 1-11. Expected indicative final energy mix EJ/year in a zero-carbon economy. Adapted from [18].</i>	13
<i>Figure 1-12. Potential pathway to meet the 2025 CO<sub>2</sub> targets in HD vehicles [30].</i>	16
<i>Figure 1-13. Low Carbon Fuels production process for transport decarbonization.</i>	18
<i>Figure 1-14. Current Euro VI ATS and potential emissions control configuration for future Euro VII requirements. Adapted from [34].</i>	21
<i>Figure 1-15. Comparison of the incremental direct technology cost estimates obtained by NREL [35] and ICCT [36] for compliance with the California Heavy-Duty Omnibus Regulation.</i>	21
<i>Figure 1-16. NO<sub>x</sub> and soot formation zones as a function of the local equivalence ratio and local temperature with the operating zone illustration of conventional diesel combustion, RCCI, PCCI, and HCCI. Adapted from [38].</i>	23
<i>Figure 1-17. Graphical representation of the argument line followed in the investigation.</i>	28
<i>Figure 2-1. Average loads of road freight transport in 2019 and 2020. Adapted from [49].</i>	33
<i>Figure 2-2. Road transport performed by empty vehicles in 2019 and 2020 was calculated as a percentage share of total vehicle kilometres. Adapted from [49].</i>	33
<i>Figure 2-3. Road freight transport by maximum permissible laden weight of the vehicle in 2020. Adapted from [49].</i>	34
<i>Figure 2-4. Fuel types of new trucks for the European market share in 2019. Adapted from [50].</i>	36

*Figure 2-5. Engine operating map for the Ram pickup with the 6.7-liter diesel on the US06 cycle at zero (a) and 11 ton (b) payload. Source [52].. 37*

*Figure 2-6. Fuel consumption increased, and payload-specific fuel consumption decreased in percentage for three payload variations. Source [53]..... 38*

Figure 2-7. Conceptual description of DI diesel combustion during the mixing-controlled burn phase illustrates the different zones and processes in the diffusive combustion. Adapted from [55]. ..... 40

Figure 2-8. CI Diesel engine's new technology impacts peak brake thermal efficiency (BTE). Adapted from [30]. ..... 41

Figure 2-9. Example of an ATS for EU VI in Heavy-Duty: Volvo D13K EUVI. Adapted from [61]. ..... 43

*Figure 2-10. Weight breakdown of main truck components for diesel and battery-electric trucks with different battery sizes. Adapted from [64]. 46*

*Figure 2-11. The driving range of different BEVs is divided by type of vehicle and world region. Source [63]. ..... 47*

*Figure 2.12. Comparison of different advanced combustion modes. Adapted from [89]. ..... 52*

Figure 2-13. Optimized piston bowl templates to reduce the compression ratio while maximizing gross indicated efficiency. Adapted from [107]. ..... 56

*Figure 2-13. Conceptual description of the Dual-Mode Dual-Fuel combustion and the respective constraints that are generally used for each one of the operating zones. Source [107]. ..... 58*

Figure 2-14. Gross indicated efficiency percentage difference between compression ratio of 15.3:1 and CR 12.75:1. Source [107]. ..... 59

Figure 2-15. Maps of the DMDF concept in a Multi-Cylinder 8L engine in terms of a) Emission constraints, b) Brake Thermal Efficiency, c) Brake specific NO<sub>x</sub>, and d) Brake specific soot. Adapted from [108]..... 61

Figure 2-16. Tailpipe emissions (after DOC) of a) Unburned hydrocarbons and (b) Carbon monoxide. Source [108]..... 62

Figure 2-17. Dependence of (a) nitrogen oxides and (b) soot emissions concerning the different engine loads evaluated considering diesel, OME<sub>x</sub>, and e-FT as high reactivity fuels. Source [108]..... 68

Figure 2-18. Engine maps for (a) brake efficiency difference between OME<sub>x</sub>-gasoline and Diesel-Gasoline calibration and (b) Brake Specific NO<sub>x</sub> emissions. Source [108]. ..... 69

Figure 2-19. Examples of electrified HD trucks powertrain available in Europe. .... 71

Figure 2-20. Schematic representation of the different Parallel hybrid electric architectures: P0, P1, P2, and P3. .... 75

Figure 2-21. Schematic representation of Series hybrid electric architectures. .... 76

Figure 2-22. Schematic representation of Power-split e-CVT hybrid vehicle. .... 77

Figure 2.23. Battery characteristics depend on the technology used. Li-ion (Lithium-Ion), Na-S (Sodium Sulfur), Flow (Supercapacitors), Ni-Cd (Nickel Cadmium), and Lead Acid. Source [129]. ..... 78

Figure 2.24. Comparison of different Li-ion cell shapes used in electric vehicles..... 79

Figure 2.25. Li-ion cell technologies are based on active material chemistry. Adapted from [134]. ..... 81

*Figure 2-26. Typical EM curve with the main characteristic regions for Power and Torque against the rotational speed. Source [139].* ..... 84

*Figure 2-27. Shapes of Interior Permanent Magnet (IPM) rotors: (a) V shape, (b) double magnet shape, (c) delta shape with a bar magnet in a V shape, (d) improved shapes using a delta shape, and (e) improved shapes using a double V shape. Source [140].* ..... 85

*Figure 2-28. Torque (a) and efficiency (b) compare different IPM rotor design shapes. Source [140].* ..... 85

Figure 2.29. Comparison between (a) Induction Motor and (b) Permanent Magnet Synchronous Motor. Adapted from [141]. ..... 86

Figure 2.30. Typical electric power net of HEVs. HVB: high voltage battery; AUX: auxiliaries; HV DC: high voltage direct current; LV DC: low voltage direct current. .... 87

Figure 2.31. Structure of multilevel hierarchical control system for MHEV, FHEV, or PHEV. EMC: Energy management control, ECU: Engine control unit, EMU: Electric machine unit, BMS: Battery management system, and BCS: Brake control system. .... 89

Figure 2.32. Classification of supervisory energy management system strategies at state of the art. Source [145]. .... 91

Figure 2.34. Overview well-to-wheel and full life cycle. Adapted from [149]. .... 93

*Figure 2.33. Average engine efficiency over the test cycles for different hybrid architectures and hybridization levels. Source [181].* ..... 100

*Figure 2.34. Energy losses distribution for conventional and hybrid trucks operating over the FDHDT cycle. Source [179].* ..... 101

*Figure 2.35. Well to wheel GHG ( $CO_{2eq}$  g/tkm) emissions of all alternative drivetrains with low and high carbon energy fuel supply on short (a) and long (b) haul cycles. Source [182].* ..... 102

*Figure 2-36. Higher speed (80 km/h to 90 km/h), engine downsizing (466 kW to 410 kW) and partial load (100% to 75% payload) impact on fuel consumption decrease for a 60-ton long-haul truck. Source [53].* ..... 103

Figure 3-1. Maximum power (a) and torque (b) output curve for the same 8L engine considering different calibration setups [183]. ..... 111

Figure 3-2. Compressor (a) and turbine (b) map for the modeling of the turbocharger. .... 114

Figure 3-3. Exhaust gas recirculation system illustrates the differences in removing the moisture and particles from the exhaust gases. .... 115

Figure 3-4. Test cell facility scheme presenting the different subsystems and the measurement devices used to assess the DMDF concept on the multi-cylinder engine. .... 119

Figure 3-5. Calibration strategy with combustion types by power and rotational engine speed (a) and example of 5 CAD ATDC local equivalent ratio and local temperature distribution for the three phases (b). .... 122

Figure 3-6. Dual Fuel dual-mode brake specific consumption and emissions for Diesel-Gasoline (left) and OMEx-Gasoline (right). Adapted from [108]. .... 126

Figure 3-7. Dual Fuel dual-mode EU VI normative comparison for NOx and soot for Diesel-Gasoline (left) and OMEx-Gasoline (right). .... 127

Figure 3-8. Numerical model of the non-hybrid truck in GT-Suite. 131

Figure 3-9. Forces involved in the numerical simulation of the vehicle. .... 132

Figure 3-10. FL 18-ton CDC no-hybrid powertrain layout and sensor position for on-route fuel consumption measurements .....	134
Figure 3-11. Total and rate of fuel consumption against time for the Local Hilly driving cycle measured with the FL 18-ton CDC no-hybrid truck with 50% of payload.....	135
Figure 3-12. Testing methodology scheme (a), operational conditions marked in red over the calibration map for tank-to-wheel (tailpipe) CO <sub>2</sub> with RCCI diesel-gasoline (b), and Series hybrid optimum ICE load requirements at 0%, 50%, and 100% payload in the WHVC under diesel-gasoline RCCI Series hybrid. ....	137
Figure 3-13. Experimental ICE test bed versus simulated ICE 0D vehicle model results in instantaneous emissions. WHVC with 50% payload Series hybrid RCCI. ....	138
Figure 3-14. Experimental ICE test bed versus simulated ICE 0D vehicle model results in cumulative emissions. WHVC with 50% payload Series hybrid RCCI. ....	139
Figure 3-15. Engine calibration map with the 36 operative points and test matrix for e-components calibration. ....	141
Figure 3-16. 0D-engine model for the DMDF ICE configuration with LP and HP EGR lines.....	143
Figure 3-17. Combustion rate profiles were obtained experimentally with Diesel-Gasoline multi-cylinder engine for the GT-Power 1D model. Example for 25% load (a) and 50% load (b) for 950, 1500 and 2000 RPM. ....	144
Figure 3-18. Pressure-volume diagram including the experimental and simulation traces for 950 RPM of engine load for the DMDF LP+HP EGR configuration. ....	145

Figure 3-19. Pressure-volume diagram including the experimental and simulation traces for 950 RPM of engine load for the DMDF LP+HP EGR configuration. .... 146

Figure 3-20. Pressure-volume diagram including the experimental and simulation traces for 950 RPM of engine load for the DMDF LP+HP EGR configuration. .... 147

Figure 3-21. Experimental versus simulation results of the 0D-engine model for DMDF LP+HP EGR configuration in terms of IMEP (a) and BMEP (b). .... 148

*Figure 3-22. Experimental versus simulation results of the 0D-engine model for DMDF LP+HP EGR configuration in terms of turbine inlet (a) and outlet temperature (b), and turbine inlet pressure (c). .... 148*

Figure 3-23. Experimental versus simulated conversion efficiencies for (a) unburned hydrocarbon and (b) carbon monoxide, considering the calibration and validation operating points. .... 151

Figure 3-24. Engine speed and torque evaluate experimental and simulated conversion efficiency (a). Comparison between experimental and simulated conversion efficiency for unburned hydrocarbons (black) and carbon monoxide (blue) (b). .... 152

Figure 3-25. Inlet temperature and comparison between experimental and simulated temperature results at the DOC outlet. .... 153

Figure 3-26. Map characteristic zones and points for a PMSM in brake torque output and rotational speed. .... 154

Figure 3.27. Efficiency map of a PMSM electric machine for Heavy-Duty vehicles HTM-3500. Only the first and fourth quadrants are shown. Adapted from [198]. .... 157



Figure 3.28. Efficiency map of a PMSM electric machine for high-speed requirements. Only the first and fourth quadrants are shown. Adapted from [197] ..... 157

Figure 3.29. Effect of length-scaling on electric machine maximum torque characteristic. The plot shows three lengths, referred to as the baseline dashed blue line. Source [199]..... 158

Figure 3.30. Scheme representing a conceptual description of the different approaches used for battery modeling: resistance (a), resistance-capacitance (RC branches model) (b), and electrochemical (c)..... 159

*Figure 3.31. Steps in order to obtain the RC branches parameters from the electrochemical model..... 163*

*Figure 3.32. Cell validation for NMC (left) and LFP (right) for constant current discharge (top) and conduction cycle (bottom)..... 168*

*Figure 3.33. Equivalent circuit maps for OCV,  $R_o$ ,  $R_1$ , and  $C_1$  against battery state of charge (SOC) and surface temperature for LFP (left) and NMC (right)..... 170*

Figure 3.34. Cells arrangements in a battery pack (a) and electric circuit model with one cell (top-b) and all battery packs (bottom-b)..... 172

Figure 3.35. LFP and NMC selected cells to have power limitations in terms of maximum charge and discharge power. .... 173

*Figure 3.36. The ideal braking curve (a) and the comparison between the ideal curve and normative depend on the vehicle's deceleration (b)... 176*

*Figure 3.37. The split ratio between axles in order to perform the regenerative braking. .... 177*

*Figure 3.38. The Regenerative Brake System controller scheme with the split ratio and Battery and EM limits. .... 178*

<i>Figure 3.39. Homologation and real driving cycles with vehicle speed and altitude against time.....</i>	179
<i>Figure 3.40. Regenerative braking analysis for FL 18ton truck in WHVC and 100% of payload. Post-processing analysis with working points (a) and frequency map in the percentage of occurrence and the lines of power braking (b). .....</i>	181
<i>Figure 3.41. Frequency map in the percentage of occurrence and the lines of power braking for driving cycles Urban (a), Local (b), and Flat (c) with 100% payload. ....</i>	181
<i>Figure 3.42. Optimization strategy with test matrix with 12 simulated cases.....</i>	183
<i>Figure 3.43. The flow chart scheme of the methodology was used to optimize a Medium-Duty truck platform under reactivity-controlled compression ignition combustion mode. ....</i>	183
<i>Figure 3.44. Brake specific Well-to-Wheel CO<sub>2</sub> emissions for Diesel-Gasoline (a) and OME<sub>x</sub>-Gasoline (b) for the MD8 engine.....</i>	187
<i>Figure 3.45. Marginal emissions rate versus electricity generation for 2019 and 2030 in Spain. Adapted from [215].....</i>	188
<i>Figure 4-1. EGR percentage (a) and boost pressure (b) for Only HP EGR loop against the HP &amp; LP EGR loop experimentally characterized.</i>	196
<i>Figure 4-2. VGT rack position for Only HP EGR loop against the HP &amp; LP EGR loop experimentally characterized. ....</i>	197
<i>Figure 4-3. Brake-specific fuel consumption for successful cases with Only HP EGR loop against the HP &amp; LP EGR loop experimentally characterized.....</i>	198
<i>Figure 4-4. EGR pump example of EATON design.....</i>	199

<i>Figure 4-5. 0D-engine model for the DMDF with e-EGR pump in the HP EGR line. ....</i>	200
<i>Figure 4-6. EGR percentage (a) and boost pressure (c) for EGR pump case against the HP &amp; LP EGR loop experimentally characterized. ....</i>	202
<i>Figure 4-7. VGT rack position for EGR pump case against the HP &amp; LP EGR loop experimentally characterized. ....</i>	203
<i>Figure 4-8. Pump speed and power for EGR pump case. ....</i>	203
<i>Figure 4-9. Brake-specific fuel consumption for successful cases with EGR pump case against the HP &amp; LP EGR loop, experimentally characterized. ....</i>	204
<i>Figure 4-10. Electrified turbocharged example of Garret. ....</i>	205
<i>Figure 4-11. 0D-engine model for the DMDF with e-TC. ....</i>	206
<i>Figure 4-12. Air management parameters (a), e-motor of the turbocharging operation condition (b), and equivalent brake specific fuel consumption (c) for 950 RPM and 10% engine load. ....</i>	207
<i>Figure 4-13. Air management parameters (a), e-motor of the turbocharging operation condition (b), and equivalent brake-specific fuel consumption (c) for 1500 RPM and 50% engine load. ....</i>	207
<i>Figure 4-14. Air management parameters (a), e-motor of the turbocharging operation condition (b), and equivalent brake-specific fuel consumption (c) for 2000 RPM and 80% engine load. ....</i>	208
<i>Figure 4-15. Brake-specific fuel consumption for successful cases with e-Turbo pump case against the HP &amp; LP EGR loop experimentally characterized. ....</i>	209

*Figure 4-16. 0D-engine model for the DMDF with e-components (e-EGR pump in the HP EGR line and the e-TC).*..... 210

Figure 4-17. Power delivered/recovered by the e-TC (a), the power delivered/recovered by the e-EGR pump (b), and pumping mean effective pressure difference concerning the DMDF LP+HP EGR calibration (c) for different VGT rack positions at 1500 RPM. .... 211

Figure 4-18. Power delivered by the e-TC (a), turbine inlet pressure (b), and boost pressure (c) at 1500 RPM and 80% engine load for different VGT rack positions. .... 212

Figure 4-19. Total power (a) and equivalent brake-specific fuel consumption for different VGT rack positions at 1500 RPM and different engine loads. .... 213

Figure 4-20. Power calibration maps for the e-TC (a) and e-EGR pump (b) work together to achieve the same calibration targets as the DMDF LP+HP EGR calibration. .... 214

Figure 4-21. Rotational speed maps for the e-TC (a) and e-EGR pump (b) work together to achieve the same calibration targets as the DMDF LP+HP EGR calibration. .... 214

Figure 4-22. Calibration maps of the VGT rack position (a) and pumping mean effective pressure difference versus the DMDF LP+HP EGR calibration (b). .... 215

Figure 4-23. Brake-specific fuel consumption of the DMDF e-components calibration against DMDF HP+LP EGR (a) and CDC (b) calibration maps. .... 216

Figure 4-24. GT-Power model for the electrically heated oxidation catalyst assessment. .... 217

Figure 4-25. EHC post-heating scheme with the EHC signal in engine on-off signal and OC wall temperature..... 218

Figure 4-26. Heat addition effects at 1200 RPM and 6 bar BMEP on the HC tailpipe emissions normalized EUVI (a) and derivate HC tailpipe emissions normalized (b) with heat addition. .... 220

Figure 4-27. Light-off time map for three engine-out temperatures: steady state (a), steady-state minus 25°C, and (c) steady-state minus 50°C without EHC..... 221

Figure 4-28. Light-off time map for three engine-out temperatures: steady state (a), steady-state minus 25°C, and (c) steady-state minus 50°C with 5 kW in the EHC..... 221

Figure 4-29. OC wall temperature (a) and HC conversion efficiency (b) for steady-state temperature and the steady-state temperature minus 50°C with and without EHC at 1200 RPM and 6 bar BMEP..... 222

Figure 4-30. Diagram of the ICE starts (example of 4 starts) in the same steady-state point for the WHVC (1800 s). .... 223

Figure 4-31. HC (a), CO (b) emissions after the OC and OC wall temperature (c) against the number of ICE starts..... 224

*Figure 4-32. OC wall temperature distribution for the extreme ICE starts cases and the worst case in terms of HC emissions..... 225*

Figure 4-33. P0 performance curves for boost and EV mode at different transmission gear ratios. The Non-Hybrid is included for comparison. .... 227

Figure 4-34. 0D vehicle model for 48V mild hybrid P0 truck with the belt alternator starter (BAS), e-TC, and e-EGR pump. .... 228

Figure 4-35. P0 Hybrid scheme of Rule-Based Controller strategy. 230

Figure 4-36. Optimization of the P0 MHEV without e-components (a) and with components (b) in terms of CO <sub>2</sub> reduction versus CDC non-hybrid. ....	231
Figure 4-37. Relative sensitivity of the parameters optimized for the P0 MHEV DMDF truck. ....	231
Figure 4-38. Battery size effect on the CO <sub>2</sub> reduction versus CDC non-hybrid for P0 MHEV without e-components (a) and with components (b). ....	232
Figure 4-39. Engine speed (a) and engine torque (b) for the non-hybrid CDC and the P0 DMDF with e-components cases in homologation conditions. The WHVC driving cycle speed profile is added in the background for reference. ....	233
Figure 4-40. Belt assist starter power (a) and e-components voltage and power (b) for the P0 DMDF with the e-components case in homologation conditions. ....	234
Figure 4-41. Cumulative fuel consumption (a) and cumulative NO <sub>x</sub> engine-out emissions for the four cases studied in homologation conditions. The WHVC driving cycle speed profile is added in the background for reference. ....	235
Figure 4-42. Summary of the FL truck results in total fuel consumption difference against the non-hybrid CDC along with the WHVC, Urban, Local and Flat cycles at 0%, 50%, and 100% payloads. ....	236
Figure 4-43. Engine on-off (a) and HC emissions before/after the OC (b) for the WHVC with 50% payload in an RCCI P0 hybrid Truck without EHC. ....	238

Figure 4-44. OC wall temperature (a) and HC and CO normalized emissions with respect to EUVI (b) for the WHVC with 50% payload in an RCCI P0 hybrid truck without and with the EHC..... 238

Figure 4-45. HC tailpipe emissions (a), CO tailpipe emissions (b), and CO<sub>2</sub> tailpipe reduction compared with CDC non-hybrid for DMDF non-hybrid, P0 hybrid with/without EHC. .... 241

*Figure 4-46. EHC power sweep results in terms of absolute values (a) and relative values (b) for CO<sub>2</sub>, HC, and CO tailpipe emissions. .... 242*

Figure 5-1. P2 Hybrid architecture layout with main components in an FL-18-tons truck. The architecture (a) and component layout scheme in vehicle chassis (b). .... 248

Figure 5-2. P2 Hybrid performance graph with the two modes and compared against the non-hybrid configuration..... 251

Figure 5-3. P2 Hybrid scheme of the Rule-Based Controller strategy. .... 253

Figure 5-4. P2 Hybrid genetic algorithm cases evolution in terms of average fuel consumption and final battery state of charge (SOC<sub>end</sub>). ... 258

Figure 5-5. P2 Hybrid parameters sensitivity in terms of final average fuel consumption and final battery state of charge (SOC<sub>end</sub>). .... 259

Figure 5-6. P2 battery size and gear shift strategy influence in the final fuel consumption benefits against CDC non-hybrid..... 260

Figure 5-7. Internal combustion engine (a) and Electric Motor (b) operative conditions over the fuel consumption and efficiency map, respectively. .... 260

Figure 5-8. Battery and individual cell parameters during WHVC with 50% payload for Parallel Hybrid. .... 261

Figure 5-9. Series Hybrid architecture layout with main components in an FL-18-ton truck. The architecture (a) and component layout scheme in vehicle chassis (b). .....	264
Figure 5-10. Series Hybrid performance compared against the non-hybrid configuration. Gear iteration for high and low-speed ratio (a) and final selection (b). .....	267
Figure 5-11. Generator efficiency map (fraction) and ICE efficiency map (BTE%) with a gear ratio of 1.0.....	268
Figure 5-12. Series Hybrid scheme of the Rule Based Controller strategy.....	270
Figure 5-13. Series Hybrid genetic algorithm cases evolution in terms of average fuel consumption and final battery state of charge (SOC <sub>end</sub> )...	273
Figure 5-14. Series Hybrid parameters sensitivity in terms of final average fuel consumption and final battery state of charge (SOC <sub>end</sub> ).....	273
Figure 5-15. Series Hybrid battery size and gear shift strategy influence the final fuel consumption benefits against CDC non-hybrid.....	274
Figure 5-16. ICE RCCI operative conditions (a) and electric machines operation with Gen (b) and TM (c) for WHVC 50% payload in Series hybrid. ....	275
Figure 5-17. Battery and individual cell parameters during WHVC with 50% payload for Series hybrid. ....	276
Figure 5-18. Power Split Hybrid architecture layout with main components in an FL-18-ton truck. ....	279
Figure 5-19. Electrical continuously variable transmission (e-CVT) is also called epicyclical transmission for power-split hybrid architecture....	281



Figure 5-20. Schematic diagram showing the transmission of force in a planetary transmission. ....	282
Figure 5-21. Power Split Hybrid performance graph with the two modes and compared against the non-hybrid configuration.....	288
Figure 5-22. Power Split Hybrid genetic algorithm cases evolution in terms of average fuel consumption and final battery state of charge (SOC <sub>end</sub> ).....	293
Figure 5-23. Power Split Hybrid parameters sensitivity in terms of final average fuel consumption and final battery state of charge (SOC <sub>end</sub> ).....	293
Figure 5-24. Power Split Hybrid battery size and gear shift strategy influence the final fuel consumption benefits against CDC non-hybrid....	294
Figure 5-25. ICE RCCI operative conditions (a) and electric machines operation with Gen (b) and TM (c) for WHVC 50% payload in Series hybrid. ....	295
Figure 5-26. Battery and individual cell parameters during WHVC with 50% payload for Power Split hybrid.....	296
Figure 5-27. ICE operative conditions for WHVC and 100% payload in the four powertrains: non-hybrid DMDF (a), P2 (b), Series (c), and Power Split (d). ....	299
Figure 5-28. TTW CO <sub>2</sub> emissions benefits (a), engine-out NO <sub>x</sub> emissions (b), and engine-out soot emissions (c) for four driving cycles and three payload conditions. ....	301
Figure 5-29. Engine average efficiency (a), percentage of energy recovery during braking with respect to the total tractive energy (b), and electric losses (c) for four driving cycles and three payload conditions. ...	302

Figure 5-30. Gasoline fraction for four driving cycles and three payload conditions..... 303

Figure 5-31. Spider graph resume for the results average under 4 driving cycles and 3 payload conditions..... 304

Figure 5-32. Engine on-off (a) and HC emissions before/after the OC (b) for the WHVC with 50% payload in an RCCI P2 hybrid Truck without EHC..... 306

Figure 5-33. OC wall temperature (a) and HC and CO normalized emissions with respect to EUVI (b) for the WHVC with 50% payload in an RCCI P2 hybrid truck without and with the EHC..... 307

Figure 5-34. HC tailpipe emissions (after the OC) against the ICE start times and ICE minimum time control for the new calibration without EHC (a) and with EHC 5 kW (b)..... 309

Figure 5-35. Fuel consumption against the ICE start times and ICE minimum time control for the new calibration without EHC (a) and with EHC 5 kW (b). ..... 310

Figure 6-1. Volvo FL Power Splitt FHEV truck fueled with OMEx as High Reactivity fuel. Similar scheme can be repeated for P2 and Series hybrid. .... 315

Figure 6-2. Driving cycles results (TTW CO<sub>2</sub>, GF and Fuel volume consumption) for P2 operating with RCCI OMEx-Gasoline. The results are compared against CDC non-hybrid (baseline). In addition, the DMDF Diesel-Gasoline non-hybrid and RCCI Diesel-Gasoline P2 are added for comparison (results chapter 5)..... 318

Figure 6-3. Driving cycles results (TTW CO<sub>2</sub>, GF and Fuel volume consumption) for Series operating with RCCI OMEx-Gasoline. The results are compared against CDC non-hybrid (baseline). In addition, the DMDF

Diesel-Gasoline non-hybrid and RCCI Diesel-Gasoline Series are added for comparison (results chapter 5). ..... 321

Figure 6-4. Driving cycles results (TTW CO<sub>2</sub>, GF and Fuel volume consumption) for Power Split operating with RCCI OME<sub>x</sub>-Gasoline. The results are compared against CDC non-hybrid (baseline). In addition, the DMDF Diesel-Gasoline non-hybrid and RCCI Diesel-Gasoline Power Split are added for comparison (results chapter 5)..... 323

Figure 6-5. Operational conditions for P2, Series, and Power Split over the calibration maps of TTW (a), GF (b), and WTW CO<sub>2</sub> emissions with OME<sub>x</sub>-Gasoline..... 325

Figure 6-6. Driving cycles results in terms of WTW CO<sub>2</sub> emissions for P2, Series and Power Split operating with RCCI OME<sub>x</sub>-Gasoline. The results are compared against CDC non-hybrid (baseline). In addition, the DMDF Diesel-Gasoline non-hybrid and RCCI Diesel-Gasoline Power Split are added for comparison..... 328

Figure 6-7. Driving cycle results (engine-out NO<sub>x</sub> and soot) for P2 operating with RCCI OME<sub>x</sub>-Gasoline. The results are compared against CDC non-hybrid (baseline). In addition, the DMDF Diesel-Gasoline non-hybrid and RCCI Diesel-Gasoline P2 are added for comparison (results chapter 5)..... 329

Figure 6-8. Volvo FL Series FHEV truck fueled with Methanol as Low Reactivity fuel..... 330

Figure 6-9. Diesel-Methanol calibration for Series hybrid operation at 1800 RPM and 0-100% engine load. Diesel-Gasoline calibration is added as reference..... 332

Figure 6-10. Diesel-Methanol optimization for a Series Hybrid operation in the WHVC and 50% payload..... 333

Figure 6-11. Diesel-Methanol operative condition in the ICE brake specific fuel consumption map (a) and traction motor efficiency map (b).334

Figure 6-12. Diesel-Methanol ICE power output (a) and battery SOC (b) along WHVC for 0%,50% and 100% payload. .... 335

Figure 6-13. Diesel-Methanol Series hybrid TTW CO<sub>2</sub> versus CDC non-hybrid. Previous results of D-G and OMEx-G in non-hybrid and Series hybrid is added for comparison..... 336

Figure 6-14. Diesel-Methanol Series hybrid WTW CO<sub>2</sub> versus CDC non-hybrid. Previous results of D-G and OMEx-G in non-hybrid and Series hybrid is added for comparison. .... 337

Figure 6-15. Brake-specific fuel consumption map of D-G EU VI calibration and the selected points for the EUVII new re-calibration. .... 339

Figure 6-16. ICE operative condition setting in terms of EGR and outputs as brake-specific fuel consumption, NO<sub>x</sub>, and soot emissions for the new ICE re-calibration towards EUVII for Diesel-Gasoline (left) and OMEx-Gasoline (right)..... 341

Figure 6-17. ICE brake specific HC and CO emissions for the new ICE re-calibration towards EUVII for Diesel-Gasoline (left) and OMEx-Gasoline (right). .... 342

Figure 6-18. TTW and WTW CO<sub>2</sub> emission difference between the Series hybrid with different engine calibration and CDC non-hybrid at twelve driving scenarios..... 344

Figure 6-19. Brake specific NO<sub>x</sub> and soot emissions at engine-out for the Series hybrid at twelve driving scenarios. .... 346

Figure 6-20. Series PHEV truck concept with RCCI dual-fuel engine and external charging ..... 348

Figure 6-21. Cycle test for PHEV. The phase pure electric mode, charge depleting, and charge sustaining are marked as a function of the battery state of charge (SOC). .....	350
Figure 6-22. Utility factor used for PHEV Light-Duty vehicles (UF) and the scale version by two (UF*) and by three (UF**). .....	352
Figure 6-23. Pure electric truck GT-Suite model for model a complementary baseline case among the CDC non-hybrid. ....	353
Figure 6-24. Energy consumption, vehicle range, battery mass, and cargo mass reduction percentage due to the weight of the battery for WHVC 50% load with a BEV truck with two types of cells. ....	354
Figure 6-25. Distance traveled (a) and energy consumption (b) in charge depleting and charge sustaining mode for the PHEV series truck in several WHVC with 50% payload. ....	356
Figure 6-26. Brake specific NOx (a) soot (b) in charge depleting and charge sustaining mode for the PHEV series truck in several WHVC with 50% payload.....	357
Figure 6-27. Energy consumption is divided by type of energy in charge depleting and charge sustaining mode for the PHEV series truck in several WHVC with 50% payload.....	358
Figure 6-28. Well-to-Wheel CO <sub>2</sub> emissions divided by type of energy in charge depleting and charge sustaining mode for the PHEV series truck in several WHVC with 50% payload. ....	359
Figure 6-29. Combined CD and CS Tank-to-Wheel CO <sub>2</sub> absolute values (a) and relative with respect to CDC non-hybrid (b) for the PHEV series truck in several WHVC with 50% payload under several UF. ....	360

Figure 6-30. Well-to-Wheel CO<sub>2</sub> emissions with respect to CDC non-hybrid for the PHEV series truck in several WHVC with 50% payload under several UF..... 361

Figure 6-31. Life Cycle Analysis CO<sub>2</sub> emissions with respect to CDC non-hybrid for the PHEV, FHEV, and EV trucks under WHVC with 50% payload. .... 362

Figure 6-32. Life Cycle Analysis CO<sub>2</sub> emissions for different technologies applied in a Medium-Duty truck at 50% payload and under WHVC..... 365

Figure 6-33. Life Cycle Analysis CO<sub>2</sub> emissions percentage difference against CDC non-hybrid for different technologies applied in a Medium-Duty truck at 50% payload and under WHVC..... 366

Figure 6-34. Upstream electricity scenarios. Adapted from [227]. ... 367

Figure 6-35. e-fuel cost analysis compared with conventional fuels. Adapted from [228]. .... 369

# Index of Tables

Table 2-1. Drivetrain efficiency of current powertrains in the market. Adapted from.....	45
Table 2-2. Characteristics of the original piston bowl template as well as the two optimized bowls for CR 15:3 and 12.75.....	57
<i>Table 2-2. Physical and chemical properties of OME<sub>x</sub> with n=1–6. Adapted from [112].</i> .....	64
Table 2-3. Main characteristics of Heavy-Duty Vehicles in the USA available in 2020. Adapted from [123]. .....	72
Table 2-5. CO <sub>2</sub> associated to the fuel production in the literature....	96
Table 2-6. CO <sub>2</sub> associated to the battery production in the literature. ....	97
Table 3-1. Main characteristics of the modified engine D8k 350.....	112
Table 3-2. Fuel injection system characteristics for both direct injection and port fuel injection subsystems.....	113
Table 3-3. Diesel oxidation catalyst characteristics of the stock after-treatment system. ....	115
Table 3-4. Horiba MEXA 7100 D-EGR components, measurement principles range and associated uncertainty.....	116
Table 3-5. Physical-chemical properties of the high reactivity fuels evaluated during the investigation. ....	120
Table 3-6. Aerodynamic and geometric characteristics of the VOLVO FL 280 truck. Source [190]. .....	129

<i>Table 3-7. Comparison of experimental ICE test bed versus simulated ICE 0D vehicle model results in cumulative fuel consumption and emissions in grams and percentage differences. Case WHVC with 0%, 50%, and 100% payload Series hybrid RCCI.</i> .....	140
Table 3-8. Operating points for the OC model calibration and validation.....	150
Table 3-9. Electric motor main characteristics. Source [196] and [197]. .....	156
<i>Table 3-10. Electrochemical lithium-Ion cell equations in GT-Autolion.</i> .....	162
<i>Table 3-11. Li-Ion battery cell main specifications. Source [206] and [207].</i> .....	165
Table 3-12. Li-Ion battery cell electrochemical model optimum parameters. ....	167
<i>Table 3-13. Driving cycle main characteristics.</i> .....	179
<i>Table 3-14. CO<sub>2</sub> impact by fuel production, component production, maintenance and disposal of the vehicle components.</i> .....	185
Table 4-1. GA optimization parameters for P0 MHEV. ....	229
Table 5-1. Conditions for each operative mode of the RBC supervisory controller in P2 FHEV. ....	254
Table 5-2. GA optimization parameters for P2 FHEV. ....	257
Table 5-3. Optimum parameters of the GA for P2 FHEV.....	262
Table 5-4. Conditions for each operative mode of the RBC supervisory controller in Series FHEV. ....	271



Table 5-5. GA optimization parameters for Series Hybrid.....	272
Table 5-6. GA optimum parameters for Series Hybrid. ....	277
<i>Table 5.7. RBC strategy for the power-split HEV. Main states of operation.....</i>	<i>290</i>
Table 5.8. RBC strategy for the power-split HEV Rules for the transitions between the states. ....	291
Table 5-9. GA optimization parameters for Power Split Hybrid.....	292
Table 5-10. GA optimum parameters for Power Split Hybrid. ....	297
Table 5-11. Optimum powertrain set-up for FHEV P2, series, and power split. ....	298
Table 5-12 Summary results in homologation conditions (WHVC and 50% payload) including WTW CO <sub>2</sub> analysis. ....	305
Table 5-13. Summary of the main parameters for the RCCI P2 hybrid truck without and with the EHC in the WHVC with different payloads. ....	308
Table 5-14. Summary of the main parameters for the RCCI P2 hybrid Truck without and with EHC in the WHVC with different payloads with a new dedicated OC calibration. ....	311



# Nomenclature

## *Latin*

A/F - Air Fuel Ratio

C - Carbon

$C_p$  - Specific heat capacity at constant pressure

CO - Carbon Monoxide

CO<sub>2</sub> - Carbon Dioxide

C<sub>3</sub>H<sub>6</sub> - Propylene

C<sub>2</sub>H<sub>4</sub> - Ethylene

C<sub>2</sub>H<sub>6</sub> - Ethane

1,3-C<sub>4</sub>H<sub>6</sub> - 1,3-Butadiene

C<sub>6</sub>H<sub>6</sub> - Benzene

C<sub>7</sub>H<sub>8</sub> - Toluene

C<sub>7</sub>H<sub>16</sub> - Heptane

C<sub>8</sub>H<sub>18</sub> - Octane

m - Mass

$\dot{m}$  - Mass flow

h - Hours

$\bar{h}$  - Enthalpy

H - Unimolecular Hydrogen

HC - Hydrocarbon

H<sub>2</sub>O - Water

N<sub>2</sub> - Nitrogen

NO - Nitrogen monoxide

NO<sub>2</sub> - Nitrogen dioxide

NO<sub>x</sub> - Nitrogen oxides (NO and NO<sub>2</sub>)

O<sub>2</sub> - Oxygen

OMEx - Oxymethylene dimethyl ether

OH - Hydroxyl radical

p - Pressure

Q<sub>w</sub> - Heat transfer to the walls

t - Time

T - Temperature

u - Internal energy

V - Volume

X - Molar fraction

Y - Mass Fraction

Z - Zeolite

### *Greek*

$\gamma$  - Specific heat ratios ( $C_p/C_v$ )

$\Delta$  - Variation

$\eta$  - Efficiency

$\mu$  - Micro

$\rho$  - Density

$\phi$  - Equivalence Ratio

### *Superscripts*

o - Standard conditions

### *Subscripts*

a - relative to air

b - relative to brake power

bb - Relative to blow-by

cyl - Relative to in-cylinder conditions

exh - relative to exhaust conditions

evap - Relative to evaporation conditions

f - relative to fuel

g - grams

i - relative to indicated power

in - relative to intake conditions

inj - relative to injection

out - relative to outlet conditions

O<sub>2</sub> - relative to oxygen

### *Initials and Acronyms*

ASC - Ammonia Slip Catalyst

ATS - Aftertreatment System

BMEP - Brake Mean Effective Pressure

BSFC - Brake Specific Fuel Consumption

CA50 - Crank Angle at 50% mass fraction burned

CAD - Crank angle degree

CFD - Computational Fluid Dynamics

CI - Compression Ignition

CDC - Conventional Diesel Combustion

COV - Covariance

CR - Compression Ratio

D - Diesel

DAC - Direct Air Capture

CFR - Cooperative Fuel Research

CN - Cetane Number

EHC - Electrical heater catalyst

DF- Diesel Fuel

DI - Direct-Injection

DMDF- Dual-Mode Dual-Fuel

DOC - Diesel Oxidation Catalyst

DPF - Diesel Particulate Filter

Ea - Energy of activation

ECU - Electronic Control Unity

EGR - Exhaust Gases Recirculation

ES - Engine Speed

EU - European

FCEC - Fuel Consumption Equivalent Cycle

FID - Flame Ionization Detector

FIS - Fuel Injection System

FSN - Filter Smoke Number

FTIR - Fourier Transformed Infrared Spectroscopy

G - Gasoline

GIE - Gross Indicated Efficiency

GF - Gasoline Fraction

GHG - Greenhouse gases

HCCI - Homogeneous Charge Compression Ignition

HP - High Pressure

HRF - High Reactivity Fuel

HRR - Heat Release Rate

HTHR - High Temperature Heat Release

ICE - Internal Combustion Engines

IMEP - Indicated Mean Effective Pressure

ISC - In-Service Conformity

ISFC - Indicated Specific Fuel Consumption

J - Joule

Kde - Kernel Density Estimation

K - Kelvin

L - Liters

LCA - Life Cycle Analysis

LRF - Low Reactivity Fuel



LHV - Lower Heating Value

LP - Low Pressure

LTC - Low Temperature Combustion

LTHR - Low Temperature Heat Release

MFB - Mass Fraction Burned

MCE - Multi-Cylinder Engine

MON - Motor Octane Number

NDA - Non – Disclosure Agreement

NTC - Negative Temperature Coefficient

NVH - Noise Vibration and Harshness

OEM - Original Equipment Manufacturers

PEF - Pre-Exponential factor

PER – Premix energy ratio

PFI - Port Fuel Injection

PLIF - Planar Laser Induced Fluorescence

PM - Particulate matter

PMEP - Pumping Mean Effective Pressure

PN - Particulate number

PPC - Partially Premixed Combustion

PCCI - Partially Premixed Compression Ignition

PRR - Pressure Rise Rate

PRR - Primary Reference Fuel

PT - Pressure Temperature

RCCI - Reactivity Controlled Compression Ignition

RWGS - Reverse Water-Gas Shift

RON - Research Octane Number

S - Sensitivity

SCE - Single Cylinder Engine

SCR - Selective Reduction Catalysts

SET - Supplementary Engine Test

SI - Spark Ignition

SoI - Start of Injection

PDF - Probability Density Function

TCO - Total Cost of Ownership

TDC - Top Dead Center

ToI - Time of Injection

TRF- Toluene Reference Fuel

VGT - Variable Geometry Turbine

TRL - Technology readiness levels

TTW - Tank - to - Wheel

WHSC - World Harmonized Stationary Cycle

WHTC - World Harmonized Transient Cycle

WHVC - World Harmonized Vehicle Cycle

WTW - Well-To-Wheel



# Chapter 1

## Introduction

### **Content**

---

1.1 Introduction.....	2
1.2 Energy and emissions impact of the transport sector .....	2
1.3 Future CO <sub>2</sub> European targets .....	14
1.4 Euro VI and VII pollutant emissions limits for the Heavy-Duty transport.....	19
1.4.1 ATS solution for Euro VII.....	20
1.4.2 Advanced combustion concepts for Euro VII.....	22
1.5 Summary .....	24
1.6 Document content and structure .....	25

## 1.1 Introduction

This Thesis provides an overview of the different low carbon footprint technologies for delivery trucks as near-term solution in the way of decarbonizing the road transport sector. This first chapter establishes the bases around which the investigation is focused. The second subsection gives a quick summary of the global energy mix and the associated CO<sub>2</sub> emissions to the transport sector, one of the main responsible for the global energy consumption. Later, the trends of the past and future emissions regulations for the transport sector are analyzed in detail. Moreover, the two most expected emissions scenarios for the upcoming years set by the European Commission (EC), 2025 and 2030, and the expected evolution of the technology to fulfill them are discussed. Finally, the organization of the Thesis is presented, describing the contents of each chapter and the interaction between them.

## 1.2 Energy and emissions impact of the transport sector

The world is facing a challenging situation where it is mandatory to reduce greenhouse gases (GHG) and pollutant emissions. The main concerns are the continuous rise of the world average temperature as well as the continuous worsening of the air quality in urban regions in spite of the measurements implemented in various sectors, such as road transport [1–4].

*Figure 1-1* shows the equivalent carbon dioxide (CO<sub>2eq</sub>) emitted in 2016 (the last global report available) by sectors [5]. CO<sub>2eq</sub> is understood as a measure of how much a pollutant contributes to global warming relative to carbon dioxide. The estimated global GHG emissions are 49.4 billion tons of CO<sub>2eq</sub>, 73.2% of which corresponds to energy usage, 18.4% to agriculture and forest, and the rest is distributed between industry and waste. Inside the energy sector, transport accounts for 22.1% (16.2% of the total) and road

transport for about 16.25%. This means that the transport sector is responsible for about 12% of the global GHG emissions (5.9 billion tons of CO<sub>2eq</sub> per year).

According to the international energy agency (IEA), the GHG emissions from the transport sector have not decreased in the last years [6]. To address this issue, the European Commission recently announced stringent policies for shifting to low-emission mobility, with the main goal of reaching a net-zero scenario for 2050 [7]. The global strategy integrates a large set of measures to support Europe's transition to a low-carbon economy. In their communication, it is possible to identify two priority areas for action:

- Increasing the efficiency of the transport system, removing obstacles to the electrification of transport.
- Speeding up the deployment of low-emission alternative energy for transport, namely: advanced biofuels, electricity, hydrogen, and renewable synthetic fuels.

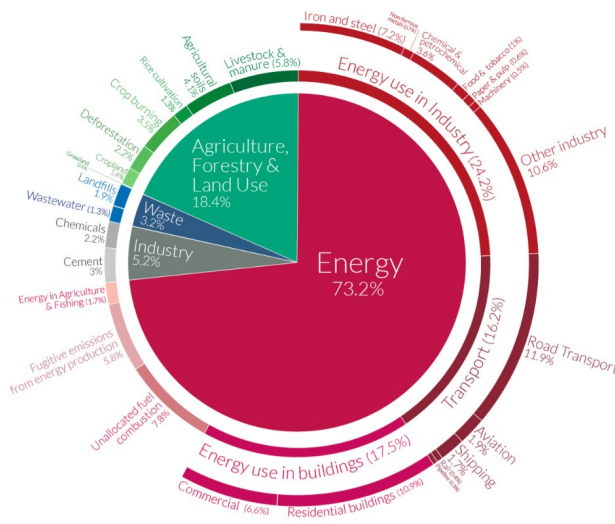


Figure 1-1. Global greenhouse gas emissions sector by sector in 2016 [5].

While CO<sub>2</sub> emissions are one of the main focuses of the latest scientific research and political efforts, it is not a unique concern of the transport sector. The local air pollution is also a crucial aspect of improving the health quality in the cities, so other pollutants must also be considered. In particular, NO<sub>x</sub> and particle matter (PM) has been proven to cause different problems to human health [8]. Figure 1-2 shows the results reported by Bar et al. [9] about the NO<sub>2</sub> concentration during the 2020 lockdown due to the COVID pandemic. The results show that the mean NO<sub>2</sub> concentration over the northern hemisphere was  $64 \mu\text{mol}/\text{m}^2$  in 2019 (*Figure 1-2a*), while it dropped to  $52 \mu\text{mol}/\text{m}^2$  in 2020 (decreased by 19%). Despite some industries stopped during this period, the greatest change was the strong reduction of the people mobility. This evidence that NO<sub>2</sub> emissions in cities are mostly coming from road transport. In cities like Madrid, Milan, and Paris, the variation between the same months in 2019 and 2020 was over 25% on average (see *Figure 1-3*). Similar results are shown for PM of size below  $2.5 \mu\text{m}$ . Despite the fact that studies have shown significant reductions in NO<sub>2</sub> and PM during COVID lockout, Singh et al. [10] emphasize the crucial necessity of separating emissions changes from climatic variables in order to prevent overestimating the effects of lock-down. According to their investigation in Oxford, UK, the observed NO<sub>2</sub> reductions of 38% at roadside and 17% at urban backdrop locations actually represent decreases in emissions of 22% and 2%, respectively. They emphasize that reducing traffic in the city center by 70% would have some positive effects on public health. PM concentrations would not decrease, nevertheless, and more effective emissions control methods might be more focused.



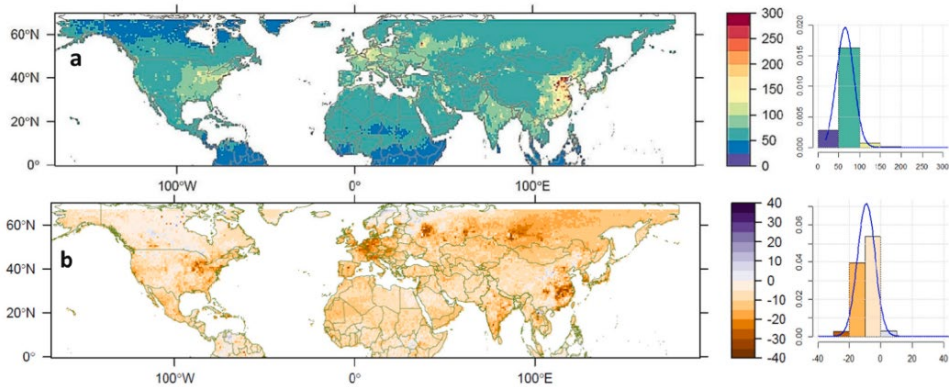


Figure 1-2. Mean tropospheric  $\text{NO}_2$  concentration ( $\mu\text{mol}/\text{m}^2$ ) in 2019 (1<sup>st</sup> March–18<sup>th</sup> May) (a), and the percent deviation of  $\text{NO}_2$  concentration in 2020 (b)[9].

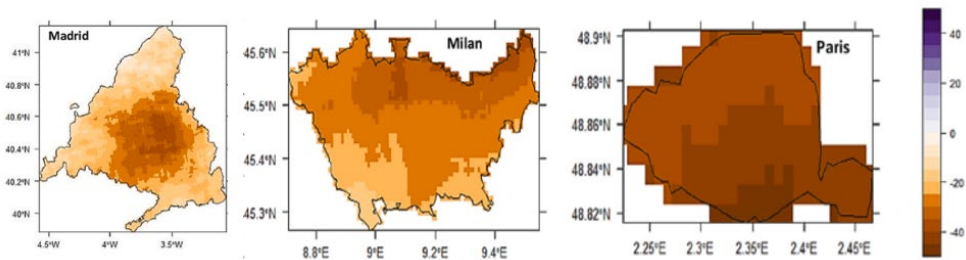



Figure 1-3. Present average relative percentage deviation (RPD) of tropospheric  $\text{NO}_2$  concentration during the effective lockdown period in 2020 (8<sup>th</sup> March–8<sup>th</sup> May) in Madrid, Milan, and Paris. Adapted from [9].

In the EU, Heavy-Duty (HD) vehicles account for over 40% of the  $\text{NO}_x$  emissions from road transport [11], while they only represent 2.4% of the total vehicle fleet [12]. To mitigate the pollutants at the tailpipe level, the EC established the Euro regulation for engines, which sets the emissions limits for transient and stationary conditions depending on the type of application. It is important to note that European emission standards for new heavy-duty diesel engines are commonly referred to as Euro I to Euro VII (Roman numerals). Arabic numerals (Euro 1 to Euro 7) are reserved for

light-duty vehicle standards. In addition, the light duty emissions are defined base on distance specific values (g/km, #/km) making them intrinsic to the complete vehicle platform. On the other hand, heavy-duty standard was defined considering only the engine system. Therefore, the emissions values are expressed in power specific values (g/kWh, #/kWh).

Figure 1-4 shows the NO<sub>x</sub> and PM limits for the different Euro regulation stages for HD vehicles. Comparing the limits imposed by the current emissions regulation, EU VI, to those proposed by the EUI (1992), it can be seen that the levels of NO<sub>x</sub> and PM are 20 and 61 times lower, respectively, than 21 years before [13].

			EU-I 1992	EU-II 1996	EU-III 2000	EU-IV 2005	EU-V 2008	EU-VI 2013
 Test cycles EU-I+II 13-Mode EU-III+IV ESC EU-VI WHSC	CO	g/kW-h	4,50	4,00	2,10	1,50	1,50	1,50
	THC	g/kW-h	1,10	1,10	0,66	0,46	0,46	0,13
	NMHC	g/kW-h						
	CH4	g/kW-h						
	NOx	g/kW-h	8,00	7,00	5,00	3,50	2,00	0,40
	PM	g/kW-h	3,60	0,15	0,10	0,02	0,02	0,01
	NH3	ppm				25	25	10
	PN	#/kWh						8 E11
	CO2, FC	g/kW-h						no
	NO2	g/kW-h						
Test cycles EU-III+IV ETC EU-VI WHTC	CO	g/kW-h			5,40	4,00	4,00	4,00
	THC	g/kW-h						0,16
	NMHC	g/kW-h			0,78	0,55	0,55	
	CH4	g/kW-h			1,60	1,10	1,10	
	NOx	g/kW-h			5,00	3,50	2,00	0,46
	PM	g/kW-h			0,16	0,03	0,03	0,01
	NH3	ppm				25	25	10
	PN	#/kWh						6 E11
	CO2, FC	g/kW-h						no
	NO2	g/kW-h						

(a)

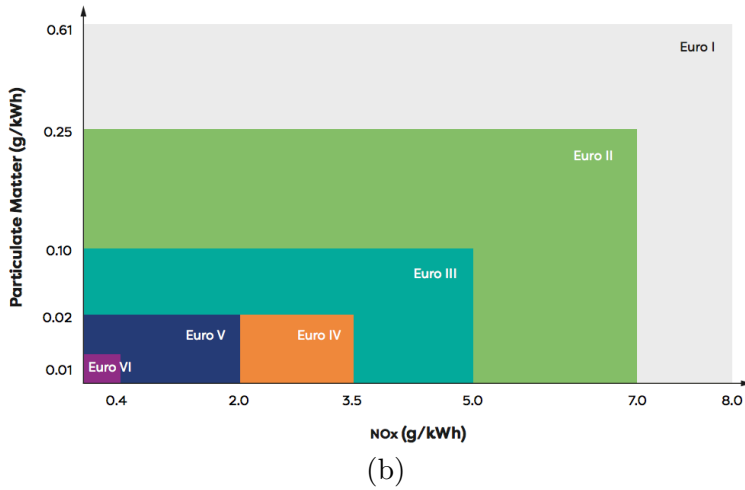


Figure 1-4. Heavy-Duty emission limits [14] (a) and evolution of the Euro emissions standard for NO<sub>x</sub> and PM [15] (b).

In other countries, the road map to reduce the emissions from the transport sector is similar to that in Europe. However, there is a large number of countries (mainly developing countries) that are far from achieving the targets set in Europe or the USA. *Figure 1-5* shows that countries such as Brazil, Mexico, and India still have legislations equivalent to EU V (two times higher in PM and five times higher in NO<sub>x</sub> than EUVI). *Figure 1-6* shows that the behavior will not change for most countries soon. Other countries do not even have emission legislation, such as the African continent or some Latin American countries. This slows down the process of achieving a global reduction of pollutant emissions and also impedes the companies from developing engines and powertrains that can be easily adapted to the different scenarios.

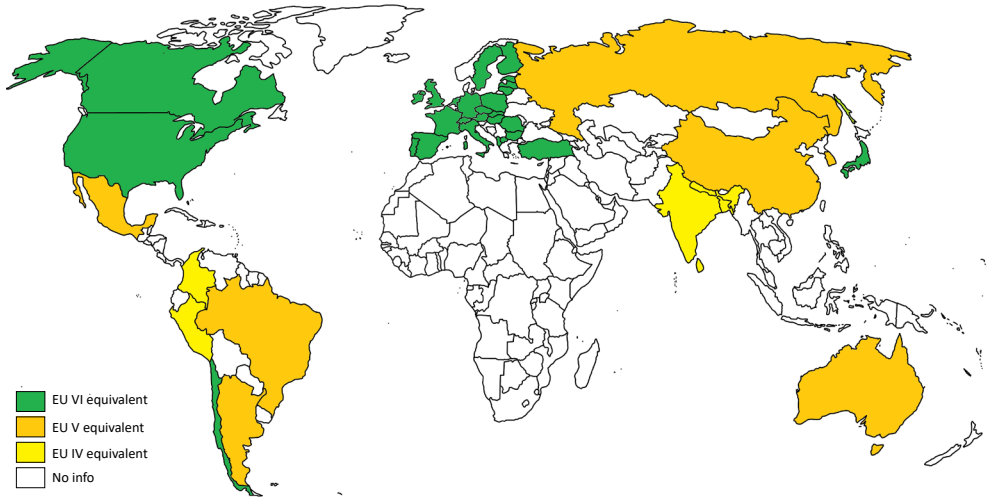


Figure 1-5. Worldwide emission legislation overview HD on-road CI engines in 2020.

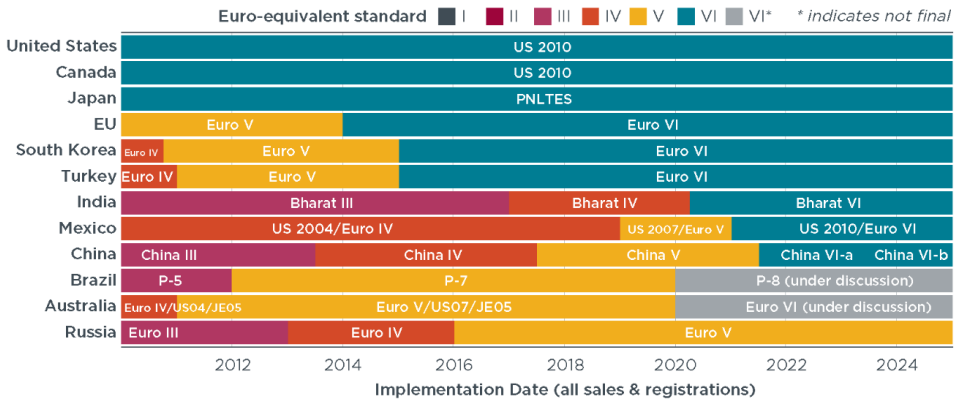


Figure 1-6. Timeline of the HD emissions standards implementation in major vehicle markets [16].

As shown in Figure 1-7a, since the EU I regulation entered into force in 1992, newly registered HD vehicles have to certify emissions limits for NO<sub>x</sub>, PM, CO, and HC, among other pollutants, below a certain value. However, CO<sub>2</sub> emissions are not limited by the Euro regulation. The new

European proposal is to apply penalties to the OEMs according to their fleet-average CO<sub>2</sub> emissions to control the CO<sub>2</sub> emissions. In a first step, for 2025, the target is to decrease the CO<sub>2</sub> fleet-average emissions by 15% with respect to the value measured in 2019 of each OEM fleet. The penalty for the OEMs that do not reach that level is estimated to be 4,250 € per gram of CO<sub>2</sub> and tons of cargo mass per kilometer (gCO<sub>2</sub>\*tkm). As a second step, for 2030, a reduction of 30% with respect to 2019 is estimated, with a penalty of 6,800 €/gCO<sub>2</sub>\*tkm. Considering the average CO<sub>2</sub> emissions of a Volvo FL 18-ton non-hybrid truck produced in 2019 along the world harmonized vehicle cycle (WHVC) with 50% payload, 60 gCO<sub>2</sub>/tkm, the penalty in 2025 would be 38,250 €/truck produced, and in 2030 of 122,400 €/truck. Considering that the purchase price of the truck is around 40,000 €, it is clear that these penalties will force the manufacturers to develop sophisticated technologies that can together decrease CO<sub>2</sub> and pollutant emissions. USA has implemented similar penalties with up to US\$37,500 per vehicle if it does not achieve the targets. China imposed a limit on the maximum fuel consumption of Heavy-Duty vehicles. A summary of the target for these three world areas is shown in Figure 1-7.

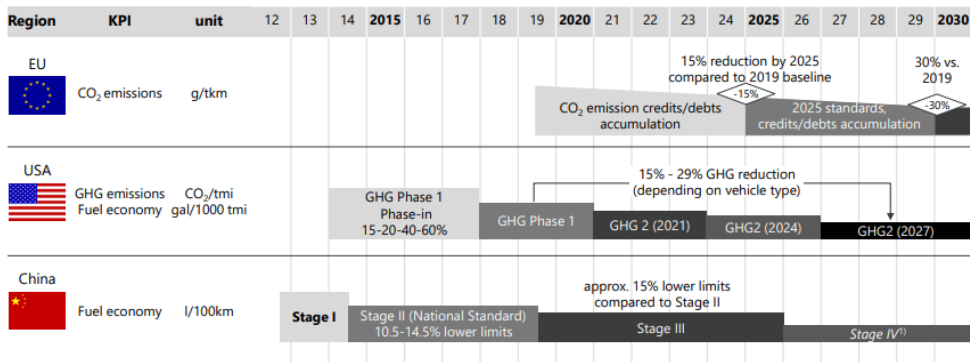


Figure 1-7. Worldwide CO<sub>2</sub> emission regulations will be tightened for commercial vehicles: in US and CN are already effective, EU recently introduced standards for 2025 and 2030 [17].

Unlike Light-Duty (LD) vehicles, in the HD industry (trucks and buses ranging from 3.5 to over 50 tons), there is more ambiguity about the future technology mix. The reduction of the battery costs, the increase of the battery energy density, and the faster-charging stations seen in the last years make xHEV attractive also for HD vehicles. The xHEV abbreviation is used to refer to mild hybrid electric vehicles (MHEV), full hybrid electric vehicles (FHEV), plug-in hybrid vehicles (PHEV), and battery electric vehicles (BEV). *Figure 1-8* shows a continuous decrease in the battery cost from 2010 up to 2020 at an average rate of 19%/year. Moreover, another 8% is expected from 2020 to 2024 and an additional 5% from 2024 to 2035. The precise balance between various types of vehicles will be determined by future technological advancements, pricing, legislative actions, and the availability of charging infrastructure along long-distance routes. In this sense, some specialists foresee that to achieve the “net zero” scenario in 2050 proposed by the EC, the future share of HD vehicles would be around 80% of BEVs and 20% of FCEVs [18]. Biofuels are expected to be not cost-competitive compared to non-bio, low-emissions alternatives for any road transport segment by 2050, with the exception of sustainably produced biofuels or synthetic fuels in internal combustion engines (ICEs) powertrains used for ultra-long-distance, very HD trucking or remote areas [19].

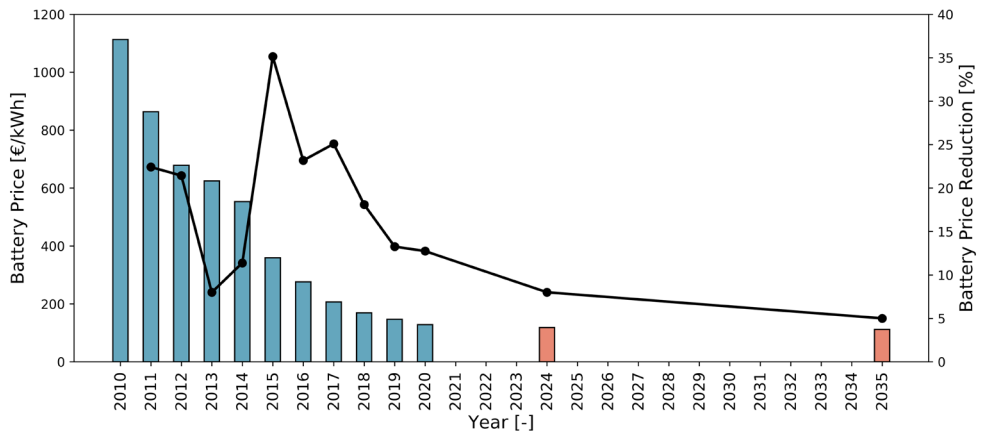


Figure 1-8. Lithium-Ion battery prices from 2010 to 2020. Cost is in €/kWh of battery storage energy. Adapted from [20].

Due to the fast development of battery technology, long-term predictions (2050 and beyond) that consider the transport sector based on electric technology are not questioned. However, hard steps need to be taken to improve the battery and fuel cell technology, as well as to increase the production of clean electric energy. Figure 1-9 shows that to cover the expected energy demand by 2050, electricity production needs to be increased 3.5 to 5 times depending on the prevalence of two future scenarios: 1) Decarbonization of the energy supply or 2) Decarbonization of the energy supply together with an increase in systems efficiency. In both cases, a high energy production increase needs to be done in only 20 years. In addition, the expansion of the electricity production sector needs to be done in a renewable and clean way. This means low land impact and ultra-low CO<sub>2</sub> and other pollutant emissions.

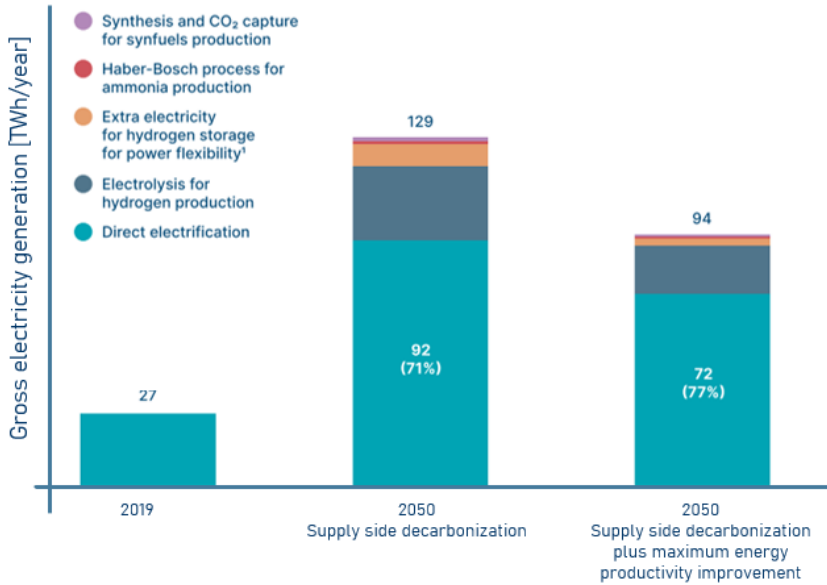


Figure 1-9. Total electricity generated by 2050 in the energy transitions commission indicative pathways. Adapted from [18].

Figure 1-10 shows the requirements in terms of wind and solar installed capacity to deal with the 2050 transport technology scenario, assuming that all LD vehicles will be BEV and HD vehicles will be distributed by BEV (80%) and FCEV (20%) in 2050. This estimation was performed by the Energy Transitions Commission (ETC). The basis of the analysis is performed by estimating the constant annual growth of the installed capacity of wind and solar power. This annual growth is called a compound annual growth rate (CAGR). In addition, the analysis added the scenario where almost all the energy generation installed is renewable. This type of energy is called variable renewable energy (VRE). The wind electricity capacity would have to increase from 640 GW to 15,000 GW, while solar capacity would have to increase from 650 GW to 30,000 GW.

Figure 1-11 shows the expected energy mix by 2050 performed by the ETC considering the same two scenarios of Figure 1-9 [18]. Both options



show that solar, wind, hydro, and nuclear need to be the main sources of energy, with biomass and waste energy recovery in second place. This totally shifts the current scenario with coal and oil as the main sources.

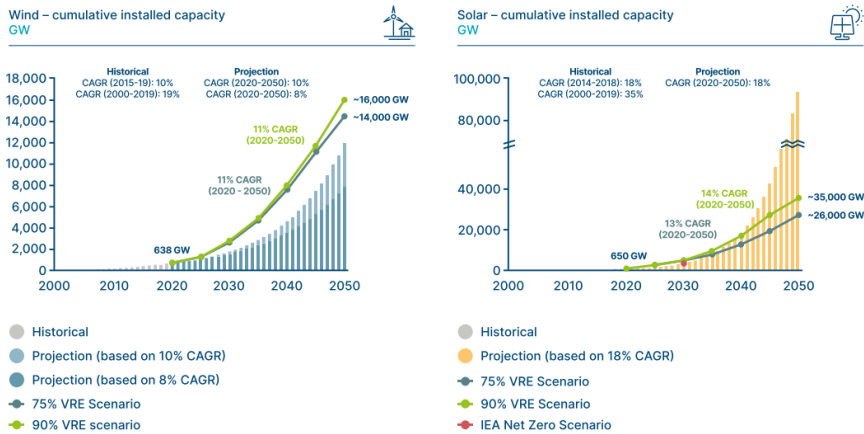


Figure 1-10. Required growth of installed wind and solar capacity in GW [18].

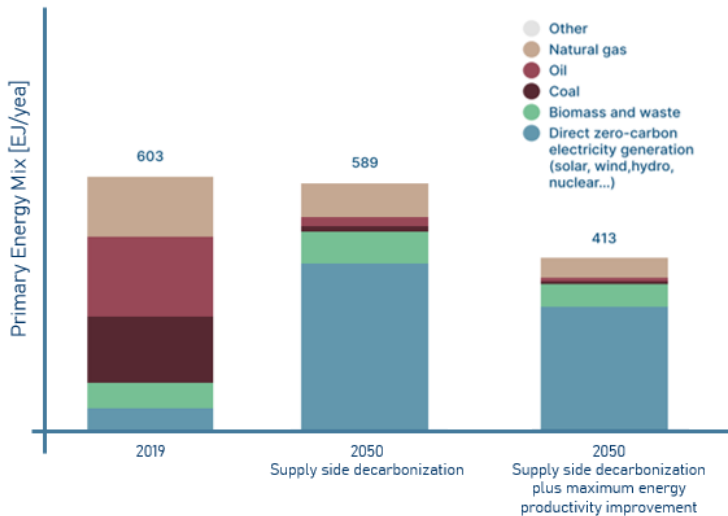


Figure 1-11. Expected indicative final energy mix EJ/year in a zero-carbon economy. Adapted from [18].

Finally, it is interesting to note that current reports consider the vehicles without tailpipe emissions (BEVs, FCEV...) as “zero-emissions.” However, zero-emission technology does not exist because transport technology will always require different energy conversion processes where CO<sub>2</sub> or other pollutant emissions are emitted. An interesting work addressing this issue was presented by Kelly Senecal and Felix Leach [21]. The well-to-wheel (WTW) [22] and life cycle analysis (LCA) [23] approaches are necessary to be applied to account for the global emissions from a given technology. However, there is not an agreement on how to consider these methodologies and the required databases yet. Considering different studies in the literature, the adoption of only BEV and FCEV technology for the transport sector seems to be not the best option in the near-term [24,25]. Thus, the lack of support in developing efficient HEVs to be used as technology-bridge could generate a global negative environmental impact. The next subsections discuss how partial electrification of the trucks can enable them to reach the CO<sub>2</sub> levels proposed for the 2025 and 2030 scenarios.

### 1.3 Future CO<sub>2</sub> European targets

For 2025 HD applications, the EC established a target of 15% fleet-average tank-to-wheel (TTW) CO<sub>2</sub> reduction compared to 2019 values [26]. This measure was established after introducing a similar target for LD vehicles, specifically a 28% fleet-average TTW CO<sub>2</sub> reduction for 2025 (68 gCO<sub>2</sub>/km) with respect to 2020 (95 gCO<sub>2</sub>/km) [27].

*Figure 1-12* shows a summary of potential solutions to improve the current commercial HD powertrains (Diesel compression ignition in non-hybrid powertrain with standard chassis and body) presented by FEV at the Vienna Motor symposium 2020 [28]. Aerodynamic and tire upgrades could aid by 6%. However, vehicle size restrictions make it difficult to improve aerodynamics, such as with additional air deflectors in Europe. Furthermore, reducing rolling resistance by 13% is not always an easy undertaking because it is also affected by the road surface. Engine improvements such as higher

compression ratio, friction improvements, and more complicated EGR systems can help to other 5% improvement. However, an additional 4% is required to achieve the proposed 15%. At this point, the introduction of electrification in the powertrain is mandatory.

Hybrid electric powertrains can be a possible solution to improve the current powertrain efficiency while transitioning, in an affordable way, to pure electric vehicles. The definition of a hybrid vehicle, according to the world forum for the harmonization of regulations on vehicles of the United Nations, is "a vehicle with at least two energy storage systems and at least two energy converters" [29]. In general, the two-energy sources are the ICE and the electric motor (EM), while the two energy storage systems are the fuel tank and the battery package. With correct energy management, the increase of the system components allows for an increase the global vehicle efficiency. The main benefits are a better use of the ICE and the energy recovery during braking.

In addition, depending on the powertrain architecture, benefits in terms of pollutant emissions can be gained by means of proper control of the ICE. *Figure 1-12* shows that a mild hybrid vehicle (48V battery system) can bring a CO<sub>2</sub> benefit of around 5% compared to the non-hybrid vehicle, fulfilling the 2025 CO<sub>2</sub> target. However, this prediction introduces the challenging task of arriving at up to 50% of brake thermal efficiency (BTE) in the ICE and the complete vehicle body design. So, these improvements give tentative values not always attainable for all applications. Then, some questions arose:

- How much is the potential reduction of the MHEV technology in a delivery truck?
- Can an FHEV be an alternative to directly achieve the 15% CO<sub>2</sub> emissions reduction? What about other pollutants?
- Which technology, or a mix of technologies, can achieve both CO<sub>2</sub> emissions and EU VI targets?

These questions will be answered in Chapter 4 and Chapter 5 of this Thesis.

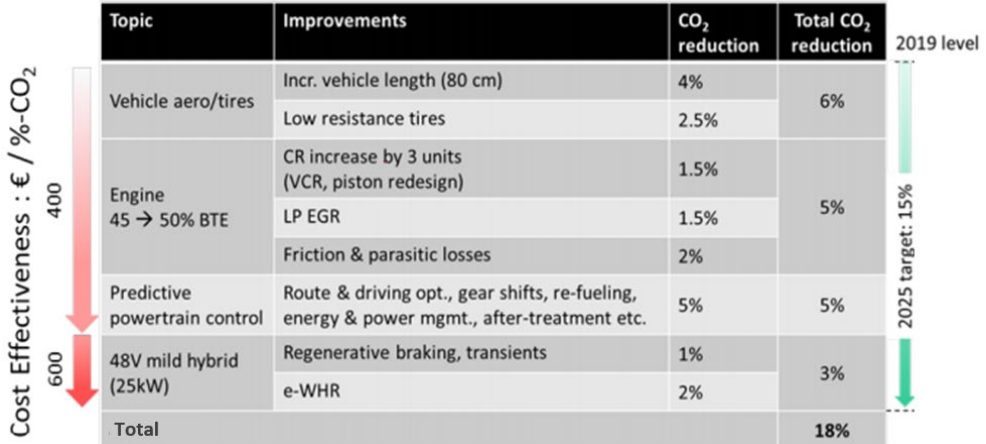


Figure 1-12. Potential pathway to meet the 2025 CO<sub>2</sub> targets in HD vehicles [30].

For 2030, the EC established for the HD transportation a 30% fleet-average TTW CO<sub>2</sub> reduction compared to 2019 values [27]. Going further, the 2050 scenario is expected to be net-zero CO<sub>2</sub> emissions [31]. Net-zero means that it is not possible to only consider the tailpipe emissions but also the indirect emissions associated with the vehicle manufacturing, use, and disposal processes, as well as those to the energy sourcing, among others. This quantification must be done by means of a WTW or LCA basis [32]. Thus, to achieve the 30% CO<sub>2</sub> reduction compared to 2019, additional technological improvements, apart from those referred to the vehicle itself, need to be done.

To reach the 2030 levels, the increase of the electric-to-thermal energy level with respect to the possible solution for 2025 (MHEV and FHEV) could be a solution. Plug-in Hybrid Vehicles (PHEV) trucks can be an affordable option with medium size battery packs without the necessity of fast charging. The mileage reduction will not be as problematic as with BEVs, and the

battery aging -a hot topic in BEVs- can also be reduced by means of intelligent management of the energy split. Thus, zero tailpipe emissions in urban zones together with long trip distances can be achieved. The ICE equipped needs also to be able to achieve low pollutant emissions in the case that charging infrastructure is not available. In this work, the PHEV technology will be evaluated in Chapter 6, trying to answer the next question:

- What is the effect of the battery size on the emissions reduction from a PHEV delivery truck?
- Is it possible to reduce the total battery energy with respect to a BEV truck?

Another option to reach the 2030 target that has been growing in the last years is the use of low-carbon fuels in ICE. One type is synthetic fuels, which are defined as an effective and environmentally benign duplicate of gasoline or diesel, with the goal of allowing ICEs to run as they presently do on fossil fuels while drastically reducing CO<sub>2</sub> emissions and hazardous pollutants. This definition includes certain synthetic fuels such as e-gasoline or e-diesel. These fuels are also called drop-in fuels and are an alternative to rapidly decarbonize the transport sector without big infrastructure changes. The lower CO<sub>2eq</sub> associated with these fuels is due to the fuel production process, where a large amount of CO<sub>2</sub> is captured from the atmosphere and combined with hydrogen taken from the water electrolysis with renewable energy sources (wind and solar power).

Other synthetic fuels produced with recovered CO<sub>2</sub> and green H<sub>2</sub>, typically via methanol, are DME and OMEx, which are attracting attention due to the potential to reduce the WTW CO<sub>2</sub> emissions but also other pollutant emissions such as soot and NO<sub>x</sub>. The high oxygen content and reduced carbon bounds make it ideal for CI engines in order to avoid the soot generation. However, engine recalibration and changes in the fuel systems are necessary due to the low heating value of these fuels.

Low carbon fuels also include fuels from biomass, such as biodiesel or bioethanol. These fuels have controversial attention due to the food versus crop debate. Clean hydrogen, carbon capture, storage or use (CCS/U), and sustainable bioenergy are all necessary to be able to generate the aforementioned fuels. *Figure 1-13* shows a scheme of the different possible green fuel pathways. There are several possible synthetic fuels or biofuels to be used in truck applications. In this work, the topic is assessed using OME<sub>x</sub>, and methanol in a hybrid dual-fuel engine. This also will be presented in Chapter 6.

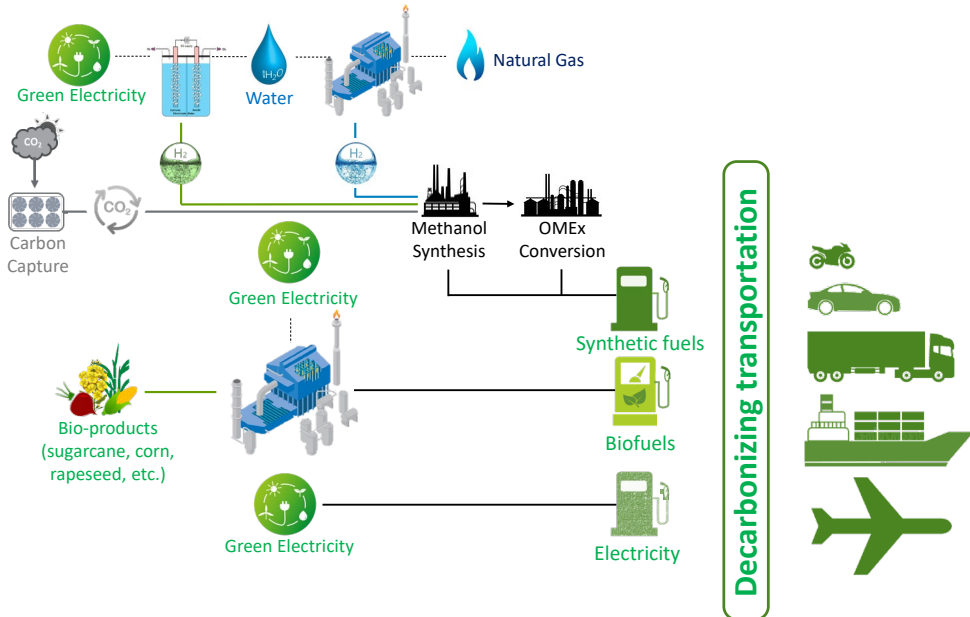


*Figure 1-13. Low Carbon Fuels production process for transport decarbonization.*

## 1.4 Euro VI and VII pollutant emissions limits for the Heavy-Duty transport

For the EC, the CO<sub>2</sub> emissions are not the unique concern in the transport sector. Pollutant emissions produced by ICEs are on the spot after the *Diesel Gate* scandal. Euro VI legislation for HD vehicles already imposes a high restriction on the tailpipe composition. Thus, the current powertrains use a complex after-treatment system (ATS) to fulfill the legislation.

However, the EC is currently formulating new regulations for the future Euro VII standard in terms of tailpipe emissions. Compared to the Euro VI standard, Euro VII is expected to require lower emissions levels over a wider range of on-road operating situations. Specifically, the regulation will give more emphasis to low-load conditions, corresponding to urban driving and at low temperatures, when the ATS is less efficient. Thus, special attention will be paid to ensure that NO<sub>x</sub> emissions stay low. According to the most recent proposal from the consortium for ultra-low vehicle emissions (CLOVE) [33], the new set of limitations should result in a 50% of pollutant reduction with respect to Euro VI. In addition, it will be requested a 90% reduction in NO<sub>x</sub> emissions during low-load and cold-start operations, which corresponds to urban driving conditions. Another requirement is that the vehicle must meet pollutant emission restrictions during its entire useful life of 1,200,000 kilometers. As a result, manufacturers will almost certainly need to invest in new technologies to meet the increased regulatory standards.

While the exact date of implementation of the Euro VII standard has yet to be defined, the new standards are projected to take effect between 2025 and 2030 [34]. Furthermore, the California air resources board (CARB) adopted the Heavy-Duty Omnibus Regulation in 2020, which establishes increasingly strict pollutant emission limitations for 2024 and 2027. China has begun laying the groundwork for the development of China VII standards, with an application deadline of 2030.

### 1.4.1 ATS solution for Euro VII

For the NO<sub>x</sub> emissions control, the current Euro VI emission control systems rely mostly on selective catalytic reduction (SCR). Ammonia slip catalysts (ASC) are frequently employed to meet the 10-ppm ammonia limit averaged across the World Harmonized Vehicle Cycle (WHVC). All Euro VI compliant systems have diesel particulate filters (DPFs), which rely largely on a diesel oxidization catalyst (DOC) for passive and active regeneration. SCR is particularly efficient in reducing NO<sub>x</sub> emissions to very low levels under favorable engine operating conditions, but it has limits in achieving similar performance under low-load and cold-start situations, such as those seen in urban driving. There are four major ways in which these technologies can be assisted:

- 1) Improving the NO<sub>x</sub> conversion efficiency of the warmed-up system.
- 2) Accelerating the SCR warm-up.
- 3) Keeping the SCR warm.
- 4) Reducing engine-out NO<sub>x</sub> emissions.

While some innovations may result in a fuel economy reduction, this is not always the case. Figure 1-14 depicts a hypothetical ATS design for achieving Euro VII. It employs two DOC and SCR+ASC with one DPF and an electrical heater catalyst (EHC). The latter is crucial for cold start operation.

International Council on Clean Transportation (ICCT) and National Renewable Energy Laboratory (NREL) assessed the estimated incremental cost of this type of system. The final numbers are shown in *Figure 1-15*. All costs were calculated using a 13-liter, 330-kW HD truck engine. Operational expenditures, such as the purchase of urea exhaust fluid and maintenance charges, are not considered. Each truck is projected to cost an additional US\$2000 to US\$4000 due to the new ATS to achieve Euro VII emissions in terms of CO, HC, NO<sub>x</sub> and soot. Considering that the purchase price of the truck is around 40,000 €, this means a price increase of around 10%.



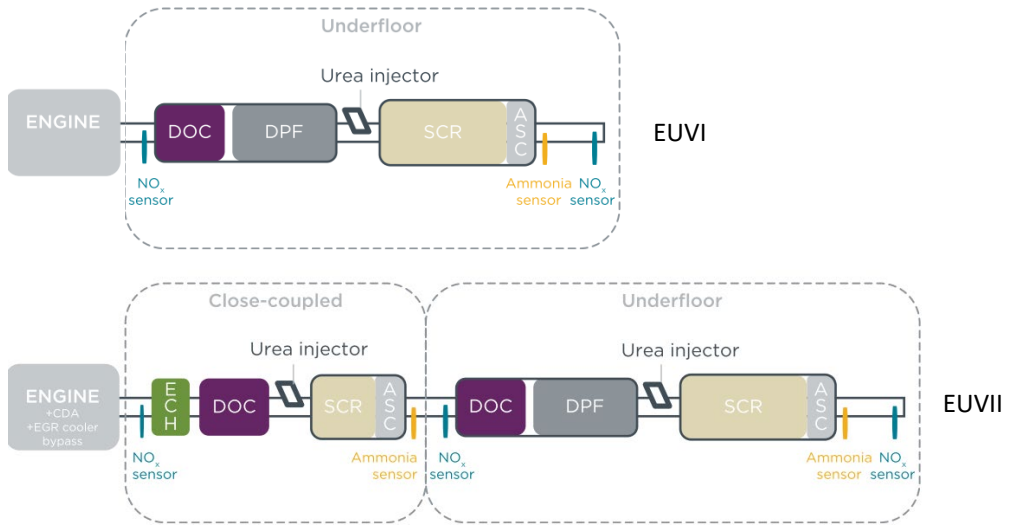


Figure 1-14. Current Euro VI ATS and potential emissions control configuration for future Euro VII requirements. Adapted from [34].

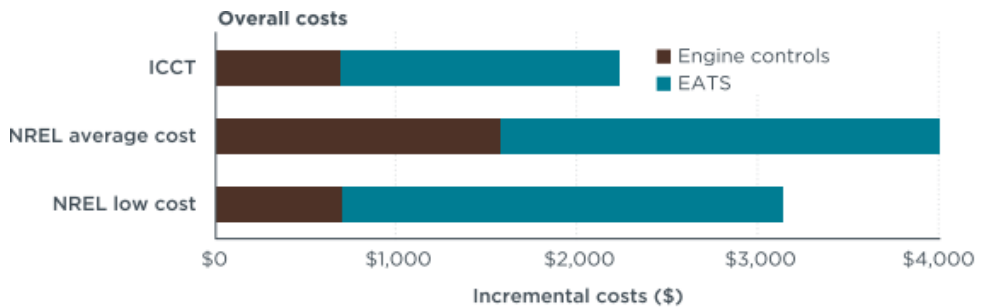


Figure 1-15. Comparison of the incremental direct technology cost estimates obtained by NREL [35] and ICCT [36] for compliance with the California Heavy-Duty Omnibus Regulation.

### 1.4.2 Advanced combustion concepts for Euro VII

The Euro VII regulation will almost certainly introduce a stringent reduction in NO<sub>x</sub> emissions. Thus, it is expected that the regulated emissions levels will be reached not only by means of the ATS but also by reducing the engine-out emissions through improved engine control. According to a previous study [37], reducing the engine-out NO<sub>x</sub> emissions from about 5.0 g/kWh to 2.0 g/kWh would give the ATS an additional 200 seconds to reach the light off temperature (maximum NO<sub>x</sub> conversion efficiency) under WHVC transient cycle. Nonetheless, in conventional powertrains operating under conventional diesel combustion, the in-cylinder NO<sub>x</sub> emissions reduction would entail a penalty in fuel consumption and PM emissions. Therefore, the use of advanced high-efficiency combustion modes that enable breaking the NO<sub>x</sub>-soot trade-off is pointed as a promising alternative to enable the required pollutant emissions reductions without the use of complex and expensive ATS.

Low-temperature combustion (LTC) allows controlling the engine-out NO<sub>x</sub> and soot emissions simultaneously by reducing the in-cylinder temperature and promoting premixed combustion, at least from part of the in-cylinder charge, instead of diffusive conventional diesel combustion. Among the different advanced combustion modes that have been proposed over the years, the Reactivity Controlled Compression Ignition (RCCI) showed advantages in terms of combustion controllability and load range extension. *Figure 1-16* illustrates the conventional operation zone of some LTC concepts such as homogeneous charge compression ignition (HCCI), premixed charge compression ignition (PCCI), and RCCI compared to the conventional diesel combustion on a  $\Phi$ -T diagram based on the work performed by Neely et al. [38].

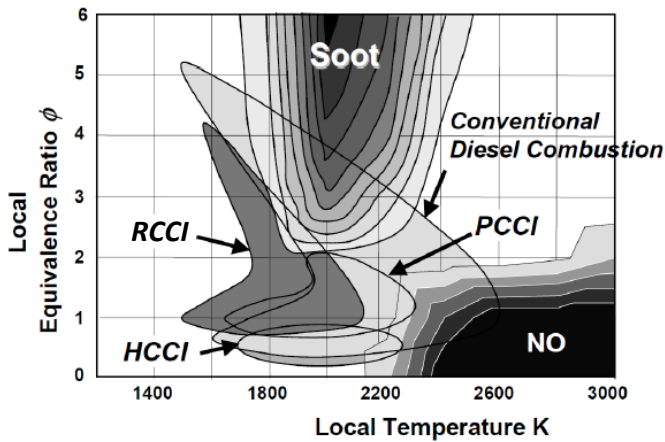


Figure 1-16. NO, and soot formation zones as a function of the local equivalence ratio and local temperature with the operating zone illustration of conventional diesel combustion, RCCI, PCCI, and HCCI. Adapted from [38].

This combustion concept can be easily implemented by adding a port fuel injector (PFI) to a CI engine to inject a second fuel with different reactivity than that injected directly into the combustion chamber [39]. Experimental and simulation studies have demonstrated that RCCI is capable of achieving diesel-like or better efficiency [40] together with near-zero NO<sub>x</sub> and soot emissions [41]. The effect of different variables on RCCI efficiency and emissions has been deeply investigated. In this sense, the engine settings [42], piston geometry and compression ratio [43], fuels used [44], and air management conditions [45] have been optimized. The majority of the investigations found in the literature rely on RCCI to achieve NO<sub>x</sub> values in steady-state conditions below Euro VI regulation (0.4 g/kWh) and soot emissions in the range of 0.1-0.2 FSN [46]. These results would confirm the great potential of the RCCI concept, meaning that nearly 60% of the total after-treatment costs of Heavy-Duty vehicles could be reduced by removing the SCR system. However, the main limitation is the impossibility to achieve an entire engine map calibration suitable for real applications.

Benajes et al. [47] proposed a multi-mode dual-fuel combustion concept moving from fully premixed combustion (as RCCI) at low loads towards a diffusive dual-fuel one at high loads to overcome the difficulties of achieving high engine loads. The multi-mode combustion concept allows the dual-fuel operation in the whole engine map; however, some calibration constraints such as NO<sub>x</sub> and soot emissions must be relaxed as compared to the levels achieved with the fully premixed dual-fuel strategies. Therefore, depending on the operative conditions, such as driving cycle or vehicle total weight, it could not be possible to achieve the EU VI emissions levels. One possible solution is the use of an electric machine (EM) in the powertrain to compensate for the lack of power of the ICE. Therefore, a de-rated RCCI engine in a hybrid powertrain sounds like a potential solution to reduce both CO<sub>2</sub> and pollutant emissions.

Other critical aspect of LTC concepts is the low exhaust temperature. When the concept achieves the emissions legislation limits without using an ATS it is not an issue. However, as the government limits not only considers NO<sub>x</sub> and PM, instead includes for example HC and CO it is not possible to not use any ATS in the engine exhaust. Therefore, a challenge enters that it is to make efficient ATS systems as an oxidation catalyst. In addition, hybrid powertrain operation with large number of ICE on/off makes the problem even bigger. Heaters in the exhaust can be applied or powertrain energy management to increase the ICE operations appears as potential solutions.

## 1.5 Summary

Hybrid electric vehicles (HEVs) were extensively studied in passenger car applications, and they are currently a relatively mature technology, being commercially available on a large scale [48]. However, for Medium- and Heavy-Duty applications, the studies in this field are in the first steps, and vehicle prototypes are only found at this moment. Compared to conventional internal combustion engine vehicles, HEVs incorporate more electrical components featuring many available patterns of combining the power flows

to meet the load requirements. Due to the multiple power sources, there exist several powertrain topologies and different control strategies to control the vehicle power. Dynamic interactions among various components and their multidisciplinary nature make it difficult to predict interactions among various vehicle components and systems. Prototyping and testing each design combination is cumbersome, expensive, and time-consuming. Modeling and simulation are therefore indispensable for concept evaluation, prototyping, and analysis of HEVs. The main advantage of the hybrid technology is the possibility to increase the powertrain operating efficiency and regenerate braking energy into onboard energy storage. Even if the operation of Heavy-Duty vehicles is typically over a long distance and consists mostly of constant speed driving, a significant amount of braking energy can be regenerated because of the road elevation changes. Depending on the location of the electric machine, different hybrid vehicle configurations can be found. In passenger vehicles can be found several commercial applications. However, the benefits of the above-mentioned powertrains are not extensively addressed in Trucks.

In this work, both LTC and electrification will be combined to reduce CO<sub>2</sub> emissions and pollutants simultaneously as NO<sub>x</sub> and PM. As a result, Chapter 6 of this Thesis examines the EUVII scenario beyond 2025.

## **1.6 Document content and structure**

The main novel of this work is to combine the powertrain electrification together with advanced combustion strategies to reduce the CO<sub>2</sub> and pollutant emissions simultaneously. Experimental and numerical tools will be used to answer the proposed questions in the most efficient and cost-effective way. The work includes fundamental and applied concepts in the topic of combustion, fluid dynamics, electrochemistry systems as well as energy management.

This Thesis is structured into seven chapters. The main contents of each subsequent chapter can be outlined as follows:

Chapter 2 details the literature review, addressing the most relevant advancements considering electrified powertrains and novel combustion strategies for internal combustion engines. Benefits, drawbacks, and challenges will be clearly stated. This first discussion will enlighten which should be the gaps to be filled by this research, justify it, and define the main objectives to be pursued.

Chapter 3 presents the experimental and numerical tools used in this research. First, the experimental facility in which a multi-cylinder engine was installed is described. Secondly, the numerical vehicle and components models are described, evidencing the most relevant aspects of each software. To conclude, the powertrain optimization strategy methodology is presented in detail.

Chapter 4 describes the benefits and drawbacks of the application of the first level of electrification, MHEV, in an 18-ton Truck. The methodology proposed in Chapter 3 to obtain the best powertrain configuration to meet the 2025 targets is applied. Taking advantage of the 48 V system, different electrified components such as an electric pump in the high-pressure EGR loop, an electrified turbocharger, and an electric heater in the ATS are tested. The 48 V MHEV system with e-components is compared to the original experimentally tested high pressure (HP) + low pressure (LP) EGR engine and the OEM conventional diesel combustion (CDC) engine. The fuel consumption, TTW CO<sub>2</sub> emissions as well as the main pollutant emissions are estimated by means of numerical simulations in homologation (WHTC) and real driving cycles and different truck payloads. Finally, the main drawbacks of the concept are identified, and the potential solutions are the bases of the next chapter.

Chapter 5 aims to assess the impact of different powertrain architectures in a full hybrid powertrain (600 V). Parallel pre-transmission

(P2), series (SHEV), and power split (PSD) hybrid are evaluated by means of numerical models fed with the experimental calibration obtained in the engine test bench. As in Chapter 4, the fuel consumption, TTW CO<sub>2</sub> emissions as well as the main pollutant emissions are estimated by means of numerical simulations in the homologation WHTC and real driving cycles at different truck payloads. Finally, a summary of the possibilities to achieve the 2025 targets is discussed. The main challenges for 2030 targets are identified, and the potential solutions are the bases for the last result chapter.

Chapter 6 evaluates different solutions to meet the targets beyond 2025. In particular, the 30% of CO<sub>2</sub> reduction for 2030 is set as the main target. The 600 V PHEV technology is studied. In addition, the use of synthetic fuels in FHEV powertrains is evaluated with the introduction of the WTW analysis. Moreover, an LCA is included to evaluate the differences between the OEM truck, MHEV, FHEV, PHEV, FHEV with synthetic fuels, and BEV truck. This brings a general picture of the possible scenarios and the benefits of each technological proposal.

Chapter 7 summarizes the contributions of the investigation and draws the most significant conclusions from this work. Moreover, enhancements and additional investigations for this topic are proposed as future works.

*Figure 1-17* depicts the argument line that was followed from the Thesis definition to the conclusions.

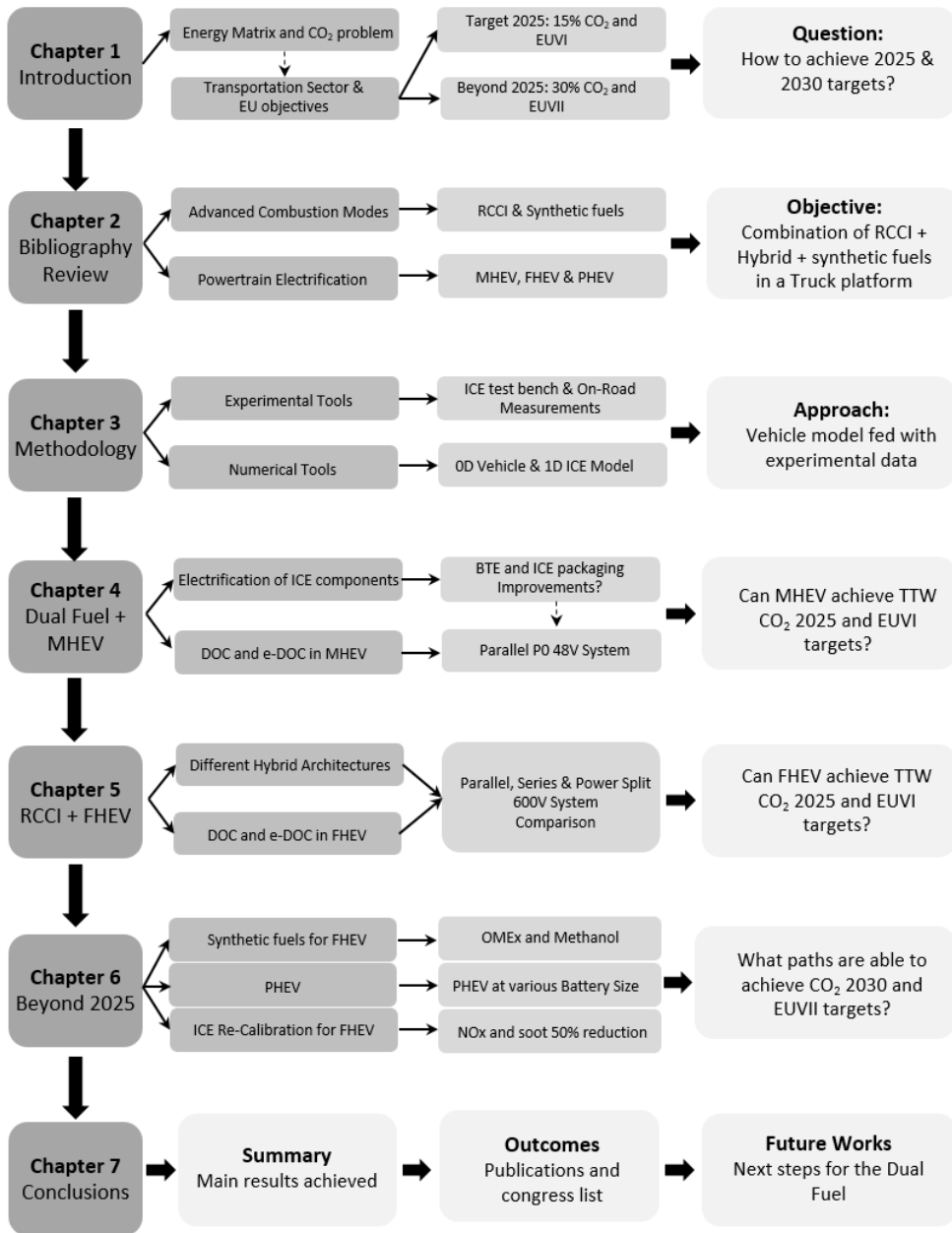


Figure 1-17. Graphical representation of the argument line followed in the investigation.



# Chapter 2

## Electrified powertrains and advanced combustion modes for Heavy-Duty vehicles

### **Content**

---

2.1 Introduction.....	31
2.2 Overview of the Heavy-Duty sector .....	31
2.3 Current powertrain challenges .....	35
2.4 Advanced combustion modes for emission reduction.....	49
2.4.1 RCCI: Reactivity Controlled Compression Ignition .....	52
2.4.2 Alternative fuels for compression ignition engines.....	63
2.5 Powertrain electrification for CO <sub>2</sub> and battery reduction .....	69
2.5.1 Hybrid powertrain classification.....	72
2.5.2 Battery storage system .....	77
2.5.3 Electric machine and power electronics.....	82
2.5.4 Control strategies.....	88
2.5.5 Life Cycle Analysis in Transportation.....	92
2.5.6 Hybrids in the Heavy-Duty sector .....	99
2.6 Literature review conclusions .....	104

2.7 The objective of the study and proposed methodology..... 106

## 2.1 Introduction

This chapter presents an overview of the current transportation sector, focusing on trucks in Europe. It is identified a predominance of Diesel non-hybrids and a small market penetration of battery-electric powertrains. Therefore, the main advantages that justify the current market share and challenges to be tackled is shown.

Subsequently, potential solutions to overcome these challenges are introduced. Two subsections are presented, divided into Advanced Combustion Modes to overcome pollutant emissions and electrified powertrains to improve vehicle efficiency and, consequently, CO<sub>2</sub> emissions.

The main conclusions are listed in a separate subsection, followed by the objective of this work based on the gap found in the research bibliography. Lastly, the methodology proposed is outlined.

## 2.2 Overview of the Heavy-Duty sector

Heavy-Duty transport, defined as trucks, buses, and coaches, is a critical sector to the European economy. In particular, trucks that are used for the transportation of goods account for more than 75% of freight movement by weight in the EU [49]. All commodities purchased in Europe are transported by truck for at least part of their journey to the consumer. Furthermore, many critical public services, such as waste collection, fire, and construction, are provided by trucks. There are currently over 6.6 million trucks in use across the European Union [49]. Therefore, the improvement of the vehicle energy economy and emissions is crucial. In addition, around 190,277 trucks (with a maximum payload of over 5 tons) were exported worldwide in 2019, worth €5.6 billion. For example, around half of all heavy trucks made in the United States originate from European-owned plants using European technology [50]. Despite that this Thesis focuses on the

European legislation (CO<sub>2</sub> targets and EU emissions limits) and current EU truck technology, the bibliography and results can be extended to other countries.

*Figure 2-1* shows the average cargo mass by country in 2019 and 2020 to understand the European truck transportation scenario. The comparison between 2019 and 2020 is interesting due to the modifications generated by the COVID situation. The average cargo mass for national and international transport was 14.3 tons in 2019 and 2020. *Figure 2-2* shows the percentage of empty travel for trucks to complement the previous information. Empty vehicles made for one-fifth of all road freight journeys at the EU level. The majority of countries have a percentage of empty vehicle kilometers ranging from 10% to 35%. The ratio for Cyprus and Montenegro, on the other hand, was higher than 45.0 percent, owing to one-way journeys carrying commodities imported through ports and construction traffic. This shows the importance of improving the vehicle performance at zero cargo mass.

While considering the type of truck (*Figure 2-3*), it is possible to see that the most used variety in 2020 had between 30-40 tons of maximum permissible laden weight (52%). With lockdowns and high urban delivery, the pandemic situation shows an increase in the number of medium-sized trucks (10-20 tons). There was a shift from 10% in 2019 to 16% in 2020 and a decrease in large trucks from 40% in 2019 to 27% in 2020. This seems to be a trend that will continue in the next years due to the drastic increase in the delivery business.

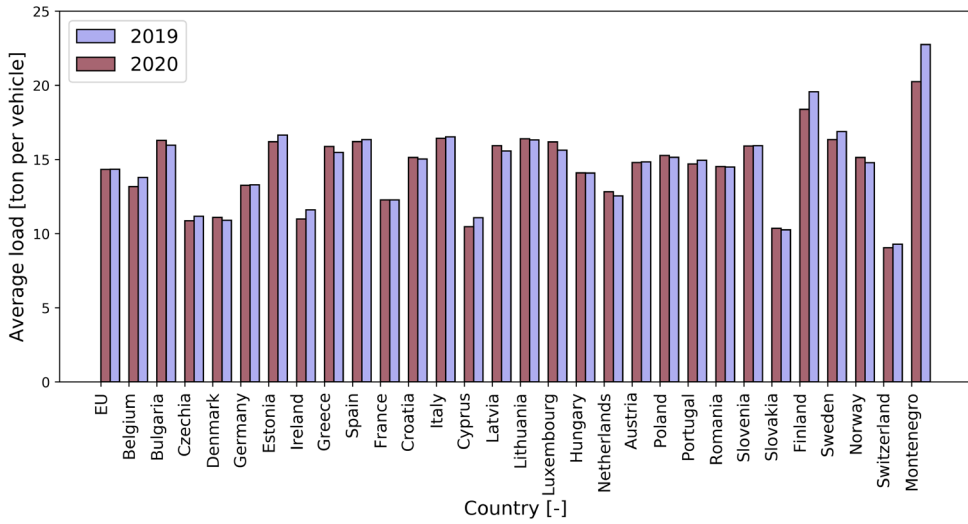


Figure 2-1. Average loads of road freight transport in 2019 and 2020. Adapted from [49].

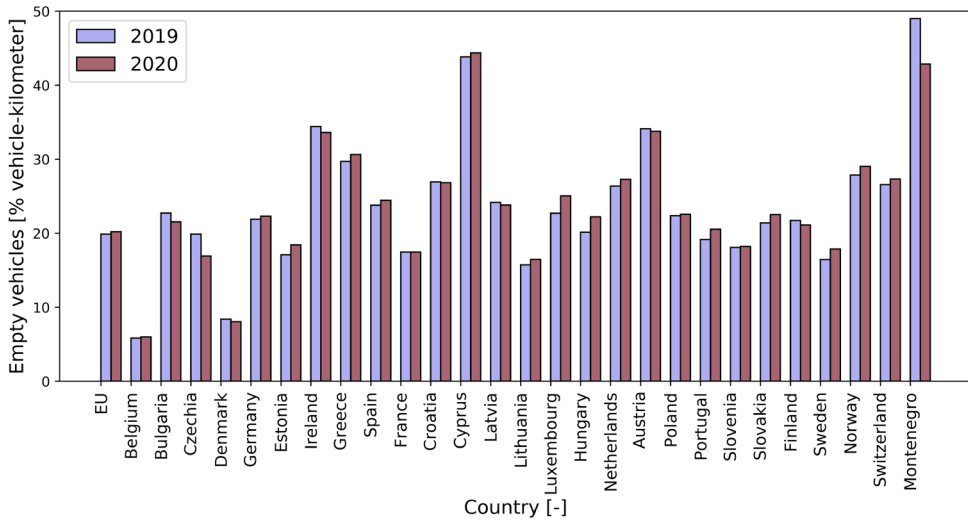


Figure 2-2. Road transport performed by empty vehicles in 2019 and 2020 was calculated as a percentage share of total vehicle kilometres. Adapted from [49].

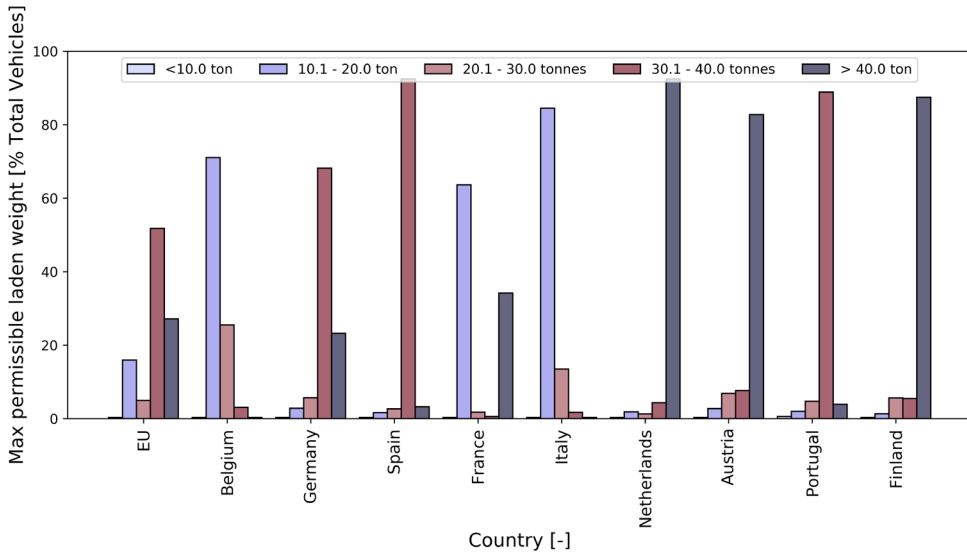


Figure 2-3. Road freight transport by maximum permissible laden weight of the vehicle in 2020. Adapted from [49].

Other interesting information found in the literature is the average age of Europe's trucks: 12.4 years [49]. Vehicles less than five years old accounted for 61 percent of total vehicle kilometers. In comparison, vehicles older than ten years accounted for only 20 percent. Therefore, the expected lifespan of the trucks and fleet renewal is also important aspect. This data also gives an idea of the years it can take to have a large market penetration of new technology.

In terms of manufacturers, Volkswagen leads (32%) the truck market, followed by Volvo (24%) and Daimler (19%) [51]. When looking at the road freight transport by axle configuration, all major economies had more than 70% of their transport performed by road tractors and semi-trailers in 2018. From 1.660.888 trucks evaluated, 144.254 were lorry (9%). The rests are Lorry plus Trailer or road tractor plus semi-trailer [37].

After an overview of the EU truck scenario, the next sections of this chapter aim to set the fundamentals of the research scope by evidencing the

different challenges that have been faced during the last years the Heavy-Duty powertrains and possible solutions presented by researchers and Original Equipment Manufacturers (OEMs).

## 2.3 Current powertrain challenges

The market is shared by mostly non-hybrid powertrains operating with CI engines under conventional diesel combustion (CDC), a small part with natural gas in non-hybrid powertrains, and an almost negligible part is composed of electrified vehicles. *Figure 2-4* shows that in Europe, non-hybrid CDC accounts for 97.9% of the total number of new registrations in 2019. Along with this work, this technology will be considered a conventional powertrain.

The new registrations of chargeable trucks (BEVs and PHEVs) represent 0.2% of the EU new registrations (mainly in Germany and the Netherlands) [50]. HEV held a smaller share of new truck sales in 2019, with only 0.1% of the EU new registrations. Other types of vehicles, like petrol-fueled, represent just 0.1% of the total (mainly Finland and Germany), and alternative fuels (Natural gas, LPG, biofuels, and ethanol vehicles) account for 1.8% (mainly France, Italy, and Germany). Despite non-conventional powertrains being small in numbers, they gradually see an increase due to the newer European legislation. BEV between 2018 and 2019 increased by 109%, alternative fuels by 70%, and hybrid powertrains by 10%.

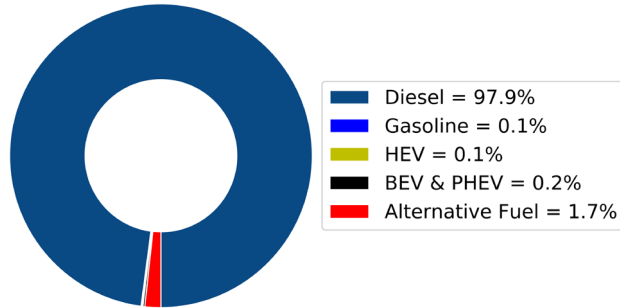


*Figure 2-4. Fuel types of new trucks for the European market share in 2019. Adapted from [50].*

Focusing on conventional powertrains, one of the major problems is the engine's dependence on the truck payload and driving cycle. Southwest Research Institute's [52] created a numerical model for evaluating vehicle performance and fuel economy. With less than 5% fuel consumption variances, this tool was validated against existing chassis dynamometer test data. It stressed the need to understand how the engine runs during different vehicle driving cycles so that engine technology development can concentrate on the parts of the operating map that spend the most time. For a Dodge Ram 6.7-liter diesel non-hybrid truck, *Figure 2-5* was created to help visualize engine operation during drive cycles. It comprises the engine torque curve, the engine fuel map, and points of different sizes to represent the amount of time spent in a particular section of the fuel map (Medium-Duty vehicle). Each point's area is proportional to the time spent in that speed/load bin.

In addition, *Figure 2-5* shows that the increase in payload shifts the operating conditions to higher loads ( $>600$  Nm) and engine speeds ( $>2000$  RPM). This part of the map is more efficient with a BSFC of 205-220 g/kWh instead of 300 g/kWh of low engine load ( $<400$  Nm). The idle zone (around 0 Nm) is similar in both cases because the truck is stopped depending on the driving cycle. The authors studied the operational engine points for the



European homologation cycle for Heavy-Duty (WHVC) with a 4-ton payload for the same vehicle. This mild cycle never operates the engine above 1750 RPM or 300 Nm torque. As a result, the engine never gets into the more efficient portion of the operating map.

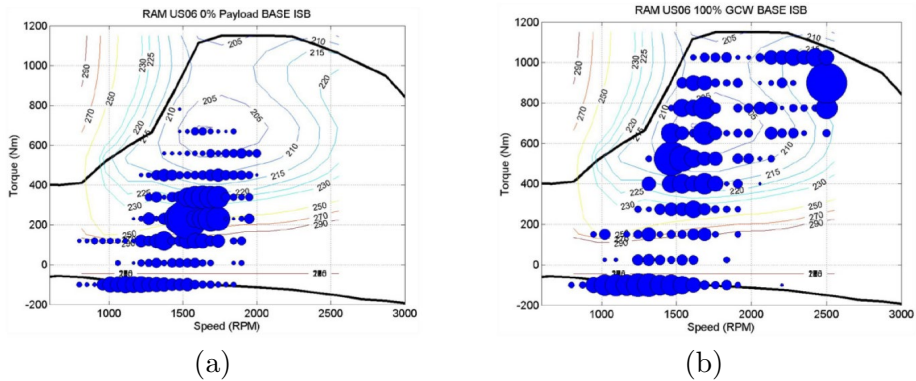


Figure 2-5. Engine operating map for the Ram pickup with the 6.7-liter diesel on the US06 cycle at zero (a) and 11 ton (b) payload. Source [52].

Lajunen [53] studied, by numerical simulation, long-haul trucks with 40-90 tons (Figure 2-6). For a conventional powertrain, the increase in the payload directly impacted the fuel consumption with an increase of 38%, 65%, and 90% when passing from 40 tons to 60, 76, and 90 tons, respectively. However, considering the specific fuel consumption (grams of fuel per kilogram of vehicle weight), the vehicle is more efficient with a decrease of 18%, 22%, and 25% for 60, 76, and 90 tons with respect to the 40-ton case. The decrease in specific fuel consumption is due to the change in engine operation from low load to high load with the increase of the cargo mass, as seen in *Figure 2-5*.

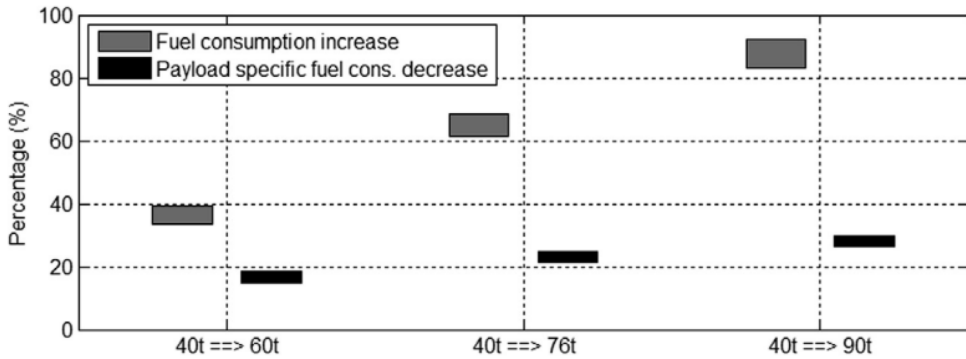


Figure 2-6. Fuel consumption increased, and payload-specific fuel consumption decreased in percentage for three payload variations. Source [53].

Zhu et al. [54] investigated the energy flow in a Heavy-Duty truck dynamometer test bench. The vehicle was tested under the China-World Transient Vehicle Cycle (C-WTVC). The findings demonstrate that the vehicle's operating conditions have the most significant impact on the energy flow distribution of a Heavy-Duty diesel-powered vehicle. Under C-WTVC, the vehicle's effective power, exhaust energy flow, coolant energy flow, pump loss energy flow, and other loss are 35.7%, 35.1%, 19.6%, 2.1%, and 7.5%, respectively. Due to the vehicle's frequent acceleration and deceleration, the variability range of the diverse energy flows is significant. The Heavy-Duty vehicle's brake thermal efficiency under C-WTVC remains between 20% and 43% except for idle conditions. The discrepancy between the maximal BTE and what can be achieved under transitory conditions shows one of the crucial problems of non-hybrid powertrains. Zhu et al. [54] also show that coolant and exhaust energy flow can reduce energy consumption in transient conditions if it is recovered.

As was previously shown, almost all Heavy-Duty vehicles are compression ignition with Diesel as fuel. The reason is the high efficiency and reliability with respect to other types of engines (spark ignited) or fuels (gasoline, natural gas). However, there are several problems to be tackled.

The high NO<sub>x</sub> and particle matter (PM) that the compression-ignition engine has at tailpipe emissions are well known. In addition, the ICE efficiency is reduced when compared with other mechanical converting systems used in transport, such as electric machines or fuel cells. An electric motor can transform electricity into mechanical energy with an 85-97% efficiency, while for a fuel cell, this efficiency ranges from 40-60%. As shown previously, the ICE ranges between 20-48%.

Going deep into the Conventional Diesel Combustion (CDC), it can be phenomenologically described as a sequence of processes from the fuel injection at the end of the compression stroke up to the well-controlled diffusion combustion during the expansion stroke. Briefly, the injection process takes place on a high-density flow, originated by the compression of the fresh air and residuals during the compression stroke. The liquid fuel is injected with high velocity (high injection pressure) into this environment to allow a proper spray penetration and atomization. During this injection process, various simultaneous phenomena can be found as the gas-liquid phase interaction, spray atomization, evaporation, and droplet-wall interaction. The evolution of the mixing process coupled with the high pressure and temperatures inside the combustion chamber enables the spontaneous ignition of the mixture, burning part of the already premixed fuel.

The period from the start of the injection process up to the ignition of the mixture is defined as the ignition delay. It lasts a few crank angle degrees. Once the combustion is established, the fuel continues to be injected into a more reactive environment, reducing the vaporization and ignition delay. This sequence of steps is generally known as the mixing-controlled part of the diesel combustion. Figure 2-7 shows the characteristics zone in terms of the fuel state, flame, and pollutant formation of the conventional diesel combustion.

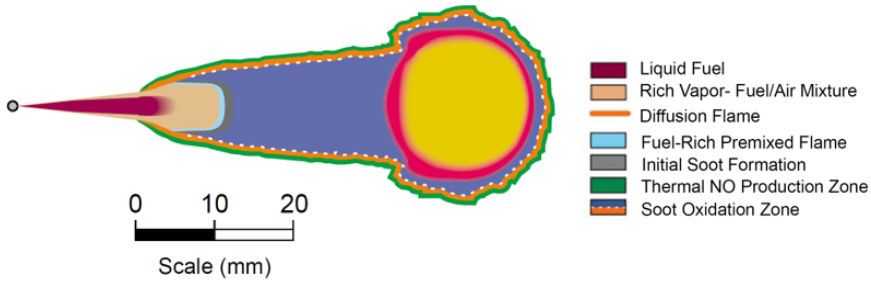


Figure 2-7. Conceptual description of DI diesel combustion during the mixing-controlled burn phase illustrates the different zones and processes in the diffusive combustion. Adapted from [55].

Advantages of CI engines include no-knock limit, low cycle-by-cycle volatility at lean conditions, and reduced pumping losses owing to unthrottled operation, resulting in extremely high efficiency as compared to SI engines. Previous works [56–58] provide a thorough examination of how engine design and operational characteristics affect diesel engine efficiency.

The first Rudolf Diesel’s engines were only approximately 26% efficient. Modern compression-ignition diesel engines dominate the commercial trucking industry, which converts roughly 44 percent to 48 percent of fuel energy into engine work. New diesel engines, despite their already highly efficient, continue to improve. Advanced coating materials to reduce heat transfer losses, novel materials to reduce friction losses, sophisticated piston shapes to reduce emissions, adjusting injection settings to be more efficient, and waste heat recovery are the primary study areas.

According to EPA estimates, diesel engines will cut fuel consumption (CO<sub>2</sub> emissions) per unit of work by 4.2 percent between 2017 and 2027. By 2030, CO<sub>2</sub> emissions from engines would be lowered by an average of 0.3 percent to 0.4 percent per year. To accomplish these results, teams led by Cummins, Daimler, Navistar, and Volvo exhibited engine improvements of 12–17 percent over a 2010 baseline. These improvements are part of the US Department of Energy’s Super Truck initiative, aiming for a BTE of more than 50%. Currently, the program has a peak brake thermal efficiency of 50–

51 percent. The follow-up aim for the Super Truck program would be a brake thermal efficiency of 55 percent under peak conditions.

FEV presented an estimation of the potential to achieve above 50% peak BTE by starting from a 46% BTE engine (2020 Heavy-Duty Diesel engine) [29]. The compression ratio, injection pressure, and combustion control increase can give additional 2 points of BTE (major step). Improving the air management, parasitic and friction losses can allow achieving the first target of 50% BTE. In addition, a low-pressure EGR and waste heat recovery allow going further, to almost 54% BTE. Figure 2-8 shows the peak BTE achievable with FEV predictions.

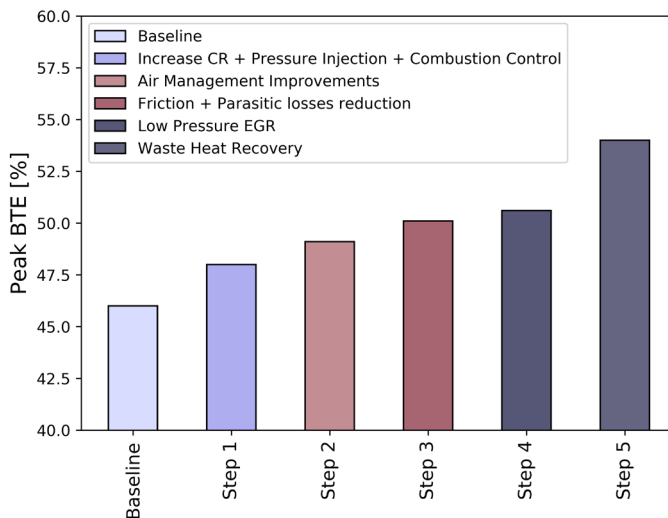


Figure 2-8. CI Diesel engine's new technology impacts peak brake thermal efficiency (BTE). Adapted from [30].

An example of this is the 13-liter commercial engine developed by China-based automaker Weichai Group with a brake thermal efficiency above 50% (50.26%) in 2020 [59]. The main improvements declared are: 1) Increase combustion speed by 30% by optimizing the architecture of the air passage, fuel injection, and combustion chamber shape. 2) The engine's general structure is strengthened to withstand high peak firing pressure. 3) Adapting

the turbocharger to the demand for exhaust gas recirculation while maintaining turbine efficiency according to rules and norms and obtaining a 1% increase in brake thermal efficiency. 4) A subzone lubrication method was created based on the various characteristics of the system's friction pairings to minimize overall friction by 20%. 5) Develop a succession of more precise control predictive models to advance control technology.

Despite the efficiency being improved to around 54% BTE (Figure 2-8), the emissions of NO<sub>x</sub> and particle matter (PM, mainly soot) are still a challenging issue. Once the combustion is established in a Diesel engine, the injected fuel is progressively vaporized and mixed by diffusion from the rich fuel zone near the spray to the leaner mixture near the thin reaction sheet. This rich zone is prone to agglomerate polycyclic aromatic compounds. Therefore, initiating the soot formation (see Figure 2-7). On the outer side of the flame, the high temperature with the excess oxygen and nitrogen environment gives space to the thermal NO<sub>x</sub> formation mechanism, which consists of the decomposition of N<sub>2</sub> by unimolecular oxygen and its subsequent reactions, producing nitrogen oxides. These emissions are the primary concern in Diesel engines and are necessary to be decreased. Despite the intensive research on reducing the conventional diesel combustion hazardous products, it was concluded that soot and NO<sub>x</sub> emissions coexist, and strategies to reduce one of them penalize the other, called the NO<sub>x</sub>-soot trade-off. In this sense, the technological answer to the current normative was the introduction of after-treatment systems to reduce the emissions levels after leaving the combustion chamber. Nonetheless, these devices have increased the vehicle price and the total cost of ownership (TCO).

Figure 2-9 shows the Volvo D13 Euro VI engine, similar to the engine used in this Thesis. The engine is an in-line six-cylinder engine with a Diesel Oxidation Catalyst to reduce CO and HC, catalytic exhaust treatment (SCR) to control NO<sub>x</sub> emissions, and a diesel particulate filter (DPF). Exhaust gas recirculation (EGR) is also used. A seven injector (one additional fuel injection in the exhaust pipe to the six injectors of the cylinders) is added to increase the ATS temperature during a cold start. This device inject fuel in

the exhaust pipe, after the turbine outlet, to warm up the engine during cold start. The combustion of this fuel is only to increase of the temperature of the exhaust gases. Therefore, no work is taken from this fuel, represent a great waste of energy for the system.

In addition, NO<sub>x</sub> sensors, temperature sensors, and PM sensors are often used for ATS management. The SCR requires the use of Urea diluted in water (AdBlue) for the NO<sub>x</sub> conversion by the ammonia reaction. This implies an extra tank as well as an injector (eighth ICE injector) and control system. In addition, AdBlue increases the cost of operation. It is estimated that 5% of AdBlue [60] (0.60 €/l<sub>AdBlue</sub> Spanish market) per liter of diesel consumed (2.00 €/l<sub>Diesel</sub> Spanish market). This adds to a total operation cost of 2.03 €/l<sub>Diesel</sub>. Lastly, Ammonia Slip Catalyst (ASC) after the SCR is required to meet the NH<sub>3</sub> limits of Euro legislation. This ammonia is a residual from the AdBlue operation. Due to the dynamic driving cycle, recognizable amounts of NH<sub>3</sub> leave the SCR due to not completing the conversion.

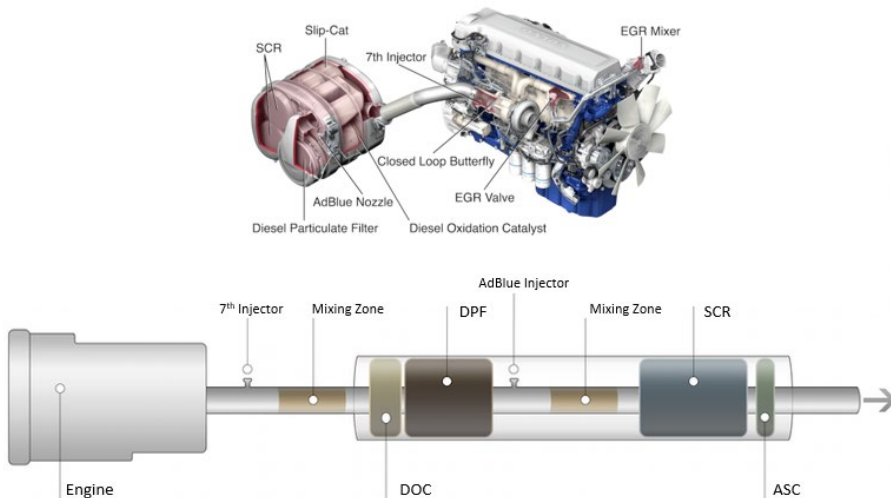


Figure 2-9. Example of an ATS for EU VI in Heavy-Duty: Volvo D13K EUVI. Adapted from [61].

Despite ATS being an effective way to reduce tailpipe emissions, there are two main concerns. 1) The differences between homologation emissions and real driving emissions. 2) The future emissions legislation, for example, the EU VII in Europe. The first is related to the widely known Dieselgate. A German automaker used false ECU control to detect dyno testing and used a lower emissions calibration, which later was not used under real driving conditions. This impacted all Diesel engines directly and in Light-Duty, provoking a massive ban of this type of ICE for that application. Customers and manufacturers shifted to gasoline ICEs or alternative propulsion systems (Gasoline-Hybrid or pure BEV).

For HD vehicles, this was not the case because another mature alternative does not yet exist for the application. Betegari et al. [62] studied the behavior of different trucks in real driving conditions. The vehicle was a Euro V truck compliant with 16 tons. The NO<sub>x</sub> emission coefficient, defined as the ratio of real road NO<sub>x</sub> emission to test bench emission, shows that the emissions were four times higher in city driving cycles. For interurban cycles, the coefficient was three, and for highway cycles, two times the chassis dyno tests. The improvement in highway settings is due to relatively higher exhaust temperature. This allows for maintaining a high temperature in the after-treatment system (>150°C). Therefore, the conversion efficiency of HC, CO, NO<sub>x</sub>, and soot is also high. An alternative to reduce pollutant emissions without complex ATS is controlling the combustion process using new combustion concepts, aiming at the active reduction of the combustion pollutant while maintaining similar efficiency levels to those found in CDC. This topic will be addressed in detail in the following subsection.

Before passing on future technology opportunities, it is important to describe the current electrified powertrain available. Customers can now purchase pure electric trucks. MAN, Volvo, Mercedes Benz, and others have started series production in the European market. Battery electric powertrains are one of the most energy-efficient human and cargo transportation modes. The difference between the efficiency of conventional and electric powertrains is more than double, as shown in Table 2-1. In



addition, the tailpipe emissions are zero with the electric powertrain. There seems to be no doubt that pure electric powertrains are the best option from this perspective. However, the ultra-low emission of CO<sub>2</sub> of this type of powertrain is not well demonstrated in all conditions.

*Table 2-1. Drivetrain efficiency of current powertrains in the market.  
Adapted from*

Efficiency	Diesel ICE	BEV
AC/DC rectification	-	95%
Battery charging	-	95%
DC/AC inversion	-	95%
Motor Operation	39% to 48%	87% to 95%
Transmission	95%	98%
Total Drivetrain	37% to 45%	73% to 80%

The main problems that can be identified to justify the current low amount of BEV HD trucks on the streets (in 2020, only 7,400 BEVs trucks were sold worldwide [63], 90% in China) are related to the battery: energy density, cost, safety, charging infrastructure and time. The energy density directly impacts the vehicle weight. For trucks delivering goods, this means reducing the cargo mass capacity to transport and lower energy efficiency. Even after accounting for the weight of the traditional engine and after-treatment systems, increasing battery capacity increases the per-mile energy requirement. It can lower payload capacity, as indicated in *Figure 2-10*. For a more extended range, the mass of the batteries reduces the possible cargo capacity, increasing load-specific fuel consumption. For trucks between 600 kWh to 900 kWh, the battery weight is the third most significant component of overall vehicle weight. For these three cases, the vehicle lost 4.5 to 6.5 tons compared with the Diesel non-hybrid, 11 to 16% of the cargo mass. For a vehicle that is designed for the transportation of goods, this means a significant disadvantage. This can be minimized in the future with the

development of high-energy-density lithium-ion cells and faster-charging methods.

Light duty vehicles are historically limited to a peak C-rate of around 1.5, which enables fast charging to 80% of a nominal full charge in 40 min. For larger battery packs as the case of Heavy-Duty, C-rates and charging times can be the same, but the power needed scales linearly with the size of the battery pack. This means that in order for BEV trucks to mimic charging patterns from personal vehicles, the limiting factors are the high-power levels and development and deployment of such chargers and not Li-ion battery technology per se. Conceptually, a straightforward method to achieve high-power charging for heavy trucks (i.e., a peak of one MW or more per truck) could be to use multiple parallel 150- or 350-kW chargers. It is, however, important to note that these values could be optimistic as frequent fast charging causes high degradation.

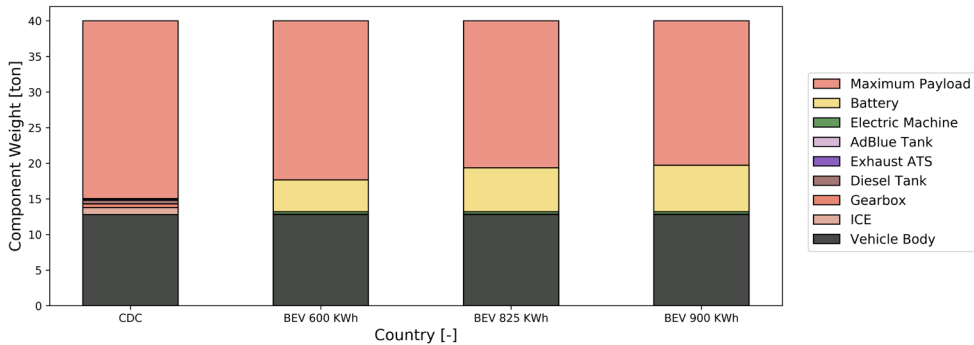


Figure 2-10. Weight breakdown of main truck components for diesel and battery-electric trucks with different battery sizes. Adapted from [64].

An alternative is the use of small batteries. However, this will directly impact the vehicle range. Figure 2-11 shows the current vehicle range for different types of BEVs. For Medium-Duty, the average is around 255 km, and for Heavy-Duty, 418 km, while a Diesel non-hybrid can easily achieve 2,000 km. In addition, the charging time can overpass 5 hours, and the

charging infrastructure is scarce for the number of vehicles and routes. This makes BEV constraints far from acceptable for customers.

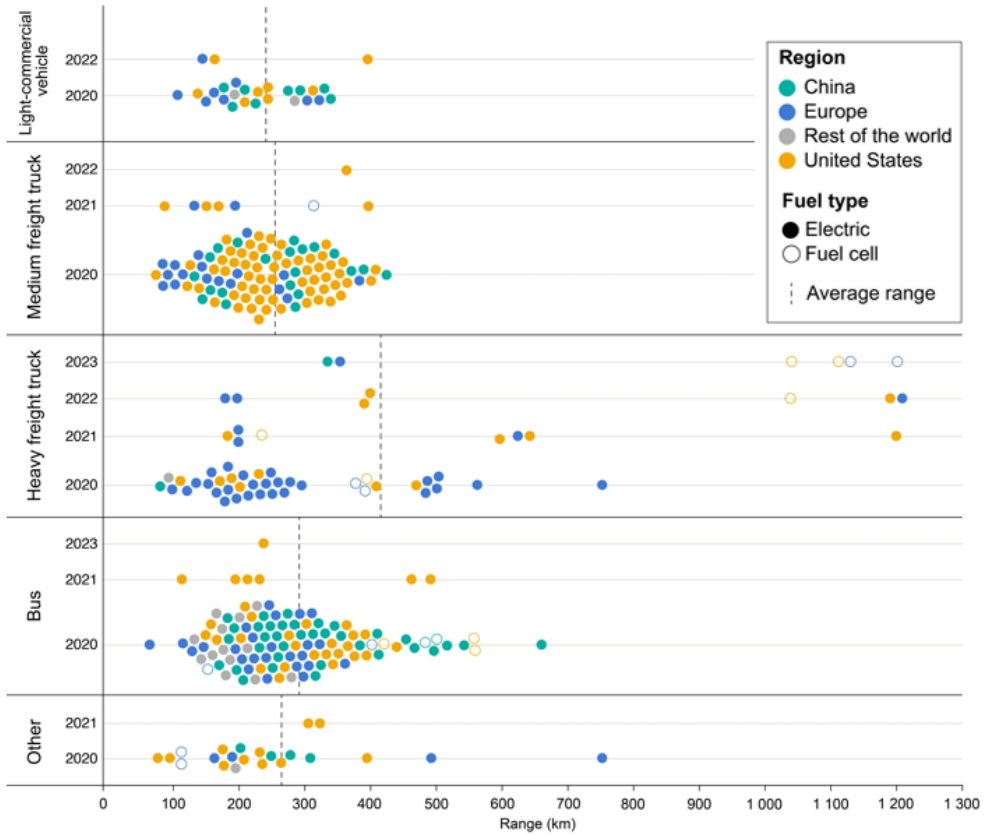


Figure 2-11. The driving range of different BEVs is divided by type of vehicle and world region. Source [63].

The cost of ownership is higher than for conventional powertrains. The battery pack change due to the aging effect can be a limitation for customers preventing them from picking BEV trucks. The main cost of the battery pack is the cathode which is 51% of the total cost, followed by the manufacturing 24%, anode 12%, separator 7%, Electrolyte 4%, and battery case 3%. In 2021 the cost hit a minimum of 101 US\$/kWh per cell and 132 US\$/kWh the pack (see Figure 1-8). However, the current market is not segmented. China has

80% of the production, and the price of the materials is increasing due to the higher demand without further extractions investments.

Due to the size of the battery required, a hybrid Medium- and Heavy-Duty truck will have a substantially lower up-front cost than a battery-electric similar model. Scania's plug-in hybrid Heavy-Duty distribution truck, for example, has a 7.4kWh battery that costs around US\$977 without the battery management system. In contrast, a similarly sized battery-electric DAF LF has a 222kWh battery that costs US\$29,304. As a battery pack is a cell arrangement, 30 battery packs for an HEV can be made with one BEV battery pack. In addition, battery manufacturing has a high CO<sub>2</sub><sub>eq</sub> associated, which will be 30 times higher than the HEV in the case of BEVs.

The assumption of 1,000 cycles is broadly representative of conservative and slightly older assumptions used in the literature analyzing electric trucks by using Li-ion batteries. 5,000 cycles are broadly representative of an optimistic outlook that considers recent literature on Li-ion batteries. It is important to note that the capital cost of the battery is not only determined by the battery cost per kWh but also by the lifetime of batteries. The 200% increase between 1,000 cycles and 3,000 cycles is very pronounced and results in a very sharp cost reduction that is more important than the 300 to 200 USD/kWh 50% price reduction.

Moreover, to define a BEV as a “green” technology, the electricity to charge the batteries needs to come from renewable or low emission sources. To put things in perspective, a European home's average yearly electricity consumption is 3.5 MWh. A truck of 300 kWh of battery size means around 12 charging times or a travel distance of 2431 km (average electric consumption of 1.44 kWh/km). The energy consumption per truck (1.44 kWh/km) can be coupled with the number of trucks in the EU (4.5 million) and the average mileage (50,000 km/year) to get an order of magnitude of the total electricity necessary to charge a European fleet of long-haul BETs. This would amount to 324 TWh or a little over 10% of the EU's total generation of 3000 TWh in 2019. Only 1000 TWh is from renewable

electricity in the European Union (around 33% of total consumption). This is one of the examples of why this type of vehicle is not zero-emissions.

## **2.4 Advanced combustion modes for emission reduction**

Traditionally, many pollutant formation control strategies have been deployed with varying degrees of success for controlling the NO<sub>x</sub> and the soot emissions in Diesel Compression Engines . Examples are optimized fuel injection strategies and high fuel injection pressures [65], exhaust gas recirculation (EGR) [66], increased in-cylinder turbulence (increased in-cylinder motion and turbocharging) [67], and redesign of the combustion chamber and piston geometry (piston waves) [68]. However, these methods struggle primarily because of the intrinsic trade-off between the soot and the NO<sub>x</sub> in diesel engines [69], where reducing one pollutant increases the other.

Primarily, NO<sub>x</sub> is formed through a thermal mechanism (although other mechanisms also exist and can be prevalent during some combustion modes) where nitrogen and oxygen in the in-cylinder mixture combine at high combustion temperatures and enough residence time [69]. Because of this, reducing the combustion temperatures and duration can reduce NO<sub>x</sub> [70]. Nonetheless, this has a counter effect on soot, as the temperatures and residence times are not high enough to burn off and reduce soot particles [71]. Advanced combustion strategies that overcome the soot-NO<sub>x</sub> trade-off have been developed over time and can also integrate the use of more advanced fuels with properties to mitigate these emissions. In particular, Low-Temperature Combustion (LTC) strategies have been developed, which improve the fuel-to-work conversion efficiency while providing low soot and NO<sub>x</sub> emissions [72].

LTC modes cover several advanced combustion strategies, including homogeneous charge compression ignition (HCCI) [73], partially premixed charge compression ignition (PPCCI) [74], premixed charge compression

ignition (PCCI) [75], and Reactivity Controlled Compression Ignition (RCCI) [76]. In all LTC modes, relatively lower in-cylinder combustion temperatures are typical, which is the main reason for extremely low NO<sub>x</sub> emissions. In addition, the reduction of the equivalent ratio ( $\phi$ ) helps to avoid the zone of soot formation [72].

The HCCI was one of the first LTC concepts to be developed [77]. Summarizing, at the end of the compression stroke, a homogenous (well premixed) air-fuel mixture auto-ignites without the use of a spark. The combustion in HCCI engines occurs in numerous areas due to the mixture's auto-ignition when it reaches its chemical activation energy [78]. The combustion is spontaneous, with no apparent diffusion flame or flame front propagation. As pressure and temperature rise during the compression stroke, hotspots are caused by synchronous auto-ignition across the whole cylinder. This prevents NO<sub>x</sub> generation by removing the high-temperature flame front and keeping local temperatures low. Soot development is also avoided by the cylinder's overall homogenous lean mixture [79]. As a result, the global composition of the air-fuel combination and the spatial in-cylinder temperature regulate ignition in HCCI engines. The idea for it comes from combining the finest qualities of both premixed mixture SI engines and compression ignition diesel engines.

Controlling the HCCI's auto-ignition over the engine's whole operating load and speed conditions is quite challenging [80]. Mixture homogeneity, inlet fuel and air temperatures, equivalence ratio, level of turbulence, fuel composition, and fuel oxidation kinetics at lower temperatures affect the quality of HCCI combustion and ignition delay [81]. Extending the operational load range, managing auto-ignition, knocking tendency, and more significant HC and CO emissions are the key obstacles for HCCI engines that prevent them from being commercialized. Another significant problem with the HCCI is the short combustion period, which results in a faster rate of pressure rise [82]. Though a high PRR improves thermal efficiency, it is detrimental to engine components and causes noise, vibration, and harshness (NVH) issues.

In order to manage the start of combustion and burn duration, researchers developed a new form of low-temperature combustion technique known as premixed charge compression ignition (PCCI) combustion, which evolved from HCCI combustion. The charges are diluted with a higher rate of EGR to lengthen the ignition delay and increase mixing time in this technique [83]. As a result, fuel-rich pockets and high-temperature regions inside the cylinder are avoided, and the premixed combustion phase is achieved, resulting in lower NO<sub>x</sub> and soot emissions [84]. At low loads, the higher auto-ignition properties of diesel fuel allow PCCI combustion without severe issues [85]. However, its strong reactivity makes it difficult to manage combustion phasing at larger loads and causes excessive pressure rise.

A new concept with the intent to solve the reactivity problems appears in the dual-fuel combustion mode [86]. The idea is to have a combustion chamber mixture with better auto-ignition characteristics. A high reactivity fuel, such as Diesel, and low reactivity fuel, like gasoline, can give this advantage [87]. This concept of controlling the in-cylinder fuel mixture and temperature is called RCCI [88]. A representation of the injection strategies of the different LTC concepts is shown in *Figure 2.12*.

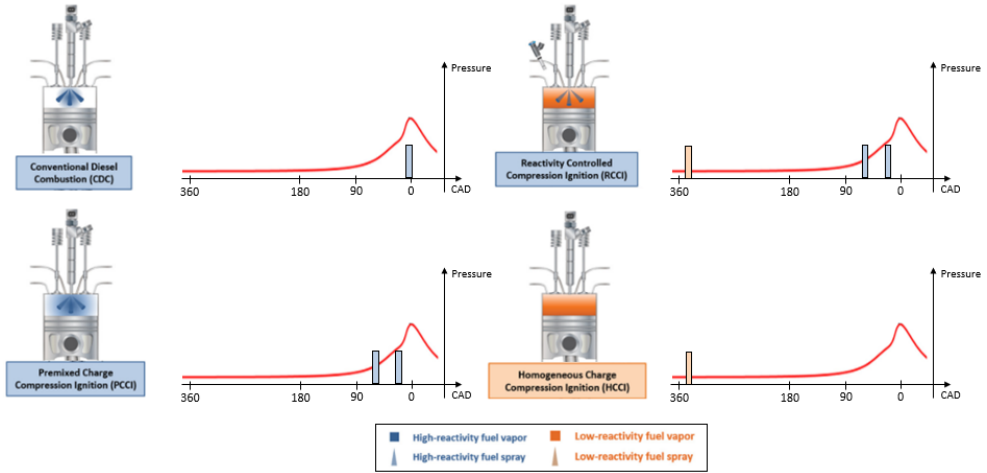


Figure 2.12. Comparison of different advanced combustion modes. Adapted from [89].

Another path explored for more than 20 years is the use of oxygenated fuels to reach practically soot-free emissions [90–92]. However, the increase in the fuel’s oxygen content (as with some alcohols) can increase NO<sub>x</sub> emissions and peak pressures if strategies that address those issues are not utilized [93]. As their characteristic properties differ from commercially available fossil fuels, dedicated calibrations and strategies also need to be developed for other alternative fuels. However, research has shown that combining both the LTC and alternative fuels in the same system can benefit both emissions and engine efficiency. The following two sub-sections summarize the work developed until now in the RCCI and synthetic fuels and the challenges that need to be tackled.

### 2.4.1 RCCI: Reactivity Controlled Compression Ignition

A new concept appeared early in 2006, which uses a dual-fuel combustion mode intending to control the combustion by controlling the in-cylinder mixture reactivity. The reactivity of the fuel is understood as the



auto-ignition characteristics. This combustion concept was named Reactivity Controlled Compression Ignition.

The concept starts with the works of Inagaki et al. [94], and Bessonette et al. [95] as modifications of PCCI and HCCI, respectively. Both works used a low reactivity fuel (gasoline) injected at the port and a high reactivity fuel injected early (diesel). By varying the gasoline and diesel fuel volumes over a wide range of engine load and speed, in-cylinder fuel blending aids in achieving the required fuel reactivity. As a result, it has been proven that managing the fuel blend in terms of spatial stratification of fuel reactivity allows for control of the combustion duration. This mixture stratification is added to the temperature stratification as with the HCCI. Similarities between RCCI and HCCI or PCCI are the low temperature in the chamber, the lean combustion zones, and high EGR rates. This allows for achieving ultra-low NO<sub>x</sub> and soot emissions (below Euro 6 for Light-Duty and EU VI for Heavy-Duty).

In RCCI, using two separate fuels by two fuel injectors allows flexibility to adopt different injection strategies depending on the operating conditions. When diesel is injected into a gasoline-air environment, it evaporates, causing non-uniform reactivity stratification in the cylinder, resulting in a shift in combustion behavior. The main characteristics of RCCI combustion are: 1) Low-temperature reactions and cool flames appear similar to conventional diesel combustion promoted by diesel injection, 2) Auto-ignition from the high reactivity zones leads to a higher heat release rate due to an increase in the mass of burnt fuel in this premixed stage, and 3) Previous multiple site combustions leads to multiple propagation flames.

Since its introduction, RCCI combustion has been extensively investigated, as shown in Chapter 1. The different studies have established the basics to realize the benefits of the RCCI mode, such as the dependence on parameters like gasoline fraction, high reactivity fuel injection, and dilution levels. These different parameters allow better control of the combustion onset, where the HRF fuel injection timing can dictate the

combustion start. Moreover, the investigations have demonstrated that the RCCI concept can be successfully implemented on both Light-Duty [96] and Heavy-Duty [47] engine platforms as a part load combustion concept by modifications in the engine injection system as the addition of a port fuel injector, low-pressure pump and a separated fuel tank for the low reactivity fuel.

Splitter et al. [97] have experimentally demonstrated that the RCCI concept can be extended to engine loads as high as 18 bar of IMEP, i.e., full load operation. As opposed to the earlier LTC concepts, RCCI allowed extending the benefits of LTC combustion to high load zones, which have a significant weight on the final emissions for this type of application. In addition, due to the flexibility of the concept, several fuels were tested in the DI port and PFI port. There exists a variety of combinations of low and high reactivity fuels, namely: diesel-ethanol [98], diesel-methanol [99], diesel-butanol [100], and biodiesel-gasoline [101]. Low reactive gaseous fuels, such as alcohol fuels, can also be used as alternative fuels to achieve RCCI combustion. Gaseous fuels have higher octane numbers (above 110) than other low reactive fuels (gasoline is 100), making them an excellent alternative for RCCI combustion. Because of the considerable reactivity difference between diesel and gaseous fuels (because of the higher octane number) allows superior control over the maximum pressure rise rate and peak cylinder temperature with a longer combustion duration [102]. The various low reactivity gaseous fuels, such as natural gas [103], biogas [104], and syngas [105], are used for RCCI combustion.

The Centro de Motores Térmicos (CMT) has extensive experience working with RCCI combustion for Light-Duty and Heavy-Duty applications. Three Ph.D. Thesis were published in this area. J. Monsalve Serrano [106] worked on calibrating a Light-Duty single-cylinder engine (SCE) with injection variation and piston bowl geometry to understand the influence on the RCCI combustion. In addition, ethanol-gasoline blends were tested as an initiative to introduce biofuels to the concept. Lastly, Monsalve did an RCCI operation limit assessment to see the limitation of the concept.

In terms of injection settings, the main diesel injection set at -50 CAD ATDC offers NO<sub>x</sub> levels that are within EURO VI norms in various engine circumstances (GF, EGR, and intake temperature).

Furthermore, the EURO VI NO<sub>x</sub> compliance was linked to the combustion cycle's CA50 position. The combustion phasing values at +5 CAD ATDC, in particular, demonstrated a proper trade-off between engine performance and NO<sub>x</sub> emissions. Two different strategies were tested to modulate the in-cylinder reactivity while providing constant combustion phasing at +5.5 CAD ATDC. First, the effect of EGR and gasoline fraction (GF) on each other was investigated. Later, the simultaneous modulation of the input charge temperature and GF was investigated. Both solutions successfully managed RCCI combustion and showed tremendous promise in reducing combustion losses and increasing thermal efficiency.

The bathtub piston provided greater gross indicated efficiency than the standard geometry in all load ranges. However, according to the testing results with varied piston geometries, its flatter bowl shape resulted in unacceptable soot emissions when using single injection techniques at high load. Ethanol-gasoline mixes (E10-95, E10-98, and E20-95), which could be available shortly due to present rules, were evaluated. The results showed that the three intermediate mixes could meet the Euro VI NO<sub>x</sub> standard with ultra-low soot emissions and acceptable PRR from low to high load, demonstrating RCCI's potential as a flexible-fuel concept. Instead of the 17.5:1 original CDC compression ratio, a rigorous experimental technique considering the engine's emissions restrictions and mechanical constraints was created and applied utilizing two different compression ratios, 14.4:1 and 11:1. For the high and low compression ratios, the maximum operable load was around 50% and 70%, respectively. Some technological issues were found, such as low exhaust temperatures and the high-performance demands placed on the turbocharger and EGR systems. As a result, it was determined that just operating in the RCCI regime could not cover the entire engine map.

The second work was developed by V. Boronat [107], where a Dual-Mode Dual-Fuel concept was presented to tackle the previous constrain. The DMDF incorporates the benefits of RCCI combustion at low and medium engine loads, while when the pressure gradients limit, it progressively switches the operating parameters to obtain a mixed controlled dual-fuel combustion at high engine loads. The work was developed in a Medium-Duty SCE engine. Considering the previous conclusions from J. Monsalve [106], modifications of the combustion process were suggested according to the different restrictions found at each operating zone (low, medium, or high load). Boronat [107] has evaluated the benefits that could be achieved in modifying the transition zone locations by using different compression ratios. The bowls templates were based on the CFD optimized pistons proposed by [88] and depicted in *Figure 2-13*. As it can be seen, compression ratios of 15.3:1 and 12.75:1 were achieved by removing the material from the piston bowl, moving from a reentrant bowl (original piston) to a non-reentrant (15.3:1) and finally to a bathtub bowl (12.75:1). The details of each bowl template are presented in *Table 2-2*.

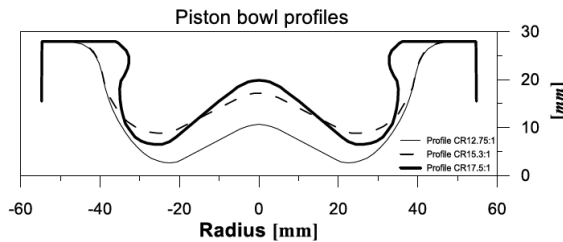


*Figure 2-13. Optimized piston bowl templates to reduce the compression ratio while maximizing gross indicated efficiency. Adapted from [107].*

Table 2-2. Characteristics of the original piston bowl template as well as the two optimized bowls for CR 15:3 and 12.75.

Production bowl (CR 17.5:1)	Non re-entrant bowl (CR 15.3:1)	Bathtub bowl (CR 12.75:1)
Area/Volume: 8.18 cm <sup>2</sup> /63.51 cm <sup>3</sup> =0.128	Area/Volume: 9.05 cm <sup>2</sup> /77.8 cm <sup>3</sup> =0.116	Area/Volume: 9.78 cm <sup>2</sup> /97.8 cm <sup>3</sup> =0.1
Depth: 20.8 mm	Depth: 20.8 mm	Depth: 24.35 mm
Min. distance to oil gallery	Min. distance to oil gallery: 5.35 mm >3.9 mm (used in bathtub design)	Min. distance to oil gallery: 4.5 mm >3.9 mm (used in bathtub design)
In distance in center: 19.3 mm	In distance in center: 16.79 mm	In distance in center: 10.37 mm

Figure 2-13 depicts a conceptual description of the DMDF concept. As it is shown, the concept is composed of two main combustion modes, a fully premixed and dual-mode diffusive combustion. Between both, a highly premixed zone is included, resulting from the progressive switch between both combustion modes (premixed and diffusive). Different constraints in terms of mechanical abuse and NO<sub>x</sub> and soot emissions were set prior to the calibration. The information about each one of these constraints can be visualized on the left-hand side of Figure 2-13.

As it is depicted, the mechanical stress was limited by setting the maximum in-cylinder pressure and PRR to 190 bar and 15 bar/CAD, respectively. Moreover, the emissions constraints were set as NO<sub>x</sub><0.4 g/kWh and soot <0.01 g/kWh. These constraints could be realized from low to medium load by implementing conventional RCCI combustion. Nonetheless, as the load was increased, the pressure gradients started to be a limitation in extending the RCCI mode. In this sense, modifications of the injection settings were proposed, including decreasing the relevance of the energy provided by the gasoline and shifting the diesel injections towards the top dead center, as it is shown in Figure 2-13.

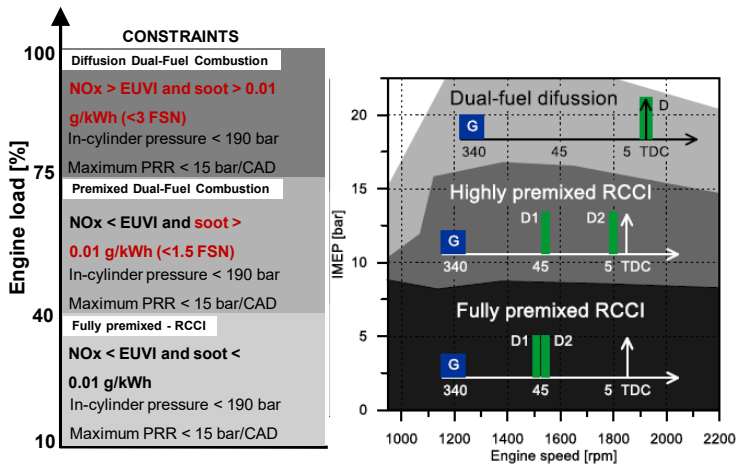


Figure 2-14. Conceptual description of the Dual-Mode Dual-Fuel combustion and the respective constraints that are generally used for each one of the operating zones. Source [107].

Although this strategy effectively reduces the pressure gradients, the increase of the diesel quantity with delayed SOIs enhances the formation of rich zones, which increases the soot formation. In this sense, this highly premixed zone requires a relaxation of the soot constraints to values up to 1.5 FSN. In the last part of the operating map, even highly premixed strategies result in excessive mechanical requirements. Then, a dual fuel diffusive combustion mode was proposed as an alternative to extend the heat release rate and smooth the combustion process. This diffusive combustion is enabled by an early gasoline injection (340 CAD bTDC) coupled with a single diesel injection near the TDC. Therefore, once the diesel is injected, the high temperature and pressure found in the combustion chamber allow a slight ignition delay, which initiates the combustion of the gasoline that was fully premixed in a highly EGR diluted environment.

The diesel injection remains once the combustion is established, providing the energy using a well-controlled conventional diffusive combustion. As the diffusive combustion is recalled, the drawbacks of its usage are again introduced. Under these conditions, both NOx and soot

emissions must be relaxed to 2 g/kWh and 3 FSN, respectively. These values are still much lower than those verified at conventional diesel combustion despite the relaxation. The gasoline provides part of the energy, and the fuel premixing is maximized to avoid soot formation. In addition, the high levels of EGR at low load, an order of magnitude higher than those from CDC, allows inhibiting by a certain degree the formation of NO<sub>x</sub> emissions by the Zeldovich mechanism.

V. Boronat [107] remarked that the width of the zones inside the operating map is highly dependent on the engine compression ratio and the fuel characteristics. As the RCCI combustion and most of the transition zone are still kinetically controlled combustion, the variation of the in-cylinder state parameters and the fuel reactivity would impact the development of the combustion process. V. Boronat [107] has evaluated the benefits of modifying the transition zone locations by using different compression ratios (15.3:1 and 12.75:1). The results of both compression ratios are presented as absolute difference maps considering the percentage variation for each parameter as CR15.3-CR12.75. This means that positive values indicate a higher value for CR 15.3, while a negative value means the opposite. As demonstrated in Figure 2-15, it was concluded that using a lower compression ratio has a negative impact on the gross indicated efficiency. In general, CR15.3 delivered higher efficiencies (2-4%) for most of the engine map, except for isolated conditions at high load operation at low engine speeds.

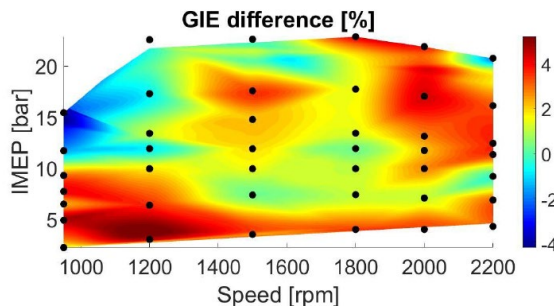


Figure 2-15. Gross indicated efficiency percentage difference between compression ratio of 15.3:1 and CR 12.75:1. Source [107].

V. Boronat [107] has also assessed the impact of the compression ratio modification on the different regulated emissions. It was concluded that a higher compression ratio demands an early transition to the dual-fuel diffusive combustion. Consequently, both NO<sub>x</sub> emissions are worsened at high loads, exceeding values of 1g/kWh (NO<sub>x</sub>) and 1 FSN (soot) in a vast part of the operating map. These results suggested that higher compression ratios should require a dedicated after-treatment system since the use of these higher engine loads could have a significant weight during normative evaluations.

With all the knowledge of the previous work, R. Lago Sari [108] developed his Ph.D. Thesis on a multi-cylinder 6L engine with the same characteristics of the SCE of V. Boronat [107]. The concept of DMDF was applied by doing a complete map calibration with Diesel-Gasoline and CR 12.75:1. Moreover, the impact of the combustion concept on the after-treatment performance was carried out to identify possible hurdles of the concept on the DOC and DPF performance. Using only HP EGR to achieve the desired dilution levels promoted a lack of energy in the turbine, requiring an excessively closed VGT, which increased the pumping losses. In this sense, the EGR was split in both LP and HP EGR routes.

Nonetheless, the use of LP EGR has increased the amount of mass flowing through the compressor, increasing its temperatures up to limiting levels. In this sense, the system could not deliver both the oxygen and EGR required to achieve the desired combustion process. Consequently, issues with pressure gradients and partial soot oxidation have appeared, requiring relaxing the emission constraints. This situation worsened as the engine load approached full load operation. Under these conditions, it was challenging to combine a setting that could provide the same power output while minimizing fuel consumption with emission levels below those from the EUVI mandates. The final calibration maps are presented in *Figure 2-15*.



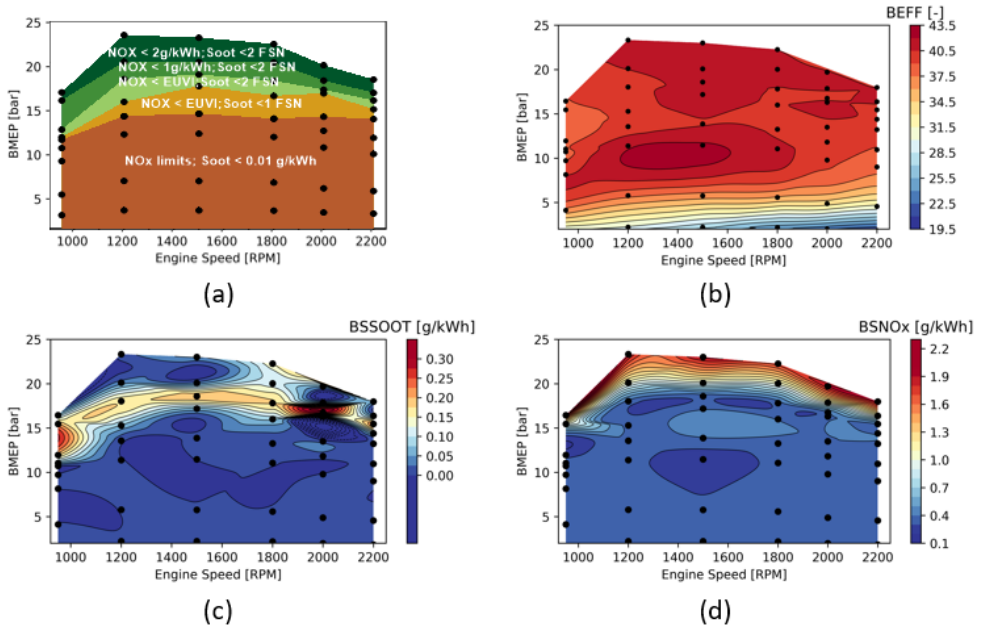


Figure 2-16. Maps of the DMDF concept in a Multi-Cylinder 8L engine in terms of a) Emission constraints, b) Brake Thermal Efficiency, c) Brake specific NOx, and d) Brake specific soot. Adapted from [108].

R. Lago [108] work also assessed the impact of DMDF on the stock ATS. Steady-state evaluations were used to assess the impact of the boundary conditions on the conversion efficiency of CO and HC in the DOC. From this analysis, it was possible to identify that low load and low engine speed conditions are the most challenging points in attaining light-off operation due to the low exhaust temperature and significant concentration of unburned products. As the engine load was increased towards medium load, the higher exhaust temperatures enabled a proper conversion efficiency, allowing tailpipe emissions for both HC and CO to be lower than the normative limits.

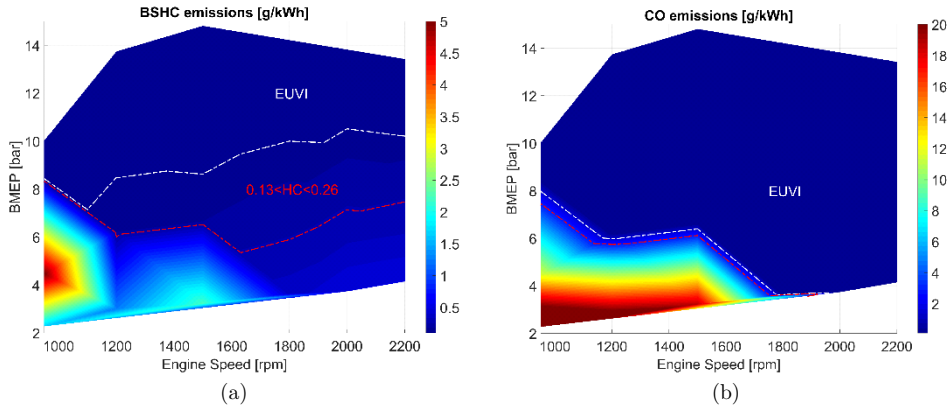


Figure 2-17. Tailpipe emissions (after DOC) of a) Unburned hydrocarbons and (b) Carbon monoxide. Source [108].

Due to the high NO<sub>x</sub> and particle emissions at high load, the DPF was also assessed by studying passive and active regeneration. The passive regeneration was studied using monitoring the ratio of NO<sub>2</sub>/NO<sub>x</sub> before and after the DPF. The main focus was to identify any consumption of this specie by reacting with the soot in the particulate filter. The results demonstrated that no passive regeneration takes place. By contrast, the active regeneration evaluation has demonstrated that the DMDF can provide conditions at the DPF inlet suitable for the active regeneration process. It was identified that the conversion of the unburned products on the oxidation catalyst was a fundamental process to realizing proper soot oxidation in DPF. In this sense, it was possible to conclude that using the stock DOC and DPF is an alternative to assure EUVI-compliant HC, CO, and soot emissions for the proposed calibration.

Lastly, R. Lago [108] uses numerical simulation with a non-hybrid powertrain to understand the compliment of EU VI in the WHVC. The results show that with 50% cargo mass, it is possible to achieve EUVI limits in all pollutant emissions. This means that the DMDF concept can avoid using an SCR, reducing the operational costs with urea while solving the issues of HC, CO, and DPF with well-established after-treatment devices. It

was remarked by R. Lago [108] that the main drawback of the concept is the impossibility of reducing the CO<sub>2</sub> footprint using conventional fuels and powertrains.

### 2.4.2 Alternative fuels for compression ignition engines

Carbon neutrality, or the goal of achieving a net-zero state, is the balance between lowering carbon dioxide emissions as much as feasible while also eliminating any remaining carbon dioxide from the environment. Synthetic fuels are circular hydrogen carriers that use hydrogen as a vector form of energy that may be carried and stored more safely than hydrogen as a single fuel source. Furthermore, rather than developing a wholly new engine, some synthetic fuels require minor modifications to current engines (such as replacing the fuel tank and injectors). Dimethyl ether (DME), oxymethylene ether (OMEx), Fischer-Tropsch (FT) are some examples.

The liquefied gas DME has the molecular formula CH<sub>3</sub>OCH<sub>3</sub>. Due to lower flame temperatures, using DME as a diesel alternative reduces NO<sub>x</sub> emission significantly compared to conventional diesel engines. DME combustion also creates far less particulate matter. The absence of C-C bonds is the cause of ultra-low soot particle emission. Another advantage of DME is the higher cetane number and lower boiling point than diesel. This allows lower auto-ignition temperature and faster vaporization leading to a reduced ignition delay and good cold-starting properties [109]. However, because of DME's lower heating value (LHV) in contrast to diesel, the equivalent fuel volume of DME to diesel is 1.8x that of diesel (m<sup>3</sup>/m<sup>3</sup>) [110]. Larger fuel tanks are required, and these fuel tanks must be equipped to handle gaseous fuel to meet the exact distance requirements.

OMEx is an alternative to DME with a formulation of CH<sub>3</sub>O-(CH<sub>2</sub>O)<sub>x</sub>-CH<sub>3</sub> with x ranging from 1 to 8. The oligomer length of the OME influences the physical qualities of the fuel. The fuel behaves similarly to LPG but has physical, chemical, and fuel qualities similar to ordinary diesel [111] due to

its extended length and higher boiling point when compared to DME. The similarities allow using of conventional diesel supply structures [112]. Therefore, OMEx is considered a drop-in fuel. OMEx also has no C-C bonds and presents oxygen in the molecule, so it has the same potential as DME to reduce soot emissions. Because this fuel has a lower heating value than diesel, it requires more volume to achieve the same brake power. This problem is mitigated by the rise in density as the oligomer length increases. For fuel equivalence, the fuel volume required is 1.7x that of diesel ( $\text{m}^3/\text{m}^3$ ). The main properties of the different OME are presented in *Table 2-2*.

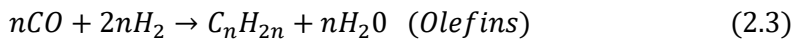
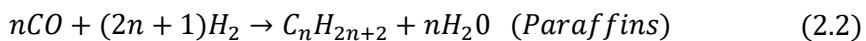
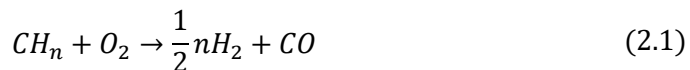
*Table 2-3. Physical and chemical properties of OMEx with  $n=1-6$ . Adapted from [112].*

Property	OME <sub>1</sub>	OME <sub>2</sub>	OME <sub>3</sub>	OME <sub>4</sub>	OME <sub>5</sub>	OME <sub>6</sub>
Chemical Formula	C <sub>3</sub> H <sub>8</sub> O <sub>2</sub>	C <sub>4</sub> H <sub>10</sub> O <sub>3</sub>	C <sub>5</sub> H <sub>12</sub> O <sub>4</sub>	C <sub>6</sub> H <sub>14</sub> O <sub>5</sub>	C <sub>7</sub> H <sub>18</sub> O <sub>6</sub>	C <sub>8</sub> H <sub>18</sub> O <sub>7</sub>
Oxygen content [wt%]	42.1	45.2	47.0	48.1	48.9	49.5
LHV [MJ/kg]	23.3	21.0	19.6	19.0	18.5	17.7
Density <sub>@15C</sub> [kg/dm <sup>3</sup> ]	0.86	0.98	1.03	1.07	1.11	1.14
Melting point [°C]	-105	-70	-43	-10	18	38
Boiling point [°C]	42	105	156	202	242	273
Flash point [°C]	-32	12	54	88	115	-
Cetane Number [-]	28	68	72	84	93	-

Various studies have demonstrated that combining OMEx with diesel reduces particulate matter (PM) and particulate number (PN) emissions, allowing for higher EGR rates to minimize nitrogen oxide (NO<sub>x</sub>) emissions. In the European Transient Cycle (ETC), operating a series of Heavy-Duty engines fueled with 20 volumetric percent of high boiling 1:1 mixtures of tri and tetraoxy-methylene dimethyl ether (OME  $n=3,4$ ) reduces PN emissions by 40% and PM emissions by 50% [113]. When OME is added to diesel fuel, particle size measurements show that the distribution shifts to smaller particles. The indicated efficiency becomes comparable to or slightly better than diesel operation [114].

Lastly, Fischer–Tropsch (FT) diesel is made by condensing syngas ( $\text{CO}/\text{H}_2$ ) and post-processing to produce a synthetic fuel with a long chain hydrocarbon structure comparable to traditional diesel. The high cetane number of fuels produced by the F-T method also can reduce the  $\text{NO}_x/\text{PM}$  trade-off experienced in traditional diesel engines.

The raw material can either be natural gas (the final liquid fuel being Gas-to-Liquid), coal (Coal-to-liquid) or residual biomass (Biomass-to-liquid) [115]. Gas-to-Liquid is already produced commercially and diesel fuels blended FT are available in several European countries [116]. A number of new large-scale Gas-to-Liquid production plants is currently being planned or under construction, resulting in a potential total Gas-to-Liquid diesel fuel production of significant volumes within the next decade. Franz Fischer and Hans Tropsch developed the process that bears their names in the 1920's [117]. The production of diesel fuels using the FT process is a set of chemical reactions in the presence of a catalyst [115]. Synthesis Gas (Syngas) Formation (Equation 2.1) and FT Synthesis Process (Equation 2.2 and Equation 2.3).



Synthesis gas can be formed from any carbonaceous material such as natural gas, coal, or biomass. Several reactions are required to obtain the gaseous reactants required for FT catalysis. Reactant gases entering an FT reactor must first be desulfurized to protect the catalysts that are readily

poisoned [118]. The following major sets of reactions are employed to adjust the H<sub>2</sub>/CO ratio with Water-Gas-Shift Reaction (Equation 2.4) and Steam Reforming (Equation 2.5).



The formation of synthesis gas from coal or biomass is called gasification, wherein the feedstock is reacted with steam and oxygen (O<sub>2</sub>). The next step in the FT production process is the conversion of synthesis gas into HC. This begins with H<sub>2</sub> and CO molecules being formed into eCH<sub>2</sub>e alkyl radicals and water in an exothermic reaction. The CH<sub>2</sub> radicals then immediately combine in an iron or cobalt catalytic reaction to make synthetic olefin and/or paraffin HC of various chain-lengths. The selectivity (the amount of desired product obtained per unit consumed reactant) is influenced by parameters such as temperature, H<sub>2</sub>/CO ratio in the feed gas, pressure and the catalyst type. The FT product can be upgraded to high quality diesel fuel through post-processing and any oxygenates formed during the FT process are often removed during this step. Addition of H<sub>2</sub> and a catalyst causes hydrocracking, rupturing long carbon chains into shorter, liquid parts to produce cuts that correspond to a range of conventional refinery products [119]. It is important to note that the distillation range of FT diesel can be customized by FT synthesis conditions and by the distillation cut after synthesis occurs. Therefore, this is not an inherent property of the FT diesel. Ideally, a compression ignition (CI) fuel would be renewable, produce useable power to current diesel standards, run in both existing and newly manufactured engines and require no engine modifications. In addition, its combustion should produce fewer emissions which would enhance the efficiency of exhaust gas after-treatment systems primarily by increasing the availability of active catalytic sites [120]. In a modern diesel engine synthetic fuels can satisfy many of the above ideal fuel requirements.

The exhaust emissions performance of Gas-to-Liquid diesel fuels has been the subject of a growing number of technical publications in recent years. Several researches have investigated the effects of F-T diesel on combustion and emission characteristics in light of these factors. Huang et al. [121] investigated the F-T diesel combustion characteristics in a direct injection diesel engine. The results showed that F-T diesel had a shorter ignition delay, a similar combustion length, and reduced combustion noise than standard diesel fuel. Shi et al. [122] used a diesel engine with a high-pressure common-rail system to explore the impact of F-T diesel on combustion parameters. The results showed a decreased heat release rate peak and a shorter ignition delay and combustion duration.

In the Thesis of R. Lago Sari [108], Diesel, OMEx, and Fischer–Tropsch as HRF and Gasoline as LRF in the DMDF multi-cylinder engine were compared performed. Similar brake thermal efficiency was achieved in the DMDF concept, but the OMEx allows NO<sub>x</sub> and soot reduction at all engine loads (see Figure 2-17). On a Well-to-Wheel (WTW) basis, and considering wind power as the power source, both OMEx and e-FT can provide savings in the CO<sub>2</sub> production and consequent decrease of the CO<sub>2</sub> footprint in the fuel lifecycle. While OMEx can reach almost an average of 20% reduction, e-FT can achieve an average reduction value of 35%.

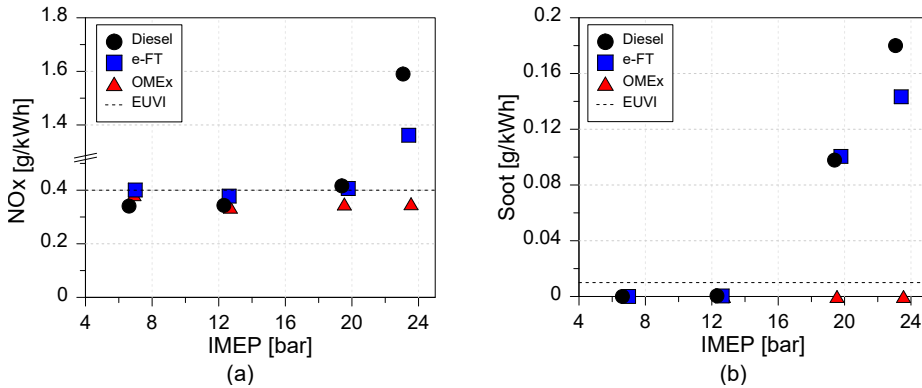


Figure 2-18. Dependence of (a) nitrogen oxides and (b) soot emissions concerning the different engine loads evaluated considering diesel, OME<sub>x</sub>, and e-FT as high reactivity fuels. Source [108].

A new engine calibration was performed considering the diesel replacement by OME<sub>x</sub> as high reactivity fuel [108]. The results are shown in Figure 2-18 for brake thermal efficiency gain and brake-specific NO<sub>x</sub> emissions. While the BTE was similar throughout all the maps, the NO<sub>x</sub> emissions were reduced compared to the Diesel-Gasoline calibration reaching EUVI on all the maps. In addition, soot emissions were negligible for all operating conditions. OME<sub>x</sub>, as a substitute for Diesel, allows removing the SCR and DPF from the ATS. Only the DOC is necessary due to the high HC and CO emissions at the engine out.



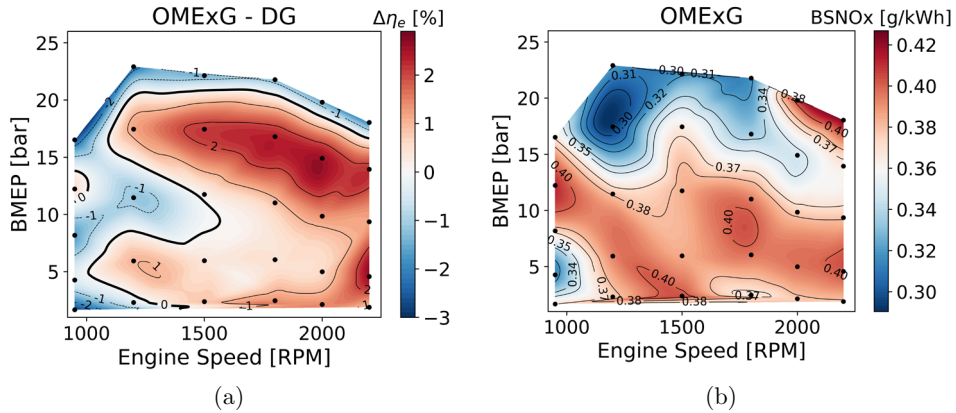


Figure 2-19. Engine maps for (a) brake efficiency difference between OMeX-gasoline and Diesel-Gasoline calibration and (b) Brake Specific NO<sub>x</sub> emissions. Source [108].

## 2.5 Powertrain electrification for CO<sub>2</sub> and battery reduction

This section aims to identify the challenges to the widespread adoption of commercial vehicle electrification technologies and prioritize the research and development gaps that must be filled to accelerate considerable market penetration.

The modern story of vehicle electrification started in 1997 with Toyota launching the first generation of Toyota Prius. The first-generation Prius (NHW10) was available only in Japan. With the second generation of Prius, it began to be sold outside of Japan in the early 2000s. The BEVs arrived in large amounts in the early 2010s with Light-Duty vehicles such as the Nissan Leaf, Tesla Model S, and the BMW i3. China provided the second impulse for vehicle electrification, with a wide range of Light- and Heavy-Duty vehicles. In the HD sector, it went from no electric bus sales to a 30% market share in 2016, making it the e-bus leader. The advantage of city buses is the

reduced necessity for vehicle range and the benefits due to many start-stops and regenerative braking.

There is now a third wave in the market: truck electrification. Electrification is a viable technology path for Heavy-Duty because it can improve freight efficiency, reduce emissions, and improve performance all at the same time. Unlike passenger vehicles, where style and image are essential in deciding between options, trucks and buses are generally driven by business case considerations. The fundamental aspect is functionality. Commercial vehicles must be able to meet employment requirements. After functional requirements, payback, return on investment, and total cost of ownership are frequently used as deciding factors in adopting new vehicle technology. The total cost of ownership (TCO) comprises both the initial investment and ongoing operating expenses.

A wide range of electrified commercial vehicles, from mild-hybrid 48V vehicles to tractor-trailer full BEVs, have been developed and tested at the prototype and commercial levels. Almost all truck manufacturers are testing electric delivery vehicles commercially available in a few years. eCanter and eActros from Daimler, Volvo FL and FE Electric from Volvo, MAN e-TGM from MAN, Renault D Z.E. from Renault, and DAF CF Electric from DAF are some examples. Scania has tested the electric catenary road infrastructure to charge battery e-trucks over long distances, with trials in Germany, Sweden, and Italy. In addition, Daimler and DAF test hydrogen fuel-cell trucks. Therefore, there are various electrified powertrains, and the right choice is not evident. Limited commercial sales of electrified HD trucks show that technology barriers need to be overtaken. *Figure 2-19* shows examples of available commercial and prototype electrified trucks (xEV) in Europe. Table 2-3 summarizes available models in the USA with the range for battery, EM, and fuel converter (ICE or fuel cell) size. The average for BEVs truck is 200 kWh while FCEV 192 kWh, PHEV 81 kWh, and HEV 28 kWh in the USA. The cases taken for Europe have an average of 267 kWh for BEV and 31 kWh for HEV.



Figure 2-20. Examples of electrified HD trucks powertrain available in Europe.

Table 2-4. Main characteristics of Heavy-Duty Vehicles in the USA available in 2020. Adapted from [123].

Truck Class	Type	Available Models	Battery Capacity (kWh)	EM max Power (kW)	Fuel Converter Max Power (kW)
3	BEV	7	48-99	70-160	-
	PHEV	1	14	92	138
4	BEV	10	61-136	20-188	-
	HEV	3	2-60	44-100	156-190
	FCEV	1	28	120	30
5	BEV	12	62-135	91-200	-
	PHEV	2	60	200-343	25-50
	HEV	3	99	36-200	120-157
6	BEV	10	99-200	134-250	-
	FCEV	2	28.4	200	30
	PHEV	1	74	200	180
	HEV	6	2-28	36-120	80-231
7	BEV	10	120-352	103-360	-
	HEV	4	2-28	44-265	150-227
8	BEV	45	88-1000	103-770	-
	FCEV	7	12-700	85-746	30-100
	PHEV	5	80-175	168-300	29.8-239
	HEV	8	2-28	44-265	150-227

### 2.5.1 Hybrid powertrain classification

The powertrain electrification by hybridization is a way to improve the fuel economy of HD vehicles with relatively small electric components compared to a fully electric vehicle. The ability to boost powertrain operating efficiency and convert braking energy into onboard energy storage is the main advantage of hybrid technology over conventional non-hybrid powertrains.

The critical point in hybrid powertrains is the correct energy management between ICE and EM. Between the different hybrid options, two types of classifications can be identified: 1) By percentage of electrification (mainly size of the battery, voltage of the system, and power of the EM) and 2) By type of powertrain architecture (mainly the type of link between the ICE and EM).

By the electrification percentage, the vehicles that can be identified are the Mild-Hybrid (MHEV, also known as 48V hybrid), Full-Hybrid (FHEV), and Plug-in Hybrid (PHEV). A small electric motor and energy storage are paired with a transmission and an internal combustion engine in mild-hybrid (MHEV) powertrains (ICE). The MHEV incorporates a motor-generator attached to the engine for regenerative braking and torque enhancement. This electric machine usually replaces the conventional engine starter motor of the non-hybrid configurations. Therefore, this motor is usually called the Belt Assistant Starter (BAS). The battery size, in general, ranges from 2 kWh to 10 kWh, with lithium-ion cells connected in series to achieve a medium voltage range ( $\approx 48\text{V}$ ). The system electrifies power steering, cooling fans, and the air compressor in some cases. Additionally, the 48V systems (BAS and battery) can be used to supplement turbocharging or supercharging boosting systems. Micro-hybrids, which solely provide stop-start operation, are also included in this powertrain group. The limited low-speed all-electric operation, brief boost, limited auxiliary load during engine-off activities, and limited brake regeneration are the main limitations [124].

An electric drive system capable of generating all or a significant portion of traction power is included in full hybrid powertrains. They can sustain all vehicle traction needs without any help from the ICE for at least half of the vehicle acceleration-speed range. A substantial portion of braking energy can be recuperated in the energy storage system due to the larger size of the components compared to MHEV. The battery storage capacity ranges between 10 kWh to 50 kWh, and the voltage is from 300V to 800V. The attributes of a plug-in hybrid (PHEV) powertrain are similar to those of the previously mentioned hybrid kinds, but they can also be recharged from an

off-board source. Because of this capability, PHEVs typically have greater energy storage systems for all-electric operation.

By powertrain architecture, it is possible to identify: 1) Parallel Hybrid, 2) Series hybrid, 3) Series-Parallel Hybrid. Parallel hybrid allows using the ICE and EM while delivering mechanical power to the shaft that propels the vehicle. Depending on the position of the EM in the powertrain, subtypes of parallel can be identified as P0, P1, P2, P3, and P4. The number increase as the EM is farther from the ICE. The P0 is generally associated with the MHEV because it substitutes the conventional alternator of diesel engines for the BAS.

The P1 locates the EM between the ICE and the transmission in the crankshaft axle. This architecture does not allow disconnecting the EM from the ICE but has higher power than P0. Therefore, more energy can be recovered during braking. The P2 is a similar version of the P1 but with a clutch in the middle to be able to operate in pure electric mode. This is the most used version for HD vehicles due to the flexibility of operation. P2 is also named parallel pre-transmission because the EM is located before the vehicle's transmission.

The following case is the P3, also named pos-transmission. The EM is located between the transmission and the differential. One advantage of P2 is that it reduces one clutch as a non-hybrid or P1 while performing pure electric drive as P2. However, several reports identify two main disadvantages: 1) The transmission is not used during the purely electric mode, so higher EM is needed, and 2) The vibration of the wheels is absorbed by the EM instead of the transmission giving several problems of reliability. Lastly, P4 is a parallel system where the ICE is traditionally connected two one pair of wheels (as non-hybrid) and the EM to the opposite pair of wheels. *Figure 2-20* shows a schematic of the parallel P1, P2, and P3 architecture.

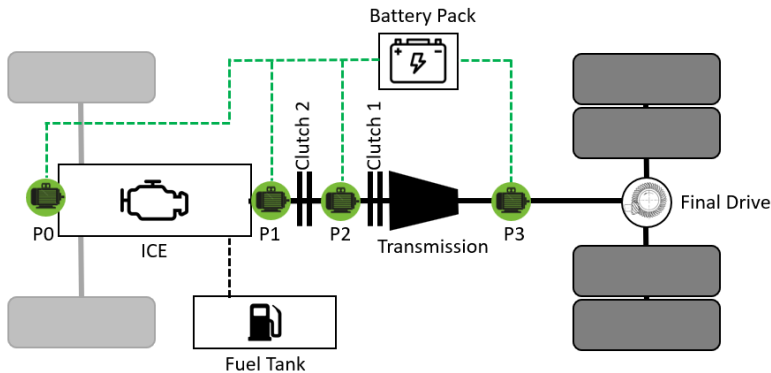


Figure 2-21. Schematic representation of the different Parallel hybrid electric architectures: P0, P1, P2, and P3.

The Series hybrid only mechanically connects the EM (traction motor) and the wheels. The ICE mechanical energy is transformed into electric energy by another EM called a generator and passed to the TM or the battery by cables. The wheels' speeds do not change the operation of the ICE because there is no mechanical connection. It avoids the transitory operation that conventional or parallel hybrid powertrains suffer [125]. Allows the ICE to be operated at high efficiency or low emissions levels. As a result, it is appropriate for use with advanced combustion modes, where the number of parameters to optimize and modify at various operating points varies greatly [126].

This type of powertrain can also be used with fuel cells due to the stationarity of the operation of the fuel converter (ICE or Fuel Cell). The most significant disadvantage of this method is the amount of electricity lost due to the ICE energy being transferred to the generator and traction motor. Due to the massive amount of power delivered to the wheels and generated in the engine, this aspect is critical in HD vehicles. *Figure 2-21* shows a schematic of the Series hybrid architecture. In some cases, such as HD trucks or buses, a two-gear transmission can be added between the TM and the Final Drive to have high torque at low vehicle speed and not over speed the electric motor on highways.

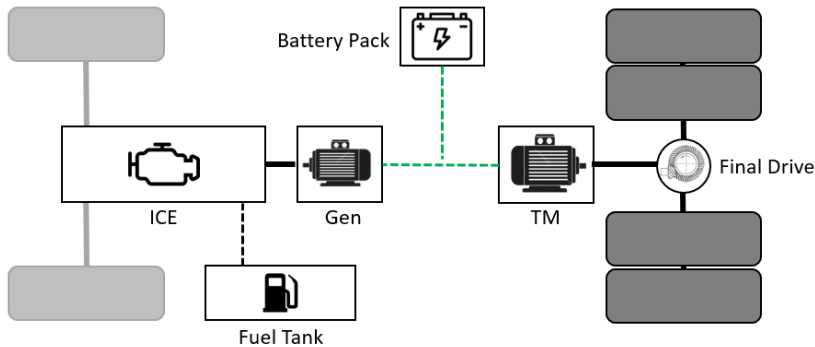


Figure 2-22. Schematic representation of Series hybrid electric architectures.

There is a third widely disseminated architecture, known as power-split, which Toyota presented as the "Toyota Hybrid System" (THS) [127]. The planetary transmissions used in this approach are unique. They allow the ICE to be adjusted independently of the wheel dynamics and produce traction power to meet the power demand. The THS has undergone various revisions since its first release in 1999, and other car manufacturers have proposed different applications for the planetary transmission in an automotive powertrain.

The planetary transmission is employed as a speed coupling device in the power-split HEV powertrain architecture. The ICE is attached to the carrier gear in *Figure 2-22*, with one electric machine (Gen) connected to the sun and the other (TM) to the ring. Finally, the torque-coupling device is the differential/final drive connected to the ring gear. The planetary transmission divides engine power into two paths: the electrical path, which sends part of the ICE's power to Gen (generator mode) and stores it in the battery or directly to the motor TM (traction mode) via a controlled power bus, and the mechanical path, which sends the remaining power to the transmission output.



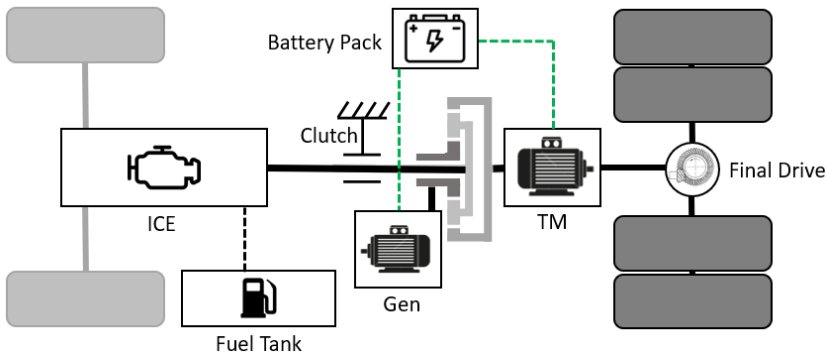


Figure 2-23. Schematic representation of Power-split e-CVT hybrid vehicle.

## 2.5.2 Battery storage system

A rechargeable electric energy storage system (REESS) is a fundamental component for xEVs to provide the electrical energy, which can be suitably used to soften the power demand to the ICE, hence, improving both fuel economy and tailpipe emissions. Moreover, it must be able to store the kinetic energy recuperated during vehicle braking events to improve the vehicle's overall efficiency. Nowadays, Lithium-Ion technology is majorly used in electrified powertrains since it offers excellent reliability in energy and power densities and can count on the expertise developed in the past decades. Some isolated cases, such as the Mercedes Benz Citaro bus [128], use Supercapacitors. However, the low energy storage capabilities make it not the best option for applications where pure electric mode is required. As shown in the Ragone plot of Figure 2.23, Li-ion batteries offer both a good energy density and power density [129].






	Energy density (kW/kg)	Round Trip Efficiency (%)	Life Span (years)	Eco-friendliness
<b>Li-ion</b> 	<b>1st</b> 150-250	<b>1st</b> 95	<b>1st</b> 10-15	<b>1st</b> Yes
<b>NaS</b> 	<b>2nd</b> 125-150	<b>2nd</b> 75-85	<b>2nd</b> 10-15	<b>2nd</b> No
<b>Flow</b> 	<b>3rd</b> 60-80	<b>3rd</b> 70-75	<b>4th</b> 5-10	<b>4th</b> No
<b>Ni-Cd</b> 	<b>4th</b> 40-60	<b>4th</b> 60-80	<b>3rd</b> 10-15	<b>3rd</b> No
<b>Lead Acid</b> 	<b>5th</b> 30-50	<b>5th</b> 60-70	<b>5th</b> 3-6	<b>5th</b> No

Figure 2.24. Battery characteristics depend on the technology used. *Li-ion* (Lithium-Ion), *Na-S* (Sodium Sulfur), *Flow* (Supercapacitors), *Ni-Cd* (Nickel Cadmium), and *Lead Acid*. Source [129].

The main elementary component of a battery pack is the cell. Multiple cells are connected in series and parallel to give the desired electrical properties of the module. Then, modules are connected in series and parallel to achieve the final electric power and energy storage capability per package, as it is shown in Figure 2.24. Recently, BYD implemented a cell package to reduce weight and volume [130]. However, this type of approach reduces the flexibility of the mounting of different vehicle capacities, is more difficult to be maintained, and issues in the REESS have been found. Therefore, a package with a module is the most common approach.

Different types of casing are used for lithium-ion batteries. As shown in Figure 2.24, the most common are cylindrical, pouch, and prismatic. Inside the cell, the main components are the cathode (positive electrode – highest potential) containing lithium and insertion materials that are transition metal oxides (active material). The metal may be Cobalt (Co), Nickel (Ni), Maganese (Mn), or Iron (Fe). The active material chemistry defines the cell type. The anode (negative electrode – lowest potential) is made of carbon in the form of graphite or hard carbon. The electrolyte is a non-aqueous, carbonate-based organic solvent mixture and acts as a medium for lithium

ions transfer between the cathode and anode. The electrolyte wets the separator. Lastly, the separator is made of an ionically conducting and electrically-insulating material. It is interposed between anode and cathode to prevent internal short-circuit.

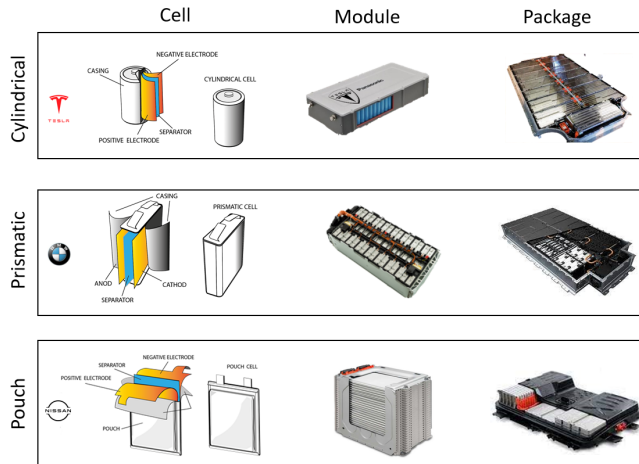


Figure 2.25. Comparison of different Li-ion cell shapes used in electric vehicles.

During discharge, the Li-ions move (intercalate) from the anode to the cathode, and vice versa during charge. A typical value for Li-ion cell voltage is 3.6V. When choosing a cell, the main parameters to observe are: 1) Nominal voltage, 2) Cut-off or minimum voltage, 3) Capacity (Ah), 4) Cycle life (number of complete discharge-charge cycles the cell can withstand before 80% of the pristine capacity) 5) Cell cost (\$/kWh), 6) Specific energy (kWh/kg) and 7) Specific power (kW/kg).

The properties of the different Li-ion cell technologies available in the market depend on their active material. The spider diagrams in Figure 2.25 give a quick overview of the cell's strengths and weaknesses. The specific energy (also gravimetric energy density) is an important property, and alongside the vehicle's energy consumption, it determines its driving range. On the other hand, the power density can be associated with the capacity of

the cell to deliver power, hence the acceleration of the vehicle instantaneously. The  $\text{LiFePO}_4$  (also LFP) has superior electrochemical performance with low internal resistance, and high C-rate, can sustain a wide temperature operating range ( $-30^\circ\text{C}$  to  $60^\circ\text{C}$ ), and has a long cycle life [131]. Moreover, LFP is less prone to thermal runaway due to phosphate stabilization [132]. However, this type of cell has a low energy density that penalizes large battery packs such as BEVs and trucks.

During the operation, the state of the charge (SoC) is one of the foremost parameters to observe and control. The SoC level must be kept within the desired range. For instance, at low SoC, the discharge power decreases, but also at high SoC, the charge power is reduced. For this reason, car manufacturers tend to oversize the battery pack so that it can meet the power and energy requirements. Also, the importance of the SoC range is related to safety and aging concerns.

A battery management system (BMS) is the interface between the battery and the vehicle. It monitors and communicates parameters describing the status of the battery. It is appointed with many tasks such as sensing and reporting cell voltages and temperatures, battery voltage, and current it also controls cell balancing to prevent battery malfunction and failure [133].

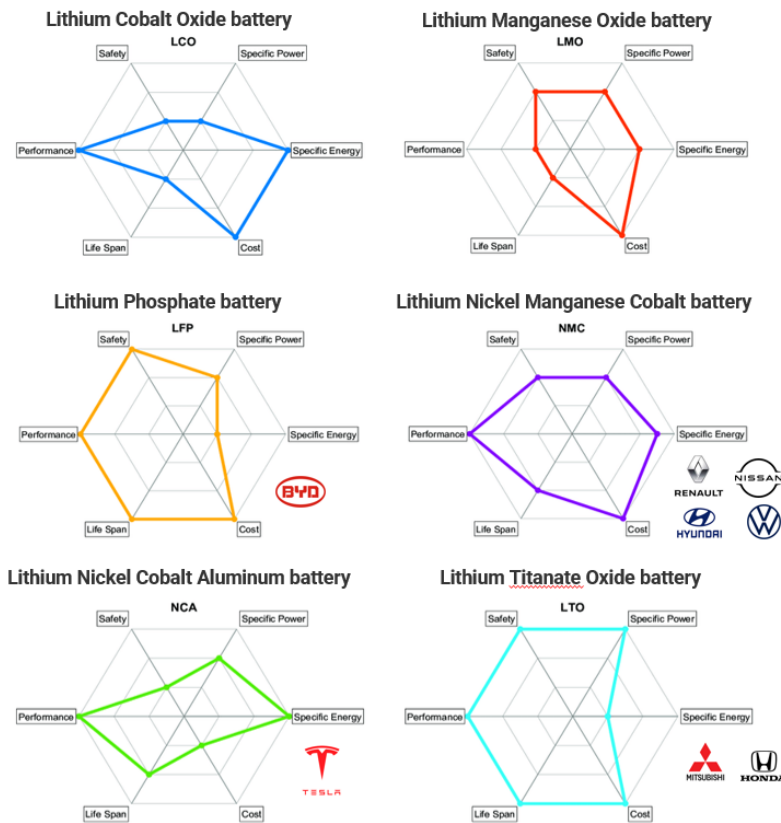


Figure 2.26. Li-ion cell technologies are based on active material chemistry. Adapted from [134].

A Li-ion battery is subject to aging, which is the capacity and power losses that occur from the moment of its first use (pristine condition). A general criterion is adopted to establish the end-of-life of a Li-ion battery pack: a Li-ion battery becomes useless for vehicle traction when a maximum of 20-30% loss of the initial nominal capacity is reached. Of course, this aspect is the primary concern for EV and HEV manufacturers since battery degradation leads to a reduced driving range for the former and reduced fuel economy. A typical automotive battery for Light-Duty has then to stay functional for at least ten years (i.e., the average life of a vehicle), which correspond to around 200,000 km. In the case of the Heavy-Duty sector, a

midlife battery replacement is recommended after six years of heavy use (~60,000 km per year), which means 360,000 km.

Battery degradation can be subdivided into two parts: cycling and calendar aging. Cycling degradation derives from the actual use of the battery, which includes charge and discharge phases. The latter is due to the battery storage when the battery is not being used. Both aging mechanisms depend on many factors, which can be classified into operational and environmental factors: the main operational factors include the SoC level, SoC range, and C-rate, while environmental factors are mainly temperature and humidity [135,136]. All these parameters should be carefully monitored, and battery use should be controlled accordingly to avoid a fast degradation of the battery pack. The BMS performs this task.

Furthermore, battery aging has two effects: capacity loss which reduces the vehicle's pure-electric driving range, and internal resistance increase, producing lower battery power output. Several indicators are adopted to estimate aging: 1) State of Health (SoH) [137,138], 2) End of Life (EoL), and 3) State of Function (SoF). Concerning HEVs, it is then clear how the energy management strategy that decides the power split between the ICE and the electric machine/s has an essential influence on battery aging since it affects how it is used.

### **2.5.3 Electric machine and power electronics**

Electric machines are crucial components of hybrid and pure electric vehicle drivetrains. Even when scientific papers are published on the issue, the design specifics are not entirely divulged. Only a few EV manufacturers have provided technical material on the design of the machinery utilized in their products. Researchers in the field and third-party reverse engineering sources provide most of what is known about the electric machinery in xEVs. ORNL purchased vehicles from the US market (Toyota Prius v2004, 2010, and 2017, Toyota Camry v2007 and 2013, Lexus v2008, Hyundai Sonata

v2008, Nissan Leaf v2008, Honda Accord v2014, and BMW i3 v2016) and performed detailed testing and teardown of their drivetrain components, producing comprehensive reports on their findings. Two types of machines have been discovered in current vehicles: induction machines and synchronous machines. Permanent magnet machines and variable reluctance machines are two types of the latter.

The electric current in the rotor required to produce torque is obtained via electromagnetic induction from the stator's magnetic field, winding in an induction motor (IM) or asynchronous motor. As a result, an induction motor can be built without any electrical connections to the rotor. The main qualities of induction machines are their simplicity, low cost, and robustness. High peak torque, good dynamic response, and very minimal maintenance requirements in all aspects of the operation are significant characteristics of these machines. The Tesla Roadster, Model S, and Model X with die-casting copper rotors are examples of this EM. Compared to aluminum die-cast rotors, copper's superior electrical conductivity (almost 60% more than aluminum) results in significant reductions in overall motor losses, estimated at 15–20%.

On the other hand, permanent magnet machines are currently employed in the majority of automobiles. The transition was prompted by rising demands for high efficiency, high specific power, and high-power density. A permanent magnet (PM) motor, often known as a synchronous motor, is an electric motor with permanent magnets and windings on its field. Consider the transition from Tesla Model S (induction EM) to Tesla Model 3 permanent magnet-based technology.

*Figure 2-26* shows a typical curve of power and torque measured in the output shaft of electric machines. The three unique operational regimes of EM, namely constant torque, constant power, and reduced power zones, are defined by the design decisions in machine design and electronic power control.

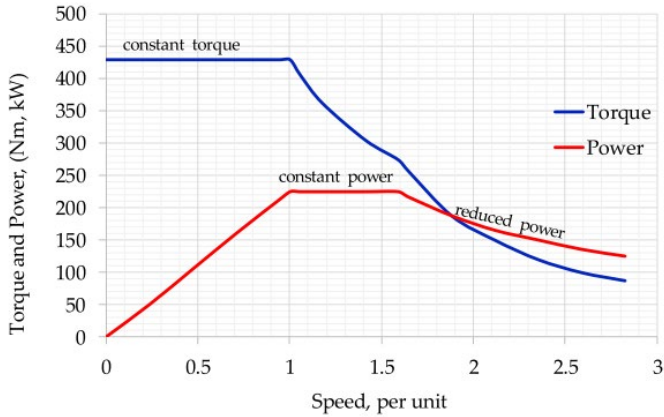


Figure 2-27. Typical EM curve with the main characteristic regions for Power and Torque against the rotational speed. Source [139].

The rotor design is the significant distinction between different permanent magnet motors: 1) surface permanent magnet (SPM) and 2) inside permanent magnet machines (IPM). The SPM machines have a relatively simple design/structure, but because the magnet is positioned on the rotor's surface, there is a bigger air gap, which affects the machine's performance. Even though SPM machines can be developed with concentrated windings to obtain a much-enhanced high constant power speed range, their use in the automotive industry is currently limited. The IPM machine and its variants appear to be preferred for automotive traction over the SPM machine.

Hwang et al. [140] studied the effect of the rotor design of IPM. Figure 2-27 shows the designs under investigation. Figure 2-28 shows the results in terms of torque output and efficiency. The same regions as Figure 2-26 are seen with 70% to 95% efficiency.



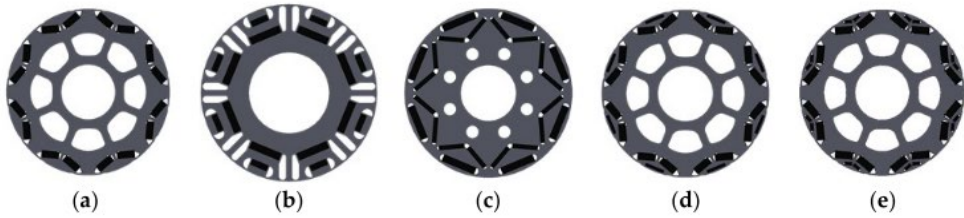


Figure 2-28. Shapes of Interior Permanent Magnet (IPM) rotors: (a) V shape, (b) double magnet shape, (c) delta shape with a bar magnet in a V shape, (d) improved shapes using a delta shape, and (e) improved shapes using a double V shape. Source [140].

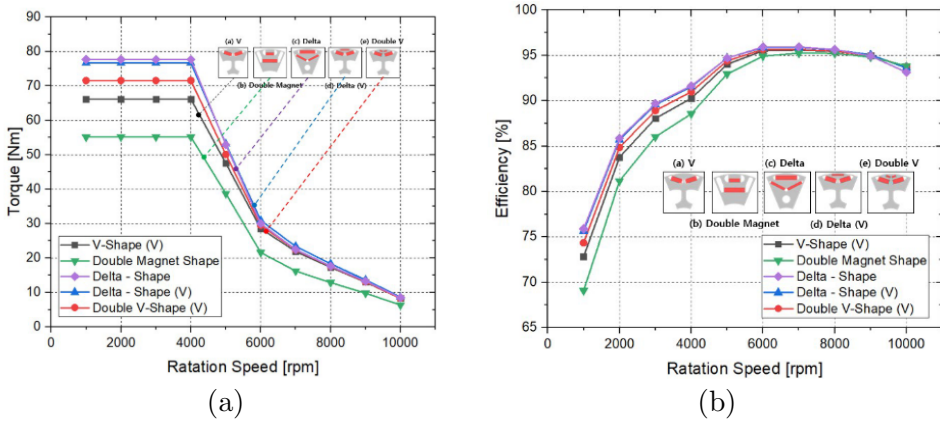


Figure 2-29. Torque (a) and efficiency (b) compare different IPM rotor design shapes. Source [140].

It is possible to obtain a map of the motor's efficiency by extending the measurements to several points of torque and speed. Figure 2.29 compares the same maximum torque of an IM and an IPM. The IPM achieves higher zones of efficiency (over 90%). However, the IM achieves higher torque for intermediate rotational speeds.

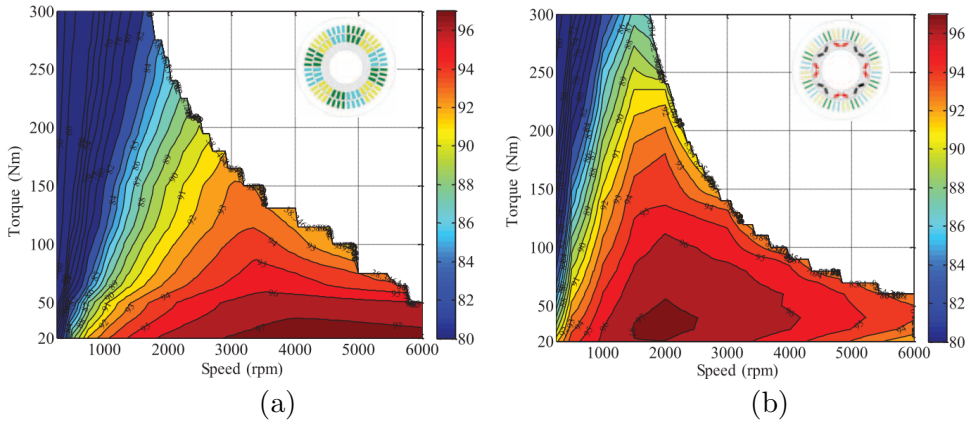


Figure 2.30. Comparison between (a) Induction Motor and (b) Permanent Magnet Synchronous Motor. Adapted from [141].

In an HEV, the net electric power is completed by the power electronic components, which distribute the energy flow and adjust the voltage and current. Two aspects that must be assessed are the stepping-up or stepping-down of the voltage level to allow the electric power flow between components at different voltages and the transformation of DC to AC and vice-versa. A scheme of the power electronics in an HEV is presented in Figure 2.30.

There are still auxiliaries that work with low voltage levels (i.e., 12V), such as the headlights, the heater fan, and the radio, among others; for this reason, a converter to step down the voltage level of the battery pack is needed, and a DC/DC converter is appointed this task. A power converter modifies the amplitude and/or the frequency of the voltage and current and ensures the bi-directional flow between electric power nets at different voltages. The power capability of inverters is related to DC input voltage. This is why FHEVs have electric power nets that operate in the range of 200-400 V. A DC/DC converter modifies the DC voltage: it can reduce it (buck mode operation) or increase it (boost mode operation). When both buck and boost modes are available, it is called buck-boost DC/DC converter.

The EMs of interest for the automotive application work with AC electric voltages and currents. The AC excites the armature windings of the EM, according to a design control sequence, to produce a rotating magnetic field. An inverter is needed to convert the DC voltage or current of the battery to AC and vice-versa and control the switching sequence and frequency of the phases of the electric machine. There are two types of inverter: voltage-source inverter (VSI), which are fed with constant voltage, and current-source inverter (CSI), which are fed with a constant current. The elemental working device of an inverter is the transistor. For each of the three phases of the EM, a couple of transistors are switched on at alternate times.

The sizing of the inverter is done by considering the desired apparent power. If the EM has a low power factor, the inverter could be oversized in terms of useful power output. The power factor is the ratio between active electric power applied to the EM measured in [W] and the modulus of the apparent electric power flowing in the circuit, measured in [VA]). The efficiency associated is around 98% for inverters and does not have significant variations. They are generally modeled or considered in calculus as a constant efficiency value. This is the approach in the present Thesis.

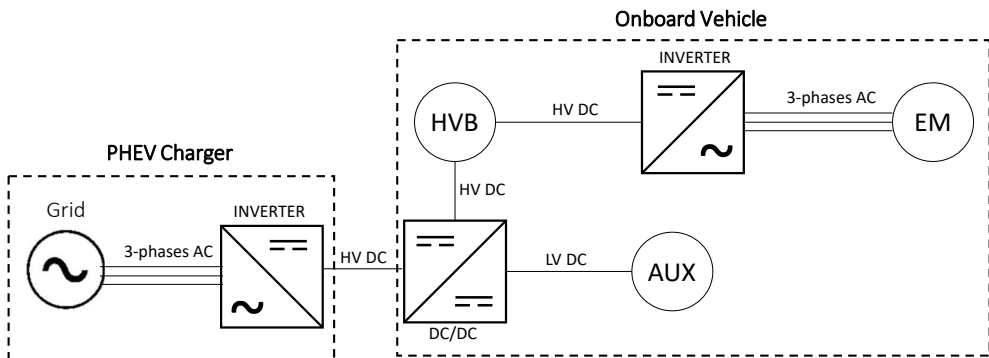


Figure 2.31. Typical electric power net of HEVs. HVB: high voltage battery; AUX: auxiliaries; HV DC: high voltage direct current; LV DC: low voltage direct current.

### 2.5.4 Control strategies

In addition to the powertrain architecture, the control strategy, responsible for coordinating the split between ICE and EMs, has a critical role in fuel consumption and emissions output [142]. The implementation of an additional source of energy in the powertrain gives additional degrees of freedom to operate it. The complexity of the powertrain and the possible operating modes which enhance the exploitation of the potential reduction of fuel consumption and tailpipe emissions depend on the chosen architecture. How the ICE is coupled to the wheels and the characteristics of the electric machine/s and battery (i.e., rated power) determines how well the power demand at the wheels can be satisfied by favoring a more efficient use of the ICE. For a given architecture, however, it is paramount to correctly coordinate the power demand among the ICE and EMs since the available electric energy stored in the battery depends on its size, but also on the type of hybridization, and it is finite, so it must be spent in the best possible way. A PHEV can be recharged with an external electric socket, while an FHEV does not have any external access for energy replenishing. In the first case, the electric charge can be extensively depleted until a specific limit of the battery SoC is reached to have a pure-electric drive.

In the second case, the electric charge must be sustained when the vehicle is driving to keep the battery SoC around the desired level. Electric energy is restored to the battery through electric regenerative braking and the ICE, which needs to output extra power to fulfill this task. This characteristic suggests that if good fuel economy and emissions reduction are to be achieved, how the ICE and the EM jointly operate must be finely controlled while also considering the battery's state of charge. This job is accomplished through an energy management control strategy implemented in a supervisory control unit.

The term “supervisory” suggests that this kind of control is put at a higher level than the single components’ control units, such as the engine control unit (ECU), the motor control unit (MCU), and the battery

management system (BMS), which have in turn the task of optimizing the requested operation for the single component: for example an ECU, according to the driver power demand, would set the suitable injected-fuel mass, timings and pressure, the EGR ratio, the VGT, among others, to calibrated maps stored in its memory. There is no need for an energy management control strategy in a conventional ICE-powered vehicle since the ICE is the only power source: the accelerator and brake pedal's positions translate the driver's power demand into signals for the low-level controller of the engine (ECU) for instance. On the other hand, is a hybrid vehicle, the driver demand cannot directly actuate the ICE and EM, but some coordination is needed first. Finally, the vehicle control system would have a more complex structure: as suggested in Figure 2.31, a multilevel hierarchical structure can be used, which is further complicated if sub-control routines are implemented to deal with specific operating conditions of the vehicle (i.e., coordination level).

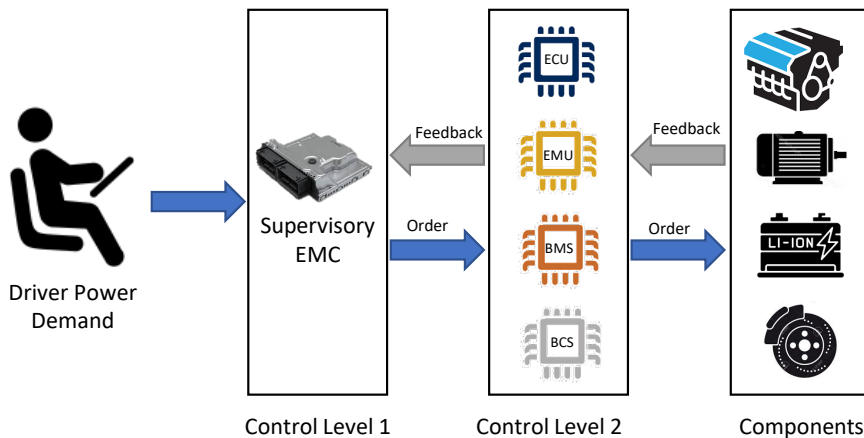


Figure 2.32. Structure of multilevel hierarchical control system for MHEV, FHEV, or PHEV. EMC: Energy management control, ECU: Engine control unit, EMU: Electric machine unit, BMS: Battery management system, and BCS: Brake control system.

Several control methods are available and can be mainly classified into rule-based and optimal control. In brief, a rule-based control (RBC) strategy is an ensemble of rules created to operate the ICE and EMs according to several specifications and states of powertrain components. On the other hand, optimization-based control (OBC) strategies are based on formulating an analytic problem that must be optimized, to which both ICE and EM are subject. Moreover, a control strategy must be implemented in a vehicle control unit and performed efficiently and in real-time: this final consideration is important to discriminate specific OBC strategies. Modern HEVs are equipped with powerful control units to solve complex functions installed onboard concerning computing power. A variety of tasks, from infotainment to security and autonomous-driving capabilities with advanced driver-assistance systems (ADAS), usually adopt artificial intelligence and advanced analytical algorithms [143].

A detailed classification of available state-of-the-art energy management control strategies is reported in Figure 2.32, following the recent review of Tran et al. [144]. Apart from RBC and OBC, the proposed classification also introduces the class of learning-based control (LBC) strategies, which compasses all those algorithms-based machine-learning techniques. Given the potential capability of self-adapting the powertrain to external disturbances (i.e., power demand, weather, traffic). The principal characteristic of these strategies is the importance of data acquisition. A detailed powertrain model, like the case for OBC algorithms, is not needed anymore. However, a large dataset of historical and real-time information needs to be analyzed to interpret the performance and predict the behavior of the power components to efficiently achieve the desired targets (i.e., fuel consumption minimization).

Rule-based control is the most common method to implement control rules to operate an HEV. The task is to coordinate the ICE and EM/s so that the ICE operates efficiently and the battery SoC is maintained within the prescribed boundaries. It is not based on any optimization algorithms. The formulation does not require analytically modeling the powertrain (as

for predictive model controls) but relies on engineering expertise and intuition. A set of rules can then be designed in the fashion of a state-machine controller (i.e., some key operational states of the powertrain are linked by transition conditions, which depend on the status of the drivetrain). As indicated by the map in Figure 2.32, there are two main approaches: deterministic and fuzzy logic. In the first case, the control logic works with a set of if-else control rules tuned using many control parameters, such as threshold values or power limitations, that must be calibrated to achieve the desired performance. For example, the EM/s may be activated only below a certain speed.

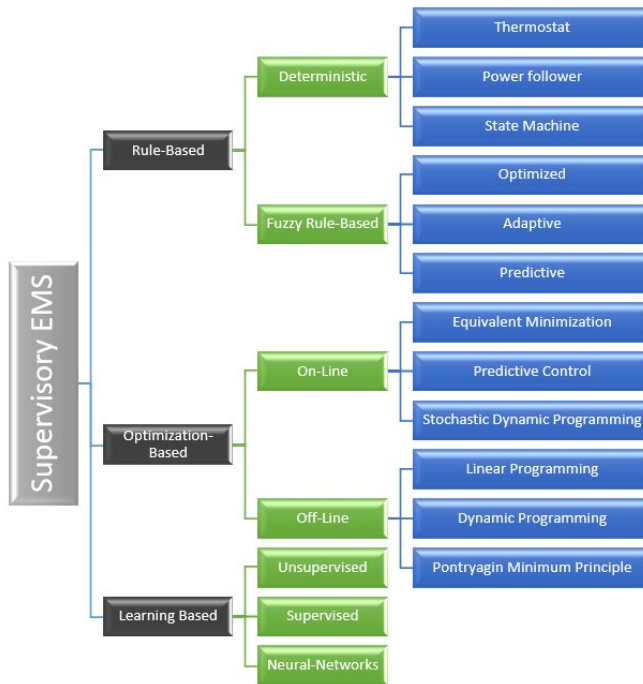


Figure 2.33. Classification of supervisory energy management system strategies at state of the art. Source [145].

### 2.5.5 Life Cycle Analysis in Transportation

Life cycle assessment (LCA) is a methodology, standardized by ISO, to analyse the environmental impacts of products or systems [146]. In transportation, LCA is a method to calculate and the environmental impact of the vehicles' entire life cycle through the raw material procurement, manufacturing, use, recycling, and disposal [147]. Often, main vehicle components considered in LCA estimations for the production and recycling stages are the battery -for BEVs and hybrid electric vehicles (HEVs)-, the powertrain system, and vehicle body. It was demonstrated that the rest of vehicle components are relatively powertrain-type agnostic [148].

Electrified vehicles offer low or no tailpipe emissions. However, as the direct tailpipe emissions are only one aspect of the environmental impacts of EVs. To ensure that the promotion of EVs to reduce greenhouse gas (GHG) emissions from transport does not lead to other undesired consequences, it is critical to conduct rigorous, scenario-based environmental assessments of proposed technologies before their wide spread adoption. Life cycle assessment is the tool of choice for comparing the environmental impacts of transportation in this work because it explicitly quantifies resource use and environmental releases along the entire life cycle of a product. Understanding the system-wide environmental impacts of replacing ICEVs with an alternate technology such as EVs involves a wide range of considerations. Moving forward, it is important to codify what is known about the environmental impacts of electrified vehicles and to identify the most important gaps in our knowledge which should be filled to create effective policy for mitigating the environmental impacts of personal transportation. In addition, considering e-fuels (synthetic fuels) as alternative or complement to the powertrain electrification will requires the LCA calculation too. In this case, the estimation is to quantify the CO<sub>2</sub> associated with the production of the fuel. In particular, e-fuels main benefits are the inclusion of clean electricity and CO<sub>2</sub> capture during the fuel production. This calculation is called Well-to-Tank. On the other hand, the tailpipe emission is called Tank-to-Wheel.



Figure 3.34 shows a basic scheme of the process considered in an LCA for a vehicle [149]. In Figure 3.34 (blue arrows) the Well-to-Tank (WTT) fuel production is shown. For the fossil fuel production, this includes crude oil/natural gas exploration as well as further processing and transport to the vehicle tank. With e-fuels, it starts with the construction and erection of renewable energy plants, including the necessary raw materials, and continues with water and CO<sub>2</sub> capture from air to produce the fuels. The next step is Tank-to-Wheel (TTW) shown in Figure 3.34 (red arrows), which is largely determined by the fuel, respective energy consumption of the vehicles. Furthermore, Figure 3.34 (green arrows) shows the vehicle life cycle (LCA). It also begins with the extraction of raw materials, further processing into intermediate products and vehicle manufacture. The end of life with recycling and landfilling is considered, as common for life cycle assessments of vehicles.

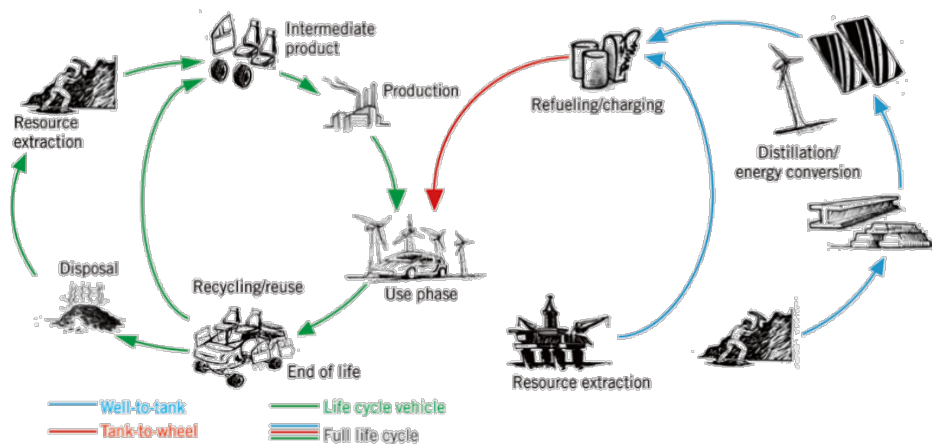


Figure 2.34. Overview well-to-wheel and full life cycle. Adapted from [149].

LCA has been widely applied to ICEVs and BEVs in the scientific literature [23,150–153]. However, existing studies found significantly different results due to their divergence in assumptions. Usually, main GHG emission from the BEVs are derived from their electricity consumption and the battery production.

In terms of the electricity CO<sub>2</sub> associated, BEVs LCA reports available in the literature consider average values of GHG emissions of certain regions, typically corresponding to the average of the total electricity mix such as in [154,155]. However, this approach does not consider the impact of the actual increase of the demand and charging times. As an example, in 2021, the electricity production share in Spain was 24% wind energy, 22% nuclear, 15% combined cycle, 10% cogeneration, and 9% solar photovoltaic [156,157]. The average GHG emissions associated to this mix was 121 gCO<sub>2</sub>/kWh. In spite of the acceptability of this value as a reference, its direct use in LCA calculations from BEVs can lead to wrong conclusions. To estimate more accurately the CO<sub>2</sub> emissions associated to charging a BEV in a certain time, the instantaneous CO<sub>2</sub> emission rate must be considered.

Koch et al. [158] showed that, for Germany, the real CO<sub>2</sub> emissions of the electricity system may be underestimated if the average CO<sub>2</sub> emissions are considered. Particularly, real CO<sub>2</sub> emissions (considering instantaneous values) would outmatch those estimated using the average CO<sub>2</sub> value by factor of two, at least, depending on the status of the electricity system when BEVs are plugged-in. Authors used the fundamental theorem of calculus to calculate the marginal emissions.

Burton et al. [159] studied the marginal emission in USA in passenger vehicles. The information from the 2019 electricity grid data was used in this study to compute the geographically and temporally resolved marginal emission rates that capture the actual carbon emissions related to the current use of the USA grid for electric vehicle charging or any other electricity need. It is discovered that there is currently no data to support the claim that BEVs uniformly reduce car emission rates when compared to HEVs, and that they frequently produce higher greenhouse gas emissions. This suggests that a combination of powertrain technologies is the best way to reduce emissions from the transportation sector until the USA grid can supply electricity for the infrastructure of the all-electric fleet and the operations of the vehicles with a carbon intensity that produces a net environmental benefit.

In this work, the marginal CO<sub>2</sub> emission and the average are used to compare both approaches. In particular, the calculation is focused in Spain during the 2019 because is the available data in terms of instantaneous electricity production source and quantity in the all year. Spain in terms of average year CO<sub>2</sub> emissions for electricity production compared with the rest of Europe is close to the average value. Therefore, is a good reference to be associated the final results to the average behaviour of Europe.

In terms of fuels production, the TTW CO<sub>2</sub> associated can be found in several works in the literature [160–163]. The green fuels or synthetic fuels uses renewable electricity and CO<sub>2</sub> capture and utilization. It is an alternative pathway for low-carbon hydrocarbon production. In the literature can be found a large range of values for the same fuel depends on the percentage and type of renewable electricity source and the use of carbon capture. Some works also includes the heat recovery in the production plant that improves the efficiency of the process. Table 2-5 shows a summary of the literature review values for Gasoline, Diesel, Methanol and OMEx.

The other important aspect of LCA in electrified vehicles is the battery manufacturing impact. Electric vehicle battery manufacturing emissions have been studied extensively. Table 2-5 lists several research studies analysing the emissions related to electric vehicle battery production. These studies vary in scope and methodology, and find a range of values for electric vehicle greenhouse gas emissions attributable to battery production. As shown in Table 2-6 the studies indicate that battery production is associated with 35 to 494 kilograms of carbon dioxide per kilowatt-hour of battery capacity (kg CO<sub>2</sub>/kWh) for electric vehicles. The average value of all the works is 108 kgCO<sub>2</sub>/kWh with a standard deviation of 42 kgCO<sub>2</sub>/kWh. The table simplifies the analytical findings, which in many cases have more scenarios and results than are basically summarized here. However, it is a good picture of the literature values used for quantify HEVs and BEVs LCA. The wide range of values found in these studies indicates the degree of uncertainty in assessing life-cycle emissions and the variety of methods and materials used in manufacturing batteries.

Table 2-5. CO<sub>2</sub> associated to the fuel production in the literature.

Fuel	Year	Battery Production emissions (kgCO <sub>2</sub> /kWh)	Work	Additional note
Gasoline	2020	13.0/16.9	[160]	Crude oil from typical EU supply, transport by sea, refining in EU (marginal production), typical EU distribution and retail
Diesel	2020	13.6/18.9	[160]	
Methanol	2021	-68.3/-52.3	[161]	Methanol considering H <sub>2</sub> from Wind and Solar sources, Nuclear energy and renewable electricity.
Methanol	2022	-93.1/264.0	[162]	Methanol production with (maximum) and without (minimum) heat recovery and CO <sub>2</sub> capture.
Methanol	2020	-68.1/-49.9	[163]	Aramco Analysis of e-fuels with blue, green, nuclear and bio methanol.
Methanol	2020	30.96/32.86	[163]	Aramco Analysis of e-fuels with grey methanol.
Methanol	2020	1.85/124.4	[160]	Piped natural gas to methanol, Wood to methanol, waste wood, farmed wood, and waste wood via black liquor gasification/synthesis plant and renewable electricity to methanol (CO <sub>2</sub> from flue gases).
OMEx	2020	-74.9/-47.1	[163]	Aramco Analysis of e-fuels with blue, green, nuclear and bio OMEx.
OMEx	2020	107.0/109.5	[163]	Aramco Analysis of e-fuels with grey OMEx.

Therefore, the methodology used for a life-cycle assessment can greatly influence its conclusions about the carbon intensity of batteries. An LCA can evaluate the environmental impacts of a system using either a bottom-up or top-down approach [164]. A bottom-up approach incorporates the activity data for each stage of each component of a battery and aggregates these different components. In contrast, a top-down analysis first determines the total emissions from a plant and attributes these emissions to different processes. Top-down inventories tend to include more auxiliary energy uses, but they may double-count certain processes and emissions. In this context, top-down inventories typically find higher emissions, often by a factor of two or more.

Table 2-6. CO<sub>2</sub> associated to the battery production in the literature.

Year	Battery Production emissions (kgCO <sub>2</sub> /kWh)	Work	Additional note
2020	91/100	[165]	The carbon footprint model of the NCM811 battery from cradle to cradle is constructed based on the Gabi software version 10.6.
2020	75/105	[166]	Evaluate NCA, NMC and LFP cathode chemistry with worldwide energy mix.
2020	125	[167]	Primary data for the assessment were collected onsite from the two Chinese leading LIB suppliers, two leading cathode material producers and two battery recycling corporations.
2019	61/106	[168]	The low value coming from an assumption of the utilization of zero-emission electricity for battery production (0 kg CO <sub>2</sub> /MWh) and the

			upper value from a fossil-fuel electricity source (1000 kg CO <sub>2</sub> /MWh).
2019	42	[169]	Use an attributional life-cycle analysis, and process-based cost models, to examine the greenhouse gas emissions associated with producing and recycling lithium-ion cells with lithium nickel manganese cobalt oxide (NMC-622).
2019	42/141	[170]	This work use GREET® model as the basis for the US, China, Japan, South Korea, and Europe.
2019	121/250	[171]	The CO <sub>2</sub> emission factor was estimated based on various works in the literature for LFP and NMC.
2017	55/185	[172]	Global Warming potential of manufacturing various Lithium battery chemistries (LFP, LTO, LCO, LMO, NMC, NCA).
2017	35/108	[173]	Uses China and USA grid for battery manufacturing. Batteries produced in U.S. create 65% less GHGs.
2017	150/200	[174]	Reviews literature, concluding manufacturing energy contributes at least 50% of battery life-cycle emissions. Assumes battery manufacturing in Asia.

These early estimates appear to have a high degree of uncertainty and may not correctly reflect the numerous electric vehicle battery production facilities already in operation worldwide, according to methodological and data input considerations [175]. There is a need for more transparent, up-to-date inventories because the majority of life-cycle assessments only use a

small number of primary sources for emissions inventories. As several of these studies demonstrate, the electricity consumed in manufacturing accounts for most of the battery carbon emissions [176]. As a result, manufacturers that use greener electricity can dramatically cut the emissions linked to battery production. It also matters what kind of battery chemistry was examined because certain chemistries contain larger quantities of energy-dense metals than others. Since there is a lot of uncertainty on how recycled materials might alter carbon footprints, these studies also often do not include battery recycling in their estimates [166]. The lithium-ion battery market is also evolving swiftly, and larger, more effective facilities often produce batteries with lower emissions per kWh [170].

Despite the LCA is an extensively used methodology to account for CO<sub>2</sub> emission in different powertrain platforms, the final results must be taken according to the hypothesis done during the LCA and the database taken. The CO<sub>2</sub> associated to the battery manufacturing and the electricity mix are the main aspects in electrified vehicles.

### **2.5.6 Hybrids in the Heavy-Duty sector**

Several works have been published exploring the electrification of the Heavy-Duty sector. Mainly related to trucks, there is interesting research on the influence of the electrification level impact [177,178], powertrain architecture [179], and driving cycles influence [180].

When applied to a Medium-Duty truck and compared to the baseline configuration, Warey et al. [181] assess the potential of electric propulsion systems in significantly decreasing CO<sub>2</sub> emissions. Many electric driving combinations were tested over the combined US FTP-72 (Federal Test Procedure) cycle and the Highway Fuel Economy Test (HWFET). Compared to the baseline vehicle, stop-start (S/S) functionality with a belt alternator starter (BAS) system resulted in a 2.5 percent reduction in CO<sub>2</sub> emissions. Various electrified drive systems reduced total CO<sub>2</sub> emissions by 8.5 percent

with a 48V P0 configuration to 25 percent with a high-voltage Series-Parallel hybrid throughout the test cycle.

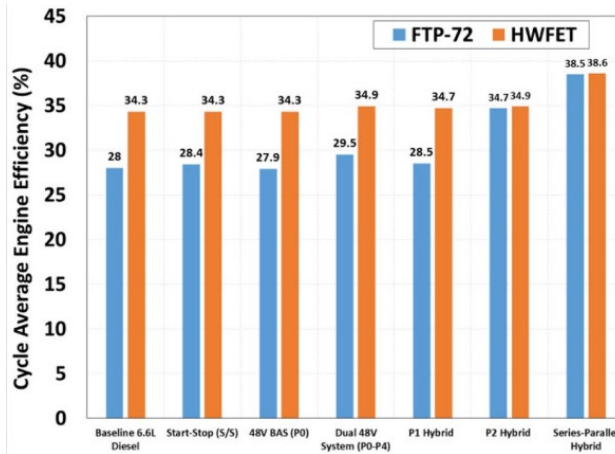


Figure 2.35. Average engine efficiency over the test cycles for different hybrid architectures and hybridization levels. Source [181].

Over a Heavy-Duty freeway truck driving cycle, Gao et al. [179] reported simulated fuel economy for parallel, series, and dual-mode hybrid electric long-haul trucks (Class 8, USA classification) and a conventional powertrain configuration powered by a commercial 2010-compliant 15-L diesel engine. According to the findings, both parallel and dual-mode hybrid powertrains were capable of boosting fuel economy by 7% to 8%. However, there was no significant fuel economy benefit for the Series hybrid vehicle due to intrinsic inefficiencies in energy exchange. There was a synergistic fuel economy benefit for appropriate hybrids when reduced aerodynamic drag and tire rolling resistance were combined with hybridization, increasing the fuel economy benefit to more than 15%.



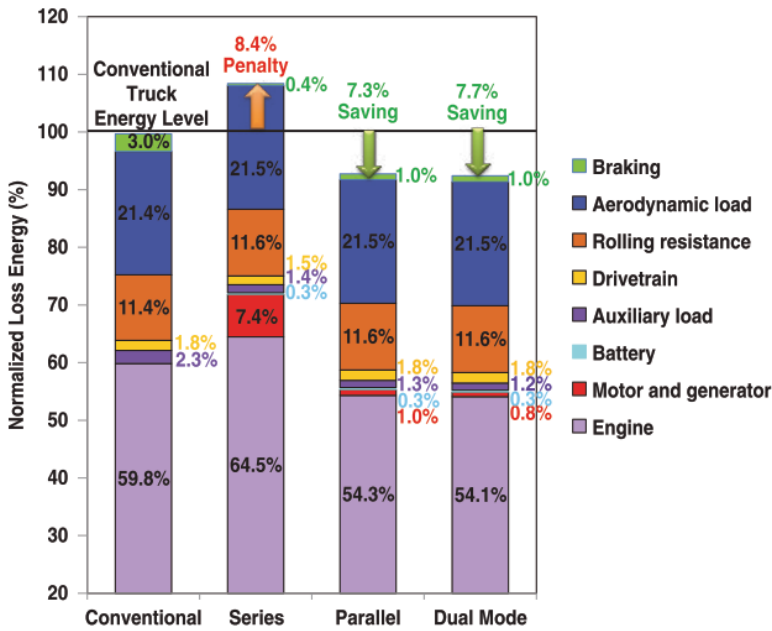


Figure 2.36. Energy losses distribution for conventional and hybrid trucks operating over the FDHDT cycle. Source [179].

Using numerical powertrain simulations, Mojtaba et al. [182] calculated well-to-wheel GHG emissions, total ownership costs, and abatement costs for 16 distinct Heavy-Duty long-haul trucks (class 8, USA classification) drivetrains, including those powered by natural gas, electricity, and hydrogen. For the conventional diesel, plug-in parallel hybrid diesel, and plug-in parallel hybrid diesel, a 13L Mack CI diesel engine was used. For the traditional CNG, plug-in parallel hybrid CNG, and plug-in parallel hybrid CNG catenaries, an 11.9 L Cummins Westport CNG engine was examined. A Panasonic NCR, 18650 lithium-ion battery pack with a 243 Wh/kg power density, was employed. Permanent magnet motors are employed, and their efficiency ranges from 70% to 95%. GREET was also used to estimate various on-road and up-stream GHGs in addition to simulated CO<sub>2</sub> emissions.

The plug-in parallel-hybrid diesel has the lowest total ownership cost (including infrastructure expenditures) for short and long-haul operations across a variety of drive cycles. The ownership expenses are divided by GHG reductions to compute abatement costs (\$/tonne). Plug-in parallel hybrid diesel offers the lowest abatement cost, with negative costs on most drive cycles using either diesel or bio-diesel. When it comes to maximum freight loads, the plug-in parallel hybrid fuel cell and traditional diesel drivetrains have the most capacity on short and long-haul routes, respectively.

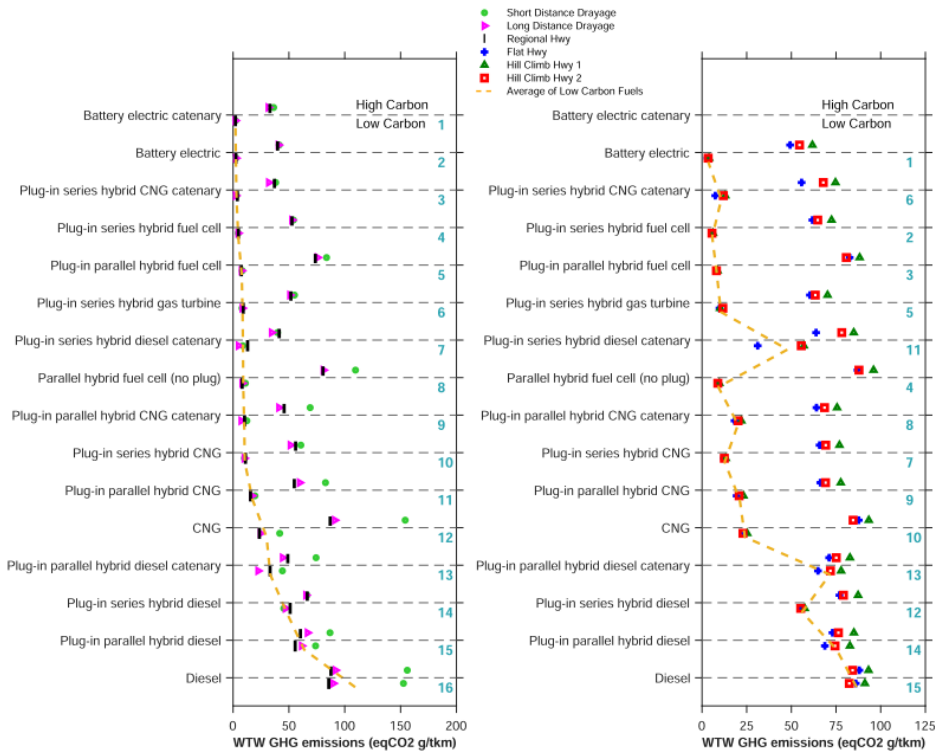


Figure 2.37. Well to wheel GHG ( $CO_{2eq}$  g/tkm) emissions of all alternative drivetrains with low and high carbon energy fuel supply on short (a) and long (b) haul cycles. Source [182].

According to Lajunen's [53] research, regenerated energy has a substantial correlation with fuel consumption, implying that increased fuel

consumption is partly due to the necessity to break. With increasing combination weights, the braking energy naturally increases. There is a 45–68% variance in regenerated braking energy between the different driving cycles. With lower weights, the difference is more significant; with larger weights, the difference is minor.

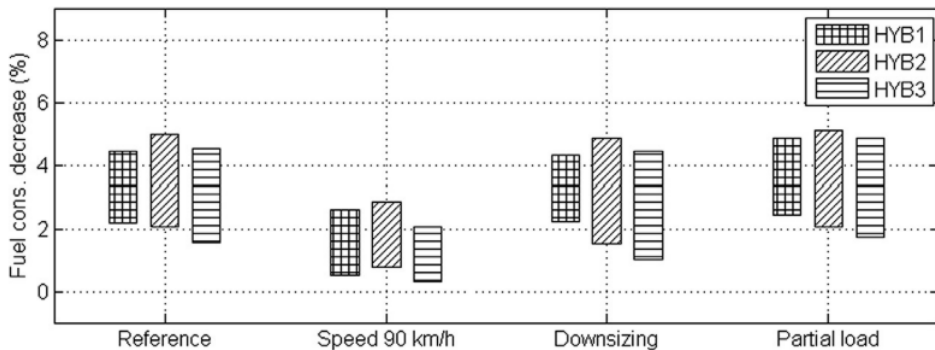


Figure 2-38. Higher speed (80 km/h to 90 km/h), engine downsizing (466 kW to 410 kW) and partial load (100% to 75% payload) impact on fuel consumption decrease for a 60-ton long-haul truck. Source [53].

Depending on the condition tested, the average reduction in fuel consumption is between 3.6 and 4.2 percent. The operating cycles differ significantly, especially between the 40-ton and 60-ton. The operational cycles, which feature less hill climbing, are one cause for this. The vehicle's working characteristics are captured by Duty cycles, including weight, route (speed, distance, and elevation), idle, and job-site power consumption. The significant impact of payload and the route/speed driving cycle on energy consumption for conventional vehicles is well established. Depending on the drive cycle, the difference in fuel consumption between fully loaded and lightly loaded vehicles might be as much as 50%. The difference in fuel usage between mostly urban and highway payloads might be more than 50%. Even small upward road gradients of 3% can triplicate the power necessary to keep a fully loaded truck moving.

## 2.6 Literature review conclusions

In spite of several works that have been published in the area of Heavy-Duty vehicles, as shown in the previous sections, there are several challenges to be tackled in order to extend the electrified powertrain and low-temperature combustion modes on a large scale.

It can be concluded that the Dual-Mode Dual-Fuel concept is a promising combustion concept to face the actual and the upcoming scenarios in the transportation sector. Nonetheless, there are still significant points to be addressed as the system packaging, issues with the high concentration of unburned products, and the challenges in translating the concept to real applications. Lastly, the short-term future will require a significant reduction of the total CO<sub>2</sub> emitted by Heavy-Duty transportation. In spite of having similar to higher efficiency than conventional diesel engines, the concept is still not able to provide the required reductions of 15% and 30% on the horizons 2025 and 2030, respectively, which requires additional investigations on techniques or fuels that could help the concept to fulfill these requirements.

In terms of electrification, the possible improvements for vehicles that travel long distances and primarily drive at constant speeds are determined by changes in road elevation and the amount of braking energy that can be regenerated. Furthermore, if the truck payload is considerable, the diesel engines are already operating in high-efficiency regions. Thus, the powertrain efficiency is unlikely to improve significantly. As a result, electrification makes more sense for urban/rural small and medium Heavy-Duty trucks. Regardless, given how much energy Heavy-Duty vehicles consume overall, even slight increases in fuel economy might be considered worthwhile.

Energy storage (battery) shortcomings continue to be a significant barrier to electrification, with needs in the areas of cost reduction, increased energy density, improved performance at extreme temperatures, achieving battery lifetimes (cycles) commensurate with commercial vehicle TCO

requirements, and developing cost-effective end-of-life solutions. In an application where the battery is used frequently, like Heavy-Duty trucks, the battery's durability might be a critical aspect of the design requirements. In addition, the large emissions produced by the battery production and the not zero electricity grid makes small batteries used in HEVs “greener” than large battery package as BEVs.

To expand the market, solutions that optimize the powertrain system and controls for certain Duty cycles that would benefit most from electrification must be developed. Methods to improve powertrain flexibility in order to achieve high efficiency over a wide variety of operations are also required. In addition, a new regulation in tailpipe emission requires an advanced combustion mode together with complex ATS to achieve the desired values in hybrid powertrains. The inclusion of synthetic fuels to reduce carbon emissions on a WTW basis is crucial. Some specific challenges for trucks found are listed below:

- The life expectancy of a Heavy-Duty (HD) vehicle can exceed 1 million kilometers, and the average age of commercial trucks on the road is about 14 years. Therefore, new powertrain concepts need to achieve the durability of a Diesel engine with a non-hybrid system.
- The power and energy flow in HD powertrains far exceed those of their LD counterparts: roughly twice the peak power, four times the peak torque, and more than five times greater per-km fuel consumption. This will require large electric machines and battery packages.
- The HD market comprises a vastly diverse set of vocational uses compared to the passenger car market. Therefore, to be cost-effective for large market penetration, the powertrain needs to be flexible.
- With high annual vehicle kilometers traveled in the HD sector and high fuel consumption per kilometer, fuel costs will typically exceed the purchase price of the vehicle in a few years.

This places a high priority on the overall vehicle efficiency and the efficiency of electrical components.

## 2.7 The objective of the study and proposed methodology

The general objective of this work is to study the powertrain electrification effect in a dual-fuel combustion concept for a truck application. In particular, CO<sub>2</sub> emissions on TTW, WTW, and LCA basis are going to be evaluated and compared with the commercial CDC non-hybrid truck (baseline). In addition, pollutant emissions such as NO<sub>x</sub>, soot, CO, and HC are considered in the different powertrain architecture calculations and compared against the European legislation (EU VI and EU VII).

Specific objectives were defined to accomplish the general objective that was proposed:

- To understand the potential of mild-hybrid electrification by a 48V battery system with different e-components.
- To evaluate full hybrid electrification to achieve 2025 CO<sub>2</sub> targets using different battery sizes and powertrain layouts.
- To analyze the potential of synthetic fuels, plug-in hybrid, and after-treatment systems to achieve 2030 CO<sub>2</sub> savings and EU VII.

Numerical tools are used in order to model a complete truck with different: 1) Electrification levels, 2) Internal engine configuration, and 3) fuels. The sub-models that are part of the vehicle model are fed and validated with experimental tools. On-route measurements of a Diesel non-hybrid truck are used to validate the baseline 0D vehicle model in GT-Suite. This model is later modified to simulate the above-mentioned cases. Experimental results of the internal combustion engine test bench are used to feed the ICE 1D sub-model and map-based ICE sub-model. Different fuels such as Diesel,

gasoline, OME<sub>x</sub>, and Methanol are used. In addition, a dedicated transient test of a hybrid powertrain is performed in order to validate the ICE sub-model. More information about the methodology is presented in the next subsection.





# Chapter 3

## Tools and methodology

### Content

---

3.1 Introduction.....	110
3.2 Experimental facilities .....	110
3.3 Fuels properties and calibration maps.....	119
3.4 Numerical tools.....	127
3.4.1 Vehicle model .....	128
3.4.2 Internal combustion engine model.....	140
3.4.3 Aftertreatment system model.....	149
3.4.4 Electric motor model .....	153
3.4.5 Lithium-Ion battery model.....	159
3.4.6 Regenerative braking .....	174
3.4.7 Driving cycles .....	178
3.4.8 Energy management and optimization strategy .....	182
3.4.9 Life cycle analysis .....	184
3.5 Conclusions.....	189

### 3.1 Introduction

This work aims to evaluate the potential of RCCI in different hybrid powertrain platforms. Experimental and numerical tools are used to achieve a virtual environment that replicates a real vehicle application. Different fuels are tested to analyze the potential of conventional (Diesel, Gasoline) and e-fuels (OMEx, Methanol).

The experimental campaign includes previous and new tests in an 8L multi-cylinder engine. The previous results include steady-state calibration of the full map with Diesel-Gasoline and OMEx-Gasoline. New tests were performed for dedicated calibration and transient engine cycles for hybrid powertrains.

The numerical simulation includes 0D vehicle modeling of an 18-ton maximum payload truck with different hybrid architectures and hybridization levels. 1D sub-models for lithium-ion cells, engine components, and after-treatment systems were developed and calibrated. Life cycle analysis was implemented to characterize the CO<sub>2</sub> emissions at a global technology level.

The combination of experiments and numerical tools allows extending the capabilities regarding the evaluation of the RCCI implementation on real applications while reducing developing cost and time. This chapter is divided into explaining the experimental devices and data coming from previous works. Next, the different 0-D and 1-D simulations will be explained in detail. A summary of the methodology section is also presented.

### 3.2 Experimental facilities

The RCCI concept was applied in a multi-cylinder (six cylinders in line) 8L, manufactured by VOLVO trucks® and used in several Medium-Duty commercial applications (Volvo FL, Volvo FE, among others) in different

power versions (250-350 hp) as shown in Figure 3-1. Originally calibrated to operate under conventional diesel combustion and equipped with an ATS that allows fulfilling the current EU VI normatively. A complex after-treatment system for each one of the engine-out pollutants: DOC (HC and CO), DPF (Soot), and SCR+ASC (NO<sub>x</sub>, NH<sub>3</sub>) is needed. In CMT-UPV, modifications were done to apply RCCI in the full operation regime of the engine. The new concept was named the dual-mode dual fuel (DMDF) combustion concept. All tests were done in a CMT-UPV test bench that equips an active dynamometer with all subsystems to correctly provide the services (water cooling, fuel, lubrication, among others) and measurements (pressure, temperature, emissions). The control is performed with the original ECU with proper modification for the dual fuel system and control injection and air management settings.

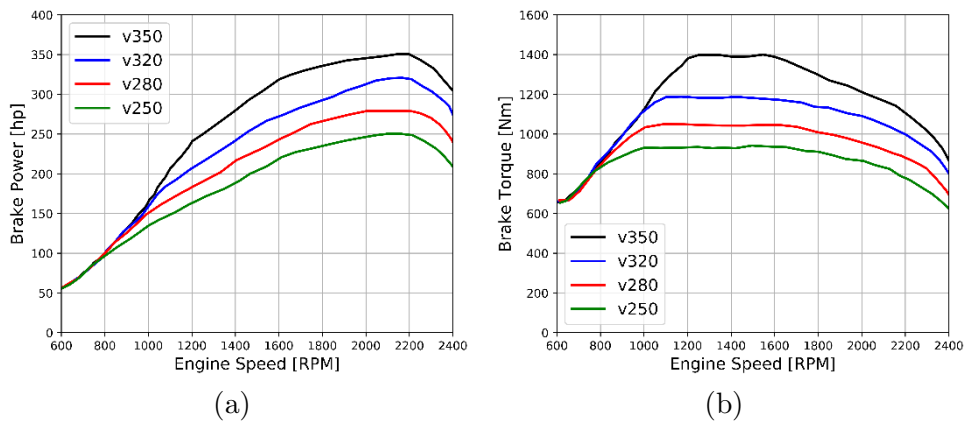


Figure 3-1. Maximum power (a) and torque (b) output curve for the same 8L engine considering different calibration setups [183].

Significant geometrical modifications were made to the original engine to enable the implementation of the DMDF combustion concept. First, the compression ratio was reduced from 17.75 to 12.75 by decreasing the piston height as shown in section 2.4.1 of this Thesis. Moreover, the piston geometry was optimized by employing CFD to realize low emissions and improve fuel consumption. Both modifications were based on the previous work from

Boronat [107]. The main characteristics of the engine are presented in Table 3-1.

*Table 3-1. Main characteristics of the modified engine D8k 350.*

Engine Type	4 stroke, 4 valves, direct injection
Number of cylinders [-]	6
Displaced volume [cm <sup>3</sup> ]	7700
Stroke [mm]	135
Bore [mm]	110
Piston bowl geometry [-]	Bathtub
Compression ratio [-]	12.75:1
Rated power [kW]	235 @ 2100 RPM
Rated torque [Nm]	1200 @ 1050-1600 RPM

As presented in the literature review (Chapter 2), the DMDF combustion concept relies on using two different fuels with contrasting reactivities, generally diesel and gasoline. Therefore, a port fuel injection system was added, composed of six PFI injectors plus a low-pressure pump for the low reactivity fuel (LRF). The original high-pressure piezoelectric injector injects the high reactivity fuel (HRF). The HRF injection system is composed of a fuel lubricated high-pressure pump (which allows achieving injection pressures up to 2000 bar), a pressure regulator, and a common rail. The main characteristics of the injectors are presented in Table 3-2.

Table 3-2. Fuel injection system characteristics for both direct injection and port fuel injection subsystems.

Direct injector		Port fuel injector	
Actuation Type [-]	Solenoid	Injector Style [-]	Saturated
Steady flow rate @ 100 bar [cm <sup>3</sup> /min]	1300	Steady flow rate @ 3 bar [cm <sup>3</sup> /min]	980
Included spray angle [°]	150	Included Spray Angle [°]	30
Number of holes [-]	7	Injection Strategy [-]	single
Hole diameter [µm]	177	Start of Injection [CAD aTDC]	340
Maximum injection pressure [bar]	2500	Maximum injection pressure [bar]	5.5

An important feature present in the commercial engine platform is its air management system. This comprises a turbocharger with a variable geometry turbine and a fixed geometry compressor. The operating map in terms of pressure ratio and reduced mass flow is presented in Figure 3-2. As it can be seen, the compressor map presents the optimum efficiency point at pressure ratios of 2.5 bar and reduced mass flow of 0.22 kg/s. Moreover, the variable geometry turbine efficiently operates a wide range of mass flows according to its vane position. This provides an additional degree of flexibility which is beneficial in the case of having huge mass flow variations and EGR concentrations.

The limits suggested by the turbocharger manufacturer is 3.8 bar of maximum pressure at the turbine inlet and compressor outlet temperature of 220 °C. The turbine inlet can achieve up to 800 °C without turbocharging damage.

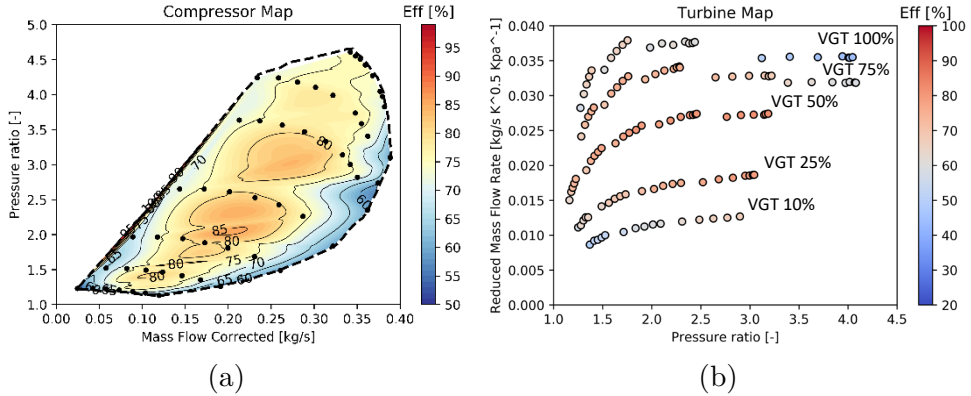


Figure 3-2. Compressor (a) and turbine (b) map for the modeling of the turbocharger.

Following previous work of J. Monsalve [106], V. Boronat [107], and R. Lago [108], it was demonstrated that to be able to achieve ultra-low emission and acceptable turbocharging demands, it is necessary a low-pressure EGR line. The use of only HP EGR would result in a lack of energy in the turbine inlet. Consequently, the turbocharger would not be able to provide the required boost pressure. By contrast, only LP EGR would result in an excessive mass flow flowing through the compressor. In this case, the stock turbocharger would not be able to deal with this mass, exceeding the temperature at the compressor.

Therefore, the first solution implemented was a dual EGR route. This allows controlling the turbine and compressor's energy and mass flow balances. Moreover, the dual-route approach also enables a way to control the temperature at the intake manifold, becoming an additional path to tailor the mixture reactivity. The LP EGR is composed of pipes, control valves, intercooler, particulate filter, and water filter, as depicted in Figure 3-3. These devices are responsible for cleaning and drying the EGR flow, eliminating both particulates and water condensates prior to entering the compressor to avoid damage of the compressor blades. The main drawback of implementing the LP EGR route is a large number of engine changes and more significant difficulties in controlling the air setting than in an only HP

EGR route. Therefore, an electrified turbocharging and a positive displacement pump for the high-pressure EGR line are proposed in this Thesis. The two alternatives alone and combined are evaluated in Chapter 4 as a solution to the DMDF combustion concept.

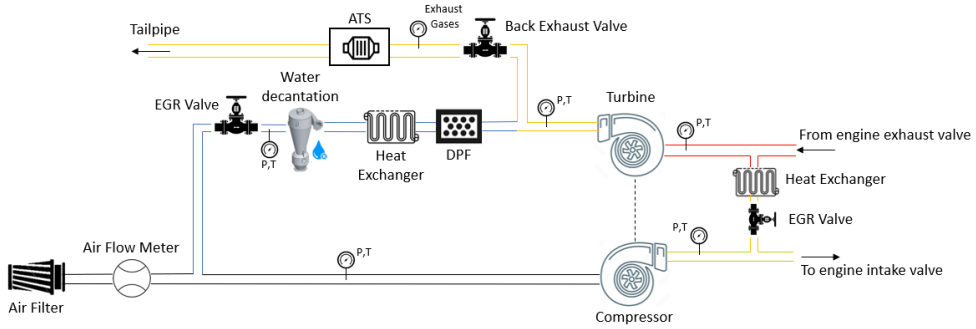


Figure 3-3. Exhaust gas recirculation system illustrates the differences in removing the moisture and particles from the exhaust gases.

In terms of ATS, the commercial engine version with CDC achieves EUVI emissions limits using a complex after-treatment system (DOC, SCR, ASC, DPF, and Urea tank). Based on the previous results presented by R. Lago [108], the DMDF concept should be able to realize engine out EUVI NO<sub>x</sub> and soot emissions at engine-out. Therefore, the SCR, ASC, and DPF systems can be removed, and only the DOC was operative during the after-treatment test. The characteristics of both DOC are presented in Table 3-3.

Table 3-3. Diesel oxidation catalyst characteristics of the stock after-treatment system.

DOC Parameters	Value
Diameter [m]	0.266
Length [m]	0.102
Cell density [cpsi]	400
Total volume [dm <sup>3</sup> ]	5.7

In terms of emission measurement equipment, Horiba Mexa 7100 D-EGR was installed after the turbine output (engine-out) and the DOC (tailpipe). It is possible to measure NO<sub>x</sub>, NO, NO<sub>2</sub>, CO, HC, O<sub>2</sub>, and CO<sub>2</sub> components. Table 3-4 relates the specie in discussion with the respective measurement principle, range, and uncertainty associated with the measurement.

*Table 3-4. Horiba MEXA 7100 D-EGR components, measurement principles range and associated uncertainty.*

Component	Model	Principle	Range	Uncertainty
CO	AIA-31	NDIR	0-12 vol%	4%
CO <sub>2</sub>	AIA-32	NDIR	0-20 vol%	4%
THC	FIA-01	FID	0-10000 ppmC	4%
O <sub>2</sub>	MPA-01	MPD	0-25 vol%	4%
NO/NO <sub>x</sub>	CLA-01	HCLD	0-10000 ppm	4%
NO, NO <sub>x</sub> , NO <sub>2</sub>	CLA-02HV	DH-CLD	0-10000 ppm	4%

It should be noted that the emission measurement system is composed of sensors that deliver their result on a different basis (wet or dry). Therefore, a regulation was proposed to establish rules that should be followed during emissions measurement. In Europe, regulation 49 from UNECE is widely accepted as an emission measurement guide [184]. Therefore, it was employed to address the emission values in this work adequately. Once the raw emissions are obtained, they can be converted to mass by employing the general equation presented in Equation 3.1.

$$Emission [g/s] = y_i[-] \cdot \dot{q}_{exhaust} [g/s] \quad 3.1$$

where  $\dot{q}_{exhaust}$  is the exhaust mass flow rate in g/s and  $y_i$  stands for the mass fraction of each component that can be obtained by Equation 3.2.

$$y_i = x_i \cdot \frac{MW_i}{MW_{exhaust}} \quad 3.2$$



Equation 3.4 can be particularized for each interest component and its measurement basis. In addition, the values can be converted to power-specific units dividing by the power delivered in each operating condition ( $P$ ). This last parameter can be given on both a brake and indicated basis:

$$SCO = \frac{\dot{m}_{CO}}{P} = \frac{x_{CO} \cdot \frac{MW_{CO}}{MW_{exhaust}} \cdot \dot{q}_{exhaust} \cdot k_{w,r}}{P} \quad 3.3$$

$$SNO_x = \frac{\dot{m}_{NO_x}}{P} = \frac{x_{NO_x} \cdot \frac{MW_{NO_x}}{MW_{exhaust}} \cdot \dot{q}_{exhaust} \cdot k_{w,r} \cdot k_{h,D}}{P} \quad 3.4$$

$$SHC = \frac{\dot{m}_{HC}}{P} = \frac{x_{HC} \cdot \frac{MW_{HC}}{MW_{exhaust}} \cdot \dot{q}_{exhaust}}{P \cdot k_{FID}} \quad 3.5$$

Additional CO<sub>2</sub> measurement line enables the online measurement of the EGR quantity by Equation 3.6.

$$EGR [\%] = \frac{CO_2 intake_{dry} - CO_2 ambient}{CO_2 exhaust_{dry} - CO_2 ambient} * 100 \quad 3.6$$

Last but not least, an AVL 415S smoke meter was employed to quantify the soot production for the different operating conditions assessed. A specific volume of exhaust gases is forwarded to the smoke meter passing through a clean paper filter. The blackening of the paper filter is measured using a reflectometer and then correlated to FSN (Filter smoke Number), which can range from 0 to 10. The AVL 415 S has a resolution of 0.001 FSN with a minim detectable limit of 0.002 FSN. Since the normative values are generally specified in g/kWh, the correlation presented in equation 3.7 proposed by Christian et al. was employed to determine the volumetric soot mass (mg/m<sup>3</sup>). A constant exhaust gas density is used to convert it to mass basis (mg/kg) and to allow the subsequent conversion to g/kWh [185].

$$Soot = \frac{1}{0.405} \cdot 4.95 \cdot FSN \cdot e^{(0.38 \cdot FSN)} \quad 3.7$$

It should be stated that the smoke meter measurements cannot quantify the totality of particulate matter mass presented in the exhaust gases. Its optical measurement system is inaccurate in accounting for condensable organics, underestimating the real particulate matter mass in the exhaust. Moreover, the DMDF particulate matter composition has deviated from the CDC once the condensable organic hydrocarbons are dominant PM mode on RCCI, affecting the accuracy of the soot estimation for this combustion concept [186].

Figure 3-4 depicts the standard test cell configuration used during this investigation. The test bench control was realized by employing the AVL PUMA interface, allowing for a selection of different operating modes and the acquisition of the most critical parameters during the evaluations. An optical encoder AVL 364 was installed on the engine's crankshaft, which has an interpolated resolution of 0.2 CAD.

Instantaneous pressure transducers are also employed at the intake and exhaust manifold to capture pressure wave interactions and flow pulsation caused by the engine operation, providing valuable information for modeling applications. In addition, average pressure and temperature sensors are included in different locations of interest to capture critical phenomena such as pressure drop and flow expansion in specific devices and track the heat transfer that occurs along the exhaust and intake lines. The test cell facility is also fully instrumented with pressure and temperature sensors and environmental monitoring systems.

The six cylinders contain instantaneous in-cylinder pressure transducer (piezoelectric Kistler 6125C sensor), which are introduced to monitor the in-cylinder dispersion from different sources as differences in empty-filling process, air distribution, or even injection differences. Moreover, the individual monitoring guarantees that none of the cylinders are operating over the mechanical limitations imposed during the evaluations. Mass flow measurement is performed through a positive displacement flow meter Elster RVG G100 rotary meter, located at the intake runner.

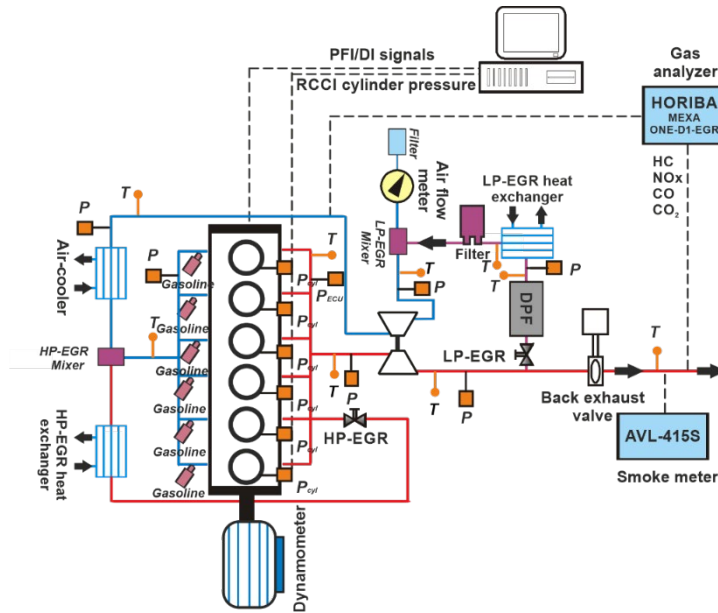


Figure 3-4. Test cell facility scheme presenting the different subsystems and the measurement devices used to assess the DMDF concept on the multi-cylinder engine.

### 3.3 Fuels properties and calibration maps

Throughout this work, different fuels for both low reactivity and high reactivity applications were used to realize the fuel characteristics to deliver the best results in both performance and emissions.

Considering LRF, most of the investigation relies on using commercial gasoline. The properties are suitable to run in the DMDF concept with low NO<sub>x</sub> and soot emissions. In addition, as can be found in any fuel station, the first option to be considered if the objective is to apply the concept on a large scale. Methanol is used to explore a synthetic fuel with the potential to reduce CO<sub>2</sub> emissions at the WTW level. Table 3-5 presents the characteristics of each LRF fuel.

Considering HRF, commercial diesel was used extensively during the investigations as a drop-in fuel for DMDF combustion. Despite this, additional high reactivity fuels were also evaluated as alternatives to push the combustion concept towards lower WTW CO<sub>2</sub> emissions. Specifically, oxymethylene ethers (OMEx) were used because this fuel can significantly reduce the CO<sub>2</sub> footprint during their production cost. OMEx allows for a drastic reduction of soot formation compared to Diesel combustion. Nonetheless, it has a low value of lower heating value (LHV), which increases its volumetric fuel consumption. The low LHV is a direct consequence of the molecule's low carbon and hydrogen content, as almost half of it is composed of oxygen [187]. Table 3-5 summarizes the chemical-physical properties of the high reactivity fuels used.

*Table 3-5. Physical-chemical properties of the high reactivity fuels evaluated during the investigation.*

Property	Gasoline	Methanol	EN 590 diesel	OMEx
Type of Fuel	LRF	LRF	HRF	HRF
Density [kg/m <sup>3</sup> ] (T= 15 °C)	720	792	842	1067
Viscosity [mm <sup>2</sup> /s] (T= 40 °C)	0.55	0.58	2.93	1.18
RON [-]	95.6	109	-	-
MON [-]	85.7	100	-	-
Cetane number [-]	-	-	55.7	72.9
Carbon content [% m/m]	84.3	37.5	86.2	43.6
Hydrogen content [% m/m]	15.7	12.6	13.8	8.8
Oxygen content [% m/m]	0	49.9	0	47.6
Lower heating value [MJ/kg]	42.4	19.93	42.44	19.04

It should be remarked that both LRF and HRF fuels present a significant dispersion on the lower heating values. In this sense, the brake-specific fuel consumption can be seen as affected by these LHV differences. Therefore, an equivalent brake specific fuel consumption ( $BSFC_{eq}$ ) was included whenever the fuel was modified to account for these differences by

normalizing the LHV of the given fuel with respect to its pair (gasoline for LRF and diesel for HRF) as presented in Equation 3.8. In addition, in Dual fuel concepts, the Premix Energy Ratio (PER) is an essential parameter for understanding the energy amount of each of the fuels (HRF and LRF). This parameter is calculated by equation 3.9.

$$BSFC_{eq} [g/kWh] = \frac{\dot{m}_{HRF} [g/h] \cdot \left( \frac{LHV_{HRF}}{LHV_{diesel}} \right) + \dot{m}_{LRF} [g/h] \cdot \left( \frac{LHV_{LRF}}{LHV_{gasoline}} \right)}{Power_{brake} [kW]} \quad 3.8$$

$$PER = \frac{m_{LRF} LHV_{LRF}}{m_{HRF} LHV_{HRF} + m_{LRF} LHV_{LRF}} \quad 3.9$$

An extensive experimental campaign was performed in the work of R. Lago [108] to obtain the calibration maps for the DMDF concept in a multi-cylinder engine. The dual-mode dual-fuel combustion consists of RCCI mode at low and medium load, and dual-fuel diffusion combustion is promoted at high load (see Figure 3-5a). The transition zone is coupled with an intermediate injection strategy between the modes mentioned above. The injection strategy of the two fuels, diesel (DI, marked with green) and gasoline (PFI, marked with blue), are illustrated in Figure 3-5a.

Figure 3-5b shows the effect of the different injection strategies in the mixture formation on an equivalence ratio-temperature map, where the NOx and soot formation peninsulas are highlighted. These data were extracted from previous work utilizing CFD analysis [188]. It is important to note that the DMDF achieved the same maximum power and torque values as the original CDC calibration. The fuel consumption and emissions were measured in 52 operating conditions between 950 and 2200 RPM and 15-350 hp (black points in Figure 3-5a). The measurements of the same operational points were repeated with the OEM configuration (CDC ICE) for a fair comparison.

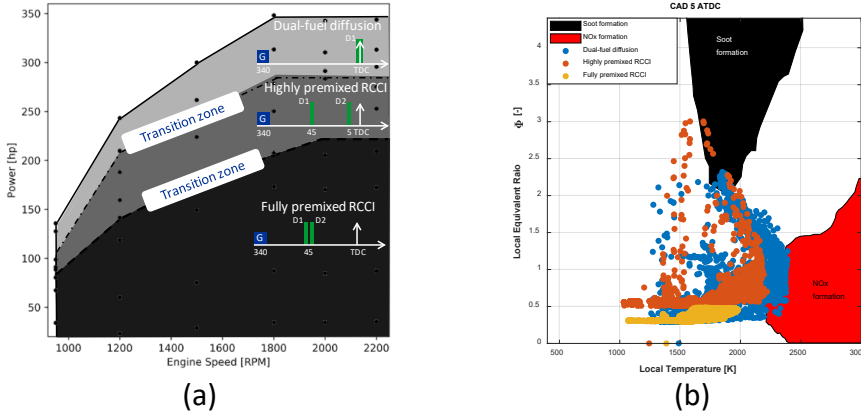


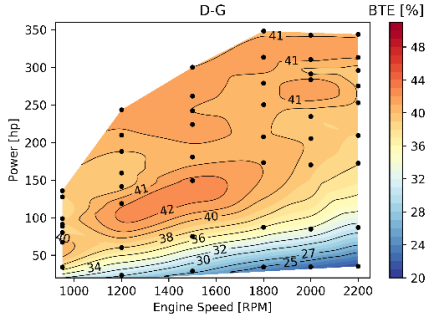
Figure 3-5. Calibration strategy with combustion types by power and rotational engine speed (a) and example of 5 CAD ATDC local equivalent ratio and local temperature distribution for the three phases (b).

The calibration maps obtained by R. Lago [108] for Diesel-Gasoline and OMEx-Gasoline for the 8L six cylinders engine are shown in Figure 3-6. The engine is calibrated up to  $\approx 210$  hp (60% of engine load) in full RCCI mode and DMDF up to  $\approx 350$  hp (100% of engine load) in 54 operational points. Brake specific fuel mass consumption, brake specific fuel volume, brake specific  $\text{CO}_2$  Tank-to-Wheel, brake specific  $\text{CO}_2$  Well-to-Wheel, Premix Energy Ratio, brake specific NOx, and brake specific Soot are presented.

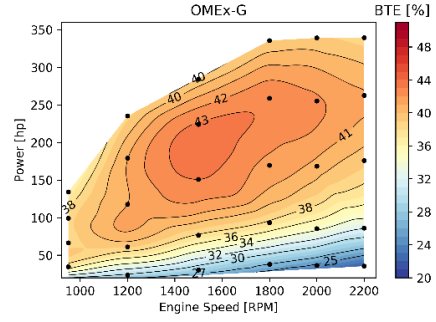
For Diesel-Gasoline calibration, the highest fuel economy (below 200 g/kWh) was achieved at medium load and speed due to the flexibility of this map zone to increase the GF ( $>80\%$ ) and EGR rate. Figure 3-6 shows that this zone achieved the lowest NOx value (0.2 g/kWh) with almost negligible soot emissions. In the transition zone, see Figure 3-6, the soot emission increases gradually with the load. However, the NOx emissions remain below 0.4 g/kWh, corresponding to the tailpipe EU VI limit for Heavy-Duty applications. The fuel economy in this region is acceptable, with values around 205 to 210 g/kWh. Moreover, the GF rate decreases due to the high-pressure gradients down to values around 60%.

Lastly, the dual-fuel diffusion zone completes the engine map up to 350 hp with lower GF rates (<50%) than the previous zone. In this zone, diesel fuel gives the engine load instead of gasoline, as was in the RCCI and transition zone. It is important to note that the gasoline fraction is equivalent to the premix energy ratio due to the similar lower heating value of both fuels. The calibration was performed in the highest load zone to achieve NO<sub>x</sub> emissions below 2.0 g/kWh and the soot emissions below 100 mg/kWh. For reference, the CDC calibration map achieves 9.0 g/kWh for NO<sub>x</sub> and 60 mg/kWh for soot. It is important to remark that the CR decrease strongly affects the calibration results. For one side, it allows achieving an entire calibration map with dual-fuel combustion and ultra-low NO<sub>x</sub> values in a multi-cylinder engine. The in-cylinder conditions are not possible to control as single-cylinder prototypes. On the other side, the fuel economy achieves values close to the CDC ICE but cannot be further improved. As it is well known, the CR directly impacts the brake thermal efficiency. In spite of this, the differences are lower than 7 g/kWh (200 g/kWh for DMDF and 193 g/kWh for CDC). The LTC modes have large CO and HC emissions due to low-temperature combustion inside the combustion chamber and the PFI gasoline injection. The maps can be found in the previous work of the author [189].

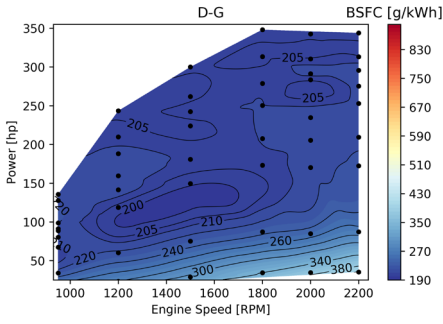
The main advantage of using OMEx-Gasoline is seen in the NO<sub>x</sub> and soot emissions with complete fulfilling of EUVI on all maps. The BTE is similar with some improvements in the case of OMEx-Gasoline thanks to the higher freedom to change air management settings due to the high oxygen content and no C-C bounds. The main drawback of OMEx substitution of Diesel is the higher mass fuel consumption. The difference is reduced for fuel volume consumption due to the higher density of OMEx compared to Diesel.



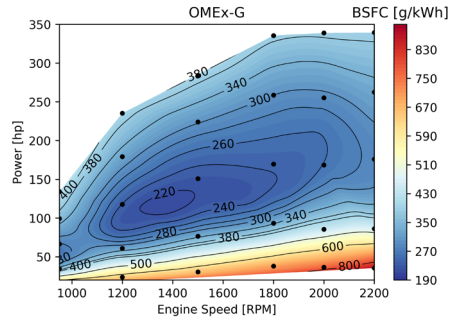
(a)



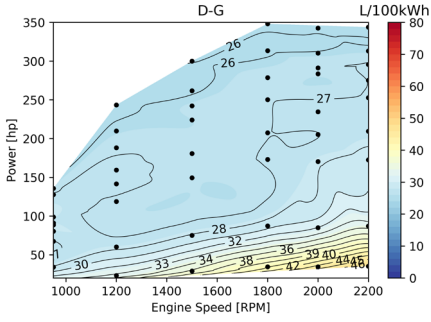
(b)



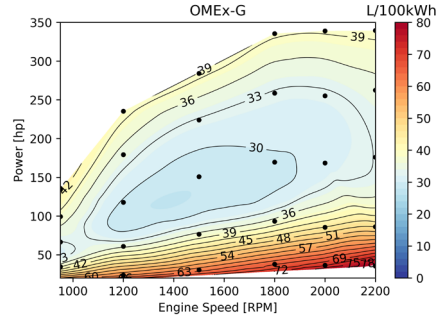
(c)



(d)

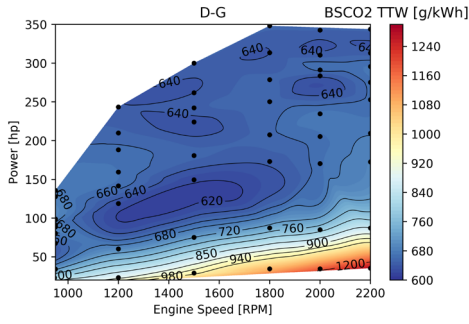


(e)

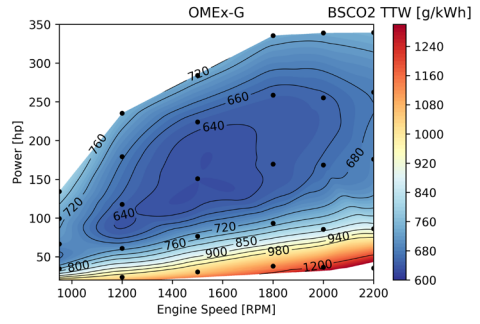


(f)

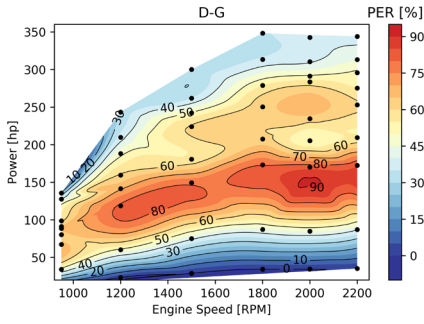




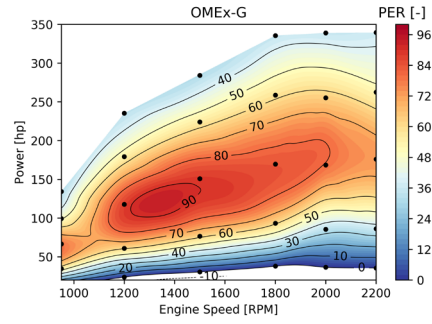
(g)



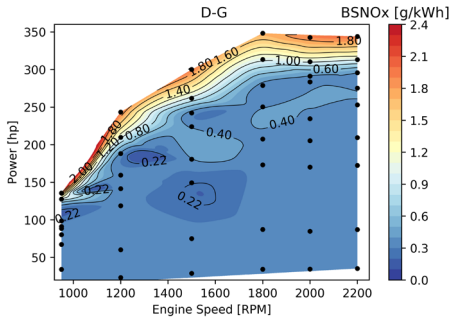
(h)



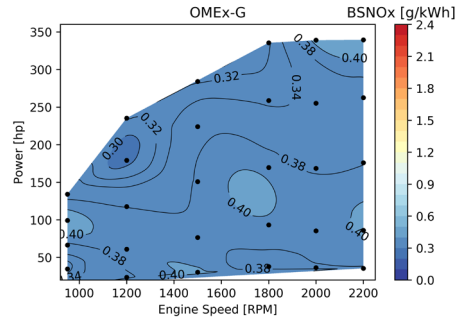
(i)



(j)



(k)



(l)

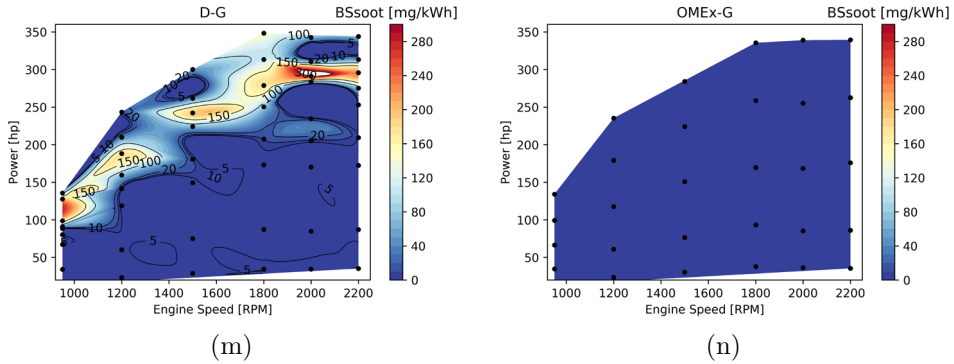


Figure 3-6. Dual Fuel dual-mode brake specific consumption and emissions for Diesel-Gasoline (left) and OMEx-Gasoline (right). Adapted from [108].

To better understand the emissions fulfillment and the power delivered, Figure 3-7 summarizes the emission maps by highlighting the zones in which the EU VI normative for stationary conditions is fulfilled for NO<sub>x</sub> and soot (0.4 g/kWh and 0.01 g/kWh, respectively). The three zones defined with dashed lines correspond to three engine calibration maps used in the different truck platforms and the work. Heavy-Duty engine manufacturers widely use the de-rating methodology to reduce the number of engine versions in the different truck applications. In this work, the calibration zone in which it is possible to achieve the EU VI NO<sub>x</sub> and soot levels simultaneously in the whole region will be referred to as RCCI 210. The nomenclature identifies the primary combustion mode and the maximum power output in horsepower. One step further is the DMDF 280, being EU VI compliant only in NO<sub>x</sub> for the complete map. Finally, the DMDF 350 is the complete map calibration presented above.

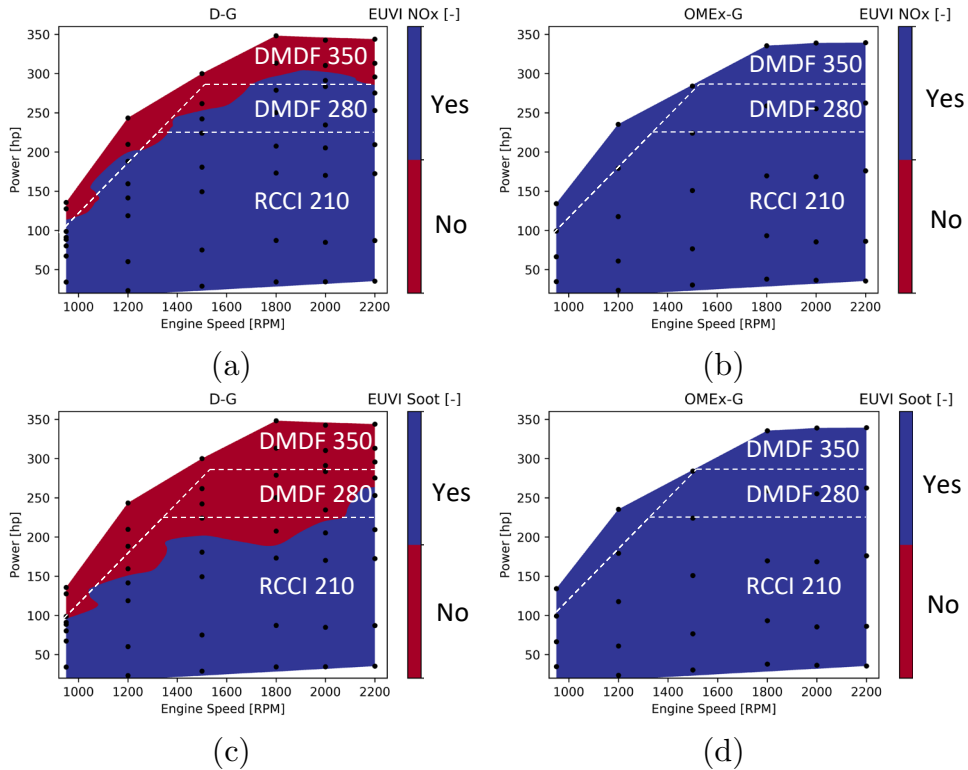


Figure 3-7. Dual Fuel dual-mode EU VI normative comparison for NOx and soot for Diesel-Gasoline (left) and OMEx-Gasoline (right).

### 3.4 Numerical tools

This section describes the numerical tools used for vehicle, engine, ATS, and electric components simulations. Despite the simplifications found in 0-D calculations, it is a powerful approach to investigating phenomena under specific assumptions and well-controlled conditions. Moreover, it allows obtaining a general overview of processes in a much fast time order than 1-D and multi-dimensional approaches. This investigation uses a 0-D vehicle model in GT-Suite (Gamma Technology®). This software allows applying already set up sub-models for vehicle components and the flexibility to create own user models.

For the engine simulation, two approaches are used. A map-based approach is used with the experimental data presented in the previous section for vehicle simulation. GT-Power (Gamma Technology®) is used to understand the effect of different e-components in the air management system. This software package consists of a multi-domain approach combining the 1-D discretization of the conservation equations by finite volumes method with a 0-D phenomenological model [30]. These equations are solved explicitly in the time, i.e., considering the solution field from the last iteration during the integration and specifying a proper time step to guarantee solver stability calling the Courant condition [31]. This software package models the combustion chamber, cooling system, and all air inlet and gas exhaust pipes. The ATS is also modeled with GT-Power by including dedicated sub-models. Experimental data to adequately describe the component operation is mandatory.

In addition, GT-AutoLion (Gamma Technology®) is used to simulate the lithium-ion battery package and linked with the vehicle model in GT-Suite. An electrochemical model is used to predict cell voltage, temperature, and aging characteristics.

Lastly, an LCA database is created and directly implemented in Matlab® to calculate each hybrid platform's modeled WTW and LCA CO<sub>2</sub> emissions.

### 3.4.1 Vehicle model

The implementation of new technology in a real platform requires a Technology Readiness Levels (TRL) 9. It is important to note that the purpose of Technology Readiness Levels (TRL) is to measure the maturity of technology components for a system. TRL 9 means that the subsystems, controls, sensors, and trials are already done. Unfortunately, reaching this level of readiness is time-consuming and expensive. Nonetheless, the concept's potential can be proved to some extent by the technology simulation in a

virtual platform. The vast number of tools and templates ready in GT-Suite and the user-friendly interface allow to model complex systems in a reduced time. Therefore, this software was employed to evaluate the developed concept and assess the advantages and drawbacks of using the RCCI combustion mode in several hybrid architectures and different levels of hybridization.

This work focuses on a delivery truck representative of Medium-Duty applications. A Volvo FL truck with a maximum payload of 18-ton was chosen because it equips the same engine as the experimental campaign. Table 3-6 summarizes the characteristics of the VOLVO FL truck (ICE of 280 hp). Additional details can also be evidenced in Table 3-6. The commercial application is a non-hybrid powertrain with a manual gearbox of six gears (Gear ratios of:  $i_{g,1} = 3.36$ ,  $i_{g,2} = 1.91$ ,  $i_{g,3} = 1.42$ ,  $i_{g,4} = 1.00$ ,  $i_{g,5} = 0.72$  and  $i_{g,6} = 0.62$ ). The conventional non-hybrid diesel truck model is shown in Figure 3-8, and in this work, it will be referenced as a baseline case for comparison. The main sub-models are the vehicle, transmission, engine, ECU, and the driver.

*Table 3-6. Aerodynamic and geometric characteristics of the VOLVO FL 280 truck. Source [190].*

Truck characteristics	Value
Engine / Max power [hp]	MD8 280K / 280 <sub>@2200RPM</sub>
Vehicle weight [kg]	5240
Max. Cargo mass [kg]	12760
Max. Total mass [kg]	18000
Drag coefficient [-]	0.65
Vehicle frontal Area [m <sup>2</sup> ]	5.52
Vehicle Wheelbase [m]	4.4
Rolling friction [-]	0.0155
Tires specification	295/80R/22.5"
Gear box models	ZF Eco Life Manual six gears
Differential drive ratio	5.29

Overall Chassis Length (A) [mm]	9915
Wheel Base (WB) [mm]	5300
Center of Gravity (Max/Min) (Y) [mm]	1532/1283
Center of rear axle to front (D) [mm]	4709

The diagram illustrates the chassis and cab dimensions of a truck. The side view of the chassis shows the overall length (A), wheel base (WB), distance from the front axle to the center of gravity (D), and the height of the center of gravity (Y). The front wheel offset is 1320 mm, and the rear wheel offset is 541 mm. The height of the rear axle is 912 mm. The cab view shows a height of 2833 mm and a width of 2282 mm.

A map-based approach is used to model the engine. This means inserting the fuel consumption and emissions matrix (z-axis) with engine speed (x-axis) and torque (y-axis) as dependency parameters. The powertrain model will calculate the torque and speed requested, and the sub-model of the engine will return a value of mass fuel consumption, PER, and emissions (NO<sub>x</sub>, soot, CO, HC, and TTW CO<sub>2</sub>). Moreover, the ECU sub-model is in charge of controlling the torque request to the engine depending on the driver's accelerator pedal position. Also, it is in charge to control the engine during the idle phase. The engine was controlled to 700 RPM for the cases without a start/stop function in this work.

The driver model is in charge of calculating the forces required to achieve the desired speed target. The forward approach is used to generate the signals of throttle and brake pedal positions. These two signals result from the PID control, which tries to match the target speed imposed by an input driving cycle based on the actual vehicle speed. This approach allows considering the component's limitations, which may hinder the capability of the vehicle concept under test to accomplish the driving cycle. In theory, this approach also allows simulating different driver behaviors (i.e., driving aggressiveness) by tuning the factors of the PID controller. In the current

study, the forward approach is used since it maintains the physical causality of the real system. The accelerator and brake signals generated by the driver PID controller are converted to a power/torque request, which is used to actuate the ICE and/or EMs, according to the power ratio strategy operated by the supervisory energy management controller.

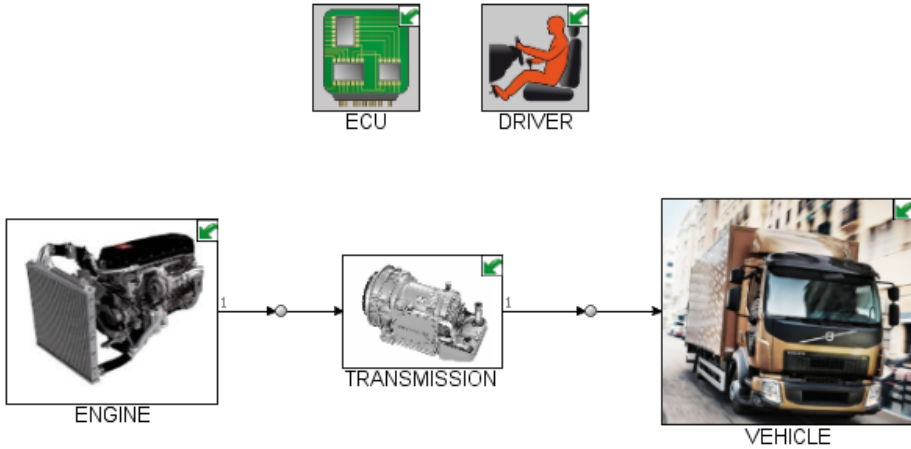


Figure 3-8. Numerical model of the non-hybrid truck in GT-Suite.

For each condition, an energy balance equation is solved as presented in equation 3.10 by solving the interaction of the forces for longitudinal analysis shown in Figure 3-9.

$$ma = F_{traction} - F_{aerodynamic} - F_{gravity} - F_{roll\ friction} \quad 3.10a$$

$$ma = \frac{T_{tract}}{r_w} - \frac{1}{2}c_D\rho_{air}S_f v_{veh}^2 - M_{veh}g\sin\alpha - c_r M_{veh}g\cos\alpha \quad 3.10b$$

with  $a$  is the longitudinal vehicle acceleration,  $T_{tract}$  the traction torque applied at the motored wheels,  $r_w$  the wheel radius,  $c_D$  the aerodynamic drag coefficient,  $\rho_{air}$  the air density,  $S_f$  the frontal vehicle surface,  $v_{veh}$  is the vehicle speed,  $M_{veh}$  is the vehicle curb mass that encompasses the unloaded mass and the passenger and cargo masses,  $g$  is the acceleration of gravity,  $c_r$

is the rolling friction coefficient,  $\alpha$  is the road grade. The  $m = M_{veh} + 4\frac{J}{r^2}$  is the equivalent mass that also considers the rotating inertias. For the hybrid cases, the extra mass related to the battery pack and EM/s will also be added after the design phase to  $M_{veh}$ .

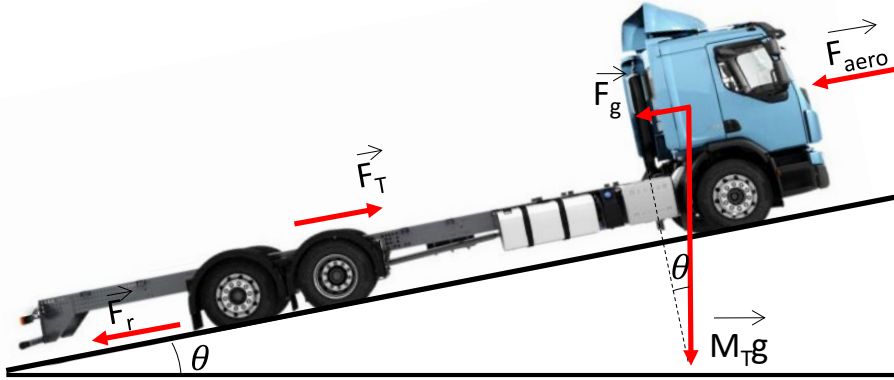


Figure 3-9. Forces involved in the numerical simulation of the vehicle.

The driveshaft rotational speed  $\omega_{shaft}$  depends on the engaged gear transmission ratio  $i_g$  for a given vehicle's speed  $v_{veh}$ . The vehicle speed is also multiplied by the differential ratio  $i_{diff}$  following Equation 3.11.

$$\omega_{shaft} = \frac{v_{veh}}{r_w} i_g i_{diff} \quad 3.11$$

The efficiency for all gears is assumed to be 0.97. The gearshift schedule is set in the driver sub-model. For the non-hybrid case, the original OEM schedule is set in which the gear upshift is at 2000 RPM. Optimization of the strategy was implemented by assuming an automatic transmission for the cases of the hybrid powertrain with transmission (P0 and P2). The same gear relationship that the non-hybrid case is adopted. The speed range from zero to the maximum vehicle speed is divided into six intervals. The values for up-shift speeds can be then regulated by means of a gear-shift coefficient  $\phi$ : the maximum ICE speed  $n_{ICE,max}$  is known to be 2200 RPM therefore the ICE speed at the moment of the gear shift  $n_{ICE,up-shift}$  can be tuned. At this



point, as the transmission ratio for each gear and the differential ratio are known, the vehicle speed for each gear shift  $v_{up-shift,k}$  with  $k$  the gear position (from 1 to 6) can be calculated with equation 3.12b. The down-shift speed is set to 4 km/h slower than the up-shift speed to avoid frequent shifts equation 3.12c.

$$n_{ICE,up-shift} = \phi * n_{ICE,max} \quad 3.12a$$

$$v_{up-shift,k} = \frac{2\pi n_{ICE,up-shift}}{60} \frac{r_w}{i_{g,k} i_{diff}} \quad 3.12b$$

$$v_{down-shift,k} = v_{up-shift,k} - 4 \text{ km/h} \quad 3.12c$$

The 0D-vehicle model with all the powertrain components was compared against on-route measurements to ensure that the model replicates the behavior of the real vehicle. Volvo Group provides the data of a commercial FL 18-ton non-hybrid diesel truck platform with torque measurements in the ICE and output of the transmission, gear position, fuel consumption, engine data (rotation speed, driver acceleration demand), and GPS data (speed, acceleration, altitude) against the time. Figure 3-10 shows the truck platform with the different measurement sensor positions. The torque measurement in the ICE and transmission output axle allows for calibrating the transmission and clutch losses and the transient behavior of the components. The fuel consumption was compared against the simulation results.

The model calibration checks the vehicle information collected and shown in Table 3-6 to adjust the power losses. The measured map of fuel consumption with the 54 operative points for CDC in the CMT-UPV test bench was used for the ICE modeling. On one side, this allows validating the map-based approach, and on the other side enables us to understand if the test bench replicates the Volvo On-road measurements. This same test bench was used for the RCCI maps presented in the previous section. Figure 3-11 shows the instantaneous and accumulated fuel consumption mass of diesel with the experimental and simulation results for a custom driving cycle called

the Local cycle. The model allows a reasonable agreement regarding total fuel consumption with a deviation below 2%.

Moreover, Figure 3-11 shows a good agreement in the transient behavior with similar peaks. The rest of the cycles show similar agreements and are not included for the brevity of the manuscript. It is important to note that the emissions measurement was not available. Therefore, this was not possible to compare this truck platform. A previous work [130] compared a Light-Duty Euro 6 diesel engine with a similar modeling approach in transient conditions. In particular, the WLTC cycle was studied with a difference between numerical and simulation results below 4% for NO<sub>x</sub> engine-out emissions.

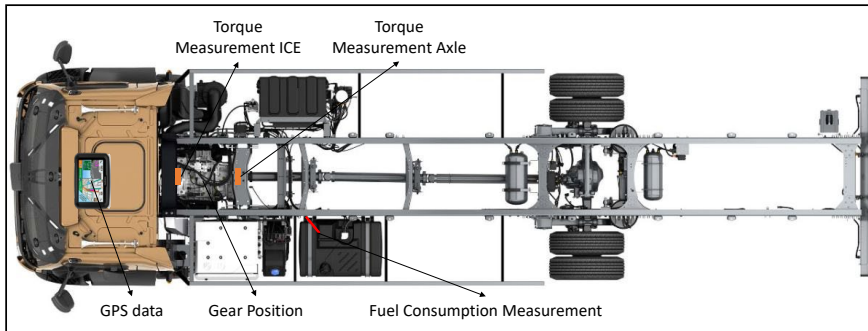


*Figure 3-10. FL 18-ton CDC no-hybrid powertrain layout and sensor position for on-route fuel consumption measurements*

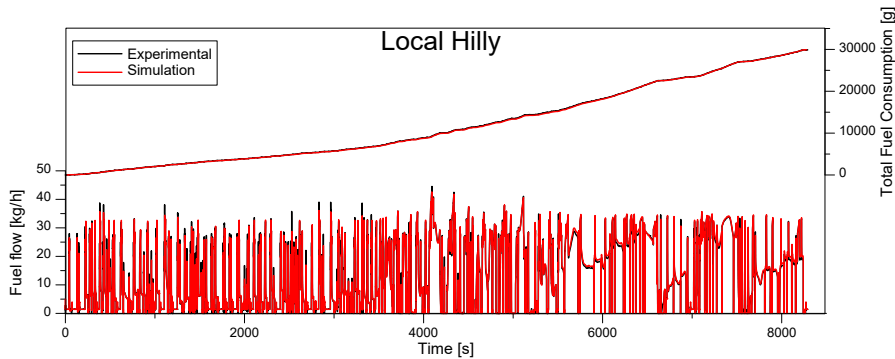
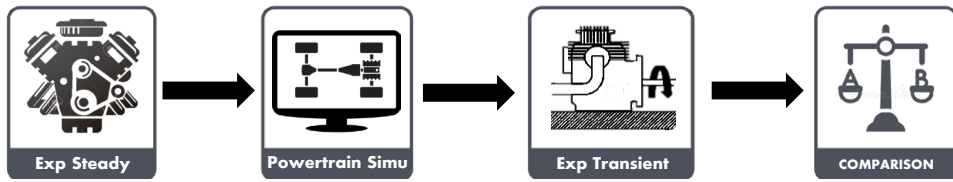


Figure 3-11. Total and rate of fuel consumption against time for the Local Hilly driving cycle measured with the FL 18-ton CDC no-hybrid truck with 50% of payload.

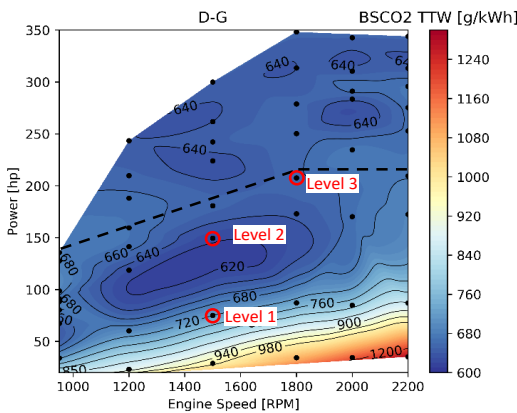
After the good agreement between the experimental results and the conventional vehicle simulation model in terms of vehicle forces and fuel consumption, the hybrid powertrains were built on the same model basis but with all the electric components and new controllers. In addition, the ICE maps were substituted by the RCCI ones. These models are presented in detail in the results chapters.

Transient experimental campaign was performed with the RCCI engine configuration to compare the 0D engine numerical model and the experimental results. In particular, a Series hybrid powertrain was simulated to compare the emissions of the engine-based map approach for RCCI with experimental data. This type of powertrain allows operating in soft transient steps in the engine instead of fast transient changes as a non-hybrid or parallel hybrid. Therefore, the homologation cycle for HD (WHVC) was tested in the experimental test bench with the FL 18-ton truck with a Series hybrid architecture. Three power steps for the ICE were set depending on the battery's state of charge and the vehicle speed. A detailed explanation of this architecture and the control strategy is explained in detail in chapter 5. However, the ICE emissions results are used to validate the map base approach used in this section. A summary of the approach is depicted in Figure 3-12.

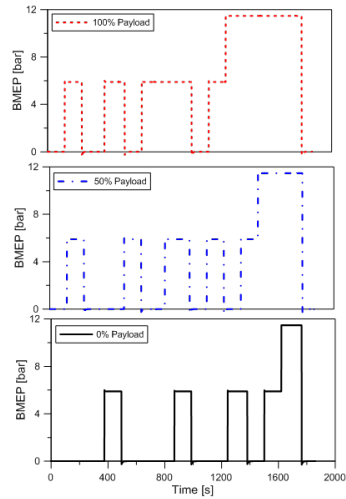
The instantaneous emissions values are presented in Figure 3-13 for the WHVC with a 50% payload. CO<sub>2</sub> tailpipe emissions (Figure 3-13a) are calculated by the Diesel-Gasoline carbon emission and the fuel consumption values. Therefore, the agreement is almost perfect due to the imposed injection settings for both fuels. Figure 3-13b shows that the model overpredicts the emissions values in almost all conditions for NO<sub>x</sub> emission. This is mainly to a lower combustion chamber temperature due to the start/stop. After 120 s, the emission achieves the stationary value in which the model sets the step value. The HC and CO show inverse behavior. The model underpredicts the emissions values. This is a consequence of the different mechanisms responsible for each emission formation. In the RCCI combustion, CO emissions are mainly produced in rich zones, where there is insufficient oxygen to oxidize the CO to CO<sub>2</sub>. Lower temperatures may reduce the reaction rates of the oxidation paths, but this mechanism does not seem to be affected in this case since the CO emission is like those of the simulation cases.



(a)



(b)



(c)

Figure 3-12. Testing methodology scheme (a), operational conditions marked in red over the calibration map for tank-to-wheel (tailpipe)  $CO_2$  with RCCI diesel-gasoline (b), and Series hybrid optimum ICE load requirements at 0%, 50%, and 100% payload in the WHVC under diesel-gasoline RCCI Series hybrid.

On the other hand, HC emissions are significantly increased compared to the simulated cases. This effect can be attributed to the HC formation mechanism in RCCI combustion. Since a high quantity of fuel is injected employing port fuel injection, it tends to be directed towards the piston crevices during the compression stroke, where it cannot be burnt due to the high heat losses near the cylinder wall. The low cylinder block temperatures enhance the heat loss process, hindering fuel oxidation. This effect reduces as

the cycle approaches the final phase, where the engine is close to warm conditions. At this period, the instantaneous HC production is like that obtained with the steady-state calibration.

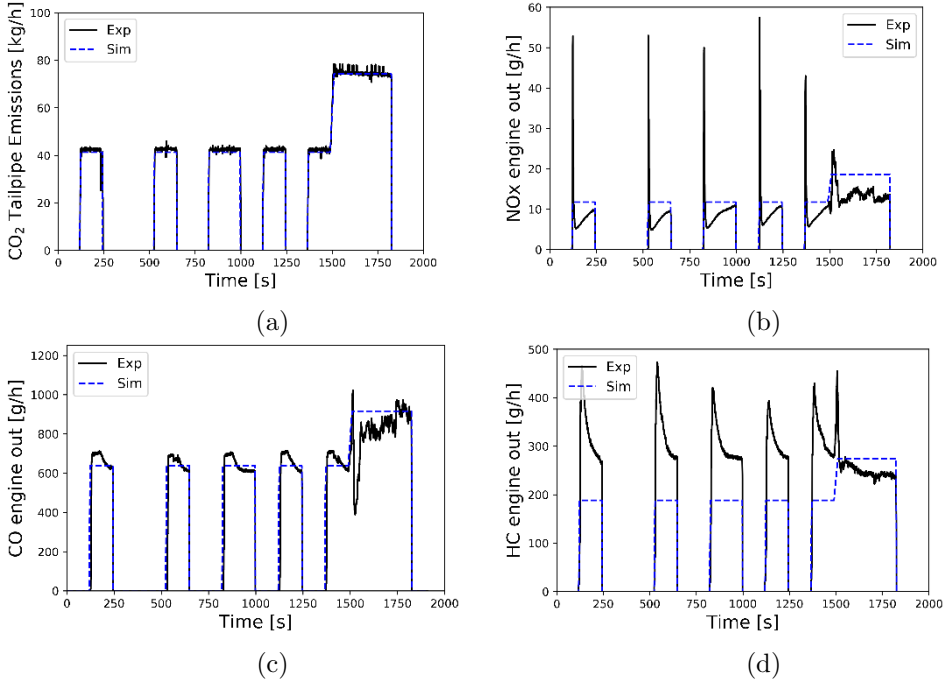


Figure 3-13. Experimental ICE test bed versus simulated ICE 0D vehicle model results in instantaneous emissions. WHVC with 50% payload Series hybrid RCCI.

The instantaneous results from fuel consumption and emissions were integrated concerning time to deliver the evolution of the cumulative profiles, allowing us to quantify the differences at the end of the transient cycle (see Figure 3-14). Fuel consumption results have demonstrated high similarity between the experimental and simulated values, attributed to the similar consumption of low and high-reactivity fuels. By contrast, emissions have demonstrated higher deviation due to the wall temperature and the combustion process in their formation compared with the steady-state conditions. NOx emissions presented a total deviation of 24% at the end of

the cycle, which is attributed to the delayed combustion process and low combustion chamber temperature. The differences are steeply increased during the cycle, as can be observed in Figure 3-14c and Figure 3-14d. The CO emissions present the major differences at the end of the cycle because of the difference in the operating condition with 50% of engine load. Nonetheless, the differences were around 7%, considering the final cumulative results. HC emissions have the opposite trend than NOx, with an underestimation of the numerical calculation totalizing more than 23% of the difference.

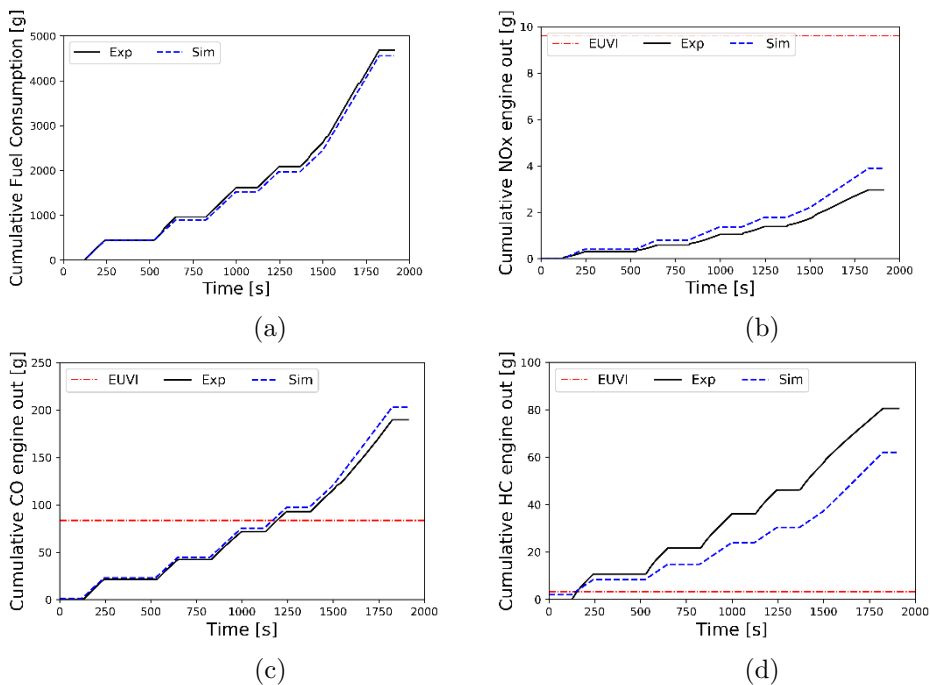


Figure 3-14. Experimental ICE test bed versus simulated ICE 0D vehicle model results in cumulative emissions. WHVC with 50% payload Series hybrid RCCI.

The same simulation methodology was applied for two other payloads (0% and 100%), enabling a comparison of the differences between the simulation and the real driving conditions for a broad set of operating

conditions. The results are presented in *Table 3-7*. It is possible to see that the increase in payload reduces the fuel consumption and emissions differences. The closest results are the fuel consumption (equivalent to the tailpipe CO<sub>2</sub> emissions) with a maximum difference of 3.6% at an empty truck. The simulation always underpredicts the experimental measurement. This behavior is attributed to the lower engine temperatures, increasing the required fuel to achieve a similar brake torque. In terms of pollutant emissions, the NO<sub>x</sub> and CO are over-predicted.

Meanwhile, the HC levels are under-predicted. The lower engine temperatures change the combustion parameters and combustion chamber temperatures. The NO<sub>x</sub> strongly decreases the prediction differences between 30% and 3% due to higher engine use requirements, increasing the overall cycle operation temperature. The HC emissions present similar behavior but only achieve a minimum of 10% at full payload. The CO shows the most stable measurement with average differences of around 5.5% for all payloads. An in-depth evaluation by the author was performed in [191].

*Table 3-7. Comparison of experimental ICE test bed versus simulated ICE OD vehicle model results in cumulative fuel consumption and emissions in grams and percentage differences. Case WHVC with 0%, 50%, and 100% payload Series hybrid RCCI.*

Payload	NO <sub>x</sub> [g]			HC [g]			CO [g]		
	Exp	Sim	Diff	Exp	Sim	Diff	Exp	Sim	Diff
<b>0%</b>	1.74	2.50	+30%	59.5	41.0	-31%	123	132	+7%
<b>50%</b>	2.97	3.88	+24%	80.5	62.1	-23%	190	203	+7%
<b>100%</b>	5.11	5.29	+3%	92.7	83.1	-10%	244	254	+4%

### 3.4.2 Internal combustion engine model

In general, numerical vehicle models use map-based due to the low computational cost and the accurate global results. In this type of approach, the main assumption is that the transient behaves as the stationary



condition. However, if the objective is to test new elements in the engine, for example, an electrified turbo, this approach is not the right approach for the evaluation. In this Thesis, three electrified components (e-components) were tested to improve the air admission (electrified turbocharging), the HP EGR line (electrified positive displacement pump), and the DOC heating time (electrified heater catalyst). To be able to model and test the RCCI combustion concept, it was necessary to calibrate a 1D engine model. This was performed in GT-Power, and the starting point was Volvo's conventional diesel combustion (CDC) MD8 GT-Power model version.

The experimental test is used to build a multi-cylinder engine model to predict engine performance, fuel consumption, and air management behavior. The emissions are not considered in this model and directly used the experimental measurements as output. All air management systems, combustion chambers, and engine crank trains, among others, are modeled. 36 of the 56 calibration points are taken for this evaluation to reduce the computational time. Figure 3-15 shows the selected operating conditions in engine speed and brake power output.

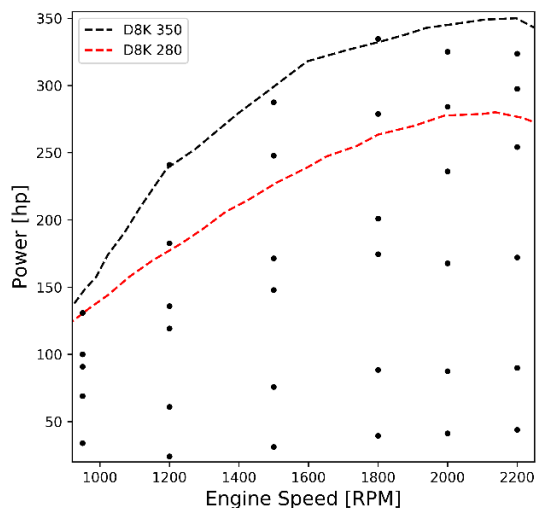


Figure 3-15. Engine calibration map with the 36 operative points and test matrix for e-components calibration.

Figure 3-16 shows the GT-Power numerical model for the DMDF Volvo engine. As can be seen, this model contains the HP EGR loop with the heat exchanger, valves, and pipes. In addition, the LP EGR loop is also modeled and connected after the turbine to the intake. All the pipes section and longitude are experimentally measured. The turbocharger was experimentally characterized by the OEM and previously used in the CDC model. This work adapted DMDF combustion by adding the LP EGR loop and the new experimentally measured heat release rate for this specific LTC combustion mode. Also, the instantaneous pressure and temperature measurements are used to calibrate the model.

The LP EGR loop comprises the DPF, heat exchanger, and pipes that model the experimental test bench loop. The combustion process is controlled by imposing the average six-cylinder combustion rate ( $1/CAD$ ) for each operative condition. This parameter is calculated by obtaining the heat release rate ( $J/CAD$ ) and normalized by the total fuel heat release energy ( $J$ ). Figure 3-17 shows an example of the fuel-burning rate for different engine operative conditions. This data is inserted in the combustion element of the GT-Power combustion chamber sub-model.

It is important to note that to speed up the simulation process, the heat exchangers are modeled as a heat transfer coefficient with a PID to enhance the cooling ratio to meet the experimental mean flow temperatures. A PID is included to control the VGT position in terms of air path calibration. A signal of intake air pressure at the entry of the cylinder collector is put as the control variable and the experimental pressure as a target. The VGT is varied between 0-1 to find the best calibration. In addition, a supplementary PID is set to control the exhaust back pressure just after the LP EGR loop in an exhaust valve equal to the experimental engine set up. Lastly, another two valves are controlled with a PID to regulate the intake's HP EGR and LP EGR exhaust mass. Each valve is inserted in the respective line. These four PIDs are optimized to calibrate the engine model to match the experimental data.

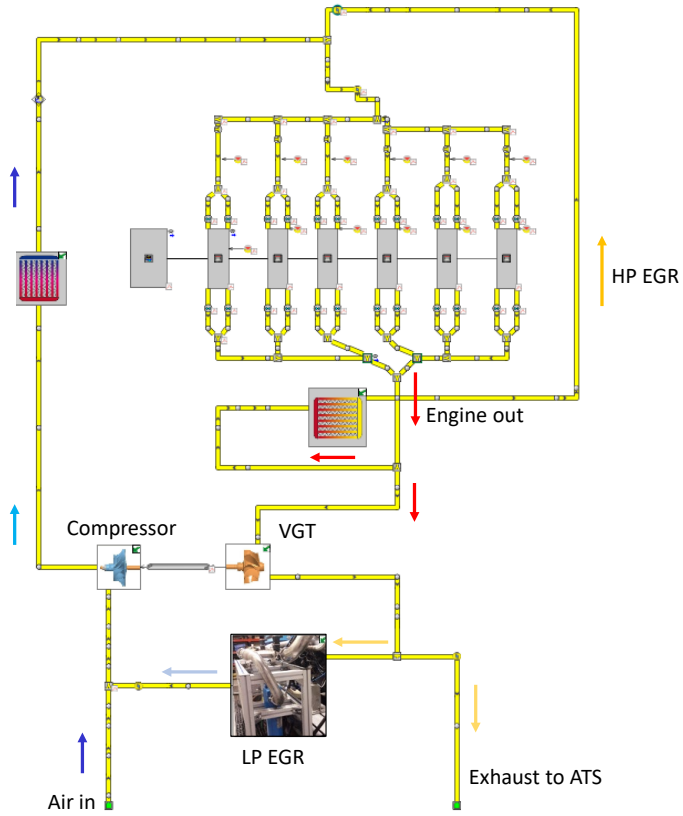


Figure 3-16. 0D-engine model for the DMDF ICE configuration with LP and HP EGR lines.

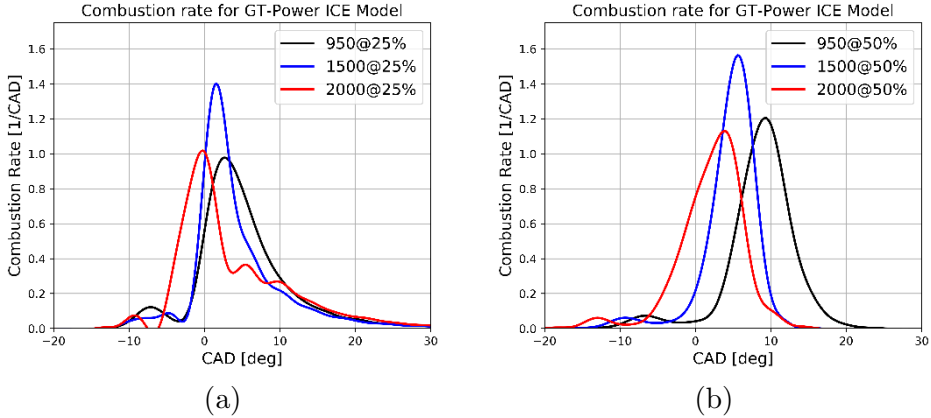


Figure 3-17. Combustion rate profiles were obtained experimentally with Diesel-Gasoline multi-cylinder engine for the GT-Power 1D model. Example for 25% load (a) and 50% load (b) for 950, 1500 and 2000 RPM.

The air management loop is adjusted to fit the experimental in-cylinder pressure, as is shown in Figure 3-18 to Figure 3-20. The same is repeated for the 36 operative conditions. Figure 3-21 shows that the IMEP and BMEP prediction agree with experimental data ( $R2 > 0.9$ ). The same agreement is also seen for turbine parameter as inlet pressure and temperature, as shown in Figure 3-22.

From this model, the work to be performed in Chapter 4 will be to modify the system to adapt an electric motor to the turbo compounding shaft (e-turbo), remove the LP EGR, and include a positive displacement pump (e-EGR pump) in the HP EGR line.

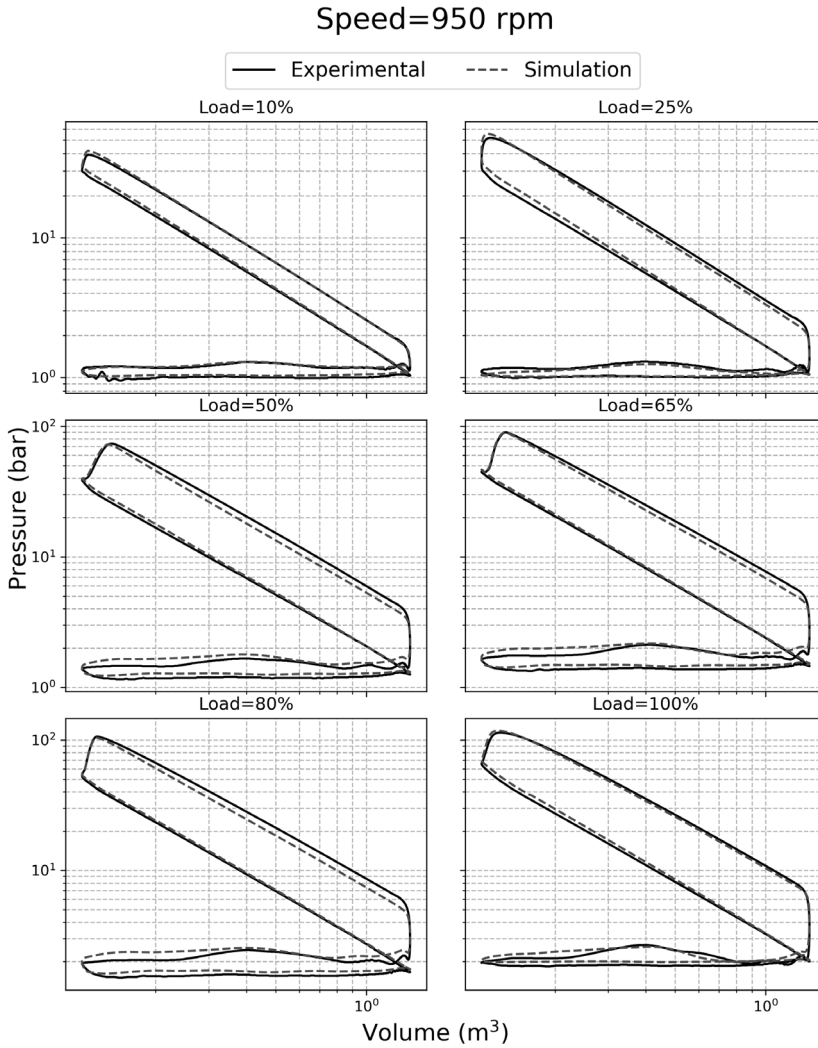


Figure 3-18. Pressure-volume diagram including the experimental and simulation traces for 950 RPM of engine load for the DMDF LP+HP EGR configuration.

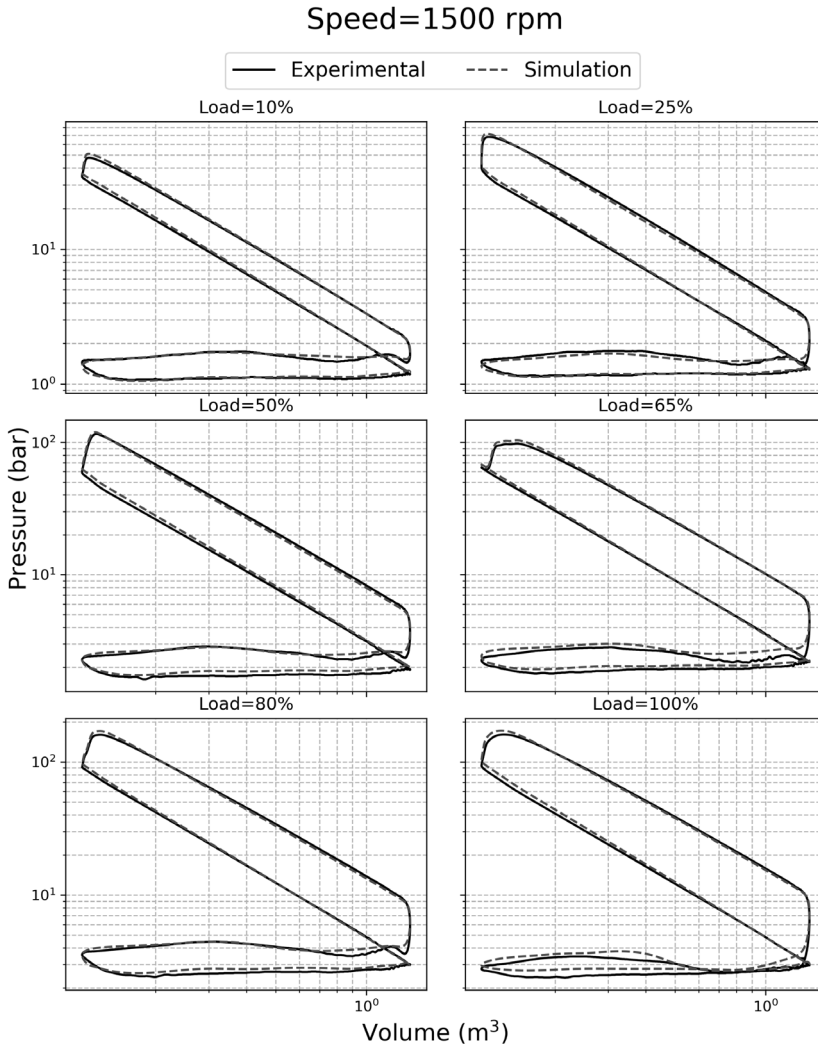


Figure 3-19. Pressure-volume diagram including the experimental and simulation traces for 950 RPM of engine load for the DMDF LP+HP EGR configuration.

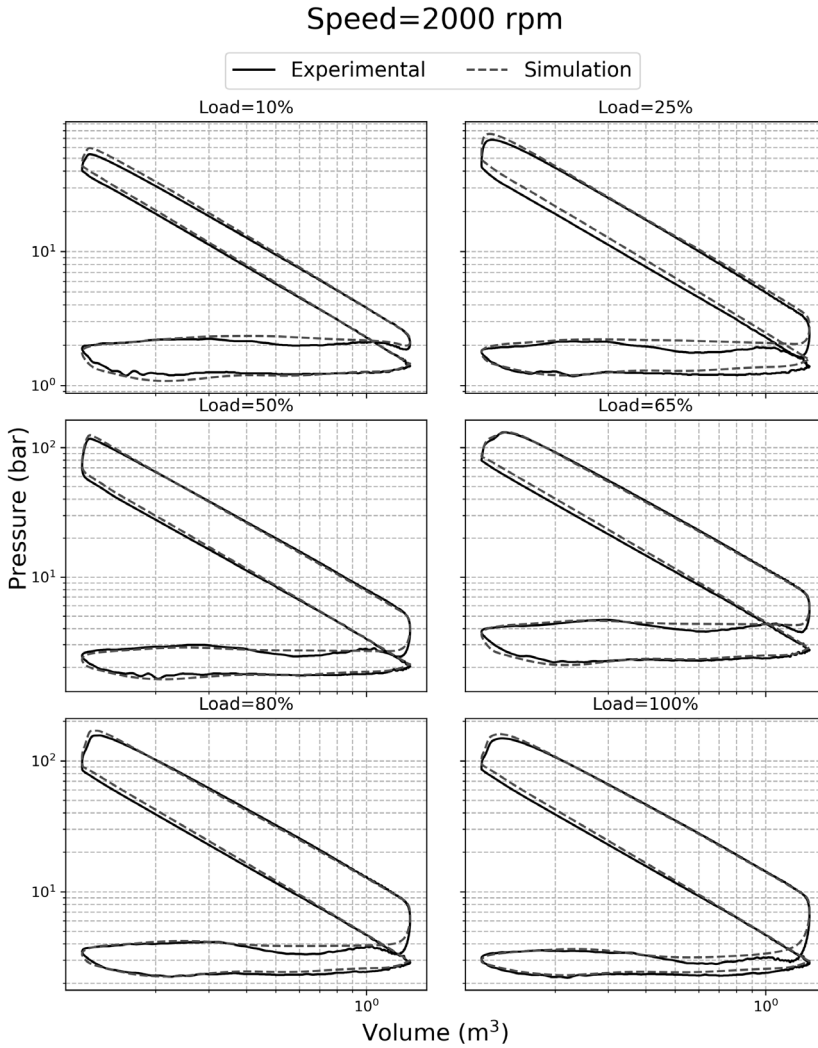


Figure 3-20. Pressure-volume diagram including the experimental and simulation traces for 950 RPM of engine load for the DMDF LP+HP EGR configuration.

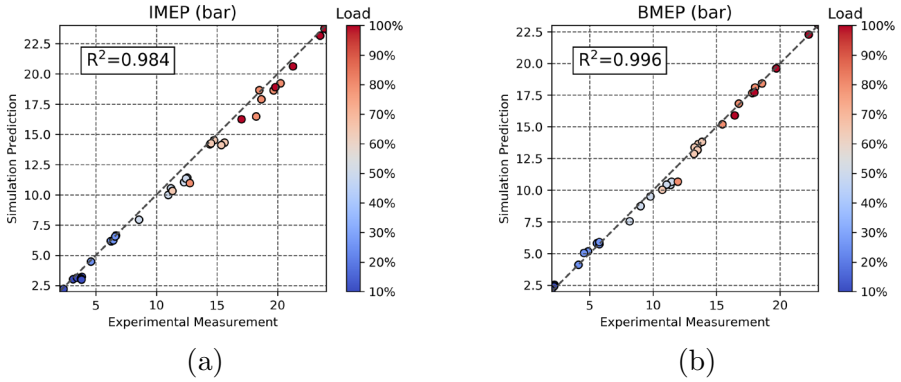


Figure 3-21. Experimental versus simulation results of the 0D-engine model for DMDF LP+HP EGR configuration in terms of IMEP (a) and BMEP (b).

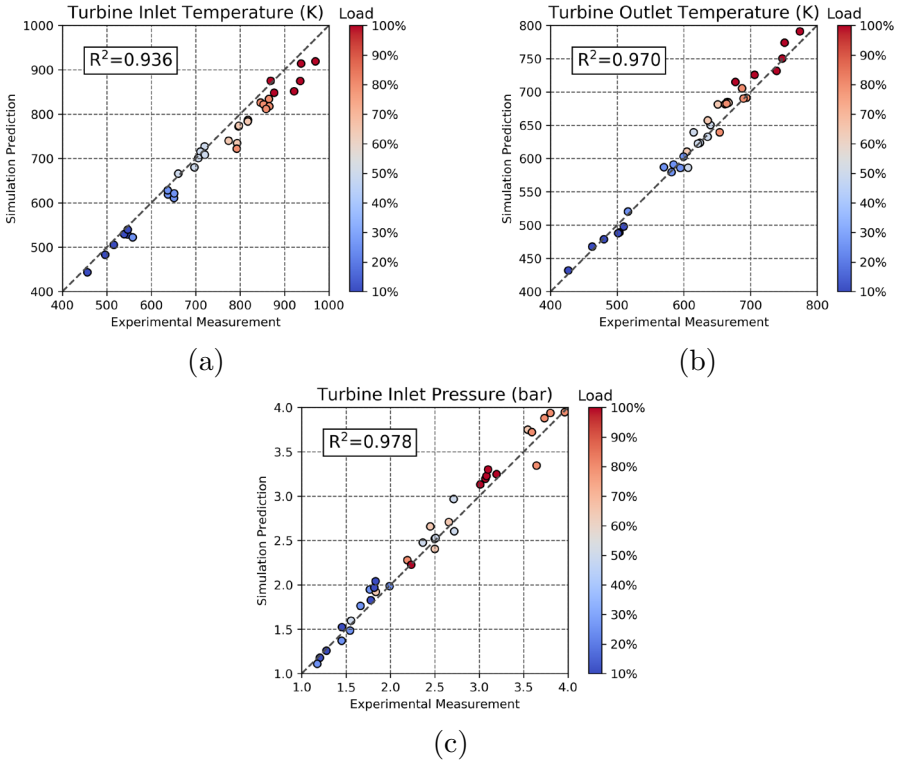


Figure 3-22. Experimental versus simulation results of the 0D-engine model for DMDF LP+HP EGR configuration in terms of turbine inlet (a) and outlet temperature (b), and turbine inlet pressure (c).



### 3.4.3 Aftertreatment system model

Only the DOC was left in the ATS system due to the ultra-low NO<sub>x</sub> and soot emissions. A 1D numerical model in GT-power was used by coupling the engine-out pipe to a catalyst sub-model to model the DOC. The oxidation catalyst reactions were solved using the Sampara et al. [192] mechanism. This model consists of two different parts. First, the geometric characteristics such as wash coat width, length, and channel density, presented in Table 3-3, are defined in the OC object. At the same time, the chemical reactions from the chemical kinetic mechanism are specified in the reaction mechanism object. The concentration specification at the oxidation catalyst inlet was determined considering the approach proposed in [193], considering the most 11 representative species.

The global chemical kinetic mechanism requires a previous calibration using six operative conditions (*Table 3-8*) to obtain the Arrhenius parameters, such as the activation energy and pre-exponential factor. The optimization process was performed using a genetic algorithm searching approach. More information about the calibration process can be seen in [86].

The calibration and validation process results are presented in Figure 3-23. It is possible to see a good agreement between the predicted and experimental conversion efficiency results for both HC and CO species. The higher deviations in CO conversion efficiency compared with HC are justified by the sensibility of this specie to the temperature.

Additionally, the HC conversion efficiency is a consequence of both low reactivity and high reactivity hydrocarbon, enhancing the mechanism's performance in harsh conditions. The highest deviations are shown in temperatures lower than the light-off conditions. These conditions are generally representative of low load conditions, where the cyclic variability of the engine may produce a significant variation in the exhaust gas composition. Despite the low deviation, the HC and CO emissions are slightly

overestimated in the validation process for low temperatures. Therefore, this allows the model to report the results on the safe side.

Table 3-8. Operating points for the OC model calibration and validation.

Op. Point	Engine Speed	BMEP	Exhaust gas mass	Temp engine-out	HC	CO	HC conv eff	CO conv eff
-	[RPM]	[bar]	[g/s]	[°C]	[ppm]	[ppm]	[%]	[%]
Cal 1	1200	2.15	43.5	176	432	2436	42.8	12.0
Cal 2	1200	5.66	57.5	256	3912	1420	96.5	99.9
Cal 3	1500	5.74	76.9	273	3432	1737	96.8	99.6
Cal 4	1800	2.10	75.7	208	742	1433	89.9	99.7
Cal 5	2000	1.91	81.0	214	720	1501	91.6	99.7
Cal 6	2200	1.78	85.3	227	329	2335	92.2	99.8
Val 1	1500	2.1	54.7	191	1599	2467	43.0	19.5
Val 2	2000	2.0	80.6	217	268	1781	87.3	99.8
Val 3	1200	5.6	59.1	282	3890	1118	98.0	99.8
Val 4	1800	5.4	91.4	287	3613	2108	97.1	99.7
Val 5	1500	7.8	76.2	287	977	1536	97.9	100.0
Val 6	2200	4.6	118.9	296	4054	2953	96.5	99.4
Val 7	2000	4.7	98.5	302	4482	2856	97.0	99.4
Val 8	2200	8.8	169.0	327	1606	1389	96.6	100
Val 9	2000	9.7	151.8	342	1404	952	97.7	100

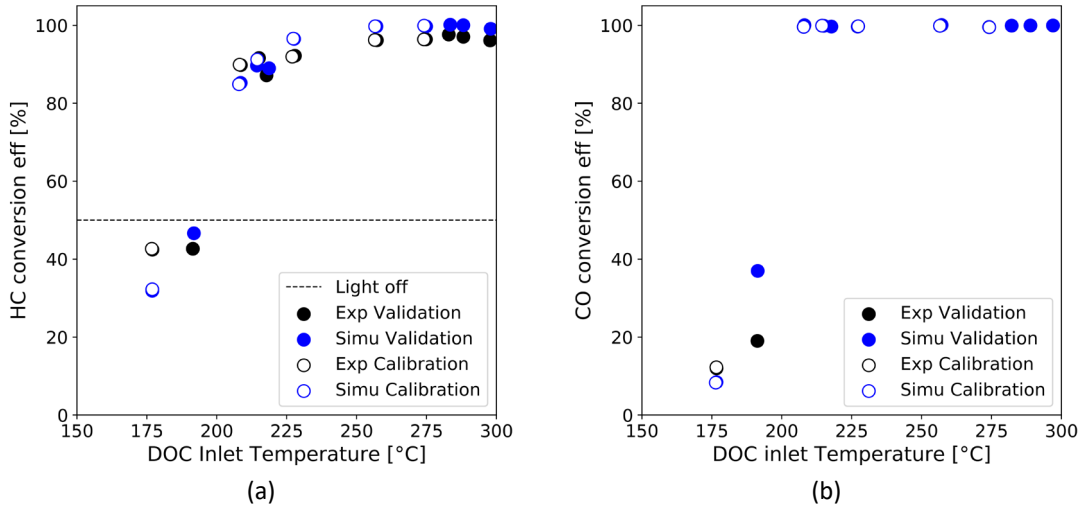


Figure 3-23. Experimental versus simulated conversion efficiencies for (a) unburned hydrocarbon and (b) carbon monoxide, considering the calibration and validation operating points.

In addition to the steady-state calibration, further verification was performed considering transient conditions. In this sense, the experimental results from previous experiments were used as boundary conditions to assess the capability of the model to reproduce the conversion efficiency of the experimental oxidation catalyst. The results of this evaluation for both HC and CO emissions are depicted in Figure 3-24. As it is shown, it is possible to obtain an accurate description of the conversion efficiency at transient operation at most of the time evaluated. The highest differences are evidenced at 400 s. This zone represents the time in which the engine speed is modified in the experiments, modifying the exhaust mass flow and the exhaust temperatures. Since the thermocouples are not designed to capture this thermal fast transient, they may lead to a delay in the temperature reading, which is the main reason for the difference observed. The delayed reading of the thermocouples can be observed in Figure 3-25, where the simulated and experimental results of temperature are depicted. As can be seen, the thermal model of the oxidation catalyst can describe the temperature variation at most of the transient steps.

The described DOC model is used to evaluate the HC and CO conversion efficiency in a hybrid architecture. Due to using a battery pack, a DOC electrified solution is tested to improve the warm-up phase. This element is a heater that heats the exhaust gases before the DOC and is known as an electric heater catalyst (EHC). This element will be virtual tested in Chapter 4 and Chapter 5 for P0 and P2 hybrid architectures.

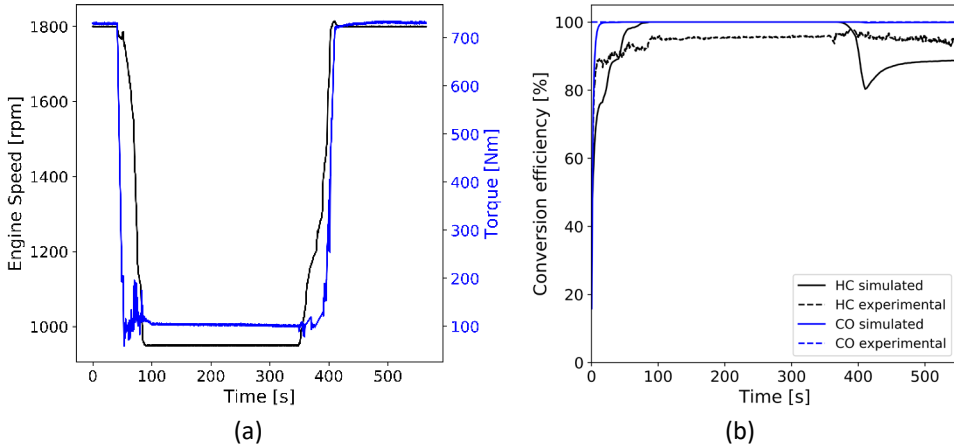


Figure 3-24. Engine speed and torque evaluate experimental and simulated conversion efficiency (a). Comparison between experimental and simulated conversion efficiency for unburned hydrocarbons (black) and carbon monoxide (blue) (b).

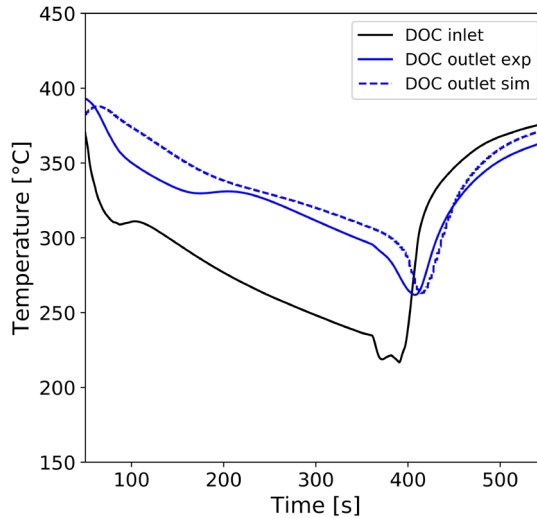


Figure 3-25. Inlet temperature and comparison between experimental and simulated temperature results at the DOC outlet.

### 3.4.4 Electric motor model

A detailed analysis of different electric machines was done in Chapter 2. As mentioned, an electric machine (EM) is a device that converts electrical power into mechanical one, and vice-versa. The EM acts as a motor and outputs positive power in the first case. In the second one, it acts as a generator and produces negative power. In addition, the EM can operate with both negative and positive angular velocities. Therefore, the speed-torque operating point can be described on a four-quadrants map. Three zones and four characteristic points can be distinguished (see Figure 3-26), analyzing one of the quadrants.

The typical performance of an EM is characterized by constant torque from zero speed until the “base speed” (speed value after which the torque output of the EM decreases). Next, the torque decreases at higher speeds, but the power is constant till the maximum EM speed. At higher speeds than the maximum/critical speed, the power decreases due to too high a back-

electromotive force. Flux weakening is the control method used in alternating current EMs to keep the voltage below the rated voltage.

The torque characteristic curve is attractive for HEVs and EVs since high constant torque is required at low speeds to start the vehicle, win the static friction, and uphill driving, while constant power is desired at high speeds.

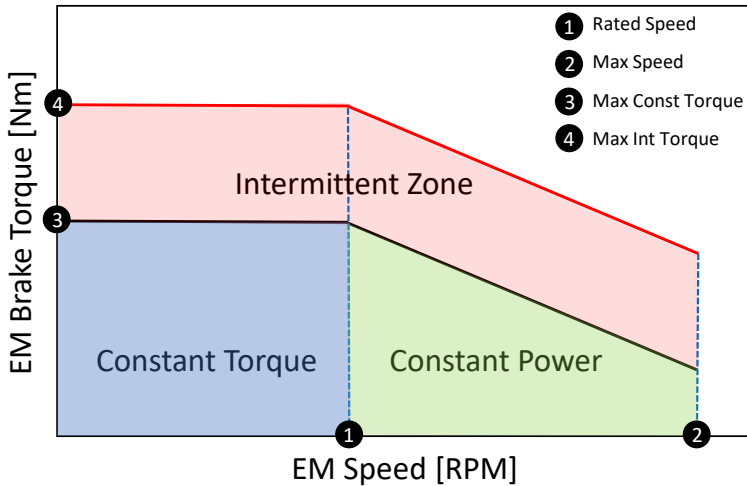


Figure 3-26. Map characteristic zones and points for a PMSM in brake torque output and rotational speed.

Additionally, the performance of an EM has two operation limits. Usually described as 1) Continuous rating: rated power operating region and 2) Intermittent overload operation: the power output is greater than the continuous rated one, but the EM can operate in this regime for a reduced time.

One of the most critical parameters is the conversion efficiency from electric to mechanical power and vice versa. The efficiency in EM is defined by equation 3.13a. Additionally, also the power electronic efficiency (i.e., the

inverter  $\eta_{inv}$ ) could be included and integrated into the previous equation by 3.13b.

$$\eta = \frac{P_{out}}{P_{out} + P_{losses}} \quad 3.13a$$

$$\tilde{\eta}_{EM} = \eta_{EM}\eta_{inv} \quad 3.13b$$

where  $P_{out}$  is the mechanical power at the EM rotor and  $P_{losses}$  accounts for the electromagnetic efficiency of the machine due to iron losses, copper losses, and permanent magnet losses that depend on the flux density amplitude and the current frequency; the mechanical efficiency is due to friction losses.

Efficiency maps are commonly used to illustrate the performance of electric machines. They are contour plots of the maximum efficiency on axes of torque versus speed. Efficiency maps show the capability envelope of the machine and the maximum efficiency at all possible operating points. In addition, efficiency maps are usually used for vehicle modeling due to the low computational cost and high precision of the global vehicle powertrain efficiency results [194,195]. This approach is suitable when aspects like the electronic control of the EM and the thermal management are not investigated.

In this Thesis, the efficiency map and the torque limits are inserted in a map-based model similar to the ICE model. The EM sub-model is in charge of calculating the conversion efficiency depending on the speed and torque requested. In addition, the limits of the delivered power depend on the limit torque curve.

When the operating torque-speed points for the EM are mainly distributed in the low-medium speed range, then the permanent magnet synchronous motor (PMSM) is the ideal choice. This is the case for the most widespread HEV architectures. Moreover, packaging could be an issue in HEV due to the additional components (ICE, transmission). The higher

power density of PMSM is definitively a plus. In addition, as was shown in Chapter 2, the most employed motor in transportation is the PMSM. Therefore, this type of motor for the HEV analysis is chosen.

*Table 3-9. Electric motor main characteristics. Source [196] and [197].*

Parameter	Unit	HTM-3500	Lexus LS 600
Type of Motor	[-]	PMSM	
Maximum Power	[kW]	400	100
Continuous Power	[kW]	210	60
Maximum Torque	[Nm]	3500	400
Continuous Torque	[Nm]	1500	230
Maximum Speed	[RPM]	3500	10000
Diameter	[mm]	540	200
Width	[mm]	251	135
Weight	[kg]	195	47
Weight Density	[kW/kg]	1.07	1.27

The map of Figure 3.27 is used when traction power at low rotational speed but high torque output has required. On the other hand, Figure 3.28 shows an efficiency map for a PMSM of 50 kW of continuous power. This map will be used for cases where high-rotational speed ( $>6000$  RPM) and low torque are required. The first map is representative of the Heavy-Duty application for BEVs trucks. The second map is used in power-split architecture such as Lexus or Toyota models.



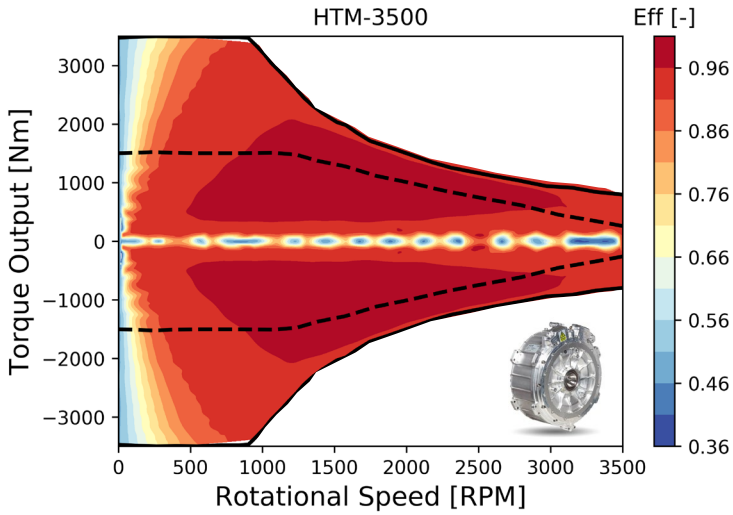


Figure 3.27. Efficiency map of a PMSM electric machine for Heavy-Duty vehicles HTM-3500. Only the first and fourth quadrants are shown. Adapted from [198].

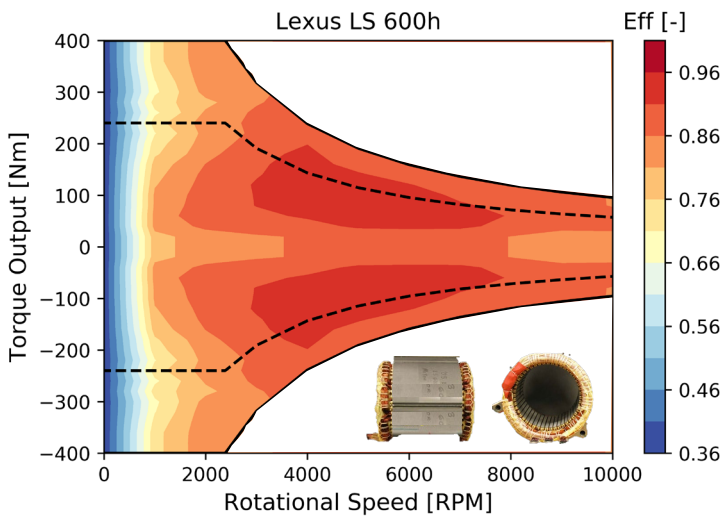


Figure 3.28. Efficiency map of a PMSM electric machine for high-speed requirements. Only the first and fourth quadrants are shown. Adapted from [197]

The EM can be sized according to the design torque output or maximum power. Several works applied a re-scale of the efficiency map by multiplying the output torque of a base experimentally measured EM by a scaling coefficient. One of the problems of this methodology is the loss of real behavior. Typically, up-scaling means better efficiency than down-scaling, as shown in Figure 3.29. However, due to the lack of several EM efficiency maps depending on the motor size required, the re-scaling approach is used with a representative EM map.

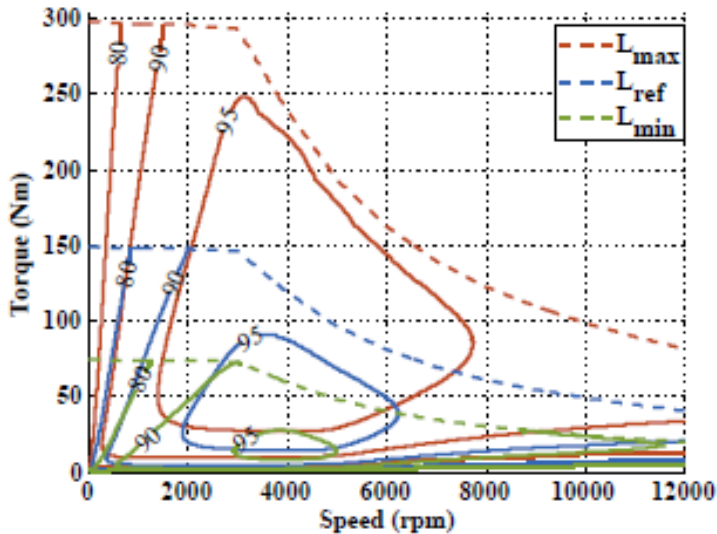


Figure 3.29. Effect of length-scaling on electric machine maximum torque characteristic. The plot shows three lengths, referred to as the baseline dashed blue line. Source [199].

The power scaling of the EM is done by multiplying the maximum torque output at each speed by a multiplier coefficient, which becomes a design parameter used in the powertrain components' optimal sizing phase. This is also consistent with the procedure described in [199]: it is explained that manufacturers do electric machine power scaling by changing the length of the machine, that is, scaling the length of the iron core, which is due to economic reasons. Thus, the cross-section of the EM remains unaltered, with

the voltage rating and maximum current density, but the maximum torque output is proportionally linear to the length scaling factor. In addition, the mass of the EM is calculated assuming the gravimetric power density of Table 3-9.

### 3.4.5 Lithium-Ion battery model

Different modeling approaches for battery cells can be found in the literature. Simple resistance circuits are used to attain a global description of the electrical properties of the system. Nonetheless, they are not able to capture the hysteresis of the system. A further step towards accurate models comprises the addition of a Thevenin resistance-capacitance branch, which benefits the model to follow dynamic conditions, mainly at load pulses [200]. Finally, electrochemical descriptions account for a conservative description obtained through differential equations [201]. Figure 3.30 shows a schematic of the different modeling approaches used for battery operation description.

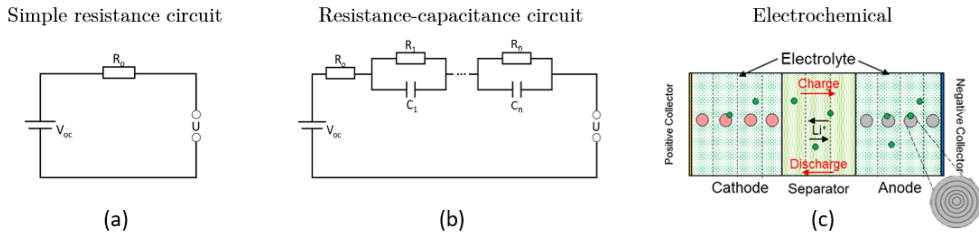


Figure 3.30. Scheme representing a conceptual description of the different approaches used for battery modeling: resistance (a), resistance-capacitance (RC branches model) (b), and electrochemical (c).

The electrical circuit was built starting from the cell model and then expanded with several cells in parallel and series arrangements. In order to understand more about the different approaches, details about RC branches and electrochemical models are addressed.

The equivalent internal series resistance model (Figure 3.30a) correctly models the polarization effect, that is, the departure of the cell's terminal voltage  $V$  (equation 3.15) from the open-circuit voltage ( $OCV$ ), hence it is good for modeling the instantaneous response of the cell to a change in input current. The resistance ( $R_{int}$ ) as well as the  $OCV$  depends on the state of charge (SOC) status and the temperature.

$$V(t) = OCV(\text{SoC}(t), \theta(t)) - R_{int}(\text{SoC}(t), \theta(t))I(t) \quad (3.14)$$

However, when a cell is subject to a current, it exhibits a non-instantaneous/dynamic response. When a current load is applied to the cell, its voltage  $V$  decreases below the open-circuit voltage  $OCV$ , but when it is unloaded, it does not instantaneously return to  $OCV$ . This behavior is due to slow diffusion processes in the cell. Thévenin circuit model, which adds a resistance-capacitor (RC) branch, is suitable to also consider this characteristic (equation 3.16) by the  $V_{C1}$ .

$$V(t) = OCV(\text{SoC}(t), \theta(t)) - V_{C1}(\text{SoC}(t), \theta(t)) - R_{int}(\text{SoC}(t), \theta(t))I(t) \quad (3.15)$$

Given the characteristic relation between the capacitor and the current balance at the RC branch:

$$I_{C1}(t) = C_1 \dot{V}_{C1}(t) \quad (3.16)$$

$$V_{C1}(t) = R_1 I_{R1}(t) \quad (3.17)$$

$$I_{R1}(t) + C_1 \dot{V}_{C1}(t) = I(t) \quad (3.18)$$

The following set of equations describes the Thévenin model with 1 RC branch:

$$\begin{cases} \frac{d\text{SoC}(t)}{dt} = -\eta_c \frac{I(t)}{Q} \\ \frac{dI_{R1}(t)}{dt} = \frac{I(t) - I_{R1}(t)}{R_1 C_1} \\ V(t) = OCV(t) - R_1 I_{R1}(t) - R_{int} I(t) \end{cases} \quad (3.19)$$

Often, an additional RC branch is added in series to one of the original Thevenin models [202], to simulate the so-called Warburg impedance, further improving the voltage response approximation [203,204], as shown in Figure 3.30b. This model also allows adding a thermal cell model to calculate the cell surface temperature depending on the heat exchanged with air or the thermal management system (cooling or heating device). However, in this Thesis, the cell temperature will maintain constant and similar to the ambient temperature. As thermal management is not the focus of this work, this simplification emulates a suitable heat exchanger. In general, the RC branches model is calibrated ( $OCV, R_{int}, V_{Cn}$ ) by constant current discharge and charge as well as dynamic current profiles. Hybrid Power Pulse Characterization (HPPC) testing is a common approach because incorporates both discharge and charge pulses that take place at various SOC, and which can be performed under various temperature stressors and current loads.

The electrochemical model is based on the conservative nature of electric charge that allows devising transport equations for this property in each of the elements that compose the battery, such as the solid and electrolyte phases (Figure 3.30c). Newman's work [141] provides a complete description of the equations. Herein, only a summary of the most relevant equations for the species and charge conservation are presented. The set of equations presented in *Table 3-10* allows to precise the behavior of an electrochemical cell concerning its assembling characteristics and materials. It is possible to use a dedicated battery sub-model in GT-Suite by adding the GT-AutoLion license. It incorporates different materials to model several cathodes, anode, and electrolyte chemistries, as well as all the equations and the solver. The main task is to calibrate a large number of parameters in order to have an accurate model at different current, temperature, and SOC conditions.

Table 3-10. Electrochemical lithium-Ion cell equations in GT-Autolion.

Description	Governing equations	
Solid-phase: conservation of $\text{Li}^+$	$\frac{\partial c_s}{\partial x} = \frac{D_s}{r^2} \frac{\partial}{\partial r} \left( r^2 \frac{\partial c_s}{\partial r} \right)$	(3.20)
Electrolyte phase: conservation of $\text{Li}^+$	$\frac{\partial}{\partial x} [\varepsilon c_e] = \frac{\partial}{\partial x} \left( D_e^{eff} \frac{\partial l c_e}{\partial x} \right) + \frac{1-t_+^0}{F} j^{Li}$	(3.21)
Solid-phase: charge conservation	$\frac{\partial}{\partial x} \left( \sigma_s^{eff} \frac{\partial \phi_s}{\partial x} \right) - j^{Li} - a_{dl} C \frac{\partial (\phi_s - \phi_e)}{\partial x} = 0$	(3.22)
Electrolyte phase: charge conservation	$\frac{\partial}{\partial x} \left( k^{eff} \frac{\partial \phi_e}{\partial x} \right) + \frac{\partial}{\partial x} \left( k_D^{eff} \frac{\partial \ln c_e}{\partial x} \right) + j^{Li} + a_{dl} C \frac{\partial (\phi_s - \phi_e)}{\partial x} = 0$	(3.23)
Electrochemical Kinetics	$j^{IC} = a_s i_0 \left\{ \exp \left[ \frac{\alpha_a F}{R_u T} \left( \eta - \frac{R_{SEI}}{a_s} j^{Li} \right) \right] - \exp \left[ \frac{\alpha_c F}{R_u T} \left( \eta - \frac{R_{SEI}}{a_s} j^{Li} \right) \right] \right\}$	(3.24)
Overpotential	$\eta = \phi_s - \phi_e - U$	(3.25)
Voltage	$V = \phi_s(x = L_{cell}) - \phi_s(x = 0) - \frac{R_c}{A} I$	(3.26)
Reaction surface area	$a_s = a_{s,0} \left[ 1 - \left( \frac{\varepsilon_0 - \varepsilon}{\varepsilon_0} \right)^\zeta \right]$	(3.27)
Energy conservation	$\frac{d(C_p T)}{dt} = -h Q A_{cell} (T - T_{amb}) + Q_{gen}$	(3.28)
Heat generation	$Q_{gen} = (U - V) - IT \frac{dU}{dT}$	(3.29)

with  $\sigma_s$  solid-phase conductivity,  $C_p$  specific heat,  $h$  heat transfer coefficient,  $T$  temperature,  $F$  Faraday's constant,  $eff$  defined as an effective parameter,  $\phi_s$  solid-phase potential,  $\phi_e$  liquid phase potential,  $j^{Li}$  reaction current of lithium,  $a_{dl}$  specific interfacial area,  $C$  specific capacitance,  $x$  the distance in the thru-plane direction,  $j^{IC}$  charge transfer,  $a_s$  volume-specific reaction surface area,  $i_0$  exchange current density,  $\alpha$  charge transfer coefficient,  $R_u$  universal gas constant,  $R_{SEI}$  resistive film layer,  $\eta$  over potential,  $U$  open-

circuit potential of the solid, and  $\varepsilon$  porosity. This model can also model aging by activating the degradation of the materials. As it is not the focus of this work, the aging parameters are disabled, and the model represents the condition of pristine cells.

Both models need to be calibrated by tuning several parameters in order to be able to predict the cell behavior (terminal voltage, SOC, etc.). The main advantage of the RC branches model is that it reduces the computational effort to solve the equations and fewer parameters to be calibrated. On the contrary, the main drawback is the no prediction of aging and material conditions. The electrochemical model has the opposite characteristics. In this work, the RC branches are preferred as the focus is to model the vehicle model efficiencies accurately, powertrain capabilities in terms of power, and hybrid operational modes. However, as the best available data was found to be more accurate in calibrating an electrochemical model, the following methodology was proposed:

- 1) Create and calibrate an electrochemical model for the cell.
- 2) Obtain an RC branches model by the use of the previous calibrated electrochemical model.
- 3) Create a battery pack model by using the RC branches model in series and parallel connections.

A summary of the three steps is depicted in *Figure 3.31*.

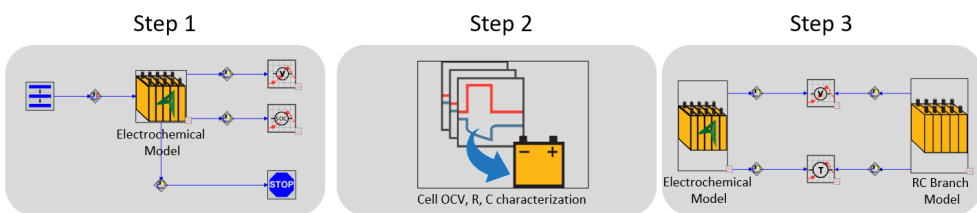


*Figure 3.31. Steps in order to obtain the RC branches parameters from the electrochemical model.*

Before calibrating the model, selecting the most suitable cell for the xHEV application is necessary and finding the necessary experimental information. For MHEV and FHEV, it is necessary to have a cell with a high specific power capacity (kW/kg). Because in the general small battery pack (low amount of cells) is used. Therefore, the maximum current to charge and discharge is crucial. For PHEV or BEV, where the battery pack is large in the number of cells, this parameter is less crucial and more important on the cell-specific energy (kWh/kg). Reducing the battery total weight is important not to impact the cargo mass capacity of the truck. As was shown in Chapter 2, the Lithium Iron Phosphate ( $\text{LiFePO}_4$  or LFP) cathode chemistry shows high specific power, and the life span and safety are also strong points. Moreover, Lithium Nickel Manganese Cobalt oxides (NMC) cathode chemistry shows an excellent specific energy ratio while the power and life span are the main drawbacks. Therefore, these two cathode chemistries are selected for this work with LFP for MHEV and FHEV and NMC for PHEV and BEV models.

The type of packaging is also a difficult task. This is evidenced by the different options of the OMEs under the same vehicle sector. For a truck application, the volumetric density of the pack is not as crucial as a passenger car. On the other hand, the gravimetry density is more critical than not, impacting cargo capabilities. Following the trend presented in Chapter 2, cylindrical cells are the best option to minimize the battery pack's volume. Following the work of Löbberding et al. [205], a high-performance cylindrical cell in 2020 can achieve 250 Wh/kg and 600 Wh/lt.

After searching for experimental data in order to be able to calibrate the GT-AutoLion model and meet the previously mentioned requirements, it was selected two cells. The main characteristics are shown in Table 3-11. A cylindrical cell of  $\text{LiFePO}_4$  produced by Lithium Werks (formerly A123 Systems) was chosen due to its high-power capabilities. The main drawback is the low specific energy ratio. For PHEV and BEV, powertrains will be modeled with an NMC 811 produced by LG with an excellent specific energy.



The main limitation is the low discharge and charge currents that make it unsuitable for MHEV and FHEV.

Table 3-11. Li-Ion battery cell main specifications. Source [206] and [207].

Parameter	Unit	ANR26650m1B	LG HG2 18650
Cathode Chemistry	[-]	LFP	NMC 811
Diameter x Length	[mm]	25.96 x 65.4	18.3 x 65.0
Weight	[g]	76.0	47.0
Nominal Voltage	[V]	3.3	3.6
Max. current to Discharge	[A]	120@10s & 50@continuous	60@10s & 20@continuous
Max. current to Charge	[A]	26@10s & 10@continuous	6@10s & 4@continuous
Max. Voltage	[V]	3.6	4.2
Min. Voltage	[V]	2.0	2.0
Capacity	[Ah]	2.6	3.0
Energy	[Wh]	8.58	10.8
Energy Mass Density	[Wh/kg]	112	230
Energy Mass Density	[Wh/lt]	248	632

The electrochemical model was calibrated with experimental data obtained from CMT test cell. Experimental tests with controlled ambient temperature can be carried out with different battery power demands. For achieving these goals, a bidirectional current source was coupled with an accelerating rate calorimeter. The bidirectional current source is an LBT 10V 100A manufactured by Arbin Instruments, with a control accuracy of 0.02%, step current input time of 5ms, and data logging rate of 2000 points per second. This equipment aims to supply current to charge the batteries while measuring the cell voltage and surface temperature. The controlled ambient temperature was performed by an accelerating rate calorimeter, model ARC THT EV+, manufactured by Thermal Hazards Technologies. The ambient temperature can be controlled with an uncertainty of  $\pm 0.2\%$ . Both types of equipment are part of the CMT laboratory battery test. For this Thesis, constant current and transient current profiles are requested for the cells.

A genetic algorithm was used to fit 14 constructive properties of the cell materials in the GT-Autolion optimizer. Constructive elements, like the

thickness of each material layer that composes the cell, which may show a significant deviation from cell to cell due to the manufacturing process. The total charge capacity of the cell is considered through a series of parameters that define the lithium inventory available and the capacity of each electrode to allocate the lithium. Finally, thermal effects have been modeled through the convective heat transfer and heat capacity, as well as other variables intimately related to heat generation, like contact resistance. All the previous variables interact in a complex manner to define the overall cell behavior.

Parameters such as cell size, the voltage at full charge and discharge, and some properties of the materials as binder and electrolyte density, are maintained fixed. The pre-defined GT-Autlion values are used. Moreover, the mentioned software already has the cell electrode materials as NMC 811, LFPO, Graphite, electrolyte as LiPF<sub>6</sub> EC EMC, and foils as aluminum, cooper among others. In addition, the main non-manipulable inputs for the computational simulation are the current, temperature, and voltage profiles from the experimental tests. Two different types of tests have been used for the calibration process, constant C-rate discharge profiles and dynamic profiles. The latter is representative of real operation in a vehicle due to the different current magnitudes and signs applied. The rationale for using the constant C-rate curves for calibrating is that this data is usually provided by the manufacturers, so it is frequently available for the end-users.

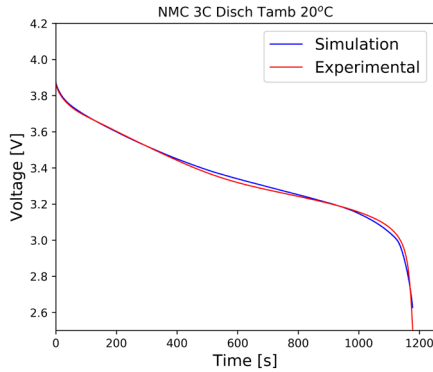
The objective function of the optimization procedure is the minimization of the voltage and temperature error between the simulated curves and the real response when a certain current profile is applied to the cell. The temperature profile is introduced in the optimization process but with a lower weight in the objective function. The relative discrepancies in the temperature profile have lower importance than in the voltage response.

The optimum values after 4000 design experiments for each cell are presented in *Table 3-12*.

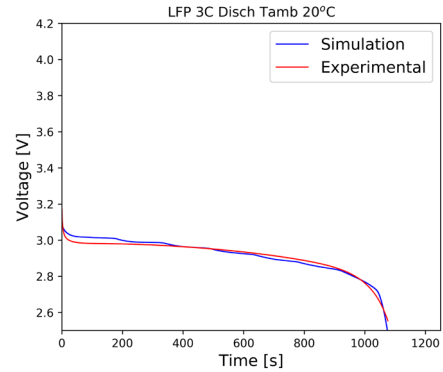
*Table 3-12. Li-Ion battery cell electrochemical model optimum parameters.*

Parameter	Unit	ANR26650m1B	LG HG2 18650
Cathode thicknesses	[ $\mu\text{m}$ ]	60	56
Anode thicknesses	[ $\mu\text{m}$ ]	35	68
Separator thicknesses	[ $\mu\text{m}$ ]	20	17
First charge capacity Cathode	[mAh/g]	171.76	197.68
First charge capacity Anode	[mAh/g]	379.36	365.86
First discharge capacity Cathode	[mAh/g]	166.10	180.83
First discharge capacity Anode	[mAh/g]	334.09	357.62
Particle size Cathode	[ $\mu\text{m}$ ]	0.07	0.05
Particle size Anode	[ $\mu\text{m}$ ]	10.5	15.6
Specific heat capacity of the cell	[J/kg.K]	1255	1132
Convective heat transfer coefficient	[W/m <sup>2</sup> .K]	26.1	90.0
Contact Resistance	[mOhm.m <sup>2</sup> ]	0.999	0.396
Cathode capacity	[Ah]	2.04	3.16
Anode capacity	[Ah]	2.06	3.05

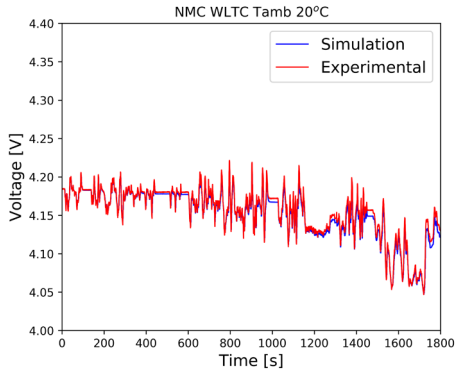
The final validation is performed by simulation of the cell profiles under 3 C-rate and a dynamic cycle representative of the homologation driving cycle for Light-Duty vehicles. The results are presented in *Figure 3.32*. The error was below 2% throughout the entire cycle. For brevity of the manuscript, the temperature profiles showed good agreement with errors below 5%.



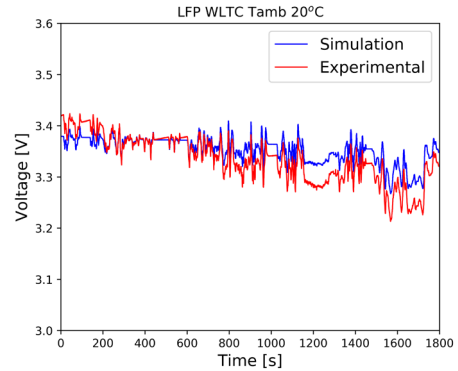
(a)



(b)



(c)

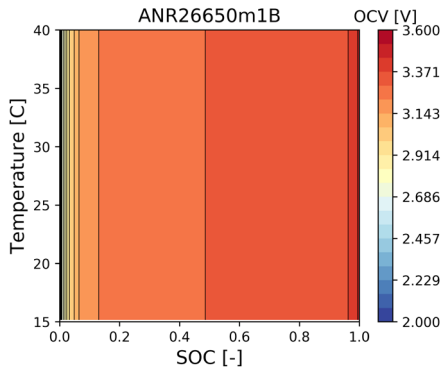


(d)

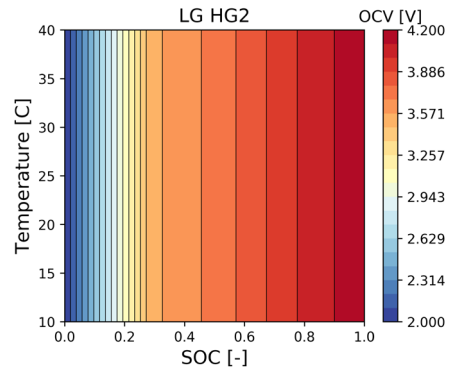
Figure 3.32. Cell validation for NMC (left) and LFP (right) for constant current discharge (top) and conduction cycle (bottom).

After obtaining the calibrated and validated electrochemical model, step 2 of Figure 3.31 was performed. The results are plotted (see Figure 3.33) in 3D maps with Open Circuit Voltage (OCV), Resistance out of RC branch ( $R_o$ ), Resistance inside RC branch ( $R_1$ ), and Capacitance inside RC branch ( $C_1$ ) against the battery state of charge (SOC) and surface temperature. As can be seen, the OCV depends on the battery SOC, while on the contrary, the  $R_0$  depends mainly on the temperature of the cell. Moreover, the internal

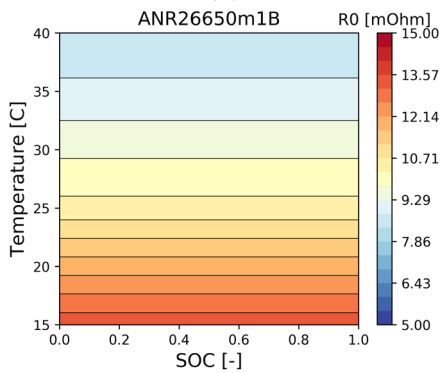
resistance of the NMC is higher as well as the OCV at high SOC. These maps are inserted in the equivalent circuit model, and the number of cells in series and parallel are increased to obtain the desired battery-package voltage and total energy.



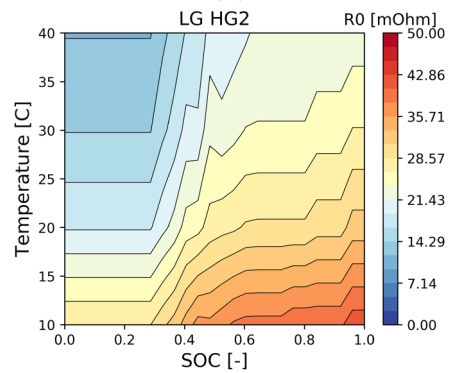
(a)



(b)



(c)



(d)

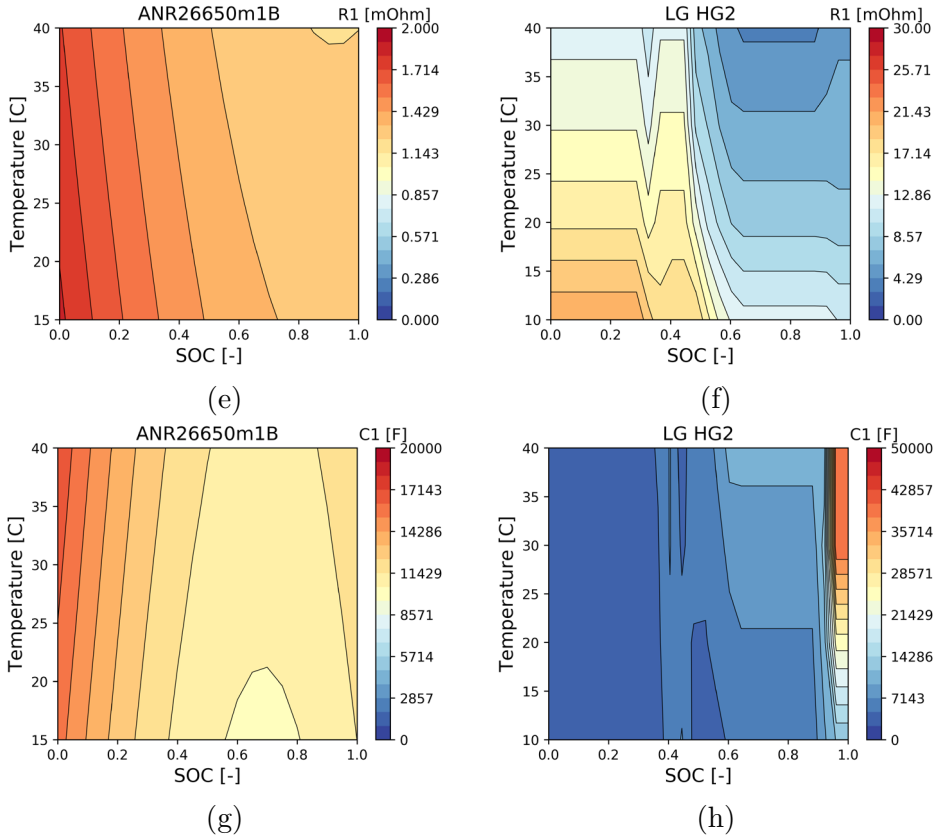


Figure 3.33. Equivalent circuit maps for OCV,  $R_o$ ,  $R_1$ , and  $C_1$  against battery state of charge (SOC) and surface temperature for LFP (left) and NMC (right).

In order to control the battery pack, the battery management system (BMS) is inserted. The BMS is in charge of monitoring the battery state of charge and must ensure that the battery is used correctly. Therefore, it also guarantees that the power request to the battery satisfies the limits of lower and upper cutoff voltages and minimum and maximum current given by the cell manufacturer (i.e., Table 3-11). The power output of the battery (when a load is applied) is:

$$P_{load} = OCV * I - R_{int} I^2 \quad (3.30)$$

Setting the derivative of (3.24) to zero and solving for the maximum power current  $I_{P,max} = OCV/2R_{int}$  allows to obtain the first theoretical constraint on maximum discharge power:

$$P_{disch,max} = \frac{OCV^2}{4R_{int}} \quad (3.31)$$

In addition, the terminal power limitations that cause the battery to reach the maximum charge and discharge current are calculated from:

$$P_{charge,I_{max}} = OCV * I_{max,charge} - R_{int}I_{max,charge}^2 \quad (3.32)$$

$$P_{discharge,I_{max}} = OCV * I_{max,discharge} - R_{int}I_{max,discharge}^2 \quad (3.33)$$

Next, substituting the relation for terminal voltage (3.15) into (3.24) gives the following terminal power limitations on the charge  $P_{charge,V_{max}}$  and discharge  $P_{disch,V_{min}}$  when  $V$  is set to the maximum cutoff voltage and lower cutoff voltages, respectively:

$$P_{charge,V_{max}} = OCV \left( \frac{OCV - V_{max,cutoff}}{R_{int}} \right) - R_0 \left( \frac{OCV - V_{max,cutoff}}{R_{int}} \right)^2 \quad (3.34)$$

$$P_{disch,V_{min}} = OCV \left( \frac{OCV - V_{min,cutoff}}{R_{int}} \right) - R_0 \left( \frac{OCV - V_{min,cutoff}}{R_{int}} \right)^2 \quad (3.35)$$

The maximum between (3.26) and (3.28) and the minimum between (3.25), (3.27), and (3.29) are used as the terminal power limits for charge and discharge, respectively. These equations are inserted in the BMS not to overpass the limits of the battery. The maximum power to discharge and charge is sent to the supervisory controller to limit the EM and control the ICE.

The battery package size (energy content) directly impacts the pure electric range, the vehicle's flexibility to operate along with the different modes, and the power losses in xHEV. Increasing the battery's total energy reduces the current through the cells, resulting in columbic losses. On the

contrary, this has a disadvantage regarding the total battery weight and cost. The battery capacity, and the number of parallel cells, will be defined using the DP algorithm with an optimal parametric study for each vehicle architecture. The battery pack nominal voltage is set to 600 V, giving many series-connected cells equal to 182 for the LFP and 167 for NMC. The selection of the battery pack voltage (600 V) was made to reduce electrical losses in the truck electrical circuit (mainly wirings) and facilitate the electric machine's control. As was demonstrated by [208], the battery nominal voltage selection cannot be made from a battery perspective. This value is fixed for all the cases studied in the present Thesis; the only design variable is the number of parallel connections. The total battery internal resistance accounts for all the series and parallel connections:

$$R_{int,pack} = \frac{N_s}{N_p} R_{int,cell} \quad (3.36)$$

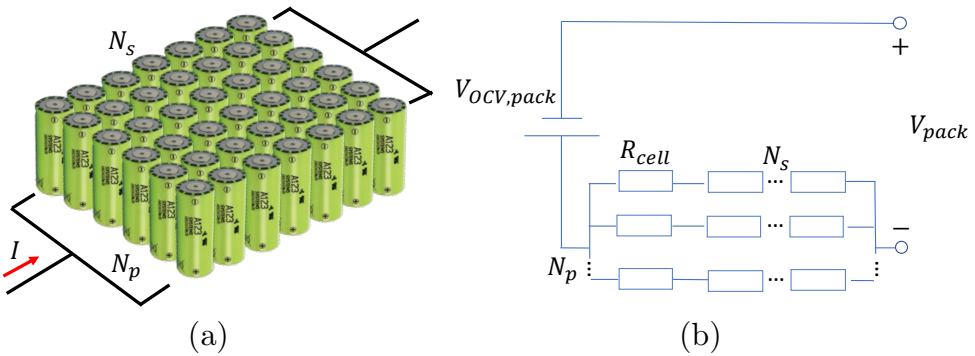


Figure 3.34. Cells arrangements in a battery pack (a) and electric circuit model with one cell (top-b) and all battery packs (bottom-b).

The number of parallel cells will be optimized in the results section of each powertrain architecture. The parallel cells are analyzed to understand how the presented power limitation can limit the EM power. Figure 3.35 shows the power limit for charging and discharging using previous equations



and Table 3-11. The main limitation is the discharging limits where LFP allows higher power charging rates. This improves the powertrain with small batteries such as MHEV and FHEV. For example, 10 kWh of battery pack allows charging ratios of 76 kW with an LFP while with NMC, only 21 kW. The discharge rates are less limited than charging rates in lithium-ion cells for both LFP and NMC.

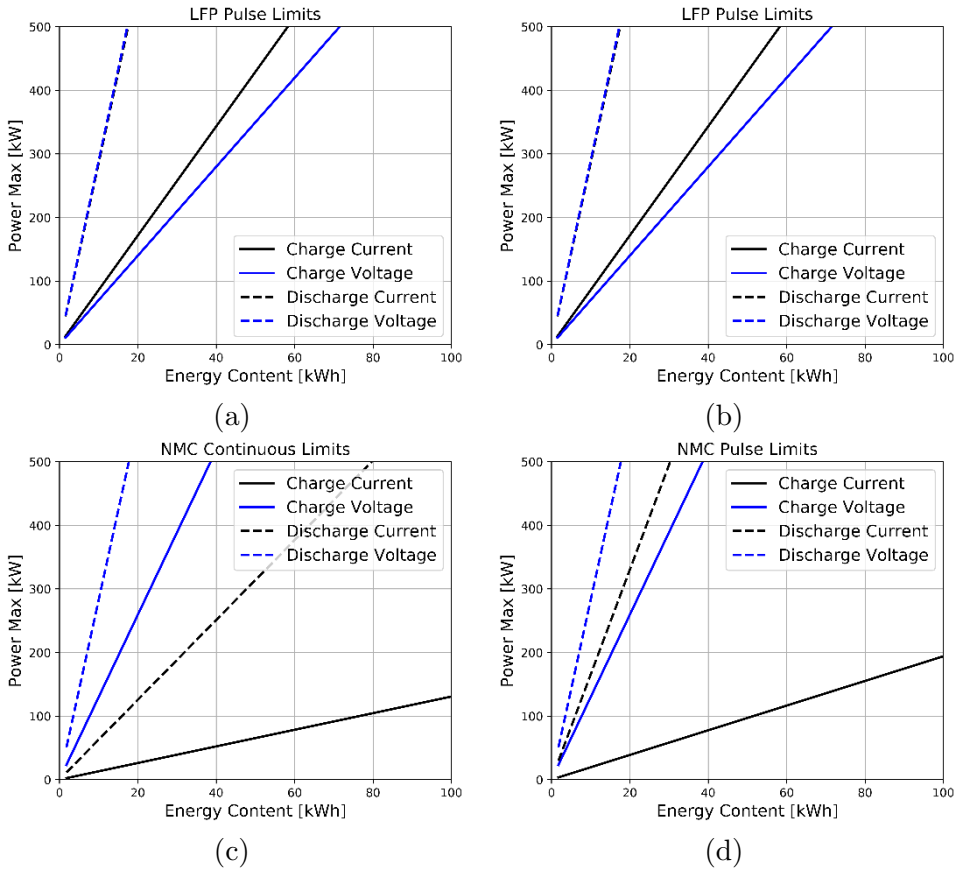


Figure 3.35. LFP and NMC selected cells to have power limitations in terms of maximum charge and discharge power.

The main advantage of the NMC is in total battery pack weight. Following the work of Löbberding et al. [205], a specific energy density of 75

Wh/kg is taken for the LFP (cell ratio of 112 Wh/kg), and 150 Wh/kg is taken for the NMC (cell ratio of 250 Wh/kg). These values are taken to calculate the new weight of the truck for the transient simulations. To have an idea of weight, a range of battery pack energy of 5 kWh to 100 kWh means 66-1333 kg for the LFP and 33-666 kg for NMC. Around 0.4-7.4% for LFP and 0.2-3.7% for NMC increase the total truck payload.

### 3.4.6 Regenerative braking

Regenerative braking represents one of the most critical features that characterize BEV and HEV powertrains. It enables vehicle kinetic energy recuperation during braking phases that conventional mechanical friction brakes would otherwise dissipate. A braking system must bring the vehicle to rest in the shortest possible distance during emergency events and always guarantee control over the vehicle's direction. These criteria can be met by adequately designing the braking system so that it can provide the necessary braking torques at the four wheels with an adequate distribution. Therefore, braking power demand might be conveniently split between front and rear axles.

In hybrid powertrains, the electrical braking system coexists with the mechanical one for safety reasons. In addition, the desired braking torque may be larger than the EM capability, especially at high vehicle speeds. A typical HEV vehicle would have one EM mechanically coupled to the driven wheels. Hence, as braking stability must always be ensured by distributing the braking forces on all four heels, it is implied that only part of the vehicle's kinetic energy can be recuperated during a braking event.

Furthermore, additional limits may reduce the amount of regenerative braking recuperated energy, which are the power limitations of the battery in charging mode, the state of charge of the battery, and vehicle speed. The limitations in the battery are controlled by the BMS that may involve the admissible current intakes of the battery and the maximum SoC level. A

good energy management strategy must ensure that it is always possible to recuperate the maximum available braking energy without breaching the BMS limitations.

Moreover, due to mechanical inefficiencies and electric inefficiencies (electric machine and inverter), only part of the available kinetic energy during braking events can be recuperated. Considering the inefficiency of the mechanical-to-electric energy conversion process, energy recuperation through regenerative braking is not always beneficial, especially at low speeds. It is argued in [209] that the energy spent to actuate the inverter and EM controls would not be compensated by the energy recuperated when the vehicle is running at low speeds. Generally, a reference value of minimum speed above which regenerative braking can be activated is 5-8 km/h. All these issues should be considered when modeling a given hybrid powertrain in order not to overestimate energy recovery, which would lead to too optimistic results in terms of fuel economy for a given driving cycle.

The ideal braking is the best braking force distribution of the vehicle when the driver presses the brake pedal. This ideal distribution gives the maximum braking force that makes the front and rear wheels lock simultaneously for each friction coefficient. Safe braking is assured when the braking force is distributed to the front and rear wheels on the ideal braking curve. This curve can be calculated by the equation 3.37.

$$F_{rear} = \frac{1}{2} \left( \frac{M g}{h_g} \sqrt{Y^2 + \frac{4h_g WB}{M g} F_{front}} - \left( \frac{M g Y}{h_g} + 2F_{front} \right) \right) \quad 3.37$$

where  $F_{rear}$  and  $F_{front}$  are the rear and front axle braking forces,  $M$  the mass of the vehicle,  $g$  the gravity acceleration,  $h_g$  height of the gravity center,  $WB$  the wheelbase, and  $Y$  distance from the center of gravity to the rear axle.

The ideal braking distribution is presented in *Figure 3.36a*. The deceleration in  $g$  can be seen in iso-lines, and the 50%/50% split between rear and front in the red dashed line. As can be seen, the braking force on the

rear axle is more significant than that one on the front axle due to the weight distribution in this type of vehicle. This remarks that regenerative braking is more effective on the rear axle.

It is important to note that when considering the braking performance of a vehicle, it is mandatory to always fulfill stability requirements according to European braking legislation. The truck modeled in this work belongs to the class N3 (vehicles for the carriage of goods and having a maximum mass exceeding 12 tonnes); Therefore, it has to fulfill the Braking regulation No. 13 “Uniform provisions concerning the approval of vehicles of categories M, N and O concerning braking” [210]. The normative established a parameter called adhesion utilized by the axle ( $f_i$ , i correspond to front or rear axle) that is calculated by dividing force exerted by the brakes on axle i under normal braking conditions on the road by the normal reaction of road surface on axle i under braking. This parameter is calculated for different decelerations of the vehicle. The deceleration is measured proportional to the gravity acceleration by the parameter  $z$  (deceleration/g). By the normative, the adhesion utilized by the rear axle must be above Equation 3.38. As seen in Figure 3.35b, the ideal braking is always over the legislation value.

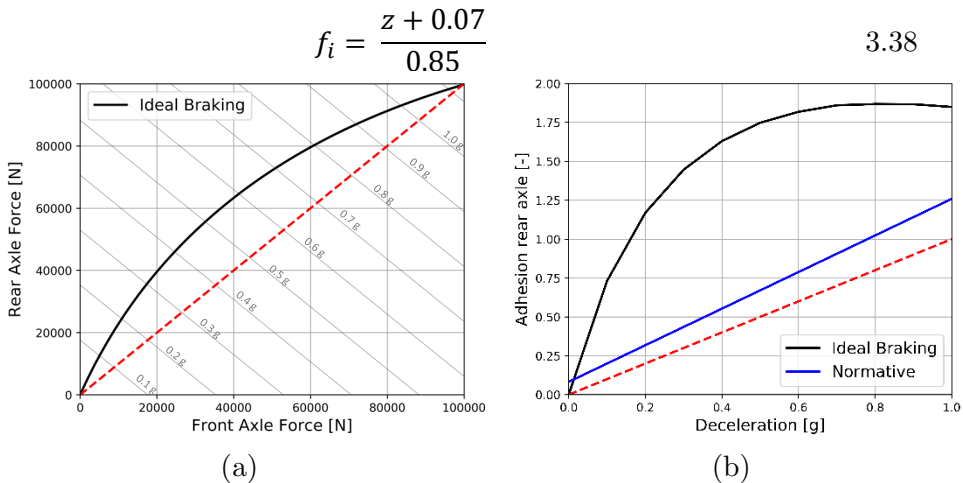


Figure 3.36. The ideal braking curve (a) and the comparison between the ideal curve and normative depend on the vehicle's deceleration (b).

The split ratio is defined as  $F_{rear} / (F_{rear} + F_{front})$  can be obtained for each deceleration value of the vehicle. This curve is added in the braking-controlled sub-model to maximize the regenerative braking and maintain the vehicle stability. The front axle will use only the friction brakes due to no connection of any EM, and the rear axle will split between EM and friction brakes to maximize EM brake force while meeting all the system requirements. In this Thesis, an RBS controller is modeled with a Boolean logic approach, which encompasses the requirements discussed so far. The diagram in Figure 3.37 represents the concept used for the RBS.

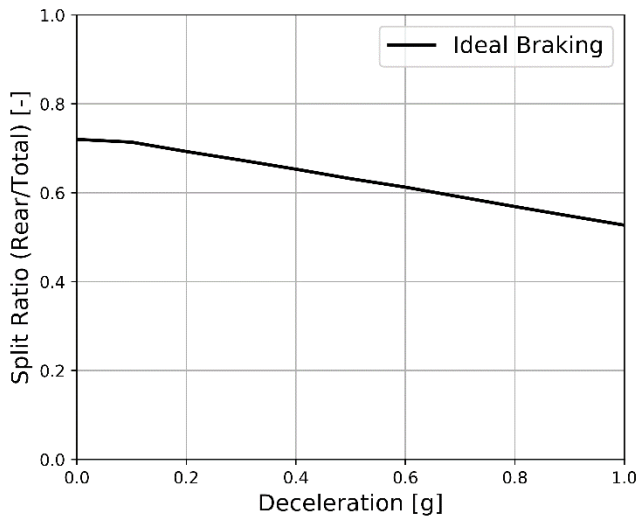


Figure 3.37. The split ratio between axles in order to perform the regenerative braking.

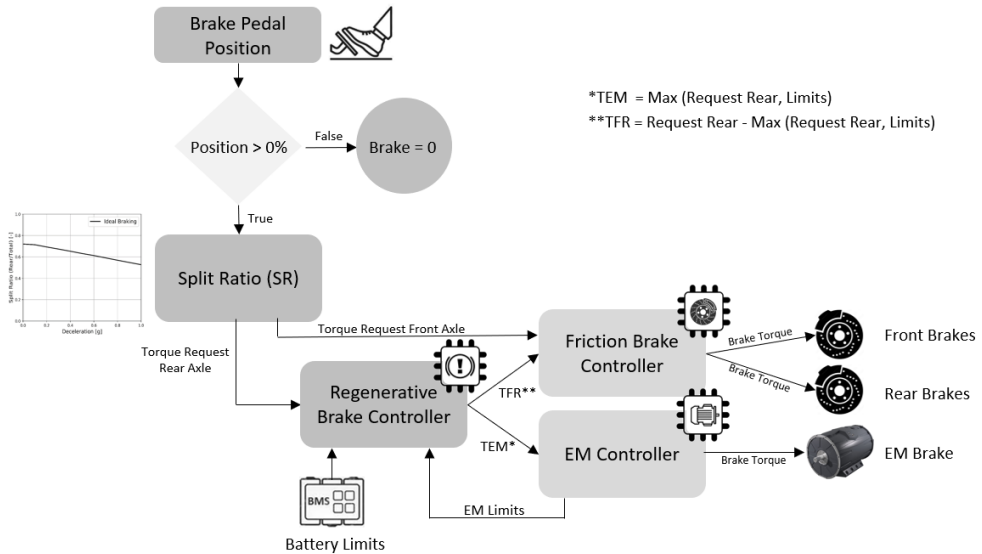


Figure 3.38. The Regenerative Brake System controller scheme with the split ratio and Battery and EM limits.

### 3.4.7 Driving cycles

As was mentioned, the truck platform is studied in transient conditions through the numerical OD-vehicle model. Different driving cycles representative of homologation conditions (WHVC) and real driving conditions were selected to understand the behavior of the concept under similar road conditions. The data to model the last-mentioned cycles was taken in real routes through a GPS in a no-hybrid commercial diesel Truck (baseline case). The cycles represent combined situations with an initial urban area and later rural and highway phases. Only one of the cycles does not contain the highway phase (Figure 3.39b). Therefore, it was called Urban. It is important to note that altitude measurements were considered in the real driving cycles. For the WHVC, the altitude is zero due to the homologation specifications. It is important to note that the duration and total distance of the real driving conditions are larger than the WHVC. More information about the cycles can be found in *Table 3-13*.

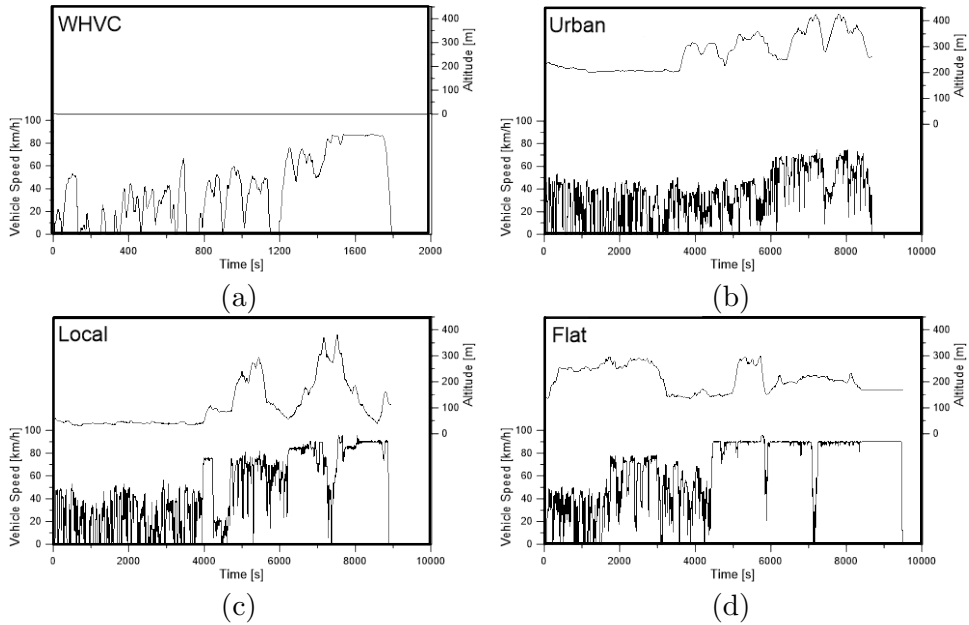


Figure 3.39. Homologation and real driving cycles with vehicle speed and altitude against time.

Table 3-13. Driving cycle main characteristics.

Parameter	WHVC	Urban	Local	Flat
Time [min]	30	145	138	158
Distance [km]	20	85	119	176
Max Speed [km/h]	88	75	96	96
Avg Speed [km/h]	40	35	48	66
Acc time [%]	46	29	29	20
Dec time [%]	32	21	24	16
Stop time [%]	26	12	13	4
Cruising [%]	28	38	34	61
RPA [m/s <sup>2</sup> ]	0.09	0.12	0.10	0.06

An additional parameter presented in Table 3-13 is the regenerative braking potential energy to be recovered. A preliminary analysis was done through the speed versus deceleration probability graphs. *Figure 3.40* shows the post-processing of the data acquired during the WHVC driving cycle. *Figure 3.40a* depicts the operative points in the braking situation (only negative acceleration) against the vehicle speed. Later, these points are passed to a probability color map in *Figure 3.40b*. The lines included in the graphs correspond to the braking power calculated with the vehicle forces for the case of an FL 18-ton truck and 100% payload.

*Figure 3.41* shows the other three driving cycles and the corresponding maximum recovery energy as *Figure 3.40c*. The Urban and Local cycles showed a high probability of braking occurrence for powers higher than 35 hp. The rest of the cycles concentrate the decelerations at low load and high speed. It is important to note that the maximum regenerative braking is limited by the maximum EM power (full line in *Figure 3.41*). The high density of points of almost all the cycles in the low deceleration region (low brake power) and the required split between the front and rear axles will cause the increase in the P2 hybrid architecture in the sizing of the electric machine will not bring high benefits.

An additional limitation in the braking system is added as maximum battery power and SOC limitation for battery safety. In addition, below 5 km/h, the truck does not recover energy due to a safety limitation. All these points directly impact fuel consumption and are considered in the result analysis.



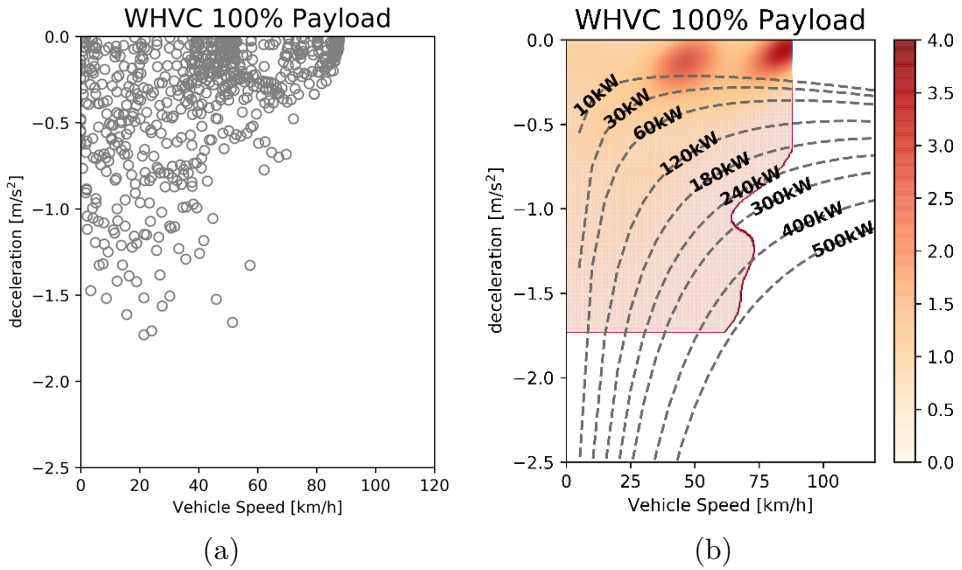


Figure 3.40. Regenerative braking analysis for FL 18ton truck in WHVC and 100% of payload. Post-processing analysis with working points (a) and frequency map in the percentage of occurrence and the lines of power braking (b).

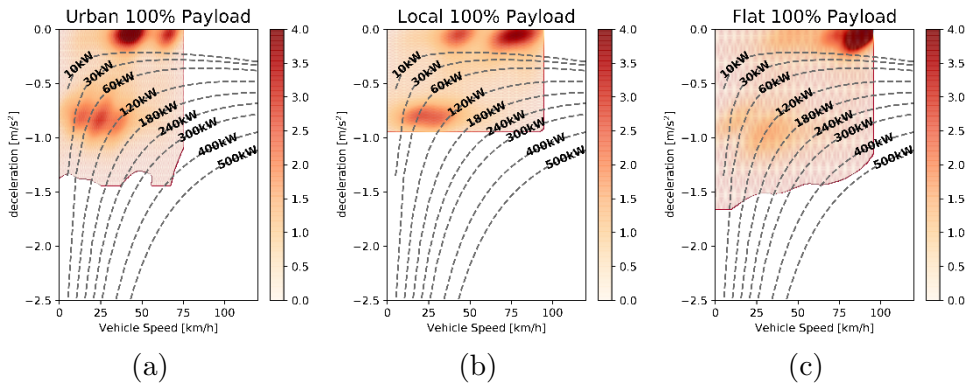


Figure 3.41. Frequency map in the percentage of occurrence and the lines of power braking for driving cycles Urban (a), Local (b), and Flat (c) with 100% payload.

### 3.4.8 Energy management and optimization strategy

Rule-based control is the most common method to implement in xHEV due to its robustness and online operation. The main task is to coordinate the split between the ICE and EM/s so that the ICE operates efficiently and the battery SoC is maintained within the prescribed boundaries. It is not based on any optimization algorithms, and its formulation does not require analytically modeling the powertrain (as is the case for predictive model controls) but relies on engineering calibration. A set of rules can then be designed depending on the desired target (examples as consumption minimization, emissions minimization, or battery SOH minimization). A deterministic RBC is used. The control logic works with a set of if-else control rules that are tuned by many control parameters, such as threshold values or power limitations, that need to be calibrated to achieve the desired performance. For example, the EM/s may be activated below a certain speed, or the battery must be recharged below a certain SOC. More details about the control strategy and parameters to be optimized will be addressed in each powertrain configuration result section.

The important aspect to keep in mind is that optimization of certain control and hardware parameters will be performed for each truck platform configuration. In particular, three payload conditions (0%, 50%, and 100% relative to the maximum payload) and four driving cycles are considered. This methodology leads to 12 possible cases to study, as shown in Figure 3.42.

For the optimization with the genetic algorithm, only the WHVC was considered due to two main reasons: 1) This homologation cycle was created to represent average conditions around the world, and it is the unique cycle used for European homologation, and 2) After a sensitivity analysis, it was seen that the payload has a more significant impact on the component and control selection than the driving cycle characteristics.

Therefore, the optimization criteria considered is to select the best case to achieve the lowest possible CO<sub>2</sub> emissions at homologation conditions (WHVC, 50% payload), as shown in Figure 3.42.

### WHVC 50% Payload Min CO<sub>2</sub>

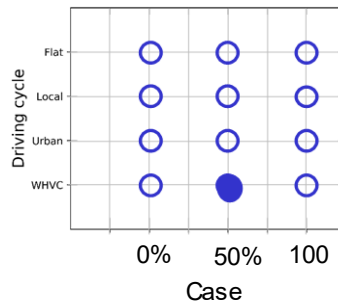


Figure 3.42. Optimization strategy with test matrix with 12 simulated cases.

A resume of the current methodology developed to optimize two truck hybrid powertrains is presented in Figure 3.43.

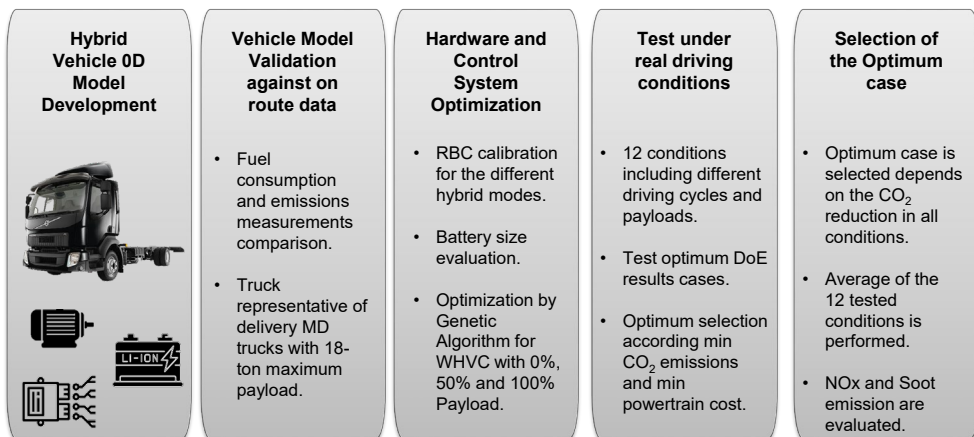


Figure 3.43. The flow chart scheme of the methodology was used to optimize a Medium-Duty truck platform under reactivity-controlled compression ignition combustion mode.

### 3.4.9 Life cycle analysis

The review of the literature on CO<sub>2</sub> emissions and the unfair comparison between engines when only tailpipe emissions are considered leads to the need for a life cycle analysis. An LCA is included considering Well-to-Tank (WTT), Tank-to-Wheel (TTW), and vehicle fabrication, maintenance, and disposal CO<sub>2</sub> generation (LCA) for each of the powertrain analysed. The main equations for the calculation of each one of the parameters are:

$$WTT\ CO_2 = Energy\ CO_2\ Production * Energy\ Consumption\ Cycle \quad (3.39)$$

$$TTW\ CO_2 = Energy\ CO_2\ factor * Energy\ Consumption\ Cycle \quad (3.40)$$

$$WTW\ CO_2 = WTT\ CO_2 + TTW\ CO_2 \quad (3.41)$$

$$LCA\ CO_2 = WTW\ CO_2 + \frac{Component\ CO_2\ Emission}{Vehicle\ Life} * Replace\ Number \quad (3.42)$$

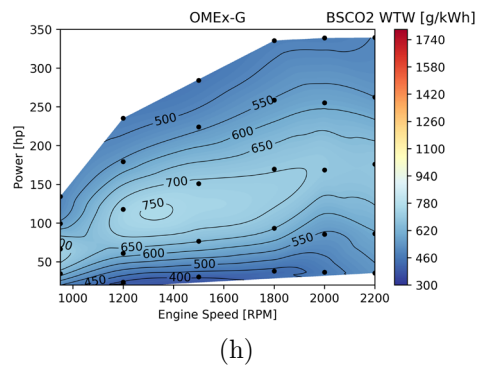
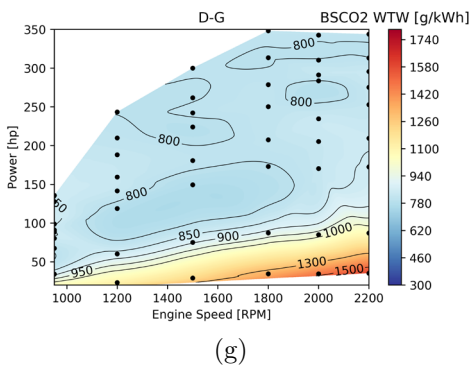
A deep research bibliography was performed to determine the CO<sub>2</sub> factor for the fuels and components of the vehicle. The values taken for this study are depicted in *Table 3-14*. The reference source is added. For the e-fuels, the work performed by Aramco [163] is used because is part of the project that this thesis is related. In addition, the green methanol and OMEx pathways is taken because to be considered a potential alternative for conventional fuels must be low carbon fuel.

Table 3-14. CO<sub>2</sub> impact by fuel production, component production, maintenance and disposal of the vehicle components.

Component	CO <sub>2</sub> Associated
Diesel WTT [g <sub>CO2</sub> /MJ <sub>Fuel</sub> ]	16.2±2.6 [Table 2-5]
Gasoline WTT [g <sub>CO2</sub> /MJ <sub>Fuel</sub> ]	14.9±2.0 [Table 2-5]
Methanol WTT [g <sub>CO2</sub> /MJ <sub>Fuel</sub> ]	-61.7±6.0 [Table 2-5]
OMEx WTT [g <sub>CO2</sub> /MJ <sub>Fuel</sub> ]	-64.5±8.9 [Table 2-5]
Electricity Average WTT [g <sub>CO2</sub> /kWh <sub>electricity</sub> ]	172 [Figure 3.45]
Electricity Marginal WTT [g <sub>CO2</sub> /kWh <sub>electricity</sub> ]	382 [Figure 3.45]
Diesel TTW [g <sub>CO2</sub> /g <sub>Fuel</sub> ]	3.17
Gasoline TTW [g <sub>CO2</sub> /g <sub>Fuel</sub> ]	3.09
Methanol TTW [g <sub>CO2</sub> /g <sub>Fuel</sub> ]	1.37
OMEx TTW [g <sub>CO2</sub> /g <sub>Fuel</sub> ]	1.60
Electricity TTW [g <sub>CO2</sub> /MJ <sub>Fuel</sub> ]	0
Battery Manufacturing [kg <sub>CO2</sub> /kWh <sub>battery</sub> ]	108±42 [Table 2-6]
Conventional Powertrain [ton <sub>CO2</sub> /Vehicle]	9.9 [211]
Hybrid Powertrain [ton <sub>CO2</sub> /Vehicle]	16.7 [211]
Electric Powertrain [ton <sub>CO2</sub> /Vehicle]	9.8 [211]
Body [ton <sub>CO2</sub> /Vehicle]	45.1 [211]
Chassis [ton <sub>CO2</sub> /Vehicle]	45.4 [211]
Conventional Powertrain End of Life [ton <sub>CO2</sub> /Vehicle]	12.2 [211]
Hybrid Powertrain End of Life [ton <sub>CO2</sub> /Vehicle]	11.9 [211]
Electric Powertrain End of Life [ton <sub>CO2</sub> /Vehicle]	13.7 [211]
Tires [kg <sub>CO2</sub> /unit]	600 [212]
Water Cooling [g <sub>CO2</sub> /lt]	1600 [213]
Oil Lubricant [g <sub>CO2</sub> /lt]	2714 [213]
Transmission Lubricant [g <sub>CO2</sub> /lt]	2140 [213]
Vehicle Life [km/years]	800,000/16
Battery expected life BEV/PHEV/HEV [years]	4/6/10
Tire replacements [-/year]	6 [214]
Water cooling replacements [lt/year]	10 [214]

Oil replacements [lt/year]	50 [214]
Transmission replacements [lt/year]	13 [214]

Regarding fuel CO<sub>2</sub> emissions by the production, it is possible to see the advantages of e-fuels such as OMEx and Methanol. The first was obtained by deep analysing the production with different renewable electricity sources such as Solar, Wind, and Nuclear by Aramco (fuel provided for the tests). The latter was obtained from an in-depth research bibliography review. The fuels are able to reduce carbon emissions due to the large carbon capture and renewable energy production. For OMEx, the WTW maps are presented and compared with Diesel-Gasoline results in *Figure 3.45*. The sum of the TTW obtains these results measured CO<sub>2</sub> emissions plus the CO<sub>2</sub> associated with the fuel production depending on each fuel injection (OMEx, Gasoline, or Diesel). *Figure 3.45* shows that on a WTW basis, OMEx-Gasoline dual-fuel combustion reverts the trend seen on a TTW basis. The carbon neutrality of OMEx allows to achieve up to 750 g/kWh in the BTE point, while for Diesel is 800 g/kWh. This means a 7% of reduction in WTW CO<sub>2</sub> emissions. In addition, at low load, due to the lower PER of the OMEx-Gasoline combustion (large injection amount of OMEx), the reduction is even higher than in the BTE (70% of CO<sub>2</sub> reduction).



*Figure 3.44. Brake specific Well-to-Wheel CO<sub>2</sub> emissions for Diesel-Gasoline (a) and OME<sub>x</sub>-Gasoline (b) for the MD8 engine.*

Generally, the CO<sub>2</sub> associated with the energy re-charging (PHEV and BEVs) is calculated with the average electricity mix. Despite being widely used, it has associated an error in terms of the impact of the vehicles being charged in the grid demand. Therefore, the CO<sub>2</sub> emission is associated with the electricity mix. The marginal emission can give a more accurate value to overtake this issue. This concept came from the marginal price that companies use for the customers. The rules of a marginalist pricing system state that every consumer pays the price per kWh of electricity driven by the cost associated with the energy given by the last power plant used to face the instantaneous demand. This means that when the demand at a given moment increases in a non-significant way, the plant which covers that additional demand is the marginal one, which has a price, and that price is the one that every consumer will pay for the energy used at that moment. The electric power is supplied at every moment by the different power plants following a merit order that establishes the use preference depending on the energy source of origin.

Based on the work of Garcia et al. [215] where the Spanish grid was analysed for 2019 and estimated for 2030, the marginal and average CO<sub>2</sub> emissions were obtained. In this work, renewable sources are the priority to supply the energy demand. When the demand overcomes their maximum generation capacity, the additional power required is supplied by non-renewable sources in the following order: 1) Waste-to-energy (0.31 kgCO<sub>2</sub>/kWh), 2) Coal (0.95 kgCO<sub>2</sub>/kWh), 3) Combined-cycle (0.37 kgCO<sub>2</sub>/kWh) and 4) Fuel-gas (0.77 kgCO<sub>2</sub>/kWh). Figure 3.46 shows the marginal emission for both scenarios. The average in Spain of power demand is 30 GW. Therefore, the marginal emission on

average is 382 g/kWh. The value taken is almost double the average emission without considering the marginal approach of 165 g/kWh. However, considering the average emission is an error because the new hybrid or EV technologies need to be considered as additional power demand sources to the exist ones. For 2030 with the introduce of new renewable sources expected in Spain electricity matrix, the marginal emissions will decay to 210 g/kWh. However, large introduction of solar and wind power sources needs to be done.

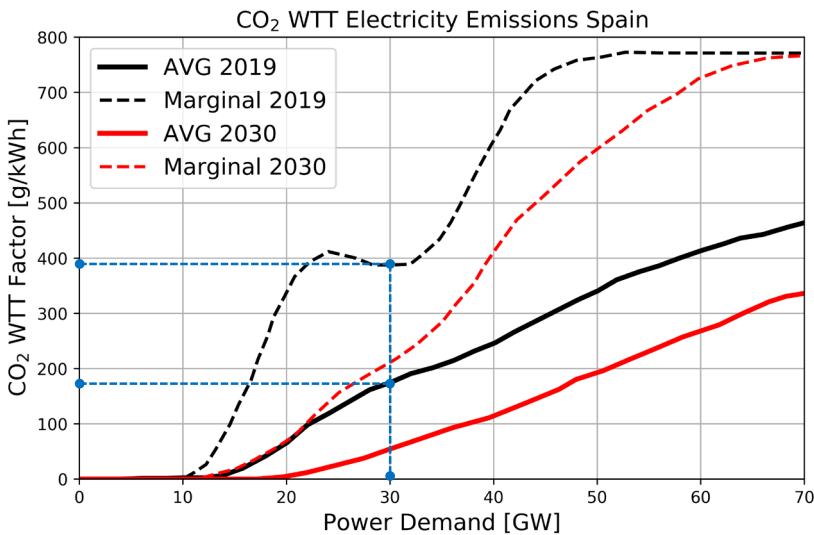


Figure 3.45. Marginal emissions rate versus electricity generation for 2019 and 2030 in Spain. Adapted from [215].

Battery manufacturing is crucial in this work for a fair comparison between non-hybrid, xHEV, and BEV. The research bibliography of [216] is taken as a reference due to the deep analysis of different scenarios. It is important to note that it is supposed that the battery will be produced in Europe. This latest evidence shows that the carbon impact of the production of batteries ranges from 61 to 106 kgCO<sub>2</sub>e/kWh according to the 2019 updated study from IVL Sweden



[168]. Their previous estimate - from 2017 - ranged from 150 to 200 kgCO<sub>2</sub>e/kWh and relied on scarce data from small-scale production, with some dating back to 2010.

The vehicle life was estimated at 16 years, which is equivalent to 800,000 km. Vehicle maintenance is separated into the maintenance of the vehicle and tire replacement. The truck production and disposal are taken from [211] due to the analysis of the vehicle CO<sub>2</sub> impact for similar conditions than are studied in the current work.

### 3.5 Conclusions

The different experimental and numerical tools used to develop this investigation was detailed in this chapter. In the first instance, the experimental setup was described evidencing the characteristics of the six-cylinder 8L engine and the active ICE test bench facility. The fuel properties used in this work are presented. Conventional fuels such as Diesel and Gasoline are used. Moreover, OMEx and Methanol properties are presented because they will be used as synthetic fuels to reduce CO<sub>2</sub> and pollutant emissions. The calibration maps performed by the research group in previous years are presented because they are used in the numerical model. In particular, two calibrations with dual-mode dual fuel concepts using Diesel-Gasoline and OMEx-Gasoline were shown.

Then, the numerical tools were introduced and divided into 0-D and 1-D simulation codes. These tools are the central point of this Thesis because they allow testing of different vehicle powertrains and engine component variations without expensive experimental tests. In addition, the models are essential to complement the empirical study in terms of fundamental understanding and give an overview of the proposed technologies applied to a commercial truck.

0D vehicle models are used in GT-Suite, fed with experimental ICE test bench data regarding fuel consumption and emissions for 54 operative conditions. The model is validated against on-road measurements in a non-hybrid diesel truck. The results show a deviation of 2% in terms of fuel consumption. In addition, transient tests in the test bench were used to verify the accuracy of the emission predictions. The results show that the NO<sub>x</sub> is overpredicted by 24%, HC underpredicted by 23%, and CO overpredicted by 7% in homologation conditions. Different combustion chamber temperatures explain the deviations due to the proposed step type.

The ICE 1D numerical simulation methodology is presented. The model was calibrated and validated against experimental engine test bench data. This model will be used in Chapter 4 to test electrified ICE components such as electrified turbocharger and electrified EGR pump. In addition, the 1D DOC model was presented in this chapter with the validation against experimental measurements.

Lastly, the different powertrain components were presented, focusing on the electric machine and the lithium-ion battery. In addition, the hybrid powertrain control system and the optimization strategy were shown. The chapter briefly summarizes the life cycle analysis used to assess the different powertrain technologies.

# Chapter 4

## Impact of mild hybridization on dual-fuel concept

### **Content**

---

4.1 Introduction.....	192
4.2 Engine model calibration with e-Components .....	193
4.2.1. Single path configuration for EGR.....	194
4.2.2. e-EGR pump.....	199
4.2.3. e-Turbo.....	204
4.2.4. e-EGR pump and e-Turbo .....	209
4.3 e-DOC model calibration .....	216
4.4 e-Component CO <sub>2</sub> tailpipe emissions.....	226
4.5 Driving cycle assessment with DOC and e-DOC.....	236
4.6 Conclusions.....	242

## 4.1 Introduction

Mild-Hybrid (MHEV) is the first level of electrification where a low voltage system is added to the powertrain to feed components such as EM and ICE subcomponents. The EM is known as Belt Assistant Starter (BAS) due to the installation in the crankshaft belt of the ICE to assist during starting, ICE boosting, and cruising. The described powertrain is also classified as P0 due to the position of the EM in the powertrain layout. The electric system allows the addition of electric ICE subcomponents that in a non-hybrid are propelled mechanically. Examples are electrified turbocharging, ATS heaters, and electric pumps of cooling and lubricant systems, among others.

Several components are numerically tested to understand the benefits that can bring the powertrain electrification. Components such as electric turbocharger, EGR assistance, and after-treatment system improver are virtually tested. In addition, the advantage of a belt assistant alternator motor is evaluated in different driving conditions by a 48V battery system.

As was shown in Chapter 3, calibration of 52 operative conditions for a Medium-Duty six-cylinder engine with dual-mode dual-fuel combustion with Diesel-Gasoline was experimentally performed. A system of low-pressure EGR was added to the originally high-pressure EGR line to meet the large EGR and air quantities needed for this low-temperature combustion mode. However, this means a complicated system that is difficult to package and adds problems to the control of the ICE. Therefore, three possible options appear: 1) Electrify the turbocharging to achieve the desired air management targets, 2) Add a pump in the HP EGR line to push more EGR mass, or 3) A combination of the previous cases.

Three targets were set before starting the study to understand the advantage and drawbacks of these components: 1) Improve engine total

efficiency, 2) Remove the LP-EGR system to reduce engine modifications with respect to the OEM design, and 3) Achieve EU VI emissions target.

Moreover, the steady-state maps show a large amount of HC and CO at engine-out is produced in the DMDF combustion. In addition, the exhaust temperature of this LTC is lower than the CDC. Therefore, there can be problems for the original DOC to handle these conditions. A hybrid powertrain as the MHEV will add start and stop events, making the DOC temperature operation even lower than a non-hybrid. Therefore, taking advantage of the 48V system, an electric heater in the DOC is numerically studied under transient conditions to understand the capabilities to convert the HC and CO.

All the new components are evaluated in driving conditions by representative homologation and real driving cycles, as shown in Chapter 3. The results are compared with the OEM case and the DMDF no-hybrid cases. The section is organized by the virtual evaluation of an e-EGR pump and e-Turbo. Later, the DOC with and without a heater is tested in controlled conditions. A step forward is testing the BAS in a 48V MHEV powertrain without ATS. Lastly, the ATS is tested in the complete vehicle with and without the electric heater.

## 4.2 Engine model calibration with e-Components

The ICE 1D model shown in Chapter 3 is used to re-calibrate the engine with the e-components. The combustion profiles, fuel mass as well as temperatures, and pressure of the fuel and gases in the intake port are maintained as the experimental measurements. The main goal of the model is to model the new air management system with the different variations proposed while maintaining the combustion behavior.

As a variable geometry turbine is installed in the engine, the optimization of the system will be done by testing different VGT positions. The most efficient position is taken for each of the 36-operative condition

(950, 1200, 1500, 1800, 2000 and 2200 RPM and 10%, 25%, 50%, 65%, 80% and 100% engine load). The tested cases are 1) Electrified EGR line (e-EGR pump), 2) Electrified turbocharger (e-TC), and 3) A combination of the two options (e-TC & e-EGR pump). The HP EGR line without LP EGR on any e-components is first simulated to understand the limitations of the baseline system.

As was mentioned, the optimization target is to maximize the brake thermal efficiency. As a new component that consumes electricity appears, the equivalent brake-specific fuel consumption is defined by equation 4.1.

$$BSFC_{eq} = \frac{\dot{m}_{fuel}}{Power_{tot}} = \frac{\dot{m}_{fuel}}{Power_{ICE\ brake} + Power_{e-components}} \quad 4.1$$

where  $\dot{m}_{fuel}$  is the fuel mass consumption,  $Power_{ICE\ brake}$  is the brake power of the ICE and  $Power_{e-components}$  is the net electrical power of the e-components. Negative power means energy delivered from the shaft of each component to the gas flow, and positive means energy recovered from the gas flow.

The final results that will be presented in the following sub-section are the behavior in stationary conditions. However, they are obtained after several iteration cycles in which the control system adjusts valves, e-Turbo power, or e-EGR pump speed to achieve the air management targets (EGR rate, intake pressure, and in-cylinder temperatures). The simulation is stopped after the settings are between 2% of the target.

#### 4.2.1. Single path configuration for EGR

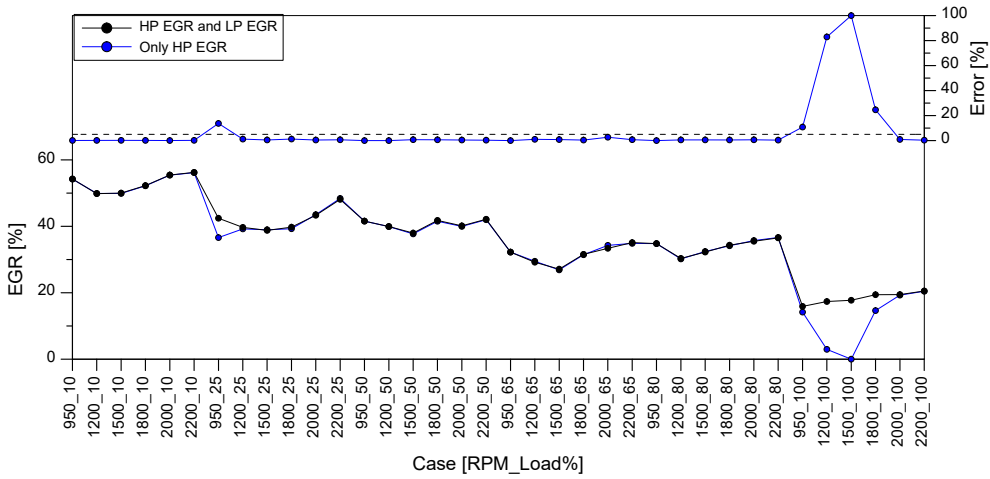
Before the evaluation of the e-components, the LP EGR loop is removed, and the 36 operative conditions are numerically analyzed. A new calibration of the VGT, exhaust back pressure EGR valve, and inlet throttle position is performed. A Proportional Derivative Integral controller performs

the optimization of the positions of the valves. The target for the back-pressure valve is to achieve the LP&HP system (baseline) EGR rate, while the VGT PID target is set the boost pressure of the baseline case. The inlet throttle controls the total intake mass by a third PID system. The model details are presented in Chapter 3. *Figure 4-1* shows the results in terms of EGR percentage, air mass flow rate, and intake pressure achieved with only the HP EGR line after the optimization. As the target is the experimental system tested in the testbed (HP and LP EGR lines), the error is defined as:

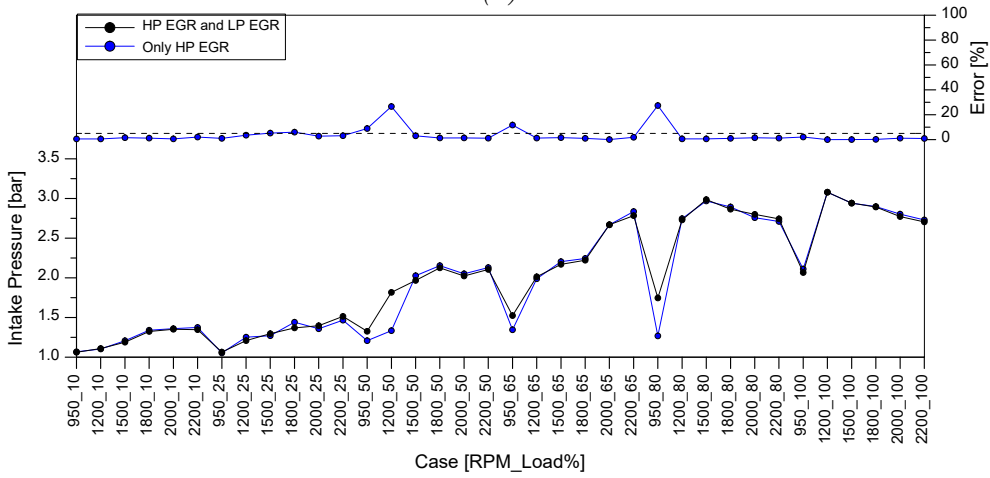
$$Error [\%] = \frac{|(Y_{New\ System} - Y_{HP\&LP\ EGR})|}{Y_{HP\&LP\ EGR}} * 100 \quad 4.1$$

With  $Y_{System\ x}$  being the parameter under investigation. If the error of the air management parameters is below 5%, it is supposed to be successful because the combustion parameters will not change.

The full load cases showed the worst behavior in terms of total EGR provided to the engine (*Figure 4-1a*). Despite being the load with the lowest EGR requirements, the high mass flow rate and boost pressure make it impossible for the HP loop to bypass the EGR required ( $\approx 20\%$ ). In terms of boost pressure (intake combustion chamber pressure), the targets were achieved in almost all cases (*Figure 4-1b*). Low engine speed (950 and 1200 RPM) presented some points without enough energy to achieve the boosted pressure, as well as low load and medium speed (25% and 1500-1800 RPM) due to significant EGR rate and high boost pressure.



(a)



(b)

Figure 4-1. EGR percentage (a) and boost pressure (b) for Only HP EGR loop against the HP & LP EGR loop experimentally characterized.

The new VGT rack position is presented in Figure 4-2 and compared with the dual loop case. For all cases, the PID tried to close the turbine to achieve the desired boost pressure. Compared with the case of both EGR lines, the VGT is half-closed. It is possible to see that the cases with high boost pressure differences (Figure 4-1b) are the same cases in which the VGT



rack position is closed. This means that it is impossible to achieve with this configuration the boost pressure desire in that case.

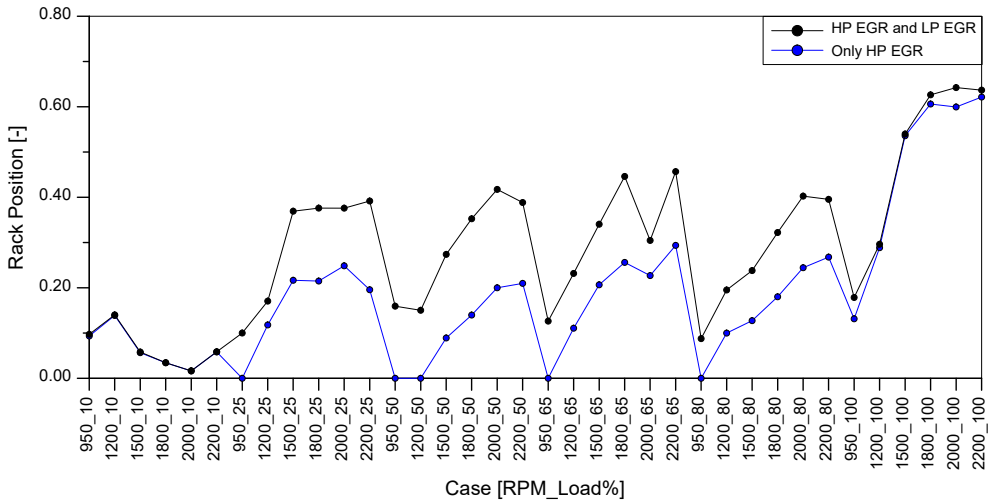


Figure 4-2. VGT rack position for Only HP EGR loop against the HP & LP EGR loop experimentally characterized.

The cases that successfully achieve the desired target -with an error below 5%- are plotted in *Figure 4-3* regarding brake-specific fuel consumption. The cases that could not achieve the desired targets have been deleted and are presented as black points. The successful cases are twenty-seven of the thirty-six cases tested. The engine cannot operate at full load and low engine speed with the DMDF combustion with only the HP EGR line. In addition, almost all cases have higher fuel consumption than the target. Only 1200 RPM/80% and 2000 RPM/65% have a slight benefit due to the reduction of pumping losses.

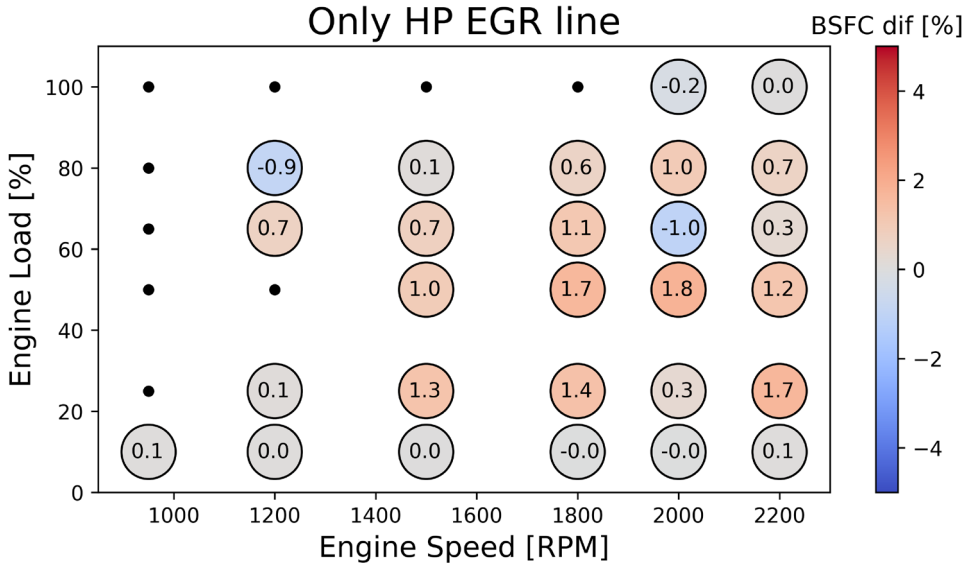


Figure 4-3. Brake-specific fuel consumption for successful cases with Only HP EGR loop against the HP & LP EGR loop experimentally characterized.

The results presented in Figure 4-3 show that the double loop EGR is better than the OEM solution for the dual-fuel combustion concept. It is important to note that the operative conditions with higher LP EGR rates in the experimental calibration are the cases with the highest penalties. Different from CDC, RCCI needs significant EGR rates. Therefore, sending the gas through the HP EGR loop (before the turbine inlet) reduces the turbine's available energy to propel the compressor. The boosting capabilities decay. In addition, the exhaust valve (after the turbine) must be quite closed to generate the required back pressure to achieve the desired EGR flow.

The question now is open to the e-components cases: Is it possible to operate under RCCI conditions and have lower fuel consumption by electrification of the air loop? The question will be answered in the following sections.

### 4.2.2. e-EGR pump

The first step in e-component testing is a positive displacement EGR pump in the HP EGR line. The pump proposed is a novel component not seen in commercial applications yet. Eaton showed recently as a prototype and designed to improve CDC engines (*Figure 4-4*). In this work, the concept of the EATON prototype pump is used and modeled as a positive displacement pump in GT-Power for the DMDF combustion.

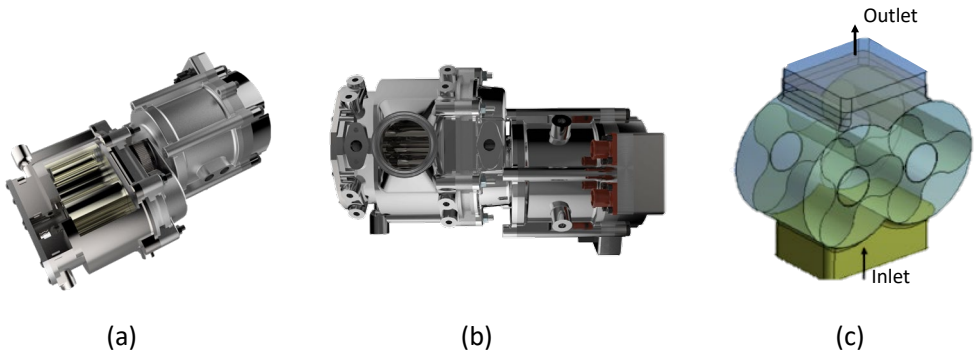


*Figure 4-4. EGR pump example of EATON design.*

The pump can move the flow just slightly above the intake pressure, and it is driven by a 48V electric motor that makes the rotational speed utterly independent from the engine speed. The main equations that describe the operation are the volumetric flow (Equation 4.2) and power consumed or delivered (Equation 4.3).

$$Q_{real} = w \cdot D \cdot \eta_{vol} \quad Eq. 4.2$$

$$W = \frac{\Delta P \cdot Q_{real} \cdot \eta_{electric}}{\eta_{isentropic}}, \Delta P > 0 \quad Eq. 4.3a$$

$$W = \frac{\Delta P \cdot Q_{real} \cdot \eta_{isentropic}}{\eta_{electric}}, \Delta P < 0 \quad Eq. 4.3b$$

with  $Q_{real}$  the volumetric flow through the pump,  $w$  the rotational speed of the pump,  $D = 400 \text{ cm}^3$  the displacement of the pump and  $\eta_{vol} = 0.90$  the volumetric efficiency measured in CMT.  $W$  is, the pump's power with two conditions depending on the pressure difference between the inlet and outlet ( $\Delta P$ ). The isentropic efficiency  $\eta_{isentropic} = 0.40$  is also needed for the power calculation and was estimated with the work of Dumont et al. [217]. The electric efficiency in the pump ( $\eta_{electric}$ ) is estimated as 96%. A scheme of the new model is presented in *Figure 4-5*. The 36 points are analyzed to understand the benefits and drawbacks of this setup, as in the case of only HP EGR.

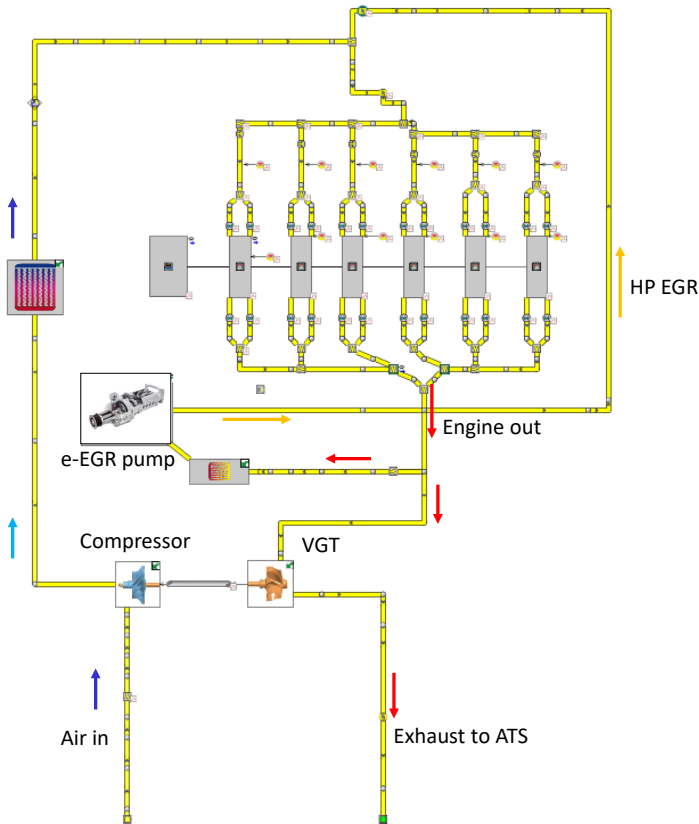
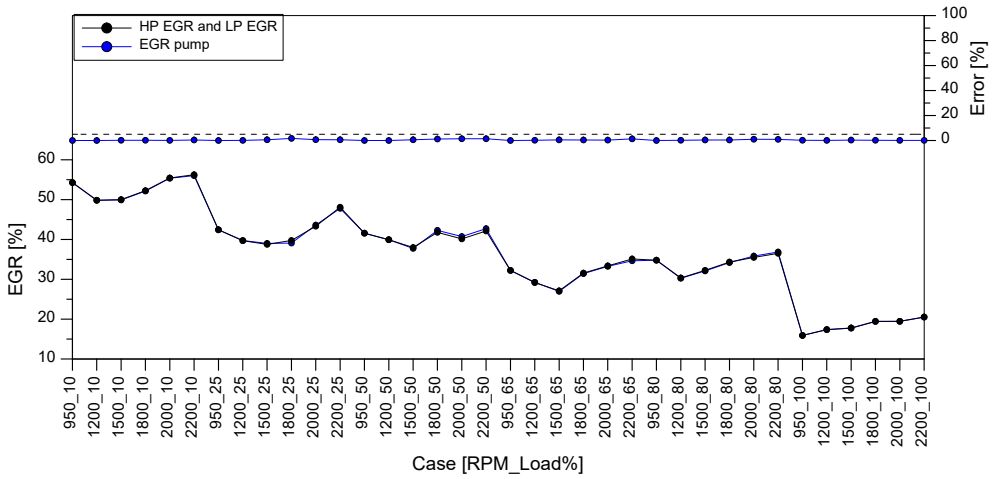


*Figure 4-5. 0D-engine model for the DMDF with e-EGR pump in the HP EGR line.*

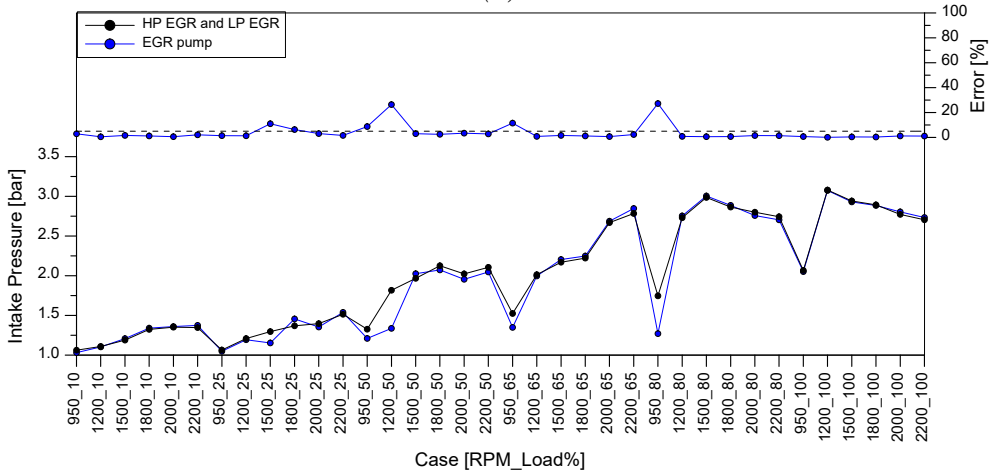
The EGR pump can provide the recirculation gas rate for all operative conditions (*Figure 4-6a*). This shows the great advantage of including the electrified component for precisely controlling the EGR. However, as it can provide the desired EGR flow, the turbine suffers a low flow rate and consequently low energy through the turbine blades. Moreover, the air mass and boost pressure are similar to the only HP EGR loop with a lack of air mainly at full load (*Figure 4-6b*). The VGT position (see *Figure 4-7*) needs to be maintained closer than the dual EGR loop case to provide the required boost pressure with lower exhaust flow mass.

*Figure 4-8* shows the EGR pump speed and power for the 36 operative conditions. The pump consumes power to deliver the required EGR mass in almost all the points, with speed increasing with the engine speed. The rotational speed was around 2000 RPM to 9000 RPM, and the power consumed around 1.5 kW. The full load cases due to the lower EGR rate and higher air mass allow recovery until 0.5 kW by braking the pump with the gas energy.

Thirty-one of the thirty-six cases were successful (see *Figure 4-9*). This is four operative conditions more than the only HP EGR loop. The main improvements are at the full load, where it was impossible to achieve the EGR levels before. With the EGR pump, this issue is solved with similar fuel consumption to the HP&LP EGR case. However, almost all cases showed higher fuel consumption at medium and high loads than the reference case. An average of around 0.2% and a peak of 1.6% in terms of equivalent BSFC were seen. The best case for the e-EGR pump is at a low load where the EGR pump makes energy recovery possible.



(a)



(b)

Figure 4-6. EGR percentage (a) and boost pressure (c) for EGR pump case against the HP & LP EGR loop experimentally characterized.

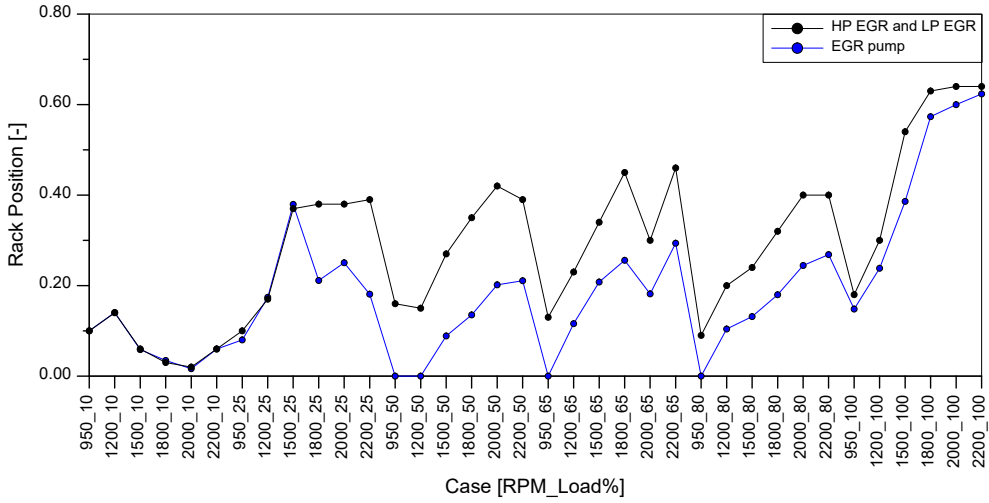


Figure 4-7. VGT rack position for EGR pump case against the HP & LP EGR loop experimentally characterized.

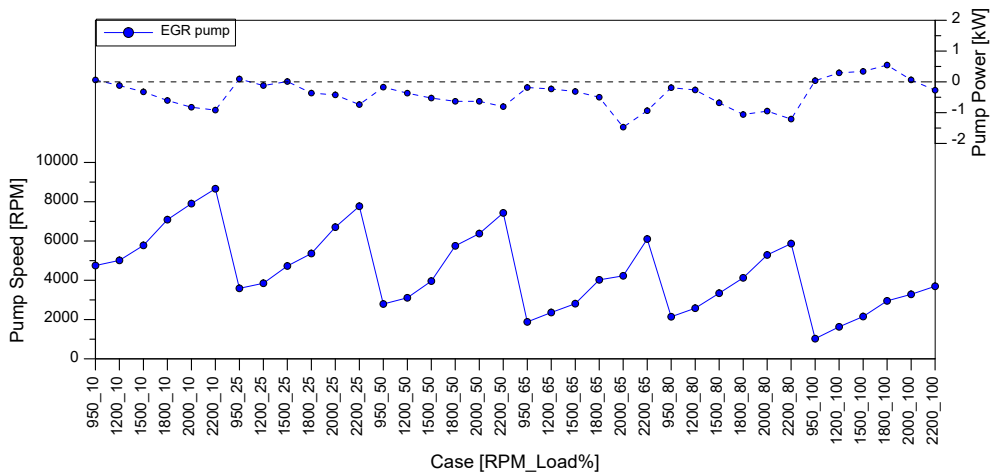


Figure 4-8. Pump speed and power for EGR pump case.

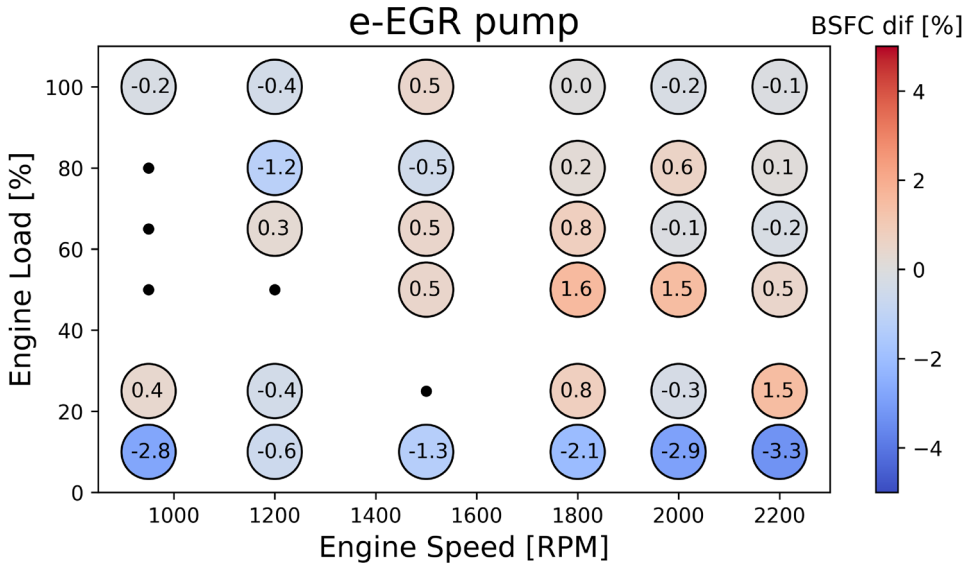


Figure 4-9. Brake-specific fuel consumption for successful cases with EGR pump case against the HP & LP EGR loop, experimentally characterized.

### 4.2.3. e-Turbo

The next step is to evaluate the benefits and drawbacks of an electric motor in the turbo-compounding axle. Well-known as e-TC or e-turbo, it allows more flexibility in terms of the energy management systems and to achieve air inlet targets that are not possible with conventional turbine arrangements. An example of an e-Turbo is shown in *Figure 4-10*, where a compact electric motor is located between the turbine housing and compressor housing. Other manufacturers prefer to locate the EM out of the two housing to avoid elevated heat transfer from turbine gases. In that case, the EM is connected to the compressor axle, reducing the EM working temperature. In this work, a generic e-Turbo layout is taken. The focus is to model the required mechanical power delivered to the turbocharger shaft to achieve the desired air management targets. The VGT design is maintained to maintain the flexibility of the component in different engine conditions.



However, the coupling of the e-components in the engine implies that several VGT positions can achieve the desired boost pressure target by varying the e-Turbo power requested. In order to optimize the component operation, a sweep of the VGT position is performed. After postprocessing, the best BSFC equivalent is taken as optimum for each of the 36 points.

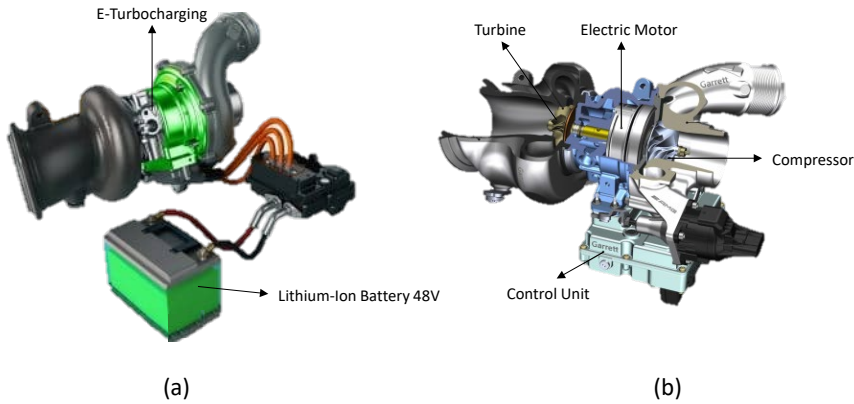


Figure 4-10. Electrified turbocharged example of Garret.

The e-TC is modeled as an electric machine coupled to the turbo compounding shaft, as shown in *Figure 4-11*. This allows to deliver or recover power depending on the engine inlet and outlet conditions and the calibration targets. Due to the high rotational speed of the turbo compounding, a gear reduction of three is included in the electric machine design.

For the control of this device, two parameters are considered. One signal corresponds to the blade position and the other to the electrical power delivery. The first signal will be calibrated in this work using a design of experiments (DoE). The second signal is calculated by employing a PID with the current intake manifold pressure and the target intake pressure for the DMDF ICE configuration. The maximum/minimum brake power of the e-TC electric machine is set at 15/-15 kW, and a maximum allowed speed of 60,000 RPM.

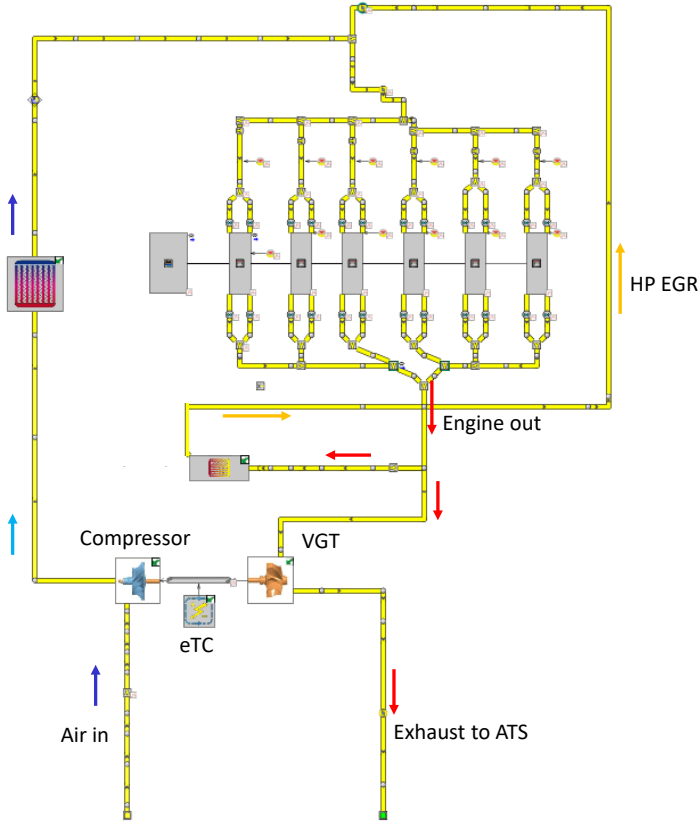


Figure 4-11. OD-engine model for the DMDF with e-TC.

For brevity of the manuscript, only three operation conditions VGT variation are shown. Figure 4-12 shows a low speed/load condition where the boost pressure, EGR rate, e-turbo operation, and BSFC are depicted. The comparison with the HP&LP EGR loop case is added. The e-turbo allows achieving the boost pressure for all VGT positions. However, the lack of back pressure makes the EGR decay. Only up to 0.22 of the VGT position can achieve the required target. The e-motor speed is around 6000 RPM, and the power delivered increases with the opening of the VGT. The optimum case is the 0.22 VGT position (the most open condition that meets the EGR rate) with a benefit of 2.2% of BSFC. This benefit came from reducing the pumping losses due to the opening of the VGT. The power delivered by the e-motor is

70 W. Similar behavior is seen for the medium operation case (*Figure 4-13*) and high operation case (*Figure 4-14*). However, no benefits are seen in these cases due to the trade-off between pumping losses and energy added by the e-Turbo.

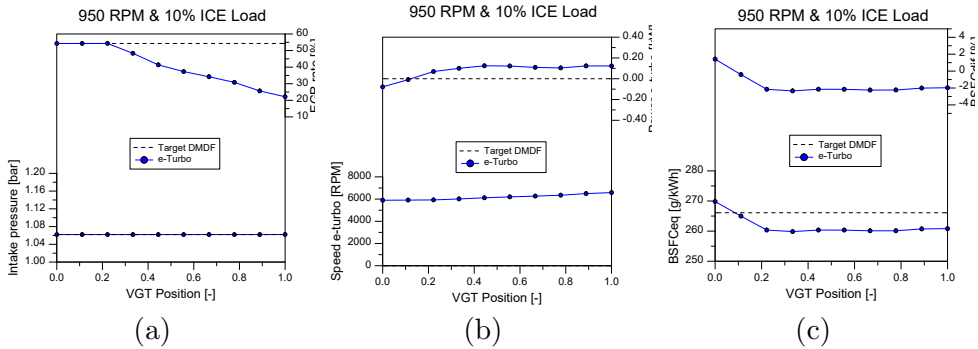


Figure 4-12. Air management parameters (a), e-motor of the turbocharging operation condition (b), and equivalent brake specific fuel consumption (c) for 950 RPM and 10% engine load.

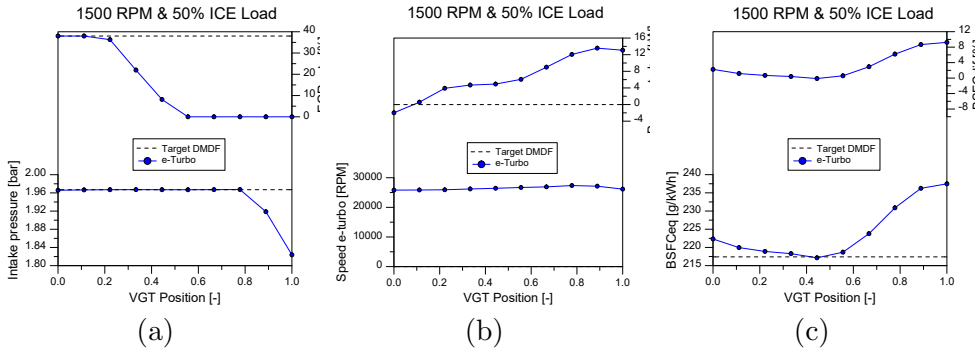


Figure 4-13. Air management parameters (a), e-motor of the turbocharging operation condition (b), and equivalent brake-specific fuel consumption (c) for 1500 RPM and 50% engine load.

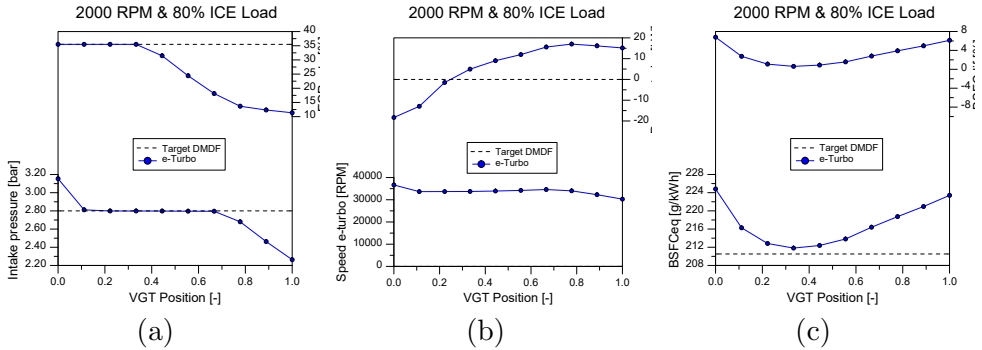


Figure 4-14. Air management parameters (a), e-motor of the turbocharging operation condition (b), and equivalent brake-specific fuel consumption (c) for 2000 RPM and 80% engine load.

A final summary of the BSFC benefits can be seen in Figure 4-15. The low load cases allow recovering a large amount of energy by pumping losses minimization with the opening of the VGT. The medium load range cannot achieve considerable benefits but allows the operation with similar consumption and without the LP EGR loop. High load again allows some benefits by the e-Turbo energy recovery. The question is: Is it possible to improve energy consumption by adding e-Turbo and e-EGR pumps? Is it beneficial to open the VGT and maintain the EGR rate by the e-EGR pump while meeting boost pressure with the e-Turbo? These questions will be answered in the following subsection.

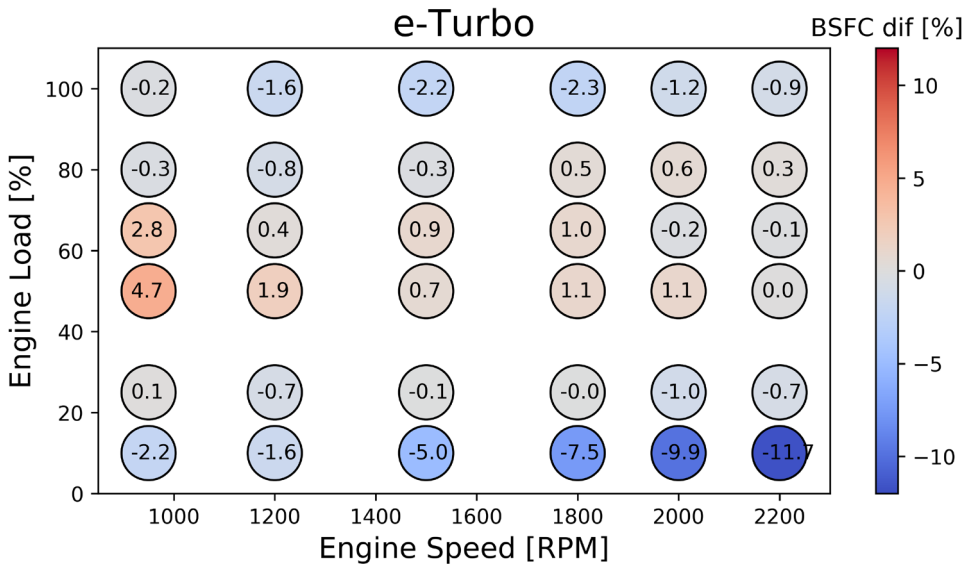


Figure 4-15. Brake-specific fuel consumption for successful cases with e-Turbo pump case against the HP & LP EGR loop experimentally characterized.

#### 4.2.4. e-EGR pump and e-Turbo

Both elements are virtually installed in the engine model and tested in the 36 operative conditions. The e-Turbo aims to achieve the boost pressure while the e-EGR pumps the EGR rate. Two independent PIDs control these two parameters. To not have interaction problems, a delay is added in the e-Turbo. The VGT varies in a DoE, and the most efficient position is selected postprocessing. The model is presented in *Figure 4-16*.

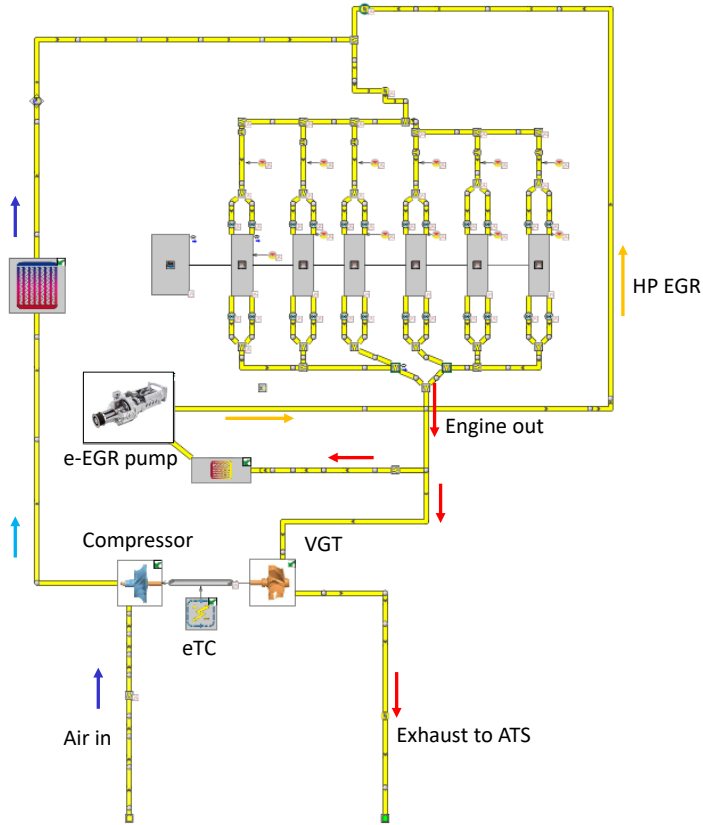


Figure 4-16. OD-engine model for the DMDF with e-components (e-EGR pump in the HP EGR line and the e-TC).

Figure 4-17 shows the effect of varying the turbine rack position over the e-Turbo (Figure 4-17a) and e-EGR pump (Figure 4-17b) energy power for six engine speeds and engine loads. Open the VGT means that the e-TC must deliver more power because the turbine blades take less energy than the closed position. This reduces the exhaust backpressure just before the engine-out pipe, where the HP EGR line is located. Therefore, the e-EGR pump needs also to deliver power to achieve the desired EGR target. Despite this disadvantage, the pumping means effective pressure (PMEP) is also reduced (Figure 4-17c), increasing the engine brake power. Interestingly,

engine loads higher than 25% do not have results for all the VGT positions because they exceeded the turbine limit (3.8 bar of turbine inlet pressure).

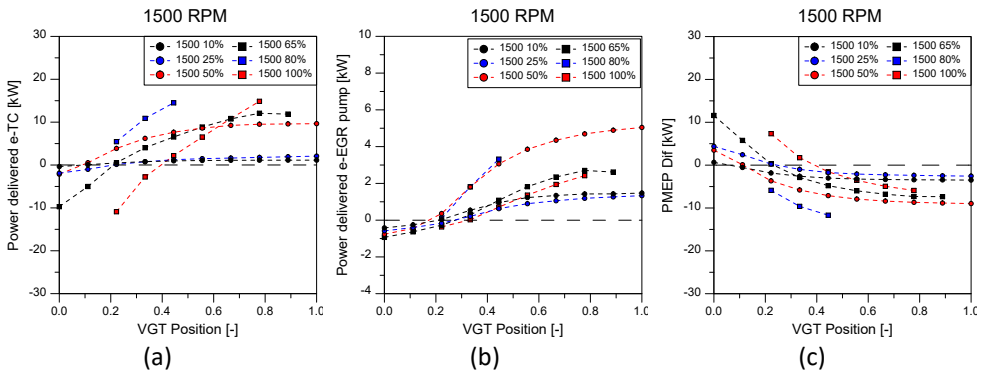


Figure 4-17. Power delivered/recovered by the e-TC (a), the power delivered/recovered by the e-EGR pump (b), and pumping mean effective pressure difference concerning the DMDF LP+HP EGR calibration (c) for different VGT rack positions at 1500 RPM.

Figure 4-18 shows the results for all the cases at 1500 RPM and 80% of engine load. When the VGT rack position is below 0.1, the turbine inlet pressure exceeds the mechanical safety limit imposed at 3.8 bar. Pasini et al. [218] noted the importance of choosing a turbine characterized by a large flow capacity to avoid high backpressure penalties, even if there is slight or no effect on fuel consumption. However, the change of turbine geometry is out of the scope of the current work. On the other hand, when the VGT rack position is higher than 0.4, the turbine inlet pressure is below 2% of the target. The main reason is that the e-TC power demand exceeds the maximum value of 15 kW. Therefore, the e-TC cannot achieve the boost pressure required at this operating condition. Despite the possibility of increasing the electric machine's maximum power of the e-TC to achieve the desired boost pressure, Figure 4-18c does not show improvements in terms of PMEP in this zone. Therefore, this zone does not represent a potential benefit to reducing fuel consumption.

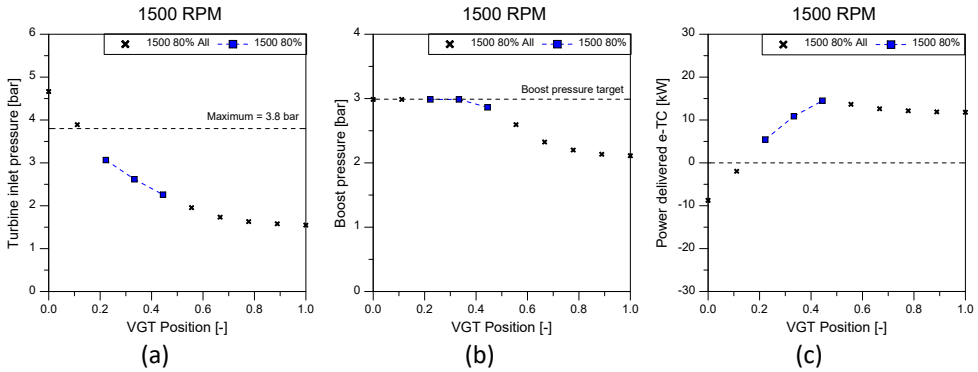


Figure 4-18. Power delivered by the e-TC (a), turbine inlet pressure (b), and boost pressure (c) at 1500 RPM and 80% engine load for different VGT rack positions.

Finally, the total power is calculated as the sum of the brake power (mainly affected by the PMEP change) and the electrical power of the e-components. Then, the new  $BSFC_{eq}$  is calculated considering the same fuel injection as the original DMDF ICE calibration. Figure 4-19 shows the results for both abovementioned parameters with the optimum marked with a star. From the  $BSFC_{eq}$  trend, it is possible to identify the engine loads that have limitations to achieve the targets and the increase of the engine efficiency with the engine load increase. For all the cases, the optimum values for VGT positions below 0.4 decrease with the engine load increase. The maximum engine load (100%) has a larger operative range than the 80% load due to the lower EGR rates required in the DMDF ICE calibration (see Figure 4-19a).



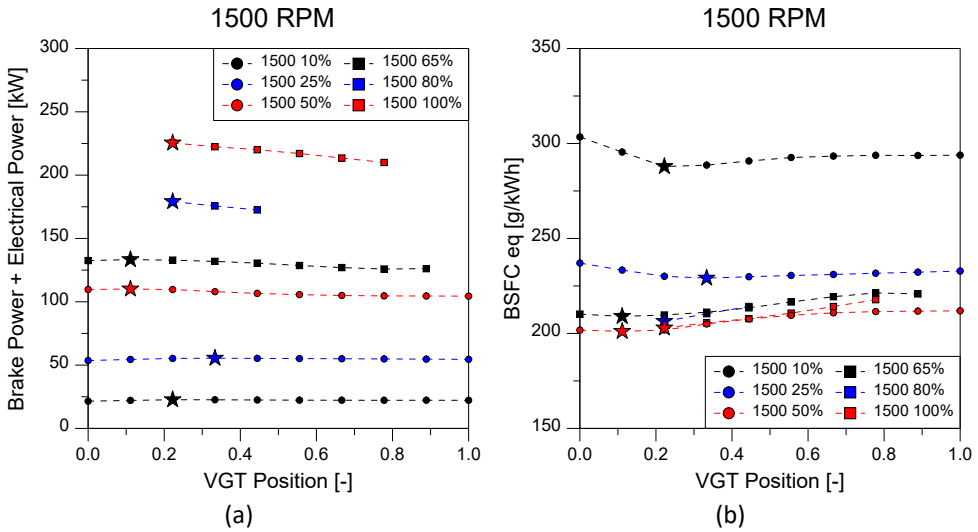


Figure 4-19. Total power (a) and equivalent brake-specific fuel consumption for different VGT rack positions at 1500 RPM and different engine loads.

The optimum operative conditions for the e-TC and e-EGR are obtained and plotted as an interpolation map for different parameters in this section. Figure 4-20 shows the e-TC and e-EGR pump power requirements in all the operative conditions. The e-TC power ranges from 6 kW in motor and -15 kW as a generator. Therefore, the sizing of the initially planned motor (15 kW) is selected correctly. In addition, the e-EGR pump shows low power requirements with 0.5 kW in traction and -1.0 kW in the generator mode. The speed set up for each e-component is shown in Figure 4-21. This is a crucial parameter for the design and can be useful in future component developments.

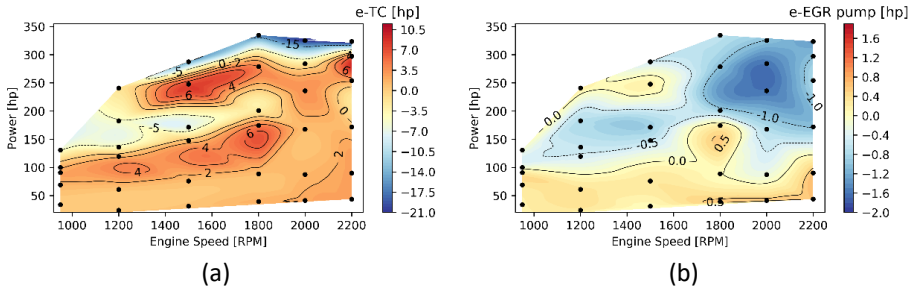


Figure 4-20. Power calibration maps for the e-TC (a) and e-EGR pump (b) work together to achieve the same calibration targets as the DMDF LP+HP EGR calibration.

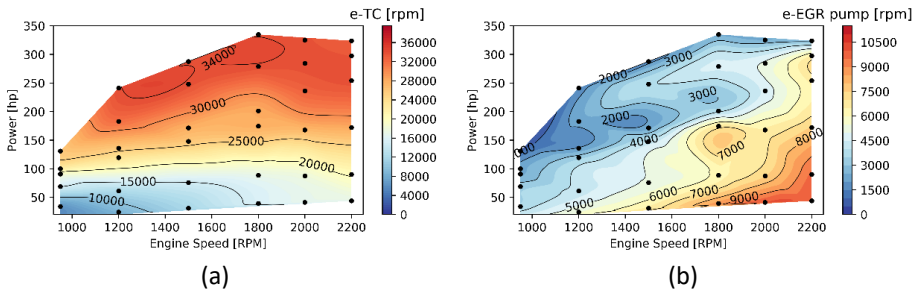


Figure 4-21. Rotational speed maps for the e-TC (a) and e-EGR pump (b) work together to achieve the same calibration targets as the DMDF LP+HP EGR calibration.

The VGT position final results and pumping work are shown in Figure 4-22. The VGT is generally near the minimum position (close to 0.1) at low and high rotational speed, close to 0.33 (see Figure 4-22a). Therefore, this increases the pumping work in middle engine load zones, as shown in Figure 4-22b. The significant benefits are found at low engine loads, where the VGT was almost closed in the original calibration to achieve the desired boost pressure.

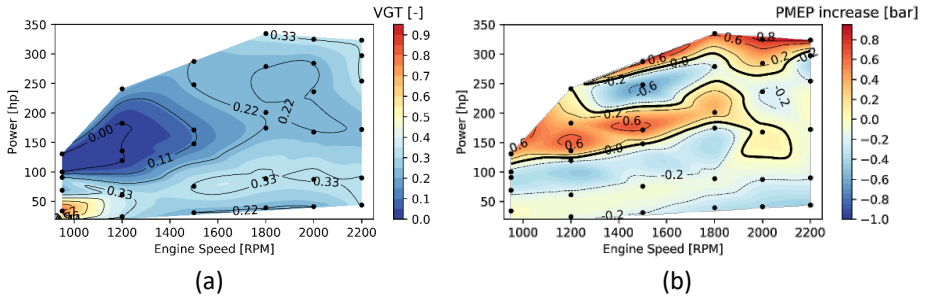


Figure 4-22. Calibration maps of the VGT rack position (a) and pumping mean effective pressure difference versus the DMDF LP+HP EGR calibration (b).

In a first step, the equivalent brake-specific fuel consumption is plotted to quantify the gains for the DMDF ICE (Figure 4-23a) and CDC calibration (Figure 4-23b). Figure 21a shows close BSFC values at medium and high loads (around  $\pm 2$  g/kWh), with the major benefits from using the e-components found at low load and high engine speed, where up to 50 g/kWh improvements are achieved. This zone allows for energy recovery with the e-TC and reduces PMEP due to the turbine rack position. In this zone, the DMDF calibration is limited due to hardware restrictions. Figure 4-23b shows that the optimum zone, compared to the CDC calibration, is around 1500 RPM and 120 hp, similar to the results shown in Figure 4-23. At low loads, the new calibration is close to the CDC values, totally different from the trend found with the DMDF configuration. It is important to remark that the new calibration achieves similar or better results in terms of BSFC but also avoids using an LP-EGR system. The NO<sub>x</sub>, soot, HC, and CO emissions remain the same as the double EGR route, which was proposed as one of the main targets for this work.

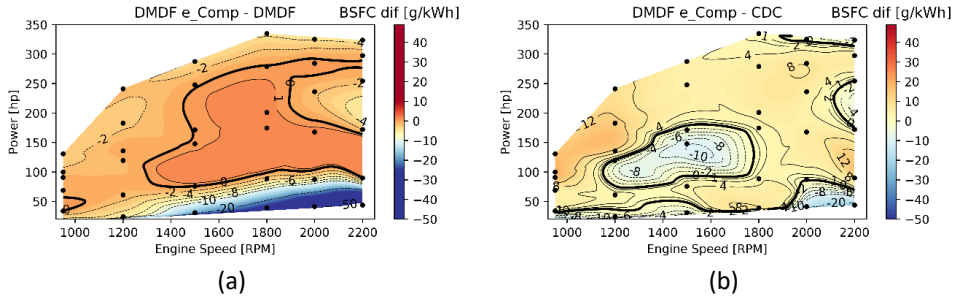


Figure 4-23. Brake-specific fuel consumption of the DMDF e-components calibration against DMDF HP+LP EGR (a) and CDC (b) calibration maps.

### 4.3 e-DOC model calibration

It is important to find an efficient thermal management strategy to heat the after-treatment device quickly without hindering the electrification benefits. As the RCCI calibration is highly sensitive to the injection strategy, delaying injections might not be the best strategy to increase the exhaust temperature. In this sense, other alternatives should be pursued. A fast catalyst heating effectively minimizes the catalyst light-off time and hence, reduces the exhaust emissions from the start-stop events. On the other hand, offering additional heat to the catalyst leads to more energy consumption, which typically results in additional fuel consumption. Various control strategies exist for catalyst heating as pre-heating and post-heating. As the control system is not predictive in terms of engine use and vehicle future speed (required for pre-heating strategies), only post-heating was used in this work. This means starting heating after a condition is achieved as a catalyst surface temperature.

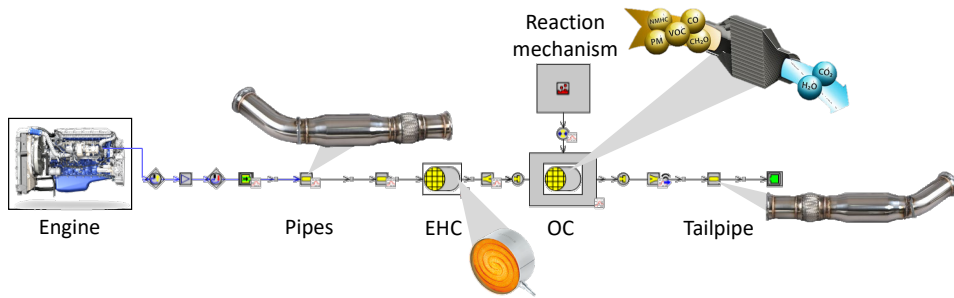


Figure 4-24. GT-Power model for the electrically heated oxidation catalyst assessment.

An electric heater catalyst (EHC) consists of an electrical resistance that provides energy to the flow at the cost of electrical consumption. The efficiency of transferring the energy to the flow is proportional to the residence time of the flow inside the EHC and the contact area. Both are directly influenced by geometric parameters of the EHC, such as length and porosity. In this study, these parameters were obtained by having as reference the EHC model proposed by Della Torre [219] for Light-Duty vehicles and scaling it considering the DOC diameter as reference. The final model of the EHC coupled with the DOC is presented in Figure 4-24. The EHC is located just in front of the DOC, with a length equal to 25% of the DOC length and the same diameter and the same substrate geometry (cell density and wall thickness). The heat is delivered to an iron mesh where the exhaust gas is heated up by convection. A 94% of conversion efficiency is set for the passage from electrical to thermal power, following the measurements found in [220].

The EHC is connected to the 48V battery system. Therefore, the energy consumption is directly seen in the battery SOC and will impact the total fuel consumption. The numerical model includes all the electrical losses and the battery cell limits. It is important to note that the cases with EHC will have a dual effect:

- 1) CO and HC tailpipe emissions levels will decrease due to the high DOC temperature.

- 2) CO and HC engine-out emissions levels will increase due to the higher fuel consumption.

For the post-heating control strategy, the EHC operation was set to be on when the ICE is also running and the DOC wall temperature is below  $150^{\circ}\text{C}$ , as shown in Figure 4-25. The temperature to start the heating was chosen because it is the breaking point where the DOC efficiency is reduced considerably. To avoid on/off troubleshooting of the EHC, the EHC is off when the temperature increases to  $200^{\circ}\text{C}$ . The first study of stationary conditions is performed to understand the EHC operation under controlled conditions with less variables than in a driving cycle.

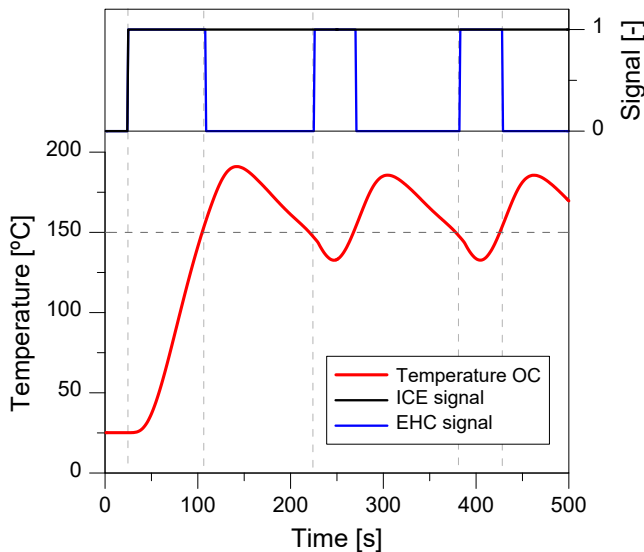


Figure 4-25. EHC post-heating scheme with the EHC signal in engine on-off signal and OC wall temperature.

The first step was to study the heat addition influence in the DOC wall temperature on the HC and CO conversion efficiency. Four cases ranging from 0 kW to 10 kW were tested in an engine operating condition selected as critical. The selected point is 1200 RPM, and 6 bar of BMEP, which is widely used in hybrid operation (see previous work [189]), and both the

amount of HC is large (4 g/kWh) and the engine-out temperature is low (210°C) for a medium load point.

Figure 4-26a shows the increase in the DOC wall temperature during the warm-up and the impact on the HC conversion (Figure 4-26b) with the heat addition. The impact on the final tailpipe HC emissions is shown in Figure 4-26c, with a decrease of 40% between the extreme cases. The derivate of the HC emissions after the DOC shows that 5 kW represents the optimum scenario for this operative condition. Therefore, it will be adopted as a proper heating rate in the subsequent EHC simulations. Even though other operating conditions can show a different optimum heat addition, the determination of each optimum is not the focus of the current manuscript.

As explained in the previous section, 36 ICE operating conditions (950 to 2200 RPM of engine speed and 2 to 18 bars of BMEP) in RCCI combustion mode were studied with the DOC starting from the ambient temperature. Figure 4-27 shows the light-off time (time required to achieve 50% of HC conversion in the DOC) for three ICE engine-out temperatures. Figure 4-27a shows the effect of steady-state temperature presented as an interpolated map of all the operating conditions. The light-off time only takes more than 20 seconds for low engine speed and load. At medium engine speed and load, where the RCCI low-temperature combustion uses the highest gasoline fraction, the DOC takes around 10 seconds to achieve the light-off temperature. For higher loads and engine speed, the time is highly reduced. Figure 4-27b and Figure 4-27c show the effect of the temperature decrease from the engine-out up to the OC inlet due to heat transfer. Since this temperature decrease depends on several factors such as pipe length and thermal insulation, among others, a parametric study was proposed using two different temperature levels: 25°C and 50°C less temperature, respectively. From the results, it is possible to observe that the light-off time highly increases at low engine speeds. The case of 950 RPM and 4 bar BMEP cannot achieve the light-off temperature. In the case of 50°C less than steady-state temperature, the central region of the map doubles the time to achieve the light-off temperature.

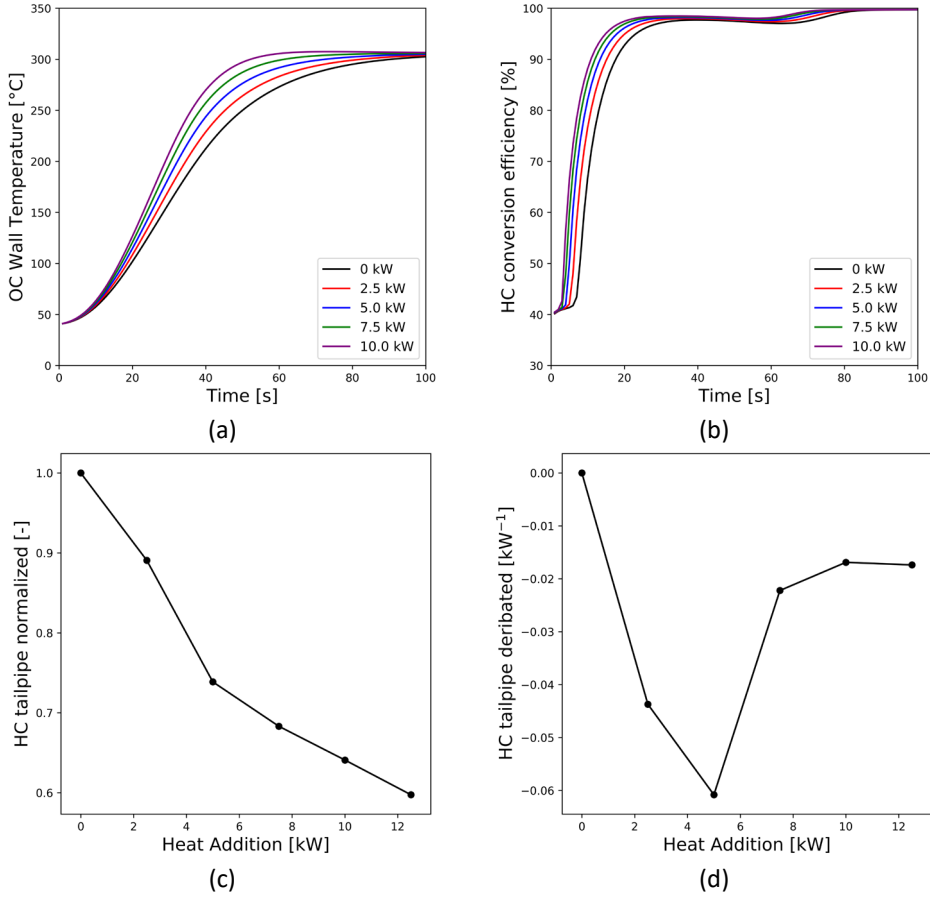


Figure 4-26. Heat addition effects at 1200 RPM and 6 bar BMEP on the HC tailpipe emissions normalized EUVI (a) and derivate HC tailpipe emissions normalized (b) with heat addition.



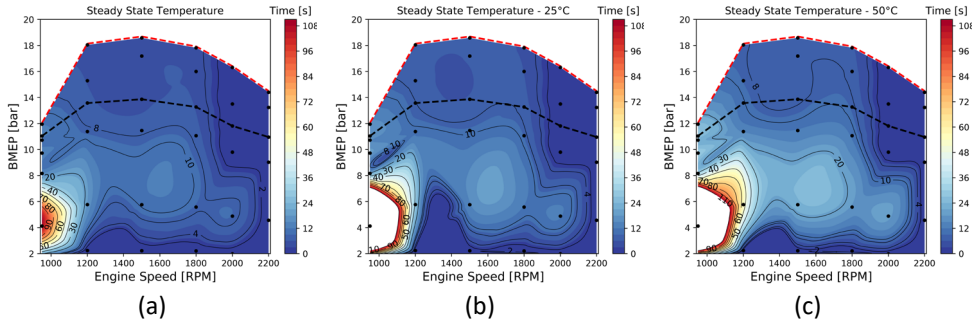


Figure 4-27. Light-off time map for three engine-out temperatures: steady state (a), steady-state minus 25°C, and (c) steady-state minus 50°C without EHC.

Adding a heater before the OC can be a potential solution to reduce the time mentioned above. Figure 4-28 shows the light-off time when 5 kW of heat is applied in the EHC for the three engine-out temperature conditions. The map is converted into blue using the same color scale as Figure 4-27. This means that the light-off temperature is achieved in all conditions and does not surpass the 10 seconds in any case.

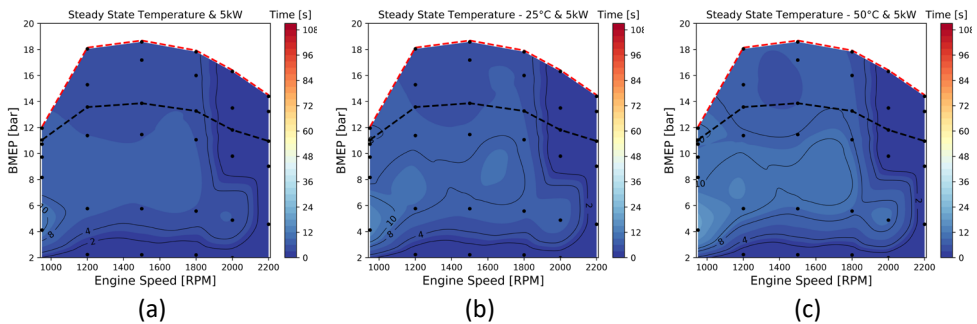


Figure 4-28. Light-off time map for three engine-out temperatures: steady state (a), steady-state minus 25°C, and (c) steady-state minus 50°C with 5 kW in the EHC.

Despite the light-off being an important condition for reference to compare with other works, due to the amount of HC and CO emitted in the

RCCI combustion, high conversion efficiencies (above 90%) need to be achieved. Figure 4-29 shows the DOC wall temperature and HC conversion efficiency at 1200 RPM and 6 bar BMEP. The EHC has a strong effect on the DOC temperature. The condition of cold engine-out gas temperature (steady-state less than 50°C) is faster than the steady-state condition without the heater. This is an essential point for the RCCI combustion during the first seconds of the engine warm-up. This is a critical aspect of the low-temperature combustion application since it combines low exhaust temperatures with excessive unburned product concentration.

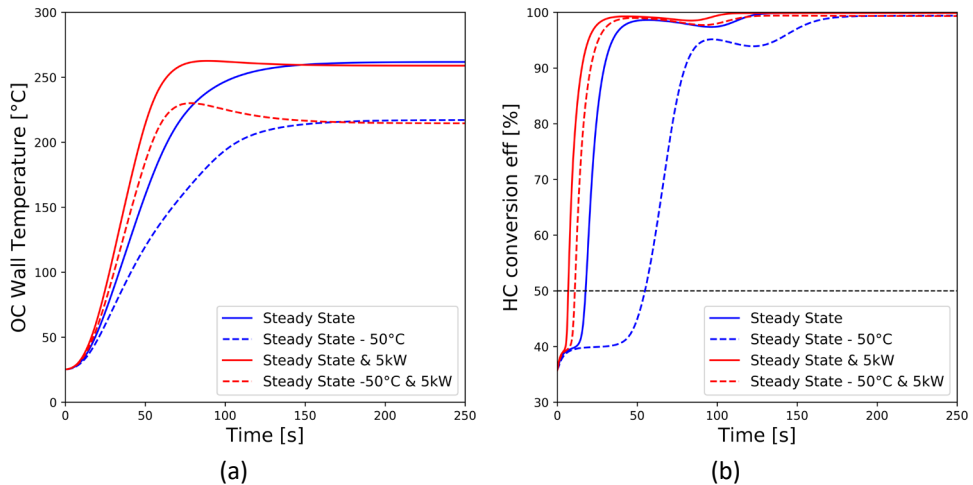


Figure 4-29. OC wall temperature (a) and HC conversion efficiency (b) for steady-state temperature and the steady-state temperature minus 50°C with and without EHC at 1200 RPM and 6 bar BMEP.

Engine steps load is proposed to understand the effect of ICE engine on/off in the DOC temperature to go further in the analysis. The steps are created and shown in Figure 4-30 based on the operative condition of 1200 RPM and 6 bar BMEP. The total energy delivered in the 1800 s is equal to the required brake output energy for a non-hybrid truck in homologation conditions (WHVC and 50% payload). It is important to note that the total

time of the engine in on mode is independent of the start and stops times ( $ICE_{on\_off\ times}$ ). However, the split is crucial for the DOC temperature.

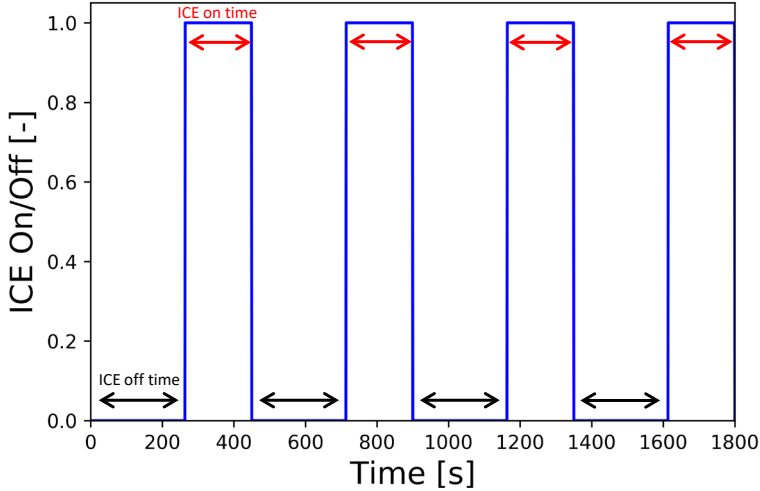


Figure 4-30. Diagram of the ICE starts (example of 4 starts) in the same steady-state point for the WHVC (1800 s).

The duration ( $ICE_{on\ time}$ ) on the driving cycle can be obtained following the equation:

$$ICE_{on\ time}[s] = \frac{E_{cycle} [kWh]}{Power_{ICE} [kW]} \frac{3600}{ICE_{on\_off\ times}[-]} \quad \text{Eq. 4.4}$$

$$ICE_{off\ time}[s] = \frac{Total\ Time_{cycle}[s]}{ICE_{on\_off\ times}[-]} - ICE_{on\ time}[s] \quad \text{Eq. 4.5}$$

with  $Power_{ICE}$  as the power delivered at the selected operative condition and the  $Total\ Time_{cycle}$  is 1800 seconds for the WHVC. In this study, a parametric analysis of the number of starts in the driving cycle ( $ICE_{on\_off\ times}$ ) is done. In addition, the use of the EHC was accomplished with 5 kW delivered if the engine is on and the DOC wall temperature is below 150°C. Figure 4-31a shows the effect of the engine starts on the HC

emissions. For both cases exist an intermediate case where the EUVI limits are not met.

In the case of CO (Figure 4-31b), the legislation limits are achieved for all the cases due to the lower CO emissions and more flexible requirements than HC. The behavior of this last pollutant can be explained by the DOC wall temperature when the engine is on. In spite of that, the average temperature of the DOC decreases with the number of starts (Figure 4-31c), and the standard deviation increases and then decreases with the number of starts as the HC emissions. This last parameter is crucial because the DOC conversion does not improve by increasing the temperature only. The main point is being above the light-of temperature ( $\approx 150^{\circ}\text{C}$ ) most of the time.

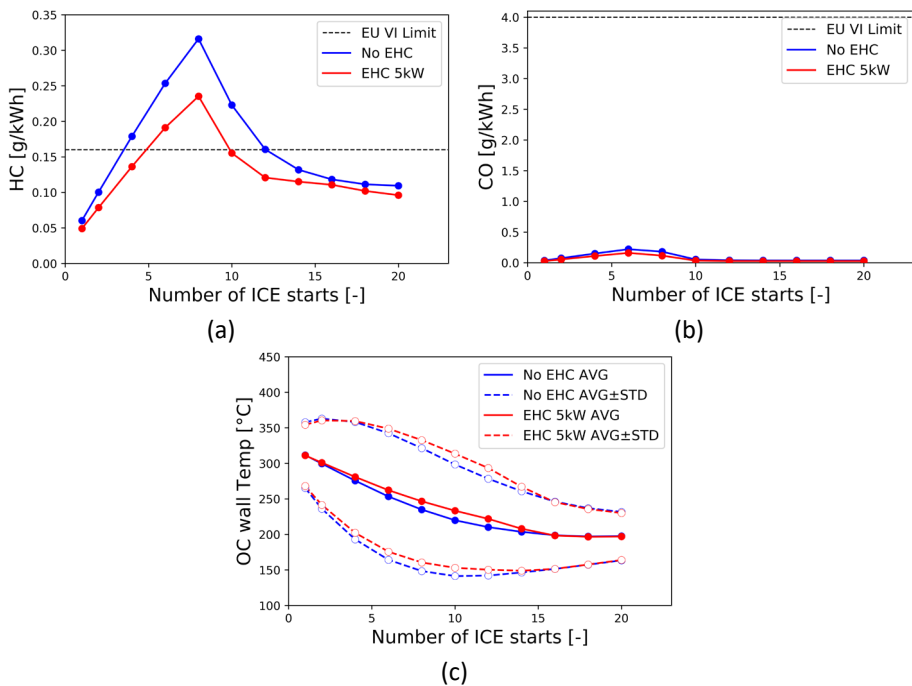


Figure 4-31. HC (a), CO (b) emissions after the OC and OC wall temperature (c) against the number of ICE starts.

Figure 4-32 shows a kernel density estimation approach to obtain insights into the temperature distribution during the DOC operation. In addition, the best fitting Gaussian curve was added to the graph, allowing to stress the effect of the number of ICE starts on the DOC wall temperature. It is interesting to see that increasing the ICE starts does not necessarily increase the OC operation. As seen in Figure 4-31, 1 start means that once the OC achieves the light-off operation, it remains at a very high temperature during most of the operation, assuring a good conversion efficiency. Nonetheless, for 8 ICE starts, the wall temperature consistently decreases as the ICE turn-off. This means that the temperature distribution is wider and also achieves lower values, impairing the conversion efficiency. In the case of 20 ICE starts, the average temperature is not too high, but it is concentrated above 150°C, which is a good temperature range for the OC operation.

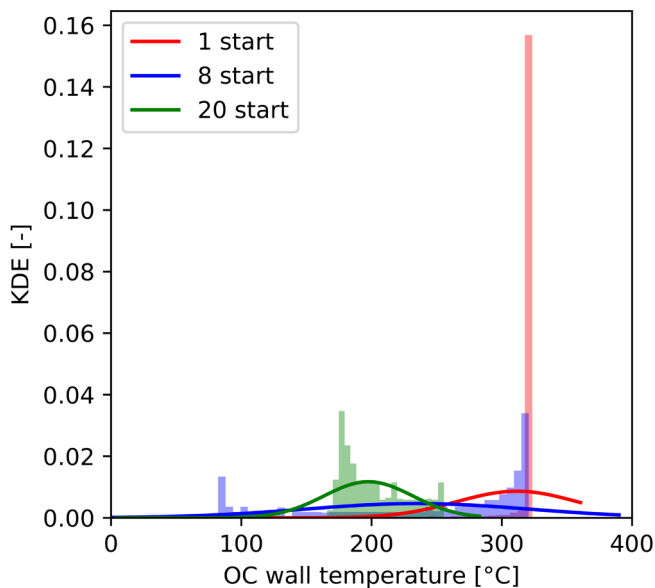


Figure 4-32. OC wall temperature distribution for the extreme ICE start cases and the worst case in terms of HC emissions.

## 4.4 e-Component CO<sub>2</sub> tailpipe emissions

A 0D vehicle numerical model is used to simulate different driving cycles to quantify the potential of using e-components in real truck operation conditions. It is important to note that this approach considers the battery losses due to charge and discharge events of the e-components. Therefore, a close scenario to real operation can be studied. The BAS is also included to simulate the start-stop and brake energy recovery along with the cycles. This component is fundamental for the re-charge of the battery. The BAS was sized at 30 hp (10% of the ICE power). The P0 hybrid equipped the DMDF engine set up with a maximum power of 280 hp. The non-hybrid CDC and non-hybrid DMDF also have the ICE with a maximum power of 280 hp (80% engine load of the full load map).

Three modes are proposed for the control of the P0 MHEV. A boost mode where the EM and ICE delivered power to the output shaft. A rechargeable model where the ICE delivers power to the output shaft and the EM to recharge the 48V battery. Furthermore, a starter mode where the EM propels the truck to move at low vehicle speed and moves the engine to 700 RPM to turn it on. All these modes are controlled by an RBC strategy where the primary inputs are driver power demand, vehicle speed, and SOC of the battery.

A preliminary analysis is done by considering the forces applied in the wheels depending on the gear ratio to understand the performance of the new MHEV powertrain. The calculation is performed in Matlab® by adding the ICE and EM maximum torque map and the transmission and final drive ratios. Figure 4-33 shows that in boost mode, the P0 has an advantage in wheel power. For example, it is possible to climb >25% of road grade with 100% payload at gear one.

The pure EV mode or starter mode allows propelling the vehicle to 30 km/h on a flat road. This is ideal for inside buildings or starts/stop events. If EM is not used, the P0 truck has the same power output as the non-hybrid. This allows flexibility to downsize the battery package and to charge when convenient.

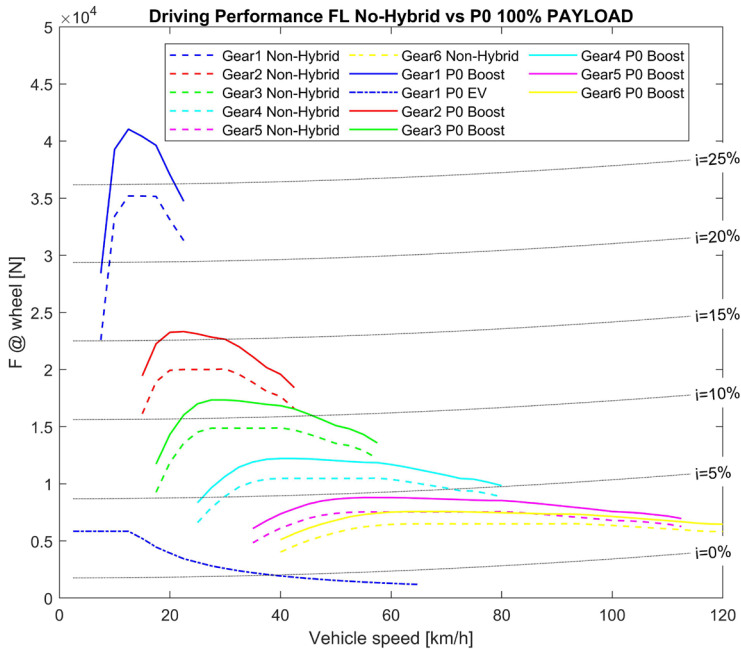


Figure 4-33. P0 performance curves for boost and EV mode at different transmission gear ratios. The Non-Hybrid is included for comparison.

After the force analysis, the driving cycles are studied with the GT-Suite 0D vehicle model (Figure 4-34). The real BSFC engine map and the maps for the e-components are used to simulate the battery's power requirements to simulate the engine operation's behavior with the 48 V e-components system.

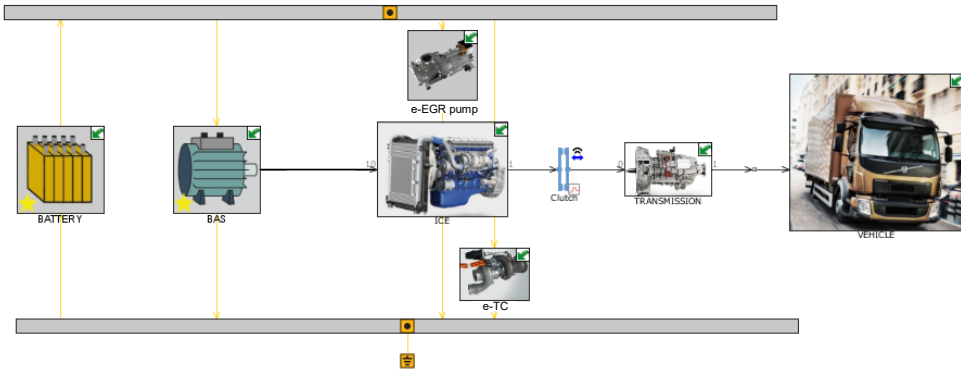


Figure 4-34. 0D vehicle model for 48V mild hybrid P0 truck with the belt alternator starter (BAS), e-TC, and e-EGR pump.

A genetic algorithm was used to optimize the powertrain RBC rules and hardware (battery size) for both cases: 1) P0 MHEV without e-components (HP & LP EGR) and 2) P0 MHEV with e-components (HP EGR line with e-turbo and e-EGR pump).

A Genetic Algorithm is used to optimize the control parameters and hardware. The target for the genetic algorithm (Genetic Algorithm NSGA-III [221]) is to minimize fuel consumption while reaching the same battery SOC at the end of the driving cycle as the initial SOC. The space over which the factors are varied is called the design space, shown in Table 4-1. The NSGA-III five key inputs required are the population size ( $P_s=40$ ), crossover rate ( $C_r=1$ ), crossover rate distribution index ( $C_{rdi}=15$ ), mutation rate distribution index ( $M_{ri}=20$ ) and number of generations to run ( $N_g=20$ ). The optimizer will stop after completing all designs according to the number of generations. This optimizer is applied in a transient condition previously set. A sensitivity analysis was also included to analyze the effect of the control parameters on the final fuel consumption and battery state of charge. The relative sensitivity values are calculated by dividing the absolute value of each regression coefficient by the sum of the absolute value of all regression coefficients. The linear regression equation would be Equation 3.1 and the



sensitivity Equation 3.2. A summary of the RBC strategy is presented in Figure 4-35.

$$y = a_0 + a_1x_1 + a_2x_2 + \dots + a_nx_n \quad (3.1)$$

$$S_i = \frac{|a_n|}{\sum|a_i|} = \text{Estimated Relative Sensitivity [-]} \quad (3.2)$$

with  $x_1$  represent standardized factors,  $a_i$  represent standardized regression coefficients,  $y$  represents the standardized response and  $S_i$  the sensitivity values.

Table 4-1. GA optimization parameters for P0 MHEV.

Parameter	Type of parameters	Range Tested
SOC Torque Assist	Control Battery pack	0.4-0.58
SOC Low Threshold	Control Battery pack	0.4-0.58
Speed Load Split	Control Electric machine	5-90 km/h
Coefficient shift	Control Transmission	0.6-1
Battery Size	Hardware	5 - 80 kWh

The optimization was performed under homologation conditions (WHVC and 50% payload), and the target was to minimize CO<sub>2</sub> tailpipe emissions. Figure 4-36 shows the CO<sub>2</sub> reduction with respect to CDC non-hybrid for both cases. The optimizer was able to reduce from positive values (higher CO<sub>2</sub> than CDC) for initial cases to around 8% of CO<sub>2</sub> reduction. The sensitive analysis shows that the most influential parameters are the shift coefficient and speed to split 50%/50% between ICE and EM (Figure 4-37). The battery size graph in Figure 4-38 shows a low influence on the CO<sub>2</sub> emissions with an optimum value of around 3 kWh. The e-component case needs a larger battery size than the case without an e-EGR pump and e-turbo due to the less battery use. The payload condition under study shows better performance for the HP&LP EGR loop than the e-components case due to the larger use of medium load zones of the DMDF map.

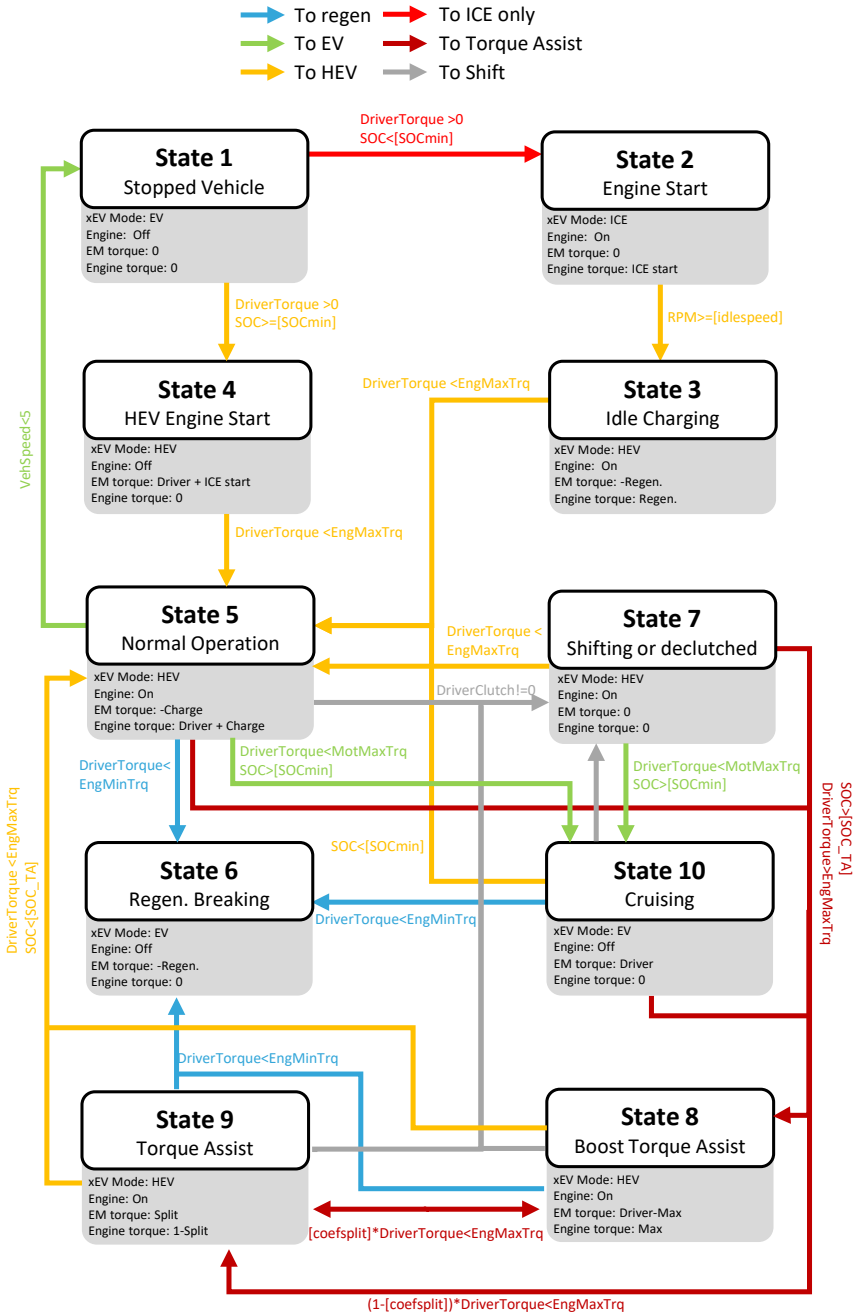


Figure 4-35. P0 Hybrid scheme of Rule-Based Controller strategy.

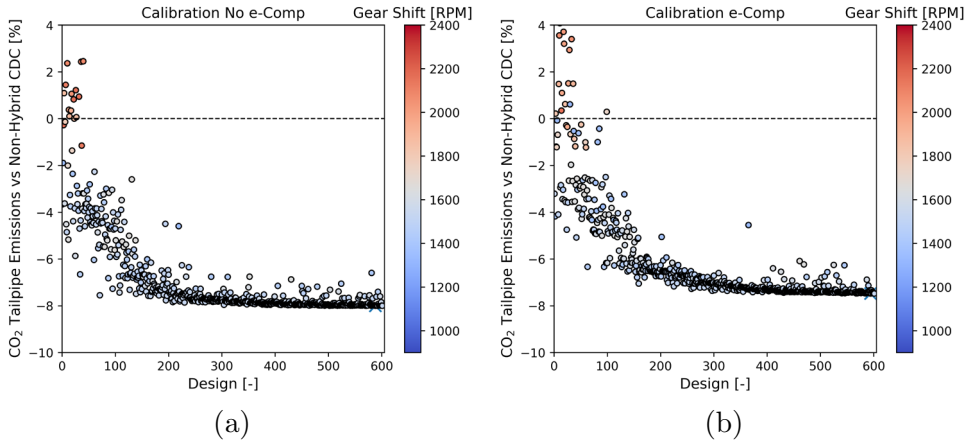


Figure 4-36. Optimization of the P0 MHEV without e-components (a) and with components (b) in terms of CO<sub>2</sub> reduction versus CDC non-hybrid.

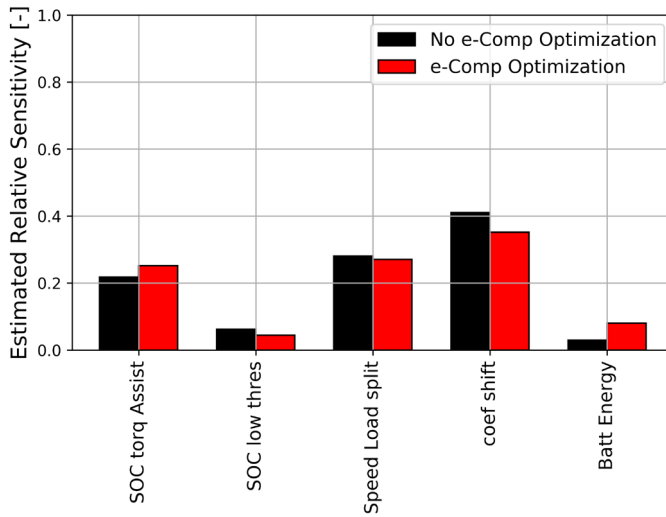


Figure 4-37. Relative sensitivity of the parameters optimized for the P0 MHEV DMDF truck.

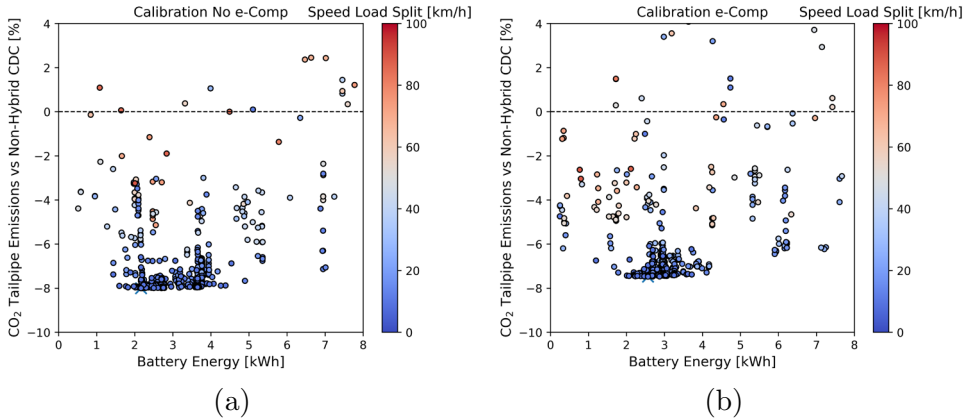


Figure 4-38. Battery size effect on the CO<sub>2</sub> reduction versus CDC non-hybrid for P0 MHEV without e-components (a) and with components (b).

The optimum configuration instantaneous values are presented in Figure 4-39. The two powertrains' engine speed-time and torque-time profiles were analyzed (non-hybrid CDC and mild hybrid P0 DMDF with e-components). The non-hybrid DMDF and P0 DMDF HP+LP EGR powertrains are not included for similarities with the previous cases. As it can be seen, the engine speed is higher for the non-hybrid CDC powertrain due to the larger gear shift strategy.

To achieve the same total power at the wheels, the P0 DMDF with e-components powertrain must deliver higher engine torque (Figure 4-39). Figure 4-40a shows the BAS operation, with positive values representing power delivery to the engine and negative values meaning energy regeneration (or battery charging) from the engine. The operation has pulsed behavior with power peaks up to 30 hp (maximum BAS power) and -30 hp in braking conditions. Figure 4-40b depicts the system voltage around 48v and the e-TC and EGR-pump power consumption. Both e-components have energy consumption from the battery (negative power values), with the e-TC having greater consumption than the e-EGR (as anticipated in Figure 4-23). For

both cases, the peak power consumption is lower than that of the BAS, so the e-components do not significantly influence the battery size and electric components selections.

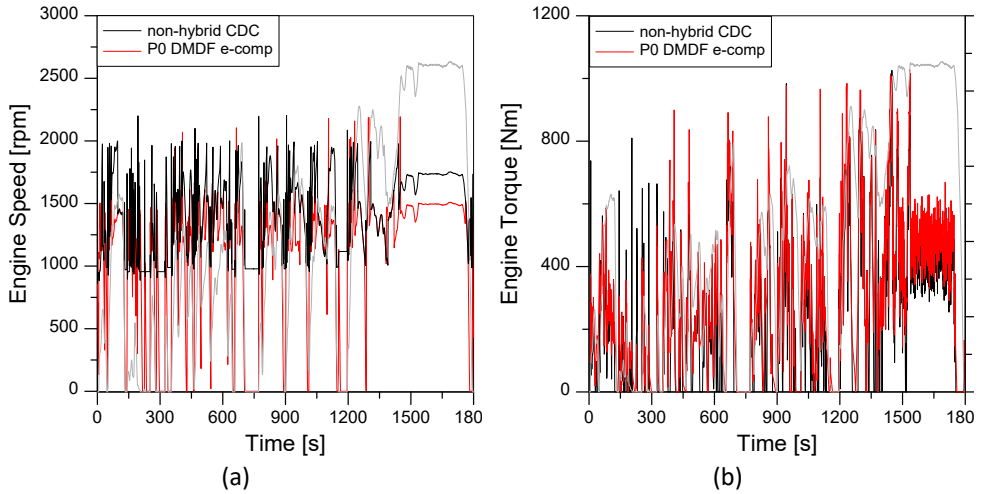


Figure 4-39. Engine speed (a) and engine torque (b) for the non-hybrid CDC and the P0 DMDF with e-components cases in homologation conditions. The WHVC driving cycle speed profile is added in the background for reference.

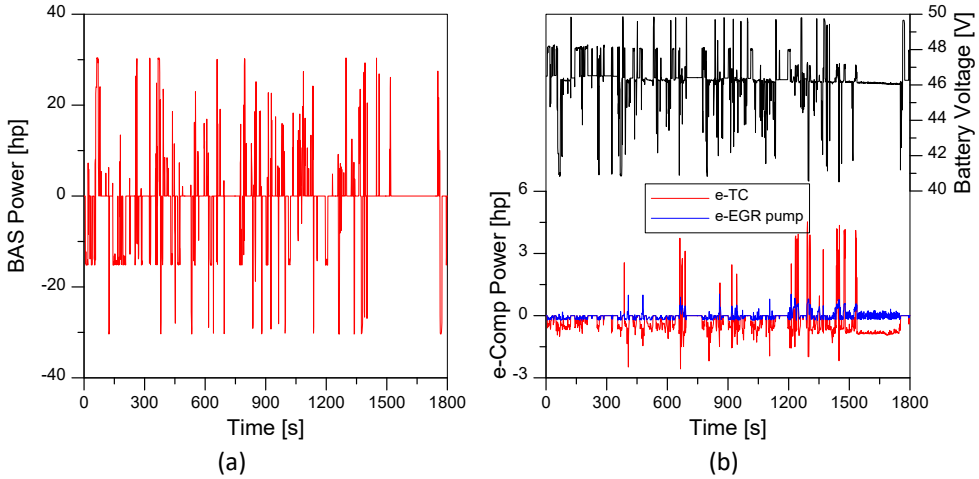


Figure 4-40. Belt assist starter power (a) and e-components voltage and power (b) for the P0 DMDF with the e-components case in homologation conditions.

The cumulative fuel consumption and NO<sub>x</sub> emissions for all the powertrains considered in this work are depicted in Figure 4-41. Figure 4-41a shows that the DMDF P0 with and without e-components achieves similar final fuel consumption, with a considerable reduction of the fuel consumption in the urban part of the WHVC as compared to the other two vehicles architectures. In the rural and highway phases, no significant differences are found in fuel consumption, but they allow to reduce the total fuel consumption with savings of CO<sub>2</sub> emissions by around 5% concerning the CDC non-hybrid case at the end of the cycle. The cumulative engine-out NO<sub>x</sub> emissions (Figure 4-41b) are strongly reduced due to the DMDF operation. The mild-hybrid and non-hybrid DMDF powertrains reduce NO<sub>x</sub> emissions by more than 90% for the CDC. These results estimate that the SCR-urea ATS would not be necessary in the DMDF cases.

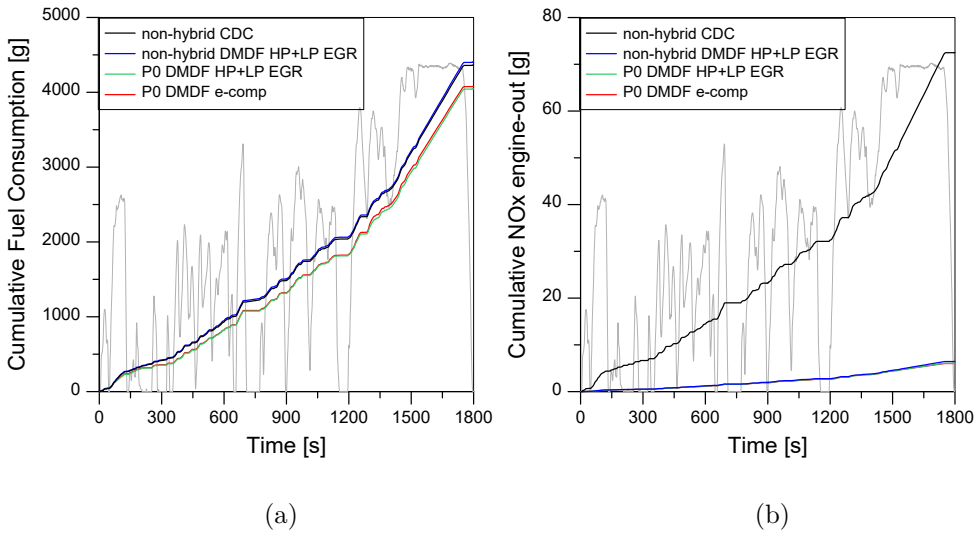


Figure 4-41. Cumulative fuel consumption (a) and cumulative NO<sub>x</sub> engine-out emissions for the four cases studied in homologation conditions. The WHVC driving cycle speed profile is added in the background for reference.

The global results for the two trucks in all the driving conditions are presented in Figure 4-42. The results show that the e-components do not improve the truck's fuel economy with respect to the DMDF HP+LP EGR in a P0 architecture, mainly when employed at the medium and high payload. As the FL 18-ton truck uses the de-rated map, 100% engine load zone Figure 4-23, that has up to 4 g/kWh of fuel consumption improvement, it is not used. Therefore, the medium zone (150 hp and 1600 RPM) is mostly used for 50% and 100% payload. In the case of the empty truck, the low load engine map zone is used, in which the fuel consumption is improved up to 30 g/kWh.

Despite not improving the DMDF HP&LP EGR case, using e-components allows improvements concerning the CDC by the P0 implementation. In homologation conditions (WHVC and 50% payload) achieves 7.3% of fuel improvement versus CDC in the conventional

powertrain. This means that similar CO<sub>2</sub> reductions can be achieved, allowing the proposed technology to remove the LP EGR line, avoid the use of DPF and potentially improve the packaging and transient behaviors.

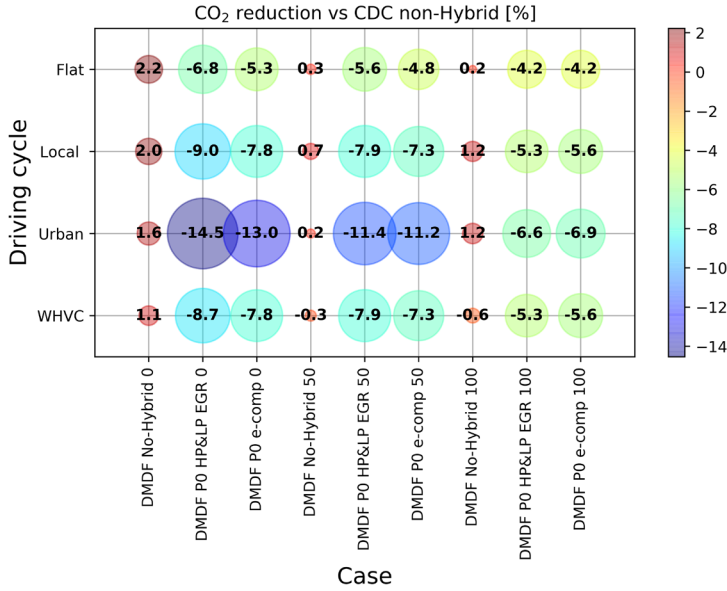


Figure 4-42. Summary of the FL truck results in total fuel consumption difference against the non-hybrid CDC along with the WHVC, Urban, Local and Flat cycles at 0%, 50%, and 100% payloads.

### 4.5 Driving cycle assessment with DOC and e-DOC

After the detailed analysis with the ICE working in steady-state conditions and the DOC warm-up behavior, the next step is studying real vehicle operation. The P0 hybrid truck operating in the homologation and real driving cycles with different payloads is modeled. For brevity of the manuscript, the HP&LP EGR engine case is studied with the optimum setup (RBC rules and battery size) for a 50% payload. One case is set without heating and the other with heating of 5kW to see the effect of the EHC.



Figure 4-43a shows the engine on-off states when 50% of a payload is applied in the case without EHC. This case represents the optimum calibrated case to fulfill the EUVI NO<sub>x</sub> and soot emissions at engine-out conditions with the lowest CO<sub>2</sub> emissions. This case is extracted from a previous work of the research group [189]. The number of starts for the optimum was 15 starts, between the range of the steady-state study (1 to 20 starts). The optimization does not consider the HC and CO emissions. Therefore, the number of starts was optimized to achieve the minimum fuel consumption/CO<sub>2</sub> emissions. It is interesting to remark that adding the chemistry simulation in the catalyst has significantly increased the computational time from 0.1 to 4 times the real-time.

Figure 4-43b shows the HC emissions before and after the OC. The first 600 s are responsible for a large amount of HC emissions. This is a direct consequence of the low DOC temperature, depicted in Figure 4-44. The amount of ICE-off time due to the urban phase makes the case without the heater to produce 70% of the total HC emissions. The HC emissions are strongly reduced when the EHC is added with 5kW under the same calibration of the case without EHC. It is possible to achieve the EUVI legislation due to the fast increase in the OC wall temperature. In both cases, the EUVI CO targets can be easily achieved. Therefore, it can be concluded that one of the main limits to implementing the RCCI combustion with hybrid architectures is the HC emissions.

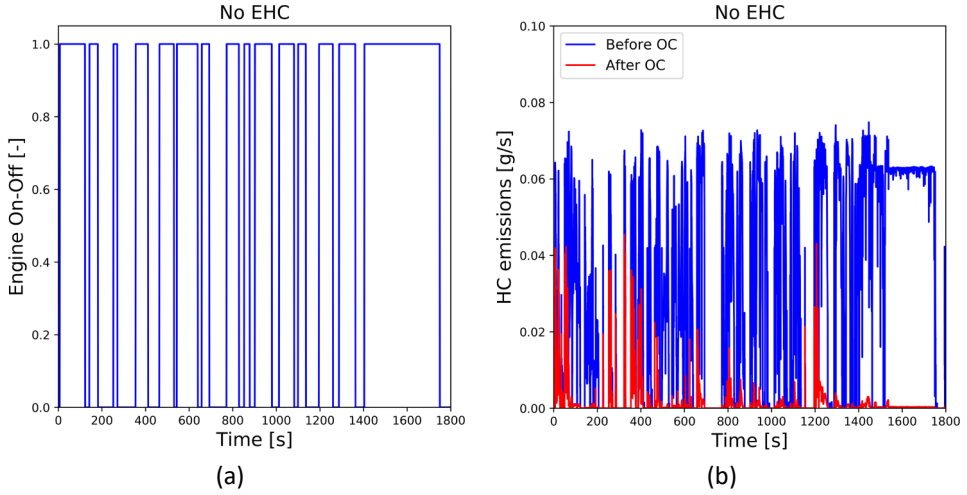


Figure 4-43. Engine on-off (a) and HC emissions before/after the OC (b) for the WHVC with 50% payload in an RCCI P0 hybrid Truck without EHC.

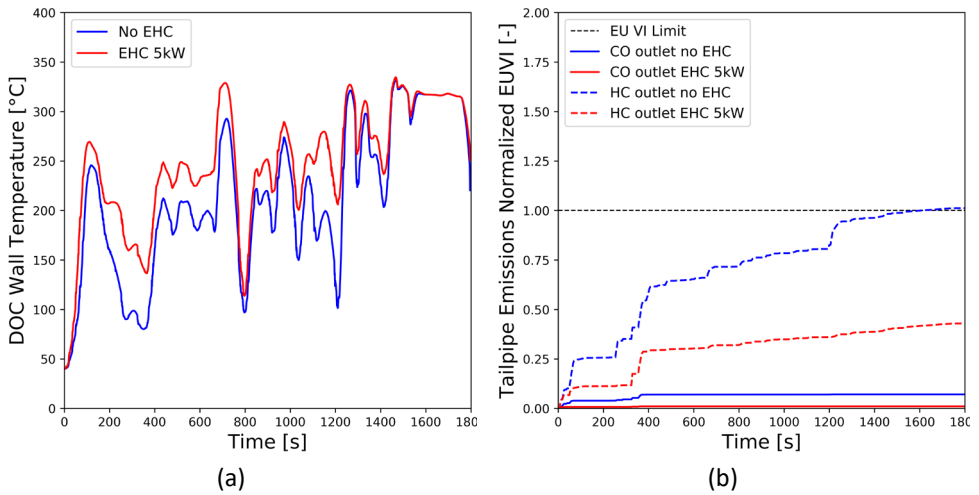
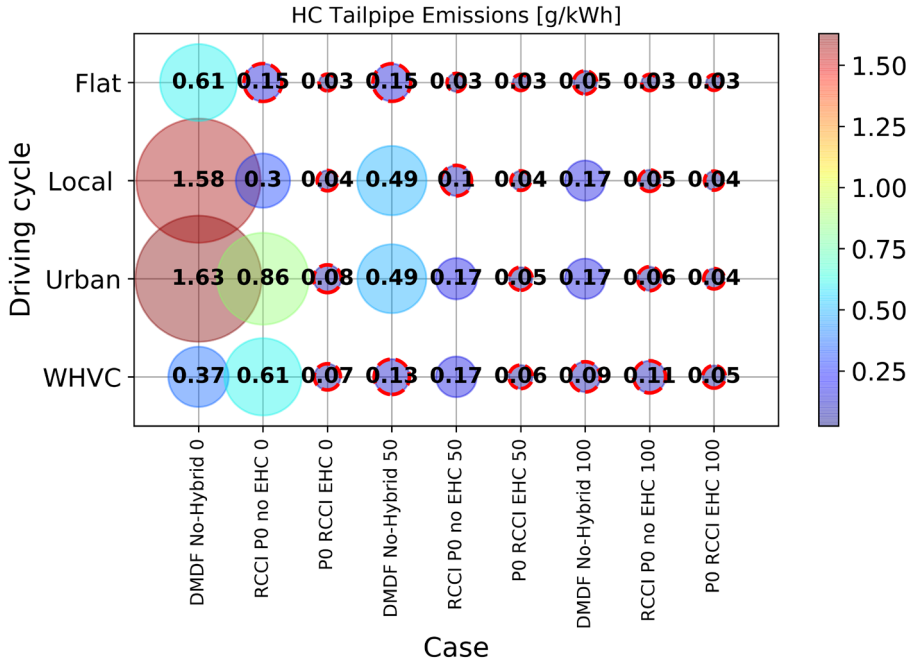


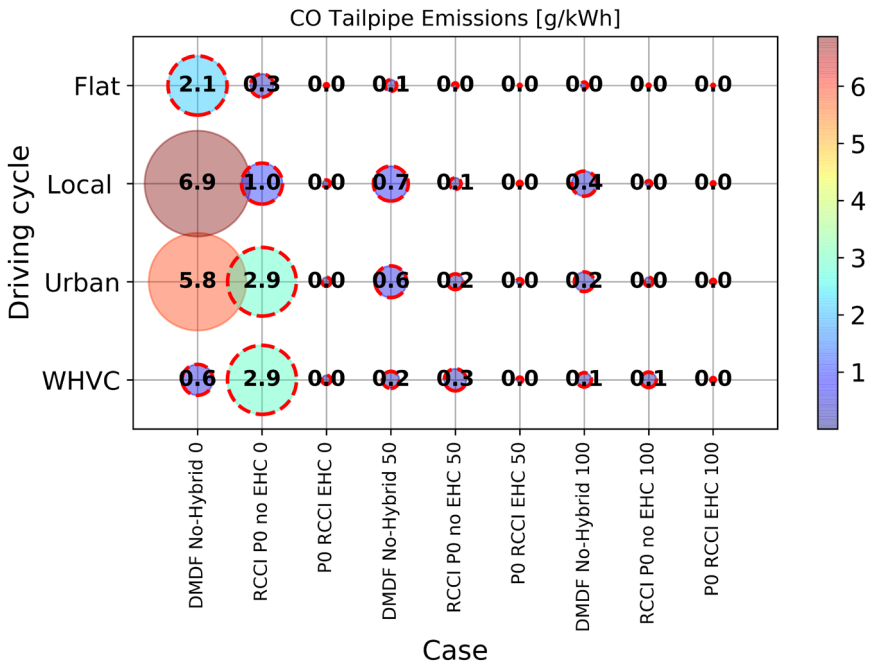
Figure 4-44. OC wall temperature (a) and HC and CO normalized emissions with respect to EUVI (b) for the WHVC with 50% payload in an RCCI P0 hybrid truck without and with the EHC.

A summary of all cases is shown in Figure 4-45. The HC and CO emissions are presented in absolute values and marked with a dashed ball when achieving EUVI emissions ( $\text{CO} = 4 \text{ g/kWh}$  and  $\text{HC} = 0.16 \text{ g/kWh}$ ). It is possible to observe a great improvement concerning DMDF non-hybrid due to the hybrid powertrain calibration. However, the use of the EHC has an impact on the final fuel consumption/ $\text{CO}_2$  emissions. Figure 4-45 shows that, on average, the heater with 5 kW increases the  $\text{CO}_2$  emissions by 2.7% for the case without the EHC. The advantage of the EHC is that it allows achieving the EUVI limits for all the emissions ( $\text{NO}_x$ , soot, CO, and HC) for the homologation case while still providing a  $\text{CO}_2$  reduction of 4.8%. It is important to note that the empty truck conditions (0% payload) are the worst scenario due to the low energy requirement. A previous study [164] showed that the non-hybrid version does not achieve the EUVI HC limits under empty cargo due to the operation only at low BMEP conditions. The hybridization enables improvements in this scenario concerning the non-hybrid case since it allows to use of the ICE at high engine loads. However, without the EHC, the EUVI limit cannot be achieved.

The 0% of the payload is a challenging condition for EUVI achievement. The Flat case that increases the cycle time and has a large phase of highway allows for achieving EUVI with the EHC. Using the heater with 5 kW of power allows for meeting EUVI CO and HC in all conditions. The  $\text{CO}_2$  emissions for the current CDC non-hybrid commercial truck show that the urban case is the best scenario for the hybrid powertrain. The low payload also allows significant improvements in all cycles. The use of EHC penalizes  $\text{CO}_2$  emissions by an average of 2.7%. For the four cycles and three payloads, the average gains for the hybrid operation were 7.8% without EHC and 5.1% for the case of EHC. The worst-case scenario is the empty truck and urban due to the elevated start/stop events. Therefore, the DOC is most of the time below the light-off temperature. For reference, the non-hybrid DMDF increases the  $\text{CO}_2$  by 0.8% with respect to the diesel case.



(a)



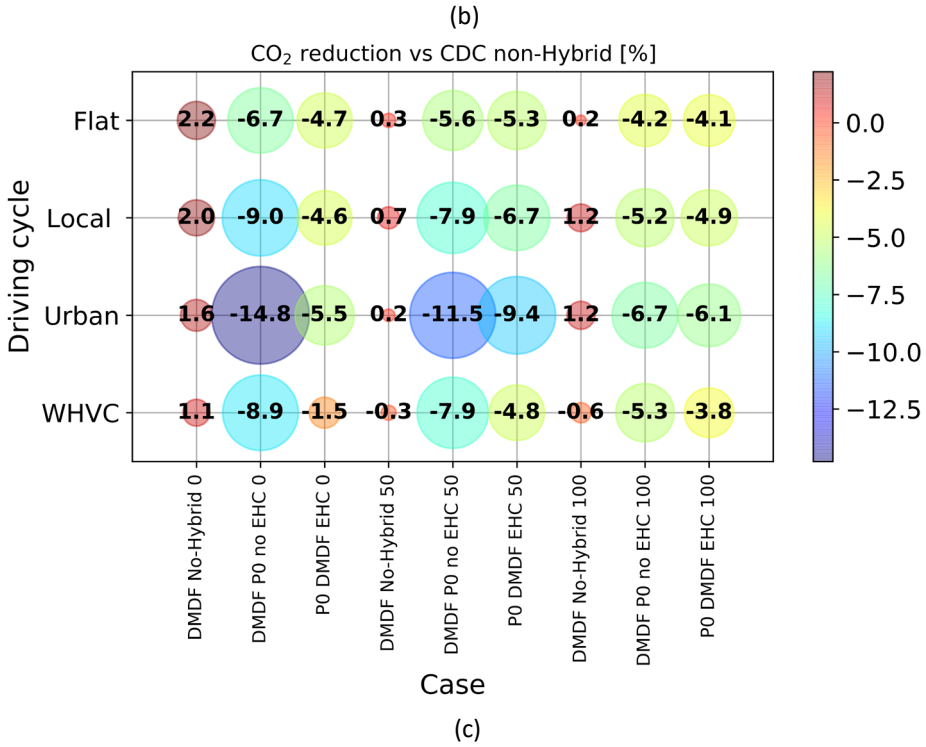


Figure 4-45. HC tailpipe emissions (a), CO tailpipe emissions (b), and CO<sub>2</sub> tailpipe reduction compared with CDC non-hybrid for DMDF non-hybrid, P0 hybrid with/without EHC.

Studying the effect of the EHC on fuel consumption (CO<sub>2</sub> emissions) is an important aspect of meeting EUVI HC and CO emissions but not losing the benefit of improving powertrain efficiency. A sweep of EHC power was done in homologation conditions. Figure 4-46 shows that with 0.5 kW is already possible to achieve EUVI limits in both pollutants with only a loss of 0.3 points in CO<sub>2</sub> with respect to the case without EHC. The increase of EHC power allows for almost 70% of HC reduction and 95% of CO reduction, but as seen in Figure 4-45, the loss in CO<sub>2</sub> is 3% points. The CO<sub>2</sub> reduction shows a flat trend between 2 and 4 kW, with a reduction of CO and HC almost linear. Therefore, 4 kW is a better choice than 5 kW as in the previous

study because it allows for greatly reduced CO and HC while with a CO<sub>2</sub> reduction with respect to CDC of 5.8% (only 1.9% points below P0 without EHC). It is important to note that as an RBC is used, the flat trend in CO<sub>2</sub> reduction can be explained as a balance of EHC starts, energy powertrain management, and available energy in the battery.

The right selection of power is a matter of homologation rules and manufacturer choice. This sub-section shows the effect of using an EHC in an MHEV powertrain and the benefits of different power heating in the ATS.

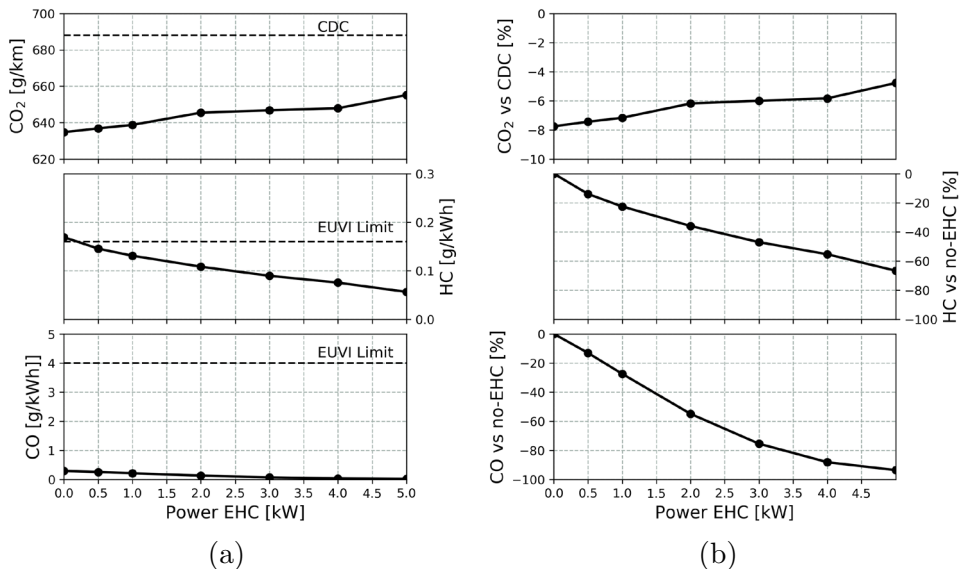


Figure 4-46. EHC power sweep results in terms of absolute values (a) and relative values (b) for CO<sub>2</sub>, HC, and CO tailpipe emissions.

## 4.6 Conclusions

Numerical 1D engine simulations evaluated electric turbo compounding and electric EGR pump. The 48 V electric components were used to achieve the same air management targets as a high-pressure/low-pressure system in

a low-temperature combustion mode. The only use of HP EGR was proposed to reduce the engine packaging and improve the transient behavior. The results show that a single path configuration does not allow to achieve all the calibration points of the engine and increases the fuel consumption for the successful cases. The introduction of the e-components allows working in an extended range of VGT rack positions. The optimum case was with both e-components working together. All the calibration map studied with both e-components shows improvements in fuel consumption in extreme cases: low engine rotational speed, low engine load, or maximum engine load. All the cases where energy recovery can be made and the baseline case has difficulties for the good operation.

The e-component results were used to feed a P0 48V MHEV truck and test in twelve driving scenarios. The new e-component calibration (P0 DMDF e-comp) was compared against the non-hybrid CDC, non-hybrid DMDF HP&LP EGR, and P0 DMDF HP&LP EGR. The results show that P0 allows advantages over the non-hybrid architecture between 4% (high payload and large highway phases) and 14% (low payload and large urban phases). The e-components show improvements with respect to the non-hybrid DMDF HP&LP EGR in low payload conditions. Overall, the P0 MHEV in both EGR configurations allows 7.5% of CO<sub>2</sub> tailpipe improvements. Despite that the system is not enough to achieve the 2025 target (15% CO<sub>2</sub> reduction), it allows large CO<sub>2</sub> savings by using a small electric machine (30 kW) and battery size (2 kWh).

A deep study of the oxidation catalyst behavior in a hybrid RCCI Medium-Duty truck was performed. The addition of an electrical heater at the inlet of the DOC was included in the analysis. The experimental validation demonstrates that the 1D DOC numerical model can accurately predict the HC and CO conversion under stationary and transient conditions. In addition, the stationary ICE analysis allows selecting the best EHC heat addition (5 kW). In the driving cycle assessment of the P0 MHEV hybrid architecture, the calibration without a heater shows that only with high payload and not urban cycles it is possible to achieve HC EUVI limits. When

the EHC is added, all cases can achieve EU VI emission in terms of CO and HC.



# Chapter 5

## Full hybridization dual-fuel concept for achieving 2025 emission targets

### **Content**

---

5.1 Introduction.....	246
5.2 Parallel (P2) hybrid optimization .....	247
5.2.1. Methodology .....	249
5.2.2. Results.....	257
5.3 Series hybrid optimization .....	262
5.3.1. Methodology .....	264
5.3.2. Results.....	272
5.4 Power split hybrid optimization.....	277
5.4.1. Methodology .....	279
5.4.2. Results.....	292
5.5 Comparison between architectures.....	297
5.6 DOC behavior in the full hybrid truck.....	305
5.7 Conclusions.....	311

## 5.1 Introduction

Full Hybrid Electric Vehicles (HEVs) were studied for more than 15 years in passenger car applications, and they are currently a mature technology being commercially available on a large scale. This type of powertrain electrification does not need a plug-in from an external source because it bases the control strategy on battery charge sustaining. This means that the initial battery state of charge ( $\text{SOC}_{\text{ini}}$ ) is similar to the final state of charge ( $\text{SOC}_{\text{end}}$ ). FHEV can be distinguished on different powertrain architectures as series, parallel, and series-parallel (also called power split). Despite the significant improvements in recent years in terms of efficiency and durability, the information about their advantage and drawbacks on truck platforms is minimal. Moreover, almost all the literature's works are focused on fuel economy and  $\text{CO}_2$  reduction without analyzing other pollutant emissions.

This chapter uses a dual-mode dual-fuel (DMDF) combustion mode to evaluate a full hybrid electric truck platform (18 tons of payload) with parallel P2, series, and power-split hybrid architectures. Chapter 4 has demonstrated the benefits of a mild hybridization in a P0. This chapter goes a step forward in terms of electrification level by analyzing several powertrains that have the advantage of pure electric mode and hybrid mode without the requirements of external charging. Specifically, parallel P2 (pre-transmission) is modeled. For brevity of the Thesis, the P3 and P4 are not studied because they will allow similar results to the P2.

Moreover, the Series hybrid will be studied in this chapter because of its particular operation that allows the engine's operation in steady-state points due to the independence of the wheels with the engine operating conditions. Lastly, the power split is also investigated due to the excellent success of Toyota's Light-Duty concepts. This architecture combines the benefits of both P2 and Series by a sophisticated control strategy with two EM and a novel transmission system.

In this sense, this chapter aims to evaluate the potential of combining the two technologies, LTC and full hybridization, to achieve the 2025 European targets.

## 5.2 Parallel (P2) hybrid optimization

Figure 5-1 shows the proposed P2 dual-mode dual-fuel hybrid truck concept scheme. One motor/generator (EM) is added between the ICE and the OEM transmission. Two clutches, one before and after the EM, are added to allow the pure electric mode (only the EM) and the boost mode ( $EM_{\text{tractive}}+ICE$ ). The transmission is the OEM model (six-gear automatic transmission) with the same gear ratios and the differential ratio.

As it is a full hybrid, the state of charge in the battery need to be maintained. Therefore, a charge mode ( $EM_{\text{charging}}+ICE$ ) is added in the control strategy where both clutches are closed. The battery module with 600V and customized capacity (total energy storage) is included in Figure 5-1. The battery is the third energy storage system in the truck. In this chapter, Diesel and Gasoline are the other two HR and LR fuel tanks, respectively.

The operation of a parallel P2 hybrid allows driving in pure electric mode when clutch one is disengaged and clutch two is engaged (see Figure 5-1). The P2 concept allows multiplying the EM speed in the transmission, which is different from the P3 or P4 architecture (wheel speed is only multiplied by the final gear ratio). Therefore, the P2 has the flexibility to operate in low speed and high payload or the contrary, by a suitable configuration of the gearing strategy. The concept can also work in several hybrid configurations such as boost mode, charging mode, or only ICE mode. In the last case, it operates similarly to a non-hybrid truck.

Unlike MHEV, the FHEV allows to downsize or de-rate the engine due to the high electric power of the system. The battery voltage of 600V enables the use of a large electric motor. From Chapter 3, it was possible to observe that the MD8 Volvo engine calibrated in DMDF can operate in pure RCCI

until 210 hp. This region (0-210 hp) achieves EUVI NO<sub>x</sub> and soot, which allows removing the SCR-Urea system and DPF. This is one of the main goals of the LTC concept. Therefore, to achieve similar performance to the OEM CDC MD8 powertrain, a 70 hp continuous power EM is included. The ICE with 210 hp and EM with 70 hp connected in the same drive shaft (separated by a clutch) will achieve the same maximum power output as the baseline (CDC non-hybrid with 280 hp).

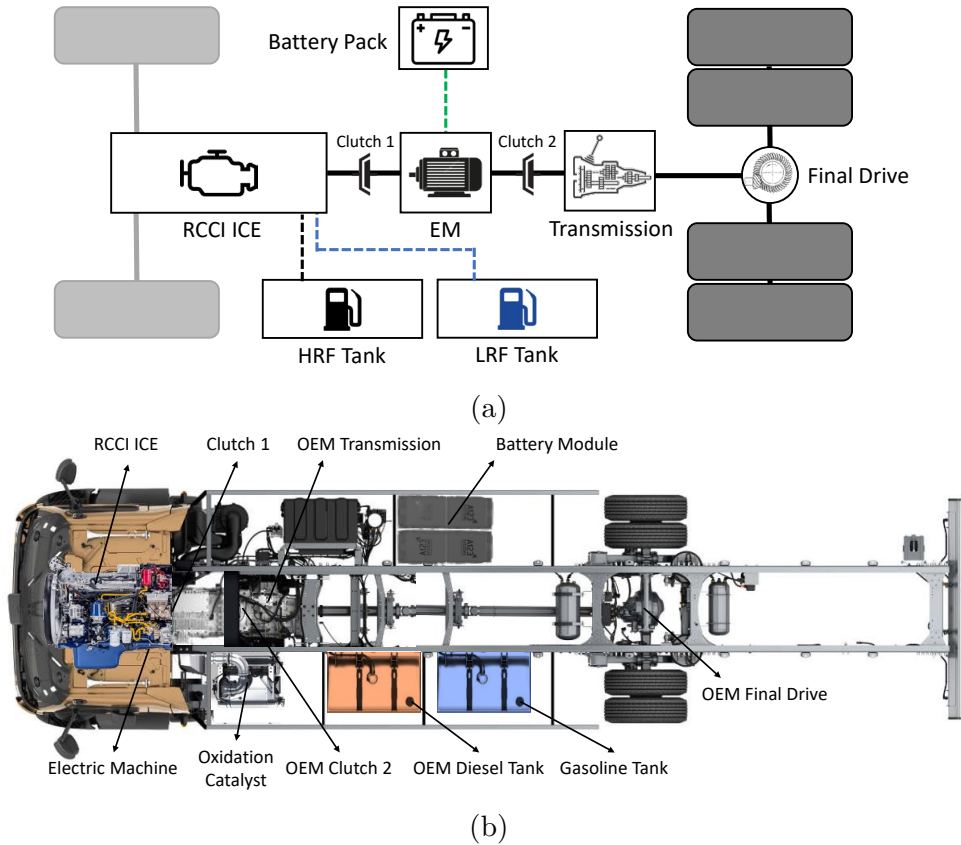


Figure 5-1. P2 Hybrid architecture layout with main components in an FL-18-tons truck. The architecture (a) and component layout scheme in vehicle chassis (b).

### 5.2.1. Methodology

The maximum power of the components in the wheel is evaluated. An in-house Matlab® code is developed to obtain the wheel forces by the propulsion system to compare the performance of a hybrid powertrain with the conventional non-hybrid. The curve of maximum torque versus rotational speed of the components (ICE and EM) is multiplied by the transmission devices. The static losses are added to the calculation. Therefore, this allows understanding if the ICE+EM selection has a similar performance on the wheel in the OEM case (non-hybrid CDC). The HTM-3500 performance curve and efficiency for the electric machine are taken and downsized from 200 kW to 52 kW by scaling with the approach shown in Chapter 3. This electric machine is suitable for P2 due to the low-speed rotation regime (0-3500 RPM) and high constant torque until 1500 RPM. It is important to note that the EM and ICE have the same rotational speed ( $\omega_{EM} = \omega_{ICE}$ ) if clutch one is closed. In other cases  $\omega_{ICE} = 0$ . Therefore, the regular EM operation will be below 2200 RPM (maximum of the ICE). The following Equation 5.1 to equation 5.5 are used to calculate the wheel force ( $F_{Wheels,tract}$ ) depending on the transmission gear ratio ( $k_{i,Transm}$ ).

$$P_{Wheels,tract} = (P_{EM} + P_{ICE}) * \eta_{Dif} * \eta_{Trans} \quad (5.1)$$

$$T_{Wheels,tract} = \frac{(T_{EM} + T_{ICE}) * \omega_{EM}}{\omega_{Wheels}} * \eta_{Dif} * \eta_{Trans} \quad (5.2)$$

$$F_{Wheels,tract} = T_{Wheels,tract} * r_{wheel} \quad (5.3)$$

$$\omega_{EM} = \omega_{Wheels} * k_{i,Transm} * k_{dif} \quad (5.4)$$

$$\omega_{Wheels} = \frac{v_{vehicle}}{r_{wheel}} \quad (5.5)$$

With  $r_{wheel}$  being the wheel radius,  $v_{vehicle}$  the vehicle speed,  $\omega_x$  the rotational speed,  $k_{dif}$  the final drive gear ratio,  $\eta_{Dif}$  and  $\eta_{Trans}$  the final

drive and transmission efficiencies and  $P_x$  and  $T_x$  the power and torque, respectively.

Figure 5-2 shows the P2 hybrid powertrain against the CDC non-hybrid in two modes. In pure electric mode (only the 70 hp EM is delivering power) the vehicle has constant force in the wheels up to a set speed, depending on the gear in the transmission, and then a continuous decay in the power curve is seen. This behavior is different from that of the conventional powertrain, which shows an increase of the wheel force up to a set speed (corresponding to the maximum ICE torque), and then decays down to the limit speed of the ICE. This behavior is due to the different characteristics of the EM versus the ICE. In addition, wheel force in pure EV mode is lower than that of the conventional powertrain due to the selection of a 70 hp EM (to reach a total of 280 hp when combined with the 210 hp ICE). However, the truck can be driven in road grades higher than 7%, with vehicle speeds up to 10 km/h. The maximum vehicle speed is 70 km/h on a flat route in pure EV mode. It is important to note that these values are calculated for the most demanding condition of 100% payload (18 tons).

The boost mode in a P2 architecture is the sum of the maximum power of the ICE and the EM. Figure 5-2 shows that it is possible to achieve higher wheel force at almost all vehicle speeds. The curves intersect at the limit speed for each gear, which corresponds to 2200 RPM of the ICE, due to the condition imposed for the P2 that forces the power of the ICE+EM to be equal to the ICE power in the conventional vehicle. This depicts the best performance of the P2 when it is working in the boost mode. As it is a full hybrid, the energy needs to be recovered by charging the batteries with the EM in generator mode. Therefore, the boost mode can be used for limited periods. The following section shows the vehicle in real driving conditions to analyze this point in detail.

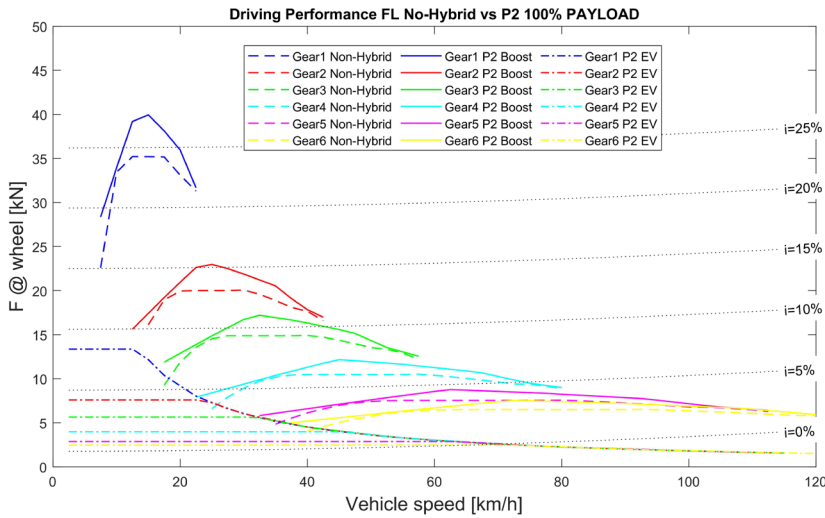


Figure 5-2. P2 Hybrid performance graph with the two modes and compared against the non-hybrid configuration.

For the powertrain study in transient conditions, a control system needs to be developed so that all sub-systems (ICE, EM, battery) work together. The control system was developed following a rule-based control (RBC) strategy due to the online application possibility and its robustness. The different control parameters are calibrated to minimize CO<sub>2</sub> emissions.

Ad-hoc rules are adopted to operate the P2 FHEV powertrain for all the possible operating modes. The control strategy characteristics are schematized in Table 5-1. The operating modes are selected according to the driver’s desired torque  $T_{driver}$  and the value of battery SoC, while ensuring that the mechanical power constraints of the ICE and EM ( $T_{ICE,max}$ ,  $T_{EM,max}$ ) are satisfied. Three main vehicle states are designed: when the traction torque demand is positive, pure electric (EV) and HEV driving modes are available, while when it is negative, the regenerative brake system (RBS) allocates the torque demand for energy recovery to the EM, which is complemented by the friction brakes. The vehicle can be propelled only by the ICE only when there is no request to charge the battery  $T_{charge}$ . The EM is set to operate

in generator mode to charge the battery, and its torque output value is determined by a PID controller that acts on the signal ( $SoC - SoC_{target}$ ). This allows to always keep the SoC level within the desired window. However, the aggressiveness of the controller is a critical aspect to calibrate to avoid frequent engine start-and-stops. Also, the control parameter  $v_{lim,EV}$  (vehicle speed limit for fully electric operation), needs to be calibrated. This rule decides the speed up to which the vehicle can run in fully electric mode. During the power assist mode, the power split between the ICE and EM is set by the control parameter  $Split_{coef}$ , which must be tuned.

In Table 5-1,  $Brake_{position} = 0\%$  when brake pedal is not actuated, 100% when fully pressed;  $Charge_{state} = [0 \text{ or } 1]$ , this control state variable is equal to 1 when  $SoC < SoC_{charge}$ , equal to 0 when  $SoC \geq SoC_{target}$ ;  $T_{EMmax}$  and  $T_{EMmin}$  are the maximum and minimum EM torque output in motor and generator modes, respectively;  $n_{ICE}$  is the rotational speed of ICE;  $T_{ICE,max}$  is the maximum torque output of the ICE. A summary of the RBC strategy is presented in Figure 5-3.



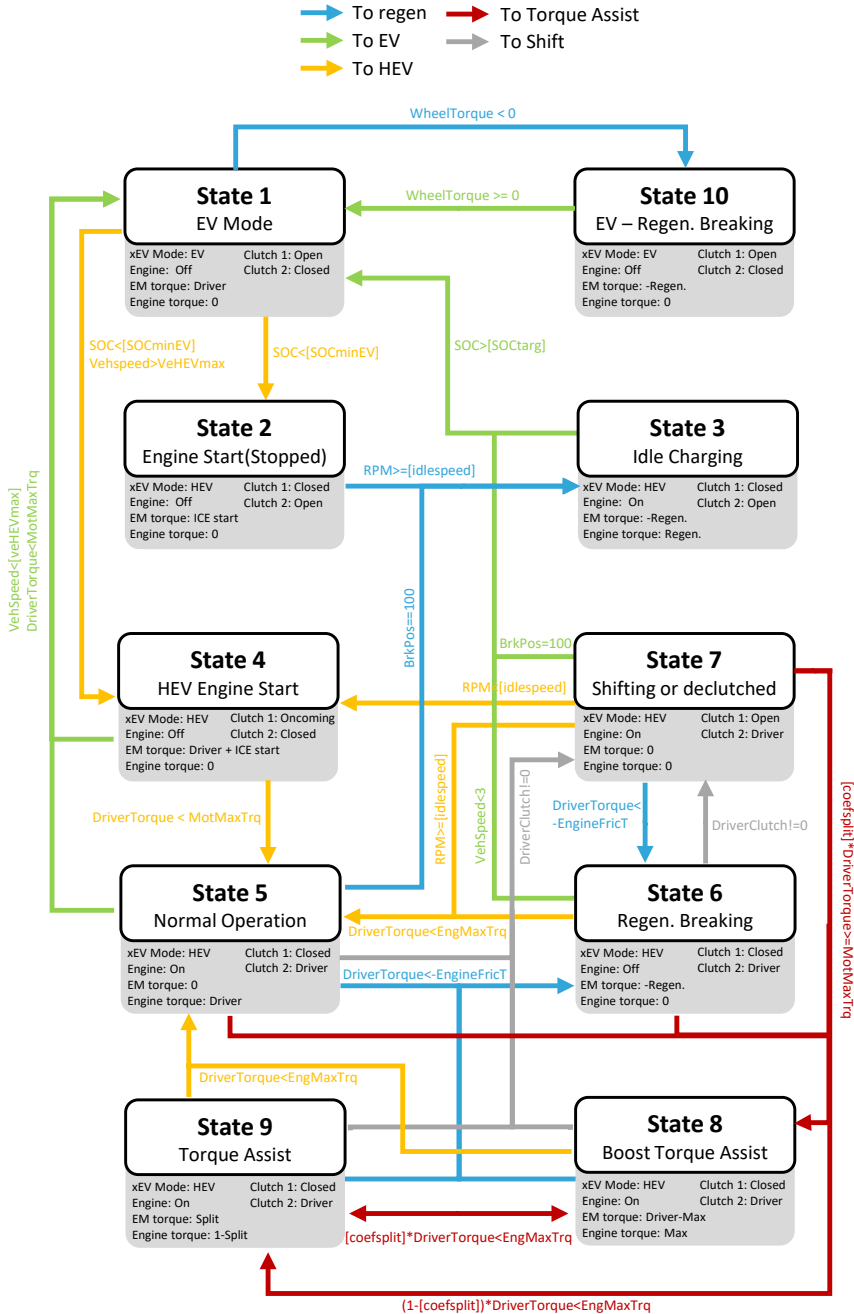


Figure 5-3. P2 Hybrid scheme of the Rule-Based Controller strategy.

Table 5-1. Conditions for each operative mode of the RBC supervisory controller in P2 FHEV.

Vehicle State	Sub-State	Conditions		ICE	EM
EV	EV traction	$T_{driver} > 0$ & $0 < v_{veh} < v_{lim,EV}$	$Charge_{state} = 0$	$T_{ICE} = 0$	$T_{EM} = T_{driver}$
HEV – Tractio n	ICE Start	$T_{driver} > 0$ & $v_{veh} > v_{lim,EV}$	$n_{ICE} < 1000$	$T_{ICE} = 0$	$T_{EM} = T_{driver} + T_{ICE\ start}$
	Charging		$Charge_{state} = 1$	$T_{ICE} = T_{driver} + T_{charge}$	$T_{EM} = -T_{charge}$
	Power Assist		$Charge_{state} = 0$ & $Split_{coef} * T_{driver} < T_{EMmax}$	$T_{ICE} = (1 - Split_{coef}) * T_{driver}$	$T_{EM} = Split_{coef} * T_{driver}$
	Power Assist Max ICE (EM boost)		$T_{driver} > T_{ICE,max}$ & $SoC > SoC_{min}$	$T_{ICE} = T_{ICEmax}$	$T_{EM} = T_{driver} - T_{ICEmax}$
HEV – Brakin g	Regenerati ve Braking	$T_{driver} < 0$ & $v_{veh} > 0$	$SoC < SoC_{max}$ & $T_{driver} > T_{EMmin}$	$T_{ICE} = 0$	$T_{EM} = T_{driver}$
	Parallel Braking		$SoC < SoC_{max}$ & $T_{driver} < T_{EMmin}$	$T_{ICE} = 0$	$T_{EM} = T_{min}$
	Mechanical Friction Braking		$SoC \geq SoC_{max}$ or $v_{veh} < 5km/h$	$T_{ICE} = 0$	$T_{EM} = 0$

From the control strategy proposed, six parameters are chosen to be calibrated. The first parameter is the maximum vehicle speed at which the operation mode changes from pure electric (generally used at low vehicle

speed) to hybrid mode. The EM propels the vehicle with the ICE switched off by disengaging the clutch 1 (Figure 5-1). Therefore, pure electric travel with zero tailpipe emissions can be performed. This operating mode is mainly used in urban areas, helping local pollution reduction and avoiding excessive ICE start and stop.

The second parameter is the boost mode split ratio, which divides the required torque between the ICE and EM. Moreover, the battery needs to be recharged to return the SOC to the initial value. From the charging mode, two additional parameters arise. The first one corresponds to the SOC value to start the battery charging. This determines the energy window (from SOC<sub>initial</sub> to SOC<sub>charge</sub>) the battery must operate. The second parameter is the intensity at which the battery is charged. For this, a PID in which the proportional gain was set as a function of the maximum EM power and the SOC limit is used. When SOC<sub>actual</sub> is equal to SOC<sub>limit</sub>, the full EM power machine is used to recharge the battery. A proportional value is used for conditions in which the SOC<sub>actual</sub> is greater than the SOC<sub>limit</sub>.

As a full hybrid, the battery state of the charge (SOC) needs to be the same at the initial and the end of the driving cycle. Depending on the cycle, it is possible not to achieve this target. Therefore, a tolerance of 5% SOC was set to accept or discard the control configuration. The initial SOC is set at 60% for having up and down range to move during the cycle. The maximum SOC is 95%, and the minimum acceptable SOC is 30% to avoid overcharging or over-discharging the battery. For compensating the cases with lower or higher battery energy in the end of the cycle than at the beginning, Equation 5.6 is proposed for a fair comparison.

$$BSCO_2_{corrected} = \frac{CO_2 + BSCO_2((SOC_{ini} - SOC_{end})Batt_{energy})}{Energy_{cycle}} \quad (5.6)$$

with  $CO_2$  the total mass of carbon dioxide,  $Energy_{cycle}$  the tractive energy is measured at the wheels. It is important to note that to be comparable in

hybrids, the energy of the ICE cannot be taken as is normal in non-hybrid powertrains. Equation 5.6 is also used in the other powertrain architectures.

Moreover, the target vehicle speed deviation was considered with a maximum accumulative variation of 3% in the total distance. The last control parameter is the gear shift strategy. This is a crucial point due to its notable impact on the ICE and EM operation speeds. The gear shift was optimized by a single parameter that establishes the rotational speed at the transmission's input (ICE and EM rotational speed) at which the gear changes. A six-gear automatic transmission is used. The parameter was swept between the minimum and maximum allowed speed of the ICE.

The battery package size (energy content) is also optimized in terms of hardware. This directly impacts the pure electric mode range, the vehicle's flexibility to operate along with the different modes, and the power losses. The increase of the battery's total energy reduces the current through the cells and the columbic losses. On the contrary, this has a disadvantage in terms of the entire battery weight and cost.

For optimizing the abovementioned parameters, a Genetic Algorithm is used, as was the case of MHEV P0. The target for the genetic algorithm is to minimize fuel consumption while reaching the same battery SOC at the end of the driving cycle as the initial SOC. The space over which the factors are varied is called the design space, and it is shown in Table 5-2. All cases out of the constrained conditions are eliminated.

Table 5-2. GA optimization parameters for P2 FHEV.

Parameter	Type of parameters	Range Tested
Battery Size	Hardware	5 - 80 kWh
Gear shift Strategy	Control Transmission	1300 - 2200 RPM
Max Pure Electric mode	Control Electric machine	5 - 90 km/h
Boost mode split	Control Electric machine	0 - 100 %
SOC start charge	Control Battery pack	0.45 - 0.59
Charge aggressiveness	Control Battery pack	0.45 - 0.59

### 5.2.2. Results

The proper selection of the battery size and the optimization of the energy management control in hybrid powertrains are essential to obtain fuel consumption and emissions benefits. This work aims to obtain the minimum CO<sub>2</sub> emissions (minimum fuel consumption) while meeting EU VI engine-out NO<sub>x</sub> and soot emissions under the WHVC at 50% payload (homologation conditions). The genetic algorithm optimizes the design parameters for the target mentioned above. Figure 5-4 shows the CO<sub>2</sub> emissions compared with CDC at the same driving cycle and payload with the evolution of the genetic algorithm generations for the P2 hybrid architecture. The difference is calculated with equation 5.7. Therefore, negative values represent a gain for the hybrid powertrain.

$$BSCO_{2dif} = \frac{BSCO_{2P2} - BSCO_{2CDC non-hybrid}}{BSCO_{2CDC non-hybrid}} * 100 \quad (5.7)$$

The final battery state of charge in the color bar is added. This parameter is inserted in the optimization as a constrain, which needs to arrive close to the SOC<sub>initial</sub> (range accepted 0.55-0.65). The cross marks show the cases in which this constraint is not achieved. After the first 500 cases, the genetic algorithm concentrates the generated points in a narrow CO<sub>2</sub>

emissions zone. It is possible to see that the 15% of CO<sub>2</sub> reduction 2025 target is achieved.

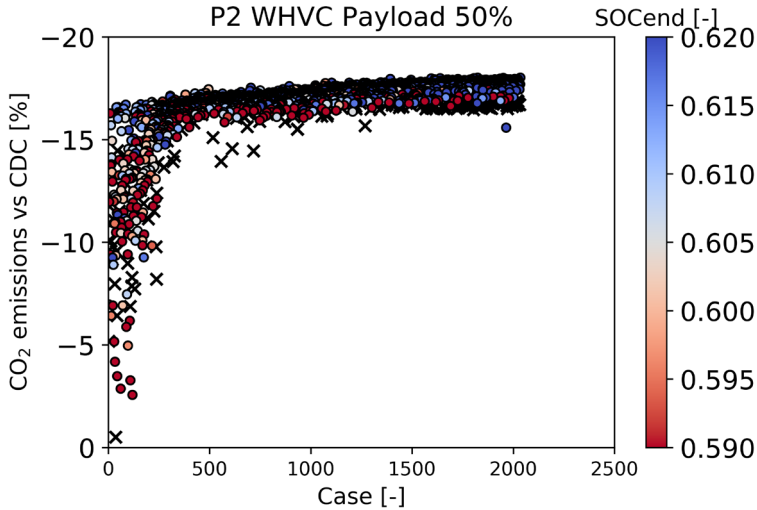


Figure 5-4. P2 Hybrid genetic algorithm cases evolution in terms of average fuel consumption and final battery state of charge (SOCend).

An important aspect is the effect of the calibration parameters on the CO<sub>2</sub> emissions and the final battery SOC. Figure 5-5 shows the sensitivity of the parameters in the abovementioned outputs. For the P2, the most sensitive parameter is the shift strategy. This parameter controls the engine speed and torque delivered by the ICE. The battery is an important aspect of the final SOC but does not significantly affect fuel consumption (CO<sub>2</sub> emissions). This is a positive point because it reduces the battery size and the powertrain cost. The constraints sensitivity is also shown with the final SOC is dependent on the battery size; high energy in the battery makes it hardest to control the battery SOC. The final vehicle distance equivalent to the vehicle performance is linked with the shift strategy. The shorter the ICE regime, the harder it is to achieve the desired power output.

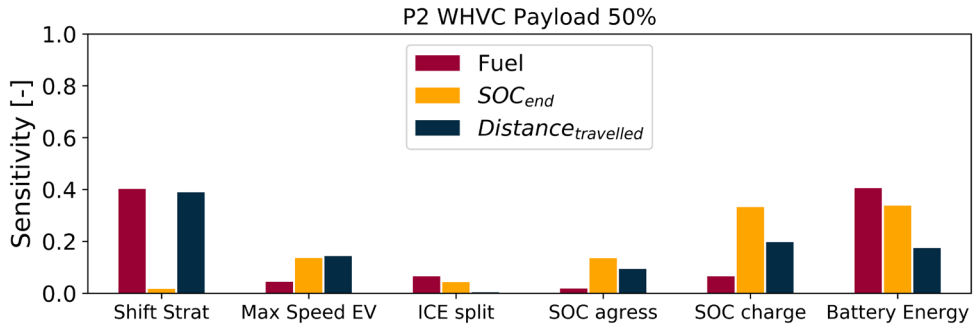


Figure 5-5. P2 Hybrid parameters sensitivity in terms of final average fuel consumption and final battery state of charge ( $SOC_{end}$ ).

Considering the most influencing parameters and the importance of the battery size in the final powertrain cost, Figure 5-6 shows the  $CO_2$  emissions difference with respect to the battery size and the shift strategy in the color bar. For the P2, the battery size has an optimum at 10 kWh (value in the low range tested). The battery is an LFP with high power for charge and discharge but low energy density. The best case is a configuration that allows high energy regeneration during braking but without adding significant weight to the vehicle. On the other hand, the shift strategy is preferred close to 1500 RPM because is possible to shift the operative points to high engine loads, as shown in Figure 5-7a. The ICE operative points are close to maximum power, almost always avoiding the wrong efficient zone at a low load. The dependence on the wheel's speed makes the ICE's operation not concentrated on a single point—instead, it variates between 950 and 1500 RPM and 10 to 100% of RCCI load.

Figure 5-7b shows the operative points of the P2 EM in tractive mode (positive torque values) and battery charging (negative torque values). As the ICE, the regime used is until 1500 RPM due to the gear shift. In addition, it is possible to see that almost all the EM torque range is used for the 50% payload. The EM use allows an average efficiency higher than 95% almost all the time.

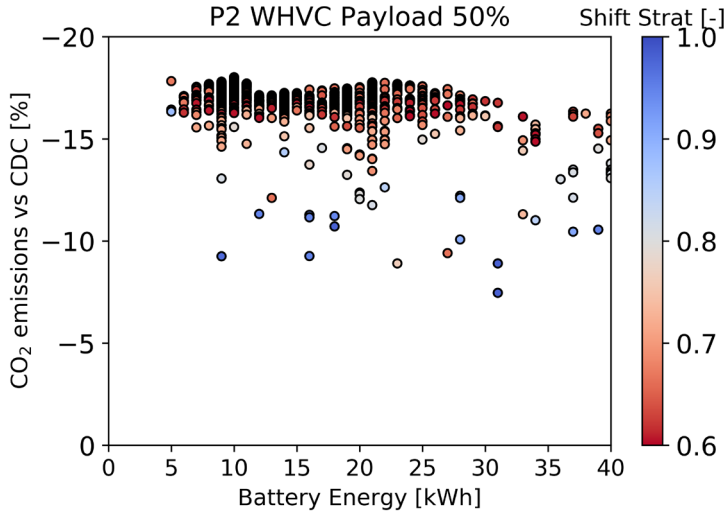


Figure 5-6. P2 battery size and gear shift strategy influence in the final fuel consumption benefits against CDC non-hybrid.

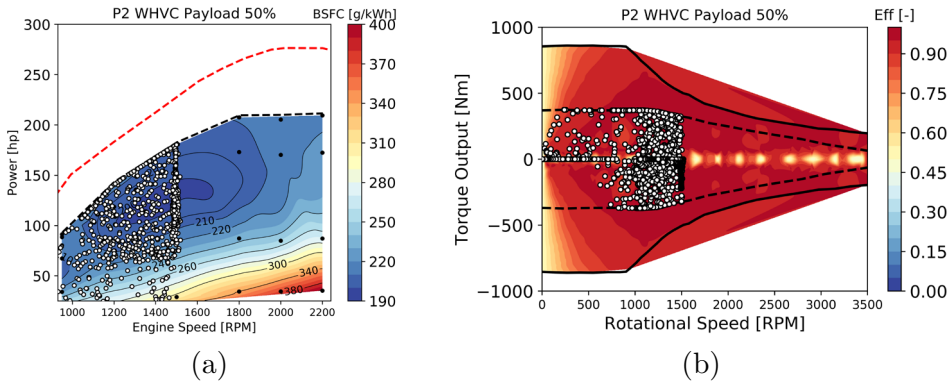


Figure 5-7. Internal combustion engine (a) and Electric Motor (b) operative conditions over the fuel consumption and efficiency map, respectively.

The battery behavior is depicted in Figure 5-8 by the SOC, voltage, current, and WHVC time. The size of the battery is selected at 10 kWh; this means 181 series cells (600 V) and 6 parallel cells (15.6 Ah). Figure 5-8a shows that the SOC is around 60% almost all the time with extra energy. This is compensated later with equation 5.6. Figure 5-8b and Figure 5-8c



show the battery package and cell parameters, respectively. The C-rate used on the cell indicates that ten is the maximum to discharge and 6 to charge. The limits following the specifications shown in Chapter 3 were 46/19 C-rate in pulse/continuous mode for discharging and 10/3.8 in pulse/continuous mode for charging. Therefore, the cell is more demanded in charge than discharge due to the considerable regenerative braking power.

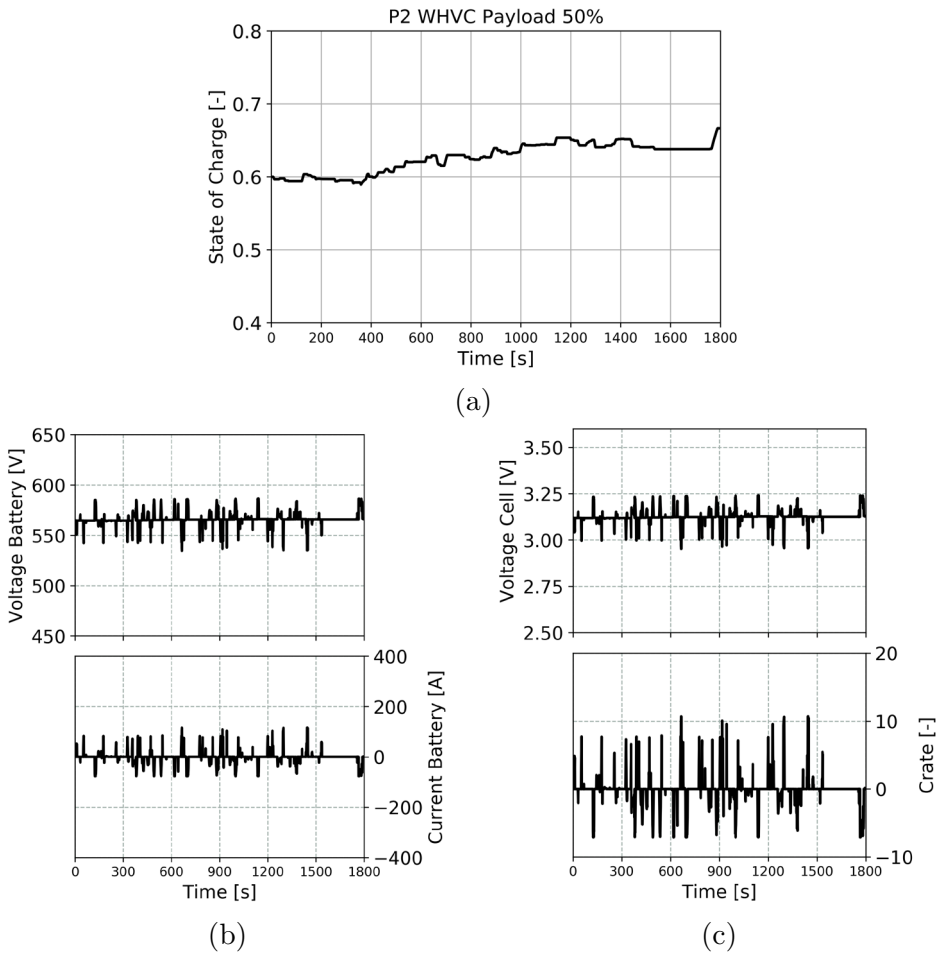


Figure 5-8. Battery and individual cell parameters during WHVC with 50% payload for Parallel Hybrid.

The optimum parameters of the GA optimization are presented in Table 5-3. The next powertrain to be optimized is the Series hybrid. A comparison of the P2 with the other powertrains will be made in Section 5.5. More payload and driving cycles will also be shown, maintaining the optimum RBC and hardware presented above.

*Table 5-3. Optimum parameters of the GA for P2 FHEV.*

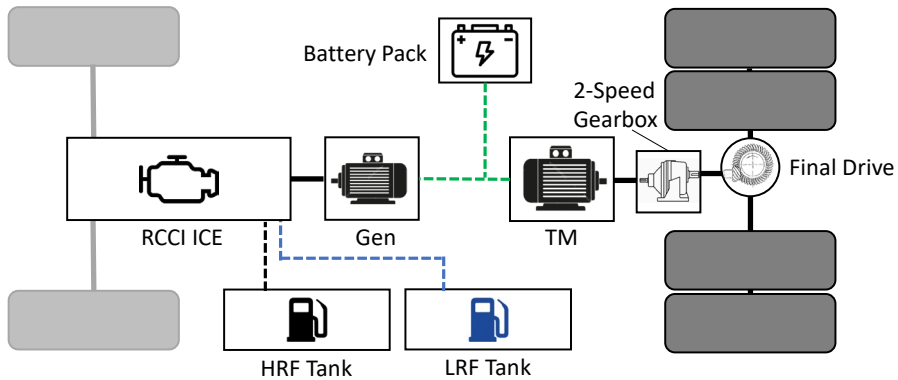
Parameter	Type of parameters	Final Opt Value
Battery Size	Hardware	10 kWh
Gear shift Strategy	Control Transmission	1462 RPM
Max Pure Electric mode	Control Electric machine	40 km/h
Boost mode split	Control Electric machine	100 %
SOC start charge	Control Battery pack	0.476
Charge aggressiveness	Control Battery pack	0.450

### 5.3 Series hybrid optimization

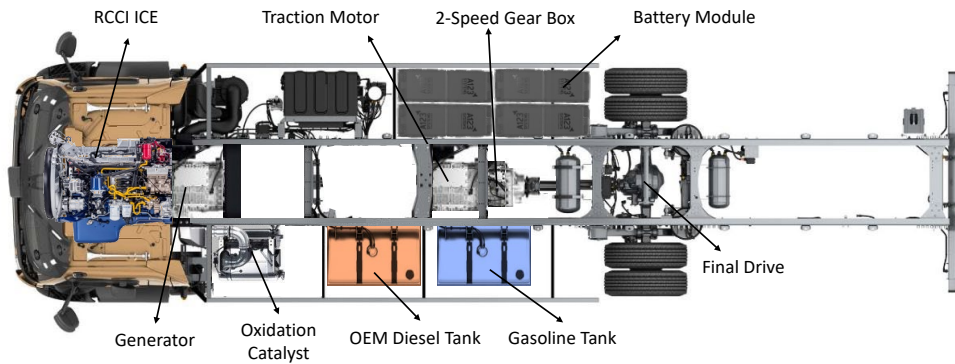
The Series hybrid is a concept that allows disconnecting the wheels from the engine totally. An ICE-generator and an electric traction motor connected to the wheels are used for battery recharging and propelling the vehicle. A pure electric mode is available at low vehicle speed and a high battery state of charge. When the battery achieves a low charge level, the ICE is turned on.

One of the significant benefits of the series architecture for the LTC RCCI concept is that a small amount of operative conditions is needed. In addition, the transitions between operative states are smoother than in a P2 or a conventional powertrain. Therefore, the ICE control is more accessible than the mentioned concepts. However, the battery needs to be greater than in a P2 to allow high discharge and charge current rates due to the two EM.

A layout of the series architecture in the Volvo FL truck is seen in Figure 5-9. As can be seen, the ICE and generator are mechanically connected, and on the other side is the TM to the wheels. Heavy-Duty vehicles have the particularity of requiring high torque at low vehicle speeds and large engine rotational speeds at high vehicle speeds. Despite the maximum vehicle speed being lower than in a passenger car (120 km/h instead of 200 km/h), the TM needs a large final drive to deliver high torque. Therefore, a two-speed gearbox is required. A similar configuration can be seen in the pure electric Volvo FL truck [222]. The main difference between this HEV and BEV is the ICE as a range extender. With the advance in EM design, a motor that delivers extra-high torque at low speed could be found in the future and can be run until large rotation speed ( $>12000$  RPM). For now, using commercially available solutions, the gear box solves the problem. Compared with P2, the Series hybrid reduces the gearbox complexity and control operation. In addition, as was the case of the P2, the ATS is only the Oxidation Catalyst. DPF and SCR-Urea systems are removed.



(a)



(b)

Figure 5-9. Series Hybrid architecture layout with main components in an FL-18-ton truck. The architecture (a) and component layout scheme in vehicle chassis (b).

### 5.3.1. Methodology

The Series hybrid powertrain was designed using the RCCI engine map calibration (210 hp) connected to a generator motor. Therefore, the generator motor (Gen) needs to be able to deliver 210 hp at continuous power. The

ICE map selection was similar to that in the P2, with total NOx and soot compliance and the highest BTE region.

For the TM, there are at least two interesting options: 1) Design to achieve the same continuous power output as the non-hybrid (280 hp), 2) Design to achieve the same continuous power as the ICE-generator, so it can be used in direct connection avoiding the battery in some particular phases. Based on bibliography research and the nature of EM to achieve a peak power near double the nominal continuous power, choice number two was taken. The Volvo pure electric truck has a TM of 180 hp continuous power. Moreover, the traction motor HM-3500 of 280 hp continuous power is recommended for Truck Class 6 to 8 (long-haul trucks) due to the 470 hp peak power. In addition to a BEV truck, the Series FHEV will equip a lower-sized battery. Therefore, in the case of high-power requirements, all the power will be provided by the ICE generator. For the TM and Gen, a scaled version of the HTM-3500 is used with a coefficient of 0.739 (210/284 hp), following the methodology shown in Chapter 3.

The two-speed gearbox and the final drive need to be designed together to achieve high torque in all vehicle speed ranges. In order to decide the gear ratios, the wheel force is calculated to understand the performance compared to the non-hybrid.

$$P_{Wheels,tract} = P_{TM} * \eta_{Dif} * \eta_{gearbox} \quad (5.8)$$

$$T_{Wheels,tract} = \frac{T_{TM} * \omega_{EM}}{\omega_{Wheels}} * \eta_{Dif} * \eta_{gearbox} \quad (5.9)$$

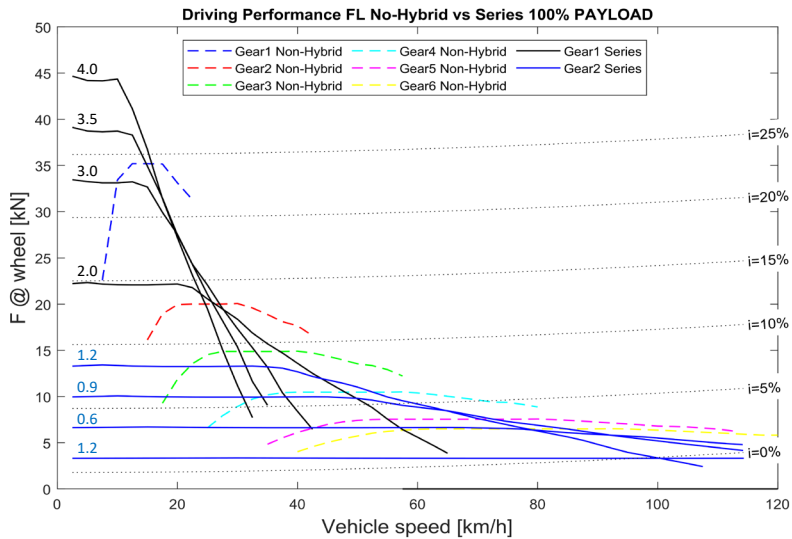
$$F_{Wheels,tract} = T_{Wheels,tract} * r_{wheel} \quad (5.10)$$

$$\omega_{TM} = \omega_{Wheels} * k_{dif} * k_{gearbox,i} \quad (5.11)$$

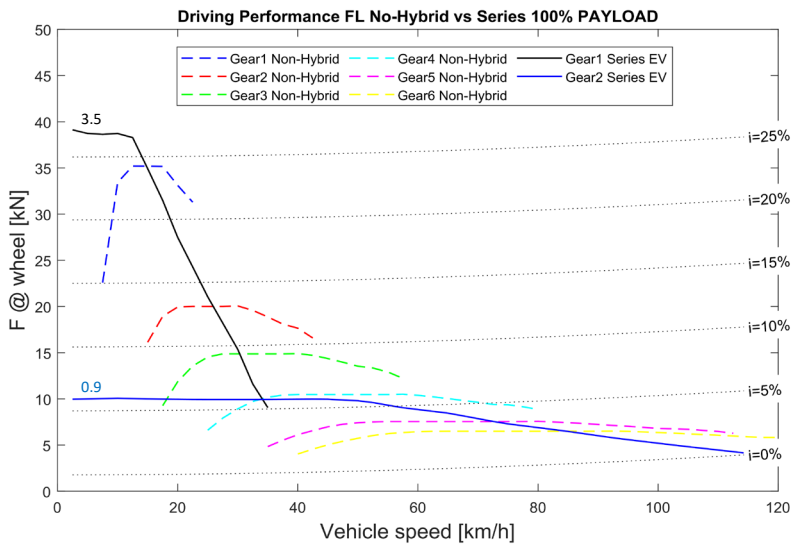
$$\omega_{Wheels} = \frac{v_{vehicle}}{r_{wheel}} \quad (5.12)$$

The  $k_{dif} = 5.29$  is chosen equal to the P2 and the non-hybrid due to the flexibility to adjust the speed with the gear box. After several iterations, a ratio of:  $k_{gearbox,1} = 3.5$  and  $k_{gearbox,2} = 0.9$  are selected to achieve similar torque output at low vehicle speed than the non-hybrid and cover all vehicle range with the second gear. Figure 5-10a shows the performance when varying the two-speed gear ratios. The combination of 3.5 and 0.9 allows operating over all the regimes with high torque at low speed and a smooth change between gear one and gear two.

The final gear selection gives the performance results in Figure 5-10b. The Series hybrid loses performance at moderate vehicle speeds compared with the non-hybrid. However, it has excellent torque output at low vehicle speeds and similar characteristics at higher vehicle speeds. The driver will not see the lack of power due to the ability to deliver higher peak power for short times. In this work, only continuous power is used due to the type of driving cycles tested.



(a)



(b)

Figure 5-10. Series Hybrid performance compared against the non-hybrid configuration. Gear iteration for high and low-speed ratio (a) and final selection (b).

A single-gear transmission is used between the ICE and the generator in some series powertrain. A comparison between efficiency map operations can be made to understand if it is necessary the gear ratio. Figure 5-11 shows the EM map of the generator over the ICE brake thermal efficiency map in case of no using a gear transmission. It can be seen that as the EM selected operate between 0 and 3500 RPM, both high-efficiency zone is overlapped. This is beneficial because adding a gear box will mean more complexity to the powertrain and additional mechanical losses.

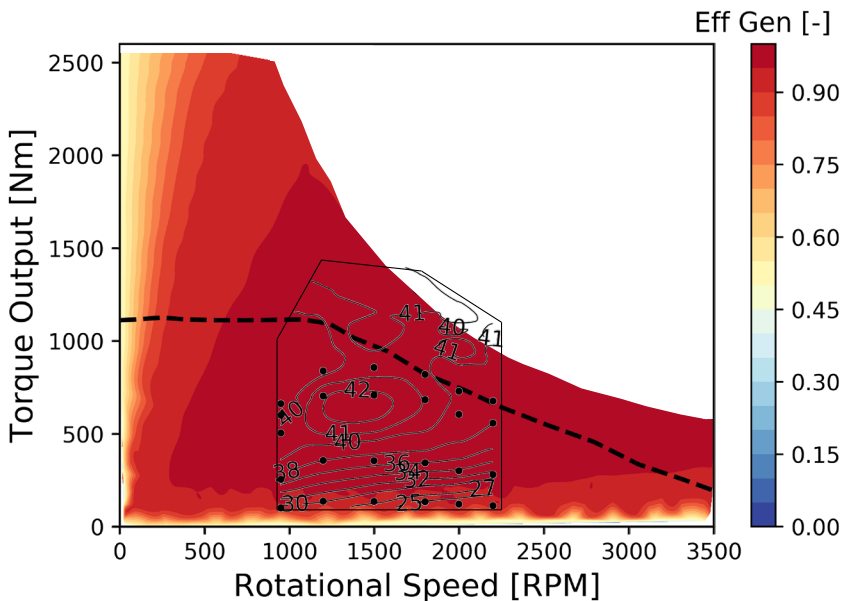


Figure 5-11. Generator efficiency map (fraction) and ICE efficiency map (BTE%) with a gear ratio of 1.0.

Regenerative braking is a critical aspect that needs to be considered and studied when a hybrid electric vehicle is under evaluation. As in the P2, the control system is an RBC with rules to change between modes. During traction, the primary operating mode is EV drive: the vehicle is propelled by TM, which discharges the battery, and the ICE-generator assembly is switched off. Another mode during traction is the ICE circulation: the ICE



is the power source since its power output matches the wheels' power demand. In this way, the battery is neither charged or discharged. This mode is helpful for sustaining charge operations. Lastly, Hybrid drive: the battery SoC level can be increased or decreased depending on whether the ICE provides more or less power than the one required for traction.

Regenerative braking is performed at the wheels coupled to the electric machine, and hence according to Figure 5-9, it can take place only at the back-driven wheels. Moreover, the battery can be simultaneously charged during a braking event by both the TM and Gen, if the ICE is switched on. The operating mode in which the ICE can charge the battery when the vehicle is stopped may also be possible given the decoupling of the ICE from the driveline. A resume of the RBC strategy for the Series hybrid is presented in Figure 5-12, and the conditions to change in Table 5-4.

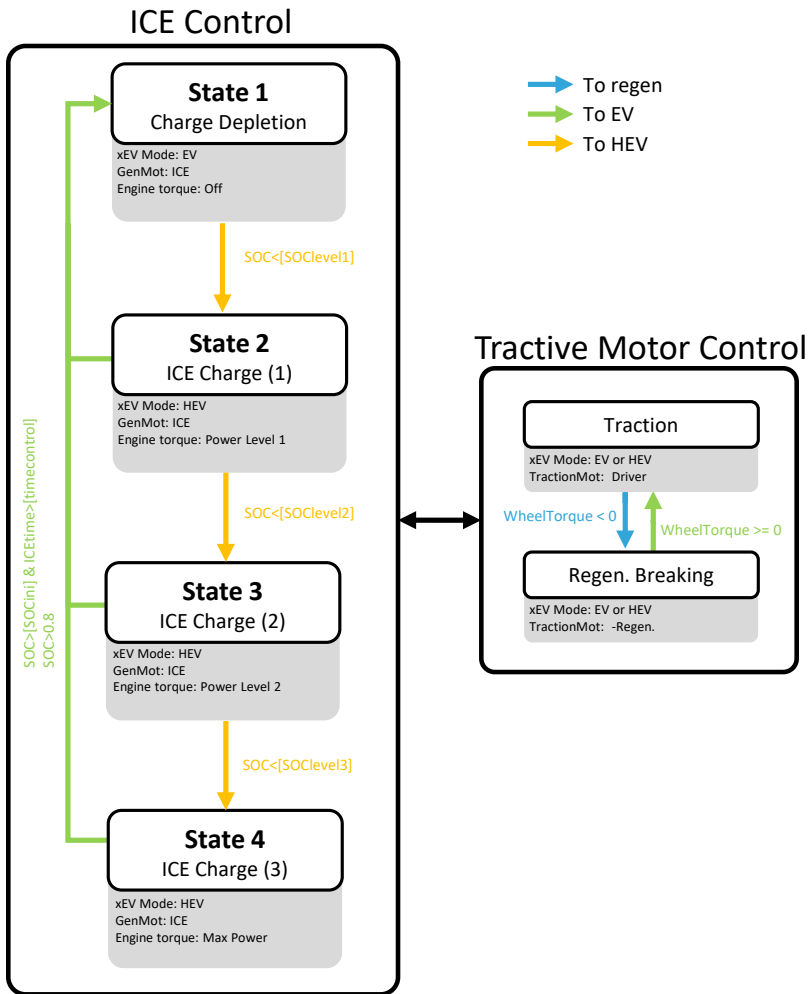


Figure 5-12. Series Hybrid scheme of the Rule Based Controller strategy.

Table 5-4. Conditions for each operative mode of the RBC supervisory controller in Series FHEV.

Vehicle State	Sub-State	Conditions		ICE	TM	Gen
EV	EV traction	$T_{driver} > 0$ & $0 < v_{veh} < v_{lim, EV}$	$Charge_{state} = 0$	$T_{ICE} = 0$	$T_{TM} = T_{driver}$	$T_{Gen} = 0$
	EV braking	$T_{driver} < 0$	-	$T_{ICE} = 0$	$T_{TM} = \min(\text{split} * T_{driver}, T_{batt charging})$	$T_{Gen} = 0$
HEV	Power level 1	$T_{driver} > 0$ & $0 < v_{veh} < v_{lim, EV}$ &	SOC < level 1	$T_{ICE} = T_{level 1}$	$T_{EM} = T_{driver}$	$T_{Gen} = -T_{level 1}$
	Power level 2		SOC < level 2	$T_{ICE} = T_{level 2}$		$T_{Gen} = -T_{level 2}$
	Power level 3	$Charge_{state} = 0$	SOC < level 3	$T_{ICE} = T_{ICE max}$		$T_{Gen} = -T_{ICE max}$

Therefore, three control parameters need to be calibrated by the genetic algorithm as in the case of P2. Additionally, the battery size and the vehicle speed to change gear one to gear two are optimized. The control parameters of the RBC intend to set the level of battery charging by two levels. Power 1 and Power 2 are used to search the torque and speed in the most efficient ICE line for each level. Level 3 is used when the SOC is low, so the maximum power of the ICE-generator is used. The search space for the GA is shown in Table 5-5.

Table 5-5. GA optimization parameters for Series Hybrid.

Parameter	Type of parameters	Range Tested
Shift Change	Control Gearbox	5 - 40 km/h
Battery Size	Hardware	5 - 80 kWh
Power level 1	Control ICE	30 – 100 kW
Power level 2	Control ICE	110 – 156 kW
SOC window for power level	Control Battery pack	1 – 12 %

### 5.3.2. Results

The optimization results for the Series hybrid are shown in Figure 5-13. After 250 cases, the GA was allowed to achieve a high CO<sub>2</sub> reduction with a final value of 14.8% lower than the CDC non-hybrid. This means almost the 2025 CO<sub>2</sub> target of 15%. The color bar shows the SOC at the end of the cycle, which must be around 0.6. The sensitivity analysis of the optimization parameters (Figure 5-14) shows that power level 1 and the battery size are the most influential parameters. Power level 1 has more influence than power level 2 because the first is most used in this payload condition. The battery energy is essential to correctly deliver power to the two EM and be able to recover the energy from the braking.

On the other hand, the shift change speed is important in performance to achieve the desired vehicle speed/total distance. The optimum was 36 km/h to delay the change to the second gear and have more torque in the output. This parameter does not have much influence on the CO<sub>2</sub> emissions due to the large high-efficiency zone of the TM. The initial SOC to charge is the most influential parameter in this restriction in terms of final SOC.

As expected, in terms of battery size, the Series hybrid optimum is higher than P2 with 41 kWh (see Figure 5-15). This means 181 series cells (600V) and 27 parallel cells (70.2 Ah). Total cells are 4887 instead of 1086 of the P2. For Series hybrid is a balance of delivering/recovering power capability and weight influence. In addition, the increase in battery size

reduces the heat losses in the battery due to the lower C-rate requested for each cell. This improves powertrain efficiency.

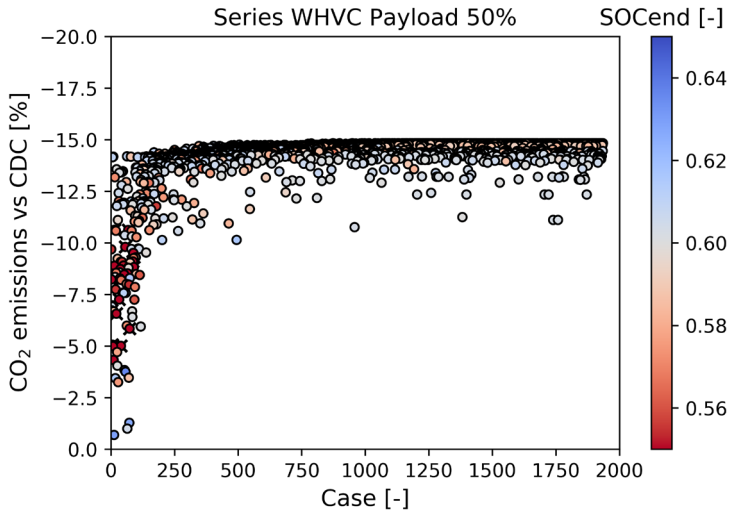


Figure 5-13. Series Hybrid genetic algorithm cases evolution in terms of average fuel consumption and final battery state of charge ( $SOC_{end}$ ).

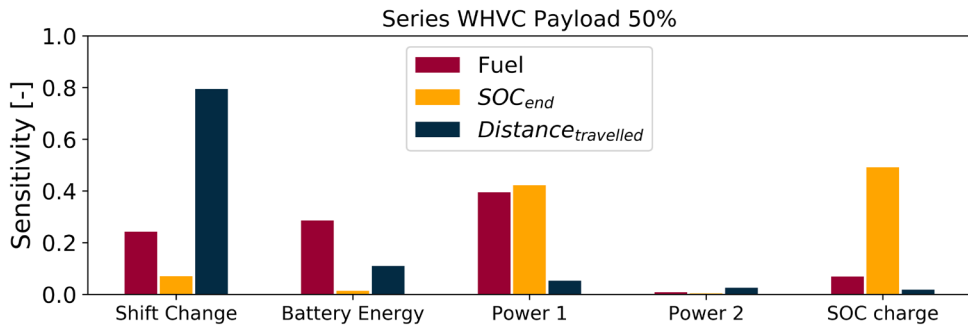


Figure 5-14. Series Hybrid parameters sensitivity in terms of final average fuel consumption and final battery state of charge ( $SOC_{end}$ ).

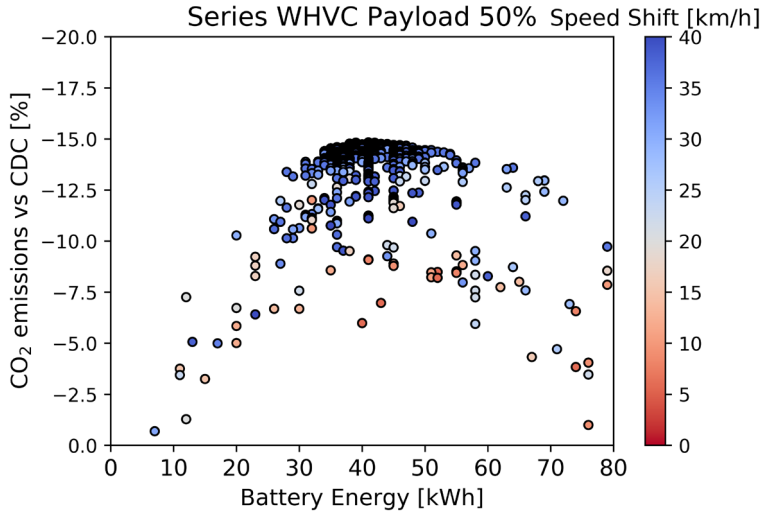


Figure 5-15. Series Hybrid battery size and gear shift strategy influence the final fuel consumption benefits against CDC non-hybrid.

Figure 5-16 shows the ICE and EM operation. As mentioned in the methodology, this powertrain architecture uses a narrow ICE region. Power level 1 (107 kW) and level 2 (141 kW) were necessary for this payload. The maximum ICE power was not requested (Power level 3). The Gen operation is opposite to the ICE, and the traction motor operates at several points due to the link of the wheels. The gear change allows extending the TM operation from almost 0 RPM to 3500 RPM.

The battery parameters are presented in Figure 5-17, where it can be seen that the current request is higher than in the P2, but as the battery size increase, the C-rate is lower. A summary of the final parameters is presented in Table 5-6.

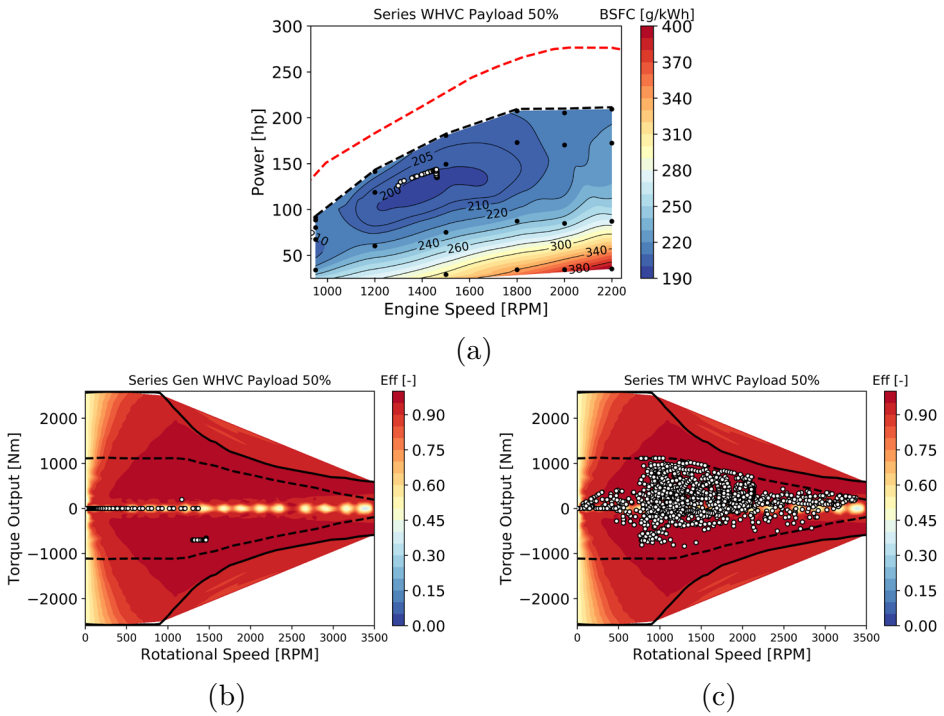


Figure 5-16. ICE RCCI operative conditions (a) and electric machines operation with Gen (b) and TM (c) for WHVC 50% payload in Series hybrid.

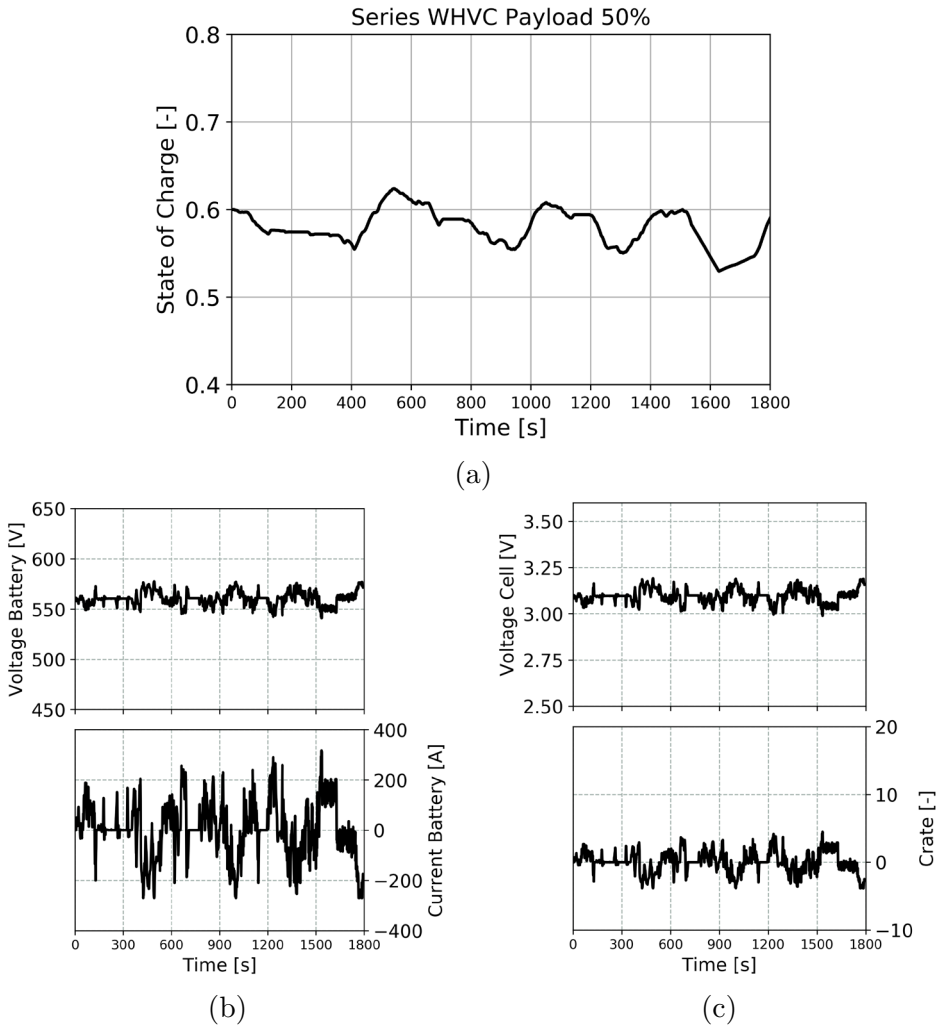


Figure 5-17. Battery and individual cell parameters during WHVC with 50% payload for Series hybrid.



Table 5-6. GA optimum parameters for Series Hybrid.

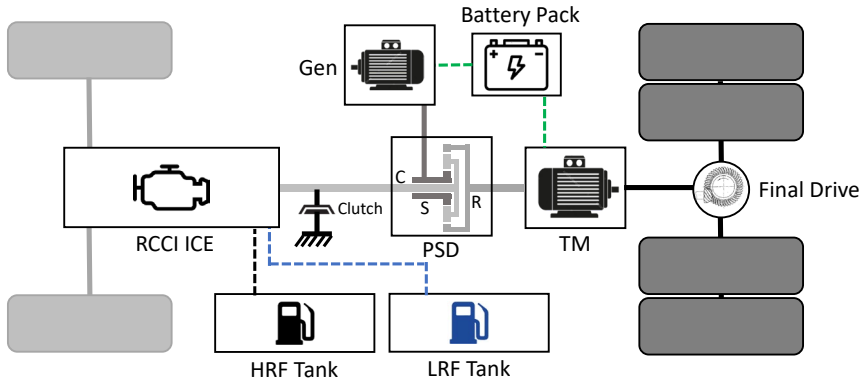
Parameter	Type of parameters	Final Opt Value
Shift Change	Control Gearbox	36 km/h
Battery Size	Hardware	41 kWh
Power level 1	Control ICE	107 kW
Power level 2	Control ICE	141 kW
SOC window for power level	Control Battery pack	7.5 %

## 5.4 Power split hybrid optimization

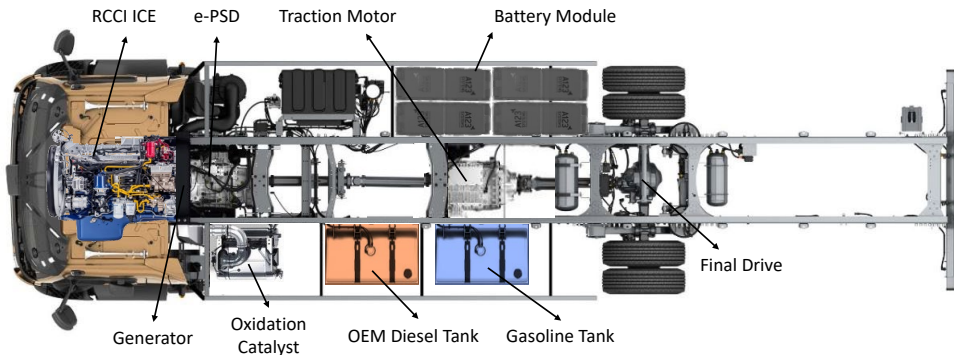
The power split is the most sophisticated architecture due to an epicyclic transmission with two electric machines to link the ICE to the final drive. It allows to decouple the speed of the ICE from the rotational speed of the wheels but connects the mechanical ICE to the wheels. Therefore, it is also known as series-parallel architecture. It can take advantage of both the parallel and the series architectures with proper system design.

The ICE is coupled to a generator to produce electrical energy for the battery like in a Series hybrid. Still, it can also have helpful traction power in parallel to the power output of the TM (see Figure 5-18). This is possible through the mechanical transmission, which is the heart of the power-split architecture. This epicyclic or planetary transmission allows to re-distribute the power from an input shaft between two output shafts. A planetary transmission is made of a sun gear, a set of planet gears that are coupled to a carrier, and a ring gear that can be externally or internally in contact with the planet gears. The number of planets determines the torque load capability of the transmission: the lower the number of planets, the higher the load acting on the teeth of the planet gears. The planetary transmission has many advantages over the conventional one, such as reduced weight, compactness, higher load-carrying capacity, and more speed ratios between input and output.

As was mentioned, this hybrid powertrain requires two electric machines. The ICE is coupled to the carrier gear, one electric machine -which is called Gen the main purpose is to charge the battery in generator mode- is connected to the sun, and the other electric machine -which is called TM because the primary goal is to propel the vehicle in traction mode- is connected to the ring. Finally, the differential/final drive is the torque-coupling device, and it is linked to the ring gear. The planetary transmission enables splitting the engine power between two paths: the electrical path, where part of the power delivered by the ICE is sent to Gen and stored in the battery or directly sent to the motor TM via a controlled power bus, and the mechanical path that brings the remaining power to the transmission output. The clutch allows another operating mode because the ICE can be grounded so that the vehicle can operate in pure electric driving mode. Figure 5-18 shows a scheme of the powertrain architecture and its look in the vehicle chassis. More explanation about the operating modes and control will be detailed in the following sub-section.



(a)



(b)

Figure 5-18. Power Split Hybrid architecture layout with main components in an FL-18-ton truck.

### 5.4.1. Methodology

The ICE power split into the mechanical and electrical paths depends on two aspects. First, the torque requested by Gen is related to the ICE through the planetary transmission ratio  $K$ ; Second, the speed of the ICE and Gen depends both on the transmission ratio  $K$  and on the ring speed

(final drive output speed that is equal to TM speed). This suggests the possibility of conveniently regulating the ICE operation to operate in the best efficiency zone. It is achieved by correctly controlling the generator motor to set the speed and torque output of the ICE in the desired operation zone. A layout of the gears and connections in the epicycloid transmission is shown in Figure 5-19.

The torque acting on the sun gear, given by the Gen, is always opposite to the ICE torque. To increase ICE speed, Gen has to rotate in the positive direction (same as the ICE). Therefore, Gen supplies a negative power and works as a generator. Gen hence absorbs part of the ICE power, and the remaining portion is transferred to the ring gear that is mechanically connected to the wheels. On the other hand, if the vehicle speed is too high and the ICE is already active, the angular speed of Gen can fall to zero.

In some cases, it can even turn negative (opposite to the ICE speed): in this particular condition, Gen absorbs no power (zero Gen speed) or outputs positive power, and all the ICE power is output for traction. In this case, TM modulates the ICE power by working in generator mode: this situation is called "re-circulation". This mode of operation is not efficient since the power flow undergoes many mechanical-to-electrical conversions and vice-versa.

In an engine-centric view, the role of Gen is to regulate the angular velocity of the ICE for a given vehicle speed. Moreover, it can be inferred that Gen speed needs to decrease as the vehicle speed increases progressively to keep the ICE at the desired regime. On the contrary, at low vehicle speeds, Gen speed has to rapidly increase to high rotational speeds if the ICE has to work above the idle speed. This is the purpose of the planetary transmission with this kind of arrangement. This device is also known as e-CVT (electrical continuously variable transmission), since the Gen can regulate the engine speed with a continuously variable ratio according to the vehicle speed. This suggests that the generator motor needs to operate in a large rotational regime to control the ICE.

The role of TM, which is coupled to the output shaft at the ring, is to complement the power output at the transmission to satisfy the power request at the final-drive input. It is important to note that the values of the planetary transmission ratio ( $K$ ) and final drive ratio ( $\tau_{FD}$ ) are fundamental parameters that make the vehicle's performance characteristics (i.e., gradeability, maximum vehicle speed, and acceleration) and determine how Gen, TM, and the ICE can work together.

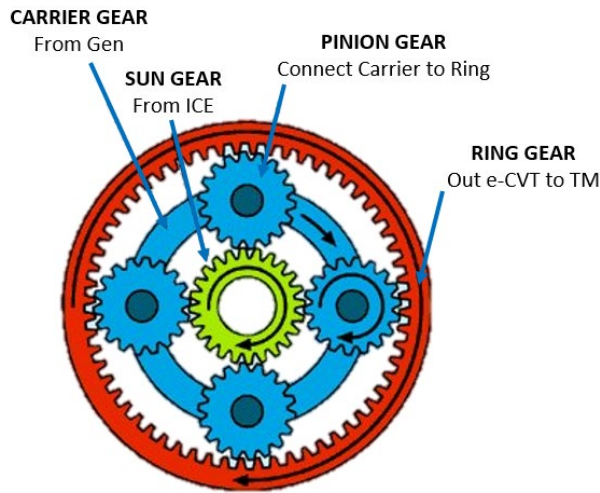


Figure 5-19. Electrical continuously variable transmission (e-CVT) is also called epicyclical transmission for power-split hybrid architecture.

Figure 5-20 shows a scheme of the forces acting in an e-CVT. The letters s for sun, p for planetary, c for the carrier, and r for the ring. For a given pair of gears  $i$  and  $j$  in mesh, the basic condition of tangent velocity at the point of contact on the primitive circumference states is Equation 5.13. The module ( $m$ ) defined as the ratio of the reference diameter ( $2r$ ) of the gear divided by the number of teeth ( $z$ ) are equal between the mentioned gears (Equation 5.14). Due to dynamic equilibrium, the forces need to be equal (Equation 5.15). It can be obtained the gear relationship  $K_{i-j}$  by

Equation 5.16. The previous relations lead to the following set of equivalent relations that define the transmission ratio for the meshing gears.

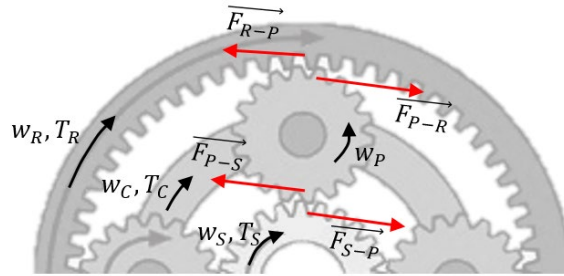


Figure 5-20. Schematic diagram showing the transmission of force in a planetary transmission.

$$v_{contact\ i-j} = \omega_i r_i = \omega_j r_j \tag{5.13}$$

$$m_i = m_j \rightarrow \frac{2r_i}{z_i} = \frac{2r_j}{z_j} \tag{5.14}$$

$$F_i = F_j \rightarrow \frac{T_i}{r_i} = \frac{T_j}{r_j} \tag{5.15}$$

$$K_{i-j} = \frac{\omega_j}{\omega_i} = \frac{r_i}{r_j} = \frac{z_i}{z_j} = \frac{T_i}{T_j} \tag{5.16}$$

For an epicyclical transmission, there can be defined two intermediate transmission ratios for the planet-sun (Equation 5.15) and planet-ring (Equation 5.16) couples and a global transmission ratio for the sun-ring (Equation 5.17) couple that previously was called  $K$ . The modulus is equal for all the gears of the transmission. A minus sign multiplies the transmission

ratio since the primitive circumference of the two gears is external to each other.

$$K_{ring-planet} = K_{ring-carrier} = \frac{\omega_c}{\omega_r} = \frac{r_r}{r_c} = \frac{z_r}{z_c} = \frac{T_r}{T_c} \quad (5.15)$$

$$K_{planet-sun} = K_{carrier-sun} = \frac{\omega_s}{\omega_c} = \frac{r_s}{r_c} = \frac{z_s}{z_c} = \frac{T_s}{T_c} \quad (5.16)$$

$$-K_{ring-sun} = K_{ring-carrier} * -K_{carrier-sun} = \frac{\omega_s}{\omega_r} = \frac{r_r}{r_s} = \frac{z_r}{z_s} = \frac{T_r}{T_s} \quad (5.17)$$

The previous Equations justified the fact that if the carrier were blocked ( $\omega_c = 0$ ), the planetary transmission would turn into an ordinary gear train, for which the pinion gears would act as idler gears. For the kinematics theorem of Arhold-Kennedy [223], three bodies that lie on the same plane must have the centers of relative instantaneous rotation aligned: this leads to the state that the relative instantaneous centers of rotation of the ring and sun gears concerning the carrier must match (Equation 5.18). Using equation 5.17, the relationship between carrier, sun, and ring speed (Equation 5.20).

$$(\omega_r - \omega_c)r_r = (\omega_s - \omega_c)r_s \quad (5.18)$$

$$\frac{(\omega_s - \omega_c)}{(\omega_r - \omega_c)} = \frac{r_r}{r_s} = -K \quad (5.19)$$

$$\omega_c = \frac{1}{(K + 1)} \omega_s + \frac{K}{(K + 1)} \omega_r \quad (5.20)$$

In addition, the dynamic equilibrium on the transmission gives:

$$T_s + T_c + T_r - T_{load} = J_s \dot{\omega}_s + J_c \dot{\omega}_c + J_r \dot{\omega}_r \quad (5.21)$$

with  $T_{load}$  is the load torque applied at the transmission output, which corresponds to the shaft coupled to the ring gear of the transmission;  $J$  is the inertia of a gear. Also, the power balance is:

$$(T_s - J_s \dot{\omega}_s) \omega_s + (T_c - J_c \dot{\omega}_c) \omega_c + (T_r - T_{load} - J_r \dot{\omega}_r) \omega_r = 0 \quad (5.22)$$

Relating the angular velocities to the carrier's one ( $\omega_c$ ), the previous equations can be used to derive some characteristics relations of the planetary transmission and divide all terms by  $(\omega_r - \omega_c)$  and recalling Equation (Equation 5.17), the previous one becomes:

$$-K(T_s - J_s \dot{\omega}_s) + (T_r - T_{load} - J_r \dot{\omega}_r) = 0 \quad (5.22)$$

Finally, combining Equation 5.22 with Equation 5.21 results in a relationship between the torque applied on the sun gear and that applied on the carrier gear:

$$T_s = J_s \dot{\omega}_s - \frac{1}{(K + 1)} (T_c - J_c \dot{\omega}_c) \quad (5.23)$$

This Equation can be interpreted as the torque transferred from the carrier to the sun or vice-versa, depending on the power flow. In this mechanical conversion, inefficiency losses also rely on the quality of the meshing between the sun and planets gears. To account for the meshing efficiency  $\eta_{ps}$ , Equation 5.23 becomes:



$$T_s = J_s \dot{\omega}_s - \frac{1}{(K+1)} (T_c - J_c \dot{\omega}_c) \eta_{ps}^q \quad (5.24)$$

where the exponent  $q = 1$  when the input torque is  $T_c$ , while  $q = -1$  when  $T_s$  is the input torque. Substituting Equation (5.24) into the torque equilibrium Equation 5.21 it is also possible to obtain the relationship between the torque applied on the ring gear, the load torque, and the one used on the carrier:

$$T_r = T_{load} - \frac{K}{(K+1)} (T_c - J_c \dot{\omega}_c) \eta_{ps}^q \eta_{pr}^t + J_r \dot{\omega}_r \quad (5.24)$$

The second term of this Equation 5.24 stands for the torque transferred from the carrier to the ring. The efficiency of the meshing between planets and the ring gear  $\eta_{pr}$  may be considered, and the exponent  $t = 1$  if power flows from the transmission to the ring output, and  $t = -1$  when the power flow is opposite.

At steady-state (i.e., no member is accelerating), the presented relations further simplify, as highlighted by the following system of equations:

$$\begin{cases} T_s = -\frac{1}{(K+1)} T_c \eta_{ps}^q \\ T_r = T_{load} - \frac{K}{(K+1)} T_c \eta_{ps}^q \eta_{pr}^t \end{cases} \quad (5.25)$$

$$\begin{cases} P_s = -\frac{1}{(K+1)} P_c \frac{\omega_s}{\omega_c} \eta_{ps}^q \\ P_r = P_{load} - \frac{K}{(K+1)} P_c \frac{\omega_r}{\omega_c} \eta_{ps}^q \eta_{pr}^t \end{cases} \quad (5.26)$$

Considering the torque demand at the wheels, the torque at the final-drive input  $T_{FD,in}$  can be calculated with the final-drive ratio  $\tau_{FD}$  and its efficiency  $\eta_{FD}^v$  (the exponent  $v = 1$  when  $T_{wheels} > 0$  and  $v = -1$  when  $T_{wheels} < 0$ ):

$$T_{FD,in} = \frac{T_{wheels}}{\tau_{FD}\eta_{FD}^v} \quad (5.27)$$

Also, the input shaft speed, which is connected to the ring gear of the planetary transmission, is calculated from the vehicle speed  $v_{vehicle}$ :

$$\omega_{FD,in} = \omega_r = \frac{v_{vehicle}}{R_{wheel}}\tau_{FD} \quad (5.28)$$

Hence from Equation 5.20 it is possible to derive the kinematic relationship between the angular velocities of ICE  $\omega_{ICE}$ ,  $\omega_{Gen}$  for Gen and  $\omega_{TM}$  for TM:

$$\omega_{ICE} = \frac{1}{(K+1)}\omega_{Gen} + \frac{K}{(K+1)}\omega_{TM} \quad (5.29)$$

The load torque  $T_{load} = T_{FD,in}$  and the torque Equation 5.25 becomes:

$$\begin{cases} T_{Gen} = -\frac{1}{(K+1)}T_{ICE}\eta_{ps}^q \\ T_{TM} = T_{load} - \frac{K}{(K+1)}T_{ICE}\eta_{pr} \end{cases} \quad (5.30)$$

At this stage, the exponent of  $\eta_{pr}$  is always assumed to be one since the power flow should always go from the planetary transmission to the output shaft. Moreover, the relationship between the ring torque  $T_r$  at the transmission output and the two input torques  $T_{ICE}$ ,  $T_{Gen}$ , is:

$$T_r = -\frac{K}{(K+1)}T_{ICE}\eta_{pr} = KT_{Gen}\eta_{ps}^{-q}\eta_{pr} \quad (5.34)$$

As can be inferred from previous equations, the power split has a complex operation. Therefore, the maximum performance needs to be obtained after several iterations of  $K$  and  $\tau_{FD}$ . As this solution is a combination of parallel and series, both behaviors are seen in this powertrain (Figure 5-21).

The selected motor for the traction is the HTM-3500 with the original power output. The continuous maximum power is 280 hp, and the full rotational speed is 3500 RPM. In the case of the generator, the Toyota Prius generator motor is used due to its capability to operate up to 10,000 RPM. The scaling methodology increased the torque to 120 hp.

The pure EV mode, where only the TM is propelling the vehicle, has the same trend as the series but less wheel torque due to lower TM power and lower differential ratio. However, the truck can achieve the maximum vehicle speed on a flat road and operate on routes with 15% of grade at a vehicle speed of less than 20 km/h. The boost mode depends on the generator's rotational speed. A well-calibrated controller mode makes it possible to achieve a similar curve to a pure EV. The wheel torque is almost above the non-hybrid for all the vehicle range. From the previous analysis, it can be said that all hybrid versions have better performance than the non-hybrid case with the selected components. The electric machines well compensate for the de-rated RCCI ICE to achieve higher wheel torque in almost all conditions. However, some modes have a limitation in the time of use. Therefore, the battery size needs to be deeply studied in real driving cycles to understand the requirements and benefits of fuel consumption and emissions.

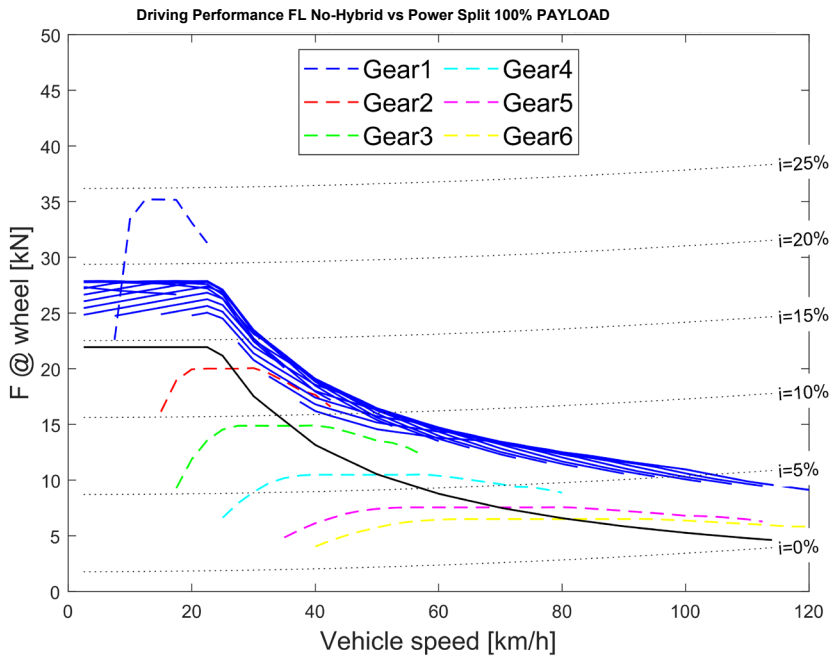


Figure 5-21. Power Split Hybrid performance graph with the two modes and compared against the non-hybrid configuration.

As was mentioned, this architecture allows several operating modes. During traction, the following modes can be activated:

- EV drive: the clutch is closed, TM can drive the vehicle, and if more power demand is also requested Gen can be used (although it is efficiently less convenient due to the mechanical losses of the transmission).
- Input-split: the clutch is opened (the carrier is not grounded), and the ICE can be used as the main power source.
- Input-split circulation: if the battery SoC needs to be kept constant, no battery discharging or charging can take place; this mode is used. This means that the ICE power must suffice for the vehicle propulsion alone. However, due to the mechanical link with Gen, part of its power is converted to electrical energy by the generator motor to

maintain the ICE speed. Without charging the battery, this energy can be entirely transferred directly to TM via the high voltage bus bar. Of course, this mode is limited by the operational capabilities of the electric machines. Although electric circulation encounters two electric/mechanical efficiency losses, it can be repaid by the e-CVT operation that allows setting the ICE on its best efficiency point.

- Input-split boost: TM complements the power output of the ICE to the ring gear to satisfy the driver power demand. The power that the ICE directly transfers to the wheels depends on the split between the mechanical path and the electrical path, which is established by the rotational speed of the Gen.
- Input-split re-circulation: TM supplies negative power to modulate the power output of the ICE to the ring to satisfy the driver demand. This situation may happen when the ICE is made to work in the best efficiency region (i.e. medium-high loads) while the power request at the wheel is low.

During braking events, regenerative braking is operated at the driven wheels linked to the EM/s. In theory, the Gen could also provide extra braking power to support TM in this case.

The RBC control strategy implemented for the power-split HEV combines the thermostat and power follower control strategies. The power output of the ICE and EM is decided mainly on the traction power demand. The battery SoC level is the most critical parameter determining the switching between the operating modes. Like the P2-parallel, the RBC control is structured with a state machine: the main operational modes are the states, and precise rules govern the transitions.

The sub-states "boost" and "circulation" are reported to indicate that under "HEV drive" mode, according to the speed of the Gen and the power output of the ICE, the TM may output positive power to aid the ICE (boost), or it may exert a negative power to absorb the extra ICE power output concerning the one required at the wheels (circulation).

The following Table 5.7 and Table 5.8 give information regarding the ICE, Gen, and TM actuation for each state and the transition rules. The signal of the desired power ( $P_{des}$ ) is calculated by the driver PID control. The abbreviation means:  $T_{des}$  – desired driver torque demand,  $P_{losses}$  – estimated mechanical power losses of the transmission,  $P_{ring}$  – ring output power,  $P_{ICE}^{idle}$  – ICE power output at idle,  $P_{charge}$  – battery charging power request,  $P_{ICE}^{min}$  – minimum ICE power,  $P_{ICE}^{max}$  – maximum ICE power. Also,  $v_{veh,des}$  – desired vehicle speed,  $v_{EM2,max}$  – maximum vehicle speed to enable EV drive,  $SoC_{min}$  – minimum battery SoC,  $SoC_{charge,max}$  – maximum battery SoC,  $\Delta t$  – time spent in a state,  $\Delta t_{min}^{ICE}$  – minimum time for continuous engine operation.

Table 5.7. RBC strategy for the power-split HEV. Main states of operation.

State	Gen torque	TM power	ICE power
Vehicle Stop	0	0	0
EV drive	$\max_{T_{des} > 0} [(T_{des} - T_{EM2}), 0]$	$P_{des} - P_{ring} + P_{losses}$	0
	$\min_{T_{des} < 0} [(T_{des} - T_{EM2}), 0]$		
ICE start	$T_{EM1}$	$P_{des} - P_{ring} + P_{losses}$	$P_{ICE}^{idle}$
HEV drive	$T_{EM1}$	$P_{des} - P_{ring}$	$\min[\max[(P_{des} > 0) + P_{charge} + P_{losses}, P_{ICE}^{min}], P_{ICE}^{max}]$

Table 5.8. RBC strategy for the power-split HEV Rules for the transitions between the states.

States transitions rules		
1	Vehicle Stop – EV drive	$v_{veh,des} > 0$ AND $SoC > SoC_{min}$
2	Vehicle Stop – ICE start	$v_{veh,des} > 0$ AND $SoC \leq SoC_{min}$
3	EV drive – Vehicle Stop	$v_{veh,des} = 0$
4	EV drive – ICE start	$v_{veh,des} > 0$ AND ( $SoC \leq SoC_{min}$ OR $P_{des} > P_{TM,max}$ )
5	ICE start – Vehicle Stop	$v_{veh,des} = 0$
6	ICE start – EV drive	$\Delta t > \Delta t_{min}^{ICE}$ AND $\omega_{ICE}^{act} < \omega_{ICE}^{idle}$ AND $v_{veh,des} > 0$
7	ICE start – HEV drive	$\omega_{ICE}^{act} > \omega_{ICE}^{idle}$ AND $v_{veh,des} > 0$
8	HEV drive – Vehicle Stop	$v_{veh,des} = 0$
9	HEV drive – EV drive	$\Delta t > \Delta t_{min}^{ICE}$ AND $SoC \geq SoC_{charge,max}$ AND $P_{des} < P_{TM,max}$ AND $v_{veh,des} > 0$
10	HEV drive – ICE start	$v_{veh,des} > 0$ AND $SoC \leq SoC_{min}$

The vehicle starts moving under EV mode unless the battery SoC is below a given threshold  $SoC_{min}$ : its value can be calibrated, and it may be higher than the lower boundary of the admissible SoC range (0.4-0.8). When the ICE is switched on, the "ICE start" state is enabled, and the clutch that grounds the engine is opened. The power request to recharge the battery  $P_{charge}$  is produced by a PID controller whose proportional and integral factors must be tuned ( $K_I^{SoC}$ ,  $K_P^{SoC}$ ). Table 5-9 shows the range tested for the abovementioned parameters.

Table 5-9. GA optimization parameters for Power Split Hybrid.

Parameter	Type of parameters	Range Tested
SOC start charge	Control	0.4-0.58
Maximum Speed EV	Control	10-90 km/h
Battery Size	Hardware	5-80 kWh
SOC aggressiveness	Control	0.5-1.0

### 5.4.2. Results

Following the same approach of previous architectures, the power split was optimized under WHVC 50% payload. The target function was optimized with 2400 cases. However, before the case 500 it was possible to achieve CO<sub>2</sub> reduction of over 15% (2025 target) with a final optimum of 17.1% (see Figure 5-22). The optimum was achieved at case 2254 with a final SOC of 0.572. As it is between the constraints (0.55 – 1), it is taken as valid, and the proposed re-calculation is done to adjust the difference between SOC<sub>ini</sub> and SOC<sub>end</sub>.

The sensitivity analysis of Figure 5-23 shows that the most significant parameter is the maximum speed at which EV mode is changed to HEV mode. In the second place, both the SOC at which starts the charging and the charging aggressiveness. Lastly, the battery size (energy storage) shows a minor impact on CO<sub>2</sub> reduction (see Figure 5-24). The EV max is important to the FHEV due to the requirement to return the energy used during the ICE off. The hybrid mode reduces the efficiency difference from the pure electric mode at high speed. Therefore, after 60 km/h, the results are preferred to use the hybrid mode than pure electric. The power-split means the ICE is on in a controlled rotational speed condition by the Gen delivering power to the battery to recharge and the wheels to propel the vehicle.



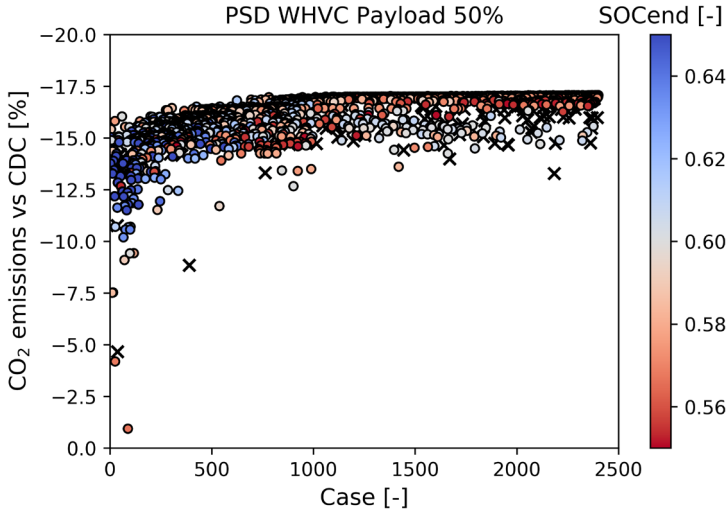


Figure 5-22. Power Split Hybrid genetic algorithm cases evolution in terms of average fuel consumption and final battery state of charge (SOC<sub>end</sub>).

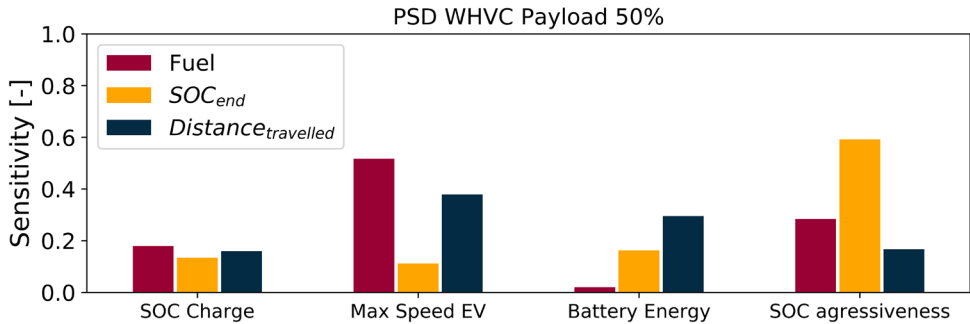


Figure 5-23. Power Split Hybrid parameters sensitivity in terms of final average fuel consumption and final battery state of charge (SOC<sub>end</sub>).

Despite the battery size not showing a high impact in the sensitivity analysis, the optimum battery size is 42 kWh. In addition, it is required at least 25 kWh to be 1% closer to the optimum. As in this work, the battery price is not included in the optimization can be seen in high CO<sub>2</sub> reduction with a battery size of 13 kWh (-15.4%) or 25 kWh (-17.0%).

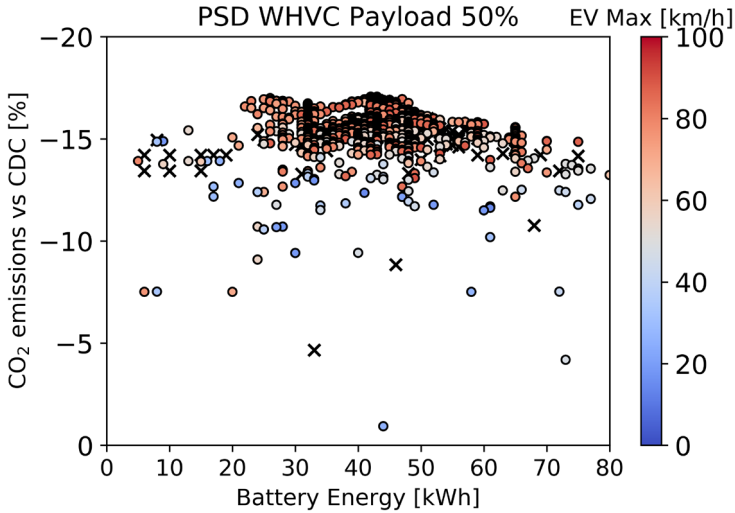


Figure 5-24. Power Split Hybrid battery size and gear shift strategy influence the final fuel consumption benefits against CDC non-hybrid.

The ICE behavior in the power split is different from the other powertrains because it can operate in the best efficiently continuously line (see Figure 5-25a). The main change from the Series hybrid is that instead of changing by steps, the control sets the power required depending on the SOC level, and the Gen manages to set the ICE speed by controlling the torque delivered. The traction motor is shown in Figure 5-25b. It works at a wide rotational speed (0-3000 RPM), and for 50% payload, it uses 70% of the positive torque and almost 100% of the regenerative braking limit (negative torque). Due to the large size of the TM, this powertrain can recover a large energy quantity from braking. Lastly, the Gen (see Figure 5-25c) has an entirely different behavior with significant rotational speeds in both directions and almost constant negative torque output. These conditions are required to maintain the engine in the operative line shown in Figure 5-25a. In addition, during the ICE off period, the Gen rotates in free mode. This explains the large negative speed with 0 torque.

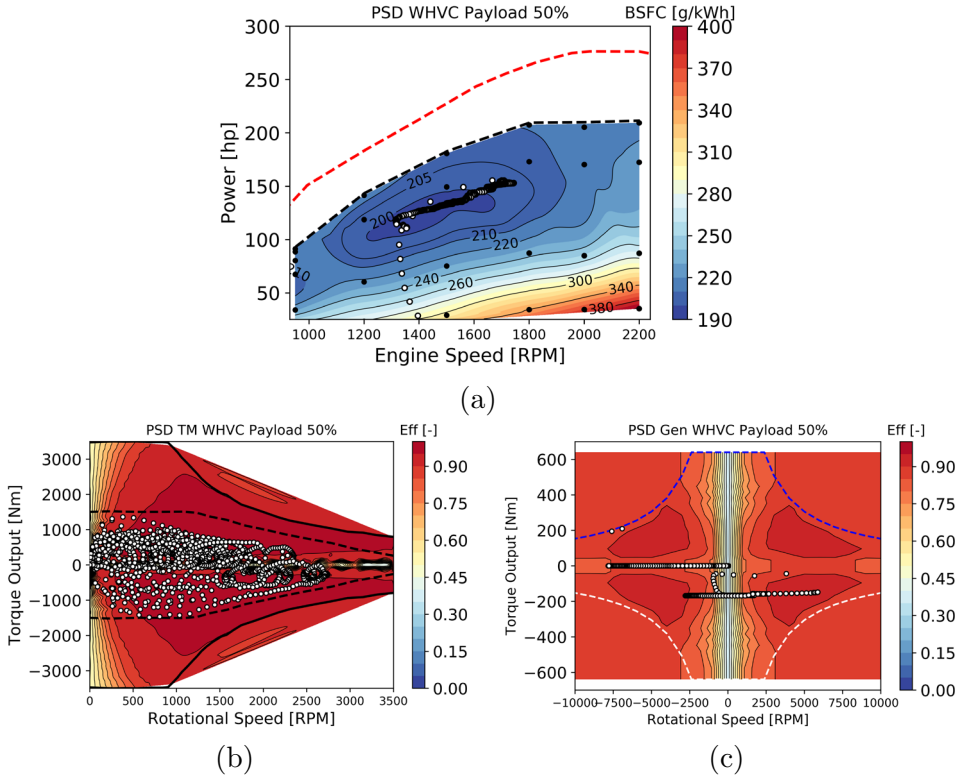


Figure 5-25. ICE RCCI operative conditions (a) and electric machines operation with Gen (b) and TM (c) for WHVC 50% payload in Series hybrid.

The lithium-ion storage device's main parameters are shown in Figure 5-26. The battery is discharged until 0.41 because the power split uses the EV mode until high speeds (80 km/h) and then starts charging to reach the initial SOC (0.6). The spikes show a regenerative braking event when they are positive and high power delivered to the wheels when they are positive. The cell C-rate is between  $\pm 5$  due to the large final battery package size.

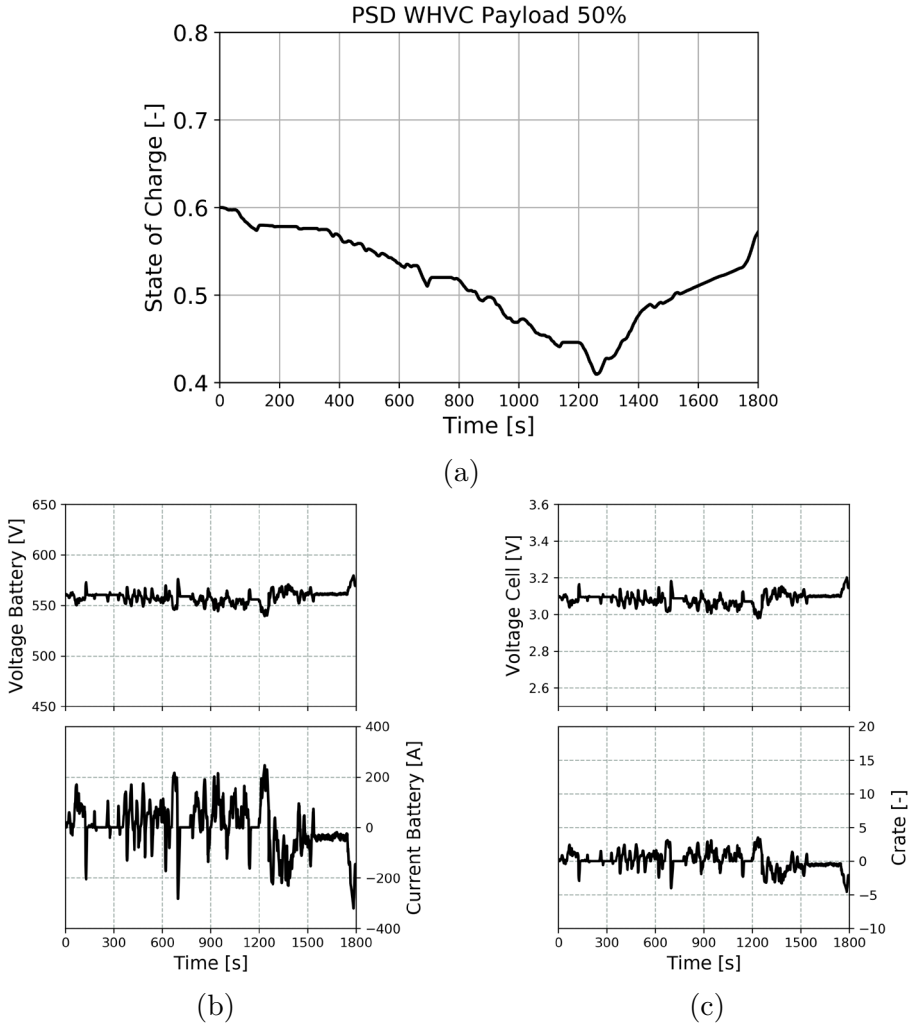


Figure 5-26. Battery and individual cell parameters during WHVC with 50% payload for Power Split hybrid.

The optimum control and hardware parameters are presented in Table 5-10. The next sub-section compares the architectures by using the optimum cases and simulated in 4 driving cycles and 3 payload conditions.

Table 5-10. GA optimum parameters for Power Split Hybrid.

Parameter	Type of parameters	Final Opt Value
SOC start charge	Control	0.410
Maximum Speed EV	Control	81 km/h
Battery Size	Hardware	42 kWh
SOC aggressiveness	Control	0.643

## 5.5 Comparison between architectures

The optimum powertrain design is listed in Table 5-11 for the three FHEV architectures studied in this chapter.

The ICE operative conditions for WHVC and 100% payload is depicted in Figure 5-27. It is important to note that, for confidentiality reasons, the BSFC CDC map was not represented as a non-hybrid case. On the contrary, the DMDF map was presented. As the main purpose of this graph is to see the operation of the different architectures, this figure still meets the abovementioned objective. The non-hybrid DMDF and P2 have operative points in several engine speeds and almost all loads. The main difference between these two architectures is that the P2 reduces the operative conditions at low loads. In this sense, the optimization of the energy management system, by controlling the gear shift strategy and the electric machine operation, allows concentrating the operative conditions in a range of intermediate engine speed (950 RPM to 1500 RPM) and ICE high load zone, where it is more efficient. In addition, it is possible to see that the engine de-rating from 280 hp to 210 hp does not represent any limitation at full payload.

On the other hand, the series and power split show a different operation behavior. The series is only operated in two operative conditions, 1200 RPM and 125 hp and 1900 RPM and 170 hp, both in the optimum fuel consumption zones (below 210 g/kWh). The level 3 of charge, which corresponds to 210 hp, is not used due to the high energy content of the battery selected.

However, it would be used for more demanding cases such as the Flat driving cycle with long routes. The power-split has similar behavior but uses a line of operative conditions that are under the best BSFC line. The transient variation is more significant than the series for the power split but more controlled than in the P2. This behavior is thanks to the dedicated generator that controls the ICE by the decoupling from the wheel speed. In advanced combustion concepts, this is a benefit because it helps solve issues such as combustion control and high EGR rate changes, among other parameters.

*Table 5-11. Optimum powertrain set-up for FHEV P2, series, and power split.*

Type of parameters	Parameter	Architecture	Optimum
Hardware	EM Max continuous power	P2	70 hp
		Series	210/210 hp
		Power Split	280/120 hp
	Final drive ratio	P2	5.29
		Series	
		Power Split	
	Gear box ratio	P2	3.36/1.91/1.42/1.0/0.72/0.62
		Series	3.5/0.9
		Power Split	3.33
	Battery Size	P2	10 kWh
		Series	41 kWh
		Power Split	42 kWh
ICE Max power	P2	210 hp RCCI	
	Series		
	Power Split		
Gear Shift Control	Gear shift strategy	P2	1462 RPM
		Series	36 km/h
		Power Split	-
Supervisory Control	Pure EV mode	P2	40 km/h
		Series	-
		Power Split	81 km/h

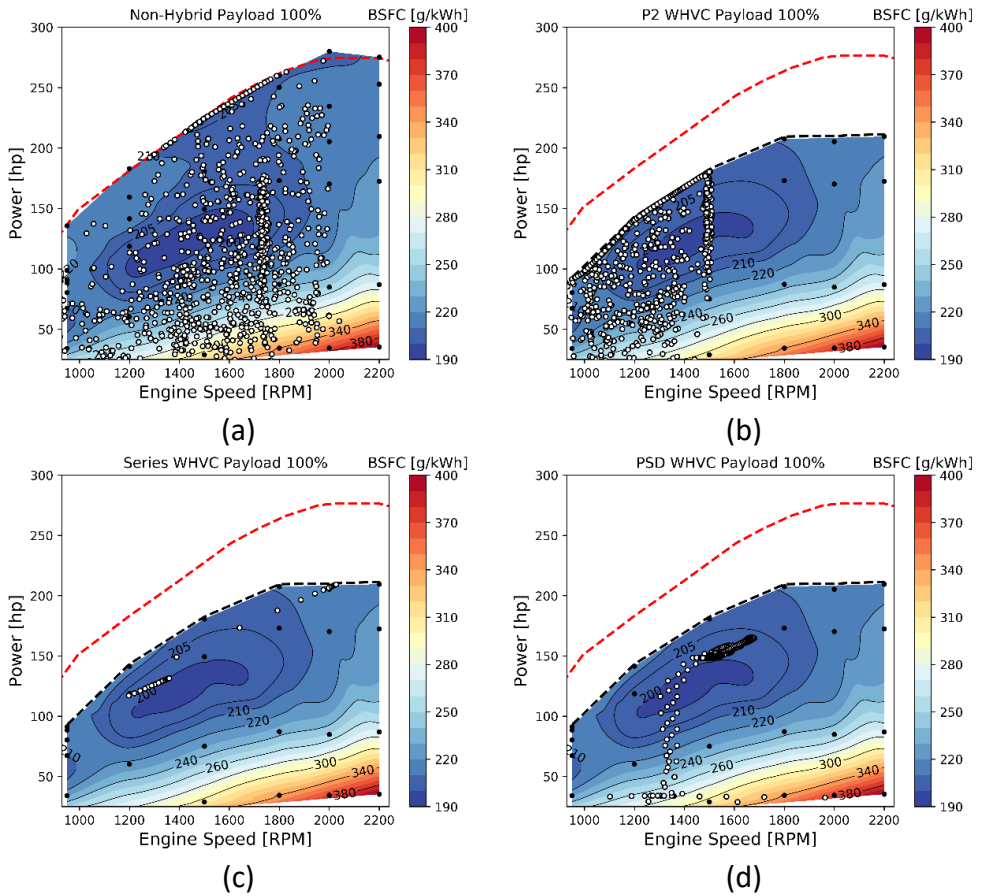


Figure 5-27. ICE operative conditions for WHVC and 100% payload in the four powertrains: non-hybrid DMDF (a), P2 (b), Series (c), and Power Split (d).

The optimum powertrain selection is studied in the other three driving cycles at 0%, 50%, and 100% payload. Figure 5-28a shows the tank-to-wheel CO<sub>2</sub> emissions reduction concerning the baseline. In addition, the 2025 European Target (15% with respect to 2019) is marked in a dashed line. All the hybrid powertrains show CO<sub>2</sub> reductions when the truck is unloaded. In addition, the urban case also has the highest benefits in all load conditions. The P2 has the largest benefits compared to the powertrain architectures,

only improved in the series and power split at low payload and large combined cycles (local and flat). The engine-out NO<sub>x</sub> and soot emissions are shown in Figure 5-28b, and Figure 5-28c depicts the benefits of using RCCI combustion. For all the cases, the emissions achieved the EU VI legislation limits and an improvement of around 90% with respect to the baseline.

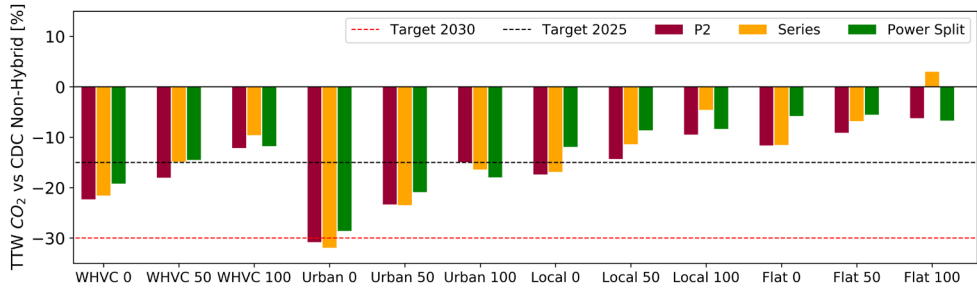
Figure 5-29 includes an energy analysis to investigate the benefits of fuel consumption (TTW CO<sub>2</sub> emissions). Figure 5-29a depicts the ICE average brake thermal efficiency of the cycle. It is possible to see that the biggest ICE improvements are at low payload conditions where the non-hybrid operates in low efficient zones. In addition, due to the totally or partially uncoupling of the wheels, the Series and Power Split achieve almost 42% global BTE independently on the payload.

Figure 5-29b shows the energy recovered during braking with respect to the tractive energy necessary to meet the speed during acceleration. The urban cycle is the only cycle that increases the recovery with the payload. The other cycles, in general, show the highest recovery at 0% payload. The P2 is the powertrain with the lowest brake recovery due to electric machine limitations. However, Figure 5-29c shows that using one electric machine as the case of P2 reduces electric losses compared to the Series and Power Split, which require a traction motor and generator separately. Although the electric losses consider the battery losses, it is not seen a large variation between powertrains.

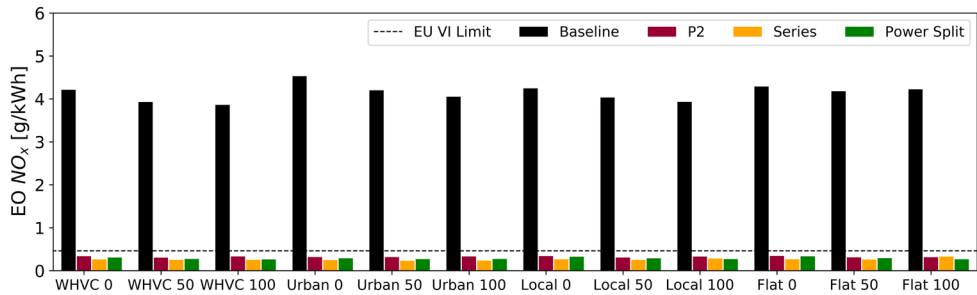
One crucial point is the amount of gasoline used in the combustion concept with respect to the diesel amount. This is evaluated using the gasoline fraction (GF). When the GF is higher than 50%, more gasoline than diesel is used in the driving cycle. Figure 5-30 shows that the P2 is the hybrid powertrain with the lowest GF due to the transient operation in the low load zone of the map (lowest GF). For the P2, the GF only overpasses the 50% in full payload conditions. The Series and Power Split used more gasoline than diesel, with an average of around 75%. This result suggests that if a renewable fuel is used in the low reactivity port, the hybrid powertrain can



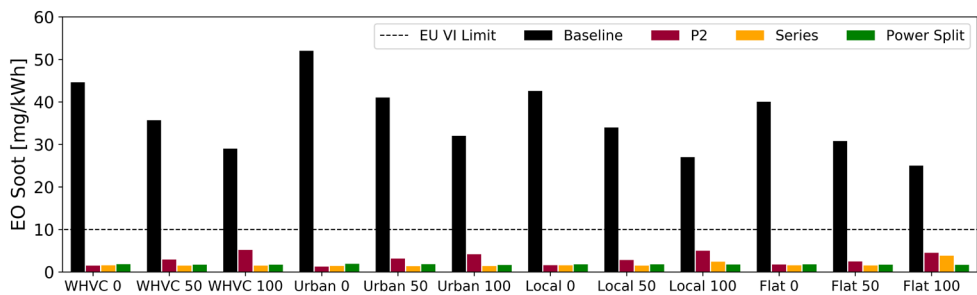
help to large well-to-wheel CO<sub>2</sub> reduction. Synthetic gasoline is a potential e-fuel due to the renewable pathway in fuel production.



(a)

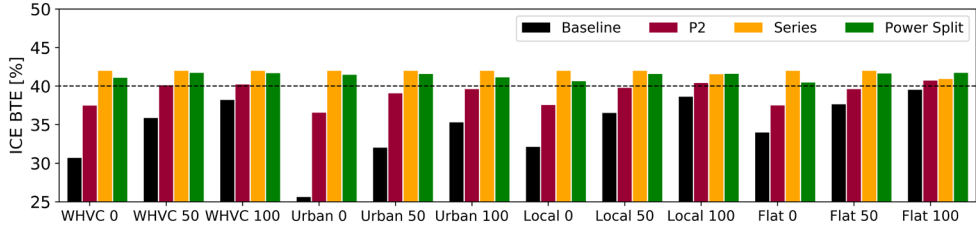


(b)

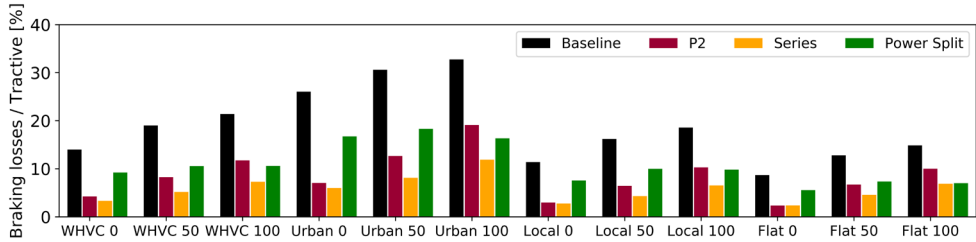


(c)

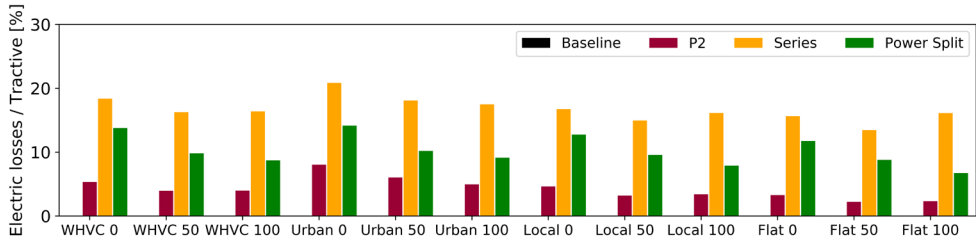
Figure 5-28. TTW CO<sub>2</sub> emissions benefits (a), engine-out NO<sub>x</sub> emissions (b), and engine-out soot emissions (c) for four driving cycles and three payload conditions.



(a)



(b)



(c)

Figure 5-29. Engine average efficiency (a), percentage of energy recovery during braking with respect to the total tractive energy (b), and electric losses (c) for four driving cycles and three payload conditions.

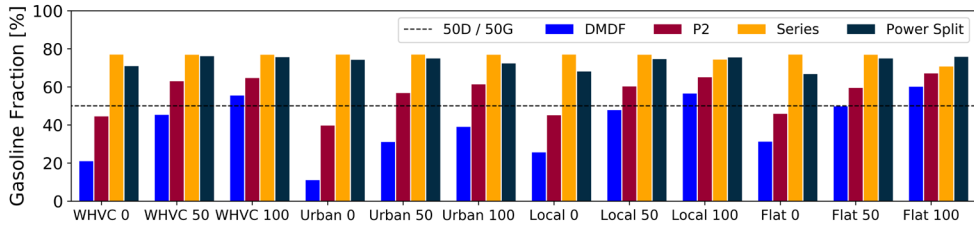


Figure 5-30. Gasoline fraction for four driving cycles and three payload conditions.

To summarize the results, a spider graph with the main components selected and performance values is depicted in Figure 5-31. The performance results are the average value for the 12 driving conditions tested. The series and power split used the highest electric machines (the spider shows the total power of the traction motor and generator) and battery size in terms of components. Specifically, due to the separated ICE-wheels configuration, the series requires two large EM, and the optimum battery size is 42 kWh. At the same time, the P2 only uses an EM seven times lower than the series and a battery size of only 8 kWh. The fuel energy savings are similar for all the hybrids, consuming around 10% lower fuel than the non-hybrid version. Similar behavior is seen for the tailpipe CO<sub>2</sub> emissions.

The other two main emissions that are wanted to be reduced using RCCI combustion are NO<sub>x</sub> and soot. The hybrid versions promote engine-out emissions levels under the EU VI normative (NO<sub>x</sub><0.4 g/kWh and soot <10 mg/kWh). The dual-fuel dual-mode combustion (DMDF) non-hybrid case is also added to have a complete vision of the powertrain potential. This concept uses the same operative condition as the RCCI ICE and changes to more diffusive combustion from 210 hp to 280 hp. The DMDF allows reaching the NO<sub>x</sub> limit. However, due to the diffusive operation zone at high load, the average engine-out soot for all the DMDF conditions is 15 mg/kWh, above the EU VI limit. Therefore, the hybrid powertrain allows using the RCCI map with almost negligible soot emissions. This allows the removal of the particle filter device (or at least simplifying), reducing the after-treatment system costs.

A final summary of the performance results at homologation conditions (WHVC at 50% payload) is included in Table 5-12.

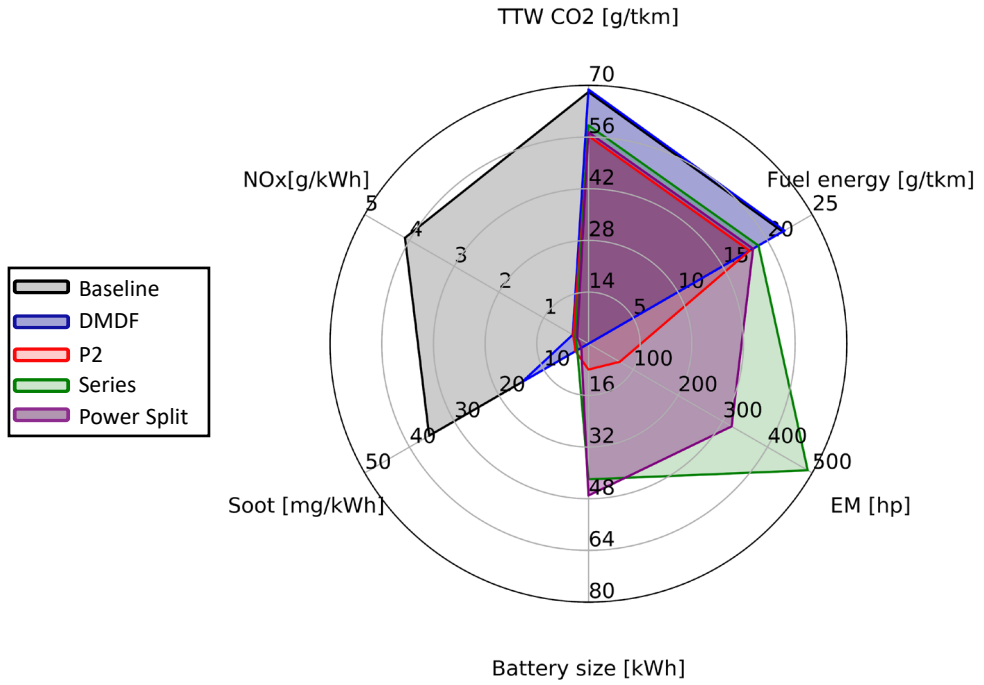


Figure 5-31. Spider graph resume for the results average under 4 driving cycles and 3 payload conditions.

Table 5-12 Summary results in homologation conditions (WHVC and 50% payload) including WTW CO<sub>2</sub> analysis.

Parameter	Non-hybrid		P2	Series	Power Split
	CDC	DMDF	RCCI	RCCI	RCCI
BSFC	244 g/kWh	0.9%	-17.3%	-14.5%	-16.5%
BSNO <sub>x</sub>	3.9 g/kWh	-91%	-91%	-92%	-92%
BSsoot	36 mg/kWh	-93%	-93%	-95%	-92%
BSHC	0.11 g/kWh	2882%	2791%	2127%	1744%
BSCO	0.47 g/kWh	1567%	1228%	786%	917%
CO <sub>2</sub> TTW	59.2 g/tkm	-0.2%	-18.0%	-14.8%	-17.1%
CO <sub>2</sub> WTW	71.9 g/tkm	-1.4%	-19.3%	-16.7%	-19.9%

## 5.6 DOC behavior in the full hybrid truck

After analyzing different powertrain architectures in terms of energy consumption, CO<sub>2</sub> emissions, and NO<sub>x</sub>/soot engine out, this subsection analyzes the DOC's effectiveness in converting the HC and CO engine-out emissions. A similar approach performed for the P0 is made in this subsection with the P2. Only one architecture is studied for the brevity of the manuscript. The P2 is selected due to the high potential to increase powertrain efficiency.

The P2 hybrid truck operating in the homologation driving cycle WHVC with different payloads is modeled without and with EHC. Figure 5-32a shows the engine on-off states when 50% of the payload is applied. This case represents the optimum calibrated case to fulfill the EUVI NO<sub>x</sub> and soot emissions with the lowest CO<sub>2</sub> emissions at engine-out conditions. The number of starts for the EHC was 12 starts. The optimization does not

consider the HC and CO emissions. Therefore, the number of starts was optimized to achieve the minimum CO<sub>2</sub> emissions. It is interesting to remark that adding the chemistry simulation in the catalyst has significantly increased the computational time from 0.1 to 4 times the real-time.

Figure 5-32b shows the HC emissions before and after the OC. The first 600 s are responsible for a large amount of HC emissions. This is a direct consequence of the low OC temperature depicted in Figure 5-33. The ICE-off time due to the urban phase makes the case without the heater to produce 70% of the total HC emissions. When the EHC is added with 5kW under the same calibration of the case without EHC, the HC emissions are strongly reduced. It is possible to achieve the EUVI legislation due to the fast increase in the OC wall temperature. In both cases, the EUVI CO targets can be easily achieved. Therefore, it can be concluded that one of the main limits to implementing the RCCI combustion with hybrid architectures is the HC emissions.

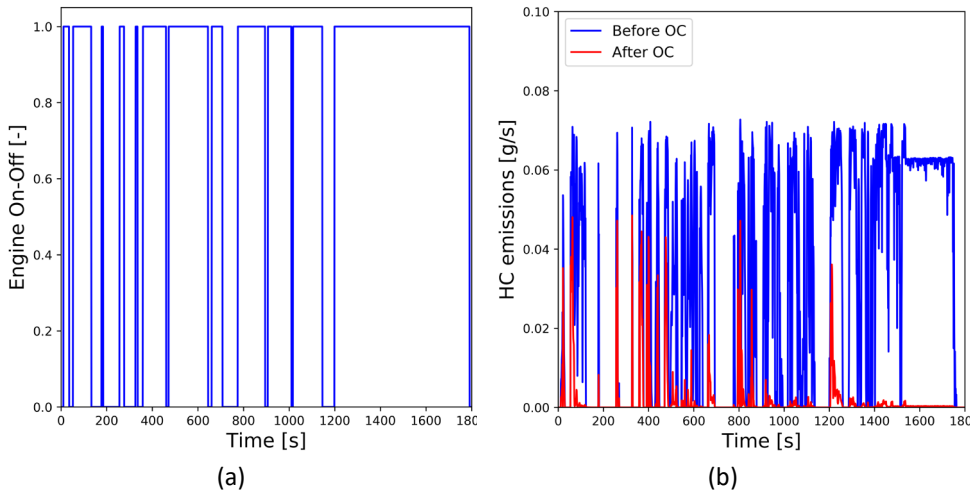


Figure 5-32. Engine on-off (a) and HC emissions before/after the OC (b) for the WHVC with 50% payload in an RCCI P2 hybrid Truck without EHC.

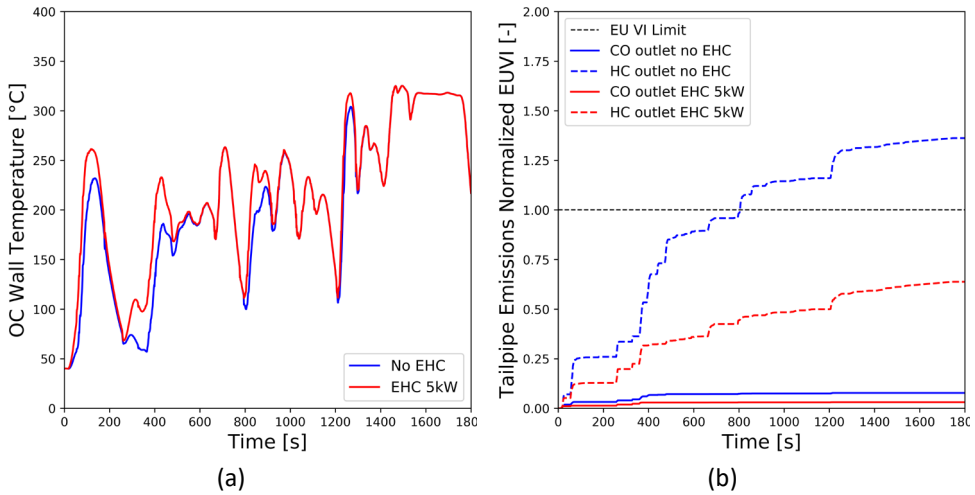


Figure 5-33. OC wall temperature (a) and HC and CO normalized emissions with respect to EUVI (b) for the WHVC with 50% payload in an RCCI P2 hybrid truck without and with the EHC.

However, the use of the EHC impacts the final fuel consumption/ $\text{CO}_2$  emissions. Table 5-13 shows that, on average, the use of the heater with 5 kW increases the  $\text{CO}_2$  emissions by 1.0% with respect to the case without the EHC. The advantage of the EHC is that it allows achieving the EUVI limits for all the emissions ( $\text{NO}_x$ , soot, CO, and HC) for the homologation case while still providing a  $\text{CO}_2$  reduction of 15.7% (the European target for 2025 is to achieve 15% of  $\text{CO}_2$  reduction for Heavy-Duty transportation with respect to 2020). It is important to note that the empty truck conditions (0% payload) are the worst scenario due to the low energy requirement. A previous study of the research group showed that the non-hybrid version does not achieve the EUVI HC limits under empty cargo due to the operation only at low BMEP conditions [108]. The hybridization enables improvements in this scenario with respect to the non-hybrid case since it allows to use of the ICE at high engine loads. However, without a dedicated calibration to reduce the ICE on-off times, the HC limit is not achieved for 0% of payload even with an EHC, as shown in Table 5-13.

Table 5-13. Summary of the main parameters for the RCCI P2 hybrid truck without and with the EHC in the WHVC with different payloads.

Case	Tailpipe CO <sub>2</sub> emissions vs CDC non-hybrid	HC emissions [g/kWh]	CO emissions [g/kWh]
0%	-22.3%	0.66	2.34
0% EHC	-20.6%	0.20	0.27
50%	-18.0%	0.19	0.27
50% EHC	-17.5%	0.09	0.11
100%	-12.1%	0.10	0.17
100% EHC	-11.2%	0.06	0.10

\*Red colour means values out EUVI limit or below 2025 European CO<sub>2</sub> target.

In this sense, a DoE with all the hybrid calibration parameters, including the OC in the simulation. Unlike the previous results, a controller for the ICE on-off time is added. This control forces the ICE to maintain the same state condition for a set time, reducing the number of on-off events. However, this time cannot always be achieved due to the small electric machine (ratio of hybridization is 25%) and battery package (10 kWh, 5% of an equivalent pure electric truck) used. When the desired wheel torque exceeds the EM maximum torque, or the battery is full or depleted, the ICE will change the state without following the on-off minimum time rule. In any case, this parameter helps to control the ICE behavior.

Figure 5-34 shows the new calibration results in HC tailpipe emissions (after the OC) versus the ICE start times and the ICE control parameter for both cases, with and without the EHC. The new calibration allows to achieve the EUVI HC limit by reducing the number of the engine also starts in the case without the EHC. Despite the fact that the ICE minimum time helps to decrease the number of engines starting after 100 seconds (transition from red to a blue color bar), the effect is null due to driving cycle requirements for this payload condition. The range of starts was between 6 and 22, and the best cases were achieved below 10 starts. It is seen that reducing the



number of starts reduces the HC tailpipe emissions as the case of the steps. However, the main difference is that the further increase in the number of starts from 20 does not improve the results. Therefore, increasing the control time to reduce the number of starts is the best option in real transient conditions.

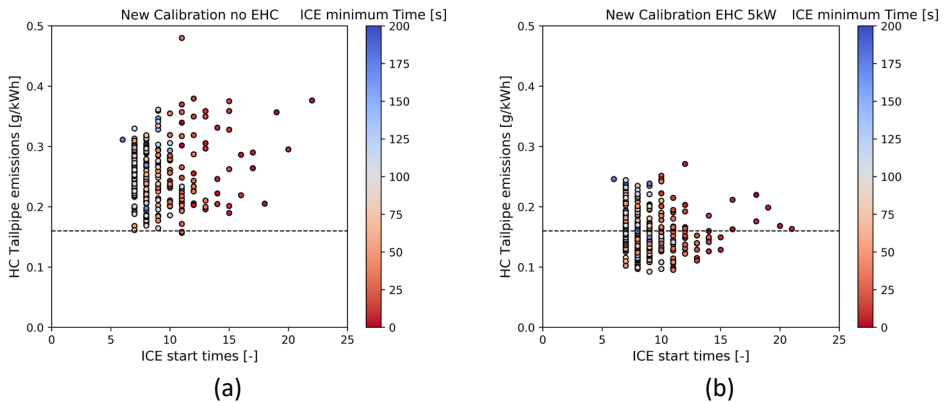


Figure 5-34. HC tailpipe emissions (after the OC) against the ICE start times and ICE minimum time control for the new calibration without EHC (a) and with EHC 5 kW (b).

Figure 5-35 shows that the CO<sub>2</sub> tailpipe emissions increases by reducing the ICE starts and the use of the EHC. Both strategies reduce the improvements with respect to the baseline case of around 1.25% of the CO<sub>2</sub> emissions. Therefore, if both strategies are applied, the penalties achieve a 2.5% of CO<sub>2</sub> reduction. However, the EHC impact allows not to need a high decrease in ICE starts. The lowest CO<sub>2</sub> emissions and HC and CO under EUVI limits differ only in a 0.7% CO<sub>2</sub> penalty.

To summarize, Table 5-14 shows the effect of controlling the ICE on-off times and using the EHC in other payloads. For the most challenging condition (0% payload), the new calibration allows achieving the EU VI limits. These results suggest that a hybrid RCCI truck can reach the EUVI limits for all the emissions under homologation conditions for the entire range

of payloads with the OEM OC and an EHC with 5kW of heat addition with a dedicated controller.

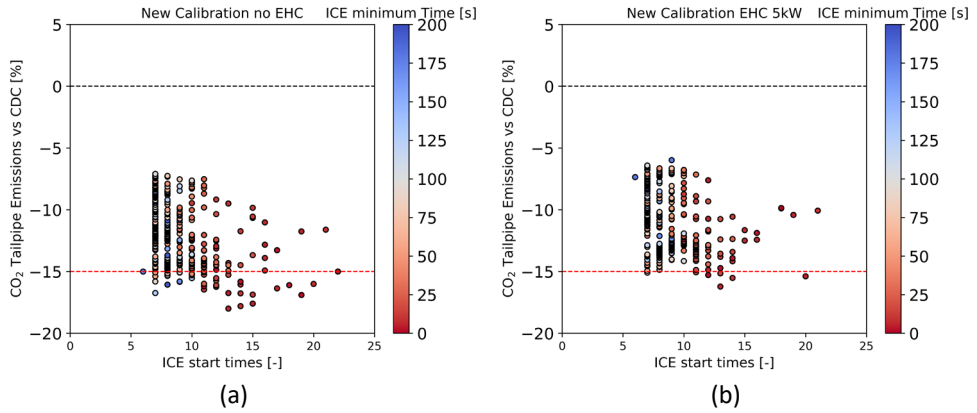


Figure 5-35. Fuel consumption against the ICE start times and ICE minimum time control for the new calibration without EHC (a) and with EHC 5 kW (b).

*Table 5-14. Summary of the main parameters for the RCCI P2 hybrid Truck without and with EHC in the WHVC with different payloads with a new dedicated OC calibration.*

Case	Tailpipe CO <sub>2</sub> emissions vs CDC non-hybrid	HC emissions [g/kWh]	CO emissions [g/kWh]
0% New cal	-19.2%	<b>0.33</b>	0.39
0% EHC New cal	-21.1%	0.14	0.30
50% New cal	-16.9%	0.16	0.22
50% EHC New cal	-16.2%	0.10	0.20
100% New cal	<b>-12.2%</b>	0.09	0.10
100% EHC New cal	<b>-11.2%</b>	0.07	0.09

\*Red colour means values out EUVI limit or below 2025 European CO<sub>2</sub> target.

## 5.7 Conclusions

This chapter analyzed the potential of different full hybrid architectures in representative European Medium-Duty trucks. The ICE was calibrated in RCCI combustion mode with the target of reducing ATS. Moreover, the results are compared with the OEM diesel truck. In addition, the components and control strategy optimization were done with a genetic algorithm under homologation conditions. The optimum was evaluated in 12 different conditions, including several payloads and real driving cycles.

The main findings are summarized as follows:

- The hybrid configurations allow achieving EU VI engine-out NO<sub>x</sub> and soot emissions without SCR and DPF for all conditions by following a de-

rating ICE strategy. The performance analysis shows higher wheel forces than the OEM truck. This goal was not achieved yet by any other combustion technology in a Heavy-Duty truck.

- The hybrid platforms allow achieving from 14% (series and power split) to 18% (P2) of tailpipe CO<sub>2</sub> reduction with respect to the CDC non-hybrid case. These results are closer to or even higher than the 2025 European Target for the Heavy-Duty sector.
- The higher electric machine for series and power split does not show a considerable advantage over the P2 for the conditions tested. The extra regenerative braking between 70 hp and 280 hp of the electric machine is limited.
- The HC and CO emissions are the main drawback of this technology. However, the DOC investigation demonstrates that using a heater in the ATS can solve this issue in almost all payloads.

# Chapter 6

## Dual-fuel combustion concept for 2030 targets

### **Content**

---

6.1 Introduction.....	314
6.2 Synthetic fuels for WTW CO <sub>2</sub> reduction.....	314
6.2.1. Synthetic high reactivity fuel.....	315
6.2.1.1. Methodology .....	316
6.2.1.2. Results .....	316
6.2.2. Synthetic low reactivity fuel .....	329
6.2.2.1. Methodology .....	330
6.2.2.2. Results .....	333
6.3 Potential of dual-fuel combustion for EUVII.....	338
6.3.1. Methodology .....	338
6.3.2. Results.....	342
6.4 Plug-in Hybrid towards 2030 LCA CO <sub>2</sub> targets .....	347
6.4.1. Methodology .....	348
6.4.2. Results.....	355
6.5 Conclusions.....	369

## 6.1 Introduction

From the previous discussions presented in both chapter 4 and chapter 5, it was evidenced that the dual-mode concept implemented in a mild and full hybrid powertrain is able to reduce CO<sub>2</sub> emissions while meeting EUVI limits. However, the European Commission will implement further CO<sub>2</sub> and pollutant emissions reduction in the next years. As explained in Chapter 1, 2030, it was affirmed the EU a 30% of CO<sub>2</sub> reduction with respect to 2019, and for 2050 it claims zero emissions targets. There are some indications that the TTW base will be changed to WTW or LCA. This will allow for the introduction of technologies such as synthetic fuels or a fair comparison of plug-in technology such as BEV or PHEV.

In addition, EUVII is going to be implemented. Despite not having clear pollutant limits for EUVII, there is some prediction that the pollutant emission will be reduced by 50% with respect to EUVI [33].

In this chapter, both targets (CO<sub>2</sub> and pollutant emissions) are studied by the use of synthetic fuels, plug-in hybrid, and dedicated engine recalibration for hybrids. Moreover, tools such as WTW or LCA analysis are introduced to more fairly contrast the different technologies.

## 6.2 Synthetic fuels for WTW CO<sub>2</sub> reduction

Synthetic fuels can have the double potential of reducing CO<sub>2</sub> emissions on a Well-to-Wheel (WTW) basis and pollutant emissions as particle matter. In this Thesis, OME<sub>x</sub> is investigated as a potential replacement for Diesel while Methanol for replacing the Gasoline. Therefore, the study is divided into two sub-sections differentiated by high reactivity fuel (HRF) or low reactivity fuel (LRF).

### 6.2.1. Synthetic high reactivity fuel

Oxymethylene ethers (OMEx) main characteristics are the high oxygen content (47.6 % m/m) and no C-C bonds, which allow the avoidance of particle matter at engine-out. The dual-fuel concept allows changing the setting parameters to reduce NO<sub>x</sub> engine-out too. The fabrication process of this fuel is based on carbon capture. In addition, if renewable electricity is used, the experts predict ultra-low WTW emissions. As was shown in Chapter 3, the OMEx used in this work was estimated to have a WTW index of  $-67.2 \text{ gCO}_2/\text{MJ}_{\text{fuel}}$  [224]. This means that saving in CO<sub>2</sub> is done only by fabrication. The CO<sub>2</sub> associated with the combustion in the engine for propelling the vehicle will be calculated in this sub-section.

The potential of this fuel with gasoline as LRF is studied in the already developed full hybrid powertrains shown in Chapter 5. In particular, P2 parallel, Series, and Power Split hybrid are studied for OMEx-gasoline. A scheme of the proposed idea is shown in Figure 6-1.

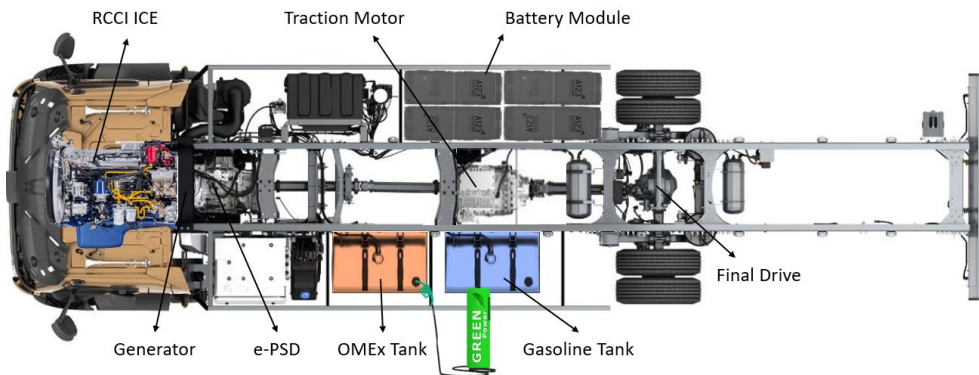


Figure 6-1. Volvo FL Power Splitt FHEV truck fueled with OMEx as High Reactivity fuel. Similar scheme can be repeated for P2 and Series hybrid.

### 6.2.1.1. Methodology

Chapter 3 presented a full calibration map with OMEx replacing the Diesel in the MD8 six-cylinder engine. It was possible to achieve NO<sub>x</sub> EUVII in all the engine maps, including up to 350 hp and negligible soot emissions. These maps are changed in the place of the D-G maps used in Chapter 5. The 0D vehicle model is re-optimized under WHVC 50% payload. The decision of re-optimization of the control parameters was adopted because the ICE best efficient zones change from D-G to OMEx-G. Therefore, the control parameters can change too. However, the battery size is maintained to simplify the comparison between fuels.

### 6.2.1.2. Results

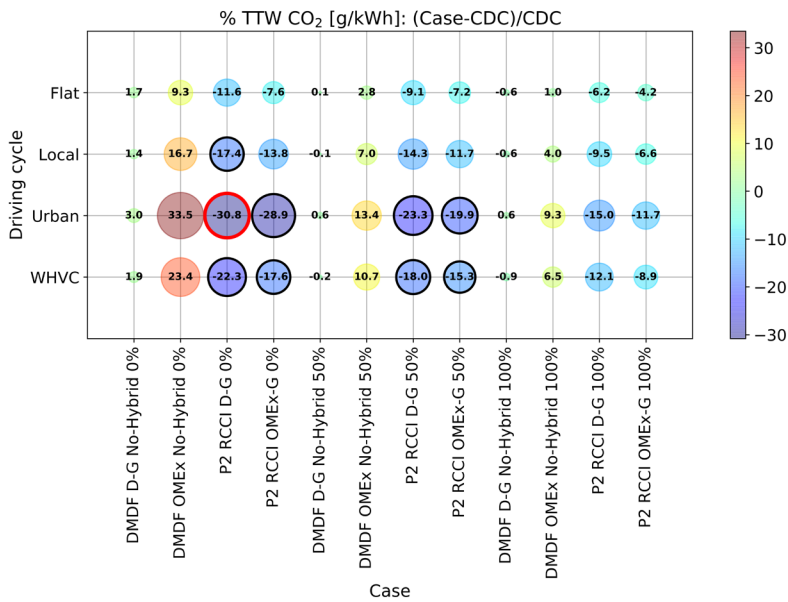
The optimization of the full hybrid platforms was performed in homologation conditions, and then the 12 cases were run with the optimum value. Figure 6-2 shows the results in terms of tailpipe emissions (TTW CO<sub>2</sub>), gasoline fraction, and liter consumed for the P2 FHEV. These last two parameters are important to understand the effect of the lower heating value and density of the OMEx. Considering the twelve conditions, the OMEx-Gasoline P2 hybrid allows reducing 12.8% of TTW CO<sub>2</sub> with respect to the CDC non-hybrid with 15.3% at homologation conditions. Despite the fact that the benefits for OMEx-G are lower than in the D-G P2 hybrid (3.0%), it achieves the 2025 target in homologation conditions and allows benefits up to 28.9% in the urban case with an empty truck. The main disadvantage for the OMEx-G with respect to D-G in the hybrid architecture is low payload due to the worse brake thermal efficiency in low engine load.

The GF graph (see Figure 6-2) shows evidence that the gasoline amount used in OMEx-Gasoline calibration operating under hybrid P2 is higher than in the non-hybrid case. This is due to the operation at a high load by the hybrid, where the calibration increments the LRF injection. This allows reducing the volume fuel consumption gap between conventional and synthetic fuels. For homologation conditions, the OMEx-G P2 consumes



10.3% more volume than the CDC non-hybrid. However, the non-hybrid case is 34.4% more fuel volume than the baseline. This evidences a clear disadvantage of using OMEx in non-hybrid powertrains due to the effect on vehicle range and storage space, and it will be difficult to achieve a price where the use of OMEx can be feasible due to the large volume of fuel consumption. Therefore, the hybridization together with dual fuel combustion tackles one of the most challenging aspects of the use of OMEx in transport.

To summarize the fuel volume consumption results, on average of the 12 cases: the OMEx-G non-hybrid consumes 55.5% more volume, and the OMEx-G P2 hybrid 12.7% more fuel volume than the CDC non-hybrid. As a reference, the D-G P2 is 8.2% less volume than the baseline case.



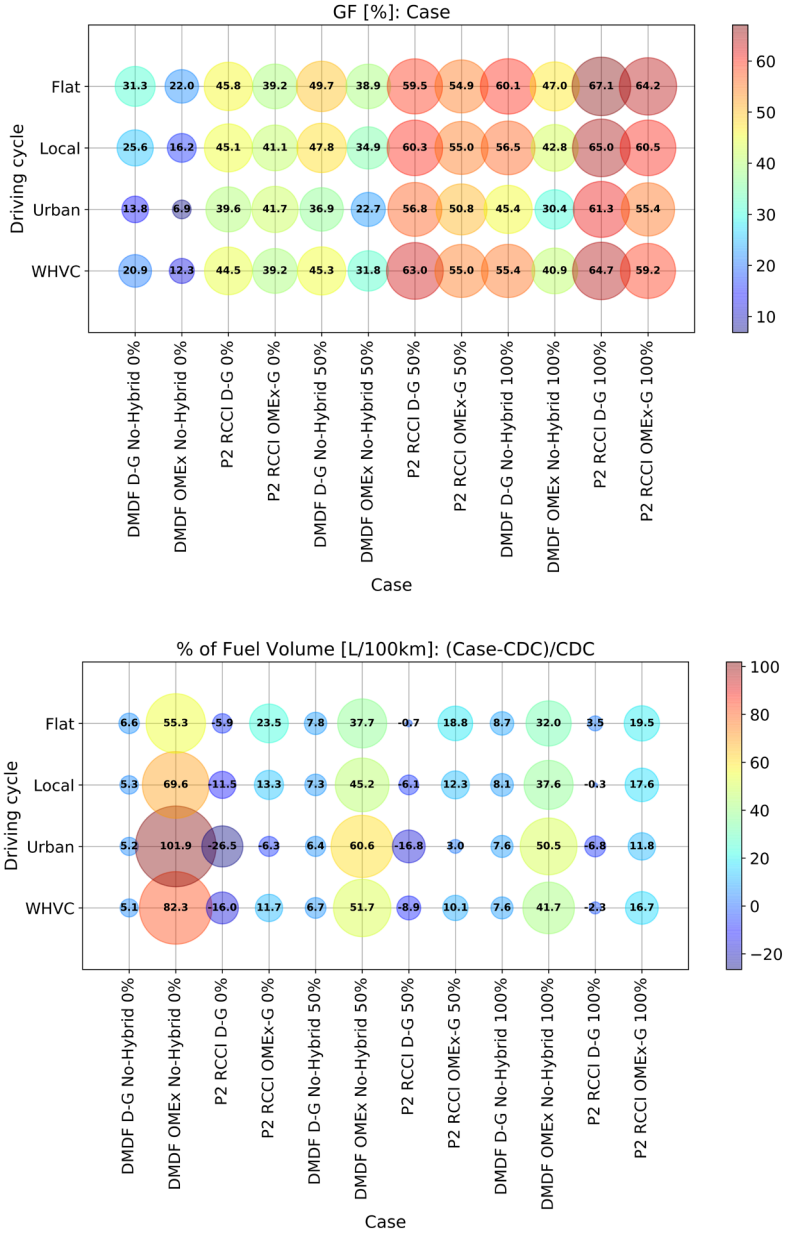
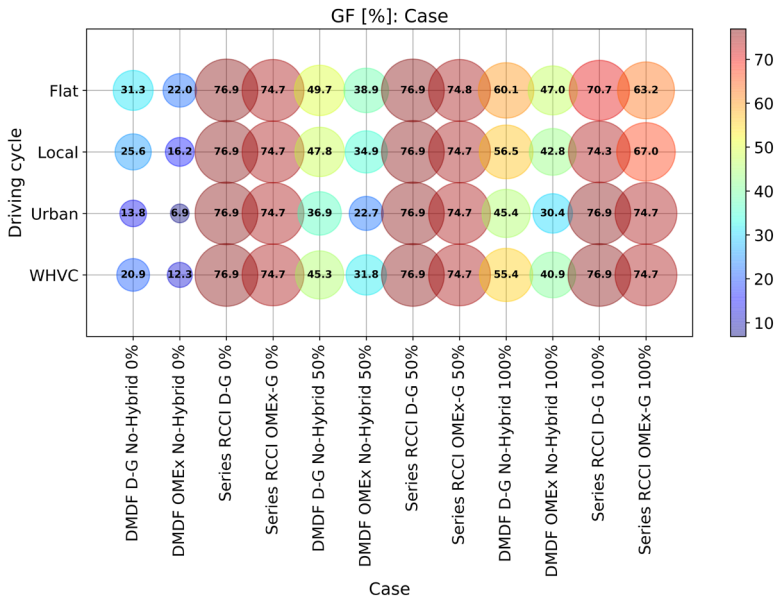
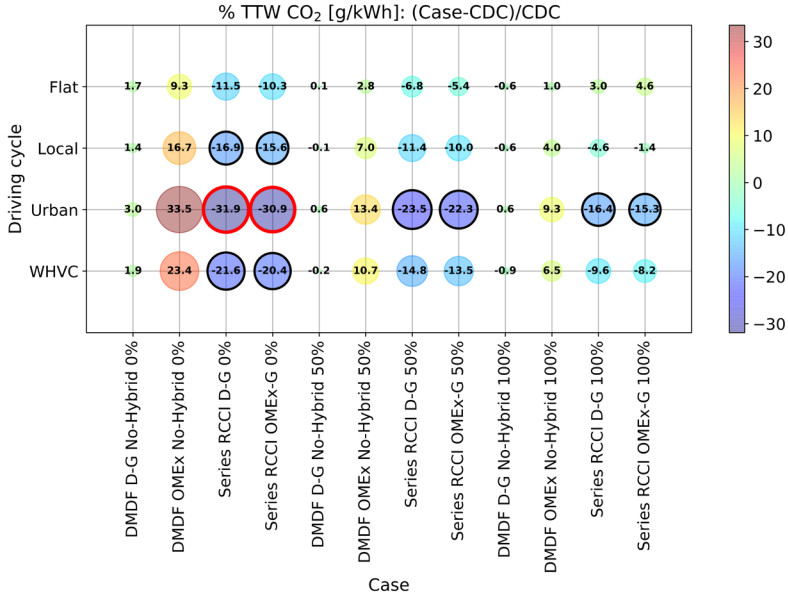


Figure 6-2. Driving cycles results (TTW CO<sub>2</sub>, GF and Fuel volume consumption) for P2 operating with RCCI OMEx-Gasoline. The results are compared against CDC non-hybrid (baseline). In addition, the DMDF Diesel-

*Gasoline non-hybrid and RCCI Diesel-Gasoline P2 are added for comparison (results chapter 5).*

The Series hybrid was also optimized for the new fuel. Figure 6-3 shows the tailpipe CO<sub>2</sub>, gasoline fraction, and volume fuel consumption. Different from P2, this hybrid architecture uses an even higher gasoline fraction due to the concentration of ICE operative conditions in a narrow, highly efficient zone. As the RCCI is more efficient where the premix combustion is present, the LRF is higher consumed than the HRF. For the case of OMEx-G, the GF is always higher than 80%. Therefore, the volume fuel consumption in the case of the Series hybrid is lower than in the P2 for OMEx-G.

On average, of the 12 cases for Series hybrid, the TTW CO<sub>2</sub> emission is reduced by 12.4%, and the volume fuel consumption is increased by 6.6% for OMEx-G with respect to CDC non-hybrid. The Series Hybrid shows a reduction of the gap between fuels (D-G to OMEx-G) than the seen for P2. The Series hybrid only increases 1.4% in TTW CO<sub>2</sub> emission when passing from conventional fuel to synthetic fuel instead of 2.7% of P2. It can be explained by the increase of the peak BTE from 43% in OMEx-G to 42% in D-G. As the series is able to use for a long time in this operative condition, it improves the behavior of the synthetic fuel.



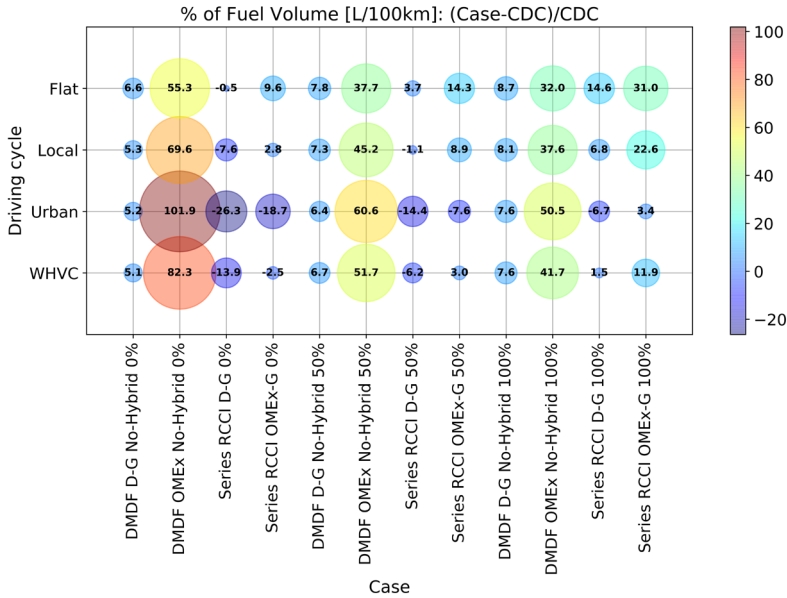
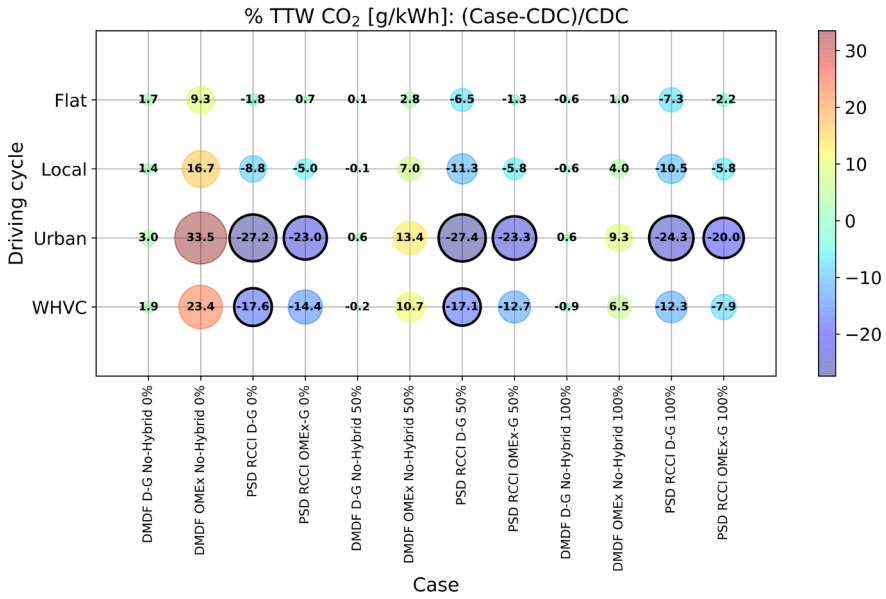


Figure 6-3. Driving cycles results (TTW CO<sub>2</sub>, GF and Fuel volume consumption) for Series operating with RCCI OME<sub>x</sub>-Gasoline. The results are compared against CDC non-hybrid (baseline). In addition, the DMDF Diesel-Gasoline non-hybrid and RCCI Diesel-Gasoline Series are added for comparison (results chapter 5).

Lastly, the power split is optimized. Figure 6-4 shows that, as with the previous hybrid powertrains, losses in terms of TTW CO<sub>2</sub> emissions are seen introducing OME<sub>x</sub>. At homologation conditions, it is reduced a 4.4%, while in the twelve cases, from 14.3% to 10.1% of CO<sub>2</sub> reduction for power split D-G and OME<sub>x</sub>-G, respectively. Therefore, around 4% worst in tailpipe emission is the power split with OME<sub>x</sub>. The main reasons are the worse energy to CO<sub>2</sub> conversion of OME<sub>x</sub> and a decrease in the gasoline fraction (GF). As can be seen in Figure 6-4, the GF is lower than in the case of D-G due to the use of an extended engine load region as in the case of P2. The series is maintained in almost a single operation condition. It can achieve up to 80% GF. At the same time, the power split was on average 65.7% for OME<sub>x</sub>-G.

This also impacts the fuel volume consumption where the power split OMEx-G was, on average, 7.2% higher than CDC non-hybrid. Compared to P2 and series, the power split is in the middle in terms of fuel volume consumption, being the best in the Series due to the high GF achieved.



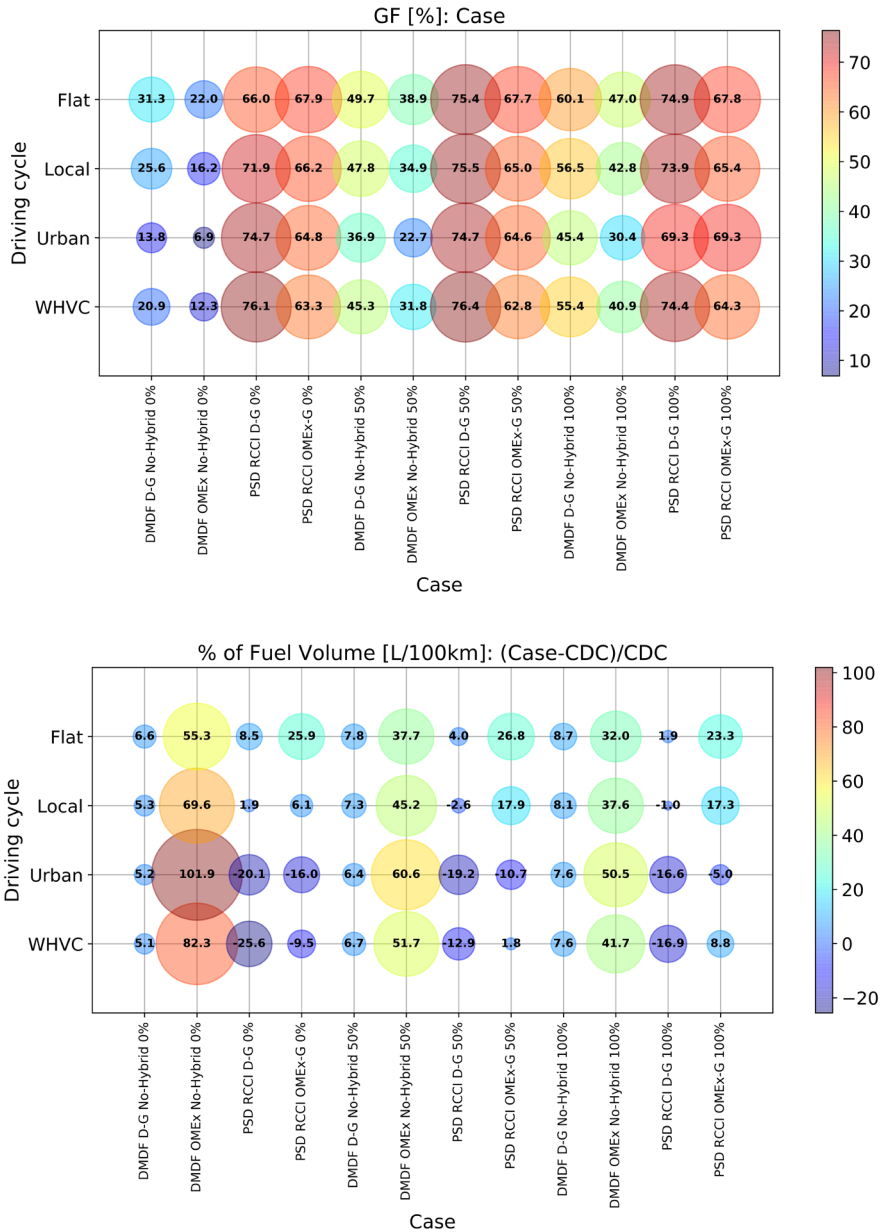
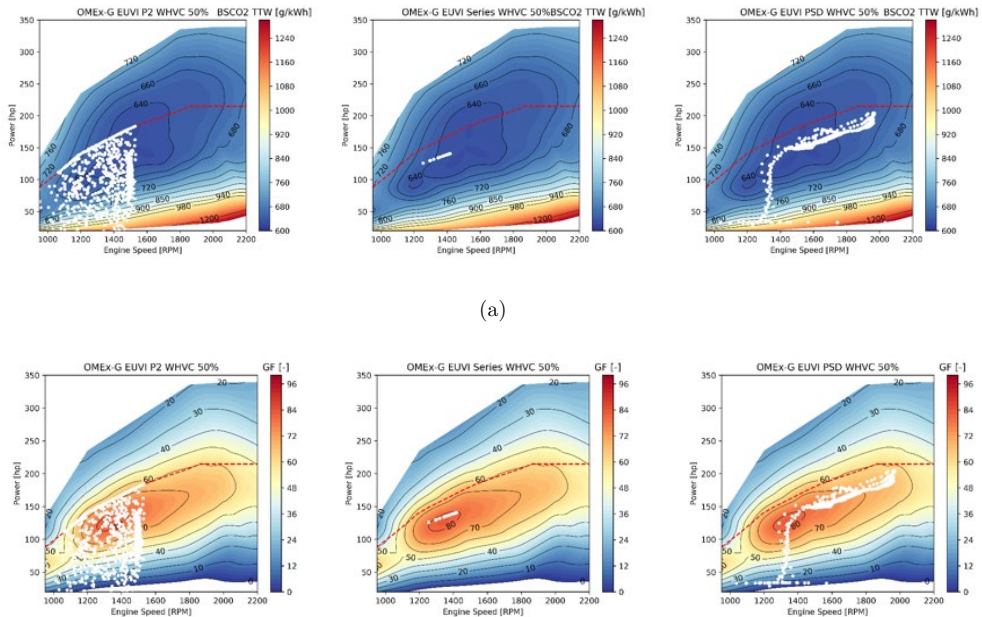


Figure 6-4. Driving cycles results (TTW CO<sub>2</sub>, GF and Fuel volume consumption) for Power Split operating with RCCI OMEx-Gasoline. The results are compared against CDC non-hybrid (baseline). In addition, the

*DMDF Diesel-Gasoline non-hybrid and RCCI Diesel-Gasoline Power Split are added for comparison (results chapter 5).*

In terms of operative conditions, Figure 6-5 shows that the behavior of the engine is completely different for the three architectures. The P2 operates at a wider rotational speed with points of low and high load. On the other hand, the series concentrates the operation in a single zone that corresponds to the most efficient (lowest fuel consumption and TTW emissions). As is a dual fuel concept, the WTW emissions depend on the GF and the WTT CO<sub>2</sub> of OME<sub>x</sub> production. The WTW map shows that where the OME<sub>x</sub> is more present or where the concept is more efficient is finding the islands of minimum WTW CO<sub>2</sub> emissions. However, optimizing to obtain the minimum WTW emissions is dangerous. The concept can suffer limitations in terms of vehicle range and OME<sub>x</sub> price because the fuel volume will drastically increase. Therefore, in this work, the TTW CO<sub>2</sub> optimization is maintained, and the benefits in terms of WTW CO<sub>2</sub> emissions will be only computed and analyzed.



(a)



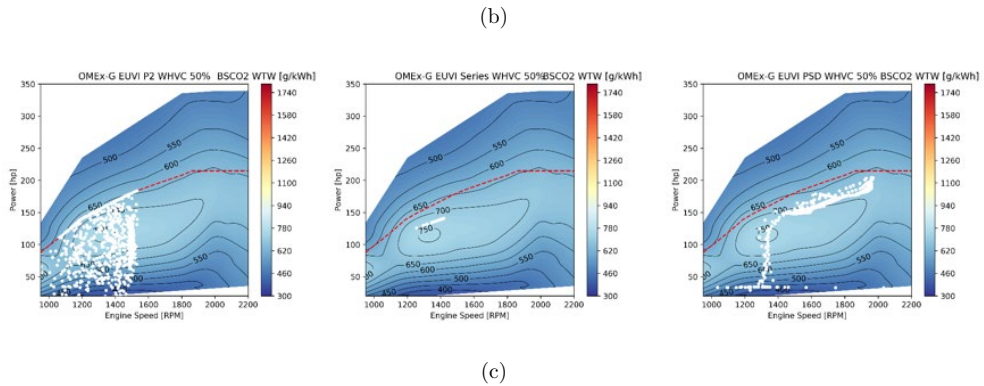
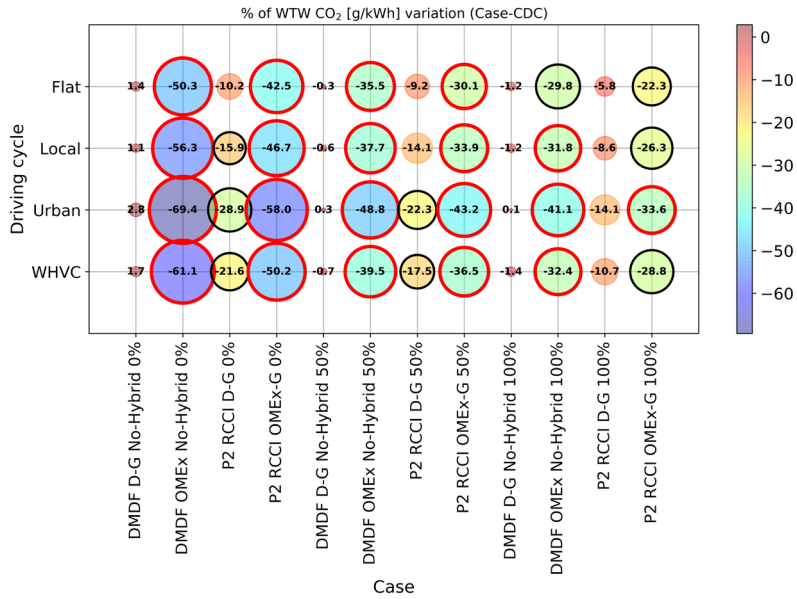


Figure 6-5. Operational conditions for P2, Series, and Power Split over the calibration maps of TTW (a), GF (b), and WTW CO<sub>2</sub> emissions with OMEx-Gasoline.

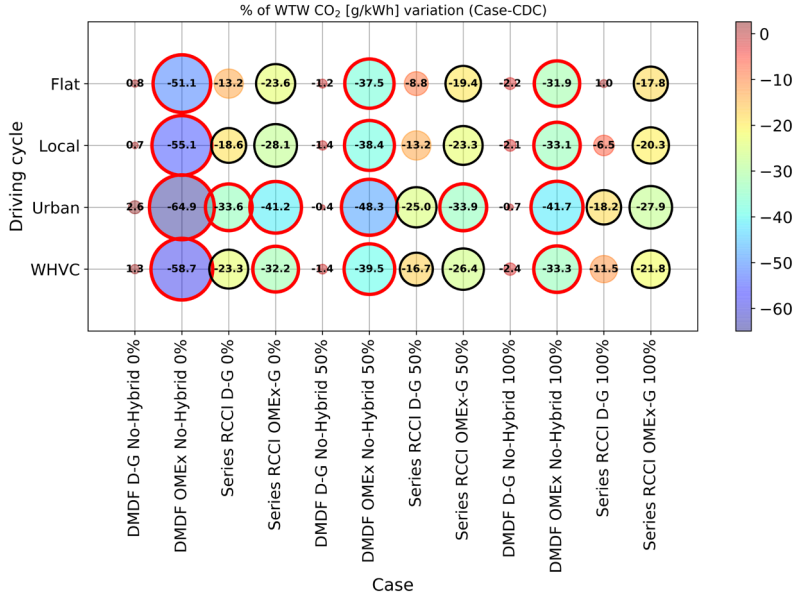
The results in terms of WTW CO<sub>2</sub> are presented in Figure 6-6 by using the WTT CO<sub>2</sub> values for each fuel presented in Chapter 3. Figure 6-6a shows the benefits of using OMEx for the P2 FHEV case. This powertrain with synthetic HRF can achieve 38% CO<sub>2</sub> savings compared with the baseline (CDC Non-Hybrid). The best case is in urban conditions due to the combination of an efficient powertrain and the negative WTT OMEx associated CO<sub>2</sub>. It is important to note that the OMEx-G non-hybrid achieves ultra-high WTW CO<sub>2</sub> savings due to the large amount of OMEx used. As was shown previously, the non-hybrid uses the low engine zones that are mainly OMEx injection (low GF). On average, the non-hybrid achieves 44.5% WTW CO<sub>2</sub> reduction. However, have limitations such as large fuel volume and energy consumption as well as high TTW CO<sub>2</sub> emissions. Therefore, both concepts using OMEx can achieve the 2030 CO<sub>2</sub> target, but it seems that the P2 FHEV has a better balance between all the output parameters.

Similar behavior can be seen for Series, and Power Split WTW CO<sub>2</sub> emissions in Figure 6-6b and Figure 6-6c, respectively. The Series with the lower OMEx consumption was able to reduce on average 26.3%, while the power split 27.9% with respect to CDC non-hybrid. As the WTW CO<sub>2</sub>

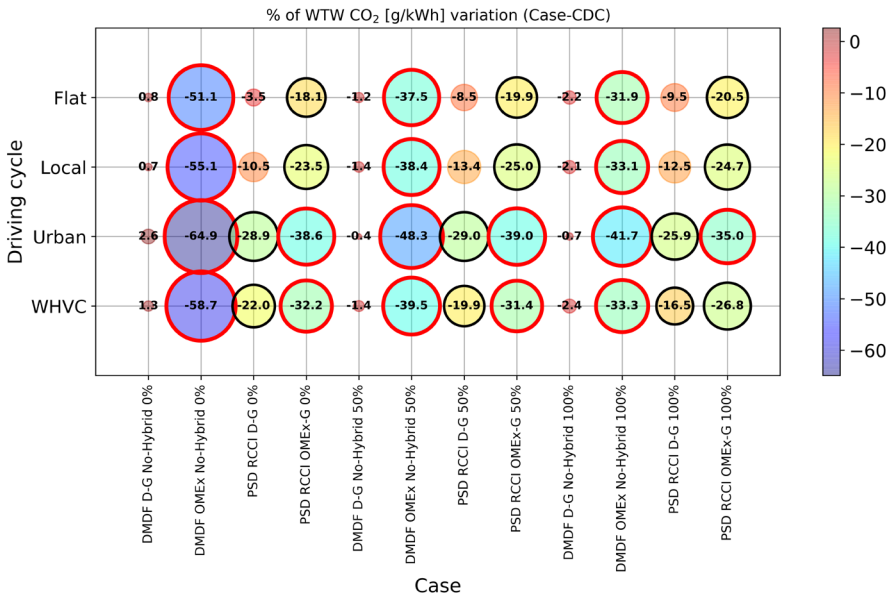
reduction mainly depends on the amount of synthetic fuel injected, the P2 is the best case for the hybrid powertrain for this application.



(a)



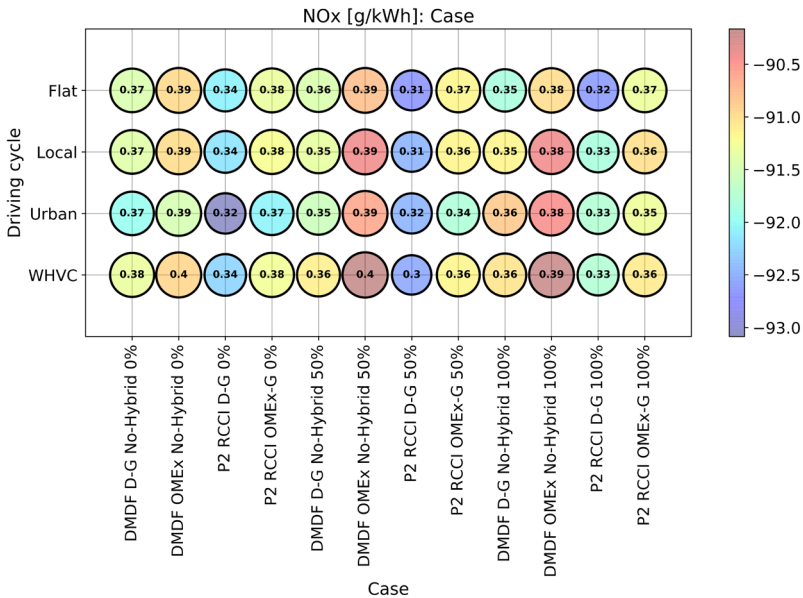
(b)



(c)

Figure 6-6. Driving cycles results in terms of WTW CO<sub>2</sub> emissions for P2, Series and Power Split operating with RCCI OME<sub>x</sub>-Gasoline. The results are compared against CDC non-hybrid (baseline). In addition, the DMDF Diesel-Gasoline non-hybrid and RCCI Diesel-Gasoline Power Split are added for comparison.

The NO<sub>x</sub> and soot with OME<sub>x</sub>-Gasoline and Diesel-Gasoline under different vehicle concepts and the driving situation are shown in Figure 6-7. For brevity of the manuscript, only P2 is shown from the FHEV perspective. The other hybrid powertrain has similar behavior. The Dual Fuel concept with both fuels allows a high NO<sub>x</sub> reduction, and the engine out with EUVI meets all conditions. The main difference is in terms of soot emissions. OME<sub>x</sub>-G achieves zero soot in all concepts. The D-G calibration in hybrid architectures achieves EUVI due to the de-rating of the ICE to 210 hp. The next subsection will be studied the use of synthetic fuel but in the low reactivity injector as a replacement for the gasoline.



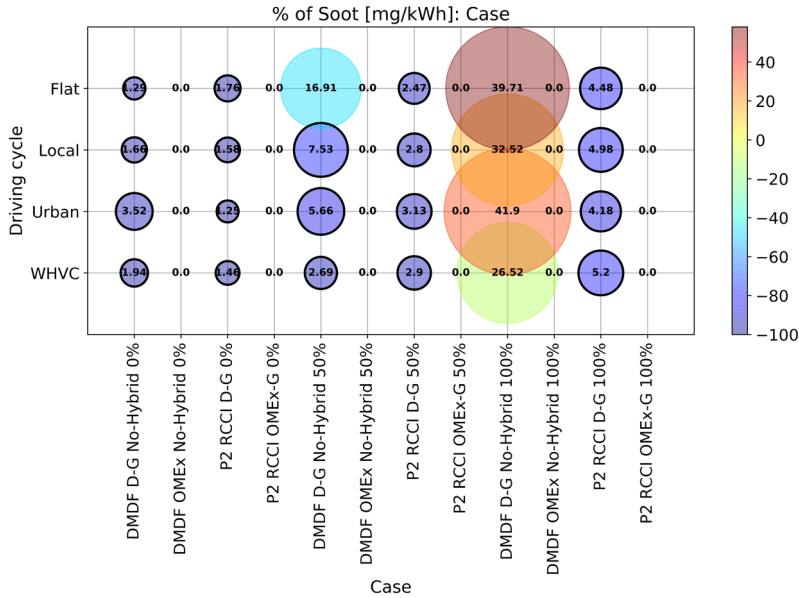


Figure 6-7. Driving cycle results (engine-out NO<sub>x</sub> and soot) for P2 operating with RCCI OME<sub>x</sub>-Gasoline. The results are compared against CDC non-hybrid (baseline). In addition, the DMDF Diesel-Gasoline non-hybrid and RCCI Diesel-Gasoline P2 are added for comparison (results chapter 5).

### 6.2.2. Synthetic low reactivity fuel

As an alternative to gasoline, methanol is tested due to the low CO<sub>2</sub> associated with the fabrication and the high oxygen content (49.9% m/m) in the molecule that makes it suitable for reducing soot emission. As for the OME<sub>x</sub>, the LHV of methanol is low (19.93 MJ/kg instead of 42.4 MJ/kg of gasoline). Therefore, the dual-fuel concept makes sense to reduce the fuel volume consumption and injection times with respect to a single fuel combustion concept.

The Series hybrid powertrain is used to reduce ICE calibration time. As was seen in Chapter 5, two to three operative conditions are enough to have a high reduction of CO<sub>2</sub>. Therefore, an ICE experimental calibration

with Diesel-Methanol is performed dedicated to the Series hybrid. After the experimental campaign, the obtained operative conditions are inserted in the 0D vehicle model, and a re-optimization of the concept is performed. In the case of OMEx-Gasoline, the control parameters of the FHEV are optimized by a genetic algorithm while the battery size is kept fixed to be comparable with the other fuels. Figure 6-8 shows the concept to be used in this section.

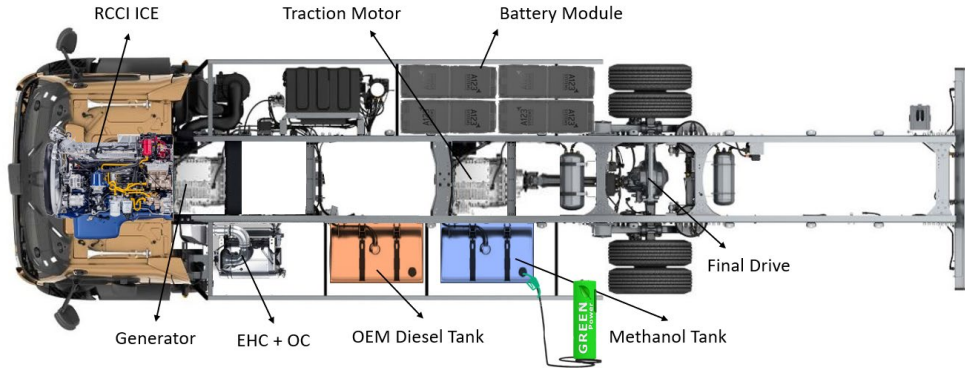


*Figure 6-8. Volvo FL Series FHEV truck fueled with Methanol as Low Reactivity fuel.*

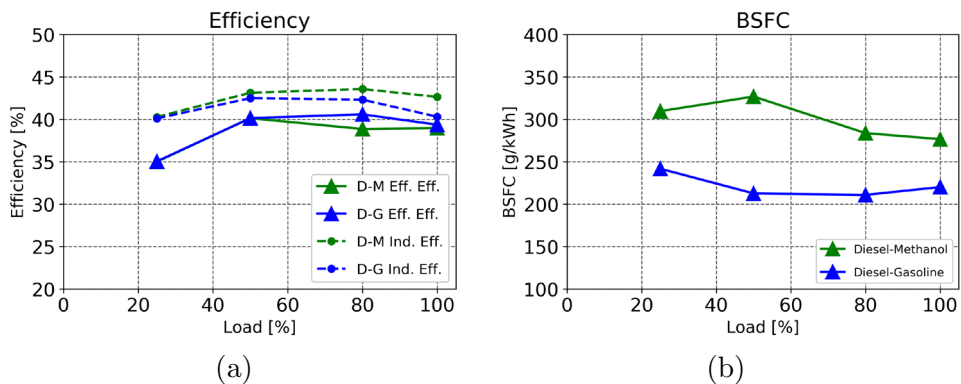
### 6.2.2.1. Methodology

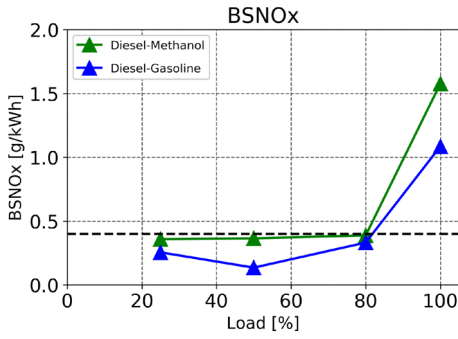
For the experimental ICE calibration with Diesel-Methanol, LP and HP EGR lines are used. The only modification in the test bench is the gasoline deposit that is changed by the methanol deposit. Other hardware such as injectors, fuel pumps, or control components is maintained as the D-G.

All the operative conditions selected are at 1800 RPM and between 0 to 100% engine load. The decision of these cases was performed because it is possible to achieve 210 hp of engine power output under fully premixed combustion mode. This condition of max power of the Series hybrid is necessary for cases of high payload or demanding driving cycles. Another rotational speed that could be taken due to the potential of high efficiency

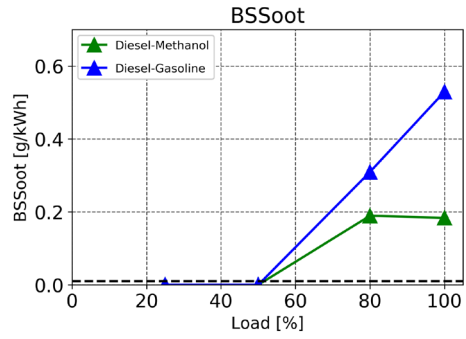
under dual-fuel combustion is 1500 RPM. However, due to hardware limitations, the maximum power is 180 hp under RCCI. The calibration of four operative conditions is performed by the sweep of EGR rate, GF, and injection timing. The main target of the ICE calibration was to achieve the same power output as the conventional fuels and achieve EUVI NO<sub>x</sub> and soot emission limits.

The results in Figure 6-9 show a similar BTE between the two calibrations with a peak after 50% engine load of 40%. The mass fuel consumption was higher for D-methanol due to the low LHV of the synthetic fuel proposed. Moreover, the NO<sub>x</sub> and soot emissions at engine out were maintained similar to D-G and under the EUVI limit. The problems appear at higher engine loads (80% and 100%) because the premixed combustion cannot be maintained, and diffusive combustion appears. Therefore, NO<sub>x</sub> and soot increased for both fuel combinations. The high oxygen content of methanol allows to reduce the soot emission with respect to D-G, but the zero soot emissions of OME<sub>x</sub> are not achieved. This is because the oxygen content of HRF benefits soot formation, while LRF creates an environment that is less prone to soot but not prevented. It is not a concern to this work because the 80% and 100% engine load are out of the 210 hp necessary for the Series hybrid concept. The results are shown to demonstrate the advantages and drawbacks of methanol and the limitation of its application in a non-hybrid vehicle.

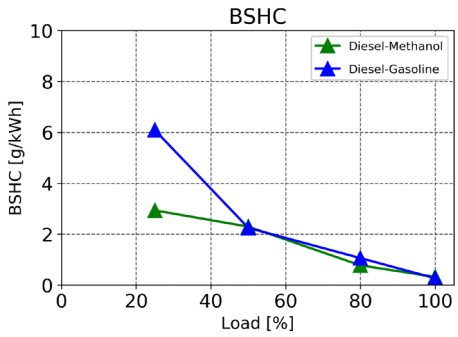




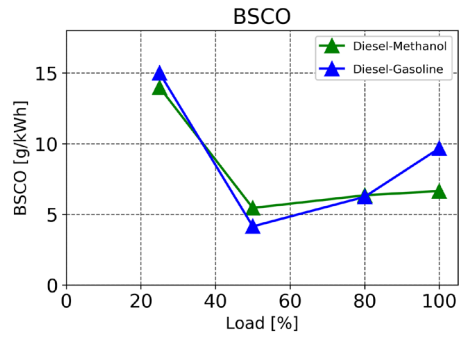
(c)



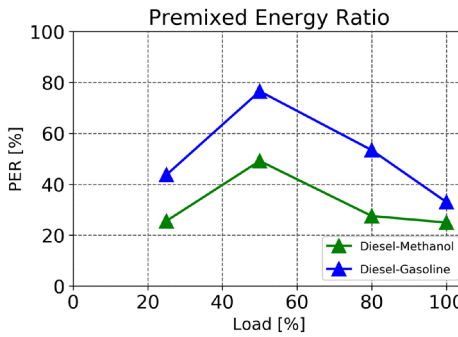
(d)



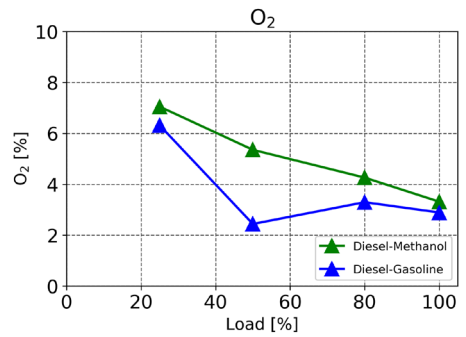
(e)



(f)



(g)



(h)

Figure 6-9. Diesel-Methanol calibration for Series hybrid operation at 1800 RPM and 0-100% engine load. Diesel-Gasoline calibration is added as reference.



### 6.2.2.2. Results

The results of the experimental campaign are inserted in the ICE sub-model, and the optimization of the control parameters is performed. Figure 6-10 shows the 600 cases simulated with an optimum at case 569 with 7.9% of TTW CO<sub>2</sub> reduction with respect to CDC non-hybrid. The benefits are lower than in the case of D-G and OMEx-G, with a reduction of 6% at homologation conditions. The main reason is that the D-G has the complete map, so it can operate at a different engine speed where 42% of BTE is achieved instead of the 35-40% of the D-Methanol calibration.

The operation point at WHVC 50% payload is shown in Figure 6-11. The ICE needs only use the first operation level with a power output of 150 hp. The TM propels the vehicle using the highest power in traction mode and up to 80% in regenerative braking mode.

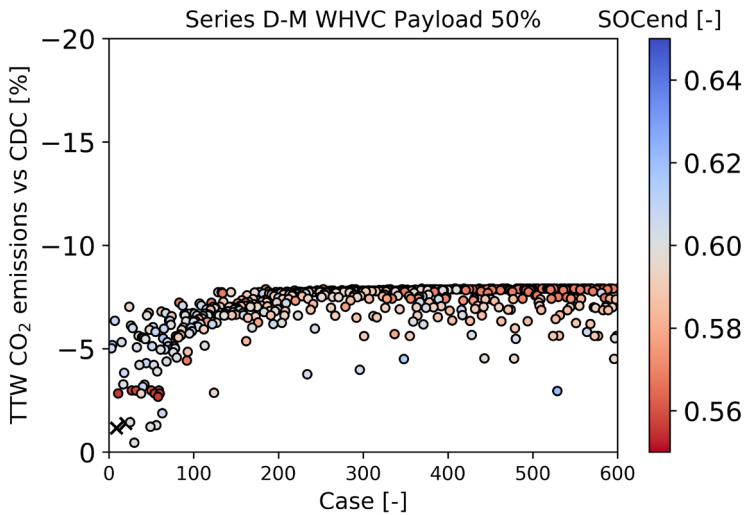


Figure 6-10. Diesel-Methanol optimization for a Series Hybrid operation in the WHVC and 50% payload.

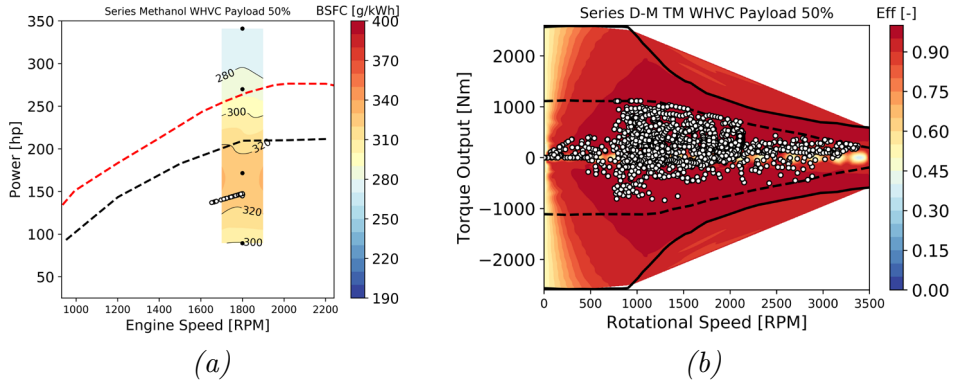
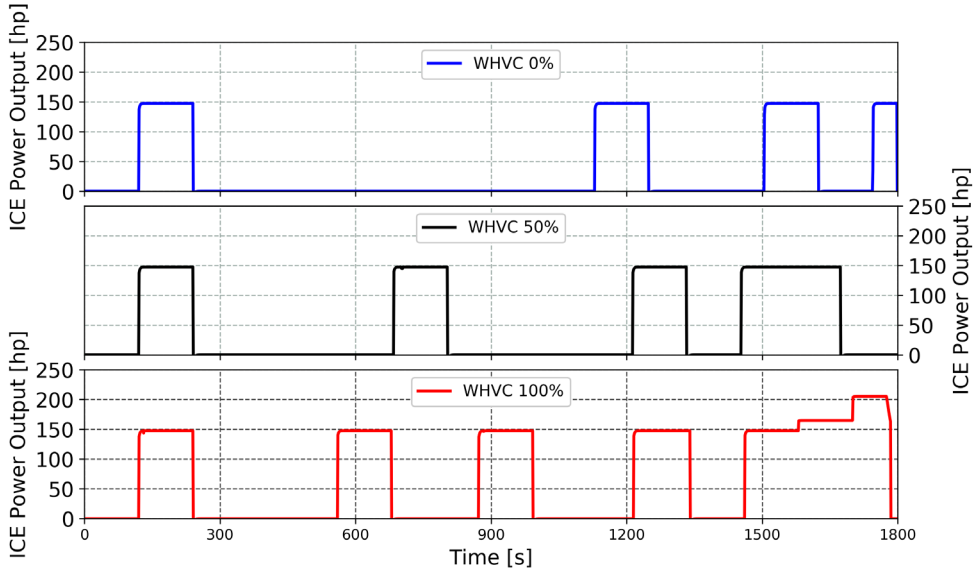
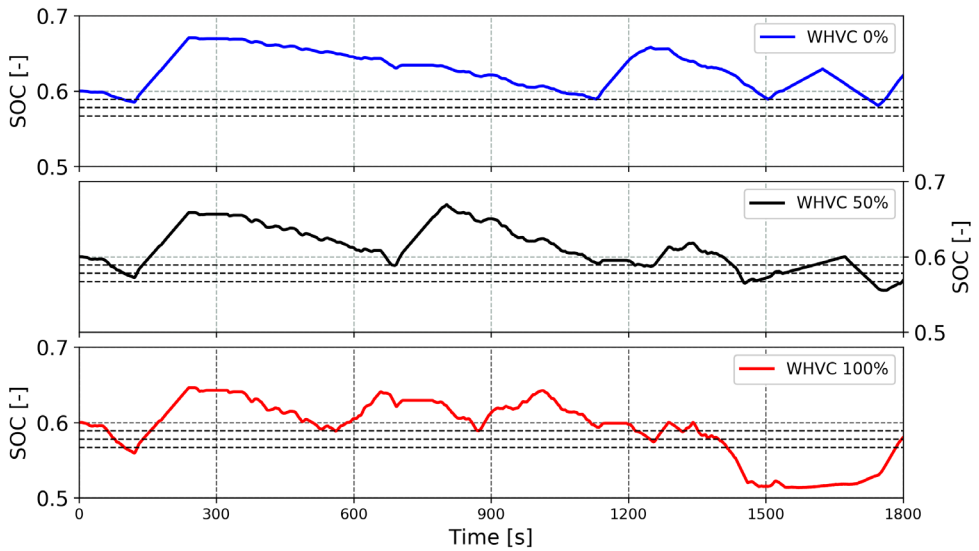


Figure 6-11. Diesel-Methanol operative condition in the ICE brake specific fuel consumption map (a) and traction motor efficiency map (b).

A comparison between 0%, 50%, and 100% payload is depicted in Figure 6-12 for ICE output power (a) and battery SOC (b). Only the 100% payload uses the three power levels (150, 164, and 210 hp) due to a high-power demand in the highway phase of the WHVC. The power levels are shown as dashed lines in Figure 6-12b. It is important to remark that to change of operative condition, at least 60 seconds have to pass. Despite that the SOC is below the power threshold of the next level, the RBC maintains the first level.



(a)



(b)

Figure 6-12. Diesel-Methanol ICE power output (a) and battery SOC (b) along WHVC for 0%,50% and 100% payload.

For the other cycles, the tailpipe CO<sub>2</sub> emissions are depicted in Figure 6-13. The series with conventional fuels as well as OME<sub>x</sub>-Gasoline is included for reference. Figure 6-13 can be taken as a resume of the benefits of different fuels when applied in a Series hybrid architecture with respect to the CDC non-hybrid. All the non-hybrid dual fuel versions are included. For the twelve cases tested, the average TTW CO<sub>2</sub> reduction for Series hybrid was: D-Methanol 8.3%, D-G 14.0%, and OME<sub>x</sub>-G 12.5%. The differences seen in an average of twelve cases are similar to homologation cases due to the lower BTE of the new experiments with D-Methanol with respect to D-G. Similar to other fuels, D-Methanol has a large CO<sub>2</sub> reduction in urban cases for all payloads and also for combined cycles with an empty truck. Cycles with large highway phases as the Flat and the Series hybrid, have low or no gain with respect to the non-hybrid.

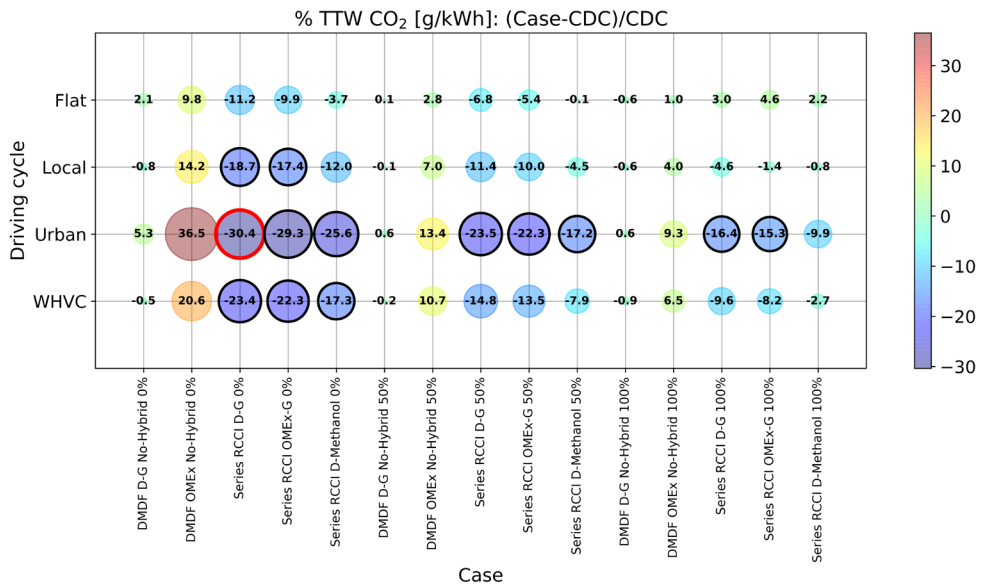


Figure 6-13. Diesel-Methanol Series hybrid TTW CO<sub>2</sub> versus CDC non-hybrid. Previous results of D-G and OME<sub>x</sub>-G in non-hybrid and Series hybrid is added for comparison.

Finally, to understand the benefits of using a synthetic fuel as methanol in terms of global CO<sub>2</sub> emissions, a WTW analysis is included in Figure 6-14. In red balls is seen the cases in which the 2030 target is achieved (30% CO<sub>2</sub> reduction) while in black balls, the 2015 target (15% CO<sub>2</sub> reduction). In terms of WTW, it is possible to obtain higher CO<sub>2</sub> reduction with an LRF than with an HRF synthetic fuel. Figure 6-14 shows that under homologation conditions, the D-methanol improves by 30.8% while the OMEx-G is 26.4%. This is because the LRF fraction is higher than the HRF injected in the RCCI calibration proposed. Therefore, the negative WTT CO<sub>2</sub> value (-42.0 g<sub>CO2</sub>/MJ<sub>Fuel</sub>) of methanol has a higher impact than the OMEx (-67.2 g<sub>CO2</sub>/MJ<sub>Fuel</sub>) savings in the total WTW CO<sub>2</sub> results. Despite the fact that the OMEx is ‘greener’ than Methanol, the latter is better to be applied in dual-fuel combustion as RCCI purely considering the global CO<sub>2</sub> footprint.

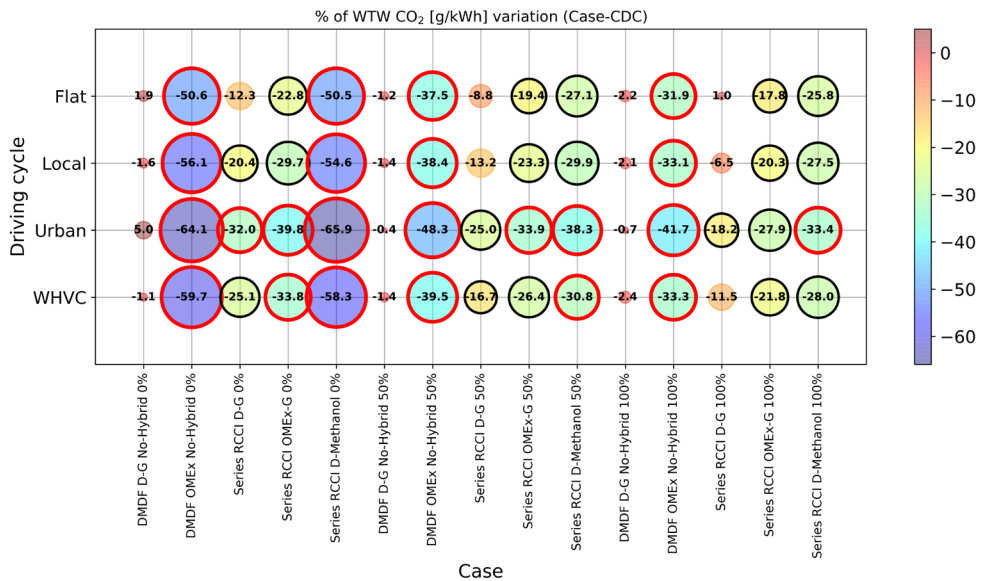


Figure 6-14. Diesel-Methanol Series hybrid WTW CO<sub>2</sub> versus CDC non-hybrid. Previous results of D-G and OMEx-G in non-hybrid and Series hybrid is added for comparison.

## 6.3 Potential of dual-fuel combustion for EUVII

The new coming restrictions in terms of pollutant emissions with EUVII will have a big impact on ICE applications. The estimation is to be forced to decrease by 50% the tailpipe pollutant emissions like NO<sub>x</sub>, soot, HC, and CO. This will mean: 0.23 g/kWh of NO<sub>x</sub>, 5 mg/kWh of particle matter, 2 g/kWh of CO, and 0.08 g/kWh of HC.

Increasing the complexity of the after-treatment system is an option but will increase the powertrain price, and the packaging of all components will be compromised. Some estimations of the new ATS affirm that two to three SCR are necessary with several heaters in the pipeline.

On the other hand, dual-fuel combustion can be an option to highly decrease engine-out pollutant emissions. Using the D-G, OMEx-G, or D-Methanol calibration with current EUVI CDC ATS (1 SCR, 1 DPF, 1 DOC) is an option. However, intended to simplify the ATS, a step forward in the calibration of RCCI dual fuel can be done. Thanks to the hybridization, it is possible to focus on the re-calibration of the ICE at certain points of the map and not be necessary to evaluate the concept in 54 operative conditions as a non-hybrid. This sub-section will show results in terms of ICE re-calibration with D-G and OMEx-G to achieve EUVII NO<sub>x</sub> and soot targets.

### 6.3.1. Methodology

A similar approach to the showed with Diesel-Methanol was followed in this sub-section. The operative conditions selected for the re-calibration were thinking of the Series hybrid. With the learning of the methanol calibration in terms of not selecting only one ICE rotational speed due to brake thermal efficiency limitations, three rotational speeds were tested. The ICE load was chosen considering where the most premixed combustion can be achieved and the points with less hardware restriction. The main limitation of this multi-cylinder engine is the air path and the in-cylinder peak pressure rate. The strategy to decrease the emissions is to increase EGR

to avoid NO<sub>x</sub> production and tune the gasoline fraction to maintain the soot to a minimum. Therefore, 50% load at 1500, 1800, and 2000 were selected. The RCCI combustion was achieved until 60% engine load, so 50% has some margin to operate. Lastly, 2000 RPM and 60% engine load were tested in order to have an operative condition in which 210 hp is achieved. This power is necessary for the level of maximum ICE power of the Series hybrid strategy. A scheme of the point selected is shown in Figure 6-15.

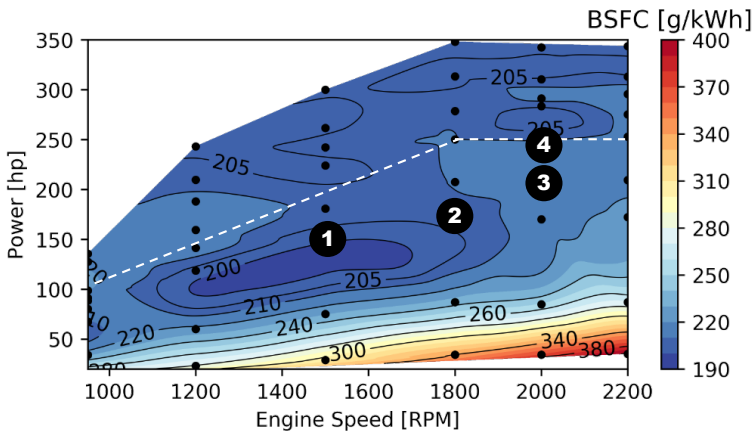
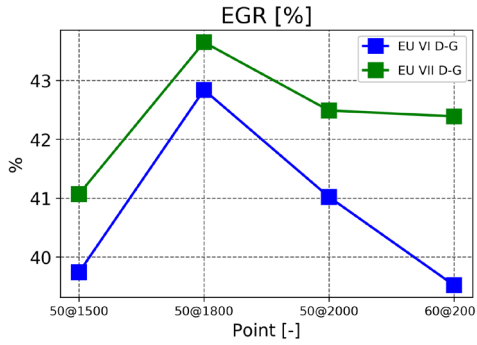


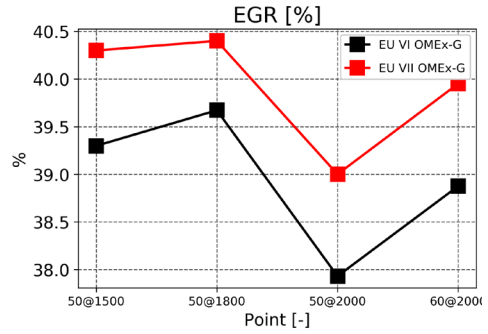
Figure 6-15. Brake-specific fuel consumption map of D-G EU VI calibration and the selected points for the EUVII new re-calibration.

The increase of around 1% in terms of the total EGR rate allows for a decrease in the NO<sub>x</sub> up to the target 0.23 g/kWh of EUVII (Figure 6-16). These results show the great potential of RCCI to decrease emissions. For D-G, up to 43.5% of EGR was necessary at 1800 RPM, while the OMEx-G requires 40.4%. The brake-specific fuel consumption did not suffer big changes due to the ability to tune several parameters in the multi-cylinder engine. The soot emissions were maintained for both combinations of fuel, similar to the EUVI calibration that was by large below that emission limit. The only conflict point was 2000 RPM and 60% due to the limit to the RCCI application frontier. This particular point was out of EUVII in soot for the

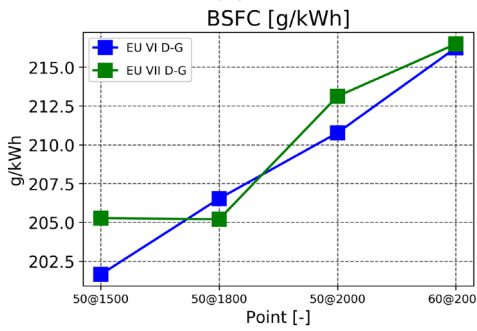
case of D-G. The next sub-section results will show the impact on driving conditions.



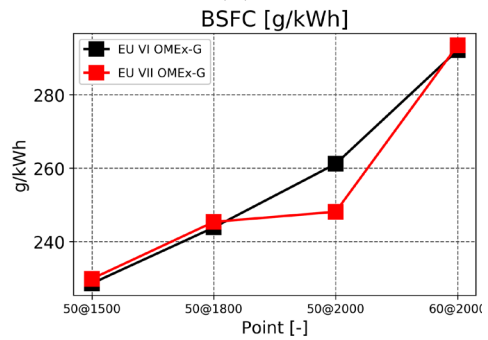
(a)



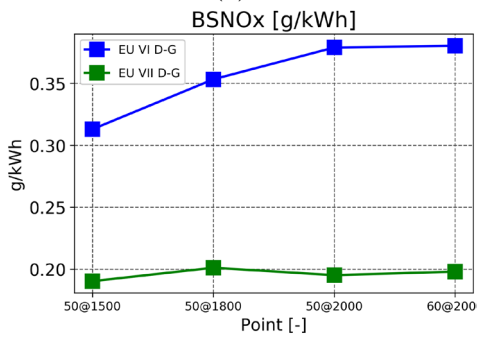
(b)



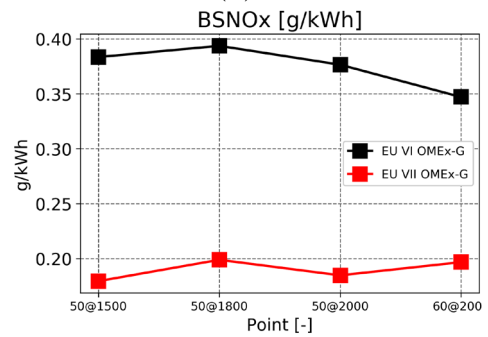
(c)



(d)



(e)



(f)



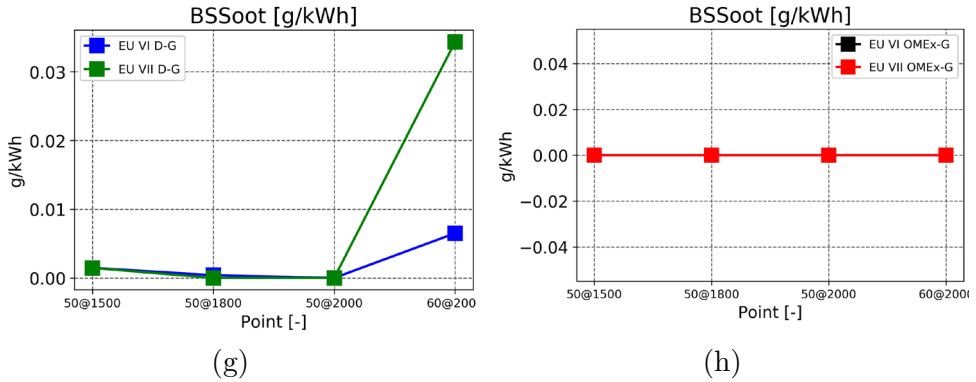


Figure 6-16. ICE operative condition setting in terms of EGR and outputs as brake-specific fuel consumption,  $NO_x$ , and soot emissions for the new ICE re-calibration towards EUVII for Diesel-Gasoline (left) and OME $x$ -Gasoline (right).

The HC and CO suffer penalties (Figure 6-17) with an increase for both combinations of fuels due to the delayed combustion and less premixed zones. In the case of D-G RCCI, a consistent penalty for both HC and CO is observed from the increase of rich zones and lack of oxygen due to the increased EGR rate, promoting quenching and partial or incomplete oxidation processes. In the case of OME $x$ , the penalty is only observed on CO emissions while HC remains practically the same. This is a consequence of oxygen availability in the fuel molecule that permits it to reach partial oxidation even in very rich conditions. The emissions of HC, in this case, are mainly related to the quenching of fuel near the crevices and the walls. On the other hand, since the oxygen availability from the fresh air is reduced with the increase in EGR, the final stages of the combustion process, where the mixture tends to be rich, have a lack of oxidizer, leading to an increase of CO emissions in the same trend as for D-G. It is important to highlight that, in general, CO emissions coming from OME $x$ -G are significantly lower than those of D-G due to the improved reactivity of the fuel.

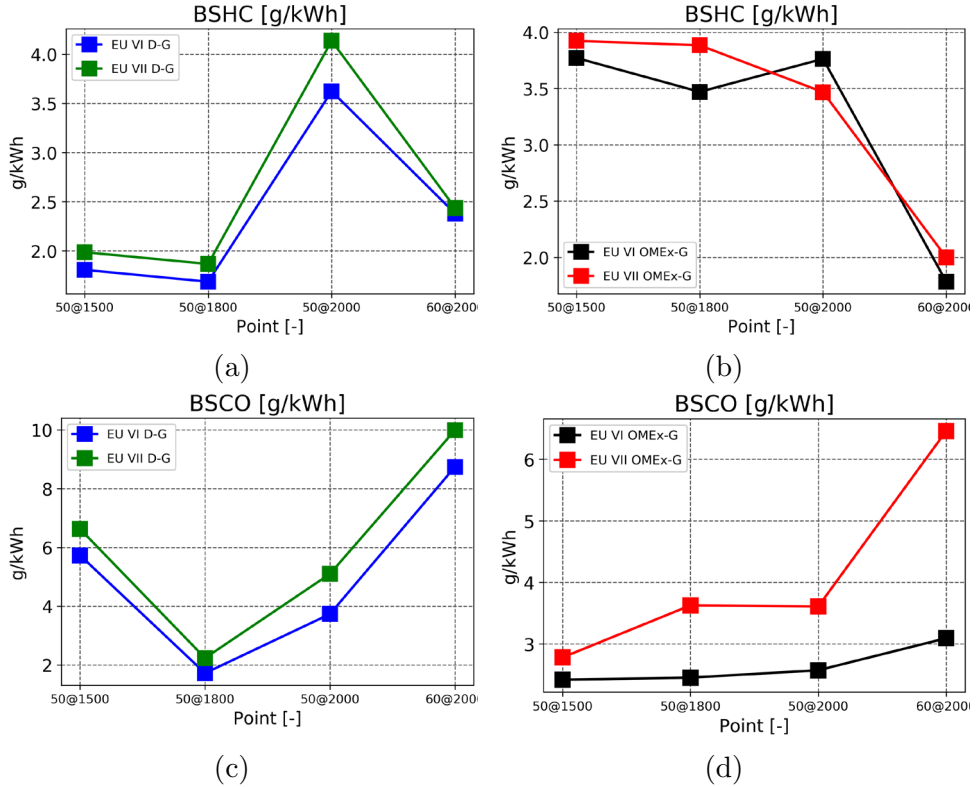


Figure 6-17. ICE brake specific HC and CO emissions for the new ICE recalibration towards EUVII for Diesel-Gasoline (left) and OME<sub>x</sub>-Gasoline (right).

### 6.3.2. Results

The optimum of the EUVI hybrid truck configuration was taken, and change the operation points with the results obtained in the ICE test bench. As the series operate in power level, the first level was assigned to 1500 RPM and 50% engine load (147 hp), while the second level to 1800 RPM and 50% engine load (171 hp). The point of 2000 RPM and 50% engine load produce similar power output to the case of 1800 RPM and 50% but with the worst brake-specific fuel consumption for both fuel combinations. The operative

condition of 2000 RPM and 60% engine load was kept as the level 3 or maximum ICE power output.

The results in terms of CO<sub>2</sub> (TTW and WTW) are presented in Figure 6-18. The non-hybrid cases were avoided for the brevity of the manuscript but can be found previously in the manuscript. Instead, the Series hybrid with EUVII new calibration and the previously found results with EUVI are presented. On average, the EUVII to EUVI lost 1.7% of the TTW CO<sub>2</sub> gains for D-G and 0.9% for OMEx-G. This is mainly due to the higher flexibility of OMEx combustion to tune the parameters to reduce pollutant emissions without large penalties in brake thermal efficiency. The Series hybrid is close to achieving 2025 CO<sub>2</sub> targets in homologation conditions, but at a high payload, it penalizes due to the large electric inefficiencies in converting the fuel power to mechanical wheel power.

Another scenario is seen in terms of WTW CO<sub>2</sub> emissions reduction with respect to CDC non-Hybrid with above 15% (2025 target) reduction at homologation conditions for all cases (EUVI and EUVII calibration). The cases with OMEx achieve almost 25% of reduction under homologation conditions and urban cases with low payload with 40% CO<sub>2</sub> reduction. These are large savings of CO<sub>2</sub> in conditions where a delivery truck is submitted every day. On average, of the twelve tested cases, the EUVII calibration allows achieving 14.6% for D-G and 24.0% for OMEx-G instead of the 15.6% and 26.3% of the EUVI calibration for D-G and OMEx-G, respectively.

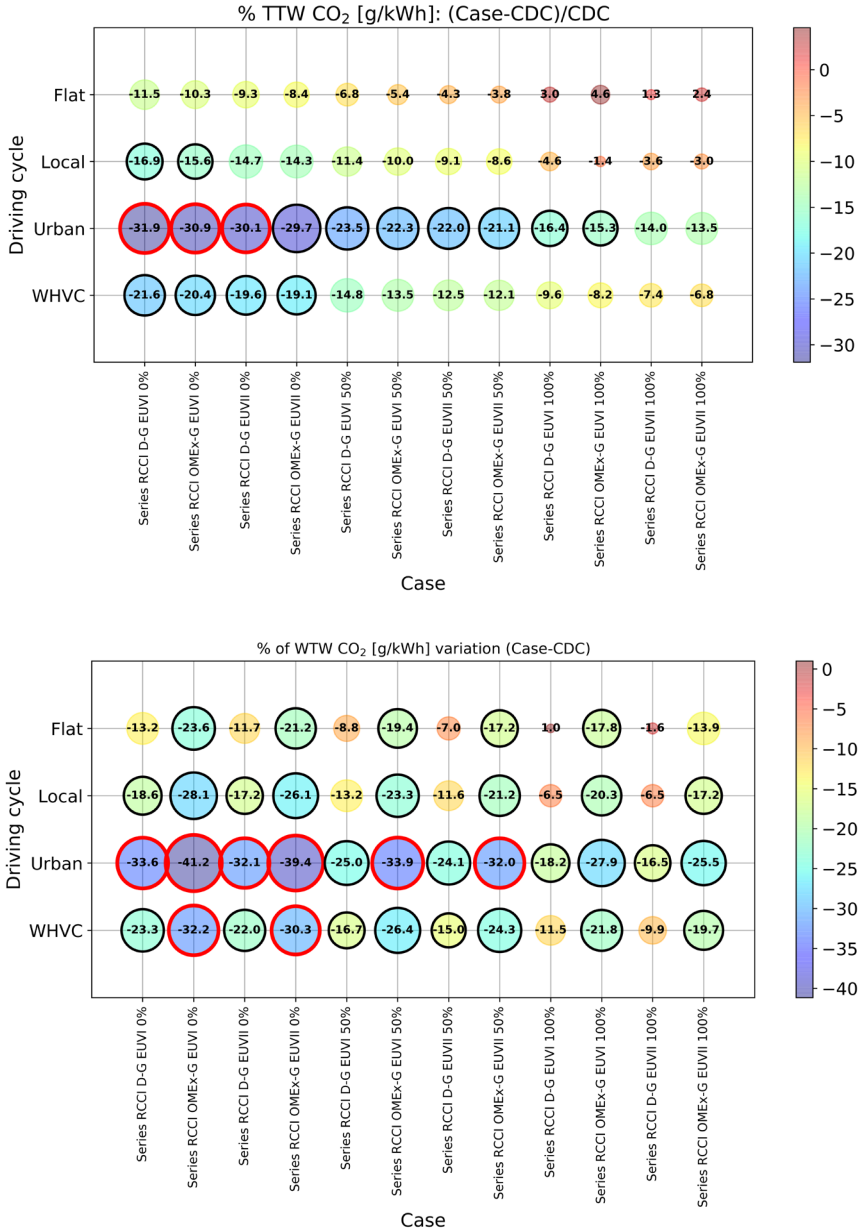


Figure 6-18. TTW and WTW CO<sub>2</sub> emission difference between the Series hybrid with different engine calibration and CDC non-hybrid at twelve driving scenarios.

The main purpose of these two new calibrations was to achieve EUVII in terms of NO<sub>x</sub> and soot. Figure 6-19 shows that both fuel cases achieve the desired target (red balls) while the previously EUVI calibration in some cases is close to achieving but at high payload is close to the EUVI limit. The NO<sub>x</sub> reduction with respect to CDC non-hybrid achieves an average of 94.5% for both fuel cases. In the case of EUVI, calibration was around 90% engine-out NO<sub>x</sub> reduction. The case of soot emissions is more favorable, with negligible emissions for OME<sub>x</sub> cases and a reduction of around 95% for both EUVI and EUVII D-G calibration.

Lastly, CO suffers penalties for the new proposed calibration. On average, the engine-out CO for D-G EUVII was 7.3 g/kWh, while for EUVI was 4.9 g/kWh. In the case of OME<sub>x</sub>, the gap is lower, with 3.8 g/kWh for EUVII and 3.3 g/kWh for EUVI. The HC was around the same level for both calibrations, with 2.1 g/kWh for D-G and 3.0 for OME<sub>x</sub>-G. The graph is not shown for the brevity of the manuscript.

The next sub-section will address the potential of a higher level of electrification as a plug-in hybrid. The advantages and drawbacks of using electricity on the net will be studied and contrasted with synthetic fuels results.

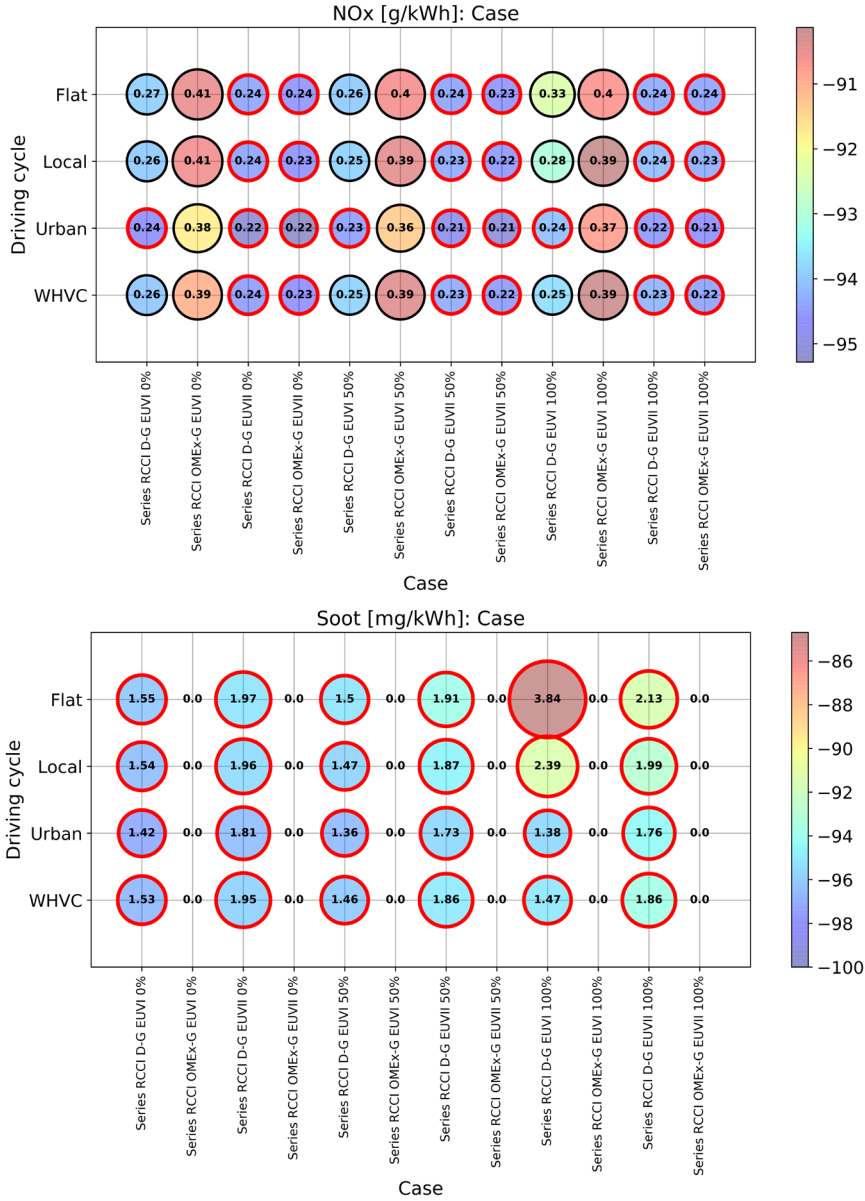


Figure 6-19. Brake specific NOx and soot emissions at engine-out for the Series hybrid at twelve driving scenarios.

## 6.4 Plug-in Hybrid towards 2030 LCA CO<sub>2</sub> targets

The plug-in hybrid allows using the electric mode for a higher distance/time while having the ICE extend the range when the battery is depleted. Following the classification of the type of hybrid, PHEV is a step forward in the electrification level. It can be implemented in architectures such as P2, Series, or Power Split. In this section, the Series hybrid will be evaluated due to the already sizing of the TM to operate in pure electric. The P2 or power-split needs re-sizing of the electric motor to have the capabilities to operate in pure electric mode in all situations. For brevity of the manuscript that hybrid architectures are not evaluated. It is expected similar results to the Series hybrid following the results obtained for FHEV.

A series PHEV maintain the architecture and components of the FHEV, shown in Chapter 5 but increases the battery package energy/size and adds the power electronics for external charging. In addition, small changes need to be made in the RBC strategy. The SOC to start to charge is fixed at 0.3, and the three power levels are set at: 0.25, 0.20, and 0.15. These values are set to be able to use all battery energy (SOC 1.0 to SOC 0.3 in pure electric) but without overpassing the minimum recommended of 0.1 to not damage the cells. Figure 6-20 shows a schematic of the concept proposed for this section. The WTW of the electricity mix in Spain and LCA using the values presented in Chapter 3 are included in the analysis.

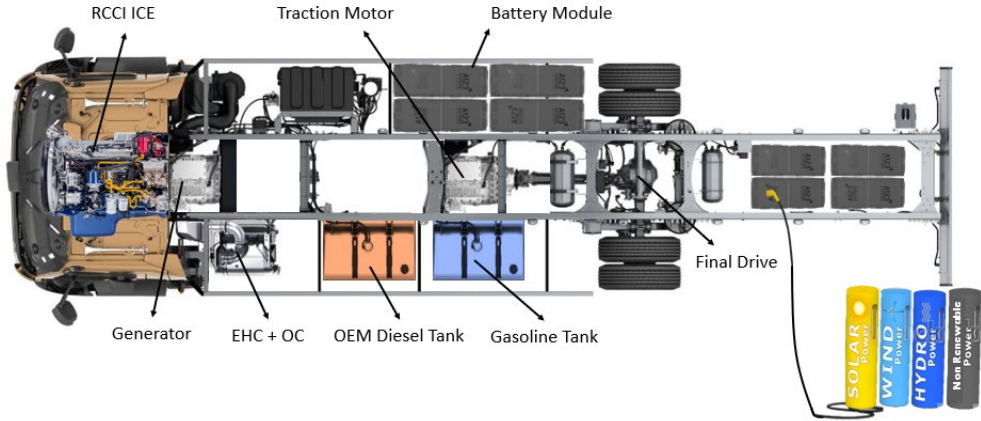


Figure 6-20. Series PHEV truck concept with RCCI dual-fuel engine and external charging.

### 6.4.1. Methodology

The Series hybrid is equipped with a TM, generator, and ICE of 210 hp. The RCCI dual-fuel engine is fueled with Diesel and Gasoline. For external charging, an efficiency of 5% is considered due to electricity losses in the charge station, cabling, and battery. In this work, full charge means SOC=1.0 and depleted battery to SOC=0.2.

The simulations were carried out under the World Harmonized Vehicle Cycle (WHVC), which is the homologation cycle currently in force for trucks to evaluate the PHEV system. It should be noted that for Heavy-Duty, there is no special annex for the test of the plug-in hybrid systems as in the case of Light-Duty vehicles. The PHEVs are vehicles that can be fueled by both conventional liquid fuels and grid electricity. Therefore, variations from the original normative must be done in the next years. For this work, an adaptation of the passenger cars Light-Duty WLTP normative in Europe was made.



For PHEVs, two operation modes were established: charge depleting (CD) and charge sustaining (CS). In charge depleting mode, the traction motor (TM) is mainly responsible for the vehicle propulsion while the ICE is switched off. The battery package feeds the TM. In charge sustaining mode, the battery has been fully depleted (up to a minimum of around 0.30 of state of the charge (SOC)), so that the combustion engine is turned on and used to charge the batteries through the generator motor (GEN) and the TM propels the vehicle. In this phase, the normative establishes that the battery SOC must be in a narrow range around the minimum. After that, the vehicle is stopped, and the battery is fully charged with electricity from the grid. The rule that defines the start of the charge depleting mode is described in Equation 6.1.

$$REEC_i = \frac{|\Delta E_{\text{Battery},i}|}{E_{\text{cycle}}} * 100 < 4.0\% \quad (6.1)$$

with  $REEC_i$  being the relative electric energy change in cycle  $i$  [%],  $\Delta E_{BATT\ i}$  the change of battery energy content  $i$  [Wh] and  $E_{\text{cycle}}$  the energy required to complete one WHVC [Wh]. The WLTP normative establishes that after CD mode ends, one CS phase must be accomplished before the test is finished. Figure 6-21 illustrates a typical WHVC for PHEV, where the initial state of charge is set to its maximum (SOC=1.0), then the WLTC is repeated until the battery reaches its minimum allowed CD charge state (SOC = 0.30). After that, a complete WHVC is performed in charge of sustaining operation (the vehicle is propelled by the ICE, and the SOC is maintained around the minimum).

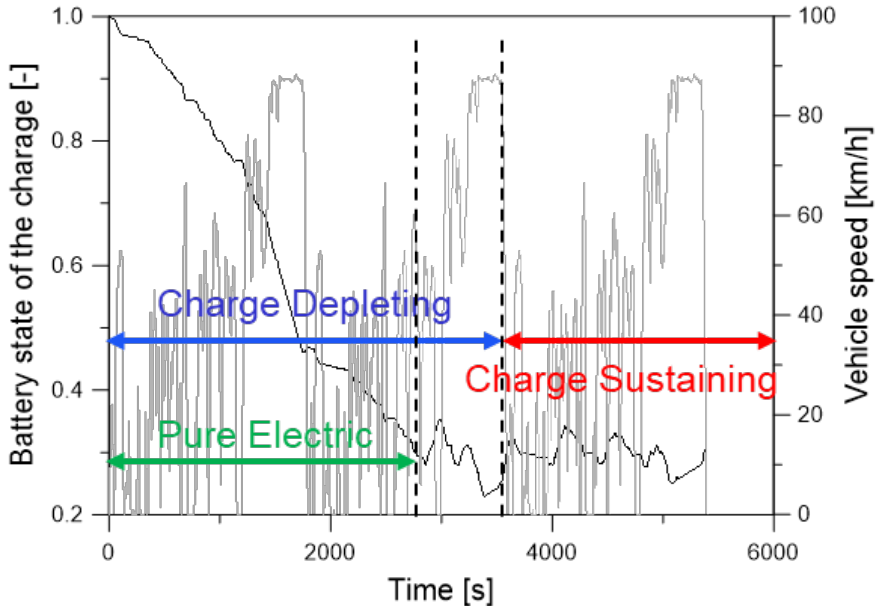


Figure 6-21. Cycle test for PHEV. The phase pure electric mode, charge depleting, and charge sustaining are marked as a function of the battery state of charge (SOC).

In this work, by GT-Suite PHEV modeling will be obtained the CD and CS energy consumption (fuel and electricity), CO<sub>2</sub>, and other pollutant emissions. However, depending on the battery size and initial energy, the truck can perform all WHVC cycles (20 km) in pure electric. Or, in the worst-case scenario, all cycle in CS because it was not charged. Therefore, to have global energy consumption and emissions, it is necessary to combine both scenarios. The charge depleting and charge sustaining fuel consumptions are used to estimate the equivalent fuel consumption of the vehicle in a single WHVC. As the full electric range increases with the battery size, the WLTP for Light-Duty normative creates a utility factor (UF) that compensates for the electric vehicle range to be comparable between the different options. Some authors explain the UF as the fraction of the distance covered in charge depleting over the total distance covered between two external battery charges. The Society of Automotive Engineers (SAE) has proposed a

standard method (SAE J2841) [225,226] that defines this weighting between charge depleting driving and charge sustaining driving as a utility factor that intends to represent the real-world driving habits of a vehicle fleet for Light-Duty operation. The SAE J2841 method assumes that the vehicle is fully charged at the beginning of the test, and it is charged only once per day. To obtain the final weighted result, Equation 6.2 is used.

$$M_{i,weighted} = \sum_{j=1}^k (UF_j \times M_{i,CD,j}) + (1 - \sum_{j=1}^k UF_j) \times M_{i,CS} \quad (6.2)$$

where  $M_{i,weighted}$  is the weighted mass emission of the compound  $i$ , in g/km;  $UF_j$  is the utility factor of the phase  $j$  (see Figure 6-22);  $M_{i,CD,j}$  is the mass emission of compound  $i$  in phase  $j$  of the CD mode, in g/km;  $M_{i,CS}$  is the mass emission of compound  $i$  in CS mode. As was explained, there is no Heavy-Duty normative to PHEV. The phase  $j$  depends on the type of cycle. Despite the WLTC and WHVC having 1800 s and both having urban, rural, and highway areas, it is not possible to use the same compensation. Therefore, the formula is simplified to Equation 6.3.

$$M_{i,weighted} = (UF \times M_{i,CD}) + (1 - UF) \times M_{i,CS} \quad (6.3)$$

However, the UF was created for Light-Duty vehicles where the travel distance is lower than in a Heavy-Duty truck. Therefore, another adaptation was performed by extending the UF compensation by the double and triple of distance. Figure 6-22 shows the compensation for the original (UF) and the new proposed compensations (UF\* and UF\*\*).

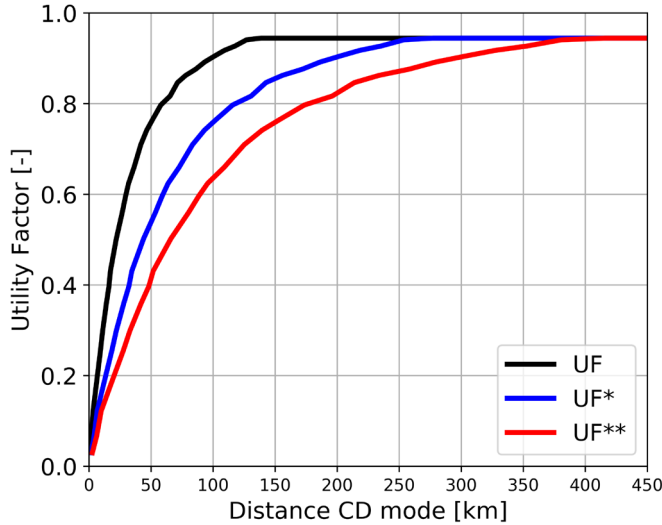


Figure 6-22. Utility factor used for PHEV Light-Duty vehicles ( $UF$ ) and the scale version by two ( $UF^*$ ) and by three ( $UF^{**}$ ).

As it was shown in Chapter 3, two lithium-ion cell models are available to use in the GT-Suite model. The LFP ANR 26650 is more suitable for small battery pack application as MHEV or FHEV, while the NMC HG2 18650 model is for a large pack. The first cell has high power capabilities, while the second has better characteristics in terms of energy density. For vehicles such as PHEVs or BEVs, it is important the energy density due to the large battery size. In this section, both cells will be compared, and the best in terms of energy consumption will be selected.

To have an extra reference than CDC non-hybrid, the pure BEV Volvo FL is modeled. The 0D vehicle model is built on the platform of the Series hybrid but removes the ICE. The transmission of two gears (ratio:  $G1=3.5:1$ ,  $G2=0.90:1$  and final drive of  $5.29:1$ ) is maintained as the Series hybrid as well as the traction motor size (210 hp continuous power). A DoE of several battery sizes is performed in a range between 40 to 700 kWh for both cells. The ANR 26650 has an energy density of 75 Wh/kg, while the NMC LG 18650 of 150 Wh/kg.

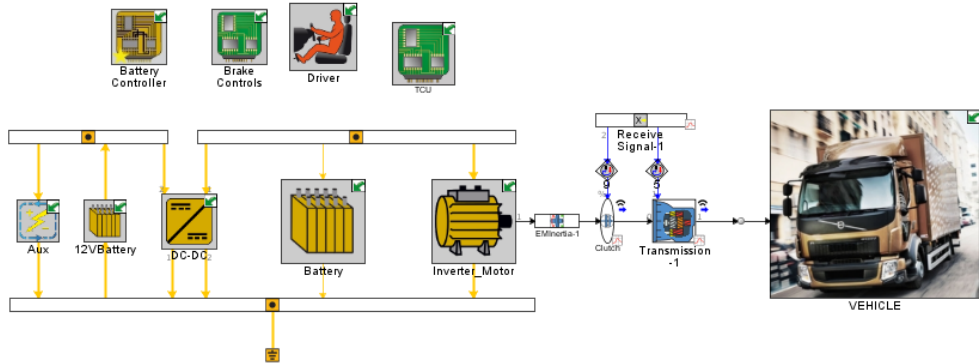


Figure 6-23. Pure electric truck GT-Suite model for model a complementary baseline case among the CDC non-hybrid.

The results of the BEV truck in WHVC with a 50% payload are presented in Figure 6-24. The NMC with high energy density shows better energy consumption due to the lower total vehicle weight. The results are more evident after 200 kWh, where the battery mass is 2.5 tons for the LFP and 1.3 tons for the NMC. In addition, the high-power capabilities of the LFP allow more recovery energy for a small battery pack size. However, the increase in terms of battery pack size eliminates the mentioned restriction for the NMC, and the vehicle weight is the most important factor. It is interesting to note that the results presented correlate with the manufacturer's declared range values of 300 km with a battery size of 395 kWh [222]. It can be concluded that for a PHEV that generally equips a battery size lower than 200 kWh, the cell chemistry will not have a large impact but for the BEV must be NMC due to the high energy density.

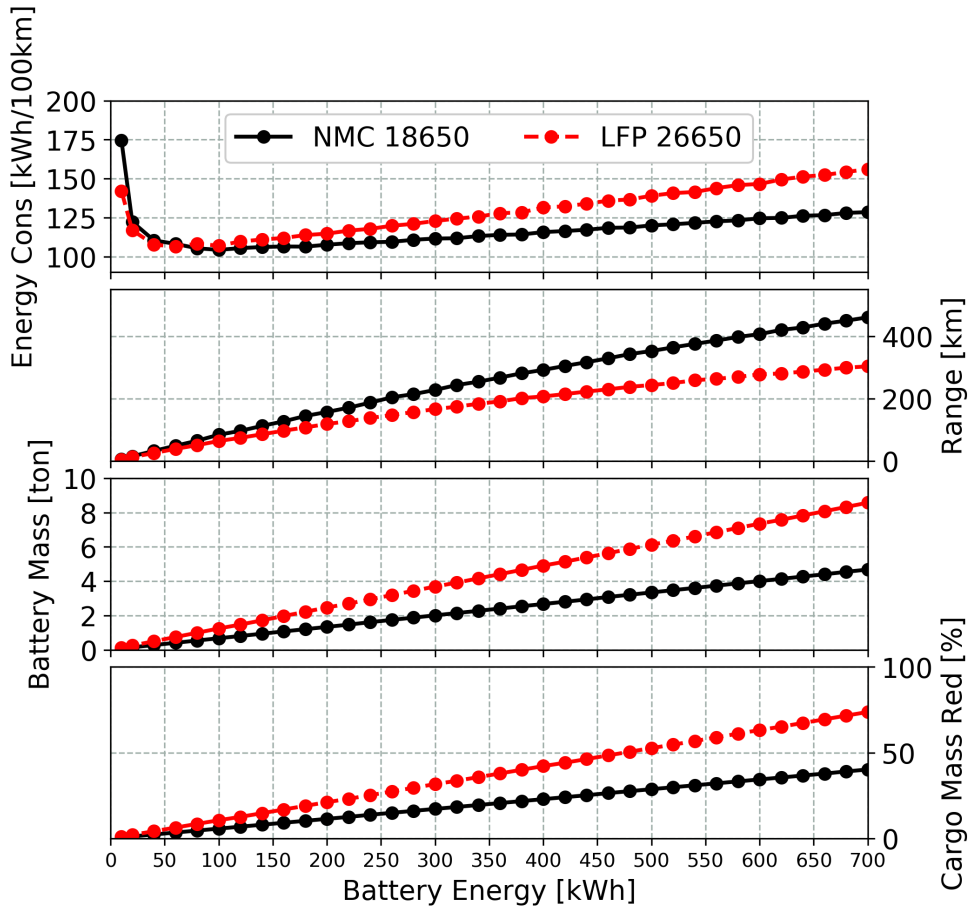


Figure 6-24. Energy consumption, vehicle range, battery mass, and cargo mass reduction percentage due to the weight of the battery for WHVC 50% load with a BEV truck with two types of cells.

After the model of the pure BEV truck, the PHEV Series truck is modeled in the WHVC and 50% payload. The results are presented in the next sub-section.

### 6.4.2. Results

The PHEV series truck was tested in two scenarios. The charge depleting -CD- which the truck starts with full battery energy (SOC =1) and runs under WHVC with 50% payload until de minimum SOC is reached. In case that happens in the middle of a WHVC, the truck finishes the cycle in sustaining mode. The other test is under charge sustaining, where the truck starts with SOC = 0.3 and completes only one WHVC (20.1 km). The test is performed under several battery-size packages (20 to 200 kWh) with the LFP 26650 cell. The distance traveled obtained from simulations is depicted in Figure 6-25a. The CD mode allows a range of almost pure electric drive of 140 km above 180 kWh. The energy consumption in that cycle is shown in Figure 6-25b. For the case of CS, the increase in the battery size makes to increase the energy consumption due to the added weight that is not used to propel the vehicle. The optimum in the CS mode is close to the FHEV battery size of 41 kWh.

The main difference between the FHEV and PHEV series trucks is that the first one uses the battery around SOC=0.6 and the latter around SOC=0.3. In spite that the battery efficiency is not the same in both scenarios and the FHEV has a larger SOC range to move, the energy consumption optimum is similar following the results obtained. The average CS consumption is 235 kWh/100km, while under CD is 126 kWh/100km. It is important to note that the CD energy is divided into electricity used for almost all the travel and fuel to end the last WHVC cycle. On average, of the different battery size, 73% of the cycles is performed in purely electric mode, with cases of 94% depending on the battery range and the cycle phase.

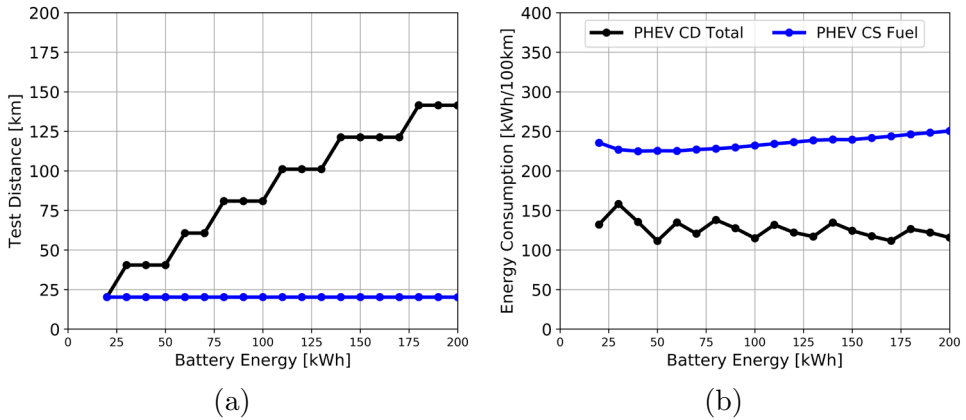


Figure 6-25. Distance traveled (a) and energy consumption (b) in charge depleting and charge sustaining mode for the PHEV series truck in several WHVC with 50% payload.

The next analysis is the NO<sub>x</sub> and soot emissions that, as can be seen in Figure 6-26, are below the EUVI limit. It can also be seen that also due to the Series operation in the pure RCCI zone, EUVII limits can also be achieved with this powertrain configuration. Therefore, the PHEV is able to achieve 2030 CO<sub>2</sub> targets and EUVII NO<sub>x</sub> and soot emissions without SCR and DPF. The DOC needs to be maintained with an EHC to achieve CO and HC targets.



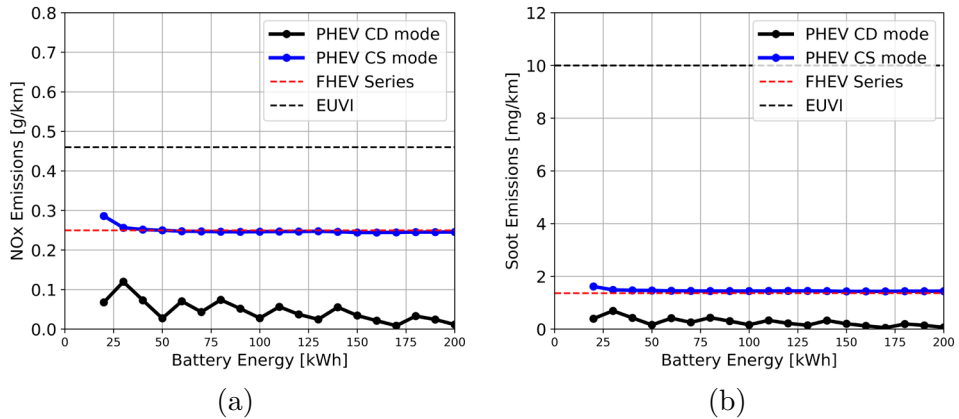


Figure 6-26. Brake specific NO<sub>x</sub> (a) soot (b) in charge depleting and charge sustaining mode for the PHEV series truck in several WHVC with 50% payload.

To better understand the energy consumption in the PHEV, Figure 6-27 shows the energy divided by electricity to re-charge the battery and fuel (Diesel + Gasoline). The series FHEV, the CDC non-hybrid, and the EV truck are added as a reference. The PHEV under CS achieves similar efficiency as the FHEV at load battery size, but when to increase the size, the values achieve the non-hybrid diesel version. This can explain by the increment of battery weight that is not used during the single WHVC because it needs to be under the 4% of energy variation.

On the other hand, the CD shows large energy improvements with respect to the CS mode. The total energy consumption is similar to the pure EV truck at the same battery size. It is possible to see in Figure 6-27 that the fuel energy decreases with the increase of battery size while the electrical energy has the opposite trend. From this graph, it can be affirmed that the PHEV with a full charge can achieve efficiencies of the EV truck.

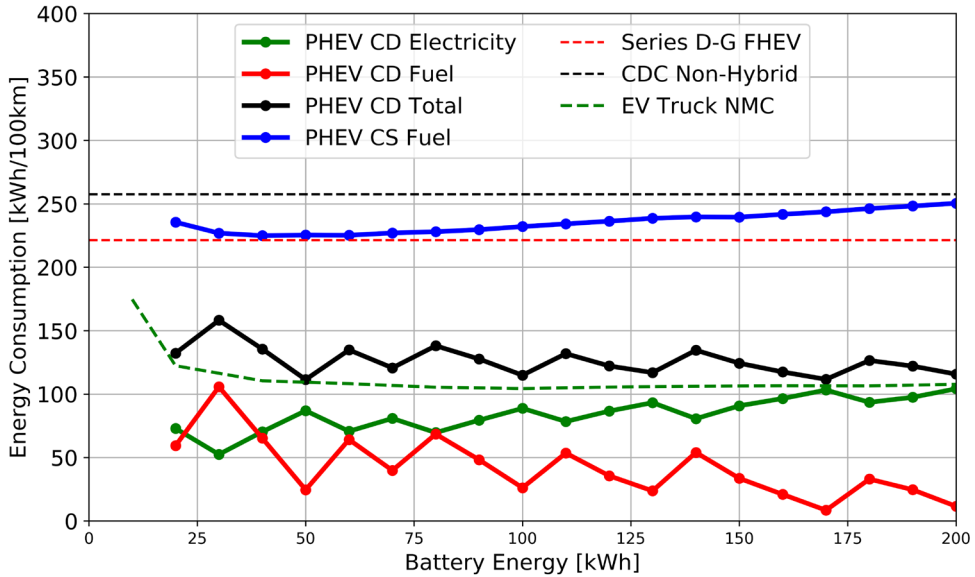


Figure 6-27. Energy consumption is divided by type of energy in charge depleting and charge sustaining mode for the PHEV series truck in several WHVC with 50% payload.

The WTW analysis of the CO<sub>2</sub>, including tailpipe emissions and the production of the fuel, can give valuable information in the comparison between technologies. The values presented in Chapter 3 are used to calculate the WTW CO<sub>2</sub> presented in Figure 6-28. The marginal emission is considered for the electricity (382 g<sub>CO2</sub>/kWh<sub>electricity</sub>) in this analysis because represents the real impact of adding PHEV and EV to the net.

The first thing to note is that the concepts using Gasoline (FHEV and PHEV) increase the gap with respect to CDC non-hybrid due to the lower WTT CO<sub>2</sub> of gasoline with respect to Diesel. In addition, the gap seen in energy consumption is reduced in WTW CO<sub>2</sub> between PHEV CD and EV trucks due to the lower emissions in WTT of Diesel/Gasoline with respect to the electricity mix of Spain, accounting for the marginal value. On average, the PHEV CS emits 735 g<sub>CO2</sub>/km and PHEV CD 541 g<sub>CO2</sub>/km. The references

account for: CDC non-hybrid 835 g<sub>CO2</sub>/km, FHEV Series D-G 696 g<sub>CO2</sub>/km, and EV truck 468 g<sub>CO2</sub>/km.

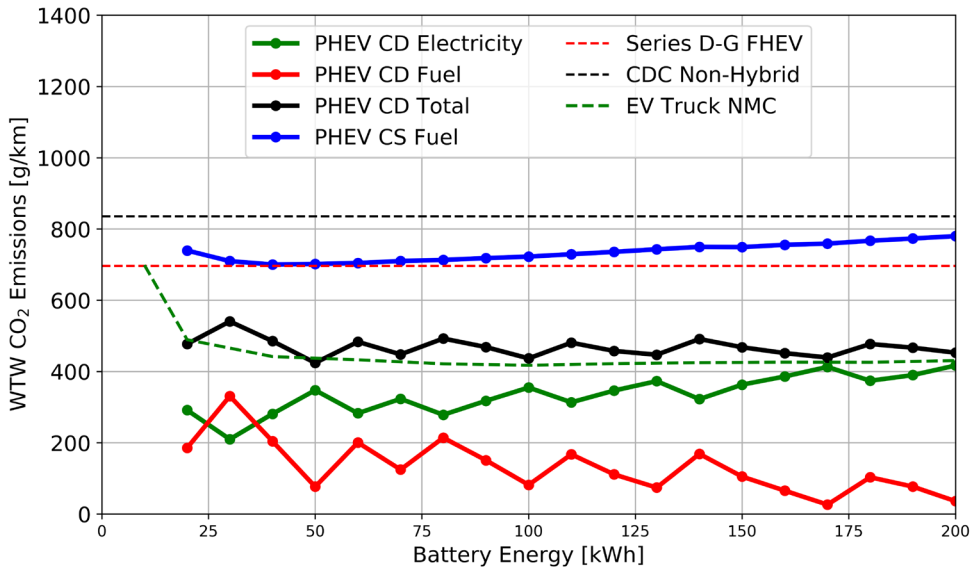


Figure 6-28. Well-to-Wheel CO<sub>2</sub> emissions divided by type of energy in charge depleting and charge sustaining mode for the PHEV series truck in several WHVC with 50% payload.

The utility factor methodology presented in the previous sub-section is used to obtain a combined CO<sub>2</sub> emission between CD and CS for the PHEV. The TTW CO<sub>2</sub> emissions are calculated considering the UF for Light-Duty and two-scale UF by double and triple of travel distance per day. The results obtained are shown in Figure 6-29 in absolute and relative values with respect to CDC non-hybrid. The range of TTW CO<sub>2</sub> saving is from 30% to 90%, depending on battery size. The difference between the UF approach can make vary the TTW around 40% to the double distance and 70% to the triple distance. These results highlight the importance of defining an appropriate compensation for CD and CS in Heavy-Duty transportation in the next years in order to have a fair comparison.

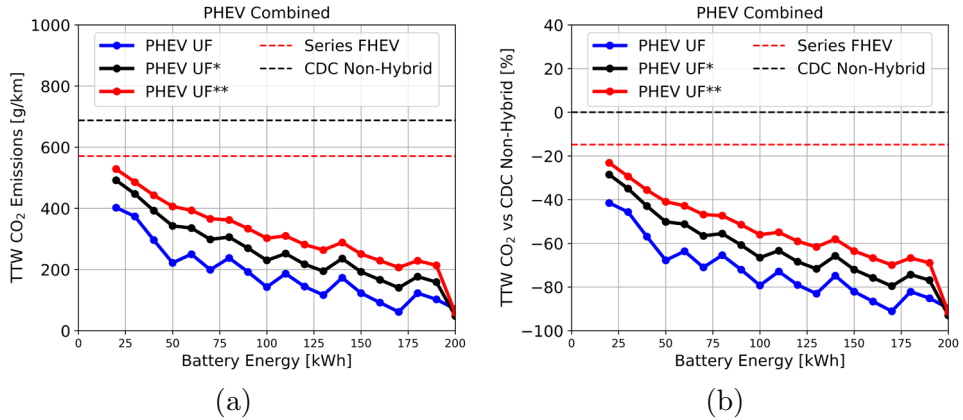


Figure 6-29. Combined CD and CS Tank-to-Wheel CO<sub>2</sub> absolute values (a) and relative with respect to CDC non-hybrid (b) for the PHEV series truck in several WHVC with 50% payload under several UF.

The WTW CO<sub>2</sub> emissions are calculated and compared against FHEV and EV, considering the different UF approaches. The values in Figure 6-30 are presented relative to CDC non-hybrid. It is possible to see that all PHEV evaluations are able to achieve 2030 CO<sub>2</sub> targets with battery size above 50 kWh. The average reduction for the PHEV series truck is 39% for UF of Light-Duty, 34% for UF\*, and 31% for UF\*\*. The EV CO<sub>2</sub> savings in WTW is 44%, while the FHEV is 15%.

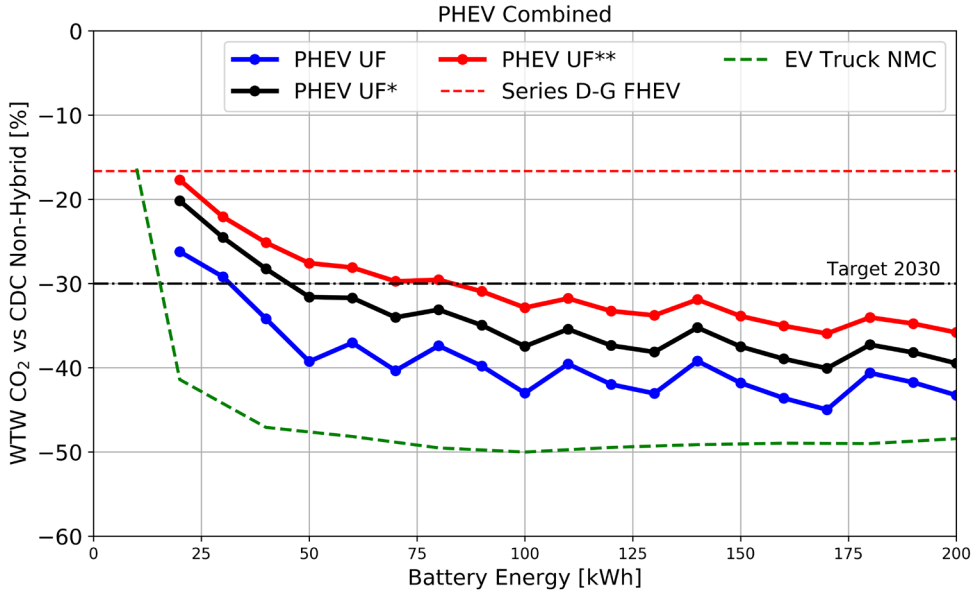


Figure 6-30. Well-to-Wheel CO<sub>2</sub> emissions with respect to CDC non-hybrid for the PHEV series truck in several WHVC with 50% payload under several UF.

The LCA following the values presented in Chapter 3 is performed to PHEV with the utility factor of the WLTP normative, the Series Hybrid, and the EV. The results are presented in Figure 6-31. All range of the EV is shown because, until 200 kWh, the vehicle range (understand as the distance travelled with a complete battery charge) is too low (<180 km). The commercial version is around 400 kWh, which is just above the 2030 CO<sub>2</sub> target. The optimum selection for the EV in terms of CO<sub>2</sub> will be 320 kWh because it allows an acceptable range and 30% CO<sub>2</sub> reduction. On the other hand, the PHEV does not show improvements after 100 kWh, where the minimum is achieved. After this battery size, the values of LCA savings oscillate due to the WHVC repetition and the split between fuel and electric energy used. Therefore, the optimum for the PHEV with conventional fuels is selected with 100 kWh.

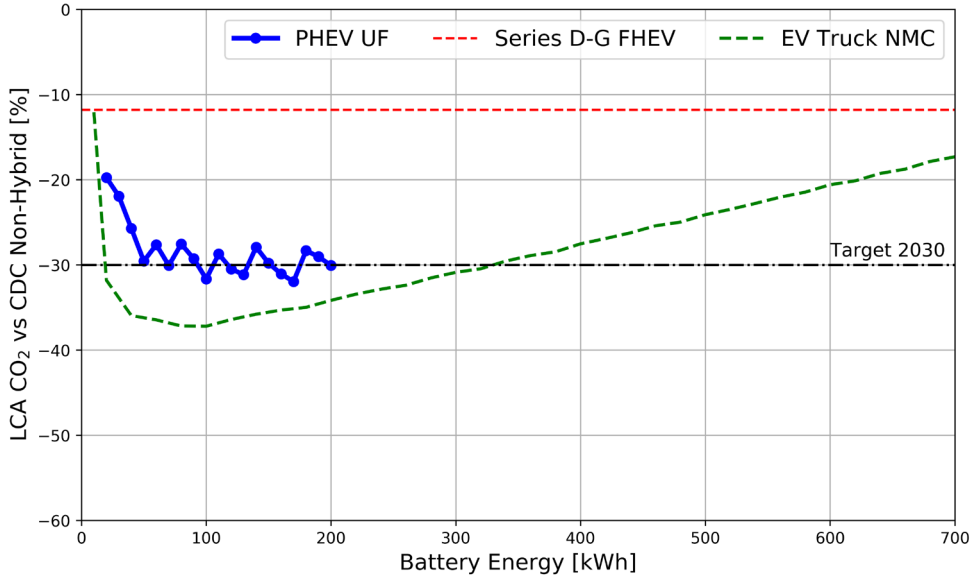


Figure 6-31. Life Cycle Analysis  $\text{CO}_2$  emissions with respect to CDC non-hybrid for the PHEV, FHEV, and EV trucks under WHVC with 50% payload.

The LCA for the different technologies presented in this work is presented in Figure 6-32. The values of *Table 3-14* are used for the LCA calculation. The point in the graph shows the LCA using the average value for each component and the error bar is obtained with the range of each component presented in *Table 3-14*. For the EV and PHEV the marginal emissions of the electricity net is taken as the maximum of the range and the average emissions as minimum. The differences between each new technology and the baseline CDC non-hybrid truck are presented in Figure 6-33. In addition, the targets in dashed lines are presented for both 2025 15% and 2030 30% reduction. Despite the European targets are not considered in LCA level, are inserted in the Figure 6-33 for reference.

The results show that e-fuels are a potential solution to achieve 2030 targets, with the best case the Series RCCI D-Methanol, P2 OMEx-G and non-hybrid OMEx-G. The first cases achieve high powertrain efficiency and uses large quantities of e-fuel (OMEx) due to the operation in a wide range

of the operation map. The series with methanol is able to large reduce the LCA CO<sub>2</sub> emissions due to the high PER, which allows to large mass injection of the e-fuel. On the other hand, the non-hybrid with OMEx does not reduce the energy consumption but uses a large amount of e-fuel. Therefore, the OMEx negative WTT emissions make the non-hybrid a low LCA CO<sub>2</sub> emission vehicle. In addition, does not have extra emissions from the battery or electric components. Despite having low CO<sub>2</sub> emissions, the high fuel consumption in volume and the dependency of being the OMEx from renewable sources can limit their usage.

The PHEV (100 kWh) with conventional fuels achieves in average 39.7% of CO<sub>2</sub> reduction. The minimum of the error bar (average electricity net emissions and low CO<sub>2</sub> during battery manufacturing) shows that PHEV can reduce 48% while the maximum (marginal electricity net emissions and high CO<sub>2</sub> during battery manufacturing) allows to reduce 32% compared with the commercial truck. In the case of the EV with 400 kWh, the best-case scenario reduces 53% while the worst-case scenario is 25%. The EV has more variation due to large battery size and high electricity consumption. Both incomes values have a large range than the conventional fuels. Therefore, in average value both have large CO<sub>2</sub> reduction (39.7% the PHEV and 38.7 the EV) and using the worst-case scenario PHEV achieves 2030 target while EV is medium way between 2015 and 2030.

The battery manufacturing CO<sub>2</sub> for the average emission case is the 5% for the PHEV and 19% for the EV of the total CO<sub>2</sub> emissions. On the other hand, the WTW CO<sub>2</sub> emission is 66% and 61% of the total CO<sub>2</sub> for the PHEV and EV, respectively. Overall, the high electrification is a solution for the CO<sub>2</sub> targets, and as shown previously, it allows to achieve EUVI NO<sub>x</sub> and soot emissions without required ATS. The PHEV with 100 kWh is the best case in order to reduce LCA CO<sub>2</sub> emissions.

Other technologies that allow high CO<sub>2</sub> reduction but without achieving 2030 targets are Power Split hybrid with OMEx (21.9%), Series hybrid with OMEx (17.9%), and P2 with conventional fuels (13.6%). As was

demonstrated in Chapter 5, the parallel hybrid has the largest energy consumption saving compared with the other powertrain, but the synthetic fuel extra CO<sub>2</sub> saving allows higher LCA CO<sub>2</sub> reductions.

A step below is the Power Split and Series hybrid with conventional fuels with 13.2% and 10.6%, respectively. The non-hybrid with DMDF and conventional fuels only allows 0.5% of CO<sub>2</sub> saving. Therefore, hybrid technologies with high electrification levels or synthetic fuels allow significant CO<sub>2</sub> reductions.

Nevertheless, in 2018, there was only around 1 GW of electrolysis capacity in the EU, corresponding to around 1.6% of total hydrogen (H<sub>2</sub>) production capacity and the current estimated capacity in EU is 2.6 GW if 70% efficiency of electrolysis is assumed. This could suggest that the implementation of e-fuels has been to some extent, hindered by the regulatory framework and low incentives, as well as the uncertainty of the future market demands, resulting in not attractive business cases.



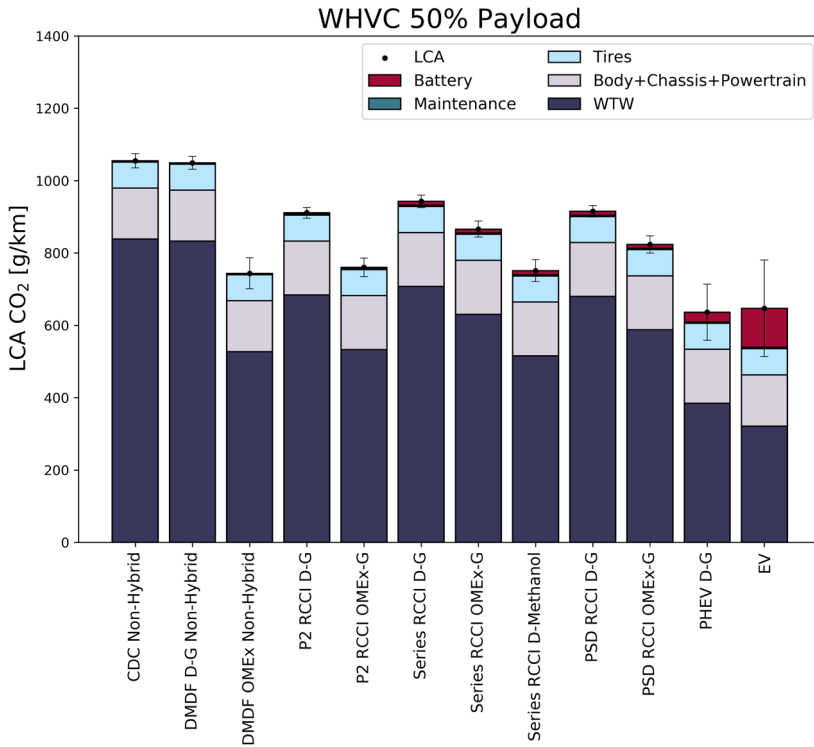


Figure 6-32. Life Cycle Analysis CO<sub>2</sub> emissions for different technologies applied in a Medium-Duty truck at 50% payload and under WHVC.

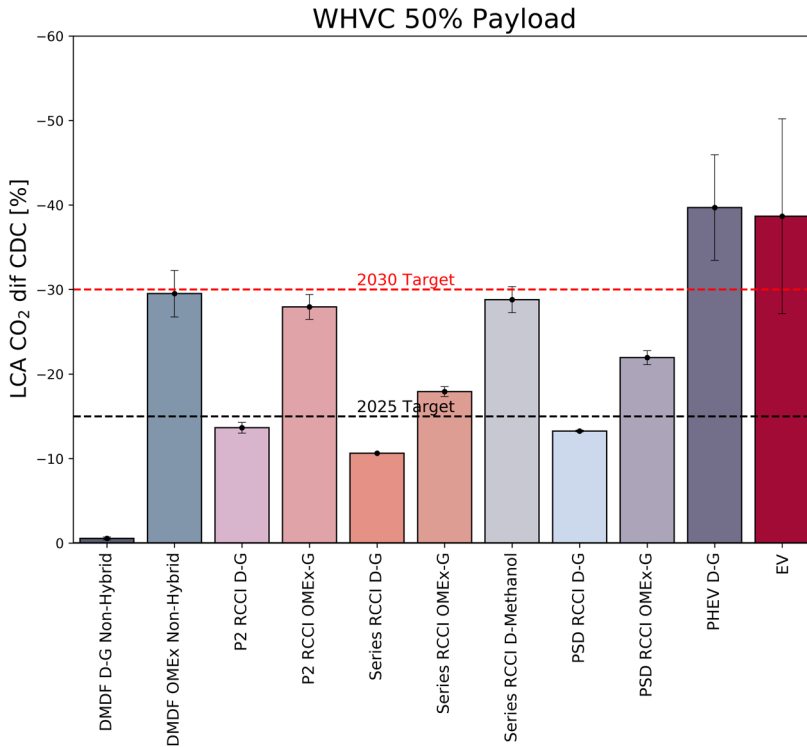


Figure 6-33. Life Cycle Analysis CO<sub>2</sub> emissions percentage difference against CDC non-hybrid for different technologies applied in a Medium-Duty truck at 50% payload and under WHVC.

Despite the large reduction of CO<sub>2</sub> emissions of the e-fuels showed in this work, a downside is the cost and availability. This type of fuels suffers from inherent inefficiencies, creating sustainability risks particular to the industry. Around half the input energy in the electricity used to make e-fuels is lost during the production process; for hydrogen, around one-quarter of input energy is lost. Using renewable electricity as e-fuels in an internal combustion engine is about five times less efficient than supplying that electricity directly to battery electric vehicles when the electricity energy is produced locally. An interesting work from Little [227] compared two scenarios: First, 100 percent local green energy, and second, imports of green energy from the Middle East. Figure 6-34 shows that locally produced

hydrogen is much less efficient than local green electricity. But when energy is imported from, for example, the Middle East, hydrogen's efficiency roughly doubles of that of electricity. From an energy production point of view, BEVs are favourable if clean electricity is regionally available all year. On the other hand, if the electricity and fuel production is performed in Middle East or Africa (large photovoltaic availability), e-fuels are potential solution.

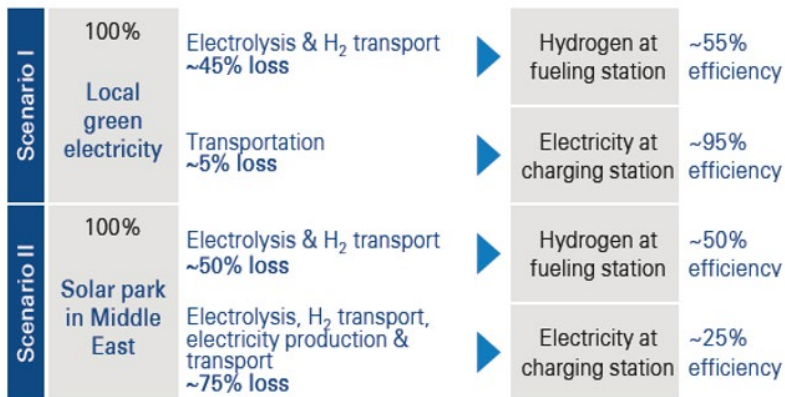


Figure 6-34. Upstream electricity scenarios. Adapted from [227].

The work of Ueckerdt et al. [228] derive levelized costs of e-fuels for a case in which hydrogen is produced in a renewable-rich country, stored and synthesized with direct air capture (DAC) based CO<sub>2</sub>, liquefied (in the case of methane) and shipped 3500 km to an importing country's harbour where it is fed into the existing fossil fuel infrastructure (without additional costs). The analysis focusses on large-scale average production costs and electricity costs are calculated without taxes and levies and based on cost developments for wind and solar PV, combined with empirical data on hourly price variability.

For 2020, it is estimate production costs for liquid e-fuels to reach ~220 €/MWh, based on green hydrogen (~80 €/MWh, ~2.7 €/kg) and direct air capture. These estimates are based on today's technology; yet, as only few demonstration and pilot plants exist. Therefore, large-scale production

assumptions are hypothetical and shall solely indicate the potential competitiveness and required policy support. Methane can be produced slightly cheaper than liquid e-fuels as it requires ~20% less CO<sub>2</sub> per energy, while long-distance transport costs are higher. Given historic natural gas and gasoline prices (mean of 2010-2020 values), this translates into a breakeven CO<sub>2</sub> price of ~690 €/tCO<sub>2</sub> for liquids and ~920 €/tCO<sub>2</sub> for gases. This means the necessary penalty for carbon fuel base production to equal the cost of the e-fuel. Abatement costs for replacing natural gas are higher because both natural gas prices and per-energy emissions savings (carbon intensities) are lower than for gasoline. For 2030 and 2050 the improvement in efficiency of the production of the e-fuels makes that the incentive in CO<sub>2</sub> abatement 240€/tCO<sub>2</sub> in 2030 and 30 €/tCO<sub>2</sub> in 2050 compared with gasoline.

Despite this work is based in several assumptions, give an idea of the expensive that is right now to produce e-fuels and the necessity of incentives to achieve a competitive price.

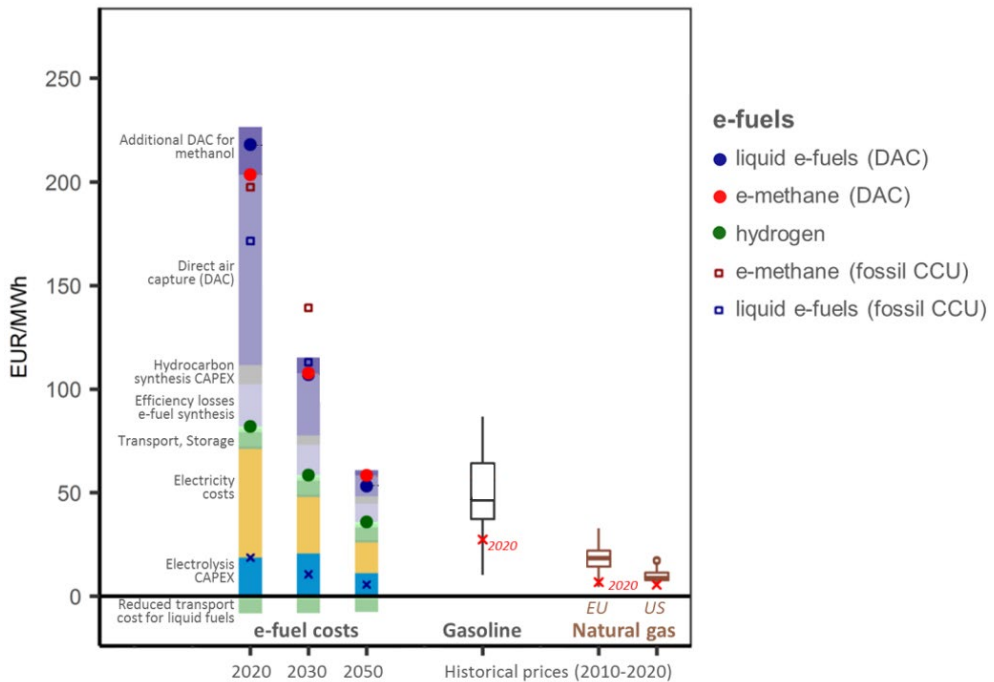


Figure 6-35. e-fuel cost analysis compared with conventional fuels. Adapted from [228].

## 6.5 Conclusions

Chapter 6 has presented a comprehensive evaluation of the different technologies in order to achieve the targets beyond 2025. In particular, the focus was put on 30% of CO<sub>2</sub> reduction estimated for 2030 and EUVII emissions pollutant limits (50% reduction of EUVI). Synthetic fuels such as OME<sub>x</sub> and Methanol were evaluated by numerical and experimental tools. The OME<sub>x</sub> shows higher potential than Methanol for soot and NO<sub>x</sub> reduction. However, due to the large low reactivity fuel ratio used in RCCI combustion, the Methanol shows a large CO<sub>2</sub> saving than OME<sub>x</sub> in different driving situations. In homologation conditions, OME<sub>x</sub> allows saving 26.4% of WTW CO<sub>2</sub> while Methanol 30.8% with respect to CDC in the same Series powertrain architecture. However, the P2 hybrid was also evaluated due to the complete ICE calibration of OME<sub>x</sub>, with WTW benefits in homologation conditions of 36.5%.

Dedicated calibration for Series hybrid powertrain was performed with Diesel-Gasoline and OME<sub>x</sub>-Gasoline RCCI to achieve EUVII NO<sub>x</sub> and soot limits. The results show that both fuel combinations allow for achieving EUVII in all driving conditions. The high oxygen content of OME<sub>x</sub> allows for highly reduced NO<sub>x</sub> with negligible soot emissions while not having large fuel consumption penalties. The Diesel-Gasoline suffers small penalties due to the narrow range of calibration settings.

Lastly, plug-in hybrid technology was evaluated combined with dual-fuel combustion. The electric driving ratio was shown for several battery capacities. The results are compared with the non-hybrid diesel truck and with a battery-electric truck. In terms of energy consumption, the PHEV can achieve similar values to the BEV when operating in charge-depleting mode. On the other hand, the charge-sustaining mode of the PHEV achieves similar

values to the full hybrid truck. In terms of WTW CO<sub>2</sub>, the combined CD and CS mode allows reducing above 30%. The BEV is around 50% and the FHEV 15% compared to CDC non-hybrid. However, including battery, powertrain, vehicle body, and maintaining the CO<sub>2</sub> saving changes. The LCA results show that for the PHEV, the best case is the 100 kWh battery size with a reduction higher than the 2030 targets. The EV shows high CO<sub>2</sub> reduction at low battery size, but when increasing the electric range, the benefits decays. The commercial truck with 400 kWh and 300 km vehicle range allows 28.1% CO<sub>2</sub> reduction. On the other hand, synthetic fuels such as OMEx and Methanol show large benefits due to the ultra-low WTW emissions. The best case was the P2 with OMEx due to the large use of the synthetic fuel together with high powertrain efficiency.

# Chapter 7

## Conclusions, outcomes, and suggestions for future work

### **Content**

---

7.1 Introduction.....	372
7.2 Summary and conclusions.....	372
7.3 Contributions and publications.....	377
7.4 Suggestions for future work.....	380
7.4.1 Assessment of the particle composition in dual-mode dual fuel with conventional and synthetic fuels. ....	381
7.4.2 Impact of aggressive transient engine operation in Dual-Mode Dual-Fuel combustion.....	381
7.4.3 Implementation in a real truck demonstrator.....	382
7.5 Bibliography .....	383

## **7.1 Introduction**

This last chapter provides a global summary of the main conclusions obtained throughout this investigation. This will also enable the verification the objectives initially proposed were fulfilled or not. In addition, the outcomes of the Thesis are presented to the reader to understand the impact of this work in the research field. Finally, suggestions for future works are presented and discussed based on the different observations that were evidenced during the work.

## **7.2 Summary and conclusions**

This Thesis was developed as an attempt to create a novel and cleaner powertrain with electrified components and an internal combustion engine with a low-temperature combustion mode to solve relevant issues of current diesel powertrains engines as CO<sub>2</sub>, NO<sub>x</sub>, and soot emissions.

During the literature review, it was evidenced that LTC concepts are a potential path to improve the conversion efficiency while solving the NO<sub>x</sub> soot dilemma from the conventional diesel combustion. The former LTCs such as HCCI, PCCI, and RCCI generally have a limited operating range inside the engine map, being limited at high load due to excessive pressure gradients and at low load by significant combustion instabilities. Moreover, the kinetically controlled nature of these concepts presents a hurdle in controlling the combustion development since low dynamic variables such as temperature are dominant factors in the combustion development. DMDF appears to be a possible solution to extend the operating range to the complete engine map. However, it has excessive soot and NO<sub>x</sub> emissions at a high engine load. Therefore, the ATS can not be removed, and the benefits of the LTC are reduced.

On the other hand, Chapter 2 shows that the electrification of the powertrain allows for improving overall vehicle efficiency. Different



powertrain architectures and electrification levels can be used. Despite the several options already studied or applied in the transport sector, there is a lack of work with Heavy-Duty vehicles and, in particular, with the study of pollutant emissions. Therefore, the combination of low-temperature combustion modes and an electrified powertrain can allow achieving high vehicle efficiency and low pollutant emissions.

The objective of the Thesis is set in Chapter 2 to understand the potential of a 48V battery system with various engine electric components for mild hybrid electrification (e-components), using various battery capacities and powertrain configurations, analyze full hybrid electrification benefits, examine the potential for synthetic fuels and plug-in hybrid systems to reduce CO<sub>2</sub> emissions and to meet EU VII limitations, re-calibrate the engine utilizing the dual-fuel combustion idea.

Chapter 3 shows the numerical and experimental tools together with the validation of the different models. The engine tested is a Volvo six-cylinder 8L originally calibrated by the OEM to meet EUVI emissions limits. The combustion is conventional diesel and coupled with a DOC, DPF, SCR, and ASC to meet the current 2022 European legislation. In previous work of CMT, changes in the engine setup were performed to be able to use a dual fuel combustion mode such as RCCI. A complete engine calibration with Diesel-Gasoline and OME<sub>x</sub>-Gasoline was taken as starting point. Along with this Thesis, the already available data was introduced in a vehicle model for testing non-hybrid and hybrid technologies. In addition, a pure electric truck model is developed for comparison.

The vehicle model is validated against on-road measurements with a non-hybrid commercial truck. The power discrepancies were below 1%, and the fuel consumption was below 2%. In addition, the RCCI combustion concept was tested in the transient cycle to compare emissions against the modeling approach. The results show that the model overpredicted the NO<sub>x</sub> and CO emission and underpredicted HC emissions due to differences in the warm-up of the engine. At 100% payload, the NO<sub>x</sub> was only 3% over the

experimental measurements, while the CO and HC were 4% and 10%, respectively. The Thesis includes several driving cycles representative of homologation and real conditions. Lastly, Chapter 3 presents the database to perform a Life Cycle Analysis. This approach allows a fair comparison between different technologies. Different from a tailpipe comparison as usual in the bibliography or web reports.

The mild-hybrid powertrains with e-components are discussed in Chapter 4. The coupling of an electrified turbocharging and positive displacement EGR pump allows for achieving similar calibration outputs to the double route EGR case in DMDF combustion. The use of one route without electrical assistance or any of the electric components alone does not allow to achieve the emissions targets in the complete map. The main benefits of the EGR pump are at the low and high loads, where energy recovery can be made. The electrified turbocharger gives more benefits than the EGR pump due to greater control of the air settings. The e-component results were fed into a P0 48V MHEV powertrain, which was put through its paces in twelve different driving scenarios. The non-hybrid CDC, non-hybrid DMDF HP&LP EGR, and P0 DMDF HP&LP EGR were compared to the new e-component calibration (P0 DMDF e-comp). The results reveal that P0 provides 4 percent (high payload and big highway phases) to 14 percent (non-hybrid architecture) advantages over non-hybrid design (low payload and large urban phases). In low payload settings, the e-components perform better than the non-hybrid DMDF HP&LP EGR. Overall, the P0 MHEV provides for 7.5 percent CO<sub>2</sub> tailpipe improvements in both EGR settings.

Despite the fact that the system is insufficient to meet the 2025 CO<sub>2</sub> reduction target (15 percent), it provides for significant CO<sub>2</sub> reductions by utilizing a small electric machine (30 kW) and battery size (2 kWh). In addition, an electrified heater (EHC) in the ATS is tested in the P0 hybrid architecture. The DOC is included in the calculation to understand the HC and CO emissions with the DMDF combustion concept and the hybridization. A sweep in the heating power demonstrates that 4 kW is the best solution for highly reducing the CO and HC emissions without high CO<sub>2</sub>

penalties due to the higher energy consumption. The mentioned power heating allows 6% of CO<sub>2</sub> reduction with HC below 0.1 g/kWh and CO below 0.01 g/kWh at homologation conditions (WHVC and 50% payload). The main benefits of the EHC are at low payload and urban cycles where the high start/stop makes that ATS below the light-off temperature. The use of the EHC allows the DMDF hybrid to achieve EUVI CO and HC emissions under all driving conditions.

Chapter 5 assesses the full hybridization with different powertrain architectures. The powertrain was designed in this section by performance analysis. Later, the battery size and control strategy was optimized by a genetic algorithm to obtain the best configuration to reduce CO<sub>2</sub> emissions. The results show that the hybrid platforms allow achieving from 14% (series and power split) to 18% (P2) of tailpipe CO<sub>2</sub> reduction with respect to the CDC non-hybrid case. These results are closer to or even higher than the 2025 European Target for the Heavy-Duty sector. Moreover, the higher electric machine power for series and power split does not show a considerable advantage over the P2 for the conditions tested. The extra regenerative braking between 70 hp and 280 hp of the electric machine is limited. The optimum case in terms of battery size is 10 kWh for the P2 and around 40 kWh for Series and Power Split. Therefore, the parallel hybrid allows a considerable reduction of the battery size with respect to a fully electric version (400 kWh).

The last section of the chapter analyzes the effect of the electric heater in the ATS. The higher engine off periods of the P2 with respect to the P0 increases the HC and CO emissions. The DOC is less efficient in this hybrid architecture. Therefore, the use of the EHC is mandatory. A re-calibration of the RBC strategy was performed, including the EHC and DOC in the genetic algorithm. The results show that the EHC penalizes 0.7% and allows HC and CO EUVI fulfillment. In addition, the P2 with EHC achieves 2025 CO<sub>2</sub> targets with a reduction of 16.2% with respect to CDC non-hybrid.

The last chapter of the results (Chapter 6) analyzes the impact of synthetic fuels, engine recalibration, and plug-in hybrids. In particular, the focus was put on 30% of CO<sub>2</sub> reduction estimated for 2030 and EUVII emissions pollutant limits (50% reduction of EUVI). Synthetic fuels such as OMEx and Methanol were evaluated by numerical and experimental tools. The OMEx shows higher potential than Methanol for soot and NO<sub>x</sub> reduction. However, due to the large low reactivity fuel ratio used in RCCI combustion, the Methanol shows a large CO<sub>2</sub> saving than OMEx in different driving situations. In homologation conditions, OMEx allows saving 26.4% of WTW CO<sub>2</sub> while Methanol 30.8% with respect to CDC in the same Series powertrain architecture. However, the P2 hybrid was also evaluated due to the complete ICE calibration of OMEx, with WTW benefits in homologation conditions of 36.5%.

Dedicated calibration for Series hybrid powertrain was performed with Diesel-Gasoline and OMEx-Gasoline RCCI to achieve EUVII NO<sub>x</sub> and soot limits. The results show that both fuel combinations allow for achieving EUVII in all driving conditions. The high oxygen content of OMEx allows for highly reduced NO<sub>x</sub> with negligible soot emissions while not having large fuel consumption penalties. The Diesel-Gasoline suffers small penalties due to the narrow range of calibration settings.

Lastly, plug-in hybrid technology was evaluated combined with dual-fuel combustion. The electric driving ratio was shown for several battery capacities. The results are compared with the non-hybrid diesel truck and with a battery-electric truck. When the PHEV operates in charge depletion mode, the PHEV can attain identical energy usage figures as the BEV. The PHEV's charge-sustaining mode, on the other hand, delivers similar results to the full hybrid truck. In terms of WTW CO<sub>2</sub>, combining CD and CS mode allows for a reduction of around 30%. In comparison to CDC non-hybrid, the BEV is roughly 50%, and the FHEV is 15%. However, the CO<sub>2</sub> savings vary depending on the battery, powertrain, vehicle structure, and maintenance. The best case for the PHEV, according to the LCA results, is a 100 kWh battery size with a decrease greater than the 2030 targets. When the battery

size is small, the EV reduces CO<sub>2</sub> emissions significantly, but as the electric range increases, the benefits diminish. The commercial truck with 400 kWh and 300 km of vehicle range reduces CO<sub>2</sub> emissions by 28.1 percent. Synthetic fuels, like OMEx and Methanol, on the other hand, provide significant benefits due to their extremely low WTW emissions. Because of the substantial utilization of synthetic fuel and good powertrain efficiency, the P2 with OMEx was the best case.

### 7.3 Contributions and publications

As part of this manuscript, the following publications have been published in international journals or presented at international conferences. The publications are listed in the order in which they were submitted.

#### International Scientific Journal (with Impact factor):

- 1) Benajes J, García A, Monsalve-Serrano J, Martinez-Boggio S.D. “Optimization of the parallel and mild hybrid vehicle platforms operating under conventional and advanced combustion modes”. *Energy Convers Manag* 2019;190:73–90. doi:10.1016/j.enconman.2019.04.010.
- 2) Luján JM, García A, Monsalve-Serrano J, Martinez-Boggio S.D. “Effectiveness of hybrid powertrains to reduce the fuel consumption and NO<sub>x</sub> emissions of a euro 6d-temp diesel engine under real-life driving conditions”. *Energy Convers Manag* 2019;199:111987. doi:10.1016/j.enconman.2019.111987.
- 3) Benajes J, García A, Monsalve-Serrano J, Martinez-Boggio S.D. “Emissions reduction from passenger cars with RCCI plug-in hybrid electric vehicle technology”. *Appl Therm Eng* 2020;164:114430. doi:10.1016/j.applthermaleng.2019.114430.
- 4) García A, Monsalve-Serrano J, Martinez-Boggio S.D, Wittek K. “Potential of hybrid powertrains in a variable compression ratio

- downsized turbocharged VVA spark ignition engine”. *Energy* 2020; 195:117039. doi:10.1016/j.energy.2020.117039.
- 5) García A, Monsalve-Serrano J, Martinez-Boggio S.D, Rückert Roso V, Duarte Souza Alvarenga Santos N. “Potential of bio-ethanol in different advanced combustion modes for hybrid passenger vehicles”. *Renew Energy* 2020; 150:58–77. doi:10.1016/j.renene.2019.12.102.
  - 6) García A, Carlucci P, Monsalve-Serrano J, Valletta A, Martinez-Boggio S.D. “Energy management strategies comparison for a parallel full hybrid electric vehicle using reactivity controlled compression ignition combustion”. *Appl Energy* 2020; 272:115191. doi:10.1016/j.apenergy.2020.115191.
  - 7) García A, Monsalve-serrano J, Martinez-Boggio S.D, Gaillard P, Poussin O, Amer AA. “Dual fuel combustion and hybrid electric powertrains as potential solution to achieve 2025 emissions targets in medium duty trucks sector”. *Energy Convers Manag* 2020; 224:113320. doi:10.1016/j.enconman.2020.113320.
  - 8) Benajes J, García A, Monsalve-Serrano J, Martinez Boggio S.D. “Potential of using omex as substitute of diesel in the dual-fuel combustion mode to reduce the global CO2 emissions”. *Transp Eng* 2020; 1:100001. doi:10.1016/j.treng.2020.01.001.
  - 9) García A, Monsalve-Serrano J, Martinez Boggio S.D, Gaillard P. “Impact of the hybrid electric architecture on the performance and emissions of a delivery truck with a dual-fuel RCCI engine”. *Appl Energy* 2021; 301:117494. doi:10.1016/j.apenergy.2021.117494.
  - 10) Serrano JR, García A, Monsalve-Serrano J, Martinez Boggio S.D. “High efficiency two stroke opposed piston engine for plug-in hybrid electric vehicle applications: Evaluation under homologation and real driving conditions”. *Appl Energy* 2021; 282:116078. doi:10.1016/j.apenergy.2020.116078.
  - 11) García A, Monsalve-serrano J, Sari RL, Martinez Boggio S.D. “An optical investigation of thermal runaway phenomenon under thermal abuse conditions”. *Energy Convers Manag* 2021; 246:114663. doi:10.1016/j.enconman.2021.114663.

- 12) García A, Monsalve-serrano J, Martinez Boggio S.D, Gaillard P. “Emissions reduction by using e-components in 48 V mild hybrid trucks under dual-mode dual-fuel combustion”. *Appl Energy* 2021; 299:117305. doi:10.1016/j.apenergy.2021.117305.
- 13) García A, Carlucci P, Monsalve-Serrano J, Valletta A, Martinez Boggio S.D. “Energy management optimization for a power-split hybrid in a dual-mode RCCI-CDC engine”. *Appl Energy* 2021; 302:117525. doi:10.1016/j.apenergy.2021.117525.
- 14) García A, Monsalve-serrano J, Sari RL, Martinez Boggio S.D. “Energy sustainability in the transport sector using synthetic fuels in Series hybrid trucks with RCCI dual-fuel engine”. *Fuel* 2022; 308:122024. doi:10.1016/j.fuel.2021.122024.
- 15) García A, Monsalve-Serrano J, Lago Sari R, Martinez Boggio S.D. “Energy assessment of an electrically heated catalyst in a hybrid RCCI truck”. *Energy* 2022; 238:121681. doi:10.1016/j.energy.2021.121681.
- 16) García A, Monsalve-serrano J, Sari RL, Martinez Boggio S.D. “Thermal runaway evaluation and thermal performance enhancement of a lithium-ion battery coupling cooling system and battery sub-models”. *Appl Therm Eng* 2022; 202:117884. doi:10.1016/j.applthermaleng.2021.117884.
- 17) García A, Monsalve-Serrano J, Sari RL, Martinez Boggio S.D. “Influence of environmental conditions in the battery thermal runaway process of different chemistries: Thermodynamic and optical assessment”. *Int J Heat Mass Transf* 2022; 184:122381. doi:10.1016/j.ijheatmasstransfer.2021.122381.
- 18) Antonio García, Javier Monsalve-Serrano, Santiago Martinez-Boggio, Wenbin Zhao, Yong Qian. “Intelligent charge compression ignition combustion for range extender medium duty applications”. *Renewable Energy* 2022, 187 (2022) 671-687; doi.org/10.1016/j.renene.2022.01.110.
- 19) Antonio García, Peng Zhao, Javier Monsalve-Serrano, Santiago Martinez-Boggio. “Optical diagnostics of the venting spray and combustion behaviour during Li-ion battery thermal runaway induced

by ramp heating”. *Applied Thermal Engineering* 2022, 218 (2023) 119308; doi.org/10.1016/j.applthermaleng.2022.119308.

Peer reviewed articles and Conferences:

- 1) Benajes J, Garcia A, Monsalve-Serrano J, Martinez S. “Dual-Fuel Ethanol-Diesel Technology Applied in Mild and Full Hybrid Powertrains”. SAE Technical Paper, 2019. doi:10.4271/2019-24-0115.
- 2) Benajes J, García A, Monsalve-Serrano J, Martinez Boggio S.D. “CO<sub>2</sub> Well-to-wheel abatement with plug-in hybrid electric vehicles running under low temperature combustion mode with green fuels”. SAE Technical Paper 2020; 2020-37-0026, 2020, doi:10.4271/2020-37-0026.
- 3) Poussin O, García A, Monsalve-serrano J, Martinez-Boggio S.D, and Gaillard P. “Dual-Fuel RCCI Diesel-Gasoline Hybrid Truck Concept to Achieve the Future Emissions Targets”. 10th Aachen Colloquium China Sustainable Mobility 2020.
- 4) Antonio Garcia, Javier Monsalve-Serrano, Rafael Sari, and Santiago Martinez. “Combining DMDF and Hybrid Powertrains: A Look on the Effects of Different Battery Modelling Approaches”. SAE Technical Paper 2022-01-0658, 2022, doi:10.4271/2022-01-0658.

## 7.4 Suggestions for future work

Throughout the investigation presented in this Thesis, a number of works were identified as additional investigations to be performed. Unfortunately, they could not be done during this Thesis either due to time restrictions or because the work required additional devices that were not available at the time. Therefore, they are here included as future work suggestions to further develop the concept as well as to address drawbacks that may enhance the applicability of the concept in real applications.



### **7.4.1 Assessment of the particle composition in dual-mode dual fuel with conventional and synthetic fuels.**

The analysis of particle emission composition was regarded as a critical task. Despite the outstanding findings achieved with the AVL 415 S smoke meter, it was impossible to determine whether or not the concept could meet EUVI requirements. As previously stated, earlier studies have indicated that the D-G DMDF particle is primarily made up of condensable hydrocarbons, which cannot be quantified using the smoke meter measurement principle. As a result, even when using OMEx to measure 0% soot, a significant amount of condensable may remain in the exhaust gases. In this regard, specific research should be conducted to better characterize and quantify the particle composition using Diesel-Gasoline, OMEx-Gasoline, and Diesel-Methanol.

Furthermore, research reveals that oxygenated fuels are more likely to produce tiny particles. The quantification of the particulate number will be done to homologate the engine prototype against the EUVI requirements in terms of particle size.

### **7.4.2 Impact of aggressive transient engine operation in Dual-Mode Dual-Fuel combustion**

Despite that Series hybrid transient cycles were tested in this Thesis, the engine driving cycle requirements in a P2 hybrid or a non-hybrid are more aggressive than the steps tested. Therefore, experimental tests need to be done to understand the effect and the possible changes to the calibration proposed. In addition, complete engine modeling with a predictive combustion model and the calibrated air management system in this Thesis can be applied to better emissions and brake output prediction.

### 7.4.3 Implementation in a real truck demonstrator

The creation and market deployment of a novel concept necessitates the completion of several stages. It is divided into TRLs (time readiness levels) according to its maturity level, which ranges from 1 to 9. The work reported in this Thesis has advanced the concept to TRL 5, which entails evaluating and validating the concept in real-world scenarios. Higher TRLs, on the other hand, need a true concept demonstrator, with all subsystems assembled in a representative vehicle and tested in various circumstances. As a result, in order to continue the development process, the engine must be assembled in an actual truck. During this implementation, there are a few things to keep in mind as adjusting the calibration maps to operate under different ambient conditions and adding the abovementioned strategies for aggressive transient load and engine speed conditions.

After the engine has been fully operational under the combustion concept and the calibration maps have been adjusted, a packing study should be performed to account for the changes in the air management and after-treatment systems. Finally, much effort needs to be done on how to accommodate the various sensors and actuators from the vehicle with the new DMDF combustion calibration configuration.

The hybrid configurations found in this work need to be tested on an experimental test bench and then passed to a real truck demonstrator. The battery and electric motor interaction with the ICE needs to be tested in transient conditions. The predicted exhaust measurements and CO<sub>2</sub> savings need to be demonstrated to achieve a high TRL.

## 7.5 Bibliography

- [1] Allen, M.R., O.P. Dube, W. Solecki, F. Aragón-Durand, W. Cramer, S. Humphreys, M. Kainuma, J. Kala NM, Y. Mulugetta, R. Perez, M.Wairiu and KZ. An IPCC Special Report on the impacts of global warming of 1.5°C above pre-industrial levels and related global greenhouse gas emission pathways, in the context of strengthening the global response to the threat of climate change, sustainable development,. 2018.
- [2] Wu Q, Li T, Zhang S, Fu J, Seyler BC, Zhou Z, et al. Evaluation of NO<sub>x</sub> emissions before, during, and after the COVID-19 lockdowns in China: A comparison of meteorological normalization methods. *Atmos Environ* 2022;278:119083. doi:10.1016/j.atmosenv.2022.119083.
- [3] Jiang Y, Tan Y, Yang J, Karavalakis G, Johnson KC, Yoon S, et al. Understanding elevated real-world NO<sub>x</sub> emissions: “Heavy-duty diesel” engine certification testing versus in-use vehicle testing. *Fuel* 2022;307:121771. doi:10.1016/j.fuel.2021.121771.
- [4] Rodrigues Teixeira AC, Borges RR, Machado PG, Mouette D, Dutra Ribeiro FN. PM emissions from heavy-duty trucks and their impacts on human health. *Atmos Environ* 2020;241:117814. doi:10.1016/j.atmosenv.2020.117814.
- [5] World O, Data I. Emissions by sector n.d. [https://ourworldindata.org/emissions-by-sector#:~:text=when it decomposes-,Agriculture%2C Forestry and Land Use%3A 18.4%25,quarter of greenhouse gas emissions.](https://ourworldindata.org/emissions-by-sector#:~:text=when%20it%20decomposes-,Agriculture%2C%20Forestry%20and%20Land%20Use%3A%2018.4%25,quarter%20of%20greenhouse%20gas%20emissions.)
- [6] IEA. Global Energy Review: CO<sub>2</sub> Emissions in 2020. 2020.
- [7] Comisión Europea. A European Strategy for low-emission mobility - Fact Sheet. *Eur Com* 2016:24.

- [8] Prasad R, Bella VR. A review on diesel soot emission, its effect and control. *Bull Chem React Eng & Catal* 2010;5:69–86. doi:10.9767/bcrec.5.2.794.69-86.
- [9] Bar S, Parida BR, Mandal SP, Pandey AC, Kumar N, Mishra B. Impacts of partial to complete COVID-19 lockdown on NO<sub>2</sub> and PM<sub>2.5</sub> levels in major urban cities of Europe and USA. *Cities* 2021;117:103308. doi:10.1016/j.cities.2021.103308.
- [10] Singh A, Bartington SE, Song C, Ghaffarpasand O, Kraftl M, Shi Z, et al. Impacts of emergency health protection measures upon air quality, traffic and public health: evidence from Oxford, UK. *Environ Pollut* 2022;293:118584. doi:10.1016/j.envpol.2021.118584.
- [11] Affairs D for EF& R. *Air Pollution in the UK 2017*. 2018.
- [12] European Commission. *Proposal for a Regulation of the European Parliament and of the Council setting CO<sub>2</sub> emission performance standards for new heavy duty vehicles*. vol. 1. 2018.
- [13] European Union. *Regulation (EC) No 595/2009 of the European Parliament and of the Council of 18 June 2009 on type-approval of motor vehicles and engines with respect to emissions from heavy duty vehicles (Euro VI) and on access to vehicle repair and maintenance informati*. *Off J Eur Union* 2009;2008:1–13.
- [14] AVL. *Emission Test Systems EMISSION: HEAVY DUTY AND OFF-ROAD*. 2019.
- [15] Continental. *Worldwide Emission Standards and Related Regulations - Passenger Cars / Light and Medium Duty Vehicles*. *Cont Futur Motion* 2019:210 pages.
- [16] ICCT. *China's Stage VI emission standard for heavy-duty vehicles (final rule)*. *ICCT Policy Updat* 2018:13.

- [17] FEV. 1ST SESSION FEV WEBINAR FUTURE TRUCK SERIES. 2020.
- [18] Making T, Possible M. Making Clean Electrification Possible 2021.
- [19] Environment T&. E-fools : why e-fuels in cars make no economic or environmental sense 2021:1–23.
- [20] Environment T&. Hitting the EV Inflection Point 2021.
- [21] Senecal K, Felix L. Racing Toward Zero: The Untold Story of Driving Green. SAE International in United States; 2021.
- [22] Zhang F, Obeid E, Bou Nader W, Zoughaib A, Luo X. Well-to-Wheel analysis of natural gas fuel for hybrid truck applications. *Energy Convers Manag* 2021;240:114271. doi:10.1016/j.enconman.2021.114271.
- [23] Hernandez M, Messagie M, De Gennaro M, Van Mierlo J. Resource depletion in an electric vehicle powertrain using different LCA impact methods. *Resour Conserv Recycl* 2017;120:119–30. doi:10.1016/j.resconrec.2016.11.005.
- [24] Guo Y, Kelly JA, Clinch JP. Road transport electrification – Is timing everything? Implications of emissions analysis’ outcomes for climate and air policy. *Transp Res Interdiscip Perspect* 2021;12:100478. doi:10.1016/j.trip.2021.100478.
- [25] Rottoli M, Dirnaichner A, Pietzcker R, Schreyer F, Luderer G. Alternative electrification pathways for light-duty vehicles in the European transport sector. *Transp Res Part D Transp Environ* 2021;99:103005. doi:10.1016/j.trd.2021.103005.
- [26] European Parliament and Council. REGULATION (EU) 2019/1242 OF THE EUROPEAN PARLIAMENT AND OF THE COUNCIL of 20 June 2019 setting CO2 emission performance standards for new

- heavy-duty vehicles and amending Regulations (EC) No 595/2009 and (EU) 2018/956 of the European Parliament and of th. Off J Eur Union 2019;198:202–40.
- [27] European Union. Regulation (EU) 2017/631 of the European Parliament and of the Council. Off J Eur Union 2017;L 168:71.
- [28] FEV Heavy Duty at International Vienna Motor Symposium n.d. <https://wiener-motorensymposium.at/en/> (accessed June 7, 2022).
- [29] Nations U, Committee IT. World Forum for Harmonization of Vehicle Regulations. vol. 16. 2020. doi:10.1017/S0020818300010845.
- [30] Fev PH, Gmbh G, Consulting TLFE V. HEAVY-DUTY POWERTRAIN CONCEPTS TO COMPLY WITH 2025 & 2030 GHG REGULATIONS PREPARED FOR AUTOMOTIVE WORLD The “ Green Deal ” aims for a CO 2 neutral economy – also in the transport sector substantial measures have to be taken to fulfill the challenging targ 2020.
- [31] Commission ET. Making the Hydrogen Economy Possible :Accelerating Clean Hydrogen in an Electrified Economy. 2021.
- [32] Lai X, Chen Q, Tang X, Zhou Y, Gao F, Guo Y, et al. Critical review of life cycle assessment of lithium-ion batteries for electric vehicles: A lifespan perspective. ETransportation 2022;12:100169. doi:10.1016/j.etrans.2022.100169.
- [33] ACEA. ACEA Position Paper Views on proposals for Euro 7 emission standard 2020:18.
- [34] Ragon AP, Rodríguez F. Estimated cost of diesel emissions control technology to meet future Euro VII standards 2021:1–27.
- [35] Lynch LA, Hunter CA, Zigler BT, Thornton MJ, Reznicek EP, Lynch

- LA, et al. On-Road Heavy-Duty Low-NOx Technology Cost Study On-Road Heavy-Duty Low-NOx Technology Cost Study 2020.
- [36] Posada F, Isenstadt A, Badshah H. Estimated Cost of Diesel Emissions-control Technology to meet future California low NOx standards in 2024 and 2027. *Int Counc Clean Transp* 2020.
- [37] Hadl K, Raser B, Sacher T, Graf G. Solutions for Lowest NOx and CO2 Emissions on Heavy Duty Engines. *MTZ Worldw* 2021;82:16–23. doi:10.1007/s38313-020-0613-z.
- [38] Neely GD, Sasaki S, Huang Y, Leet JA, Stewart DW. New Diesel Emission Control Strategy to Meet US Tier 2 Emissions Regulations 2020;2005.
- [39] Kokjohn SL, Hanson RM, Splitter DA, Reitz RD. Fuel reactivity controlled compression ignition (RCCI): a pathway to controlled high-efficiency clean combustion. *Int J Engine Res* 2011;12:209–26. doi:10.1177/1468087411401548.
- [40] Desantes JM, Benajes J, García A, Monsalve-Serrano J. The role of the in-cylinder gas temperature and oxygen concentration over low load reactivity controlled compression ignition combustion efficiency. *Energy* 2014;78:854–68. doi:10.1016/j.energy.2014.10.080.
- [41] Benajes J, Pastor J V., García A, Monsalve-Serrano J. The potential of RCCI concept to meet EURO VI NOx limitation and ultra-low soot emissions in a heavy-duty engine over the whole engine map. *Fuel* 2015;159:952–61. doi:10.1016/j.fuel.2015.07.064.
- [42] Benajes J, García A, Monsalve-Serrano J, Boronat V. Gaseous emissions and particle size distribution of dual-mode dual-fuel diesel-gasoline concept from low to full load. *Appl Therm Eng* 2017;120:138–49. doi:10.1016/j.applthermaleng.2017.04.005.

- [43] Benajes J, Molina S, García A, Monsalve-Serrano J. Effects of direct injection timing and blending ratio on RCCI combustion with different low reactivity fuels. *Energy Convers Manag* 2015;99:193–209. doi:10.1016/j.enconman.2015.04.046.
- [44] Fang W, Kittelson DB, Northrop WF. Optimization of reactivity-controlled compression ignition combustion fueled with diesel and hydrous ethanol using response surface methodology. *Fuel* 2015;160:446–57. doi:10.1016/j.fuel.2015.07.055.
- [45] Splitter D, Wissink M, Delvescovo D, Reitz R. RCCI engine operation towards 60% thermal efficiency. *SAE Tech Pap* 2013;2. doi:10.4271/2013-01-0279.
- [46] Li Y, Jia M, Chang Y, Fan W, Xie M, Wang T. Evaluation of the necessity of exhaust gas recirculation employment for a methanol/diesel reactivity controlled compression ignition engine operated at medium loads. *Energy Convers Manag* 2015;101:40–51. doi:10.1016/j.enconman.2015.05.041.
- [47] Benajes J, García A, Monsalve-Serrano J, Boronat V. Achieving clean and efficient engine operation up to full load by combining optimized RCCI and dual-fuel diesel-gasoline combustion strategies. *Energy Convers Manag* 2017;136:142–51. doi:10.1016/j.enconman.2017.01.010.
- [48] Keramydas C, Papadopoulos G, Ntziachristos L, Lo TS, Ng KL, Wong HLA, et al. Real-World Measurement of Hybrid Buses Fuel Consumption and Pollutant Emissions in a Metropolitan Urban Road Network. *Energies* 2018;11:1–16. doi:10.3390/en11102569.
- [49] Eurostat. Freight transport statistics n.d. [https://ec.europa.eu/eurostat/statistics-explained/index.php?title=Freight\\_transport\\_statistics#Modal\\_split](https://ec.europa.eu/eurostat/statistics-explained/index.php?title=Freight_transport_statistics#Modal_split) (accessed May 14, 2021).



- [50] ACEA. Medium and Heavy Buses (over 3.5 t) New Registrations by Fuel Type in the European Union. *Eur Automob Manuf Assoc* 2020;3–6.
- [51] Zayer E. European Truck Market Outlook 2022. 2022 n.d. <https://www.bain.com/insights/european-truck-market-outlook-2022/> (accessed May 25, 2022).
- [52] Reinhart T, Cooper C, Whitefoot J, MacIsaac J. Analysis Process for Truck Fuel Efficiency Study. *SAE Int J Commer Veh* 2015;8:451–9. doi:10.4271/2015-01-2778.
- [53] Lajunen A. Fuel economy analysis of conventional and hybrid heavy vehicle combinations over real-world operating routes. *Transp Res Part D Transp Environ* 2014;31:70–84. doi:10.1016/j.trd.2014.05.023.
- [54] Zhu G, Zhen D, Chen W, Zuo Q, Zhao M, Wang Y, et al. Experimental study on the engine energy flow of a heavy-duty vehicle under C-WTVC. *Energy Reports* 2022;8:4430–42. doi:10.1016/j.egy.2022.03.079.
- [55] Dec JE. A Conceptual Model of DI Diesel Combustion Based on Laser-Sheet Imaging\*, 1997. doi:10.4271/970873.
- [56] Joshi A. A Review of Emissions Control Technologies for On-Road Vehicles, 2022, p. 39–56. doi:10.1007/978-981-16-8717-4\_3.
- [57] Jayagopal S, Sreerag T, Saravanan P, Porpatham E, Senthilkumar A. Emission optimization techniques for random NOx to meet stringent emissions for medium & heavy duty diesel engine applications. *SAE Tech Pap* 2015. doi:10.4271/2015-26-0093.
- [58] Joshi A. Review of Vehicle Engine Efficiency and Emissions. *SAE Tech Pap* 2020;2020-April:1–29. doi:10.4271/2020-01-0352.
- [59] NEWS G. World’s First Commercial Diesel Engine with Brake

- Thermal Efficiency Above 50% Launched by Weichai, Boosted by Garrett 2020.  
<https://www.garrettmotion.com/news/newsroom/article/worlds-first-commercial-diesel-engine-with-brake-thermal-efficiency-above-50-launched-by-weichai-boosted-by-garrett/> (accessed May 8, 2022).
- [60] Demir U, Kozan A, Özer S. Experimental investigation of the effect of urea addition to fuel on engine performance and emissions in diesel engines. *Fuel* 2022;311. doi:10.1016/j.fuel.2021.122578.
- [61] Volvo T. D13K460, EU6SCR 2020.  
[https://stpi.it.volvo.com/STPIFiles/Volvo/FactSheet/D13K460,EU6SCR\\_Eng\\_09\\_310999631.pdf](https://stpi.it.volvo.com/STPIFiles/Volvo/FactSheet/D13K460,EU6SCR_Eng_09_310999631.pdf) (accessed May 6, 2020).
- [62] Betageri V, Mahesh R. Effects of the Real Driving Conditions on the NOx Emission of a Medium Duty Diesel Commercial Vehicle. *SAE Tech Pap* 2017;2017-Janua:1–6. doi:10.4271/2017-26-0124.
- [63] International Energy Agency. Global EV Outlook 2021 - Accelerating ambitions despite the pandemic. *Glob EV Outlook 2021* 2021:101.
- [64] Mareev I, Becker J, Sauer DU. Battery dimensioning and life cycle costs analysis for a heavy-duty truck considering the requirements of long-haul transportation. *Energies* 2018;11. doi:10.3390/en11010055.
- [65] Farhan SM, Wang P. Post-injection strategies for performance improvement and emissions reduction in DI diesel engines—A review. *Fuel Process Technol* 2022;228:107145. doi:10.1016/j.fuproc.2021.107145.
- [66] Khoa NX, Lim O. A Review of the External and Internal Residual Exhaust Gas in the Internal Combustion Engine. *Energies* 2022;15. doi:10.3390/en15031208.
- [67] Fatehi H, Lucchini T, D’Errico G, Karlsson A, Bai XS, Andersson Ö.

- Effect of In-cylinder Flow Structures on Late Cycle Soot Oxidation in a Quiescent Heavy-duty Diesel Engine. *Combust Sci Technol* 2022;194:316–36. doi:10.1080/00102202.2019.1678962.
- [68] Pastor J V., García A, Micó C, Lewiski F. Soot reduction for cleaner Compression Ignition Engines through innovative bowl templates. *Int J Engine Res* 2021;22:2477–91. doi:10.1177/1468087420951324.
- [69] Heywood JB. *Internal Combustion Engine Fundamentals*. 2018.
- [70] Reşitođlu IA, Altinişik K, Keskin A. The pollutant emissions from diesel-engine vehicles and exhaust aftertreatment systems. *Clean Technol Environ Policy* 2015;17:15–27. doi:10.1007/s10098-014-0793-9.
- [71] Rana S, Saxena MR, Maurya RK. A review on morphology, nanostructure, chemical composition, and number concentration of diesel particulate emissions. vol. 29. *Environmental Science and Pollution Research*; 2022. doi:10.1007/s11356-021-15999-5.
- [72] Agarwal AK, Singh AP, Maurya RK. Evolution, challenges and path forward for low temperature combustion engines. *Prog Energy Combust Sci* 2017;61:1–56. doi:10.1016/j.pecs.2017.02.001.
- [73] Pachiannan T, Zhong W, Rajkumar S, He Z, Leng X, Wang Q. A literature review of fuel effects on performance and emission characteristics of low-temperature combustion strategies. *Appl Energy* 2019;251:113380. doi:10.1016/j.apenergy.2019.113380.
- [74] El Shenawy EA, Elkelawy M, Bastawissi HAE, Shams MM, Panchal H, Sadasivuni K, et al. Investigation and performance analysis of water-diesel emulsion for improvement of performance and emission characteristics of partially premixed charge compression ignition (PPCCI) diesel engines. *Sustain Energy Technol Assessments* 2019;36:100546. doi:10.1016/j.seta.2019.100546.

- [75] Kiplimo R, Tomita E, Kawahara N, Yokobe S. Effects of spray impingement, injection parameters, and EGR on the combustion and emission characteristics of a PCCI diesel engine. *Appl Therm Eng* 2012;37:165–75. doi:10.1016/j.applthermaleng.2011.11.011.
- [76] Reitz RD, Duraisamy G. Review of high efficiency and clean reactivity controlled compression ignition (RCCI) combustion in internal combustion engines. *Prog Energy Combust Sci* 2015;46:12–71. doi:10.1016/j.pecs.2014.05.003.
- [77] Thring RH. Homogeneous-Charge Compression-Ignition (HCCI) Engines. 1989 SAE Int. Fall Fuels Lubr. Meet. Exhib., SAE International; 1989. doi:https://doi.org/10.4271/892068.
- [78] Saxena S, Bedoya ID. Fundamental phenomena affecting low temperature combustion and HCCI engines, high load limits and strategies for extending these limits. *Prog Energy Combust Sci* 2013;39:457–88. doi:10.1016/j.pecs.2013.05.002.
- [79] Tanaka S, Ayala F, Keck JC. A reduced chemical kinetic model for HCCI combustion of primary reference fuels in a rapid compression machine. *Combust Flame* 2003;133:467–81. doi:10.1016/S0010-2180(03)00057-9.
- [80] Tanaka S, Ayala F, Keck JC, Heywood JB. Two-stage ignition in HCCI combustion and HCCI control by fuels and additives. *Combust Flame* 2003;132:219–39. doi:10.1016/S0010-2180(02)00457-1.
- [81] Yao M, Zheng Z, Liu H. Progress and recent trends in homogeneous charge compression ignition (HCCI) engines. *Prog Energy Combust Sci* 2009;35:398–437. doi:10.1016/j.pecs.2009.05.001.
- [82] Eng J, Technical S a E, Series P. Characterization of Pressure Waves in HCCI Combustion Reprinted From: Homogeneous Charge Compression Ignition Engines. *Sae* 2002:2002-01–2859.

- [83] D'Ambrosio S, Gaia F, Iemmolo D, Mancarella A, Salamone N, Vitolo R, et al. Performance and Emission Comparison between a Conventional Euro VI Diesel Engine and an Optimized PCCI Version and Effect of EGR Cooler Fouling on PCCI Combustion. SAE Tech Pap 2018;2018-April:1–16. doi:10.4271/2018-01-0221.
- [84] Hardy WL, Reitz RD. A study of the effects of high EGR, high equivalence ratio, and mixing time on emissions levels in a heavy-duty diesel engine for PCCI combustion. SAE Tech Pap 2006;2006. doi:10.4271/2006-01-0026.
- [85] Torregrosa AJ, Broatch A, García A, Mónico LF. Sensitivity of combustion noise and NO<sub>x</sub> and soot emissions to pilot injection in PCCI Diesel engines. Appl Energy 2013;104:149–57. doi:10.1016/j.apenergy.2012.11.040.
- [86] Benajes J, García A, Monsalve-Serrano J, Lago Sari R. Experimental investigation on the efficiency of a diesel oxidation catalyst in a medium-duty multi-cylinder RCCI engine. Energy Convers Manag 2018;176:1–10. doi:10.1016/j.enconman.2018.09.016.
- [87] García A, Monsalve-Serrano J, Villalta D, Sari R. Octane number influence on combustion and performance parameters in a Dual-Mode Dual-Fuel engine. Fuel 2019;258:116140. doi:10.1016/j.fuel.2019.116140.
- [88] Benajes J, Pastor J V., García A, Monsalve-Serrano J. An experimental investigation on the influence of piston bowl geometry on RCCI performance and emissions in a heavy-duty engine. Energy Convers Manag 2015;103:1019–30. doi:10.1016/j.enconman.2015.07.047.
- [89] Lerin C, Edwards KD, Curran SJ, Nafziger EJ, Moses-DeBusk M, Kaul BC, et al. Exploring the potential benefits of high-efficiency dual-fuel combustion on a heavy-duty multi-cylinder engine for SuperTruck

- I. Int J Engine Res 2021. doi:10.1177/14680874211006943.
- [90] García A, Monsalve-Serrano J, Villalta D, Lago Sari R, Gordillo Zavaleta V, Gaillard P. Potential of e-Fischer Tropsch diesel and oxymethyl-ether (OMEx) as fuels for the dual-mode dual-fuel concept. *Appl Energy* 2019;253:113622. doi:10.1016/j.apenergy.2019.113622.
- [91] Popp T, Lechner R, Becker M, Hebauer M, O'Connell N, Brautsch M. Potentials of OME/diesel blends for stationary power production – Improving emission characteristics of a diesel CHP unit. *Appl Therm Eng* 2019;153:483–92. doi:10.1016/j.applthermaleng.2019.03.015.
- [92] Styring P, Dowson GRM, Tozer IO. Synthetic Fuels Based on Dimethyl Ether as a Future Non-Fossil Fuel for Road Transport From Sustainable Feedstocks. *Front Energy Res* 2021;9:1–22. doi:10.3389/fenrg.2021.663331.
- [93] Chen H, Su X, Li J, Zhong X. Effects of gasoline and polyoxymethylene dimethyl ethers blending in diesel on the combustion and emission of a common rail diesel engine. *Energy* 2019;171:981–99. doi:10.1016/j.energy.2019.01.089.
- [94] Inagaki K, Fuyuto T, Nishikawa K, Nakakita K, Sakata I. Dual-Fuel PCI Combustion Controlled by In-Cylinder Stratification of Ignitability 2006;2006. doi:10.4271/2006-01-0028.
- [95] Bessonette PW, Schleyer CH, Duffy KP, Hardy WL, Liechty MP. Effects of fuel property changes on heavy-duty HCCI combustion. *SAE Tech Pap* 2007;2007:776–90. doi:10.4271/2007-01-0191.
- [96] Benajes J, García A, Monsalve-Serrano J, Lago Sari R. Fuel consumption and engine-out emissions estimations of a light-duty engine running in dual-mode RCCI/CDC with different fuels and driving cycles. *Energy* 2018;157:19–30. doi:10.1016/j.energy.2018.05.144.

- [97] Splitter DA, Reitz RD. Fuel reactivity effects on the efficiency and operational window of dual-fuel compression ignition engines. *Fuel* 2014;118:163–75. doi:10.1016/j.fuel.2013.10.045.
- [98] Pan S, Cai K, Cai M, Du C, Li X, Han W, et al. Experimental study on the cyclic variations of ethanol/diesel reactivity controlled compression ignition (RCCI) combustion in a heavy-duty diesel engine. *Energy* 2021;237:121614. doi:10.1016/j.energy.2021.121614.
- [99] Panda K, Ramesh A. Parametric investigations to establish the potential of methanol based RCCI engine and comparison with the conventional dual fuel mode. *Fuel* 2022;308:122025. doi:10.1016/j.fuel.2021.122025.
- [100] Pan S, Liu X, Cai K, Li X, Han W, Li B. Experimental study on combustion and emission characteristics of iso-butanol/diesel and gasoline/diesel RCCI in a heavy-duty engine under low loads. *Fuel* 2020;261:116434. doi:10.1016/j.fuel.2019.116434.
- [101] Li J, Ling X, Liu D, Yang W, Zhou D. Numerical study on double injection techniques in a gasoline and biodiesel fueled RCCI (reactivity controlled compression ignition) engine. *Appl Energy* 2018;211:382–92. doi:10.1016/j.apenergy.2017.11.062.
- [102] García A, Monsalve-Serrano J, Villalta D, Sari R. Octane number influence on combustion and performance parameters in a Dual-Mode Dual-Fuel engine. *Fuel* 2019;258. doi:10.1016/j.fuel.2019.116140.
- [103] Ansari E, Shahbakhti M. Optimization of performance and operational cost for a dual mode diesel- natural gas RCCI and diesel combustion engine 2018;231:549–61. doi:10.1016/j.apenergy.2018.09.040.
- [104] Dalha IB, Said MA, Abdul Karim ZA, El-Adawy M. Effects of port mixing and high carbon dioxide contents on power generation and emission characteristics of biogas-diesel RCCI combustion. *Appl*

- Therm Eng 2021;198:117449.  
doi:10.1016/j.applthermaleng.2021.117449.
- [105] Sattarzadeh M, Ebrahimi M, Jazayeri SA. A detail study of a RCCI engine performance fueled with diesel fuel and natural gas blended with syngas with different compositions. *Int J Hydrogen Energy* 2022;47:16283–96. doi:10.1016/j.ijhydene.2022.03.088.
- [106] Monsalve J. Dual-fuel compression ignition: towards clean, highly efficient combustion 2016:1.
- [107] Boronat V. Dual fuel dual mode combustion strategy to achieve high thermal efficiency in compression ignition engines. 2018.
- [108] Lago Sari R. Dual-Mode Dual-Fuel Combustion: Implementation on a Real Medium Duty Engine Platform. 2021.
- [109] Sun C, Liu Y, Qiao X, Ju D, Tang Q, Fang X, et al. Experimental study of effects of exhaust gas recirculation on combustion, performance, and emissions of DME-biodiesel fueled engine. *Energy* 2020;197:117233. doi:10.1016/j.energy.2020.117233.
- [110] Taghavifar H, Nemati A, Walther JH. Combustion and exergy analysis of multi-component diesel-DME-methanol blends in HCCI engine. *Energy* 2019;187:115951. doi:10.1016/j.energy.2019.115951.
- [111] Parravicini M, Barro C, Boulouchos K. Compensation for the differences in LHV of diesel-OME blends by using injector nozzles with different number of holes: Emissions and combustion. *Fuel* 2020;259:116166. doi:10.1016/j.fuel.2019.116166.
- [112] Pélerin D, Gaukel K, Härtl M, Jacob E, Wachtmeister G. Potentials to simplify the engine system using the alternative diesel fuels oxymethylene ether OME1 and OME3–6 on a heavy-duty engine. *Fuel* 2020;259:116231. doi:10.1016/j.fuel.2019.116231.



- [113] Lump B, Rothe D, Pastötter C, Lämmermann R, Jacob E. OXYMETHYLENE ETHERS AS DIESEL FUEL ADDITIVES OF THE FUTURE. *MTZ Worldw* 2011;72:34–8. doi:10.1365/s38313-011-0027-z.
- [114] Macián V, Monsalve-Serrano J, Villalta D, Fogué-Robles Á. Extending the potential of the dual-mode dual-fuel combustion towards the prospective EURO VII emissions limits using gasoline and OMEx. *Energy Convers Manag* 2021;233. doi:10.1016/j.enconman.2021.113927.
- [115] Gill SS, Tsolakis A, Dearn KD, Rodríguez-Fernández J. Combustion characteristics and emissions of Fischer-Tropsch diesel fuels in IC engines. *Prog Energy Combust Sci* 2011;37:503–23. doi:10.1016/j.pecs.2010.09.001.
- [116] Demirbas A. Progress and recent trends in biofuels. *Prog Energy Combust Sci* 2007;33:1–18. doi:10.1016/j.pecs.2006.06.001.
- [117] Dry ME. The Fischer-Tropsch process: 1950-2000. *Catal Today* 2002;71:227–41. doi:10.1016/S0920-5861(01)00453-9.
- [118] Alleman TL, McCormick RL. Fischer-tropsch diesel fuels - Properties and exhaust emissions: A literature review. *SAE Tech Pap* 2003. doi:10.4271/2003-01-0763.
- [119] Tijmensen MJA, Faaij APC, Hamelinck CN, Van Hardeveld MRM. Exploration of the possibilities for production of Fischer Tropsch liquids and power via biomass gasification. *Biomass and Bioenergy* 2002;23:129–52. doi:10.1016/S0961-9534(02)00037-5.
- [120] Elgowainy A, Han J, Zhu H. Updates to Parameters of Hydrogen Production. 2013.
- [121] Huang Y, Zhou L, Pan K. Combustion characteristics of a direct-

- injection diesel engine fueled with Fischer-Tropsch diesel. *Front Energy Power Eng China* 2007;1:239–44. doi:10.1007/s11708-007-0033-7.
- [122] Shi J, Wang T, Zhao Z, Yang T, Zhang Z. Experimental study of injection parameters on the performance of a diesel engine with Fischer–Tropsch fuel synthesized from coal. *Energies* 2018;11. doi:10.3390/en11123280.
- [123] Smith D, Graves R, Ozpineci B, Jones PT, Lustbader J, Kelly K, et al. *Medium-and Heavy-Duty Vehicle Electrification: An Assessment of Technology and Knowledge Gaps* 2019:85.
- [124] Graf F, Lauer S, Hofstetter J, Perugini M. Optimal Thermal Management and Electrification in 48-V Hybrids. *MTZ Worldw* 2018;79:38–43. doi:10.1007/s38313-018-0086-5.
- [125] Kim DM, Benoliel P, Kim DK, Lee TH, Park JW, Hong JP. Framework development of series hybrid powertrain design for heavy-duty vehicle considering driving conditions. *IEEE Trans Veh Technol* 2019;68:6468–80. doi:10.1109/TVT.2019.2914868.
- [126] Shabbir W, Evangelou SA. Threshold-changing control strategy for series hybrid electric vehicles. *Appl Energy* 2019;235:761–75. doi:10.1016/j.apenergy.2018.11.003.
- [127] Orecchini F, Santiangeli A, Zuccari F. Hybrid-electric system truth test: Energy analysis of Toyota Prius IV in real urban drive conditions. *Sustain Energy Technol Assessments* 2020;37:100573. doi:10.1016/j.seta.2019.100573.
- [128] Magazine TB. First New Citaro hybrid buses are ready 2018. <https://truckbusnews.com/first-citaro-hybrid-buses-ready-roads/>.
- [129] ADB - ASIAN DEVELOPMENT BANK. HANDBOOK ON

- BATTERY ENERGY STORAGE SYSTEM. 2018.
- [130] Masiero G, Ogasavara MH, Jussani AC, Risso ML. Electric vehicles in China: BYD strategies and government subsidies. *RAI Rev Adm e Inovação* 2016;13:3–11. doi:10.1016/j.rai.2016.01.001.
- [131] Hannan MA, Hoque MM, Hussain A, Yusof Y, Ker PJ. State-of-the-Art and Energy Management System of Lithium-Ion Batteries in Electric Vehicle Applications: Issues and Recommendations. *IEEE Access* 2018;6:19362–78. doi:10.1109/ACCESS.2018.2817655.
- [132] Sun C, Rajasekhara S, Goodenough JB, Zhou F. Monodisperse porous LiFePO<sub>4</sub> microspheres for a high power Li-ion battery cathode. *J Am Chem Soc* 2011;133:2132–5. doi:10.1021/ja1110464.
- [133] Fujita Y, Hirose Y, Kato Y, Watanabe T. Development of Battery Management System. *Fujitsu Ten Tech J No* 2016;42:68–80.
- [134] Miao Y, Hynan P, Von Jouanne A, Yokochi A. Current li-ion battery technologies in electric vehicles and opportunities for advancements. *Energies* 2019;12:1–20. doi:10.3390/en12061074.
- [135] Su L, Zhang J, Wang C, Zhang Y, Li Z, Song Y, et al. Identifying main factors of capacity fading in lithium ion cells using orthogonal design of experiments. *Appl Energy* 2016;163:201–10. doi:10.1016/j.apenergy.2015.11.014.
- [136] Waag W, Käbitz S, Sauer DU. Experimental investigation of the lithium-ion battery impedance characteristic at various conditions and aging states and its influence on the application. *Appl Energy* 2013;102:885–97. doi:10.1016/j.apenergy.2012.09.030.
- [137] Han X, Ouyang M, Lu L, Li J. A comparative study of commercial lithium ion battery cycle life in electric vehicle: Capacity loss estimation. *J Power Sources* 2014;268:658–69.

- doi:10.1016/j.jpowsour.2014.06.111.
- [138] Lam L, Bauer P, Member S. Practical Capacity Fading Model for Li-Ion Battery Cells in Electric Vehicles. *IEEE Trans Power Electron* 2013;28:5910–8. doi:10.1109/TPEL.2012.2235083.
- [139] Agamloh E, von Jouanne A, Yokochi A. An overview of electric machine trends in modern electric vehicles. *Machines* 2020;8. doi:10.3390/MACHINES8020020.
- [140] Hwang MH, Han JH, Kim DH, Cha HR. Design and Analysis of Rotor Shapes for IPM Motors in EV Power Traction Platforms. *Energies* 2018;11. doi:10.3390/en11102601.
- [141] Yang Z, Shang F, Member S, Brown IP. Comparative Study of Interior Permanent Magnet , Induction , and Switched Reluctance Motor Drives for EV and HEV Applications 2015;1:245–54.
- [142] Lü X, Wu Y, Lian J, Zhang Y, Chen C, Wang P, et al. Energy management of hybrid electric vehicles: A review of energy optimization of fuel cell hybrid power system based on genetic algorithm. *Energy Convers Manag* 2020;205:112474. doi:10.1016/j.enconman.2020.112474.
- [143] Rethinking car software and electronics architecture | McKinsey n.d.
- [144] Tran DD, Vafaeipour M, El Baghdadi M, Barrero R, Van Mierlo J, Hegazy O. Thorough state-of-the-art analysis of electric and hybrid vehicle powertrains: Topologies and integrated energy management strategies. *Renew Sustain Energy Rev* 2020;119:109596. doi:10.1016/j.rser.2019.109596.
- [145] Saiteja P, Ashok B. Critical review on structural architecture, energy control strategies and development process towards optimal energy management in hybrid vehicles. *Renew Sustain Energy Rev*

- 2022;157:112038. doi:10.1016/j.rser.2021.112038.
- [146] Lee K-M, Inaba A. Life Cycle Assessment: Best Practices of International Organization for Standardization (ISO) 14040 Series. *Comm Trade Invest* 2004;99.
- [147] Ellingsen LA-W, Singh B, Strømman AH. The size and range effect: lifecycle greenhouse gas emissions of electric vehicles. *Environ Res Lett* 2016;11:054010. doi:10.1088/1748-9326/11/5/054010.
- [148] Bieker G. A Global Comparison Of The Life-Cycle Greenhouse Gas Emissions Of Combustion Engine And Electric Passenger Cars. *Int Counc Clean Transp* 2021;12. doi:10.3390/wevj12030138.
- [149] Lozanovski A, Dingel O, Semper T, Geß A. Technical Evaluation and Life Cycle Assessment of Long-haul Heavy Duty Vehicles in 2050. *ATZheavy Duty Worldw* 2020;13:56–61. doi:10.1007/s41321-020-0063-1.
- [150] Unterluggauer T, Rich J, Andersen PB, Hashemi S. Electric vehicle charging infrastructure planning for integrated transportation and power distribution networks: A review. *ETransportation* 2022;12:100163. doi:10.1016/j.etrans.2022.100163.
- [151] de Bortoli A. Environmental performance of shared micromobility and personal alternatives using integrated modal LCA. *Transp Res Part D Transp Environ* 2021;93:102743. doi:10.1016/j.trd.2021.102743.
- [152] García A, Monsalve-Serrano J, Lago Sari R, Tripathi S. Pathways to achieve future CO<sub>2</sub> emission reduction targets for bus transit networks. *Energy* 2022;244:123177. doi:10.1016/j.energy.2022.123177.
- [153] Correa G, Muñoz P, Falaguerra T, Rodriguez CR. Performance comparison of conventional, hybrid, hydrogen and electric urban buses using well to wheel analysis. *Energy* 2017;141:537–49.

- doi:10.1016/j.energy.2017.09.066.
- [154] Xiong S, Wang Y, Bai B, Ma X. A hybrid life cycle assessment of the large-scale application of electric vehicles. *Energy* 2021;216:119314. doi:10.1016/j.energy.2020.119314.
- [155] Li M, Zhang X, Li G. A comparative assessment of battery and fuel cell electric vehicles using a well-to-wheel analysis. *Energy* 2016;94:693–704. doi:10.1016/j.energy.2015.11.023.
- [156] Agosti L, Padilla J, Requejo A. El mercado de generación eléctrica en España: estructura, funcionamiento y resultados. *Organ y Competencia En Los Mercados Generación* 2007:17.
- [157] Red Eléctrica de España - REE. El sistema eléctrico español. *Avance* 2021. 2021.
- [158] Koch T, Böhlke T. The averaging bias - A standard miscalculation which extensively underestimates real CO<sub>2</sub>.pdf n.d.
- [159] Burton T, Science C. A Data-Driven Greenhouse Gas Emission Rate Analysis for Vehicle Comparisons n.d.
- [160] Prussi M, Yugo M, De Prada L, Padella M, Edwards R, Lonza L. JEC Well-to-Tank report v5. 2020. doi:10.2760/959137.
- [161] Zang G, Sun P, Elgowainy A, Wang M. Technoeconomic and Life Cycle Analysis of Synthetic Methanol Production from Hydrogen and Industrial Byproduct CO<sub>2</sub>. *Environ Sci Technol* 2021. doi:10.1021/acs.est.0c08237.
- [162] Rolfe A, Huang Y, Hewitt N. Methanol Production from Solid Recovered Fuel and Lignite: Techno-Economic and Environmental Assessment. *Waste and Biomass Valorization* 2022;13:3801–19. doi:10.1007/s12649-022-01757-2.

- [163] Yugo M, Gordillo V, Shafiei E, Megaritis A. A look into the life cycle assessment of passenger cars running on advanced fuels n.d.:2–9.
- [164] Abdou TR, Espinosa DCR, Tenório JAS. Life Cycle Analysis Summary for Automotive Lithium-Ion Battery Production and Recycling. 2016. doi:10.1007/978-3-319-48768-7\_49.
- [165] Chen Q, Lai X, Gu H, Tang X, Gao F, Han X. Investigating carbon footprint and carbon reduction potential using a cradle-to-cradle LCA approach on lithium-ion batteries for electric vehicles in China. *J Clean Prod* 2022;369:133342. doi:10.1016/j.jclepro.2022.133342.
- [166] Mohr M, Peters JF, Baumann M, Weil M. Toward a cell-chemistry specific life cycle assessment of lithium-ion battery recycling processes. *J Ind Ecol* 2020;24:1310–22. doi:10.1111/jiec.13021.
- [167] Sun X, Luo X, Zhang Z, Meng F, Yang J. Life cycle assessment of lithium nickel cobalt manganese oxide (NCM) batteries for electric passenger vehicles. *J Clean Prod* 2020;273:123006. doi:10.1016/j.jclepro.2020.123006.
- [168] Emilsson E, Dahllöf L. Lithium-Ion Vehicle Battery Production. 2019.
- [169] Ciez RE, Whitacre JF. Examining different recycling processes for lithium-ion batteries. *Nat Sustain* 2019;2:148–56. doi:10.1038/s41893-019-0222-5.
- [170] Kelly JC, Dai Q, Wang M. Globally regional life cycle analysis of automotive lithium-ion nickel manganese cobalt batteries. *Mitig Adapt Strateg Glob Chang* 2019:371–96. doi:10.1007/s11027-019-09869-2.
- [171] Kawamoto R, Mochizuki H, Moriguchi Y, Nakano T, Motohashi M, Sakai Y, et al. Estimation of CO<sub>2</sub> Emissions of internal combustion engine vehicle and battery electric vehicle using LCA. *Sustain* 2019;11.

- doi:10.3390/su11092690.
- [172] Maarten Messagie. Life Cycle Analysis of the Climate Impact of Electric Vehicles. *Transp Environ* 2017;14.
- [173] Hao H, Mu Z, Jiang S, Liu Z, Zhao F. GHG Emissions from the production of lithium-ion batteries for electric vehicles in China. *Sustain* 2017;9. doi:10.3390/su9040504.
- [174] Romare M, Dahllöf L. The Life Cycle Energy Consumption and Greenhouse Gas Emissions from Lithium-Ion Batteries A study with focus on Current Technology and batteries for light-duty vehicles. 2017.
- [175] Qiao Q, Zhao F, Liu Z, Jiang S, Hao H. Comparative Study on Life Cycle CO<sub>2</sub> Emissions from the Production of Electric and Conventional Vehicles in China. *Energy Procedia* 2017;105:3584–95. doi:10.1016/j.egypro.2017.03.827.
- [176] Luk JM, Kim HC, De Kleine R, Wallington TJ, MacLean HL. Review of the Fuel Saving, Life Cycle GHG Emission, and Ownership Cost Impacts of Lightweighting Vehicles with Different Powertrains. *Environ Sci Technol* 2017;51:8215–28. doi:10.1021/acs.est.7b00909.
- [177] Xu C, Guo K, Yang F. A Comparative study of Different Hybrid Electric Powertrain Architectures for Heavy-Duty Truck. *IFAC-PapersOnLine* 2018;51:746–53. doi:10.1016/j.ifacol.2018.10.136.
- [178] Samsun RC, Krupp C, Baltzer S, Gnörich B, Peters R, Stolten D. A battery-fuel cell hybrid auxiliary power unit for trucks: Analysis of direct and indirect hybrid configurations. *Energy Convers Manag* 2016;127:312–23. doi:10.1016/j.enconman.2016.09.025.
- [179] Gao Z, LaClair TJ, Smith DE, Daw CS. Exploring fuel-saving potential of long-haul truck hybridization. *Transp Res Rec* 2015;2502:99–107. doi:10.3141/2502-12.



- [180] Banjac T, Trenc F, Katrašnik T. Energy conversion efficiency of hybrid electric heavy-duty vehicles operating according to diverse drive cycles. *Energy Convers Manag* 2009;50:2865–78. doi:10.1016/j.enconman.2009.06.034.
- [181] Waley A, Bucknor N, Sutherland I, Potter M. An Exploratory Assessment of Electrified Propulsion Systems for Full-Size Heavy-Duty Truck Applications. *SAE Tech Pap Ser* 2019;1:1–7. doi:10.4271/2019-01-5002.
- [182] Mojtaba Lajevardi S, Axsen J, Crawford C. Comparing alternative heavy-duty drivetrains based on GHG emissions, ownership and abatement costs: Simulations of freight routes in British Columbia. *Transp Res Part D Transp Environ* 2019;76:19–55. doi:10.1016/j.trd.2019.08.031.
- [183] Volvo. Volvo FE Specifications. 2020.
- [184] United Nations. Addendum 48: Regulation No. 49 , 6. revision 2013:114–5.
- [185] Northrop WF, Bohac S V., Chin JY, Assanis DN. Comparison of filter smoke number and elemental carbon mass from partially premixed low temperature combustion in a direct-injection diesel engine. *J Eng Gas Turbines Power* 2011;133. doi:10.1115/1.4002918.
- [186] Morgan N, Smallbone A, Bhave A, Kraft M, Cracknell R, Kalghatgi G. Mapping surrogate gasoline compositions into RON/MON space. *Combust Flame* 2010;157:1122–31. doi:10.1016/j.combustflame.2010.02.003.
- [187] Ferraro F, Russo C, Schmitz R, Hasse C, Sirignano M. Experimental and numerical study on the effect of oxymethylene ether-3 (OME3) on soot particle formation. *Fuel* 2021;286:119353. doi:10.1016/j.fuel.2020.119353.

- [188] Xu G, Monsalve-Serrano J, Jia M, García A. Computational optimization of the dual-mode dual-fuel concept through genetic algorithm at different engine loads. *Energy Convers Manag* 2020;208:112577. doi:10.1016/j.enconman.2020.112577.
- [189] García A, Monsalve-Serrano J, Martinez-Boggio S, Gaillard P, Poussin O, Amer AA. Dual fuel combustion and hybrid electric powertrains as potential solution to achieve 2025 emissions targets in medium duty trucks sector. *Energy Convers Manag* 2020;224:113320. doi:10.1016/j.enconman.2020.113320.
- [190] Volvo T. VOLVO TRUCK SPECIFICATIONS n.d. <https://www.volvotrucks.com/en-me/trucks/volvo-fl/specifications.html> (accessed July 26, 2020).
- [191] García A, Monsalve-serrano J, Sari RL, Martinez-boggio S. Energy sustainability in the transport sector using synthetic fuels in series hybrid trucks with RCCI dual-fuel engine. *Fuel* 2022;308:122024. doi:10.1016/j.fuel.2021.122024.
- [192] Sampara CS, Bissett EJ, Chmielewski M. Global kinetics for a commercial diesel oxidation catalyst with two exhaust hydrocarbons. *Ind Eng Chem Res* 2008;47:311–22. doi:10.1021/ie070813x.
- [193] Silvis WM. An algorithm for calculating the air/fuel ratio from exhaust emissions. *SAE Tech Pap* 1997. doi:10.4271/970514.
- [194] Mayet C, Welles J, Bouscayrol A, Hofman T, Lemaire-Semail B. Influence of a CVT on the fuel consumption of a parallel medium-duty electric hybrid truck. *Math Comput Simul* 2019;158:120–9. doi:10.1016/j.matcom.2018.07.002.
- [195] Kim D-M, Benoliel P, Kim D-K, Lee TH, Park JW, Hong J-P. Framework Development of Series Hybrid Powertrain Design for Heavy-Duty Vehicle Considering Driving Conditions. *IEEE Trans Veh*

- Technol 2019;68:6468–80. doi:10.1109/tvt.2019.2914868.
- [196] Equipmake. HTM-3500. 2021.
- [197] Burress TA, Coomer CL, Campbell SL, Wereszczak AA, Cunningham JP, Marlino LD, et al. Evaluation of the 2008 Lexus LS 600H Hybrid Synergy Drive System 2008 Lexus Ls 600H Hybrid Synergy. 2009. doi:10.2172/951290.
- [198] Equipmake. HTM 3500 n.d. <https://equipmake.co.uk/products/htm-3500/>.
- [199] Grunditz EA, Thiringer T. Modelling and scaling procedure of a vehicle electric drive system. Chalmers Publ Libr 2017.
- [200] Zhang L, Peng H, Ning Z, Mu Z, Sun C. Comparative research on RC equivalent circuit models for lithium-ion batteries of electric vehicles. Appl Sci 2017;7. doi:10.3390/app7101002.
- [201] Gao Y, Zhu C, Zhang X, Guo B. Implementation and evaluation of a practical electrochemical- thermal model of lithium-ion batteries for EV battery management system. Energy 2021;221:119688. doi:10.1016/j.energy.2020.119688.
- [202] Madani SS, Schaltz E, Kær SK. An electrical equivalent circuit model of a lithium titanate oxide battery. Batteries 2019;5. doi:10.3390/batteries5010031.
- [203] Gregory L. Plett. Battery Management Systems, Volume 1. In: Plett GL, editor. vol. I. Artech Hou, Artech House; 2015, p. 346.
- [204] Plett GL, editor. Battery Management Systems, Volume II: Equivalent-Circuit Methods. Artech Hou. Artech House; 2015.
- [205] Løbberding H, Wessel S, Offermanns C, Kehrer M, Rother J, Heimes H, et al. From cell to battery system in BEVs: Analysis of system

- packing efficiency and cell types. *World Electr Veh J* 2020;11:1–15. doi:10.3390/wevj11040077.
- [206] LithiumWerks. 26650 Lithium Ion Power Cell 2019.
- [207] Shin Chorong. LG Chem INR18650HG2 3 Ah 2015.
- [208] Fischer H-M, Dorn L. Voltage Classes for Electric Mobility. *Ger Electr Electron Manuf Assoc* 2013:44.
- [209] Rizzoni G. Modelling and control of a brake system for an extended range electric vehicle equipped with axle motors Kerem Bayar \*, Ricardo Biasini , Simona Onori 2012;58:399–426.
- [210] NATIONS U. Uniform provisions concerning the approval of vehicles of categories M, N and O with regard to braking. 2014.
- [211] Nordelöf A, Romare M, Tivander J. Life cycle assessment of city buses powered by electricity, hydrogenated vegetable oil or diesel. *Transp Res Part D Transp Environ* 2019;75:211–22. doi:10.1016/j.trd.2019.08.019.
- [212] Dong Y, Zhao Y, Hossain MU, He Y, Liu P. Life cycle assessment of vehicle tires: A systematic review. *Clean Environ Syst* 2021;2:100033. doi:10.1016/j.cesys.2021.100033.
- [213] Laboratory AN. GREET® Model. 2021 n.d. <https://greet.es.anl.gov/> (accessed May 24, 2021).
- [214] García A, Monsalve-Serrano J, Martinez-Boggio S, Zhao W, Qian Y. Intelligent charge compression ignition combustion for range extender medium duty applications. *Renew Energy* 2022;187:671–87. doi:10.1016/j.renene.2022.01.110.
- [215] García A, Monsalve-serrano J, Martinez-boggio S, Soria R. Carbon footprint of battery electric instantaneous electricity mix in Spain n.d.

- [216] Transport & Environment. How clean are electric cars? 2020:1–33.
- [217] Dumont O, Parthoens A, Dickes R, Lemort V. Experimental investigation and optimal performance assessment of four volumetric expanders (scroll, screw, piston and roots) tested in a small-scale organic Rankine cycle system. *Energy* 2018;165:1119–27. doi:10.1016/j.energy.2018.06.182.
- [218] Pasini G, Lutzemberger G, Frigo S, Marelli S, Ceraolo M, Gentili R, et al. Evaluation of an electric turbo compound system for SI engines: A numerical approach. *Appl Energy* 2016;162:527–40. doi:10.1016/j.apenergy.2015.10.143.
- [219] Della Torre A, Montenegro G, Onorati A, Cerri T. CFD Investigation of the Impact of Electrical Heating on the Light-off of a Diesel Oxidation Catalyst. *SAE Tech Pap* 2018;2018-April:1–14. doi:10.4271/2018-01-0961.
- [220] Mianzarasvand F, Shirneshan A, Afrand M. Effect of electrically heated catalytic converter on emission characteristic of a motorcycle engine in cold-start conditions: CFD simulation and kinetic study. *Appl Therm Eng* 2017;127:453–64. doi:10.1016/j.applthermaleng.2017.07.180.
- [221] Deb K, Jain H. An evolutionary many-objective optimization algorithm using reference-point-based nondominated sorting approach, Part I: Solving problems with box constraints. *IEEE Trans Evol Comput* 2014;18:577–601. doi:10.1109/TEVC.2013.2281535.
- [222] Group V. Volvo FL Electric. 2022 n.d. <https://www.volvotrucks.com/en-en/trucks/trucks/volvo-fl/volvo-fl-electric.html> (accessed June 1, 2022).
- [223] Uicker JJ, Pennock GR, Shigley JE, McCarthy JM. Theory of Machines and Mechanisms. *J Mech Des* 2003;125:650–650.

- doi:10.1115/1.1605769.
- [224] Poussin O, Gaillard P, Antonio G, Monsalve-Serrano J, Fogué Robles Á. Synthetic Fuels and Dual-Fuel RCCI: A Pathway Towards Carbon Neutrality in the Road Transport Sector. 11th Aachen Colloq China Sustain Mobil 2021.
- [225] Paffumi E, De Gennaro M, Martini G, Gennaro M De, Martini G. Alternative utility factor versus the SAE J2841 standard method for PHEV and BEV applications. *Transp Policy* 2018;68:80–97. doi:10.1016/j.tranpol.2018.02.014.
- [226] Utility Factor Definitions for Plug-In Hybrid Electric Vehicles Using 2001 U.S. DOT National Household Travel Survey Data 2009. doi:[https://doi.org/10.4271/J2841\\_200903](https://doi.org/10.4271/J2841_200903).
- [227] Little AD. The Future of Hydrogen. *Futur Hydrog* 2020:1–4. doi:10.1787/1e0514c4-en.
- [228] Ueckerdt F, Bauer C, Dirnaichner A, Everall J, Sacchi R, Luderer G. Potential and risks of hydrogen-based e-fuels in climate change mitigation. *Nat Clim Chang* 2021;11:384–93. doi:10.1038/s41558-021-01032-7.